ARTICLE IN PRESS Available online http://jopr.mpob.gov.my/category/article-in-press/

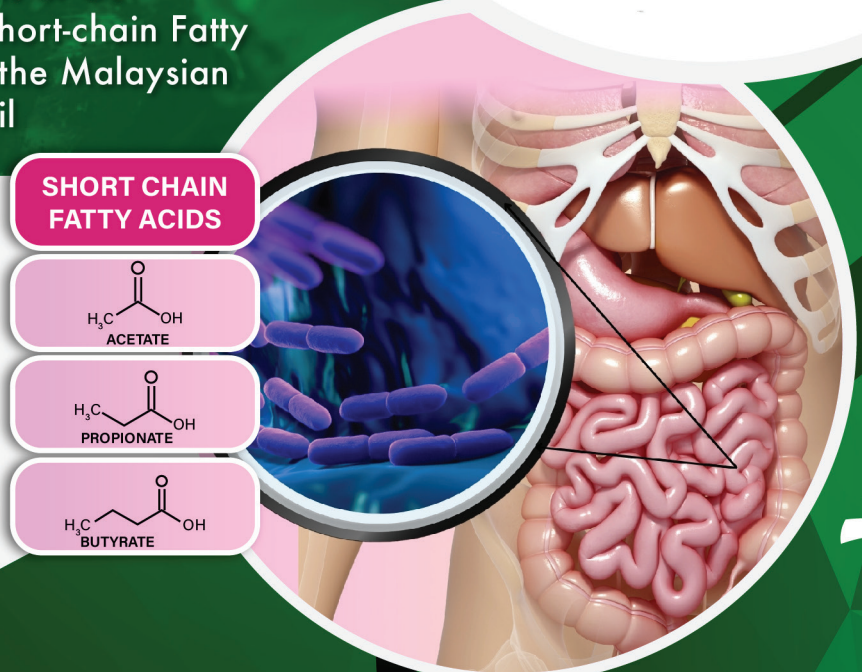
Journal of Oil Palm Research

Vol. 36 (4) • December 2024



REVIEW ARTICLES

- Patent Landscape Review on Modern Oil Palm Climatic Adaptation Strategies: Gaps and Opportunities
- Diets and Health Benefits of Gut Microbiota-fermented Short-chain Fatty Acids: A Perspective of the Malaysian Diet Containing Palm Oil



eISSN 2811-4701

MPOB

JOURNAL OF OIL PALM RESEARCH (formerly known as ELAEIS)

JOURNAL OF OIL PALM RESEARCH (JOPR), an international refereed journal, carries full-length original research papers, short communications and scientific review papers on various aspects of oil palm and palm oil and other palms. JOPR is published four times per year, *i.e.* March, June, September and December.

© Malaysian Palm Oil Board (MPOB), 2024

All rights reserved. No part of this publication may be reproduced in any form or by any means without the written permission of MPOB.

Impact Factor:
1.2
data from *2023 Journal Citation Report*® Science Edition
– A Clarivate Analytics product.

For more information on advertisement for the JOPR, please write to:

Editor-in-Chief
Journal of Oil Palm Research
Malaysian Palm Oil Board
6, Persiaran Institusi, Bandar Baru Bangi
43000 Kajang, Selangor, Malaysia

Tel: *+603-8769 4400*
E-mail: *jopr.admin@mpob.gov.my*
Website: *jopr.mpob.gov.my*

DISCLAIMER
Views of writers expressed in this publication are not necessarily endorsed by or represent the views of MPOB.

MPOB Press
Malaysian Palm Oil Board
6, Persiaran Institusi, Bandar Baru Bangi
43000 Kajang, Selangor, Malaysia
Tel: +603-8769 4400 | Fax: +603-8925 9446
E-mail: *jopr.admin@mpob.gov.my*

JOURNAL OF OIL PALM RESEARCH

Vol. 36 (4) December 2024

CONTENTS

REVIEW ARTICLES

547 Patent Landscape Review on Modern Oil Palm Climatic Adaptation Strategies: Gaps and Opportunities
Yeong Sheng Tey and Mark Brindal

560 Diets and Health Benefits of Gut Microbiota-fermented Short-chain Fatty Acids: A Perspective of the Malaysian Diet Containing Palm Oil
Sia-Yen, Yap; Phooi-Tee, Voon and Selvaduray, Kanga Rani

RESEARCH ARTICLES

586 Biology and Behaviour of *Elaeidobius kamerunicus* Faust, 1898 (Coleoptera: Curculionidae) in Two Oil Palm Cultivars in Colombia
Carlos Andrés Sendoya-Corrales; Norman Fabian Urrego-Morales; Jesús David Castaño-Martinez; Alex Enrique Bustillo and Anuar Morales Rodríguez

598 Nitrogen Uptake Model of Oil Palm in Main Nursery
Adinda N H Manurung; Suwarto; Sudirman Yahya and Budi Nugroho

608 Fish Assemblages in Artificial Drainage Systems Across Oil Palm Plantation Development Phases on Peatland in Sarawak
Angie Sapis; Bettycopa Amit; Nik Sasha Khatrina Khairuddin and Idris Abu Seman

618 Oil Palm Level of Ripeness Classification Using EfficientDet-Lite CNN Architecture
Yosua Alvin Adi Soetrisno; Eko Handoyo; Sumardi and Enda Wista Sinuraya

630 Nutritive Screening and Forage Yield of Guinea and Hybrid Napier Grass Varieties Under Dense Shade of Mature Oil Palm Plantation
Ramachandrudu Kummari; Narasimha Rao Bezawada and Manorama Kamireddy

640 Evaluation of Different Rates and Types of Moroccan Phosphate Rocks on Oil Palm Seedlings
Norakmal Khairuanuar; Tan Ngai Paing; Mohamed Hanafi Musa and Adibah Mohd Amin

650 Palm Kernel Meal Activated Carbon via Glass Wool-pyrolysis Method for Ceftriaxone Adsorption
Achmad Gus Fahmi; Zaenal Abidin; Cecep Kusmana and Erliza Noor

664 Bacterial Cellulose Production from Oil Palm Frond Juice and Its Impregnation with Silver Nanoparticles for Antibacterial Wound Dressing
Tan Sou Min; Nor Syahirah Abd Karim; Shahril Mohamad; Junaidi Zakaria; Mohd Hafiz Arzmi; Hassan Fahmi Ismail and Rohana Abu

674 Structural Alteration of Oil Palm Empty Fruit Bunch by Peracetic Acid Combined with Ultrasonic Pretreatment for Xylanase Production by *Neosartorya* sp.
Rama Mohan Poludasu; Benjamas Cheirsilp and Piyarat Boonsawang

687 Composite of ZnO/SBE as Catalyst Materials for Photodegradation of Rhodamine-B
Diah Susanti; Shafira Marellia; Azzah Dyah Pramata; I D A A Warmadewanthi; Ervin Nurhayati; Haniffudin Nurdiansah and Jhy-Chern Liu

708 Determination of Triacylglycerol Composition and Its Content in Refined and Fractionated Palm Oil by Using LC-MS/MS with Multiple Neutral Loss Scan
Seongeung Lee; Seungchul Baek; Siyoung Yang and Gyeonghweon Lee

718 *In Vitro* Evaluation of Melanogenesis Inhibition by Tocotrienol Rich Fraction
Nur Anis Albakry; Yusrabbil Amiyati Yusof and Zafarizal Aldrin Azizul Hasan

728 Development of Solid Fat Content-based Predictive Model for Margarine Formula Design
Jiajia Gong; Nanxi Shu; Xian Sun; Xinyu Cao; Yuanfa Liu and Yong-Jiang Xu

Cover picture:

1. Patent landscape review on modern oil palm climatic adaptation strategies: Gaps and opportunities.
2. Diets and health benefits of gut microbiota-fermented short-chain fatty acids: A perspective of the Malaysian diet containing palm oil.

EDITORIAL BOARD

(1 January 2024 – 31 December 2025)

Datuk Dr. Ahmad Parveez Ghulam Kadir
Malaysia (Editor-in-Chief)

Dr. Carl Traeholt
Malaysia

Prof. Dr. Matthias Finkbenier
Germany

Prof. Dr. Dirk Prufer
Germany

Prof. Dr. Douglas G Hayes
USA

Prof. Dr. Tan Chin Ping
Malaysia

Prof. Dr. Takashi Hirano
Japan

Dr. Ahmad Aldrie Amir
Malaysia

Prof. Jonathan Wong Woon Chung
Hong Kong

Dr. Tristan Durand Gasselin
France

Prof. Fikret Isik
USA

Prof. Dr. Jan Stenlid
Sweden

PUBLICATION COMMITTEE

CHAIRPERSON
Datuk Dr. Ahmad Parveez Ghulam Kadir

SECRETARY
Dr. Anita Taib

MANAGING EDITOR
Ts. Dr. Gan Sin Yee

PRODUCTION EDITOR
Dr. Laziana Ahmad

COMMITTEE MEMBERS
Dr. Zainab Idris
Dr. Ramle Moslim
Dr. Sivaruby Kanagaratnam
Dr. Astimar Abdul Aziz
Dr. Rajinder Singh
Dr. Meilina Ong Abdullah
Dr. Aki @ Zaki Aman
Dr. Zafarizal Aldrin Azizul Hasan
Ruba'ah Masri
Johari Minal
Mohd Saufi Awang
Iptisam Abdul Wahab

REVIEW ARTICLES

Journal of Oil Palm Research Vol. 36 (4) December 2024 p. 547-559
DOI: https://doi.org/10.21894/jopr.2024.0011

PATENT LANDSCAPE REVIEW ON MODERN OIL PALM CLIMATIC ADAPTATION STRATEGIES: GAPS AND OPPORTUNITIES

YEONG SHENG TEY[1]* and MARK BRINDAL[2]

ABSTRACT

Climate change is evolving at both a speed and magnitude that necessitates oil palm adaptation through innovation. This study both tracks and synthesises climate change adaptation patents applicable to oil palm cultivation. Oil palm patent applications filed between 1960 and 2022 were analysed through a network analysis, and compared to patents applied for soybean, rapeseed, and sunflower sectors. Findings indicate that the existing pool of oilseed adaptation patents is small. Oil palm adaptation patents primarily focus on and are concentrated on novel process innovation in plant breeding and biomass recycling techniques. Soybean patents cover both modern plant breeding technologies and plant varieties. By comparison, patent references to oil palm adaptation patents are fewer in number. These findings reveal a mismatch between oil palm adaptation requirements and technological availability knowledge. The oil palm research and development community are encouraged to better secure and disseminate intellectual property (IP) rights in order to inform adaptation diffusion and planning.

Keywords: adaptation strategy, climate change, intellectual property, oil palm, technology.

Received: 15 May 2023**; Accepted:** 19 November 2023**; Published online:** 31 January 2024.

INTRODUCTION

Adaptation innovation is critical in reducing the long-term threat of climate change in so far as it threatens oil palm's productivity advantage. The global average temperature is expected to rise by 1.5°C between 2030 and 2052 (IPCC, 2018), and the chance of occurrence is increasing over time (WMO, 2023). In such climatology, plantings of less adaptable oil palm cultivars experience increased mortality rates (Paterson, 2020). Climate change has also been linked to an increase in the occurrence of *Ganoderma boninense* fungus, causing basal stem rot disease (Abubakar *et al.*, 2022). Even when failing to account for extreme climatic shocks, 1.0°C localised warming could cause as much as 10% drop in oil palm yield (Sarkar *et al.*, 2020). The compounding of such climate-related factors could reduce oil palm productivity significantly.

National and international policies that prohibit deforestation also necessitate adaptation technology for increasing oil palm production without expanding into forest areas. Under Presidential Instruction No. 5 of 2019, issuing new licenses to clear primary forests and peatlands in Indonesia has been permanently halted (Cabinet Secretariat of the Republic of Indonesia, 2019). The Malaysian Sustainable Palm Oil Certification Scheme (MSPO), which all oil palm growers are required to comply, forbids the inclusion of oil palm land converted from forest after 31 December 2019. Furthermore, the Deforestation-Free Regulation of the European Union prohibits the importation of palm oil products derived from forest land cleared after 31 December 2020. Productive adaptation technology is desirable under the deforestation-free supply chain regime to enable greater production from existing lands, thus reducing the demand for new oil palm plantations.

Using global patent data, this study tracks innovations that can help oil palm and three

[1] Institute of Tropical Agriculture and Food Security, Universiti Putra Malaysia, 43400 UPM Serdang, Selangor, Malaysia.

[2] School of Agriculture, Food and Wine, The University of Adelaide, Urrbrae SA 5064, Australia.

* *Corresponding author e-mail: tyeong.sheng@gmail.com*

other major oilseeds adapt to climate change. This comparison is motivated by the expectation that temperatures will rise above the oilseed threshold, threatening yield stability (Ahmad *et al.*, 2021). Oil palm yield losses will be more severe than in other major oilseeds (Makowski *et al.*, 2020). Moreover, the global vegetable oil and fat market is highly competitive, with soybean, rapeseed and sunflower oils competing with the cost per hectare of oil palm production (Zimmer, 2016). Technological advancements (*e.g.*, in farm mechanisation) is one common initiative that has been undertaken to improve the efficiency of annual oilseeds and to address their adaptation to climate change. Adaptation strategies for oil palm cultivation, in comparison, have primarily relied on conventional agricultural practices (Abubakar *et al.*, 2021). General awareness concerning available oil palm adaptation technologies appears to be lacking. This study attempts to fill that knowledge gap.

This study adds to the body of knowledge in three ways. This is the first study to consider modern adaptation strategies for oil palm. Prior efforts have focused on common agricultural practices that can assist climate-resilient agricultural practices. Secondly, this study identifies technological hotspots in climate change adaptation. Climate policy could be modified to accelerate or to take advantage of their emergence. Thirdly, and most importantly, this research identifies the technological gaps that exist between oil palm and other oilseeds. This has important implications for the oil palm research and development (R&D). Closing the R&D gap is an important step toward achieving climate-resilient, competitive oil palm production.

Patent systems raise technology awareness in the context of climate change (Behles, 2009). When required or desirable technology becomes objectively available and widely disseminated, technology diffusion becomes most efficient and useful. It should serve to at least discourage "techno-optimism", the belief that technology will become more widely available to address climate change (McLaren and Markusson, 2020). Efficient diffusion should also aim to prevent postponement of R&D and adaptation investment, which frequently occur under the assumption that the longer the wait, the better (or cheaper) the technology. This study thus informs adaptation diffusion by revealing the present state of technologies for oil palm adaption.

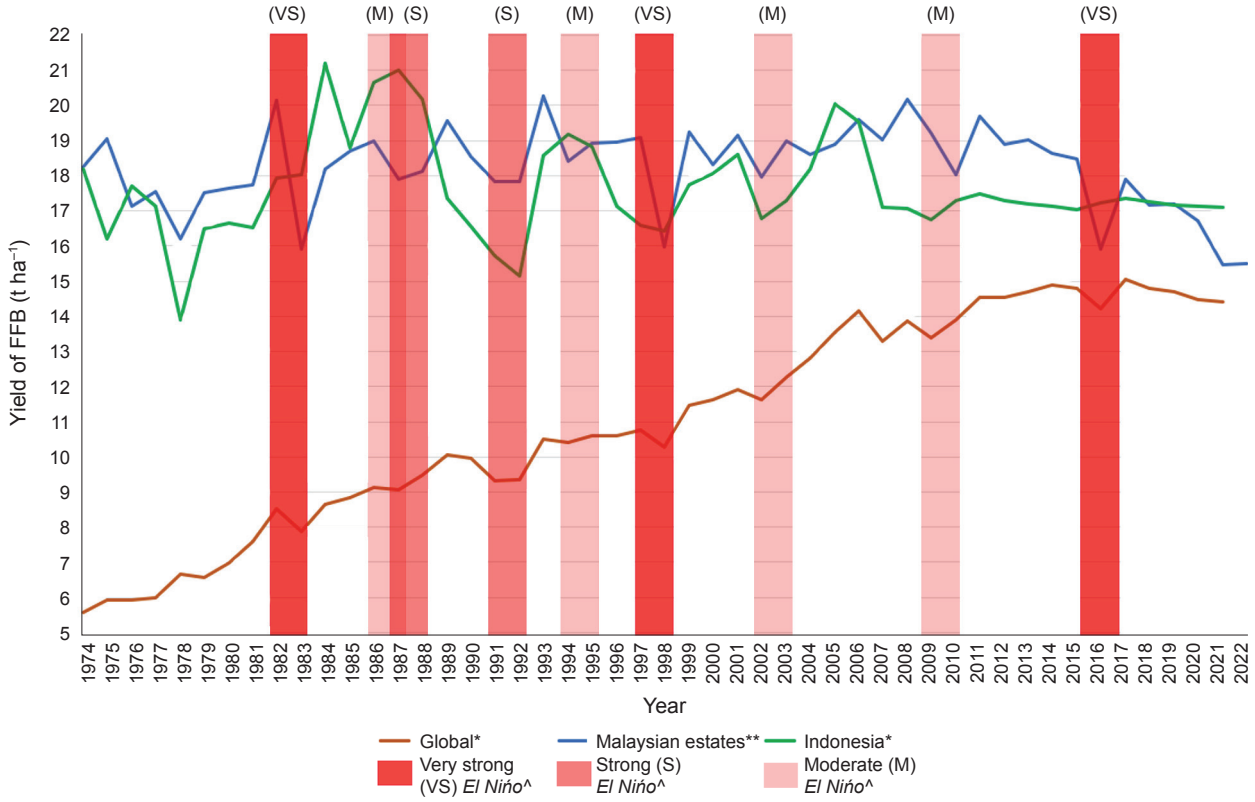
LITERATURE REVIEW

Extreme climate events have an impact on oil palm productivity. Oil palm, like other oilseed crops, is susceptible to heat stress (Ahmad *et al.*, 2021). *Figure 1* depicts the series of yield declines that correspond with various *El Niño* events for Indonesia, Malaysia and the wider world. *El Niño* weather events are associated with increased temperatures and decreased rainfall, resulting in a high level of heat and water stress (Meehl *et al.*, 2000). Most moderate *El Niño* events resulted in a decrease in oil palm yield when compared to the previous year. Strong and very strong *El Niño* events resulted in steeper declines. In addition to hot and dry weather events, higher than normal rainfall occurred during *La Niña* events in other years (Li *et al.*, 2022).

Despite these erratic global patterns, global oil palm productivity continued to rise. However, the major producing countries, Indonesia and Malaysia, demonstrated a contra trend. Their oil palm productivity has declined to levels last seen in the 1970s. Adaptation must be prioritised to ensure great resilience to both water scarcity and excess for oil palms.

Conservation of soil and water assists oil palm trees in their economic lifecycle to achieve productivity. They are carried out to aid in water infiltration and retention during prolonged droughts and soil aeration during high-intensity rainfall. Plantation tillage is preferred for oil palm (re)planting over intensive tillage, which depletes soil organic matter through aerobic mineralisation (Suresh, 2013). Oil palm trunks are logged and left to decompose during the replanting stage to improve soil fertility through carbon and mineral recycling (Uke *et al.*, 2021). Intercropping leguminous cover crops (LCC) during plantation establishment reduces soil erosion and increases nitrogen availability until the canopy of the trees reaches full shade (Agamuthu and Broughton, 1985). Mulch utilising empty fruit bunches and pruned fronds improves soil structure and fertility as well as water retention capacity (Rudolf *et al.*, 2021). The use of treated palm oil mill effluent as an organic fertiliser can produce positive results due to improvements in soil moisture regime and soil structure, as well as nutrient addition and a reduction in soil and nutrient erosion (Amelia *et al.*, 2017). Silt pits collect runoff and return nutrients into the soil (Moradi *et al.*, 2012).

There are some tradeoffs when using natural soil and water conservation measures. Some expense is incurred when purchasing and establishing LCC (Lemessa and Wakjira, 2015). However, such soft grasses are preferred by cattle that graze within young plantations when livestock integration is used as a climate change adaptation approach (Grinnell *et al.*, 2022). Due to logistical constraints, biomass-based soil nutrient recovery is usually limited to (sub)plantations near the source of availability rather than plantation-wide application (Comte *et al.*, 2013). When the carbon to nitrogen ratio is too high, improper management can turn solid biomass into a pest breeding ground (Pulingam *et al.*, 2022). Furthermore, biomass is increasing in commercial value. Empty fruit bunches, for example, are now



Note: Underestimation of oil palm yields is prevented because harvested area is the denominator. **Malaysian estates refer to private and government/state agency estates, including those with organised smallholders with area of 100 acres and above. Estates are generally more productive than smallholding farms. ^*El Niño* weather events are defined as five consecutive overlapping three-month periods with temperatures at or above the +0.5°C anomaly. *La Niña* weather events are not depicted.

Source: Authors' illustration: * - FAO (2023); ** - MPOB (2021, 2022, 2023); ^ - Golden Gate Weather Services (2023) data.

Figure 1. Oil palm yields declined in the face of El Niño *events.*

sold to produce a variety of energy, chemical and material goods (Rubinsin *et al.*, 2020). Biomass will become scarcer for *in situ* resource recycling, which will also require time to attain the desired results.

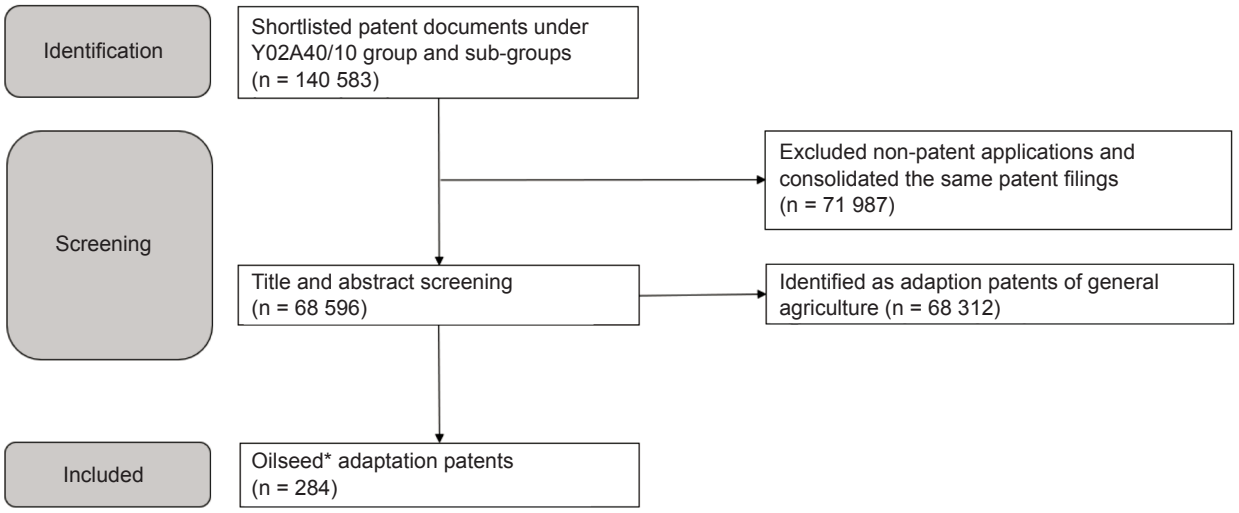
Given these considerations, external inputs for scaling climate change adaptation are required, and this begins with knowing their availability. Thus far, seed technology has received the most attention. Cultivar selection and plant breeding for abiotic and biotic stress tolerance, such as drought, flooding, soil salination, pest and disease resistance, has begun (Suresh, 2013). Understanding the responses of climate-resilient oil palm to a wide range of climate-triggered soil and nutrition uptake conditions is ongoing (Rival, 2017). Through patent analysis, Wang and Coleman (2016) discovered novel varieties suited for growing oil palm in subtropical regions, but not for assisting existing oil palm producing areas to adapt to the changing climate. Little is also known about technologies that could help oil palm become more productive under variable climatic conditions. This study thus, identifies oil palm adaptation patents, where the applications represent the early success of innovations, to inform adaptation planning.

METHODOLOGY

Data

This study's patent data was obtained from the Espacenet database. *Figure 2* illustrates the data acquisition process. Developed by the European Patent Office, it is the most comprehensive open data source (Li *et al.*, 2013), providing the most robust patent information (Jürgens and Herrero-Solana, 2015). The European Patent Office recently launched an algorithm-based classification scheme that has expanded from climate change mitigation to adaptation technologies (Angelucci *et al.*, 2018).

This study used the Cooperative Patent Classification (CPC) system to shortlist patent documents that fall under the 'technologies for adaptation to climate change in agriculture' (Y02A40/10) group and its various sub-groups. The period between 1960 and 2022 was analysed. The shortlisting process produced 140 583 patents of various document types. Only patent applications were considered since they provide the most up-to-date information on innovation. Other documents were excluded. To avoid double



Note: * - Includes oil palm, soybean, rapeseed and sunflower.

Figure 2. Data acquisition process of the study.

counting, applications for the same patent filed in different countries were consolidated. Finally, for the patent analysis, this study considered only patent applications that provided all necessary information in title and abstract.

As a result, this study's dataset contains 68 596 patent applications. These patent documents were classified as general agriculture, as well those pertaining to the four major oilseeds, *viz.* oil palm, soybeans, rapeseed and sunflower.

Patent sub-group classifications, which linked patents to technological characteristics, were extracted from the dataset. When compared to the methodology which uses unsupervised keywords in patent documents, patent classification validated on a regular basis in the Espacenet is considered relatively reliable. It has a standard error rate of less than 7% (Angelucci *et al.*, 2018).

Empirical Methods

The empirical approach of this study involves three stages. In the first stage, the trajectories of climate change adaptation patents for oil palm, soybean, rapeseed and sunflower were compared with those utilised in general agriculture. A more detailed analysis distinguished the relative growth trends in the four major oilseed sectors.

In the second stage, using disaggregation, the agglomerative hierarchical clustering method was used to analyse patent classifications for identifying structures in oilseed patent networks. It merged the most similar oilseed clusters.

A series of *n-1* clustering decisions is used to combine nodes into a hierarchical structure. Each node (patent sub-group classification) begins as a single cluster, and similar nodes are subsequently merged into a new cluster. This clustering process is repeated until only a single cluster remains. As such, any member of a cluster can trace its membership back to its origin. The visual result is a dendrogram, which becomes increasingly unwieldy with larger applications (Hair *et al.*, 2013). In other words, the agglomerative hierarchical clustering method has plausible validity with a small dataset (Marešová *et al.*, 2022).

In this study, cluster similarity was determined by the greatest distance between two nodes using the complete-linkage clustering algorithm. All nodes in a cluster were connected to each other at maximum distances through the following Equation (1):

$$D(r, s) = \text{Max} \{ d(i, j) \} \quad (1)$$

where object i is in cluster r and object j is cluster s.

The distance between every possible object pair (i,j) was computed, where object i is in cluster r and object j is in cluster s and the maximum value of these distances is said to be the distance between clusters r and s. The value of the longest link between two clusters represents the distance between them. At each stage of hierarchical clustering, the clusters r and s with the highest $D(r, s)$ were merged.

The complete-linkage clustering algorithm generates the most compact clustering solutions by joining the maximum distance of dissimilar clusters (Baeza-Yates, 1992). It is also appropriate for a variety of clustering applications (Jain and Dubes, 1988).

The number of clusters most representative of the data structure was determined in this study using an agglomeration coefficient. An agglomerative coefficient measures the dissimilarity of an object to the first cluster it joins, divided by the dissimilarity of the final merger in the cluster analysis, averaged across all samples. Small (or large) coefficients

indicate that homogeneous (or different) clusters are being merged. When the agglomeration coefficient changes significantly, the prior cluster solution is chosen. This type of rule has been shown to make reasonably accurate decisions about the number of clusters (Milligan and Cooper, 1985).

Finally, patent citations were examined to ascertain any knowledge transfer from earlier to subsequent patents. A forward citation references a subsequent patent. As a result, forward citations ascribe the technological foundation of patented inventions (Jaffe and De Rassenfosse, 2019) and the technological impact of patents (Pianta and Sirilli, 1996). The F-value was measured as Equation (2) with the null hypothesis that variance in forward patent citations is equal among oilseed crops.

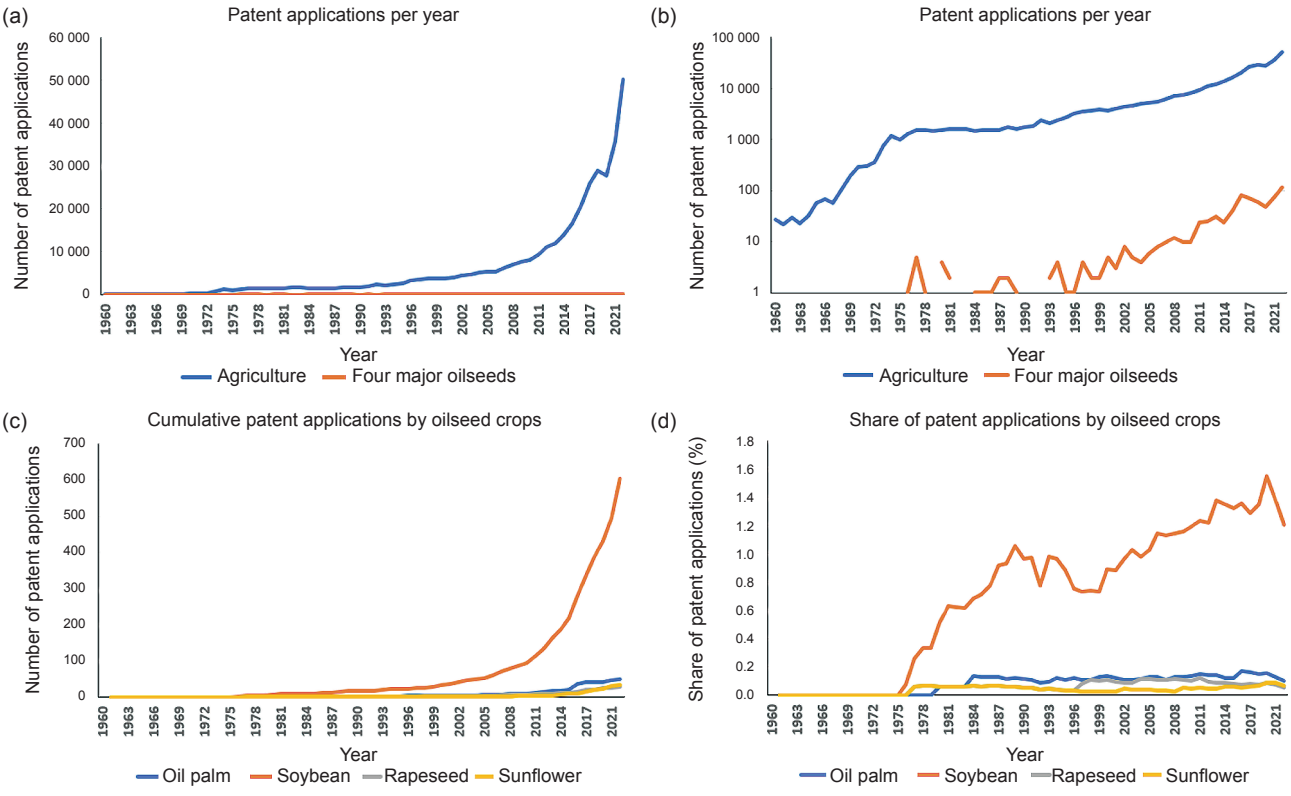
$$F\text{-}value = \frac{between\text{-}groups\ variance}{within\text{-}group\ variance} \quad (2)$$

RESULTS

The dataset was aggregated for agricultural adaptation technologies and then disaggregated into oilseeds for exploratory purposes. Agricultural patents for climate change adaptation have increased exponentially since 1960 (*Figure 3a*). Given the small number of oilseed patents, the number of patent applications was plotted on a log scale to show the rate of change. It was established that oilseed innovation in the same technological class had emerged spasmodically since the mid-1970s (*Figure 3b*). Twenty years later such innovation had evolved into a steady growth pattern. Oilseed patents grew at a faster rate than agricultural patents due to their lower starting point. This does not, however, imply that the proportion of oilseed patents within the agricultural adaptation patent pool has risen exponentially.

The disaggregated dataset contained 284 oilseed adaptation patents, with 31 oil palm patents, 14 sunflower patents, 214 soybean patents and 25 rapeseed patents. Soybean technologies have accounted for three-quarters of all oilseed inventions in patent applications since 1960 (*Figure 3c*). The other three oilseeds have significantly fewer adaptation patents in absolute terms. Similarly, soybean adaptation technology patents maintained a higher overall proportion throughout the study period (*Figure 3d*). Its annual share increased, while the other oilseed patent applications fluctuated around a much lower base.

Because of the small number of oilseed patents discovered, prior to further analysis, a validation process was carried out by referring to previous patent analyses of oilseed crops. Miao and Guo (2015) investigated patents for genetically modified (GM) soybeans, while Wang and Coleman (2016) researched palm oil production and waste treatment patents. These previous studies made no mention of climate (including climate adaptation) patents. This is still the case in Ji *et al.* (2019), who investigated soybean or rapeseed patents, and Wibowo *et al.*



Figures 3. Aggregated and disaggregated patents in the dataset.

(2019), who investigated palm oil patents. It is most likely that this has occurred due to the relative insignificance of oilseed adaptation technology in the patent pools used in those studies. As a result, this study's limited dataset was deemed valid, necessitating the employment of the agglomerative hierarchical clustering technique.

Clusters of Oilseed Adaptation Patents

The clustering analysis in this study considered sub-group classifications found in at least 10% of the observations (patents) for an oilseed. The minimum criterion used to identify eligible sub-group classifications for the analysis was three for oil palm patents, two for sunflower patents, 21 for soybean patents and three for rapeseed patents. The qualified sub-group classifications are summarised in *Table 1*.

Figure 4 show the results of the complete-linkage clustering method. The horizontal axes represent the distance between each cluster. The vertical dashed lines denote the agglomerative criterion for selecting the number of clusters. For oilseed patents, two clusters were identified. Each with an optimal number of sub-group classifications ranged from 2 to 9. Sub-group classifications that merge sooner are more alike than those that merge later.

A cluster of enabling technologies for improved plant breeding emerged among climate change adaptation patents in both the oil palm and soybean industries. In the case of oil palm (*Figure 4a*), the cluster is led by patents underlying the 'mutation or genetic engineering; deoxyribonucleic acid (DNA) or ribonucleic acid (RNA) concerning genetic engineering, vectors, with agronomic (input) traits' (C12N15/8261), the 'peptides having more than 20 amino acids; gastrins; somatostatins; melanotropins; derivatives thereof from plants' (C07K14/415), and the 'oligonucleotides characterised by their use for polymorphic or mutational markers' (C12Q2600/156) sub-groups. The focus of these patents is to use nucleic acid sequencing to predict and control (shell and membrane) phenotypes in oil palm. They aim to improve plant breeding by incorporating desirable agronomic traits.

In terms of soybean (*Figure 4b*), the enabling technologies cluster is characterised by patents classified for the 'measuring or testing processes involving enzymes, nucleic acids or microorganisms; compositions therefore; processes of preparing such compositions for plants, fungi or algae' (C12Q1/6895), the 'angiosperms, seeds' (A01H5/04), 'angiosperms, glycine max (soybean)' (A01H6/542), and the 'oligonucleotides characterised by their use for plant traits' (C12Q2600/13) sub-groups. Many of these patents describe a transgenic soybean with an event that expresses the DNA molecules produced by transgenic DNA insertion into a soybean plant's genome. They also developed techniques for detecting these transgenic events. Methods which enhance gene composition and selection for soybean were also improved. They aim to strengthen resistance to plant parasitic (*i.e.*, root knot and cyst) nematodes and insects (*i.e.*, aphid). Innovations were also developed to improve drought and herbicide tolerance in soybean.

Further, another soybean cluster (*Figure 4b*) shows that soybean climate change adaptation technology fundamentally centres on improving varieties with agronomic (input) traits. Many of these patents were primarily obtained because of 'genetic modifications' (Y02A40/146). Plant breeding through 'mutation or genetic engineering; DNA or RNA concerning genetic engineering, vectors, with agronomic (input) traits for insect' (C12N15/8286), 'herbicide' (C12N15/8274), and 'nematode resistance' (C12N15/8285) has remained a major goal for soybean crop improvement. Some new soybean varieties have been patented for their "overall" benefits rather than for any specific trait. These traits include improved oil composition and "healthier" properties.

Besides such plant breeding innovation, a cluster of biofertiliser processing technologies predominated among both oil palm and rapeseed climate change adaptation patents. In the case of oil palm (*Figure 2a*), the cluster is dominated by 'fertilisers of biological origin' (Y02A40/20), 'technologies for solid waste management through bio-organic fraction processing; production of fertilisers from the organic fraction of waste or refuse' (Y02W30/40), 'technologies relating to chemical industry from the feedstock being materials of biological origin' (Y02P20/145), and 'fertilisers from solid waste from mechanical processing of material' (C05F5/002). Given that these sub-groups are closely related and significant, the oil palm cluster clearly focuses on recycling both the solid and liquid waste generated on and off-farm. Patents underlying this cluster prescribe preparation methods, treatment processes, and conversion and extraction procedures for producing biofertilisers from palm biomass and biogas.

The biofertiliser processing cluster for the rapeseed industry (*Figure 4c*) has sub-group classifications that are like those of oil palm, with one exception: Patents in this cluster are primarily aimed at extracting oil from hulled rapeseed, with secondary descriptors as to how to convert rapeseed meal and cake into organic fertilisers.

Another rapeseed cluster centres on general agricultural adaptation innovation such as planting methods and irrigation technologies. Similarly, the sunflower clusters (*Figure 4d*) do not refer to any specific climate change adaptation strategy. They were likely constrained by the large variation among the small number of observations.

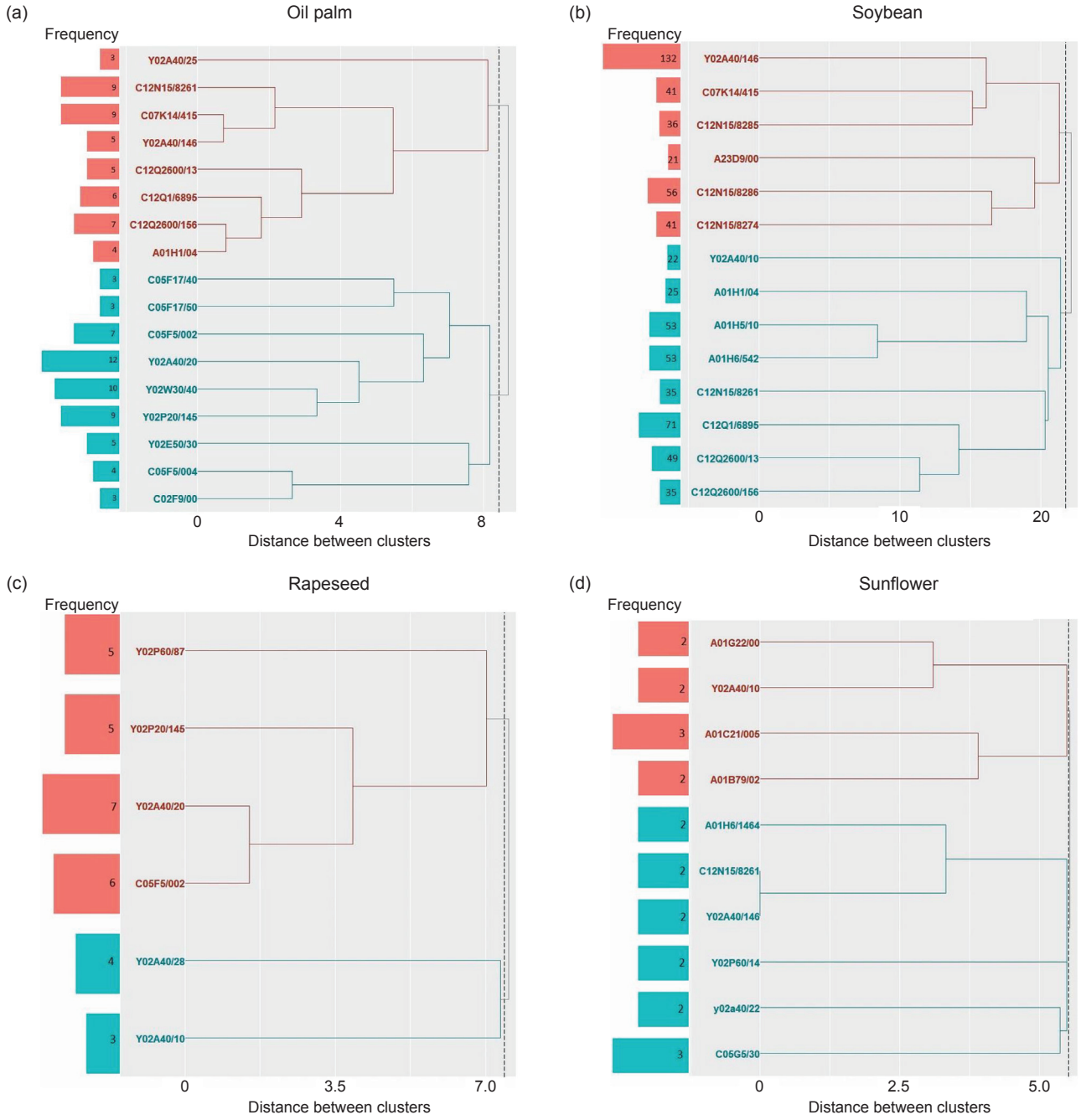
TABLE 1. QUALIFIED SUB-GROUP CLASSIFICATIONS OF CLIMATE CHANGE ADAPTATION PATENTS OF OILSEEDS

Sub-group	Description
A01B79/02	Methods for working soil combined with other agricultural processing
A01C21/005	Methods of fertilising following a specific plan
A01G22/00	Cultivation of specific crops or plants not otherwise provided for
A01H1/04	Processes for modifying genotypes involving genotypic or phenotypic markers; methods of using phenotypic markers for selection
A01H5/10	Angiosperms, seeds
A01H6/1464	Angiosperms, *Helianthus annuus* (sunflower)
A01H6/542	Angiosperms, *Glycine max* (soybean)
A23D9/00	Other edible oils or fats
C02F9/00	Multistage treatment of water, wastewater, or sewage
C05F17/40	Preparation of fertilisers characterised by biological or biochemical treatment steps for treatment of liquids or slurries
C05F17/50	Preparation of fertilisers characterised by biological or biochemical treatment steps treatments combining two or more different biological or biochemical treatments
C05F5/002	Fertilisers from solid waste from mechanical processing of material
C05F5/004	Fertilisers from liquid waste from mechanical processing of material
C05G5/30	Fertilisers characterised by their form of layered or coated
C07K14/415	Peptides having more than 20 amino acids; gastrins; somatostatins; melanotropins; derivatives thereof from plants
C12N15/8261	Mutation or genetic engineering; deoxyribonucleic acid (DNA) or ribonucleic acid (RNA) concerning genetic engineering, vectors, with agronomic (input) traits
C12N15/8274	Mutation or genetic engineering; DNA or RNA concerning genetic engineering, vectors, with agronomic (input) traits for herbicide resistance
C12N15/8285	Mutation or genetic engineering; DNA or RNA concerning genetic engineering, vectors, with agronomic (input) traits for nematode resistance
C12N15/8286	Mutation or genetic engineering; DNA or RNA concerning genetic engineering, vectors, with agronomic (input) traits for insect resistance
C12Q1/6895	Measuring or testing processes involving enzymes, nucleic acids, or microorganisms; compositions therefor; processes of preparing such compositions for plants, fungi, or algae
C12Q2600/13	Oligonucleotides characterised by their use for plant traits
C12Q2600/156	Oligonucleotides characterised by their use for polymorphic or mutational markers
Y02A40/10	Adaptation technologies in agriculture
Y02A40/146	Adaptation technologies in agriculture: Genetically modified plants
Y02A40/20	Adaptation technologies in agriculture: Fertilisers of biological origin
Y02A40/22	Adaptation technologies in agriculture: Improved land use
Y02A40/25	Adaptation technologies in agriculture: Greenhouse technology
Y02A40/28	Adaptation technologies in agriculture: Specially adapted for farming
Y02E50/30	Technologies to produce fuel from waste
Y02P20/145	Technologies relating to chemical industry from the feedstock being materials of biological origin
Y02P60/14	Technologies relating to agriculture for saving energy
Y02P60/87	Technologies relating to agriculture for re-use of by-products of food processing for fodder production
Y02W30/40	Technologies for solid waste management through bio-organic fraction processing; production of fertilisers from the organic fraction of waste or refuse

Source: Espacenet (2023).

Patents as a Knowledge Base for Subsequent Innovation

According to the F-test statistic (p>0.05) in *Figure 5*, the mean difference between forward citations of oilseeds is statistically insignificant. However, the distribution and mean scores of the four oilseed industries differ markedly. Half of the oil palm patents received one citation based on the box length, which represents the interquartile range and contains 50% of its forward citations. On average, five subsequent patents cited each oil palm



Note: Refer to *Table 1* for the description of patent sub-group classifications.

Figure 4. Clusters of climate change adaptation patents of oilseed crops, 1960-2022.

patent. One patent for a zero-discharge treatment system for palm oil mill effluent attracted five times the average number of forward citations.

Soybean and rapeseed patents had similar box lengths, beginning with a zero citation. The upward whiskers protruding from the box indicate that they have a higher number of forward citations than the oil palm industry. On average, approximately 34 subsequent patents cited soybean patents and 12 subsequent patents cited rapeseed patents. As evidenced by the number of forward patent counts that exceeded the whisker, 16 (7.5%) soybean patents were highly cited, with 10 involving soybean transgenic events and the remainder focusing on plant varieties with improved agronomic traits (*i.e.*, insect resistance and herbicide tolerance). The only rapeseed patent (4.0%) with a high number of forward citations invented a rapeseed variety with a lower saturated fatty acid content.

DISCUSSION

Climate change threatens the productivity of oil palm trees. Rising to this challenge requires not only the maintenance of existing (good) agricultural

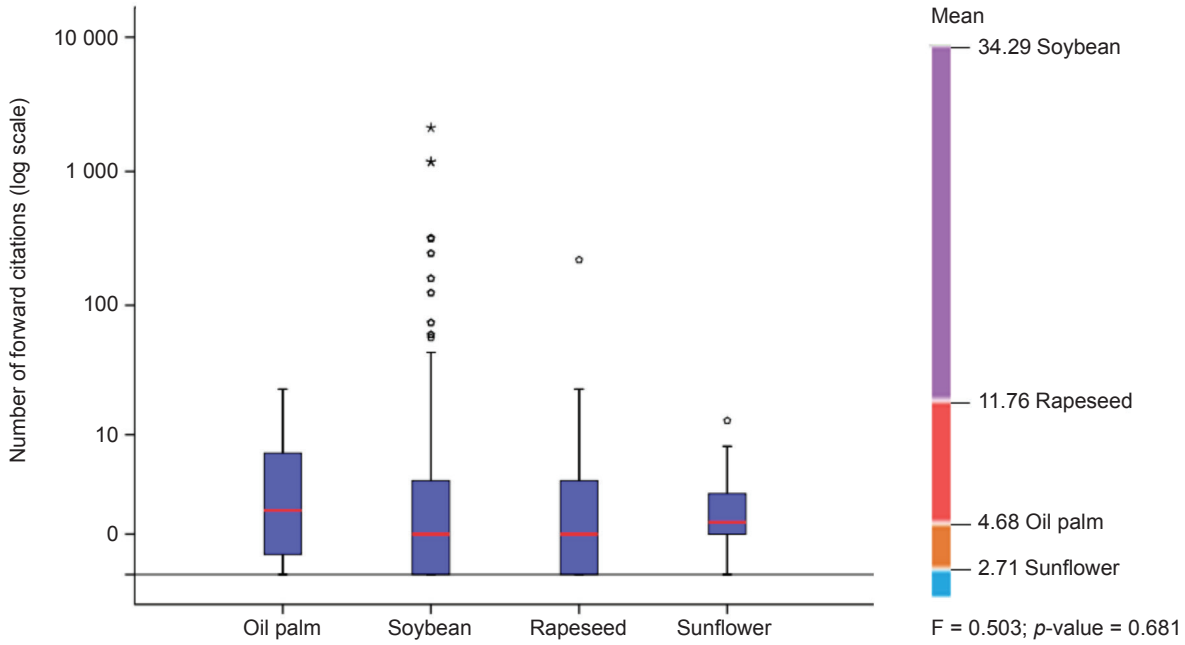


Figure 5. Forward citations in climate change adaptation patents of oilseed crops.

practices, but also the acceleration of innovation to provide strategies for coping with increasingly difficult production conditions. Understanding options for adaptation becomes necessary to ensure climate-resilient oil palm production. In this study, expanding the oil palm knowledge base was compared to adaptation innovation developed for other oilseed seeds, specifically soybean, rapeseed and sunflower.

Findings of this study reveal that the number of oil palm climatic adaptation patents is low both in absolute terms and relative to agricultural patents. This observation holds true for all the oilseed crops studied. Oilseed innovation clusters are also highly concentrated. Oil palm adaptation patents tend to focus on plant breeding and biofertiliser processing technologies. The latter was also central to rapeseed, while the former was found in the soybean sector. Another dominant cluster in soybean focuses on plant varieties with improved agronomic (particularly input) traits. Further, the reference of oil palm adaptation patents by subsequent patents was relatively limited.

The findings suggest that trade secrecy is prevalent in the major oilseed sectors. Non-disclosure is arguably the most vulnerable form of intellectual property (IP) (Lewis, 2018). Nonetheless, other oilseed sectors are also notable for their unwillingness to share information about R&D advances. Access to R&D tools, for example, has become increasingly limited in the canola sector over time (Galushko and Oikonomou, 2007; Galushko *et al.*, 2010). In business-as-usual scenarios, these R&D output strategies may be appropriate. The discovery of a small patent pool in the global patent system reveals an important knowledge gap in identifying climate-resilient technologies. Without disseminating their availability, widespread adoption is impossible. This is especially important for the palm oil industry, because, as previously stated, oil palm yields in major producing countries have fallen to a critical level.

The findings of this study point to three specific issues that require attention to boost innovation and subsequently productivity in climate change adaptation for oil palm production. These issues are relevant to the reorganisation of oil palm R&D, management by both the public and private sectors, as well as the associated opportunity to reorient innovation and commercialisation efforts.

Firstly, patents for oil palm adaptation innovation are scarce. Oil palm R&D is relatively advanced in comparison to other agricultural sectors that suffer from a lack of local inventive capability (Govindaraju and Wong 2011). Similarly, the palm oil industry has relatively high expenditure on R&D. In Malaysia, a tax on crude palm oil and palm kernel oil production is collected to support the Malaysian Palm Oil Board's (MPOB) R&D initiatives. Innovations of the MPOB are published annually in the Journal of Oil Palm Research (*e.g.*, Parveez *et al.*, 2022) and disseminated through annual Transfer of Technology Seminars (TOT). Other channels are also used. Established plantation companies also invest extensively in in-house and collaborative R&D programmes (Tey *et al.*, 2020).

Given such available financial and technical resources, priorities should be set to increase IP awareness, facilitate IP filing, and provide market incentives to encourage patenting and / or knowledge

transfer. Such interventions should involve all R&D communities, including oil palm-specific research institutions, universities, government-linked companies, and private companies.

Secondly, product innovation resulting from oil palm process innovation has not been patented. Existing oil palm research literature (*e.g.*, Martin *et al.*, 2022) has also primarily focused on modern breeding tools. The patent database contains a significant lack of improved oil palm varieties and farm inputs, indicating a long-standing underrepresentation of oil palm technological development for sustainability progress within the patenting regime and the knowledge base.

With the growing demand for adaptability and ever more productive planting materials, a strong case exists for focusing on contemporary adaptation strategies produced by state-of-the-art techniques. The questions as to whether the institutional function of R&D organisations should be expanded to include patent filing facilitation, whether all such adaptive solutions are capable of being patented or, indeed whether they should be, is beyond the scope of this paper. However, the technological foundation required to drive innovation productivity is clear: In the absence of IP, innovation and adaptation productivity can only be accomplished through individual access to and the capacity to acquire contemporary innovate ideologies and technological knowledge. This is exemplified by the fact that the proprietary R&D outputs of integrated plantation enterprises deliberately favour their business welfare, undermining the potential of generating wider benefits for the industry.

Reinforcing that point, finally, the scarcity of subsequent oil palm patents seems directly correlated with its small patent base. As discussed previously, this does not always imply a lack of innovation. Patentable innovation may not be filed where a need for confidentiality is deemed desirable. Patent documents reveal detailed technical knowledge and are only valid in the country or region in which they are registered. However, it does indicate the opportunity cost associated with knowledge and technology growth. Patents can be and are often sought in each jurisdiction where protection is required, and the certainty of patent protection drives commercialisation (Wagner and Wakeman, 2016).

In the case of oil palm, opportunities remain to seek IP rights over inventions and build a knowledge base for future innovation. In agricultural biotechnology, for example, American IP rights have motivated private investment in applied research that has been built on a foundation of public basic research (Wright and Shih, 2010).

Given the discussion above, a shortcoming of the methodology used in this study must be acknowledged. Patent publications represent only one type of R&D output. A considerable pool of modern adaptation technologies for oilseed production have not been, or cannot, be patentable. Examples are numerous but include novel oil palm varieties resulting from genomic innovation for identifying markers or genes controlling polygenic traits such as low height, pest and disease resistance, high yield, and climate resilience (Low *et al.*, 2017).

Future research should take account of modern adaptation technologies beyond those discussed here. The broadest contemporary knowledge is required for the effective implementation of cultural practices. An initiative which consolidates public and private sector R&D outputs that are both responsive to a variety of climate and sustainability challenges seems the logical next step. Moreover, understanding the state of innovation appears critical for facilitating oil palm R&D that is better suited to a dynamic environment. It should also facilitate a comparative analysis of adaptation innovation in other oilseed industries, thus providing a better understanding of the R&D gaps.

CONCLUSION

The importance of a knowledge base in informing diffusion for both the scale and speed of adaptation strategies in oil palm production is growing. However, this study reveals a scarcity of oil palm patents directed towards climate change adaptation. Existing oil palm patents are generally concerned with process innovation and show a lack of product innovation. In contrast, soybean adaptation patents encompass both process and product innovation. Critically, oil palm adaptation patents are associated with fewer subsequent patents than soybean adaptation patents. As a result, this study reveals a mismatch between the need for oil palm adaptation and technological availability knowledge. Oil palm R&D institutions should embrace a better considered IP paradigm in order to lay the groundwork for informing technology diffusion, which is critical in accelerating oil palm adaptation to climate change.

ACKNOWLEDGEMENT

The authors received no funding for this work and would like to thank the anonymous reviewers for their constructive feedback.

REFERENCES

Abubakar, A; Ishak, M Y; Bakar, A A and Uddin, M K (2022). *Ganoderma boninense* basal stem rot induced by climate change and its effect on oil palm. *Environ. Sustain.*, *5(3)*: 289-303. DOI: 10.1007/s42398-022-00244-7.

Abubakar, A; Ishak, M Y and Makmom, A A (2021). Impacts of and adaptation to climate change on the oil palm in Malaysia: A systematic review. *Environ. Sci. Pollut. Res.*, *28(39)*: 54339-54361. DOI: 10.1007/s11356-021-15890-3.

Agamuthu, P and Broughton, W J (1985). Nutrient cycling within the developing oil palm-legume ecosystem. *Agric. Ecosyst. Environ.*, *13(2)*: 111-123. DOI: 10.1016/0167-8809(85)90054-4.

Ahmad, M; Waraich, E A; Skalicky, M; Hussain, S; Zulfiqar, U; Anjum, M Z; Rahman, M H U; Brestic, M; Ratnasekera, D; Lamilla-Tamayo, L; Al-Ashkar, I and El Sabagh, A (2021). Adaptation strategies to improve the resistance of oilseed crops to heat stress under a changing climate: An overview. *Front. Plant Sci.*, *12*: 767150. DOI: 10.3389/fpls.2021.767150.

Amelia, J R; Suprihatin, S; Indrasti, N S; Hasanudin, U; Murakami, R and Fujie, K (2017). Effects of treated palm oil mill effluent application on the soil microbial community structure and oil palm plantation productivity. *J. Water Environ. Technol.*, *15*: 77-85. DOI: 10.2965/jwet.16-039.

Angelucci, S; Hurtado-Albir, F J and Volpe, A (2018). Supporting global initiatives on climate change: The EPO's "Y02-Y04S" tagging scheme. *World Pat. Inf.*, *54*: S85-S92. DOI: 10.1016/j.wpi.2017.04.006.

Baeza-Yates, R A (1992). Introduction to data structures and algorithms related to information retrieval. *Information Retrieval: Data Structure and Algorithms* (William Frakes and Baeza-Yates, R eds.). Prentice Hall, Upper Saddle River. p. 13-27.

Behles, D (2009). The new race: Speeding up climate change innovation. *NCJL Tech.*, *11(1)*: 1-50.

Cabinet Secretariat of the Republic of Indonesia (2019). Government stops issuance of new permit for primary forests, peatlands. https://setkab.go.id/en/govt-stops-issuance-of-new-permit-for-primary-forests-peatlands/, accessed on 8 August 2023.

Comte, I; Colin, F; Grünberger, O; Follain, S; Whalen, J K and Caliman, J P (2013). Landscape-scale assessment of soil response to long-term organic and mineral fertilizer application in an industrial oil palm plantation, Indonesia. *Agric. Ecosyst. Environ*, *169*: 58-68. DOI: 10.1016/j.agee.2013.02.010.

Espacenet (2023). Cooperative patent classification. https://worldwide.espacenet.com/classification, accessed on 2 February 2023.

FAO (Food and Agriculture Organization of the United Nations) (2023). FAOSTAT: Crops and livestock products. https://www.fao.org/faostat/en/#data/QCL, accessed on 8 October 2023.

Galushko, V; Gray, R; Smyth, S and Arnison, P (2010). Resolving FTO barriers in GM canola. Paper presented at the 14th International ICABR Conference on Governance: Policy, Environmental and Health Regulation, and Public Investments in Research. Ravello. 16-18 June 2010.

Galushko, V and Oikonomou, E (2007). IP protection in Canadian agriculture: A shift to "tragedy of anticommons"? *CAIRN Policy Brief No. 4*.

Grinnell, N A; van der Linde, N A; Azhar, B; Nobilly, F and Slingerland, M (2022). Cattle-oil palm integration - A viable strategy to increase Malaysian beef self-sufficiency and palm oil sustainability. *Livest. Sci.*, *259*: 104902. DOI: 10.1016/j.livsci.2022.104902.

Golden Gate Weather Services (2023). *El Niño* and *La Niña* years and intensities. https://www.ggweather.com/enso/oni.htm, accessed on 10 October 2023.

Govindaraju, V C and Wong, C Y (2011). Patenting activities by developing countries: The case of Malaysia. *World Pat. Inf.*, *33(1)*: 51-57 DOI: 101016/jwpi201001001.

Hair, J F; Black, W C; Babin, B J and Anderson, R E (2013). *Multivariate Data Analysis*. Pearson, Upper Saddle River, NJ. 761 pp.

IPCC (Intergovernmental Panel on Climate Change) (2018). *Fifth Assessment Report*. Cambridge University Press, New York.

Jaffe, A B and De Rassenfosse, G (2019). Patent citation data in social science research: Overview and best practices. *Research Handbook on the Economics of Intellectual Property Law* (Ben Depooter and Menell, P eds.). Edward Elgar, Northampton. 167 pp. DOI: 10.4337/9781789903997.

Jain, A K and Dubes, R C (1988). *Algorithms for Clustering Data*. Prentice Hall, Upper Saddle River, NJ. 334 pp.

Ji, J; Barnett, G A and Chu, J (2019). Global networks of genetically modified crops technology: A patent citation network analysis. *Scientometrics*, *118(3)*: 737-762. DOI: 10.1007/s11192-019-03006-1.

Jürgens, B and Herrero-Solana, V (2015). Espacenet, Patentscope and Depatisnet: A comparison approach. *World Pat. Inf.*, *42*: 4-12. DOI: 10.1016/j.wpi.2015.05.004.

Lemessa, F and Wakjira, M (2015). Cover crops as a means of ecological weed management in agroecosystems. *J. Crop Sci. Biotechnol.*, *18*: 123-135. DOI: 10.1007/s12892-014-0085-2.

Lewis, L (2018). Evergreening through trade secrets as an impediment to green technology transfer to the developing world. *Asper Rev. Int. Bus. Trade Law*, *18*: 23-70.

Li, B; Duan, Y; Luebke, D and Morreale, B (2013). Advances in CO_2 capture technology: A patent review. *Appl. Energy*, *102*: 1439-1447. DOI: 10.1016/j.apenergy.2012.09.009.

Li, X; Hu, Z Z; Tseng, Y H; Liu, Y and Liang, P (2022). A historical perspective of the *La Niña* event in 2020/2021. *J. Geophys. Res. Atmos.*, *127(7)*: e2021JD035546. DOI: 10.1029/2021JD035546.

Low, E T L; Jayanthi, N; Chan, K L; Sanusi, N S N M; Halim, M A A; Rosli, R; Azizi, N; Amiruddin, N; Lee, P L A; Ong, A M; Singh, R; Manaf, M A A; Sambanthamurthi, R; Parveez, G K A and Kushairi, A (2017). The oil palm genome revolution. *J. Oil Palm Res.*, *29(4)*: 456-468. DOI: 10.21894/jopr.2017.00018.

Makowski, D; Marajo-Petitzon, E; Durand, J L and Ben-Ari, T (2020). Quantitative synthesis of temperature, CO_2, rainfall, and adaptation effects on global crop yields. *Eur. J. Agron.*, *115*: 126041. DOI: 10.1016/j.eja.2020.126041.

Marešová, P; Soukal, I; Stemberkova, R and Selamat, A (2022). Perspective and suitable research area in public research - Patent analysis of the Czech public universities. *Educ. Urban Soc.*, *54(7)*: 871-899. DOI: 10.1177/00131245211027362.

Miao, R L and Guo, L G (2015). Study on technology development status of genetically modified soybean based on patent analysis. *Adv. J. Food Sci. Technol.*, *8(9)*: 603-611.

MPOB (2021). Yield 2021. https://bepi.mpob.gov.my/index.php/yield/277-yield-2021/1060-yield-2021, accessed on 9 October 2023.

MPOB (2022). Principle statistics of oil palm estates, 1974-2019. https://www.dosm.gov.my/portal-main/time-series, accessed on 9 October 2023.

MPOB (2023). Yield 2022. https://bepi.mpob.gov.my/index.php/yield/291-yield-2022/1106-yield-2022, accessed on 9 October 2023.

Martin, J J J; Yarra, R; Wei, L and Cao, H (2022). Oil palm breeding in the modern era: Challenges and opportunities. *Plants*, *11(11)*: 1395. DOI: 10.3390/plants11111395.

McLaren, D and Markusson, N (2020). The co-evolution of technological promises, modelling, policies and climate change targets. *Nat. Clim. Change*, *10*(5): 392-397. DOI: 10.1038/s41558-020-0740-1.

Meehl, G A; Tebaldi, C; Teng, H and Peterson, T C (2007). Current and future US weather extremes and *El Niño*. *Geophysical Research Letters*, *34(20)*: L20704 DOI: 10.1029/2007GL031027.

Milligan, G W and Cooper, M C (1985). An examination of procedures for determining the number of clusters in a data set. *Psychometrika*, *50*: 159-179. DOI: 10.1007/BF02294245.

Moradi, A; Boon Sung, C T; Joo, G K; Mohd Hanif, A H and Ishak, C F (2012). Evaluation of four soil conservation practices in a non-terraced oil palm plantation. *Agron. J.*, *104(6)*: 1727-1740. DOI: 10.2134/agronj2012.0120.

Parveez, G K A; Kamil, N N; Zawawi, N Z; Ong-Abdullah, M; Rasuddin, R; Loh, S K and Idris, Z (2022). Oil palm economic performance in Malaysia and R&D progress in 2021. *J. Oil Palm Res.*, *34(2)*: 185-218. DOI: 10.21894/jopr.2022.0036.

Paterson, R R M (2020). Oil palm survival under climate change in Malaysia with future basal stem rot assessments. *For. Pathol.*, *50(6)*: e12641. DOI: 10.1111/efp.12641.

Pianta, M and Sirilli, G (1996). Innovation surveys and patents as technology indicators: The state of the art. *Innovation, Patents and Technological Strategies* (Daniele Archibugi and Pianta, M eds.). Organisation for Economic Co-operation and Development, Paris. p. 17-56.

Pulingam, T; Lakshmanan, M; Chuah, J A; Surendran, A; Zainab, L I; Foroozandeh, P; Uke, A; Kosugi, A and Sudesh, K (2022). Oil palm trunk waste: Environmental impacts and management strategies. *Ind. Crops. Prod.*, *189*: 115827. DOI: 10.1016/j.indcrop.2022.115827.

Rival, A (2017). Breeding the oil palm (*Elaeis guineensis* Jacq.) for climate change. *Ocl.*, *24(1)*: D107. DOI: 10.1051/ocl/2017001.

Rubinsin, N J; Daud, W R W; Kamarudin, S K; Masdar, M S; Rosli, M I; Samsatli, S; Tapia, J F D; Ghani, W A W A K; Hasan, A and Lim, K L (2021). Modelling and optimisation of oil palm biomass value chains and the environment-food-energy-water nexus in

peninsular Malaysia. *Biomass Bioenergy*, *144*: 105912. DOI: 10.1016/j.biombioe.2020.105912.

Rudolf, K; Hennings, N; Dippold, M A; Edison, E and Wollni, M (2021). Improving economic and environmental outcomes in oil palm smallholdings: The relationship between mulching, soil properties and yields. *Agric. Syst.*, *193*: 103242. DOI: 10.1016/j.agsy.2021.103242.

Sarkar, M; Kabir, S; Begum, R A and Pereira, J J (2020). Impacts of climate change on oil palm production in Malaysia. *Environ. Sci. Pollut. Res.*, *27(9)*: 9760-9770. DOI: 10.1007/s11356-020-07601-1.

Suresh, K (2013). Adaptation and mitigation strategies for climate-resilient oil palm. *Climate-Resilient Horticulture: Adaptation and Mitigation Strategies* (Harish Chandra Prasad Singh, Rao, N and Shivashankar, K S eds.). Springer, India. p. 199-211. DOI: 10.1007/978-81-322-0974-4_18.

Tey, Y S; Brinda,l M; Darham, S; Sidique, S F A and Djama, M (2020). Early mover advantage in Roundtable on Sustainable Palm Oil certification: A panel evidence of plantation companies. *J. Clean Prod.*, *252*: 119775. DOI: 10.1016/j.jclepro.2019.119775.

Uke, A; Nakazono-Nagaoka, E; Chuah, J A; Zain, N A A; Amir, H G; Sudesh, K; Abidin, N Z H A Z; Hashim, Z and Kosugi, A (2021). Effect of decomposing oil palm trunk fibres on plant growth and soil microbial community composition. *J. Environ. Manage.*, *295*: 113050. DOI: 10.1016/j.jenvman.2021.113050.

Wagner, S and Wakeman, S (2016). What do patent-based measures tell us about product commercialization? Evidence from the pharmaceutical industry. *Res. Policy*, *45(5)*: 1091-1102. DOI: 10.1016/j.respol.2016.02.006.

Wang, H P and Coleman, A (2016). Patent landscape report on palm oil production and waste treatment technologies. *World Intellectual Property Organization*. Kuala Lumpur. 124 pp. DOI: 10.34667/tind.28973.

Wibowo, H; Fauzi, A M and Taqi, F M (2019). Mapping of palm oil technology based on patent information analysis. *IOP Conf. Ser.: Earth Environ. Sci.*, *335(1)*: 012016. DOI: 10.1088/1755-1315/335/1/012016.

WMO (World Meteorological Organization) (2023). Global temperatures set to reach new records in next five years. https://public.wmo.int/en/media/press-release/global-temperatures-set-reach-new-records-next-five-years, accessed on 11 October 2023.

Wright, B D and Shih, T M (2010). *Agricultural Innovation*. National Bureau of Economic Research, Massachusetts. 48 pp. DOI: 10.3386/w15793.

Zimmer, Y (2016). Competitiveness of rapeseed, soybeans and palm oil. *J. Oilseed Brassica*, *1(2)*: 84-90.

Journal of Oil Palm Research Vol. 36 (4) December 2024 p. 560-585
DOI: https://doi.org/10.21894/jopr.2024.0023

DIETS AND HEALTH BENEFITS OF GUT MICROBIOTA-FERMENTED SHORT-CHAIN FATTY ACIDS: A PERSPECTIVE OF THE MALAYSIAN DIET CONTAINING PALM OIL

SIA-YEN, YAP[1]*; PHOOI-TEE, VOON[1] and SELVADURAY, KANGA RANI[1]

ABSTRACT

A healthy diet provides a favourable environment that allows the essential bacteria to grow and ferment beneficial metabolites, short-chain fatty acids (SCFA) through various metabolic pathways. SCFA, including linear- and branched-SCFA (BSCFA) are important in regulating energy haemostasis, inflammation, and appetite. A plant-based diet is associated with increased SCFA levels and SCFA-producing bacteria that regulate nutrient metabolism. Conversely, an animal-based diet is associated with lower SCFA levels and its producing bacteria. The Malaysian dietary guidelines are in line with other healthy eating recommendations that promote vegetables and fruit intake. Very few clinical studies are available to explore the association of gut microbiota and SCFA profiles following a Malaysian diet and the detailed amount of oil consumption was not reported. The available data demonstrated that acetate, propionate, and butyrate were the most abundant SCFA, while BSCFA, isobutyrate, was less abundant in Malaysian. Firmicutes and Bacteroidetes are the predominant phyla, while Faecalibacterium *and* Prevotella *are the dominant SCFA-producing genera in Malaysian.* Prevotella *is associated with metabolic pathways for carbohydrates and fatty acids. However, more long-term cohort studies are needed to further elucidate the association between gut microbiota composition, SCFA profiles and the potential health effects of palm oil consumption in Malaysian diet.*

Keywords: dietary pattern, gut microbiota, Malaysian diet, palm oil, short-chain fatty acids.

Received: 12 August 2023; **Accepted:** 16 December 2023; **Published online:** 18 March 2024.

INTRODUCTION

A healthy diet provides a friendly environment for diverse gut microbiota compositions to ferment essential metabolomes particularly short-chain fatty acids (SCFA) to improve gut health (LeBlanc *et al.,* 2017). In an increasingly fast-paced world, the traditional human healthy diet rich in whole grains, vegetables and fruits is quickly replaced with processed foods added with sugars, salt, food additives and preservatives which are low in nutritional value (Atzeni *et al.,* 2022). The long-term consumption of these ultra-processed foods has been associated with diet-related chronic diseases such as obesity, type 2 diabetes (T2D), and cardiovascular disease (CVD) (Kopp, 2019).

More recently, studies reported that unhealthy dietary patterns promote gut dysbiosis (Liu *et al.,* 2021; Zsálig *et al.,* 2023), which is characterised by a lower proportion of commensal bacteria (Levy *et al.,* 2017). The commensal bacteria have diverse gene families and are important in improving the efficiency of metabolic pathways for nutrient assimilation (Asnicar *et al.,* 2021; Bolte *et al.,* 2021; Tomova *et al.,* 2019; Xiao *et al.,* 2022). Gut dysbiosis has been linked to diseases such as diarrhoea, constipation, diverticulosis, irritable bowel syndrome (IBS), Crohn's disease (Priya *et al.,* 2022) and colorectal cancer (Sánchez-Alcoholado *et al.,* 2020).

The composition of the gut microbiota is generally stable, as evident that it is resilient to short-term dietary modification (Schwedhelm *et al.,*

[1] Malaysian Palm Oil Board,
6, Persiaran Institusi, Bandar Baru Bangi,
43000 Kajang, Selangor, Malaysia.

* *Corresponding author e-mail: syyap@mpob.gov.my*

2018). A study has shown that an abrupt shift from a purely plant-based diet to a purely animal-based diet induced a rapid change in the gut microbiota profile but this change was promptly restored within 48 hr after discontinuing the animal-based diet (David *et al.*, 2014). Similar temporal effects of diet on gut microbiota have also been reported with a low-carbohydrate or low-fat diet (Fragiadakis *et al.*, 2020), suggesting that sustained dietary change should extend beyond three months (Pagliai *et al.*, 2020), which had been shown in cross-sectional studies with different populations (De Filippo *et al.*, 2010; Wu *et al.*, 2011). Long-term adherence to a diet enriched with fruits, vegetables, legumes, and grains as is the case with the Mediterranean and vegetarian diets, leads to a constant elevate in SCFA levels and cultivation of SCFA-producing bacteria such as *Prevotella copri* and *Blastocystis* spp. (Asnicar *et al.*, 2021; Gibiino *et al.*, 2021; Pagliai *et al.*, 2020). Conversely, prolonged consumption of red meat and processed foods reduces the diversity of the gut microbiota and lowers SCFA levels (Agus *et al.*, 2016) due to insufficient fibre to support the growth of gut microbiota (An *et al.*, 2021).

Dietary pattern affects the proportion of macronutrient residues, including polysaccharides from carbohydrates, peptides from proteins, and fatty acids and glycerol from fats. These residues are fermented by bacteria into a wide range of SCFA (*Figure 1*). SCFA is a group of fatty acids consisting of six or fewer carbon atoms and exists as linear or branched chain molecules (*Figure 1*). They are typically obtained from various foods such as cheese, vinegar, yoghurt, palm kernel oil and coconut oil. Among these SCFA, acetate, propionate, and butyrate are the main linear chain SCFA, and they are mainly produced through anaerobic fermentation of dietary fibre (Wang *et al.*, 2019) by saccharolytic bacteria, and through degradation of fatty acid residues by bacteria. Furthermore, a relatively small percentage of SCFA is also obtained from the fermentation of glycerol and ketone bodies such as beta-hydroxybutyrate and acetoacetate (Puchalska and Crawford, 2017). BSCFA, namely isobutyrate, isovalerate, and 2-methylbutyrate are mainly produced through the degradation of branched amino acids such as leucine, isoleucine and valine by proteolytic bacteria (Xu *et al.*, 2020a).

The Malaysian diet is unique as it offers a wide variety of foods while still ensuring a balanced nutrient intake. Palm oil is versatile and has been extensively used in Malaysia either as cooking oil or for food preparation. Palm oil has an almost equal proportion of saturated fatty acids (SFA) and unsaturated fatty acids (UFA), with palmitic acid comprising about 45%, oleic acid about 40% and linoleic acid about 10%. Palm oil can be fractionated into palm olein (liquid) and palm stearin (solid). The UFA content of palm olein increases by 5%-7% compared to palm oil.

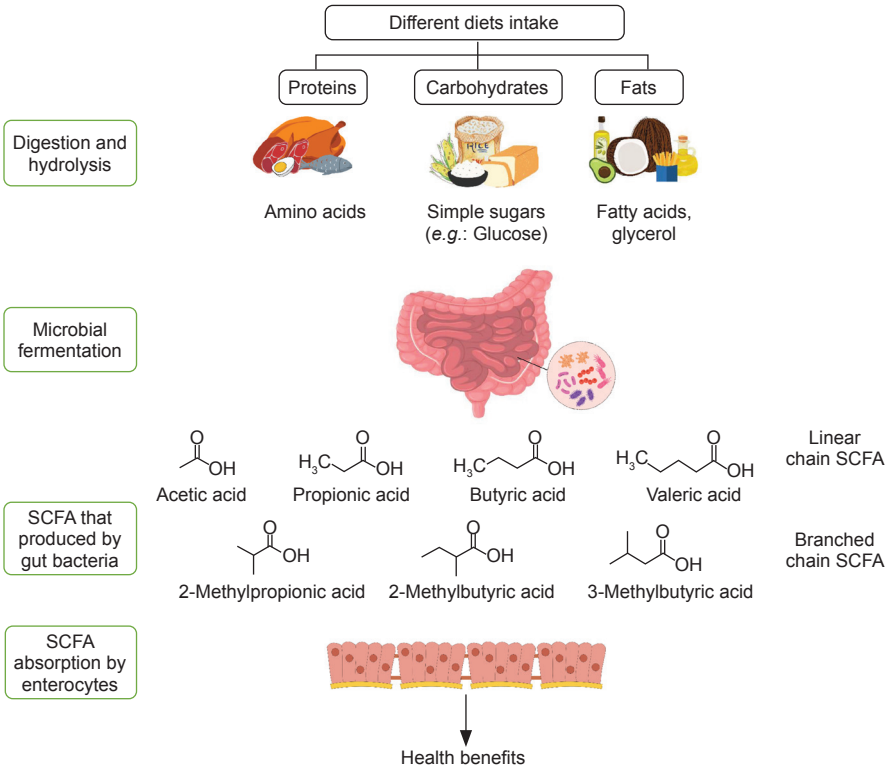


Figure 1. The roles of gut microbiota in producing SCFA after fermenting different types of food. These SCFA are absorbed into the host and provide health benefits to the host.

Palm olein has a lower proportion of linoleic acid, which makes it very stable at high temperatures and ideal for deep frying. Additionally, solid palm stearin is often used as a hard fat and is blended with other soft oils such as sunflower or soybean oil to produce margarine, and shortening which are widely used in the confectionery and food industries (Dian *et al.*, 2017).

The effects of SCFA on health are complex. Clinical randomised and cross-over trials have been conducted to investigate the effects of different individual dietary components on the profile of the gut microbiome and SCFA produced on potential health benefits, but an understanding of these effects is still lacking. Few studies have examined the effects of dietary patterns on the composition of the gut microbiota and the long-term effects of gut-fermented SCFA in healthy adults. There is limited information on the potential benefits of the effects of habitual consumption of palm oil-containing Malaysian food on the diversity of the gut microbiota and its effects on SCFA profiles. However, given the uniqueness of Malaysian cuisine and palm oil, the bacterial profile is expected to be more complex than in diets containing only SFA or UFA oils, although some core bacterial strains are previously identified in SFA and MUFA diets (Yap *et al.*, 2022). This review explains the composition of the gut microbiota and SCFA content of people following specially designed diets that are high in certain dietary components and the long-term effects of different dietary patterns to adult health. Furthermore, this review also examines the potential effect of the Malaysian diet in this context.

SCFA AND GUT HEALTH BENEFITS

A balanced physiological level of SCFA is essential to promote gut health. The direct beneficial effects of SCFA have been demonstrated in the studies of oral administration in animals (den Besten *et al.*, 2013; Vieira *et al.*, 2012). In studies in which stable acetate-, propionate-, and butyrate- isotopes were infused into mice, different SCFA were reported to regulate different pathways (den Besten *et al.*, 2013). Approximately two-thirds of the infused propionate was used for glucose production, while a higher proportion of acetate and butyrate was involved in lipid and cholesterol synthesis (den Besten *et al.*, 2013). Acetate and butyrate are precursors in lipid metabolism and are especially important for the metabolism of fatty acids and cholesterol to yield palmitate and cholesterol. Vieira and co-workers reported that mice with ulcerative colitis in the caecal lymph nodes have reduced inflammation after oral ingestion of butyrate (Vieira *et al.*, 2012).

Later, researchers have also found that a high-fibre diet increases the levels of faecal acetate as well as butyrate and reduces pathogens or toxins such as bacterial lipopolysaccharides (LPS) (Biswas *et al.*, 2022). At physiological concentrations, butyrate regulates the expression of tight junction proteins such as cladin-2 which consequently prevents LPS (Kelly *et al.*, 2015). Otherwise, high levels of LPS in the blood will trigger the immune cells in the lamina propria of the gut, leading to an increase in pro-inflammatory cytokines and interferons which increases the risk of an inflammatory response (Rowart *et al.*, 2018). Along with acetate, butyrate also stimulates mucus secretion to prevent pathogens or toxins from adhering to the colonic epithelium (Kelly *et al.*, 2015; Pelaseyed *et al.*, 2014) and to stop the growth and specification of cancer cells (Donohoe *et al.*, 2011). Therefore, faecal butyrate concentration could be a useful preliminary biomarker for the diagnosis of colonic diseases such as diarrhoea, inflammatory bowel disease (IBD), IBS, and colon cancer.

SCFA can also suppress appetite by activating the G-protein coupled receptors (GPR) 41 and 43 on L-enteroendocrine cells in the gut and pancreas (*Figure 2*). The binding of propionate and butyrate is more selective for GPR 41, while acetate and propionate have higher affinity for GPR 41 and 43 (Tazoe *et al.*, 2009) (*Figure 2*). Consequently, these activated receptors induce the secretion of gut hormones such as glucagon-like peptide 1 (GLP-1) and peptide tyrosine tyrosine (PYY) (Larraufie *et al.*, 2018) to suppress appetite, resulting in lower food intake (Byrne *et al.*, 2015).

SCFA, especially butyrate and propionate, can also ameliorate the effects of a high-fat diet on insulin resistance and obesity. These SCFA activate the AMP-activated protein kinase (AMPK) by increasing the AMP/ATP ratio and consequently trigger the expression of Peroxisome proliferator-activated receptor-gamma coactivator-1 alpha (PGC-1a). This in turn increases adiponectin secretion and, enhances glucose uptake in skeletal muscle and liver, leading to increase energy utilisation and improved insulin sensitivity (Sanna *et al.*, 2019) (*Figure 3*). Mice fed with a high-fat diet (45% calories from fat) supplemented with 5% sodium acetate lost 30% of their body weight compared to their non-supplemented counterparts (den Besten *et al.*, 2015). Moreover, SCFA particularly via the free fatty acid receptor 2 (FFAR-2) dependent pathway has been associated with an increase in leptin secretion, stimulating fatty acid oxidation (*Figure 3)* to reduce appetite and food intake (Mithieux, 2013). This concomitantly suppresses the insulin signalling to inhibit fat storage in adipose tissue.

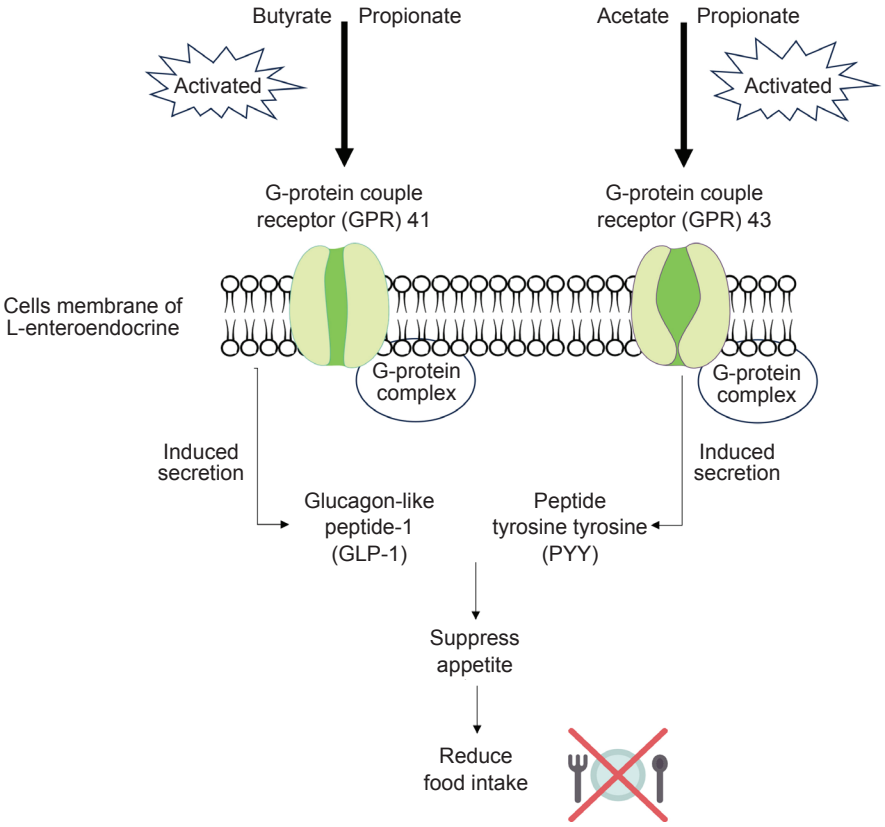
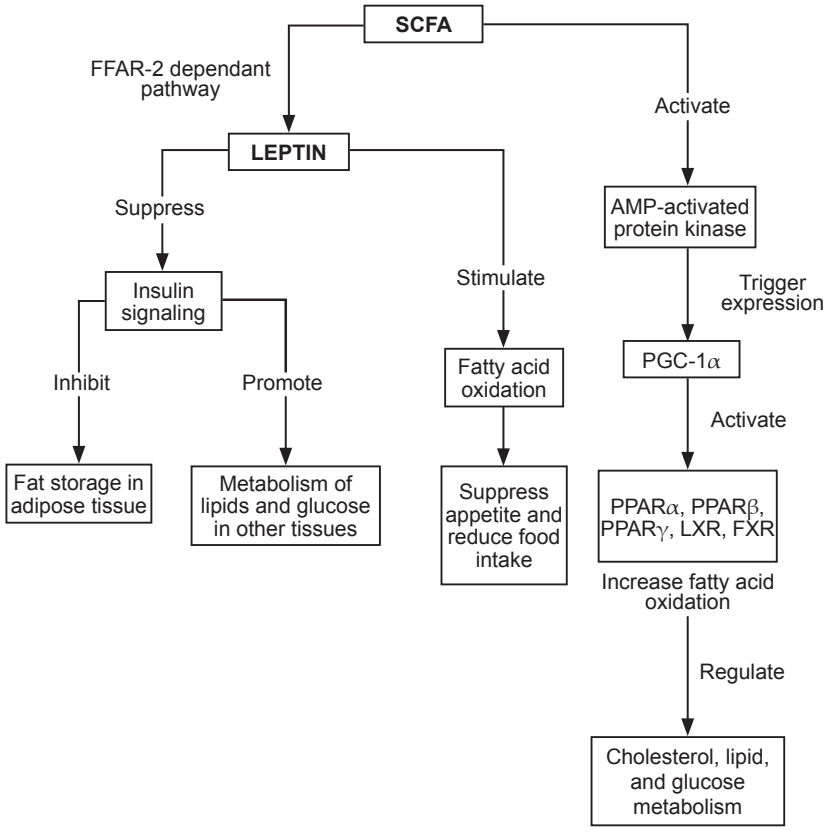


Figure 2. The important of different G-proteins couple receptor on selection of different SCFA binding and affecting the food intake.



Note: PGC-1a - peroxisome proliferator activated receptor-gamma coactivator-1 alpha; PPAR - peroxisome proliferator-activated receptor; LXR- liver X receptor; FXR - farnesoid X receptor.

Figure 3. SCFA in regulating various metabolisms in the host.

The health benefits of BSCFA are still poorly understood. A six month study of severely obese individuals who had undergone bariatric surgery found decreased total linear SCFA and increased BSCFA due to higher protein and fibre intake, resulting in increased proteolytic fermentation by gut bacteria (Farup and Valeur, 2020). Another 12-month study of obese adults who had also undergone bariatric surgery found gut isobutyrate levels that are inversely correlated with changes in BMI and insulin resistance (Martínez-Sánchez *et al.*, 2023). These results suggest that BSCFA also have the potential to promote weight loss and improve insulin sensitivity (Mohammadifard *et al.*, 2022).

GUIDELINES OF DIFFERENT DIETARY PATTERNS

Dietary guidelines serve as a reference to form a dietary pattern which is tailored to the needs of different populations to meet nutritional requirements while preventing malnutrition and deficiencies. Adherence to these dietary guidelines yields a unique SCFA and gut microbiota profile of each population. The dietary guidelines of 96 countries have been comprehensively reviewed (Rong *et al.*, 2021) and found that a healthy and balanced diet is commonly recommended, although there are minor differences due to the availability of local foods, cultural practices, and health status.

The dietary guidelines of most countries advise a high consumption of various vegetables and fruits of at least 300-500 g/day, maintaining a moderate protein intake, limiting fat intake to 25-30 g daily, reducing sugar consumption and sugary drinks, limiting salt intake to 6 g/day, and at least 1.5 to 2.0 L of water a day (Rong *et al.*, 2021). There are some minor differences in the recommendations. For example, India discourages alcohol consumption, while Mediterranean countries typically recommend 2-3 glasses of alcohol intake in their diets (*Table 1*). Some Mediterranean countries such as Spain recommend consuming olive oil instead of other oils (*Table 1*), and Greece has no limit for olive oil intake. The United States, on the other hand, recommends consuming vegetable oils instead of solid fats, and China recommends consuming 25-30 g of oil daily (Wang *et al.*, 2016). India recommends limiting the intake of ghee, butter and hydrogenated vegetable oils (Manual, 2011), while Japan advocated an adequate intake of vegetable oil and fish oil (Gabriel *et al.*, 2018) (*Table 1*).

Some common guidelines for dietary patterns used in long-term cohort or epidemiological studies are summarised in *Table 1*. The USDA dietary guidelines recommend a well-balanced diet across all food groups, emphasising a high proportion of fruits, vegetables, legumes, nuts and whole grains. It also suggests limiting fats (less than 30% of total energy, of which less than 10% is saturated fat), industrially produced *trans* fats, added sugars and salt. In a similar vein, the Dutch diet encourages a high intake of vegetables, fruits, whole grains, legumes and nuts, and reasonable quantities of dairy products, fish, fats and oils, tea and coffee (*Table 1*). The diet also discourages the consumption of red meat, *trans* fats, sugar, sweetened beverages, processed foods and salt (*Table 1*).

The Mediterranean diet, originating in Mediterranean countries such as Greece and Italy, promotes a healthy diet by reducing red meat consumption and prioritising consumption of plant foods such as fruits, vegetables, grains and legumes (*Table 1*). Poultry, seafood and dairy products are recommended to be consumed in moderate amounts, with olive oil being the main source of fat (Widmer *et al.*, 2015). Over the last two decades, vegan and vegetarian diets have increasingly gained popularity. These diets consist primarily of plant sources and exclude or limit animal products. Although vegetables are rich in fibre, they are relatively poor in protein content, leading vegetarians to rely on plant-based protein sources.

The Malaysian Ministry of Health revised the food pyramid (Ganapathy *et al.*, 2019) to improve the healthy eating habits of the Malaysian population (*Figure 4*). In line with other healthy diet recommendations, the updated guidelines recommend more than 50% of vegetables and fruits. This should be supplemented by complex carbohydrates found in brown rice, whole grains products, unprocessed cereals, and oats. These natural foods are rich in vitamins and minerals which strengthen the immune system. The guide also emphasises a moderate intake of proteins from animals, seafood and plants such as nuts and legumes. The guide also recommends staying hydrated with plain water and reducing sugar, salt and oil intake (*Figure 4*).

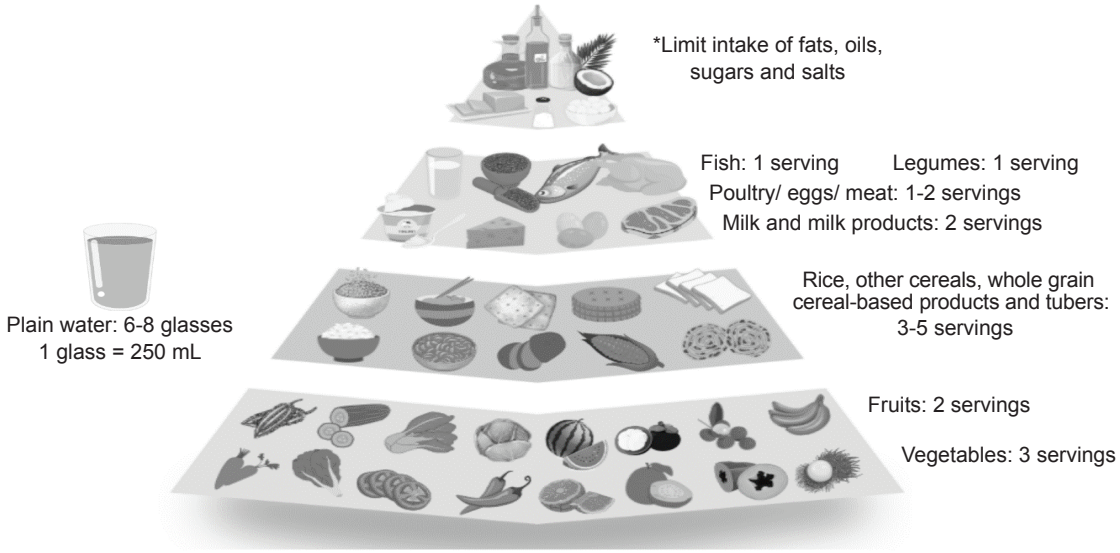
Of note, there are also specific short-term dietary patterns such as Atkins and ketogenic diets, which are mainly adopted by individuals with certain health conditions such as obesity, pre-diabetes, epilepsy, and mild cognitive impairment (Haji-Ghazi Tehrani *et al.*, 2022; Nagpal *et al.*, 2019). The Atkins diet encourages a higher protein intake from meat while reducing carbohydrate consumption. This approach has been heavily modified recently and is now known as the modified Atkins diet, serving as a transition towards the ketogenic diet (Kossoff *et al.*, 2013). The modified Atkins diet has demonstrated promising results in weight loss (Bueno *et al.*, 2013).

TABLE 1. DIFFERENT DIETARY PATTERNS AND RECOMMENDED INTAKE PORTIONS

Dietary patterns	Proximate ratio of macronutrients, % kcal	Food recommendation	Reference
USDA diet	• Carbohydrates, ~55%-60% • Proteins, ~15% • Fats, 21%≤30%	• Consume large portion of grains (preferrable whole grains), vegetable (variety of vegetables, including legumes, starchy) • Variety fruits, preferable whole fruits (2-4 servings) • Variety proteins from lean meat, poultry, fish, eggs, seafood, dry beans, soy products, lentils, peas and nuts (2-3 servings) • Moderate dairy, including milk, cheese, yogurt, fortified soy beverages (2-3 servings) • Sufficient vitamin D and calcium supplements • Sufficient intake of vegetable oils • Limit *trans* and saturated fats, red meat, butter, salt, sugars, refined grains and alcoholic beverages	DeSalvo *et al.* (2016); Fernandez *et al.* (2021)
Dutch diet	• Carbohydrates, 40%-70% • Proteins, 10%-25% • Fats, 20%-40%	• Eat plenty of vegetables, fruits, wholegrain, nuts, and legumes • Moderate dairy, fish, fats and oils, tea and coffee • Limit consumption of red meat, processed meat, sweetened beverages, alcohol, salt	Looman *et al.* (2017)
Japanese diet	• Carbohydrates, 50%-70% • Proteins, 20%-30% • Fats, 15%-25%	• 5-7 servings of grain dishes • 5-6 servings of vegetables • 3-5 servings of fish and meat dishes • 2 servings of milk or milk products • 2 servings of fruits • Moderate intake of snacks, confection and alcohol • Drink plenty of water or teas	Gabriel *et al.* (2018)
Indian diet	• Carbohydrates, 50%-60% • Proteins, 10%-15% • Fats, 20%-30%	• Eat plenty of cereals, millets, and pulses • Milk as protein source • Moderate intake of eggs, fish, and animal proteins • Reduce intake of butter, ghee, and hydrogenated fats and red meat • Eat nuts • Eat plenty of vegetables and fruits • Diversify food choice • Avoid alcohol and smoking	Manual (2011)
Chinese diet	• Carbohydrates, 55%-65% • Proteins, 20%-30% • Fats, 15%-20%	• 5-6 servings of cereals, tubers, legumes • 4-5 servings of vegetables (priorities dark-coloured vegetables) • 3-4 servings of fruits • 2-3 servings of lean meat, eggs and fish • 2-3 servings of soybeans or soy products, nuts and dairy products • Moderate intake of oil • Limit salt, sugar, and alcohol intake • Drink plenty of water	Wang *et al.* (2016)

TABLE 1. DIFFERENT DIETARY PATTERNS AND RECOMMENDED INTAKE PORTIONS (continued)

Dietary patterns	Proximate ratio of macronutrients, % kcal	Food recommendation	Reference
Spain diet	• Carbohydrates, 50%-60% • Proteins, 25%-35% • Fats, 20%-30%	• Moderate intake of meat and meat products, fish and eggs • 2-4 servings of milk and dairy products • 2 or more servings of legumes and nuts • 4-6 servings of cereals and potatoes • 2 or more servings of vegetables (250-300 g daily) • 3 servings of fruits • Moderate lean meats and plant oils intake; recommended use olive oil • Limit animal fats and *trans*-fat intake • Reduce sugary foods and drinks • Drink plenty of water, moderate intake of tea • Reduce alcohol intake	Aranceta *et al.* (2001)
Mediterranean diet	• Carbohydrates, ~55%-60% • Proteins, ~15% • Fats, 21%≤30%	• Drink plenty water • 2 portions of vegetables with a variety of colours/textures • Olive oil as the main choice of fat source • 1-2 portion(s) whole grain bread/ pasta/ rice/ couscous/ cereals/ potatoes • 1-2 portion(s) nuts/ seeds • Herbs/ spices/ garlic/ onions • Legumes • 2 portions of dairy • Variety of flavours • 1/3 portion of egg /fish/ seafood/ white meat • Less read meat and processed meat and sweet	Serra-Majem *et al.* (2020)
Vegen diet (without all flesh foods) Vegetarian diets (without all flesh foods, but also include egg (ovo) and/or dairy (lacto) products)	• Carbohydrates, ~60% • Proteins, ~10%-15% • Fats, ≤20%	• Legumes, soya foods and meat analogues, nuts and seeds, grains, potatoes, tomatoes, avocados, fruits and vegetables. • Some amounts of eggs and dairy products for those following the ovo-lacto diet • Low intake of sweets, snack foods,and soda drinks • Drink plenty of water	Orlich *et al.* (2014)
Atkins diet	• Carbohydrates, ≤40% • Proteins, ~30% • Fats, 30%-55%	• Large portion of protein sources such as fish, seafood and beef, poultry, pork and soy products • Vegetables – green leafy vegetables (2 cups per day); broccoli, cauliflower, spinach, asparagus (1 cup per day) • Fruits – blueberries, pears, raspberries, avocados • Oils – vegetable and seed oils • Unlimited eggs • Cheese and milk (4 ounces per day) • Legumes, nuts and whole grain foods • Carbohydrate (25 to 50 g per day) • 8-ounce glasses of water (at least 6 cups)	Atkins (2002)
Ketogenic diet	• Carbohydrates, ~5%-10% • Proteins, ~10%-20% • Fats, 50%-70%	• Natural fats – Olive oil, coconut oil, avocado • Moderate amounts of meats, fish, poultry • Dairy (cheese, heavy cream, butter, ghee) • Eggs • Vegetables (green leafy vegetables, avoid starchy root vegetables) • Small amounts of berries, dark chocolate (>90% cocoa) • Avoid soda drinks, milk, yogurt, candy, pastries, all starch foods including grains, limit intake of beans and lentils	Carroll and Koenigsberger (1998)



Note: 1. The recommended number of servings is calculated based on 1500, 1800 and 2000 kcal.
2. Less active/sedentary adults should choose the minimum number of servings.

Figure 4. The Malaysian Food Pyramid 2020 illustrated the proportion of food groups in a healthy Malaysian diet in daily food intake (adopted from the Ministry of Health Malaysia).

The ketogenic diet is characterised by consuming exceptionally high-fat content, moderate protein intake and very little carbohydrates (*Table 1*). Foods commonly found in the ketogenic diet include olive oil, coconut oil, avocado, moderate amounts of meat, poultry, seafood, eggs, nuts and green leafy vegetables, berries and dark chocolate (*Table 1*). This diet induces a state of ketosis, where the body utilises fat instead of glucose for energy, resulting in elevated levels of ketone-bodies. This metabolic shift has been associated with a reduction in pro-inflammatory Th17 cells in the gut and visceral adipose tissue (Ang *et al.,* 2020), which may reduce the risk of inflammation and obesity (Mohammadifard *et al.,* 2022). Notably, a meta-analysis on individuals following a ketogenic diet has shown that BSCFA levels are increased due to the degradation of branched amino acids from protein sources (Ferraris *et al.,* 2021), but total SCFA levels decrease due to limited fibre intake (Rew, 2022). These dietary changes are reflected in the gut microbiota composition, which is characterised by a lower abundance of butyrate-producing bacteria (Louis and Flint, 2017).

MACRONUTRIENTS AND PATHWAYS FOR FERMENTING SCFA

Recent studies have shown that diets rich in certain dietary components significantly affect gut microbiota compositions. These bacteria exhibit different abilities to ferment SCFA based on different rate-limiting catalytic enzyme pathways (Xu *et al.,* 2020b). Short-term dietary intervention studies, ranging from a single day to several months (David *et al.,* 2014; Pagliai *et al.,* 2020), have shown that altering macronutrient proportions can influence gut microbiota composition and SCFA profiles.

Effects of Macronutrients on SCFA-Producing Bacteria in Short-term Interventions

Carbohydrates. A diet rich in unprocessed, high-fibres foods is a good food source for the gut microbiota especially for the phyla Actinobacteria and Firmicutes, which play an important role in SCFA metabolism (Bolte *et al.,* 2021). Resistant starch (RS) is a type of carbohydrate naturally found in grains, legumes, seeds, raw bananas and potatoes, and precooked rice (Ashwar *et al.,* 2015). It serves as an excellent precursor for gut-fermented SCFA (Abreu *et al.,* 2021). A study of 20 healthy volunteers who consumed 48 g of raw potato starch, containing 50% RS for one week showed a significant increase in the relative abundance of SCFA producing bacteria, particularly *Ruminococcus bromii*, *Bifidobacterium adolescentis*, and *Eubacterium rectal* (Venkataraman *et al.,* 2016). These bacteria are responsible for RS degradation and butyrate production (Ze *et al.,* 2012). Of particular interest, *R. bromii* has a distinct organisation of some amylolytic enzymes that form complexes through cohesion and dockerin interaction, enhancing their ability to degrade starch (Xu *et al.,* 2015). Furthermore, *Clostridiales* and *Dorea* are also involved in the assimilation of starch, as

shown in a study with mice that were fed isotopically labelled RS (Herrmann *et al.*, 2018).

Other indigestible starch components such as soluble dietary fibre also increase SCFA levels. Consumption of 5-12 g of inulin or oligosaccharides, which consist of highly branched molecules, was found to result in significant fermentation by *Faecalibacterium prausnitzii* and *Bifidobacterium* (Holscher *et al.*, 2015; Vandeputte *et al.*, 2017). This finding is in accordance with a meta-analysis conducted by So *et al.* (2018), who found higher faecal butyrate with a high abundance of *Bifidobacterium* spp. and *Lactobacillus* spp. in individuals following a high-fibre diet.

Foods rich in whole grains and high in insoluble fibre such as cellulose are also excellent sources of nutrition for the gut microbiota but to a lesser extent. A diet rich in cellulosic materials promotes the growth of acetate and propionate producers, especially *Xylanibacter* and *Prevotella* (Iljazovic *et al.*, 2021; Ueki *et al.*, 2006). High proportions of *Prevotella* and *Xylanibacter* are often linked to vegetarian and high-fibre diets, suggesting their role in the hydrolysis of cellulose and xylan from dietary fibre (De Filippo *et al.*, 2010; Sánchez-Tapia *et al.*, 2019).

Proteins. The effect of proteins on gut microbiota compositions has not yet been fully researched. Depending on the type of diet, approximately 6-18 g of proteins is further degraded in the colon to peptides or amino acids daily by the host or bacterial-derived proteases and peptidases (Neis *et al.*, 2015). These degradation products can be further utilised by proteolytic bacteria and lead to the production of SCFA and BSCFA. Excessive protein consumption has been associated with an increased abundance of peptide and amino acid-fermenting bacteria that degrade branched-chain amino acids, such as *Bacteroides* and *Clostridium*, leading to increased levels of BSCFA, namely isovaleric acid and isobutyric acid, and smaller amounts of 2-methylbutyric acid (Aguirre *et al.*, 2016). These bacteria are also known to possess strong peptidase activity (Oliphant and Allen-Vercoe, 2019). A study of 17 obese men who underwent a high-protein but low-carbohydrate diet for four weeks showed that a high-protein diet increased BSCFA concentrations in the presence of toxic compounds such as phenylacetic acid and N-nitroso compounds while lowering butyrate levels and decreasing *Roseburia* and *E. rectale* (Russell *et al.*, 2011).

Some SCFA-producing bacteria such as *Prevotella bryantii* (Trautmann, *et al.*, 2020) and *Lactobacillus casei* (Chen *et al.*, 2019) can efficiently degrade peptides especially peptides that consist of more than three amino acids in their chain such as casein into nitrogen for growth (Kim *et al.*, 2017; McIntosh *et al.*, 2009). These bacteria possess dipeptidyl peptidase activity that is involved in protein digestion and the host metabolism such as regulating the secretion of glucagon-like peptide 1 (GLP-1) and gastric inhibitory polypeptide (GIP) involved in glucose haemostasis (Olivares *et al.*, 2018). Studies have also shown that different protein sources in the diet have an impact on gut bacterial species and BSCFA (*Table 2*). Consumption of chicken meat promotes the growth of *Faecalibacterium, Prevotella* 9, *Dialister* and *Megamonas*, but consumption of pork leads to the growth of *Bacteroides*, *Faecalibacterium, Roseburia, Dialister* and *Ruminococcus*. This results in different levels of SCFA and BSCFA in the gut (Shi *et al.*, 2021). Similarly, animal-derived protein sources such as fish promote the growth of *Lactobacillus* and *Oscillibacter* (An *et al.*, 2014), while consumption of dried skimmed milk and milk casein increased *Lactobacilli* and *Bifidobacterium* (Zhang *et al.*, 2020) but lower *Staphylococci, Coliforms* and *Streptococci* counts (Zhao *et al.*, 2018) in porcine and rat. Conversely, less digestible plant proteins such as peanuts and soybeans (Day *et al.*, 2022), consist of indigestible cell wall components that demonstrated a higher fermentability. This leads to an increased content of acetic and lactic acid and an increased abundance of *Bifidobacterium*. Different proteins possess different amino acids that make up the protein structure and yield different gut microbiota compositions. For example, vegetarians showed significantly higher plasma concentrations of methionine, tryptophan, alanine, glutamate, glycine, and tyrosine but lower lysine compared to meat- and fish-eaters (Schmidt *et al.*, 2016). Gut microbiota synthesises butyrate from lysine and glutamate, while propionate is mainly synthesised from alanine, methionine and threonine and acetate from glycine, alanine and lysine (*Figure 3*).

Dietary fats. The effects of fats on gut microbiota composition and SCFA production generally depend on the degree of fat saturation and the amount of dietary fat consumed. Extensive clinical studies in human and animals have consistently demonstrated that diets high in SFA promote the growth of *Firmicutes*, *Enterobacteriacea* and *Proteobacteria*, while concurrently reducing the abundance of *Bacteroidetes* and *Lactobacillus* (Heinritz *et al.*, 2016; Ley *et al.*, 2006; Wu *et al.*, 2011; Zhang *et al.*, 2012). High SFA content is often used as a comparator when studying the effects of dietary fats on gut microbiota. However, it is important to note that an increase in fat intake may inadvertently lead to lower energy intake from other macronutrients such as complex carbohydrates, and this reduces the abundance of saccharolytic bacteria such as *Bifidobacterium, F. prausnitzii,* and *Ruminococcus* (Fava *et al.*, 2013; Shen *et al.*, 2012).

In a study comparing the effects of diets high in SFA, MUFA, carbohydrate, or sugar on the gut microbiota of 88 subjects at risk of metabolic

TABLE 2. EFFECTS OF DIET COMPONENTS ON GUT MICROBIOTA PRODUCING SCFA

Diets	SCFA	Gut microbiota	Reference
Resistant starch	Butyrate, acetate	*Ruminococcus bromii, Bifidobacterium adolescentis,* and *Eubacterium rectal*	Venkataraman *et al.* (2016)
		Bifidobacterium	Alfa *et al.* (2018)
Oligosaccharides	Butyrate	*Bifidobacterium* spp. *Lactobacillus* spp.	So *et al.* (2018)
Insoluble fibres	Acetate, propionate	*Xylanibacter, Prevotella,* and *Faecalibacterium*	Holscher *et al.* (2015); Iljazovic *et al.* (2021); Ueki *et al.* (2006); Vandeputte *et al.* (2017)
Proteins	SCFA and BSCFA (isobutyric, isovaleric, and 2- methylbutyric acids)	*Bacteroides*, *Clostridium*, *Faecalibacterium, Roseburia, Dialister,* and *Ruminococcus 2*	Aguirre *et al.* (2016); Smith and Macfarlane (1998)
High SFA	SCFA	*Firmicutes, Enterobacteriacea, Proteobacteria, Lactobacillus, Prevotella,* and *Alistipes*	Heinritz *et al.*, 2016; Wu *et al.* (2011); Zhang *et al.*, 2012; Zhao *et al.* (2018)
High MUFA	Propionate	*Oscillspira, Faecalibacterium prausnitzii,* and *Roseburia*	Haro *et al.* (2016); Muralidharan *et al.* (2019)
High PUFA (EPA, DHA)	Butyrate	*Coprococcus, Roseburia,* and *Blautia*	Ochoa-Repáraz and Kasper (2016)

Note: SCFA - short chain fatty acids; SFA - saturated fatty acids; MUFA - monounsaturated fatty acids; PUFA - polyunsaturated fatty acids; EPA - eicosapentaenoic acid; DHA - docosahexaenoic acid.

syndrome over a 24 weeks period, it was found that a diet high in SFA yielded greater SCFA abundance compared to other diet groups (Fava *et al.*, 2013). Conversely, a diet rich in MUFA, akin to the Mediterranean diet, increases the abundance of SCFA-producing bacteria (Haro *et al.*, 2016; Muralidharan *et al.*, 2019). It is noteworthy that the Mediterranean diet is also high in vegetables and fruits and the effect of MUFA could be confounded by these dietary fibres. PUFA-rich diets, particularly those rich in omega-3 fatty acids, have been shown to elevate the abundance of butyrate-producing colonic bacteria, namely *Coprococcus*, *Roseburia*, and *Blautia* (Ochoa-Repáraz and Kasper, 2016) (*Table 2*).

Some researchers suggest that various dietary fats indirectly influence the gut microbiota composition by influencing bile acid secretion from the colon (Just *et al.*, 2018). It is known that a high-fat diet increases bile acid secretion, resulting in these bile acids being converted into secondary forms to prevent reabsorption in the colon (Park *et al.*, 2022). These secondary bile acids may subsequently reshape the composition of the gut microbiota by enhancing the abundance of bile-tolerant bacteria (Yokota *et al.*, 2012).

Pathways involved in SCFA production. The pathways of SCFA production have been summarised in detail by Xu and colleagues (Xu *et al.*, 2020b). Four general pathways for SCFA production have been identified. First, SCFA is produced from carbohydrates, which involves the degradation of dietary fibre to monomers (pentoses) and various sugars and oligosaccharides. These substrates are degraded by glycolysis, yielding pyruvate molecules (*Figure 5*). In addition, SCFA can be synthesised from acetate and ethanol by extending the carbon chain. Acetate, derived from beta-oxidation of dietary fats and deamination of amino acids from proteins, reacts with coenzyme A (CoA) to form acetyl-CoA (*Figure 5*). Pyruvate and acetyl-CoA serve as the main precursors in the citric acid cycle and contribute to the production of SCFA. Third, amino acids such as valine, leucine and iso-leucine undergo decarboxylation and reduction to synthesise BSCFA. Lastly, unique substrates such as carbon dioxide molecules are involved in the synthesise of acetate via the Wood–Ljungdahl pathway, while lactate contributes to the synthesise of propionate (*Figure 5*).

Recent studies have identified 74 key SCFA-producing bacterial species in different research groups (Xu *et al.*, 2020b). Approximately 80% of these SCFA-producing bacteria are members of Firmicutes phylum, mainly from the *Clostridiaceae* and *Lachnospiraceae* families. Of these, many species are recognised as butyrate producers, including *Clostridium*, *Eubacterium, F. prausnitzii, Subdoligranulum variabile, Anaerostipes, Coprococcus*, and *Roseburia*. Some of these bacteria such as *Clostridium* sp., *Coprococcus* and *Roseburia, A. muciniphila*, *Ruminococcus* spp. produce acetate and propionate in addition to butyrate (Flint *et al.*, 2015; Reichardt *et al.*, 2014).

Certain bacterial strains such as *Prevotella copri* and *P. stercorea* are major producers of longer-chain SCFA valerate (C5) (Almeida *et al.*, 2019), whereas *Veillonellaceae*, such as *Megasphaera elsdenii* and *Megasphaera* sp. *Roseburia*, *Megasphaera* and *Clostridium* have demonstrated an excellent ability

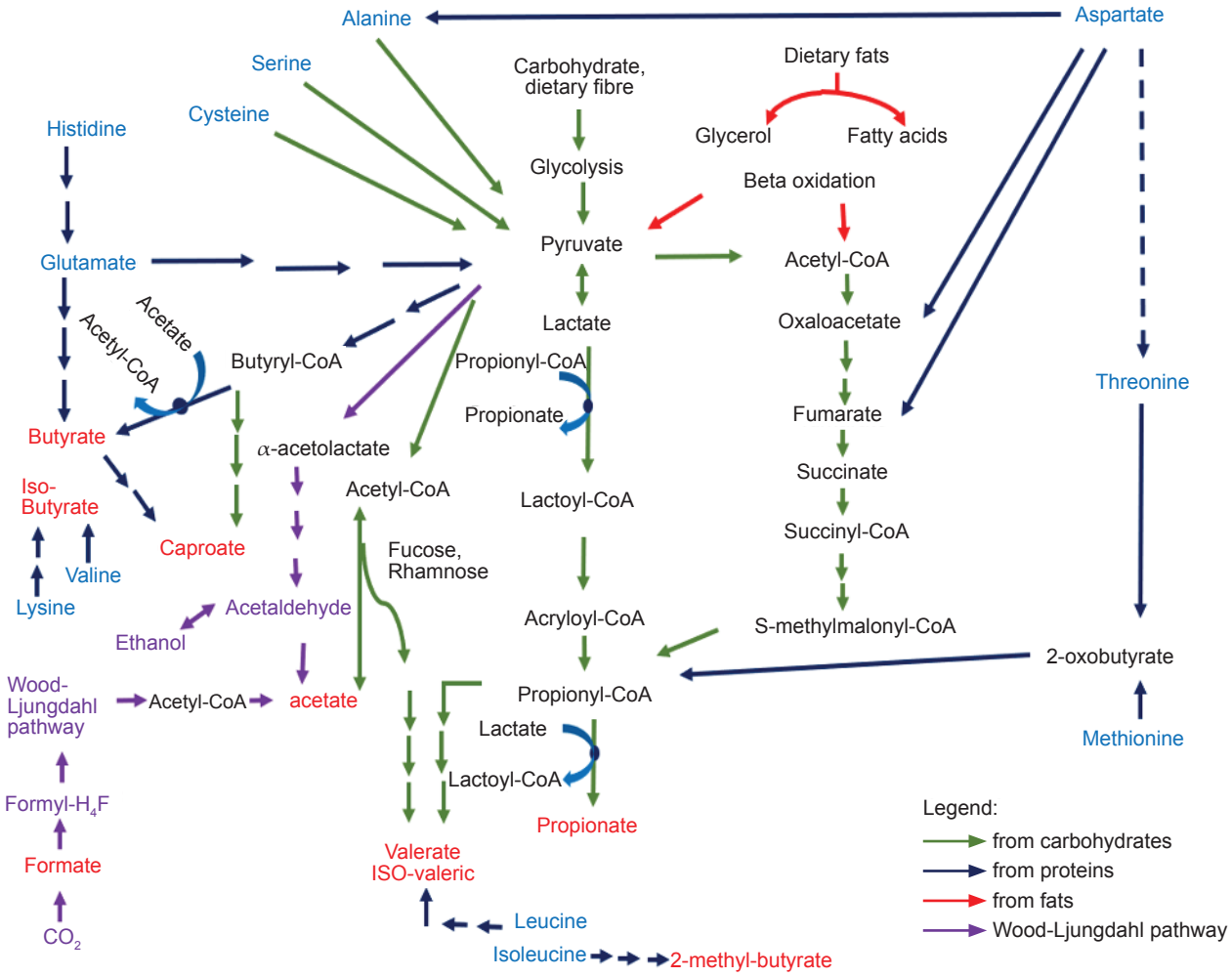


Figure 5. Pathways of SCFA production from macronutrients.

to produce multiple types of SCFA (Reichardt *et al.*, 2014). These results suggest that certain gut bacterial species can efficiently utilise different food residues, possibly highlighting the role of a few "core" gut bacteria in regulating SCFA production pathways.

Roseburia and *Faecalibacterium* (*Table 2*) are most abundant in those following high-protein and high-fat diets. These bacteria are postulated to have diverse genes which are involved in several important functional metabolic pathways or that their genes interact with other dietary components. Although short-term replacement of dietary components may affect overall gut health, the gut microbiota is resilient and tends to regenerate back to its original composition when the original diet is resumed. Therefore, holistic nutritional epidemiological studies, can shed light on the true effects of the whole diet and provide a better understanding of the complex relationship between the diet, gut microbiota composition, and the functional pathways for the production of metabolites.

EFFECTS OF LONG-TERM DIETARY PATTERNS ON GUT MICROBIOTA COMPOSITIONS AND SCFA PROFILES ON HEALTH OUTCOMES

Long-term dietary patterns have been explored in detail in several large human cohort studies. Their profound effects on gut microbiota composition, SCFA profiles, associated metabolic pathways and resulting health outcomes are summarised in *Table 3*.

In general, a plant-based diet, such as vegan or vegetarian diet, is associated with higher total SCFA content and promotes greater numbers of SCFA-producing bacteria such as *Roseburia, Ruminococcus, Lachnospira, Dorea, Lactobacillus, Bifidobacterium* and *Prevotella* (*Table 3*). Conversely, high consumption of animal foods has been associated with a reduction in gut bacterial diversity, higher levels of valeric acid, capric acid and BSCFA, and dominance of *Firmicutes*, *Streptococcus* and *Ruminococcus*, possibly stimulating endotoxin synthesis pathways.

The Mediterranean diet promotes a healthy diet high in fibre (*Table 3*). High adherence to this

diet results in increased total SCFA, particularly acetate (Mitsou *et al.,* 2017) and growth of butyrate-producing taxa such as *Roseburia faecis, R. bromii,* and *Oscillospira plautii*, with a strong association observed for *Bifidobacterium animalis*. In addition, consumption of animal proteins inhibits the growth of *Bacteroidetes*, while consumption of PUFA, particularly from fish and vegetal proteins, tends to cultivate *Prevotella copri*, *Dorea* and *Lactobacillus* (*Table 3*).

Both the Mediterranean and vegetarian diets, which are both rich in plant-based foods, exhibit slight differences in intake of animal protein and olive oil, resulting in slight variations in the composition of gut microbiota at the genus level, while alpha diversity, richness and evenness remain similar (*Table 3*). When comparing the effects of gut microbiota composition of a vegetarian and vegan diet to an omnivorous diet (*Table 3*), Shannon index, which indicates bacterial richness, are found to be significantly different between those who follow vegetarian and omnivorous diets (Ghosh *et al.,* 2020; Trefflich *et al.,* 2021). It is noteworthy that faecal SCFA levels, especially acetate, propionate and butyrate, are higher in plant-eaters, suggesting a correlation between gut microbiota composition, gut fermented SCFA, and dietary fibre content.

Comparative studies between the Mediterranean diet and different dietary habits among the British, French, Dutch, Italians, and Poles revealed some interesting patterns. Strong adherence to the Mediterranean diet for an extended period enhances the abundance of SCFA-producing bacteria. These bacteria have anti-inflammatory properties as evidenced by the negative correlation with proinflammatory markers such as the highly-sensitive C-reactive protein (hsCRP) and IL-17, and this ultimately lowers the risk of frailty in the elderly (Ghosh *et al.,* 2020). Conversely, low adherence to the Mediterranean diet is associated with an abundance of taxa such as *Collinsella aerofaciens*, *Coprococcus comes*, *Clostridium ramosum*, and *Veillonella dispar*, which are associated with a higher risk of T2D, colorectal cancer, and IBD (*Table 3*).

Vegetarian diets typically result in higher proportions of butyrate and valerate, but lower concentrations of branched-chain amino acids. However, in a small cohort study in southern India, contradictory results have reported omnivorous diets increase the abundance of *Clostridium* cluster XIVa and upregulation of the butyryl-CoA: CoA transferase gene, leading to increased butyrate production compared to vegetarian diets (*Table 3*). In a larger cohort of healthy adults following vegan or omnivorous diets, no significant difference was found between SCFA and BSCFA levels (*Table 3*).

Specific core taxa are identified in shaping the effects of a long-term dietary pattern. Omnivorous diets are dominated by three specific core taxa, namely *Lachnospira*, the NK4A136 group of the *Lachnospiraceae* and *Ruminiclostridium*. Conversely, the vegetarian diet resulted in an abundance of seven core taxa, mainly SCFA-producing bacteria together with three rare genera. The rare taxa are *Tyzzerella, Succinivibrio* and *Shuttleworthia*, which are positively correlated with SCFA and BSCFA levels (*Table 3*).

A well-studied Dutch cohort study provided insight into certain bacterial taxa with significant health implications. Of these bacterial taxa, *Christensenellaceae* stands out as being inversely proportional to the size of very-low-density lipoprotein (VLDL) particles, small high-diversity-lipoprotein (HDL) particles and triglycerides in medium HDL. These results suggest a possible role in lipid metabolism, cardiovascular risk reduction and body weight regulation (Goodrich *et al.,* 2014). *Clostridiaceae* 1 and the genus *Clostridium sensu stricto* are associated with very large and large HDL particles, suggesting an association with lower BMI and lower blood triglyceride levels, which reduces the risk of stroke and CVD. *Ruminococcaceae* is associated with acetate production, while *Lachnospiraceae* and *Blautia* are involved in upregulating 7α-dehydroxylation genes to accelerate metabolism from primary to secondary bile acids (Ridlon *et al.,* 2013; Vital *et al.,* 2019) and producing butyrate from lactate (Duncan *et al.,* 2004). Overall, these long-term cohort studies have shown that diet undoubtedly affects the gut microbiota composition at the lower phylogenetic level and the metabolome produced by these bacteria. Adherence to certain dietary patterns is important to maintain a stable "core" community of gut microbiota to perform certain core functional metabolic pathways.

PROSPECTIVE OF MALAYSIAN DIET CONTAINING PALM OIL

The Malaysian diet is unique in that it offers a wide variety of food choices. However, findings from the National Health and Morbidity Survey NHMS 2019 Technical Report (Ganapathy *et al.,* 2019) revealed a concerning high consumption of energy-dense foods and sugary beverages. Approximately, 94.9% of Malaysians have neglected to consume the recommended amounts of fruits and vegetables coupled with inadequate dietary fibre intake. Therefore, the Malaysian public is encouraged to reduce the consumption of refined sugar and sugary drinks and increase consumption of fruits, vegetables and unprocessed foods. When high adherence to this dietary guideline is achieved, a healthy gut environment with a stable gut microbiota community follows.

TABLE 3. EFFECTS OF DIFFERENT DIETS PATTERN ON SCFA PRODUCING GUT MICROBIOTA (continued)

Diet	Study design, duration, participants	Main food sources/ food components	Outcomes	Reference
Mediterranean diet	Cross-sectional, Healthy 251 F and 109 M, 45.0 ± 10.5 yo; BMI: 25-30 kg/m^2	Macronutrients intake: Carbohydrate, 54%-55% Proteins, 21%-22% Fats, 23%-24% Fibre, 24%-36%	• A strict Mediterranean diet is associated with increased abundance of butyrate-producing bacteria such as *Roseburia faecis*, *R. bromii* and *Oscillospira plautii* • *Bifidobacterium animalis* are strongly associated with the Mediterranean diet	Rosés *et al.* (2021)
Mediterranean diet	116 subjects: 61 M, 55 F; mean age 42 yo; BMI 25-30 kg/m^2. Adherence of med diet was accessed using MedDietScore. Low MedDietScore indicates high intake of fast food, high fats, sugar and processed food	Non-refined cereals, potatoes, legumes, fruits, vegetables, olive oil, fish; moderate meat, meat products, poultry, dairy; low alcohol	• 68% subjects showed moderate to high adherence to the Mediterranean diet • High adherence in MedDietScore tertiles showed higher levels of acetate but lower levels of caproic acid • A high MedDietScore was positively associated with total bacteria and *Candida albicans* counts and the ratio of bifidobacterial to *Escherichia coli* but negatively associated with the concentration of valeric acid and *E. coli* after adjusting for the BMI, gender and age • Fast food intake suppressed the abundance of *Lactobacilli* and butyrate-producing bacteria	Mitsou *et al.* (2017)
Mediterranean diet	27 healthy adults (11M, 16 F; 39.5 ± 7.3 yo; lived in Valencia-Spain): PREDIMED score	Non-refined cereals, potatoes, legumes, fruits, vegetables, olive oil, fish; moderate meat, meat products, poultry, dairy; low alcohol	• High protein intake lowers the abundance of *Bacteroidetes*, whereas animal proteins, saturated fats and sugars reduced bacteria diversity • High intake of vegetal protein was associated with high abundancy of butyrate-producing bacteria such as *Dorea, Coprococcues*; as well as *Roseburia* and *Bifidobacterium* • Higher intake of PUFA/SFA increased the abundancy of *Dorea* and *Lactobacillus* • High intake of plant-based nutrients increases the bifidobacterial counts, and total SCFA levels • Higher adherence to MedDiet Score also increased total SCFA	Garcia-Mantrana *et al.* (2018)
Mediterranean, vegan dan vegetarian diets	Cohort study: 153 healthy Italian; 51 omnivores (23M, 28F; BMI 22.1 ± 2.0 kg/m^2); 51 vegan (23M, 28F, BMI 21.3 ± 2.2 kg/m^2); 51 vegetarian (18M, 33F; 21.9 ± 2.5 kg/m^2), with 88% of them are medium or highly adhered to the Mediterranean diet.	High intake of cereals, fruits, vegetables and legumes	• Alpha diversity did not significantly vary across these three diets • Significant relationship between genus-level microbiota composition and habitual diet in PCA plot • *Lachnospira, Roseburia* and *Prevotella* was associated with a plant-based diet, while *L-Ruminococcus* and *Streptococcus* were associated with an animal-based diet • Faecal acetate, propionate and butyrate were associated with a high plant-based foods intake, while valeric and caproic acids were associated with a high protein and high fat diet intake	Filippis *et al.* (2016)

TABLE 3. EFFECTS OF DIFFERENT DIETS PATTERN ON SCFA PRODUCING GUT MICROBIOTA (continued)

Diet	Study design, duration, participants	Main food sources/ food components	Outcomes	Reference
Mediterranean diet *vs*. control diet	Mediterranean diet = 141 M, 182 F, from UK, France, Netherlands, Italy, and Poland; Control diet = 145 M, 144 F, 1 year	Mediterranean (NU_AGE) diet (tailored for elderly): Whole grains, fruits, vegetables, and legumes, dairy and cheese, seafood, meat and poultry, nuts, potatoes, rice, eggs, and olive oil Control diet: Normal habitual local diet intake Accessed with MedDiet score	• Data from these countries showed no significance, but high adherence to Mediterranean diet increased microbiota biodiversity • The control group had higher fat intake than Mediterranean Diet intervention group • Among the 44 Predictive OTUs positively associated with a high MedDiet score were *F. prausnitzzi, Roseburia hominis, Eubacterium, Bacteroides thetaiotaomicron, P. copri* and *Anaerostipes hadrus*. These bacteria are associated with SCFA or BSCFA production and possess anti-inflammatory properties, showing negative correlation with proinflammatory markers hsCRP and IL-17 • Predictive OTUs inversely associated with MedDiet score primarily belonged to taxa of *Collinsella aerofaciens, Ruminococcus torques*, *Coprococcus comes, Dorea formicigenerans, Clostridium ramosum, Veillonella dispar, Flavonifractor plautii* and *Actinomyces lingnae*. Increase abundance of these taxa has been associated with higher risk of T2D, colorectal cancer, IBD • The commercial gut microbiota is positively correlated with dietary fibre, vitamins C and D, plant proteins, and carbohydrates, resulting elevated SCFA levels and decreased secondary bile acids	Ghosh *et al*. (2020)
Vegetarian diet (VD) *vs*. omnivorous (O)	32 lacto-vegetarian and 24 omnivorous women from South India Age, 19 yo; BMI 20-21.9 kg/m^2 FFQ, 24-hr diet recall	VD, dietary intakes: Simple carbohydrate: 29.5 (g/d) Complex carbohydrate: 225 (g/d) Proteins: 30 (g/d) Fats: 21.5 (g/d) Fibre: 2.9 (g/d) O, dietary intakes: Simple carbohydrate: 25.5 (g/d) Complex carbohydrate: 246 (g/d) Proteins: 32 (g/d) Fats: 20.5 (g/d) Fibre: 2.95 (g/d)	• In the omnivorous group, the faecal microbiota composition exhibited an increase in *Clostridium* cluster XIVa, specifically *Roseburia–E. rectale* • *Clostridium* cluster XIVa and *Roseburia–E. rectale* are positively associated with faecal butyrate, with a weaker correlation observed for *Clostridium leptum* and *F. prausnitzii* • Omnivores have displayed a higher proportion of *Clostridium* cluster XIVa and butyryl-CoA:CoA-transferase gene compared to vegetarians	Kabeerdoss *et al*. (2012)

TABLE 3. EFFECTS OF DIFFERENT DIETS PATTERN ON SCFA PRODUCING GUT MICROBIOTA (continued)

Diet	Study design, duration, participants	Main food sources/ food components	Outcomes	Reference
Vegetarian diet (VD) *vs*. omnivorous (O)	Healthy vegans (n = 57) and omnivore (n = 33) subjects. Cross-sectional study 3 days dietary record	VD, dietary intakes (g/d): Carbohydrate: 250 Proteins: 69 Fats: 70 Fibre: 33 O, dietary intakes (g/d): Carbohydrate: 232 Proteins: 81 Fats: 83 Fibre: 18	• Long-term adherence to a vegan diet has greater effects (43.3%) on faecal metabolomes than the feacal bacterial genera • Vegans diet resulted in higher proportion of polysaccharide fermentation products such as MCFA, SCFA (especially butyric and valeric acids) and their derivatives in faeces, and lower proportion of branched chain amino acid compared to omnivores • Of 58 genera detected in both vegetarian and omnivorous diets, ten genera are identified as the core microbiome. Three of them (*Lachnospira*, *Lachnospiraceae* NK4A136 group, and Ruminiclostridium) were found to be more abundant in the omnivores, whereas seven genera (*Anaerostipes*, *Blautia, Alistipes, Dorea, Fusicatenibacter, Bifidobacterium, and Ruminococcaceae*_uncultured) were less abundant in the vegans compared to omnivores	Prochazkova *et al*. (2022)
Vegetarian diet (VD) *vs*. omnivorous (O)	Healthy vegans (n = 36); omnivores (n = 36) Cross-sectional study	VD: Vegetables, legumes, mushroom, confectionery, fruits, cereal, wholegrains, nuts, vegetable oils, soy milk, soy-products, vegetarian spread O: Meat, fish, poultry, processed meat, dairy products, animal fats, alcohol, vegetables, grains, fruits, confectionery, butter.	• Random forest regression analysis indicated no significant SCFA and BCFA concentration differences between vegans and omnivores, implying bacterial adaptability to diverse nutrient availability in these diets • At the species level, omnivores exhibited significantly higher Shannon diversity ($p = 0.04$) than vegans • In vegans, a cluster of *F. prausnitzii, Prevotella copri, Dialister* spp. and *Eubacterium* spp. affect • SCFA and BCFA concentrations • For omnivores, *Bacteroides* spp., *Clostridium* spp., *Ruminococcus* spp. and *Prevotella copri* affect SCFA and BCFA concentrations	Trefflich *et al*. (2021)
Dutch diet	1425 subjects from four cohorts: Crohn's disease, ulcerative colitis, irritable bowel syndrome and the general population	Dairy, cheese, meat (sausage, meatball), breads, potatoes, cereals, boiled vegetables, salad, fruits, butter, egg, legume, alcohol. Dietary intakes (g/d): Carbohydrate: 208.24-228.37 Proteins: 67.09-74.79 Plant protein: 27.34-30.85 Animal protein: 38.65-44.05 Fats: 71.77-80.66 Alcohol: 4.13-8.53	• Regular intake of processed and animal-derived foods correlated with higher abundance of *Firmicutes*, *Ruminococcus* and *Blautia*; along with pathways related to endotoxin production • Conversely, plant-based foods and fish were positively associated with SCFA-producing bacterial and pathways related with nutrient metabolism	Bolte *et al*. (2021)

TABLE 3. EFFECTS OF DIFFERENT DIETS PATTERN ON SCFA PRODUCING GUT MICROBIOTA (continued)

Diet	Study design, duration, participants	Main food sources/ food components	Outcomes	Reference
Dutch diet	2309 individuals from Rotterdam Study and the LifeLines-DEEP cohort	Grains, dairy, fruits, vegetables, legumes, potatoes, poultry, meat, processed meat, eggs, tea, coffee, soda, alcohol	• The *Christensenellaceae* family, being highly heritable, has an inverse correlation with various VLDL particle sizes, small HDL particles and triglycerides in medium HDL • *Clostridiaceae 1* and genus *Clostridium sensu stricto* are associated with very large and large HDL particles, and potentially decrease risk of stroke and CVD • *Clostridiaceae 1* is inversely related to BMI and blood TG levels • *Ruminococcus gnavus* is associated with serum triglycerides levels • *Lachnospiraceae* and *Blautia* are associated with small HDL particle • *Ruminococcaceae UCG-005* was associated with acetate • *Ruminococcaceae, Lachnospiraceae* and *Blautia* convert primary bile acids into secondary bile acids and production SCFAs	Vojinovic *et al.* (2019)

Note: RCT - Randomised cross over trial; T2D - Type 2 Diabetes; %en - percent energy; hsCRP - high-sensitivity C reactive protein; IL-17 - interleukin 17; BMI - body mass index; MCFA - medium chain fatty acid; VLDL - very low density lipoprotein; HDL - high density lipoprotein; TG - triglycerides; yo - years old.

Around 25 years ago, a study examining the fat intake of Malaysians found that the nation diet contained 40-66 g of fat daily which is equivalent to 22%-26% of total calorie intake (Ng, 1997). Two decades later, Malaysians are found to typically consume 58 g of fat, accounting for 29.2% of total calorie intake. This approaches the upper bound of the recommended limit (Lee and Muda, 2019). Malaysians are also found to have a marginal increase in protein consumption and decreased carbohydrate intake, albeit dipping slightly below the recommended range (Lee and Muda, 2019).

Malaysian Diet and SCFA-Producing Bacteria

A comprehensive understanding of the composition of gut microbiota and its SCFA profiles in the context of long-term Malaysian dietary patterns remains limited. Some noteworthy works have been conducted to investigate either the SCFA or the gut microbiota profiles alone for specific aspects. These include studies conducted in pre-adolescents (Chong *et al.*, 2015) and young adults following *Helicobacter pylori* eradication (Yap *et al.*, 2016), probiotic intake in adolescents (Joseph *et al.*, 2019) and the effects of fermentable oligosaccharides, disaccharides, monosaccharides and polyols (FODMAP) (Khoo *et al.*, 2023) in both healthy adults and patients with IBD (Huda-Faujan *et al.*, 2010), and the effect of ethnicity on gut microbiota composition and SCFA profile (Dwiyanto *et al.*, 2021) (*Table 4*). Of these, only two studies (Dwiyanto *et al.*, 2021 and Khoo *et al.*, 2023) provide detailed dietary records and explore the correlation of SCFA to gut microbiota.

Very few studies have been conducted to investigate the composition of the gut microbiota and the corresponding SCFA concentrations in people following a typical Malaysian diet. Analysis of some available data in *Table 4* suggests that the SCFA profiles of healthy adults (control) contain mainly acetate, propionate and butyrate, and relatively low levels of BSCFA such as isobutyrate (*Table 4*). The higher concentration of butyric acid compared to propionic acid suggests a higher consumption of starchy staple foods, particularly rice, by the Malaysian population (Huda-Faujan *et al.*, 2010) or subtle differences in the diets of different ethnic groups (Shafiee *et al.*, 2022).

Firmicutes and Bacteroidetes are the main phyla among healthy Malaysians, and Actinobacteria and Proteobacteria were also found in lower abundance. In addition, SCFA-producing genera such as *Faecalibacterium* and *Prevotella* have also been identified. Indigenous children were found to have a higher abundance of *Aeromonadales* and *Ruminococcaceae* (*Table 4*), which is probably related to the degradation of high-fibre foods such as *ulam*, a popular food in the indigenous diet (Shafiee

et al., 2022). A multi-ethnic study by Dwiyanto *et al.* (2021) demonstrates that the influence of ethnicity on the composition of gut microbiota is related to different lifestyles and dietary patterns of different ethnic groups (*Table 4*). Conversely, Khine *et al.* (2019) found that dietary habits affect gut microbiota composition even among individuals from the same ethnic group living in different geographical areas, including Chinese from Guangzhou city (China), Penang city (west coast of Malaysia) and Kelantan city (Malaysia). However, these studies lack detailed information on dietary intake, especially on the type and quantity of edible oils.

The inclusion of palm oil in a balanced Malaysian diet has promising health benefits and should be further explored. Palm oil is known for its unique fatty acid profile and antioxidant properties and has long been used as an important ingredient in Malaysian cuisine. High adherence to the balanced Malaysian diet, which is typically prepared with palm oil, has the potential to create a favourable environment for gut microbiota (Yap *et al.,* 2022) and improve SCFA production in promoting gut health in Malaysians.

CONCLUSION AND FUTURE PRESPECTIVES

A healthy Malaysian diet should consist of a large proportion of complex carbohydrates from fruits and vegetables which are mainly indigestible fibre, approximately 25% of proteins and 25% of fats, and the remainder being carbohydrates from fruits and vegetables, and also staple foods such as rice. This composition is broadly in line with the recommended ratios of macronutrients found in other notable dietary patterns. Strict adherence to the recommended intake promotes a healthy intestinal environment for gut bacteria.

Although the health benefits of SCFA are well known, there is limited data on the SCFA profile of healthy Malaysians who regularly consume palm oil. Therefore, more clinical data is needed to establish a link between the SCFA profile and other potential health benefits of regular palm oil consumption. This data would not only guide researchers in designing human clinical trials but also allow comparisons with other dietary oils in a balanced diet. These results can also provide valuable insights for policy makers to facilitate the effective implementation of health-conscious dietary recommendations, hopefully reducing the burden of medical costs.

Awareness of healthy diets can be achieved through collaboration between the government and private sectors to create a stable market for healthy foods while providing nutrition education programmes to enhance the public's understanding of good eating habits.

TABLE 4. STUDIES ON SCFA CONTENTS AND GUT MICROBIOTA COMPOSITIONS IN MALAYSIANS

Study	Diet	Results/outcomes	Reference
Malay (n = 24), Chinese (n = 17) and the *Orang Asli* (indigenous) (n = 20), 7-12 yo 5 weeks on normal Malaysia diet	Not provided	• The prominent phyla of gut microbiota were *Firmicutes* and *Bacteroidetes,* while *Feacabacterium* and *Prevotella* are the dominant genera • Analysis of 16S rRNA sequencing revealed elvevated abundance of *Aeromonadales* and an unclassified genus related to *Ruminococcaceae* in *Orang Asli* children compared to Malay and Chinese	Chong *et al.* (2015)
Young healthy volunteers, with Helicobacter pylori positive, 18-30 yo, n = 17	Not provided	• Alpha indexes indicated no significant diversity shifts between baseline and post-eradication; likewise, beta diversity indexes showed no substantial alternations in bacterial community composition across these time point • At baseline, the most abundant phyla were *Bacteroidetes, Firmicutes, Actinobacteria,* and *Proteobacteria* • No SCFA was tested	Yap *et al.* (2016)
Healthy and overweight (BMI ≥ 23 kg/m^2) adults. 4 weeks MCP supplement, n = 12 placebo, n = 14	No dietary record	• No notable differences were observed in fasting blood glucose, body weight, waist circumference, and SCFA content between the treatment and the control group • The content of acetate was 242.0 ± 107.7 mmol/g; propionate, 36.8 ± 16.4 mmol/g; and isobutyrate, 204.4 ± 116.3 mmol/g at the baseline. Results after MCP supplement are not of interest of this article • Gut microbiota composition was not measured	Mahadzir *et al.* (2017)

TABLE 4. STUDIES ON SCFA CONTENTS AND GUT MICROBIOTA COMPOSITIONS IN MALAYSIANS (continued)

Study	Diet	Results/outcomes	Reference

School children, 7-10 yo,
normal weight, n=19 (BMI, 16.07 kg/m^2);
overweigh, n=21 (BMI, 23.82 kg/m^2);
Probiotic drink was provided to the treatment group.
	No dietary record	• At the baseline, acetic concentration was 20.5 mmol/g, butyric, 23.07 mmol/g and propionate, 58.03 mmol/g, respectively
		• Overweight children showed higher total faecal SCFAs concentration, particularly butyrate and propionate than normal weight children
		• Only investigated the abundance of *Lactobacillus* spp and *Bifidobacterium* spp. None of these bacteria were detected in the control group
			Joseph *et al.* (2019)

Compared SCFA content in normal healthy adults (M = 18, F = 32) to IBD patients (M = 6, F = 2)	Normal Malaysian diet, details were not provided	• The concentration of SCFA µmol/g wet faeces (mean ± SEM) in healthy adults are listed below: • Acetate = 209.7 ± 14.0 • Butyrate = 176.0 ± 16.0 • Propionate = 93.3 ± 5.3 • Formic acid = 21.5 ± 9.7 • Isobutyrate = 17.9 ± 13.2 • Gut microbiota composition was not measured	Huda-Faujan *et al.* (2010)
Investigated impact of FODMAP and ethnicity on gut microbiota variation in IBS patients (n = 34, 14M, 19F, 8 Chinese, 20 Malay, 6 Indians; BMI of 23.9 kg/m^2) and healthy controls (n = 15, 6 M, 9 F, 2 Chinese, 11 Malay, 2 Indian, BMI of 20.6 kg/m^2)	3 days self-dietary record. Diet record for control group was not highlighted	• Healthy adults have higher proportions of fermenter bacteria, such as *Succinivibrio dextrinosolvens* and *Intestinibaculum porci* along with SCFA producer *F. prausnitzii* when compared to IBS patients	Khoo *et al.* (2023)
Gut microbiota composition of different ethics in Segamant area n = 214 (46 Malay, 65 Chinese, 49 Indian, and 54 Jakun), 10 to 83 yo	Main food items are *ulam*, pork, beef, chicken, fish, fermented food fruits, coffee, tea, probiotics, raw food	• When all variables were adjusted, ethnicity (Malay, Chinese, Indian, and indigenous people) emerged as the most influential factor shaping the gut microbiota compositions in Malaysian (PERMANOVA, p = 0.002). • Three distinct enterotypes were identified: *Prevotella*-dominant, *Bacteroides*-dominant and *Bifidobacterium*-dominant. Jakun volunteers exhibited a higher prevalence of *Prevetella*-dominant enterotype, Chinese had more *Bacteroides*-dominant enterotype; while Malay and Indian showed similar distribution between the first two enterotypes. • Among volunteers, Malay displayed an increased abundance of *Clostridiales*, while Jakun and Indian participants exhibited unique taxa associations attributed to variations in health-related factors. • Functional pathway analysis of the gut microbiota revealed ethnic disparities. Jakun participants displayed elevated pathways connected to pyruvate fermentation, NAD biosynthesis, protocatechuate degradation, methylglyoxal degradation, and maltose degradation. Indians had elevated in L-arginine and fatty acid biosynthesis pathways compared to Chinese and Malay and they are associated respectively to demographic and health-related factors.	Dwiyanto *et al.* (2021)

Note: FODMAP - fermentable oligosaccharides, disaccharides, monosaccharides, and polyols; BMI - body mass index; IBD - inflammatory bowel disease; MCP - microbioal cell preparation; yo - years old; M - male; F - female.

ACKNOWLEDGEMENT

The authors would like to thank the Malaysian Palm Oil Board for permission to publish this article.

REFERENCES

Abreu, A T A; Milke-García, M P; Argüello-Arévalo, G A; Calderón-De La Barca, A M; Carmona-Sánchez, R I; Consuelo-Sánchez, A; Coss-Adameg, E; García-Cedillog, M F; Hernández-Rosiles, V; Icaza-Chávez, M E; Martínez-Medina, J N; Morán-Ramos, S; Ochoa-Ortiz, E; Reyes-Apodaca, M; Rivera-Flores, R L; Zamarripa-Dorsey, F; Zárate-Mondragónn, F and Vázquez-Frias, R (2021). Review article: Dietary fiber and the microbiota: A narrative review by a group of experts from the Asociación Mexicana Degastroenterología. *Rev. Gastroenterol México., 86(3)*: 287-304. DOI: 10.1016/j.rgmxen.2021.02.002.

Aguirre, M; Eck, A; Koenen, M E; Savelkoul, P H M; Budding, A E and Venema, K (2016). Diet drives quick changes in the metabolic activity and composition of human gut microbiota in a validated *in-vitro* gut model. *Res. Microbiol., 167(2)*: 114-125. DOI: 10.1016/j.resmic.2015.09.006.

Agus, A; Denizot, J; Thévenot, J; Martinez-Medina, M; Massier, S; Sauvanet, P; Bernalier-Donadille, A; Denis, S; Hofman, P; Bonnet, R; Billard, E and Barnich, N (2016). Western diet induces a shift in microbiota composition enhancing susceptibility to adherent-invasive *E. coli* infection and intestinal inflammation. *Sci. Rep., 6*: 19032. DOI: 10.1038/srep19032.

Alfa, M J; Strang, D; Tappia, P S; Graham, M; Van Domselaar, G; Forbes, J. D; Laminman, V; Olson, N; Degagne, P; Bray, D; Murray, B L; Dufault, B and Lix, L M (2018). A randomised trial to determine the impact of a digestion resistant starch composition on the gut microbiome in older and mid-age adults. *Clin. Nutr., 37(3)*: 797-807. DOI: 10.1016/j.clnu.2017.03.025.

Almeida, A; Mitchell, A L; Boland, M; Forster, S C; Gloor, G B; Tarkowska, A; Lawley, T D and Finn, R D (2019). A new genomic blueprint of the human gut microbiota. *Nature, 568*: 499-504.

An, C; Kuda, T; Yazaki, T; Takahashi, H and Kimura, B (2014). Caecal fermentation, putrefaction and microbiotas in rats fed milk casein, soy protein or fish meal. *Appl. Microbiol. Biotechnol., 98*: 2779-2787. DOI: 10.1007/s00253-013-5271-5.

An, J; Zhao, X; Wang, Y; Noriega, J; Gewirtz, A T and Zou, J (2021). Western-style diet impedes colonization and clearance of *Citrobacter rodentium*. *Plos Pathog., 17(4):* e1009497.

Ang, Q Y; Alexander, M; Newman, J C; Tian, Y; Cai, J; Upadhyay, V; Turnbaugh, J A; Verdin, E; Hall, K D; Leibel, R L; Ravussin, E; Rosenbaum, M; Patterson, A D and Turnbaugh, P J (2020). Ketogenic diets alter the gut microbiome resulting in decreased intestinal Th17 cells. *Cell, 181(6):* 1263-1275.e16. DOI: 10.1016/j.cell.2020.04.027.

Aranceta, J and Serra-Majem, L (2001). Dietary guidelines for the Spanish population. *Public Health Nutr., 4(6a):* 1403-1408. DOI: 10.1079/PHN2001228.

Ashwar, B A; Gani, A; Shah, A; Wani, I A and Masoodi, F A (2015). Preparation, health benefits and applications of resistant starch - A review. *Starch, 68(3):* 287-301.

Asnicar, F; Berry, S E; Valdes, A M; Nguyen, L H; Piccinno, G; Drew, D A; Leeming, E; Gibson, R; Roy, L C; Khatib, H A; Francis, L; Mazidi, M; Mompeo, O; Valles-Colomer, M; Tett, A; Beghini, F; Dubois, L; Bazzani, D; Thomas, A M; Mirzayi, C; Khleborodova, A; Oh, S; Hine, R; Bonnett, C; Capdevila, J; Danzanvilliers, S; Giordano, F; Geistlinger, L; Waldron, L; Davies, R; Hadjigeorgiou, G; Wolf, J; Ordovás, J M; Gardner, C; Franks, P W; Chan, A T; Huttenhower, C; Spector, T D and Segata, N (2021). Microbiome connections with host metabolism and habitual diet from 1098 deeply phenotyped individuals. *Nature Med., 27:* 321-332. DOI: 10.1038/s41591-020-01183-8.

Atkins, C (2002). *Dr. Atkins' New Diet Revolution*. M. Evans and Company, Inc., New York. 560 pp.

Atzeni, A; Martínez, M Á; Babio, N; Konstanti, P; Tinahones, F J; Vioque, J; Corella, D; Fitó, M; Vidal, J; Moreno-Indias, I; Pertusa-Martinez, S; Álvarez-Sala, A; Castañer, O; Goday, A; Damas-Fuentes, M; Belzer, C; Martínez-Gonzalez, M Á; Hu, F B and Salas-Salvadó, J (2022). Association between ultra-processed food consumption and gut microbiota in senior subjects with overweight/obesity and metabolic syndrome. *Front. Nutr., 9*: 976547. DOI: 10.3389/fnut.2022.976547. eCollection 2022.

Biswas, V; Praveen, A; Marisetti, A L; Sharma, A; Kumar, V; Sahu, S K and Tewari, D (2022). A mechanistic overview on impact of dietary fibres on gut microbiota and its association with colon cancer. *Dietetics, 1(3):* 182-202. DOI: 10.3390/dietetics1030017.

Bolte, L A; Vila, V A; Imhann, F; Collij, V; Gacesa, R; Peters, V; Wijmenga, C; Kurilshikov, A; Campmans-Kuijpers, M J E; Fu, J; Dijkstra, G; Zhernakova, A and

Weersma, R K (2021). Long-term dietary patterns are associated with pro-inflammatory and anti-inflammatory features of the gut microbiome. *Gut, 70*: 1287-1298.

Bueno, N B; De Melo, I S V; De Oliveira, S L and Ataide, D R T (2013). Very-low-carbohydrate ketogenic diet *versus* low-fat diet for long-term weight loss: A meta-analysis of randomised controlled trials. *Br. J. Nutr., 110*: 1178-1187.

Byrne, C S; Chambers, E S; Morrison, D J and Frost, G (2015). The role of short chain fatty acids in appetite regulation and energy homeostasis. *Int. J. Obes. (Lond.), 39*: 1331-1338.

Carroll, J and Koenigsberger, D (1998). The ketogenic diet: A practical guide for caregivers. *J. Am. Diet. Assoc., 98*: 316-321.

Chen, S; Ou, Y; Zhao, L; Li, Y; Qiao, Z; Hao, Y and Ren, F (2019). Differential effects of *Lactobacillus casei* strain shirota on patients with constipation regarding stool consistency in China. *J. Neurogastroenterol. Motil., 25(1):* 148-158. DOI: 10.5056/jnm17085.

Chong, C W; Ahmad, A F; Lim, Y A L; Teh, C S J; Yap, I K S; Lee, S C; Chin, Y T; Loke, P N and Chua, K H (2015). Effect of ethnicity and socioeconomic variation to the gut microbiota composition among pre-adolescent in Malaysia. *Sci. Rep., 5*: 13338. DOI: 10.1038/srep13338.

David, L A; Maurice, C F; Carmody, R N; Gootenberg, D B; Button, J E; Wolfe, B E; Ling, A V; Devlin, A S; Varma, Y; Fischbach, M A; Biddinger, S B; Dutton, R J and Turnbaugh, P J (2014). Diet rapidly and reproducibly alters the human gut microbiome. *Nature, 505*: 559-563.

Day, L; Cakebread, J A and Loveday, S M (2022). Food proteins from animals and plants: Differences in the nutritional and functional properties. *Trends Food Sci. Technol., 119*: 428-442.

De Filippo, C; Cavalieri, D; Paola, M D; Ramazzotti, M; Poullet, J B; Massart, S; Collini, S; Pieraccini, G and Lionetti, P (2010). Impact of diet in shaping gut microbiota revealed by a comparative study in children from Europe and rural Africa. *Proc. Natl. Acad. Sci. U.S.A., 107(33)*: 14691-14696.

Den Besten, G; Bleeker, A; Gerding, A; Van Eunen, K; Havinga, R; Van Dijk, T H; Oosterveer, M H; Jonker, J W; Groen, A K; Reijngoud, D-J and Bakker, B M (2015). Short-chain fatty acids protect against high-fat diet-induced obesity via a PPARγ -dependent switch from lipogenesis to fat oxidation. *Diabetes, 64(7)*: 2398-2408. DOI: 10.2337/db14-1213.

Den Besten, G; Lange, K; Havinga, R; van Dijk, T H; Gerding, A; van Eunen, K; Muller, M; Groen, A K; Hooiveld, G J; Bakker, B M and Reijngoud, D J (2013). Gut-derived short-chain fatty acids are vividly assimilated into host carbohydrates and lipids. *Am. J. Physiol. Gastrointest. Liver Physiol., 305(12)*: G900-10. DOI: 10.1152/ajpgi.00265.2013.

Desalvo, K B; Olson, R and Casavale, K O (2016). Dietary guidelines for Americans. *J. Am. Med. Assoc., 315(5)*: 457-458. DOI: 10.1001/jama.2015.18396.

Dian, N; Hamid, R; Kanagaratnam, S; Isa, W A; Hassim, N A M; Ismail, N H; Omar, Z and Sahri, M M (2017). Palm oil and palm kernel oil: Versatile ingredients for food applications. *J. Oil Palm Res., 29(4)*: 487-511. DOI: 10.21894/jopr.2017.00014.

Donohoe, D R; Garge, N; Zhang, X; Sun, W; O'connell, T M; Bunger, M K and Bultman, S J (2011). The microbiome and butyrate regulate energy metabolism and autophagy in the mammalian colon. *Cell Metab., 13(5)*: 517-526. DOI: 10.1016/j.cmet.2011.02.018.

Duncan, S H; Louis, P and Flint, H J (2004). Lactate-utilizing bacteria, isolated from human feces, that produce butyrate as a major fermentation product. *Appl. Environ. Microbiol., 70(10):* 5810-5817. DOI: 10.1128/AEM.70.10.5810-5817.2004.

Dwiyanto, J; Hussain, M; Reidpath, D; Ong, K; Qasim, A; Lee, S; Lee, S; Foo, S; Chong, C and Rahman, S (2021). Ethnicity influences the gut microbiota of individuals sharing a geographical location: A cross-sectional study from a middle-income country. *Sci. Rep., 11:* 2618. DOI: 10.1038/s41598-021-82311-3.

Farup, P G and Valeur, J (2020). Changes in faecal short-chain fatty acids after weight-loss interventions in subjects with morbid obesity. *Nutrients, 12(3)*: 802. DOI: 10.3390/nu12030802.

Fava, F; Gitau, R; Griffin, B A; Gibson, G R; Tuohy, K M and Lovegrove, J A (2013). The type and quantity of dietary fat and carbohydrate alter faecal microbiome and short-chain fatty acid excretion in a metabolic syndrome 'at-risk' population. *Int. J Obes. (Lond), 37:* 216-223.

Fernandez, M L; Raheem, D; Ramos, F; Carrascosa, C; Saraiva, A and Raposo, A (2021). Highlights of current dietary guidelines in five continents. *Int. J Environ. Res. Public Health, 18(6):* 2814. DOI: 10.3390/ijerph18062814.

Ferraris, C; Meroni, E; Casiraghi, M C; Tagliabue, A; De Giorgis, V and Erba, D (2021). One month of classic therapeutic ketogenic diet decreases short chain fatty acids production in epileptic patients. *Front. Nutr., 8*: 613100. DOI: 10.3389/fnut.2021.613100.

Filippis, F D; Pellegrini, N; Vannini, L; Jeffery, I B; Storia, A L; Laghi, L; Serrazanetti, D I; Cagno, R D; Ferrocino, I; Lazzi, C; Turroni, S; Cocolin, L; Brigidi, P; Neviani, E; Gobbetti, M; O'toole, P W and Ercolini, D (2016). High-level adherence to a Mediterranean diet beneficially impacts the gut microbiota and associated metabolome. *Gut, 65*: 1812-1821.

Flint, H J; Duncan, S H; Scott, K P and Louis, P (2015). Links between diet, gut microbiota composition and gut metabolism. *Proc. Nutr. Soc., 74*: 13-22.

Fragiadakis, G K; Wastyk, H C; Robinson, J L; Sonnenburg, E D; Sonnenburg, J L and Gardner, C D (2020). Long-term dietary intervention reveals resilience of the gut microbiota despite changes in diet and weight. *Am. J. Clin. Nutr., 111:* 1127-1136.

Gabriel, A S; Ninomiya, K and Uneyama, H (2018). The role of the japanese traditional diet in healthy and sustainable dietary patterns around the world. *Nutrients, 10(2)*: 173. DOI: 10.3390/nu10020173.

Ganapathy, S S; Aris, H T H; Ahmad, N A; Shauki, N I H A; Kaundan, M K; Alias, N; Mohd Yusoff, M F; Jawahir, S; Perialathan, K; Kassim, M S A; Hasani, W S R; Rahim, F I A; Mat Rifin, H; Tan, L A; Yeop, N; Omar, M A; Wong, N I; Salleh, R; Lim, K K; Sooryanarayana, S; Ismail, H; Sahril, N; Chan, Y Y and Zainuddin, A A A M (2019). *National health and morbidity survey 2019: Non-communicable diseases, healthcare demand and health literacy Volume I: NCD -Non-Communicable Diseases: Risk factors and other health problems.* Institute for Public Health, National Institutes of Health, Ministry of Health, Shah Alam, Malaysia. p. 104-129.

Garcia-Mantrana, I; Selma-Royo, M; Alcantara, C and Collado, M C (2018). Shifts on gut microbiota associated to Mediterranean diet adherence and specific dietary intakes on general adult population. *Front. Microbiol., 9*: 890. DOI: 10.3389/fmicb.2018.00890.

Ghosh, T S; Rampelli, S; Jeffery, I B; Santoro, A; Neto, M; Capri, M; Giampieri, E; Jennings, A; Candela, M; Turroni, S; Zoetendal, E G; Hermes, G D A; Elodie, C; Meunier, N; Brugere, C M; Pujos-Guillot, E; Berendsen, A M; De Groot, L; Feskins, E J M; Kaluza, J; Pietruszka, B; Bielak, M J; Comte, B; Maijo-Ferre, M; Nicoletti, C; de Vos, W M; Fairweather-Tait, S; Cassidy, A; Brigidi, P; Franceschi, C and O'toole, P W (2020). Mediterranean diet intervention alters the gut microbiome in older people reducing frailty and improving health status: The NU-age 1-year dietary intervention across five European countries. *Gut, 69*: 1218-1228.

Gibiino, G; Siena, M D; Sbrancia, M; Binda, C; Sambri, V; Gasbarrini, A and Fabbri, C (2021). Dietary habits and gut microbiota in healthy adults: Focusing on the right diet. A systematic review. *Int. J. Mol. Sci., 22(13):* 6728. DOI: 10.3390/ijms22136728.

Goodrich, J K; Waters, J L; Poole, A C; Sutter, J L; Koren, O; Blekhman, R; Beaumont, M; Treuren, W V; Knight, R; Bell, J T; Spector, T D; Clark, A G and Ley, R E (2014). Human genetics shape the gut microbiome. *Cell, 159(4):* 789-799. DOI: 10.1016/j.cell.2014.09.053.

Haji-Ghazi Tehrani, L; Mousavi, S N; Chiti, H and Afshar, D (2022). Effect of atkins *versus* a low-fat diet on gut microbiota, and cardiometabolic markers in obese women following an energy-restricted diet: Randomized, crossover trial. *Nutr. Metab. Cardiovasc. Dis., 32(7):* 1734-1741. DOI: 10.1016/j.numecd.2022.04.007.

Haro, C; Rangel-Zúñiga, O A; Alcalá-Díaz, J F; Gómez-Delgado, F; Pérez-Martínez, P; Delgado-Lista, J; Quintana-Navarro, G M; Landa, B B; Navas-Cortés, J A; Tena-Sempere, M; Clemente, J C; López-Miranda, J; Pérez-Jiménez, F and Camargo, A (2016). Intestinal microbiota is influenced by gender and body mass index. *PLoS ONE, 11(5):* e0154090.

Heinritz, S N; Weiss, E; Eklund, M; Aumiller, T; Heyer, C M E; Messner, S; Rings, A; Louis, S; Bischoff, S C and Mosenthin, R (2016). Impact of a high-fat or high-fiber diet on intestinal microbiota and metabolic markers in a pig model. *Nutrients, 8(5):* 317. DOI: 10.3390/nu8050317.

Herrmann, E; Young, W; Reichert-Grimm, V; Weis, S; Riedel, C U; Rosendale, D; Stoklosinski, H; Hunt, M and Egert, M (2018). *In vivo* assessment of resistant starch degradation by the caecal microbiota of mice using RNA-based stable isotope probing-a proof-of-principle study. *Nutrients, 10(2)*: 179. DOI: 10.3390/nu10020179.

Holscher, H D; Caporaso, J G; Hooda, S; Brulc, J M; Fahey, G C and Jr Swanson, K S (2015). Fiber supplementation influences phylogenetic structure and functional capacity of the human intestinal microbiome: Follow-up of a randomized controlled trial. *Am. J. Clin. Nutr., 101(1):* 55-64. DOI: 10.3945/ajcn.114.092064.

Huda-Faujan, N; Abdulamir, A S; Fatimah, A B; Anas, O M; Shuhaimi, M; Yazid, A M and Loong, Y Y

(2010). The impact of the level of the intestinal short chain fatty acids in inflammatory bowel disease patients versus healthy subjects. *Open Biochem. J., 4*: 53-58. DOI: 10.2174/1874091X01004010053.

Iljazovic, A; Roy, U; Gálvez, E J C; Lesker, T R; Zhao, B; Gronow, A; Amend, L; Will, S E; Hofmann, J D; Pils, M C; Schmidt-Hohagen, K; Neumann-Schaal, M and Strowig, T (2021). Perturbation of the gut microbiome by *Prevotella* spp. enhances host susceptibility to mucosal inflammation. *Mucosal Immunol., 14:* 113-124. DOI: 10.1038/s41385-020-0296-4.

Joseph, N; Vasodavan, K; Saipudin, N A; Yusof, B N M; Kumar, S and Nordin, S A (2019). Gut microbiota and short-chain fatty acids (SCFAs) profiles of normal and overweight school children in Selangor after probiotics administration. *J. Funct. Foods, 57*: 103-111. DOI: 10.1016/j.jff.2019.03.042.

Just, S; Mondot, S; Ecker, J; Wegner, K; Rath, E; Gau, L; Streidl, T; Hery-Arnaud, G; Schmidt, S; Lesker, T R; Bieth, V; Dunkel, A; Strowig, T; Hofmann, T; Haller, D; Liebisch, G; Gérard, P; Rohn, S; Lepage, P and Clavel, T (2018). The gut microbiota drives the impact of bile acids and fat source in diet on mouse metabolism. *Microbiome, 6*: 134.

Kabeerdoss, J; Devi, R S; Mary, R R and Ramakrishna, B S (2012). Faecal microbiota composition in vegetarians: Comparison with omnivores in a cohort of young women in Southern India. *Br. J. Nutr., 108*: 953-957.

Kelly, C J; Zheng, L; Campbell, E L; Saeedi, B; Scholz, C C; Bayless, A J; Wilson, K E; Glover, L E; Kominsky, D J; Magnuson, A; Weir, T L; Ehrentraut, S F; Pickel, C; Kuhn, K A; Lanis, J M; Nguyen, V; Taylor, C T and Colgan, S P (2015). Crosstalk between microbiota-derived short-chain fatty acids and intestinal epithelial hif augments tissue barrier function. *Cell Host Microbe., 17(5)*: 662-671.

Khine, W W T; Zhang, Y; Goie, G J Y; Wong, M S; Liong, M; Lee, Y Y; Cao, H and Lee, Y-K (2019). Gut microbiome of pre-adolescent children of two ethnicities residing in three distant cities. *Sci. Rep., 9*: 7831.

Khoo, X-H; Chong, C-W; Talha, A M; Philip, K; Teh, C S J; Isa, A M; Wong, M S; Chew, D C H; Wong, Z; Jusoh, N S; Maksum, N M M; Mokhtar, N M; Majid, H A; Ali, R A R; Lee, Y-Y and Mahadeva, S (2023). The impact of diet and ethnicity on gut microbiota variation in irritable bowel syndrome: A multi-center study. *J. Gastroenterol. Hepatol., 38(8)*: 1259-1268. DOI: 10.1111/jgh.16174.

Kim, J N; Méndez–García, C; Geier, R R; Iakiviak, M; Chang, J; Cann, I and Mackie, R I (2017). Metabolic networks for nitrogen utilization in *Prevotella ruminicola 23*. *Sci. Rep., 7*: 7851 DOI: 10.1038/s41598-017-08463-3.

Kopp, W (2019). How Western diet and lifestyle drive the pandemic of obesity and civilization diseases. *Diabetes Metab. Syndr. Obes., 12*: 2221-2236.

Kossoff, E H; Cervenka, M C; Henry, B J; Haney, C A and Turner, Z (2013). A decade of the modified Atkins diet (2003-2013): Results, insights, and future directions. *Epilepsy Behav., 29(3)*: 437-442.

Larraufie, P; Martin-Gallausiaux, C; Lapaque, N; Dore, J; Gribble, F M; Reimann, F and Blottiere, H M (2018). SCFAs strongly stimulate pyy production in human enteroendocrine cells. *Sci. Rep., 8:* 74. DOI: 10.1038/s41598-017-18259-0.

LeBlanc, J G; Chain, F; Martín, R; Bermúdez-Humarán, L G; Courau, S and Langella, P (2017). Beneficial effects on host energy metabolism of short-chain fatty acids and vitamins produced by commensal and probiotic bacteria. *Microb. Cell Factories, 16:* 79.

Lee, Y Y and Muda, W A M W (2019). Dietary intakes and obesity of Malaysian adults. *Nutr. Res. Pract., 13*: 159-168.

Levy, M; Kolodziejczyk, A A; Thaiss, C A and Elinav, E (2017). Dysbiosis and the immune system. *Nat. Rev. Immunol., 17*: 219-232.

Ley, R E; Turnbaugh, P J; Klein, S and Gordon, J I (2006). Microbial ecology: Human gut microbes associated with obesity. *Nature, 444*: 1022-1023.

Liu, B N; Liu, X T; Liang, Z H and Wang, J H (2021). Gut microbiota in obesity. *World J. Gastroenterol., 27*: 3837-3850.

Looman, M; Feskens, E J M; De Rijk, M; Meijboom, S; Biesbroek, S; Temme, E H M; De Vries, J and Geelen, A (2017). Development and evaluation of the Dutch healthy diet index 2015. *Public Health Nutr., 20(13):* 2289-2299. DOI: 10.1017/S136898001700091X.

Louis, P and Flint, H J (2017). Formation of propionate and butyrate by the human colonic microbiota. *Environ. Microbiol., 19(1)*: 29-41. DOI: 10.1111/1462-2920.13589.

Mahadzir, M D A; Shyam, S; Barua, A; Krishnappa, P and Ramamurthy, S (2017). Effect of probiotic microbial cell preparation (MCP) on fasting blood

glucose, body weight, waist circumference, and faecal short chain fatty acids among overweight Malaysian adults: A pilot randomised controlled trial of four weeks. *Mal. J. Nutr., 23*: 329-341.

Manual, A (2011). Dietary guidelines for Indians. *Nat. Inst. Nutr., 2*: 89-117.

Martínez-Sánchez, M A; Balaguer-Román, A; Fernández-Ruiz, V E; Almansa-Saura, S; García-Zafra, V; Ferrer-Gómez, M; Frutos, M D; Queipo-Ortuño, M I; Ruiz-Alcaraz, A J; Núñez-Sánchez, M Á and Ramos-Molina, B (2023). Plasma short-chain fatty acid changes after bariatric surgery in patients with severe obesity. *Surg. Obes. Relat. Dis., 19(7)*: 727-734. DOI: 10.1016/j.soard.2022.12.041.

McIntosh, F M; Shingfield, K J; Devillard, E; Russell, W R and Wallace, R J (2009). Mechanism of conjugated linoleic acid and vaccenic acid formation in human faecal suspensions and pure cultures of intestinal bacteria. *Microbiol., 155:* 285-294. DOI: 10.1099/mic.0.022921-0.

Mithieux, G (2013). Nutrient control of hunger by extrinsic gastrointestinal neurons. *Trends Endocrinol. Metab., 24*: 378-384.

Mitsou, E K; Kakali, A; Antonopoulou, S; Mountzouris, K C; Yannakoulia, M; Panagiotakos, D B and Kyriacou, A (2017). Adherence to the Mediterranean diet is associated with the gut microbiota pattern and gastrointestinal characteristics in an adult population. *Br. J. Nutr., 117*: 1645-1655.

Mohammadifard, N; Haghighatdoost, F; Rahimlou, M; Rodrigues, A P S; Gaskarei, M K; Okhovat, P; De Oliveira, C; Silveira, E A and Sarrafzadegan, N (2022). The effect of ketogenic diet on shared risk factors of cardiovascular disease and cancer. *Nutrients, 14(17):* 3499. DOI: 10.3390/nu14173499.

Muralidharan, J; Galiè, S; Hernández-Alonso, P; Bulló, M and Salas-Salvadó, J (2019). Plant based fat, dietary patterns rich in vegetable fat and gut microbiota modulation. *Front. Nutr., 6:* 157.

Nagpal, R; Neth, B J; Wang, S; Craft, S and Yadav, H (2019). Modified Mediterranean-ketogenic diet modulates gut microbiome and short-chain fatty acids in association with Alzheimer's disease markers in subjects with mild cognitive impairment. *Ebiomedicine, 47:* 529-542. DOI: 10.1016/j.ebiom.2019.08.032.

Neis, E; Dejong, C and Rensen, S (2015). The role of microbial amino acid metabolism in host metabolism. *Nutrients, 7*: 2930-2946.

Ng, T K W (1997). Dietary fat and fibre intakes of Malaysian adults: Issues and implications when 'Western targets' are set as dietary goals. *Malays. J. Nutr., 3*: 137-147.

Ochoa-Repáraz, J and Kasper, L H (2016). The second brain: Is the gut microbiota a link between obesity and central nervous system disorders? *Curr. Obes. Rep., 5*: 51-64.

Oliphant, K and Allen-Vercoe, E (2019). Macronutrient metabolism by the human gut microbiome: Major fermentation by-products and their impact on host health. *Microbiome, 7(1)*: 1-15.

Olivares, M; Schüppel, V; Hassan, A M; Beaumont, M; Neyrinck, A M; Bindels, L B; Benítez-Páez, A; Sanz, Y; Haller, D; Holzer, P and Delzenne, N M (2018). The potential role of the dipeptidyl peptidase-4-like activity from the gut microbiota on the host health. *Front. Microbiol., 9*: 1900. DOI: 10.3389/fmicb.2018.01900.

Orlich, M J; Jaceldo-Siegl, K; Sabaté, J; Fan, J; Singh, P N and Fraser, G E (2014). Patterns of food consumption among vegetarians and non-vegetarians. *Br. J. Nutr., 112*: 1644-1653.

Pagliai, G; Russo, E; Niccolai, E; Dinu, M; Di Pilato, V; Magrini, A; Bartolucci, G; Baldi, S; Menicatti, M; Giusti, B; Marcucci, R; Rossolini, G M; Casini, A; Sofi, F and Amedei, A (2020). Influence of a 3-month low-calorie mediterranean diet compared to the vegetarian diet on human gut microbiota and SCFA: The CARDIVEG study. *Eur. J. Nutr., 59*: 2011-2024.

Park, S; Zhang, T; Yue, Y and Wu, X (2022). Effects of bile acid modulation by dietary fat, cholecystectomy, and bile acid sequestrant on energy, glucose, and lipid metabolism and gut microbiota in mice. *Int. J. Mol. Sci., 23(11):* 5935. DOI: 10.3390/ijms23115935.

Pelaseyed, T; Bergström, J H; Gustafsson, J K; Ermund, A; Birchenough, G M H; Schütte, A; Post, S; Svensson, F; Rodríguez-Piñeiro, A M; Nyström, E E L; Wising, C; Johansson, M E V and Hansson, G C (2014). The mucus and mucins of the goblet cells and enterocytes provide the first defense line of the gastrointestinal tract and interact with the immune system. *Immunol. Rev., 260*: 8-20.

Priya, S; Burns, M B; Ward, T; Mars, R A T; Adamowicz, B; Lock, E F; Kashyap, P C; Knights, D and Blekhman, R (2022). Identification of shared and disease-specific host gene-microbiome associations across human diseases using multi-omic integration. *Nat. Microbiol., 7*: 780-795.

Prochazkova, M; Budinska, E; Kuzma, M; Pelantova, H; Hradecky, J; Heczkova, M; Daskova, N; Bratova, M; Modos, I; Videnska, P; Splichalova, P; Sowah, S A; Kralova, M; Henikova, M; Selinger, E; Klima, K; Chalupsky, K; Sedlacek, R; Landberg, R; Kühn, T; Gojda, J and Cahova, M (2022). Vegan diet is associated with favorable effects on the metabolic performance of intestinal microbiota: A cross-sectional multi-omics study. *Front. Nutr., 8*: 783302.

Puchalska, P and Crawford, P A (2017). Multi-dimensional roles of ketone bodies in fuel metabolism, signaling, and therapeutics. *Cell Metab., 25*: 262-284.

Reichardt, N; Duncan, S H; Young, P; Belenguer, A; Mcwilliam Leitch, C; Scott, K P; Flint, H J and Louis, P (2014). Phylogenetic distribution of three pathways for propionate production within the human gut microbiota. *The ISME J., 8*: 1323-1335.

Rew, L; Harris, M D and Goldie, J (2022). The ketogenic diet - Its impact on human gut microbiota and potential consequent health outcomes: A systematic literature review. *Gastroenterol. Hepatol. Bed Bench, 15(4):* 326-342. DOI: 10.22037/ghfbb.v15i4.2600.

Ridlon, J M; Alves, J M; Hylemon, P B and Bajaj, J S (2013). Cirrhosis, bile acids and gut microbiota: Unraveling a complex relationship. *Gut Microbes, 4:* 382-387.

Rong, S; Liao, Y; Zhou, J; Yang, W and Yang, Y (2021). Comparison of dietary guidelines among 96 countries worldwide. *Trends Food Sci., 109*: 219-229.

Rosés, C; Cuevas-Sierra, A; Quintana, S; Riezu-Boj, J I; Martínez, J A; Milagro, F I and Barceló, A (2021). Gut microbiota bacterial species associated with Mediterranean diet-related food groups in a northern Spanish population. *Nutrients, 13*: 636.

Rowart, P; Wu, J; Caplan, M J and Jouret, F (2018). Implications of AMPK in the formation of epithelial tight junctions. *Int. J. Mol. Sci., 19*: 2040.

Russell, W R; Gratz, S W; Duncan, S H; Holtrop, G; Ince, J; Scobbie, L; Duncan, G; Johnstone, A M; Lobley, G E; Wallace, R J; Duthie, G G and Flint, H J (2011). High-protein, reduced-carbohydrate weight-loss diets promote metabolite profiles likely to be detrimental to colonic health. *Am. J. Clin. Nutr., 93*: 1062-1072.

Sánchez-Alcoholado, L; Ramos-Molina, B; Otero, A; Laborda-Illanes, A; Ordóñez, R; Medina, J A; Gómez-Millán, J and Queipo-Ortuño, M I (2020). The role of the gut microbiome in colorectal cancer development and therapy response. *Cancers, 12*: 1406.

Sánchez-Tapia, M; Tovar, A R and Torres, N (2019). Diet as regulator of gut microbiota and its role in health and disease. *Arch. Med. Res., 50*: 259-268.

Sanna, S; Van Zuydam, N R; Mahajan, A; Kurilshikov, A; Vich, V A; Võsa, U; Mujagic, Z; Masclee, A A M; Jonkers, D M A E; Oosting, M; Joosten, L A B; Netea, M G; Franke, L; Zhernakova, A; Fu, J; Wijmenga, C and Mccarthy, M I (2019). Causal relationships among the gut microbiome, short-chain fatty acids and metabolic diseases. *Nat. Genet., 51*: 600-605.

Schmidt, J; Rinaldi, S; Scalbert, A; Ferrari, P; Achaintre, D; Gunter, M J; Appleby, P N; Key T J and Travis, R C (2016). Plasma concentrations and intakes of amino acids in male meat-eaters, fish-eaters, vegetarians and vegans: A cross-sectional analysis in the EPIC-Oxford cohort. *Eur. J. Clin. Nutr., 70*: 306-312.

Schwedhelm, C; Iqbal, K; Knüppel, S; Schwingshackl, L and Boeing, H (2018). Contribution to the understanding of how principal component analysis-derived dietary patterns emerge from habitual data on food consumption. *Am. J. Clin. Nutr., 107*: 227-235.

Serra-Majem, L; Tomaino, L; Dernini, S; Berry, E M; Lairon, D; Cruz, D L N J; Bach-Faig, A; Donini, L M; Medina, F-X and Belahsen, R (2020). Updating the Mediterranean diet pyramid towards sustainability: Focus on environmental concerns. *Int. J. Environ. Res. Public Health, 17*: 8758.

Shafiee, N H; Razalli, N H; Nawawi, M K N; Mokhtar, M N and Ali, R R A (2022). Implication of food insecurity on the gut microbiota and its potential relevance to a multi-ethnic population in Malaysia. *JGH Open, 6*: 112-119.

Shen, Q; Zhao, L and Tuohy, K M (2012). High-level dietary fibre up-regulates colonic fermentation and relative abundance of saccharolytic bacteria within the human faecal microbiota *in-vitro*. *Eur. J. Nutr., 51*: 693-705.

Shi, J; Zhao, D; Zhao, F; Wang, C; Zamaratskaia, G and Li, C (2021). Chicken-eaters and pork-eaters have different gut microbiota and tryptophan metabolites. *Sci. Rep., 11*: 11934.

Smith, E A and Macfarlane, G T (1998). Enumeration of amino acid fermenting bacteria in the human large intestine: Effects of pH and

starch on peptide metabolism and dissimilation of amino acids. *FEMS Microbiol. Ecol., 25*: 355-368.

So, D; Whelan, K; Rossi, M; Morrison, M; Holtmann, G; Kelly, J T; Shanahan, E R; Staudacher, H M and Campbell, K L (2018). Dietary fiber intervention on gut microbiota composition in healthy adults: A systematic review and meta-analysis. *Am. J Clin. Nutr., 107*: 1-19.

Tazoe, H; Otomo, Y; Karaki, S; Kato, I; Fukami, Y; Terasaki, M and Kuwahara, A (2009). Expression of short-chain fatty acid receptor GPR41 in the human colon. *Biomed. Res., 30*: 149-156.

Tomova, A; Bukovsky, I; Rembert, E; Yonas, W; Alwarith, J; Barnard, N and Kahleova, N (2019). Review article: The effects of vegetarian and vegan diets on gut microbiota. *Front. Nutr., 6*: 157.

Trautmann, A; Schleicher, L; Deusch, S; Gätgens, J; Steuber, J and Seifert, J (2020). Short-chain fatty acids modulate metabolic pathways and membrane lipids in *Prevotella bryantii* $B_1$4. *Proteomes, 8*: 28.

Trefflich, I; Dietrich, S; Braune, A; Abraham, K and Weikert, C (2021). Short- and branched-chain fatty acids as fecal markers for microbiota activity in vegans and omnivores. *Nutrients, 13*: 1808.

Ueki, A; Akasaka, H; Suzuki, D; Hattori, S and Ueki, K (2006). *Xylanibacter oryzae gen. nov.; sp. nov*., a novel strictly anaerobic, Gram-negative, xylanolytic bacterium isolated from rice-plant residue in flooded rice-field soil in Japan. *Int. J. Syst. Evol., 56*: 2215-2221.

Vandeputte, D; Kathagen, G; D'hoe, K; Vieira-Silva, S; Valles-Colomer, M; Sabino, J; Wang, J; Tito, R Y; De Commer, L; Darzi, Y; Vermeire, S; Falony, G and Raes, J (2017). Quantitative microbiome profiling links gut community variation to microbial load. *Nature, 551*: 507-511.

Venkataraman, A; Sieber, J R; Schmidt, A W; Waldron, C; Theis, K R and Schmidt, T M (2016). Variable responses of human microbiomes to dietary supplementation with resistant starch. *Microbiome, 4*: 33.

Vieira, E L M; Leonel, A J; Sad, A P; Beltrão, N R M; Costa, T F; Ferreira, T M R; Gomes-Santos, A C; Faria, A M C; Peluzio, M C G; Cara, D C and Alvarez-Leite, J I (2012). Oral administration of sodium butyrate attenuates inflammation and mucosal lesion in experimental acute ulcerative colitis. *J. Nutr. Biochem., 23*: 430-436.

Vital, M; Rud, T; Rath, S; Pieper, D H and Schlüter, D (2019). Diversity of bacteria exhibiting bile acid-inducible 7α-dehydroxylation genes in the human gut. *Comput. Struct. Biotechnol. J., 17:* 1016-1019.

Vojinovic, D; Radjabzadeh, D; Kurilshikov, A; Amin, N; Wijmenga, C; Franke, L; Ikram, M A; Uitterlinden, A G; Zhernakova, A; Fu, J; Kraaij, R and van Duijn, C M (2019). Relationship between gut microbiota and circulating metabolites in population-based cohorts. *Nat. Commun., 10*: 5813.

Wang, G; Yu, Y; Wang, Y-Z; Wang, J-J; Guan, R; Sun, Y; Shi, F; Gao, J and Fu, X-L (2019). Role of SCFAs in gut microbiome and glycolysis for colorectal cancer therapy. *J. Cell. Physiol., 234:* 17023-17049.

Wang, S S; Lay, S; Yu, H N and Shen, S R (2016). Dietary guidelines for Chinese residents (2016): Comments and comparisons. *J. Zhejiang Univ. Sci. B., 17*: 649-656.

Widmer, R J; Flammer, A J; Lerman, L O and Lerman, A (2015). The Mediterranean diet, its components, and cardiovascular disease. *Am. J. Med., 128*: 229-238.

Wu, G D; Chen, J; Hoffmann, C; Bittinger, K; Chen, Y-Y; Keilbaugh, S A and Lewis, J D (2011). Linking long-term dietary patterns with gut microbial enterotypes. *Science, 334*: 105-108.

Xiao, W; Zhang, Q; Yu, L; Tian, F; Chen, W and Zhai, Q (2022). Effects of vegetarian diet-associated nutrients on gut microbiota and intestinal physiology. *Food Sci. Hum. Wellness, 11*: 208-217.

Xu, J; Lian, F; Zhao, L; Zhao, Y; Chen, X; Zhang, X; Guo, Y; Zhang, C; Zhou, Q; Xue, Z; Pang, X; Zhao, L and Tong, X (2015). Structural modulation of gut microbiota during alleviation of type 2 diabetes with a chinese herbal formula. *ISME J., 9(3)*: 552-562. DOI: 10.1038/ismej.2014.177.

Xu, Y; Wang, N; Tan, H-Y; Li, S; Zhang, C and Feng, Y (2020a). Function of *Akkermansia muciniphila* in obesity: Interactions with lipid metabolism, immune response and gut systems. *Front. Microbiol., 11*: 219. DOI: 10.3389/fmicb.2020.00219.

Xu, Y; Zhu, Y; Li, X and Sun, B (2020b). Dynamic balancing of intestinal short-chain fatty acids: The crucial role of bacterial metabolism. *Trends Food Sci. Tech., 100*: 118-130.

Yap, T W-C; Gan, H-M; Lee, Y-P; Leow, A H-R; Azmi, A N; Francois, F; Perez-Perez, G I; Loke,

M-F; Goh, K-L and Vadivelu, J (2016). *Helicobacter pylori* eradication causes perturbation of the human gut microbiome in young adults. *PLoS ONE, 11*: E0151893.

Yap, S Y; Voon, P T; Cheah, Y K; Lee, V K M and Selvaduray, K R (2022). Association of dietary fats with gut microbiota profile: How does palm oil fit in? *J. Oil Palm Res., 34*: 411-426.

Yokota, A; Fukiya, S; Islam, K S; Ooka, T; Ogura, Y; Hayashi, T; Hagio, M and Ishizuka, S (2012). Is bile acid a determinant of the gut microbiota on a high-fat diet? *Gut Microbes., 3(5)*: 455-459. DOI: 10.4161/gmic.21216.

Ze, X; Duncan, S H; Louis, P and Flint, H J (2012). *Ruminococcus bromii* is a keystone species for the degradation of resistant starch in the human colon. *ISME J., 6*: 1535-1543.

Zhang, C; Zhang, M; Pang, X; Zhao, Y; Wang, L and Zhao, L (2012). Structural resilience of the gut microbiota in adult mice under high-fat dietary perturbations. *ISME J., 6*: 1848-1857.

Zhang, C; Zhang, Y; Li, H and Liu, X (2020). The potential of proteins, hydrolysates and peptides as growth factors for *Lactobacillus* and *Bifidobacterium*: Current research and future perspectives. *Food Func., 11*: 1946-1957.

Zhao, L; Huang, Y; Lu, L; Yang, W; Huang, T; Lin, Z; Lin, C; Kwan, H; Wong, H L X; Chen, Y; Sun, S; Xie, X; Fang, X; Yang, H; Wang, J; Zhu, L and Bian, Z (2018). Saturated long-chain fatty acid-producing bacteria contribute to enhanced colonic motility in rats. *Microbiome, 6*: 1-16.

Zsálig, D; Berta, A; Tóth, V; Szabó, Z; Simon, K; Figler, M; Pusztafalvi, H and Polyák, É (2023). A review of the relationship between gut microbiome and obesity. *Appl. Sci., 13(1)*: 610. DOI: 10.3390/app13010610.

Journal of Oil Palm Research Vol. 36 (4) December 2024 p. 586-597
DOI: https://doi.org/10.21894/jopr.2023.0048

BIOLOGY AND BEHAVIOUR OF *Elaeidobius kamerunicus* FAUST, 1898 (COLEOPTERA: CURCULIONIDAE) IN TWO OIL PALM CULTIVARS IN COLOMBIA

CARLOS ANDRÉS SENDOYA-CORRALES[1]*; NORMAN FABIAN URREGO-MORALES[2]; JESÚS DAVID CASTAÑO-MARTINEZ[3]; ALEX ENRIQUE BUSTILLO[4] and ANUAR MORALES RODRÍGUEZ[4]

ABSTRACT

Elaeidobius kamerunicus *is the most efficient and abundant pollinator in oil palm plantations. We recorded biweekly observations to understand the population behaviour, habits and biological features of* E. kamerunicus*, as well as the volatile organic compound profile emitted by the inflorescences of two oil palm cultivars. Samples of the male and female inflorescences during the anthesis of* Elaeis guineensis *and the hybrid Coari × La Mé were collected.* Elaeidobius kamerunicus *adults copulated between 9:30 and 11:30 hr, and the females oviposited on the stamens of the male flowers. The life cycle of* E. kamerunicus *from egg to pupa took 8.6 days, and the life expectancy of adult males and females was 40.8 and 51.4 days, respectively. The female oviposition rate was 1.3 eggs day^{-1}, with a development time of 0.5 days. Insects such as* Pachycondyla harpax, Hololepta *sp., and members of the Chrysopidae and Dermaptera families, as well as spiders and Pseudoscorpiones, predated on this species. The main compounds emitted by the male and female inflorescences were methyl salicylate, estragole,* cis-*Anethole, and* trans-*Anethole studied in these two cultivars.*

Keywords: *Elaeis guineensis*, estragole, life cycle, pollinator, predators.

Received: 16 November 2022**; Accepted:** 1 July 2023**; Published online:** 25 September 2023.

INTRODUCTION

Oil palm is one of the most important crops in Colombia. Its high productivity and perennial nature have driven the oil palm's rapid expansion as a plantation crop. Colombia is the fourth-largest producer of crude palm oil globally, with a contribution of 1 559 065 t yr^{-1} and 595 722 ha of land planted with *Elaeis guineensis* Jacq. (Arecaceae) and the interspecific hybrid (*Elaeis oleifera* × *Elaeis guineensis*) (Fedepalma, 2022). Oil palm is a monoecious plant that requires cross-pollination (Syed, 1984). It is commonly wind-pollinated (anemophilous) or insect-pollinated (entomophilous), with the latter mechanism being the most important.

The most frequent oil palm pollinators worldwide are *Mystrops costaricensis* Gillogly, 1972 (Coleoptera, Nitidulidae), *Elaeidobius subvittatus* (Faust, 1898) (Coleoptera, Curculionidae) and *E. kamerunicus* Faust, 1898 (Coleoptera, Curculionidae) (Mondragón and Roa, 1985; Syed, 1986). Prior to 1985, *M. costaricensis*, native to America, and *E. subvittatus*, native to Africa, were the main pollinating insect species of oil palms that were identified in Colombia (Mondragón and Roa, 1985). However, given the low pollination efficiency of *M. costaricensis* and *E. subvittatus*, it was deemed necessary to introduce the *E. kamerunicus*

[1] Universidad Nacional de Colombia campus Palmira, Palmira (Valle del Cauca), 763539, Colombia.

[2] Clever Leaves. Zipaquirá (Cundinamarca), 250252, Colombia.

[3] National Coffee Research Center (Cenicafe - Colombia), Chinchiná-Manizales (Caldas), 170009, Colombia.

[4] Research Center Corporation in Oil Palm (Cenipalma - Colombia), Bogotá D.C., 111121, Colombia.

* *Corresponding author e-mail: casendoyac1987@gmail.com*

species from Malaysia. According to Syed (1986), *E. kamerunicus* is the most effective pollinator of oil palm crops and has contributed to the increase of oil palm production from 20% to 30% in Malaysia.

Dilleephan (1992) described *E. kamerunicus* male's morphological characters, which are larger than the females. Males have many setae on the outer part of the body, a characteristic absent in females, which helps to increase their body's pollen-carrying capacity (Syed, 1984; Genty, 1985). Unfortunately, improper application of chemical insecticides has caused a reduction of 10% to 20% in the *E. kamerunicus* field populations. *Elaeidobius kamerunicus* is also vulnerable to predation by ants, spiders, termites and nematodes (Prasetyo *et al.*, 2014) and is sensitive to precipitation patterns. These factors have collectively led to poor cluster formation and low oil palm extraction (Sánchez *et al.*, 2004).

Entomophilic oil palm pollination depends on the number of male inflorescences during anthesis, population size and behaviour of pollinating insects, and pollen availability with good viability and germinability. Efficient pollination of *E. guineensis* inflorescences is represented by a higher production rate of normal or fertile fruit, thereby increasing oil production by decreasing parthenocarpic fruit and abortive flowers (Corley and Tinker, 2003). While in hybrid materials, floral asynchrony and insufficient pollination cause poor conformation of the bunch, loss of bunches, and a higher percentage of parthenocarpic fruits (Hormaza *et al.*, 2011). The emission of volatile compounds that inflorescences emit to attract pollinating insects determines the pollination efficiency. Female inflorescences emit fragrances similar to those emitted by male inflorescences to ensure pollination during anthesis, attracting pollinators carrying pollen grains on their bodies (Lajis *et al.*, 1985; Yue *et al.*, 2015).

Therefore, to achieve the best conformation of fruits and the most significant potential for oil production of two of the most widely planted oil palm cultivars in Colombia, it is necessary to understand the population behaviour, habits and biological features of the pollinator *E. kamerunicus*, as well as the profile of volatile organic compounds emitted by the inflorescences in order to develop studies with attractant pheromones that improve the formation and increase the number of normal fruits in interspecific hybrids.

MATERIALS AND METHODS

Study Area

The study was carried out in the Palmar de la Vizcaína of Cenipalma Experimental Field (CEPV, Campo Experimental Palmar de la Vizcaína de Cenipalma), located 31 km from the Municipality of Barrancabermeja, in the Central Palm Zone of Colombia (06° 59′ 1.15″ N, 73° 41′ 43.35″ W, 100 m asl). On the plantation, two oil palm plots, each measuring 2 ha, were selected. One of the plots consisted of *E. guineensis* cultivar (IRHO 1001) planted in 2013 and the other plot was with interspecific hybrid *E. oleifera* × *E. guineensis* (Coari × La Mé) planted in 2014.

The Behaviour of *Elaeidobius kamerunicus* and Identification of its Natural Enemies

Twenty-four observations were made per day on a biweekly basis to determine the habits of *E. kamerunicus* and to identify its natural enemies. Each observation lasted 10 min. Two inflorescences during anthesis (bloom ≥ 80% of the flowers, phenological stage 607) (Forero *et al.*, 2017; Hormaza *et al.*, 2011) were observed from 06:00 to 18:00 hr. This process took place over a year. Following the observation, the inflorescences in Durawell 3D55 (55 × 16 × 16 cm) pollination bags were isolated (*Figure 1a*). A total of 32 inflorescences were isolated, cut, and transported to the Cenipalma entomology laboratory located in the CEPV, where the inflorescences' spikelets were removed (*Figure 1b-c*). All insects by species were separated using a brush,

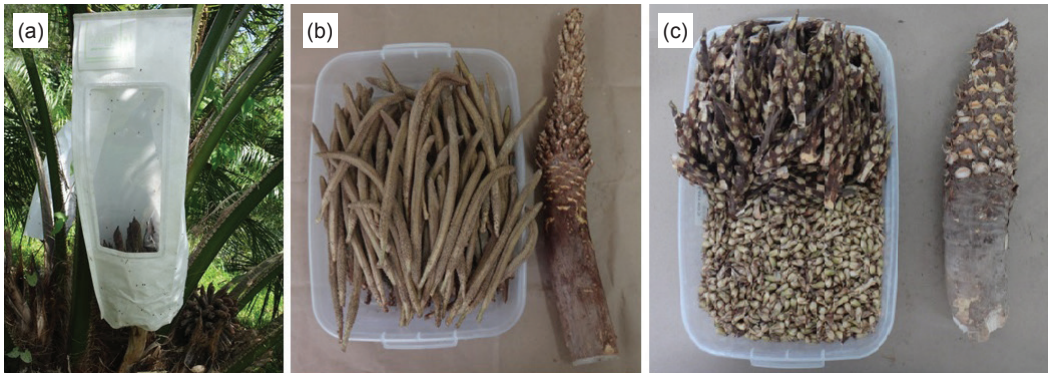


Figure 1. (a) Inflorescence isolation using Durawell 3D55 pollination bags, (b) removal of spikelets from the male inflorescence, and (c) female inflorescence.

counted, and preserved in 70% alcohol. Subsequently, via taxonomic keys, each species was identified (pollinating insects, relatives and natural enemies).

Biology of *E. kamerunicus*

Elaeidobius kamerunicus breeding stock was developed under laboratory conditions (26.0 ± 2.5°C, RH 69.7 ± 9.7%), with adults collected from the field. These adults were divided into 20 individuals (10 males and 10 females) for feeding and oviposition. These were placed in groups into acetate tubes containing a male inflorescence spikelet during the anthesis of the *E. guineensis* cultivar (IRHO 1001) (*Figure 2a*). The spikelet was set on oasis floral foam to prevent dehydration and was changed every other day.

One hundred newly oviposited eggs were extracted from the male inflorescences and placed individually in Petri dishes containing a damp paper towel. Every hour they were monitored to determine their hatching time and survival rate. The first fifty larvae to emerge were used to establish the developmental time of different larval instars. These were placed individually in Petri dishes containing a flower of the male spikelet during anthesis (as a food source) (*Figure 2b*). The larva's cephalic capsules were marked using a red fine-tip permanent marker (Sharpie, USA) (*Figure 2c*). They were checked daily to determine the instar change, which was confirmed by the presence of a new cephalic capsule. Similarly, 100 pupae were placed individually in Petri dishes and monitored until the adults emerged to determine the pupal stage's duration.

The life expectancy of the adults was determined using 100 newly emerged adults. First, their sex was determined and they were placed in acetate tubes containing a male spikelet at anthesis; these were changed daily to extract the eggs oviposited by the female, and the longevity of the adults was also monitored daily. In addition, any oviposited eggs were extracted from the spikelet using a brush and stereoscope and counted to determine the female oviposition rate.

Population Fluctuation of *E. kamerunicus*

Every 15 days from each cultivar, samples of *E. kamerunicus* were collected; six inflorescences from the cultivar at anthesis were selected (three male and three female). To estimate the abundance of pollinating insects at the inflorescences, a 5 × 5 cm white interception trap, made with Cartonplast (Compañia de Empaques, Itagui, Antioquia) with a layer of insect adhesive (Super tramp®, Inanalmet®, Bogotá, D.C.), was placed over each inflorescence (Montes *et al.*, 2018) (*Figure 3*). Every 30 min, the number of *E. kamerunicus* captured per inflorescence was counted. This activity was carried out every day for a year from 06:00 to 18:00 hr, taking 24 daily samples per inflorescence. At the CEPV weather station, humidity, temperature and precipitation were recorded.

Identification of Volatile Organic Compounds

Male and female spikelets at anthesis were collected in plastic bags from both cultivars under investigation between 10:00 and 12:00 hr. The spikelets were transported to the CEPV biochemistry laboratory in sterile, 1 L glass bottles to collect volatile organic compounds using headspace solid phase microextraction (HS-SPME), maintaining the bottles at 40°C for 1 hr. The gas chromatograph (6890N, Agilent Technologies) with a split/splitless injection port and a 5973N mass selective detector identified the volatile organic compounds. It performed injections using a split 10:1 ratio and achieved separation using a 30 m × 0.25 mm internal diameter silica capillary column with a 0.25 µm-thick film (Shinwa Chemical, Kyoto, Japan). The gas used for transportation was He at a pressure of 30 kPa and stored at 250°C.

The detector's interface temperature and ionisation voltage was 250°C and 70 eV, respectively, with electron impact ionisation. The column temperature was increased sequentially with three ramps; it was maintained initially at 45°C for 5 min. The first increase occurred at a rate of

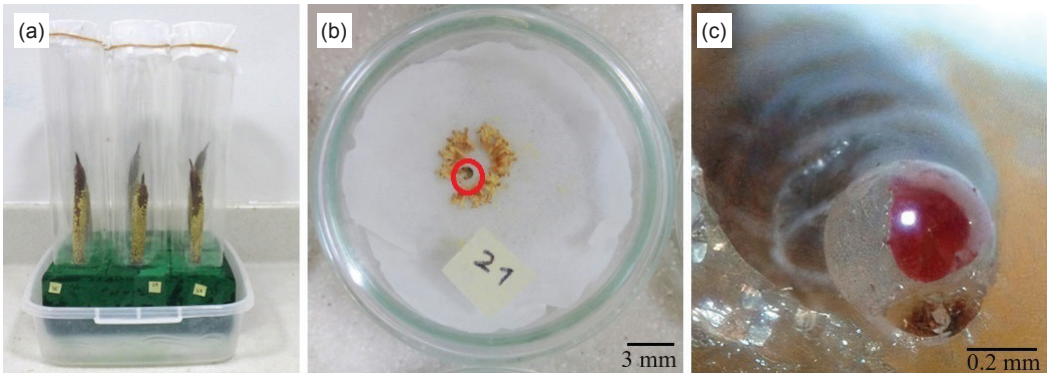


Figure 2. (a) Oviposition unit of E. kamerunicus *adult breeding stock, (b) Petri dish with flower for the larval stage development, and (c) the cephalic capsule is marked to monitor larval stage instar change.*



Figure 3. Interception trap placement for E. guineensis *inflorescences during anthesis: (a) Male inflorescence, and (b) female inflorescence.*

4°C min^{-1} up to 150°C, with a 2 min hold. A second ramp was at 5°C min^{-1} up to 250°C with a 5 min hold. As a final step, the temperature was brought up to 275°C at a rate of 10°C min^{-1} with a 20 min hold. The mass spectrometer ran with He as the carrier gas at a 1 mL min^{-1} flow rate. Between 40-400 m/z (mass/load ratio) was evaluated the mass range. Once the chromatographic profiles were known, the volatile compounds were detected using an Agilent Technologies 6890N gas chromatograph with a flame ionisation detector following the earlier methodology.

Statistical Analysis

Data recorded to determine the biology of *E. kamerunicus* were analysed using descriptive statistics. Information on the population of *E. kamerunicus* adults was plotted in population fluctuation graphs for the two cultivars during anthesis. The resulting compounds from volatiles in the cultivars were identified by referencing the Wiley/NIST mass spectrometry database.

RESULTS AND DISCUSSION

The Behaviour of *E. kamerunicus* and Identification of its Natural Enemies

Following collection from the male and female inflorescences of the two cultivars, three insect species were identified as pollinators. These were *E. kamerunicus* (*Figure 4c*), *E. subvittatus* (*Figure 4d*) and *M. costarricenses* (*Figure 4a*). *Elaeidobius kamerunicus* was the most prevalent (*Table 1*) but other insects that visited the inflorescences were also identified. These included *Cyclocephala amazona* Linnaeus, 1767 (Coleoptera: Scarabaeidae) (*Figure 5a*), *Coproporus* sp. Kraatz, 1857 (Coleoptera: Staphylinidae) (*Figure 5b*), *Apis mellifera* Linnaeus, 1758 (Hymenoptera: Apidae) (*Figure 5c*), *Trigona* sp. Fabricius, 1793 (Hymenoptera: Apidae) (*Figure 5d*).

Mondragon and Roa (1985) determined that *E. subvittatus, M. costarricenses, Coproporus* sp., *Orthoperus minutissimus* Matthews, 1899 (Coleoptera: Corylophidae), *Ahasverus* sp. Des Gozis, (1881) (Coleoptera: Silvanidae), *Thrips* sp. Haliday, 1836 (Thysanoptera), *Smicrips* sp. Le Conte, 1878 (Coleoptera: Smicripidae), *C. amazona, Cyclocephala discolor* Herbst, 1792 (Coleoptera: Scarabaeidae); are present in *E. guineensis*. While in the interspecific hybrid, they reported *Orthoperus* sp. Stephens, 1829 (Coleoptera: Corylophidae), as the most abundant. Arústegui *et al.* (2015) determined that *E. kamerunicus, E. subvittatus, Microporum* sp. Latreille, 1802 (Coleoptera: Nitidulidae), *A. mellifera* and *Melipona* sp. Illiger, 1806 (Hymenoptera: Apidae), are present in the inflorescences of *E. guineensis* (Deli × La Mé) in Peru, and *E. kamerunicus* and *E. subvittatus* are the most abundant pollinators in this cultivar. Egonyu *et al.* (2021) recorded that in Uganda, 23 insect morphospecies present in both sexes of *E. guineensis* inflorescences, including Curculionidae of the genera *Elaeidobius* and *Metamasius* (Coleoptera: Curculionidae), followed by beetles of the family Nitidulidae, Staphylinidae and Scarabidae; dipterans of the family Muscidae, Drosophilidae, and Platystomatidae; and the bee *A. mellifera*.

Natural predators of immature *E. kamerunicus* were observed, such as *Hololepta* sp. Paykull, 1811 (Coleoptera: Histeridae), *Pachycondyla harpax* (Fabricius, 1804) (Hymenoptera: Formicidae), Pseudoscorpiones, Chrysopidae, and Dermaptera, as were predators of adult *E. kamerunicus*, such as spiders (Araneae) (*Figure 6*). *Pachycondyla harpax* was the most abundant natural enemy observed in the male and female inflorescences of the interspecific hybrid with total counts of 36.0 ± 18.4 and 7.3 ± 6.7 individuals/inflorescence, respectively (*Table 1*). Muhammad *et al.* (2017) observed and highlighted the rat *Rattus tiomanicus* (Rodentia), the birds *Pycnonotus goiavier* (Pycnonotidae), *Orthotomus ruficeps* (Sylviidae), and *Prinia atrogularis* (Sylviidae), the insects *Cosmolestes picticeps* (Stal, 1859) (Hemiptera: Reduviidae), *Sycanus dichotomus*

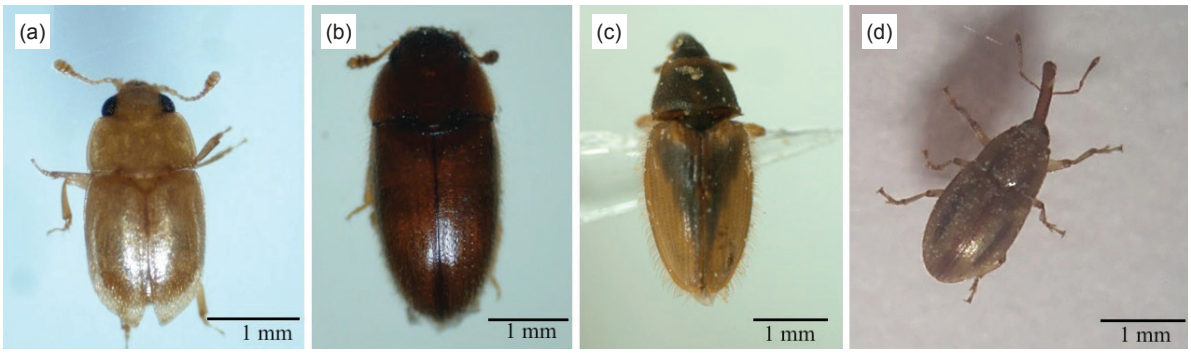


Figure 4. Pollinators collected in oil palm male and female inflorescences during anthesis: (a) Mystrops costarricenses, *(b)* Mystrops *sp., (c)* E. kamerunicus, *and (d)* E. subvittatus.

TABLE 1. INSECTS IDENTIFIED IN 32 MALE AND FEMALE *E. guineensis* (IRHO 1001) AND INTERSPECIFIC HYBRID (COARI × LA MÉ) INFLORESCENCES IN THE PALMAR DE LA VIZCAÍNA EXPERIMENTAL FIELD (CENTRAL ZONE)

Cultivar	Type of inflorescence	Type of insect	Insect name	Average number of individuals/ inflorescence day
Elaeis guineensis (IRHO 1001)	Male	Pollinator	*Elaeidobius kamerunicus* (female)	4325.6 ± 1195.6
			Elaeidobius kamerunicus (male)	1684.0 ± 340.5
			Elaeidobius subvittatus	2.1 ± 2.0
			Mystrops costaricensis	2.0 ± 1.5
		Associated	*Apis mellifera*	3.5 ± 2.1
			Cyclocephala amazona	77.5 ± 19.1
			Trigona sp.	3.5 ± 3.5
	Female	Pollinator	*Elaeidobius kamerunicus* (female)	31.8 ± 28.5
			Elaeidobius kamerunicus (male)	11.0 ± 10.8
		Associated	*Cyclocephala amazona*	28.0 ± 13.1
		Biological control	Araneae	3.1 ± 3.0
Interspecific hybrid (Coari x La Mé)	Male	Pollinator	*Elaeidobius kamerunicus* (female)	728.2 ± 559.4
			Elaeidobius kamerunicus (male)	457.3 ± 399.0
			Elaeidobius subvittatus	2.0 ± 1.0
			Mystrops costaricensis	86.0 ± 73.8
		Associated	Acari	14.5 ± 10.5
			Coproporus sp.	16.0 ± 15.4
			Cyclocephala amazona	2.5 ± 0.7
			Trigona sp.	2.0 ± 1.7
		Biological control	Dermaptera	1.5 ± 0.7
			Pachycondyla harpax	36.0 ± 18.4
	Female	Pollinator	*Elaeidobius kamerunicus* (female)	210.4 ± 147.6
			Elaeidobius kamerunicus (male)	166.5 ± 92.7
			Mystrops costaricensis	37.0 ± 9.9
		Associated	Acari	1.0 ± 0.9
			Cyclocephala amazona	1.4 ± 1.1
		Biological control	Araneae	1.8 ± 1.8
			Dermaptera	1.0 ± 0.8
			Hololepta sp.	2.1 ± 2.0
			Pachycondyla harpax	7.3 ± 6.7

Amyot and Serville, 1843 (Hemiptera: Reduviidae), *Pheidole megacephala* Fabricius, 1793 (Hymenoptera: Formicidae) and the arachnids *Argiope* sp. (Araneidae) and *Leucauge grata* (Tetragnathidae); as the predators of *E. kamerunicus* present in the palm agroecosystem in Malaysia.

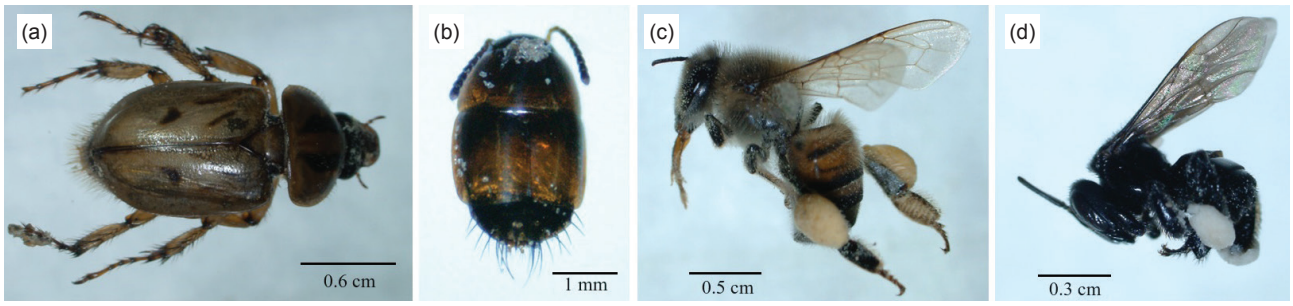


Figure 5. Insects associated with Elaeis guineensis *and interspecific hybrid male and female inflorescences: (a)* Cyclocephala amazona, *(b)* Coproporus *sp., (c)* Apis mellifera, *and (d)* Trigona *sp.*

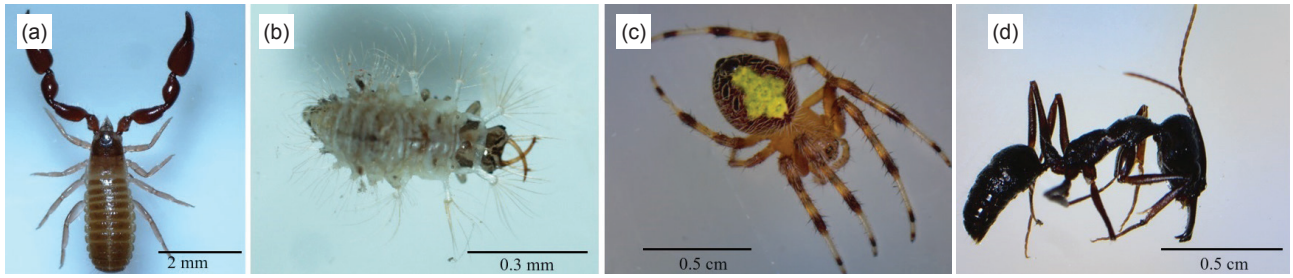


Figure 6. Natural enemies of pollinators: (a) Pseudoscorpionida, (b) Chrysopidae, (c) Araneae, and (d) Pachycondyla harpax.

Observations suggested that the activity of *E. kamerunicus* was related to environmental conditions. For instance, on days when the sky had thick clouds, the number of *E. kamerunicus* in the inflorescences was reduced. We did not observe the arrival of insects to the inflorescences on rainy days. On sunny days, their flight was more active. The insects' visits to the inflorescences were recorded from 08:00 hr to 12:00 hr, and the visits to inflorescences during anthesis took place intermittently in groups for the two cultivars studied. When the volatile compounds emitted by inflorescences were strong, pollinators arrived and settled on the peduncle of the inflorescence or the petiolar leaf fibres (*Figure 7b*); however, when these vapours were weak, pollinators settled on the underside of the leaves closest to the inflorescence (*Figure 7a*). Subsequently, they walked to the inflorescence at anthesis and hide at the base of the spikelet, where the first male flowers have bloomed, to feed on pollen. Pollinating insects reached inflorescences covered in pollen, indicating that they have come from other male inflorescences at anthesis.

Between 09:30 and 11:30 hr was estimated to be the time that *E. kamerunicus* males roam the flowers in search of females for copulation (*Figure 7d*). Later, the females oviposit their eggs on the stamens of the flowers at the base of the spikelet, where they use their proboscis to scrape at the petals and sepals to cover the oviposited eggs (*Figure 7e-f*). Abd *et al.* (2022) determined that the more active *E. kamerunicus* females spent a lot of time feeding and moving around to find the oviposition site, while the males groomed their legs to improve their grasping capacity during the copulation process, as well as to improve their sensory capacities (chemo and mechanoreceptors), they were more active after feeding and resting from the mating process.

After 12:00 hr, *E. kamerunicus* activity decreased considerably. At night (18:00 and 20:00 hr), insect movement was observed over the entire inflorescence, although the arrival of new pollinators was not evident. We found that environmental conditions play an essential role in regulating the activity of *E. kamerunicus*. Prada *et al.* (1998) reported observing similar behaviour in *E. kamerunicus* adults which visited inflorescences during the day, especially during hours of high brightness. However, they did not observe any activity on rainy or cloudy days.

The behaviour of the pollinating insects in the female inflorescence of the interspecific hybrid was minimal since few pollinators visited it. The volatiles like those emitted by the male inflorescences attracted these pollinators. They traversed the inflorescence, leaving pollen all over the flower, and finally, they searched for other flowers.

Biology of *E. kamerunicus*

The eggs of *E. kamerunicus* are a light cream color (*Figure 8*), measuring 0.6 ± 0.02 × 0.4 ± 0.01 mm (*Table 2*). They develop in 0.5 ± 0.2 days (average ± standard deviation) and have a hatching rate of

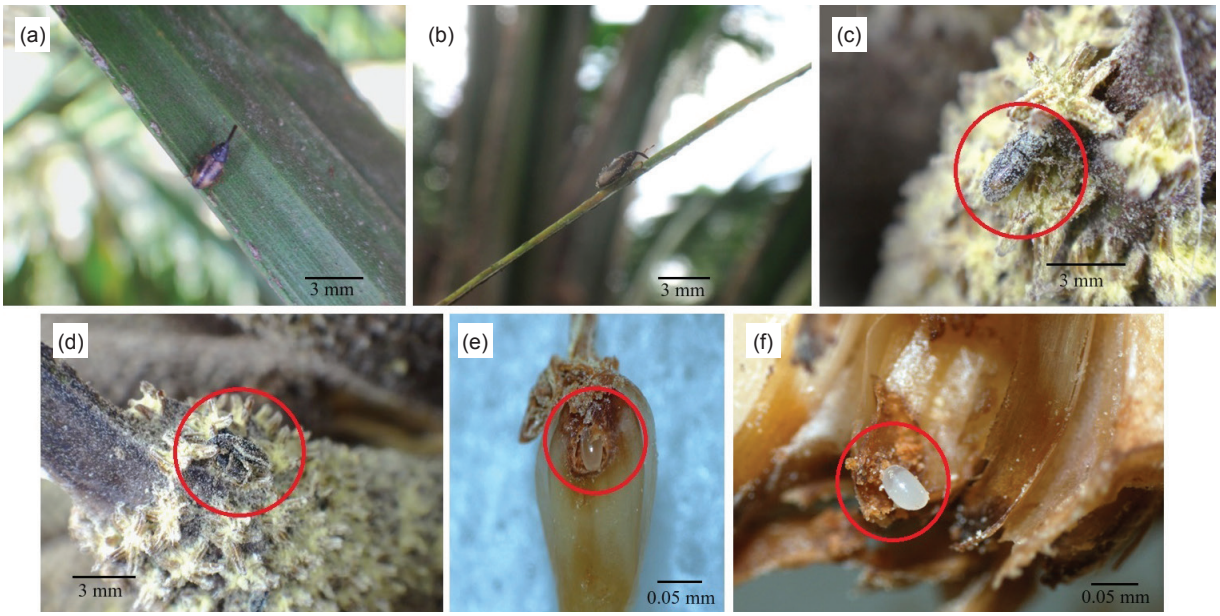


Figure 7. Elaeidobius kamerunicus *habits: (a) Adult perched on a palm leaflet, (b) adult perched on leaf petiole fibres, (c) adult feeding on pollen, (d) copulation, (e) egg oviposited inside the male flower, and (f) newly oviposited egg.*

TABLE 2. MEASUREMENTS OF *E. kamerunicus* AT VARIOUS DEVELOPMENT STAGES GROWN ON MALE INFLORESCENCES OF *E. guineensis* IRHO 1001 (26.0 ± 2.5°C, RH 69.7 ± 9.7%)

Stage of development	Body (mm)		Cephalic capsule (mm)	
	Length	Width	Length	Width
Egg	0.6 ± 0.02	0.4 ± 0.01		
Larva (first-instar)	1.2 ± 0.07		0.3 ± 0.01	0.3 ± 0.01
Larva (second-instar)	2.2 ± 0.70		0.4 ± 0.01	0.4 ± 0.01
Larva (third-instar)	3.9 ± 0.20		0.5 ± 0.01	0.6 ± 0.01
Pupa	2.9 ± 0.10	1.3 ± 0.03		

93.4%. In contrast, Tou *et al.* (2011) determined that the eggs developed in 0.2 days (5.9 hr) and presented an average hatching rate of 97.8%; this high percentage of hatching is due to the protection with sawdust that the female performs when ovipositing, generating better conditions for the development of the egg.

The larval stage shows three instars (*Figure 8*); they feed on the stamens and the internal parts of the male flower in anthesis. The first-instar larva is translucent and is 1.2 ± 0.07 mm long (*Table* 2). It has a development time of 0.5 ± 0.1 days and a survival rate of 77.0%. The second-instar larva is amber in colour and is 2.2 ± 0.7 mm long (*Table* 2). It develops in 0.9 ± 0.1 days and has a survival rate of 87.0%. Finally, the third instar is dark amber, approximately 3.9 ± 0.2 mm long (*Table* 2). It takes 4.6 ± 0.5 days to develop and has a 63.2% survival rate. For this stage of development, Tuo *et al.* (2011) reported three larval stages with a time of 0.8 days (18.2 hr) for the first instar, 1.2 days for the second instar, 1.1 days for the third instar and 4.7 days in the prepupal state.

The pupae develop within the male flower. They are exarate and yellow when they first pupate. Over time, we observed the development of the eyes and elytra. The pupae turn a grayish brown and later acquire their adult appearance (*Figure 8*). The pupal stage takes 2.1 ± 0.3 days to develop (*Figure 8*), with a survival rate of 94.0%. Tuo *et al.* (2011) reported times similar to those found in this study for this stage of development (2.03 days). The life cycle from egg to adult was 8.6 days. The results were different from those reported by Tuo *et al.* (2011), who reported a total life cycle time of 10.3 ± 0.3 days (27.4 ± 0.7°C, RH 75.2 ± 2.5%); this difference of 1.7 days probably is due to the different environmental conditions in which we carried out the studies.

It was observed that *E. kamerunicus* males have two calluses in the proximal region of the elytra, golden-colored marginal setae and a tuft-shaped crest in the dorsal part of the elytra. In contrast, these features are absent in females. Otherwise, males and females are similar in appearance; they have blackheads and brown elytra with two large black maculations (*Figure 8*). Adult life expectancy was 40.8 ± 23.0 and 51.4 ± 18.7 days for males and females, respectively (*Figure 8*), while Tuo *et al.*

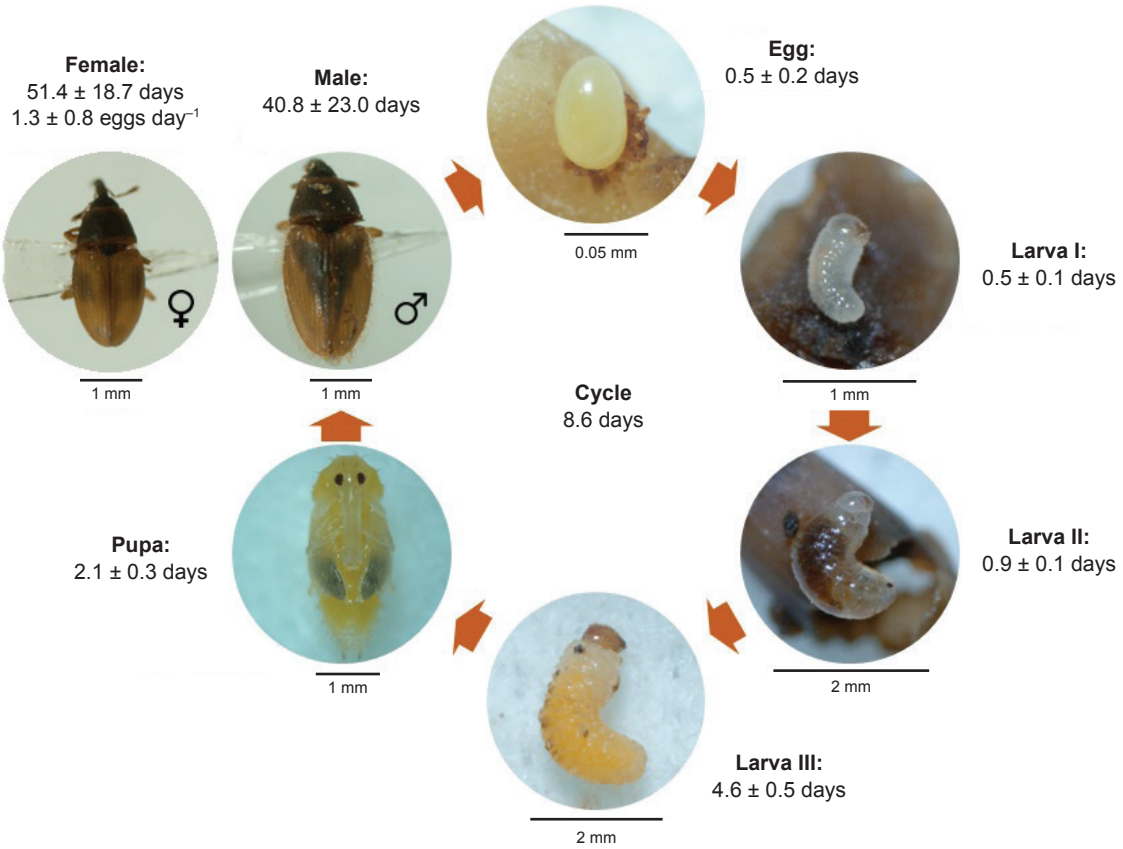


Figure 8. Life cycle of E. kamerunicus *grown on male inflorescences of* E. guineensis *(IRHO 1001) (26.0 ± 2.5°C, RH 69.7 ± 9.7%).*

(2011) reported longevity of 28.0 days for males and 31.2 days for females. We determined that *E. kamerunicus* females had an oviposition rate of 1.3 ± 0.8 eggs day^{-1}; these results coincide with what was reported by Tuo *et al.* (2011), who determined an average oviposition rate of 57.6 eggs with 1.8 daily eggs oviposited per female. Hussein *et al.* (1991) reported an average of 35.0 eggs per female of *E. kamerunicus* during her longevity. Females begin their oviposition after the fourth day of their emergence. The male-to-female sex ratio was 1:2.

The total mortality of the *E. kamerunicus* generation studied was 62.8%, with the third instar showing the highest mortality percentage. These results coincide with those reported by Husein *et al.* (1991), who obtained 60.0% mortality in the larvae during the breeding of *E. kamerunicus*, with the highest mortality rate in the first larval stage. This high mortality in the larval stage is probably due to the manipulation that monitors the change in instar and food.

Population Fluctuation of *E. kamerunicus*

It was determined that *E. kamerunicus* adults visit the inflorescences of the *E. guineensis* (IRHO 1001) cultivar in higher numbers during anthesis compared to the interspecific hybrid (Coari × La Mé). These results are similar to those of Mondragón and Roa (1985) and Yue *et al.* (2015), who determined that the number of insects attracted by *E. guineensis* is higher and more variable, compared to the interspecific hybrid, which attracts fewer insects and less variety. Also, Prasetyo *et al.* (2019) found that *E. guineensis* inflorescences were attractive to *E. kamerunicus*, while the presence of *E. kamerunicus* was lower in the *E. guineensis* x *E. oleifera* backcrosses. These population differences in *E. kamerunicus* between the evaluated cultivars are due to the presence, absence, and concentration of organic volatiles emitted by the inflorescences of each cultivar. In addition, it is essential to know the role played by these organic compounds emitted by the inflorescences in the interaction with the adults of *E. kamerunicus*, Ullah *et al.* (2015) have reported that the benzaldehyde compound is an insect repellent, and this is present in the interspecific hybrid, this may explain why the lowest visit rate of pollinating insects occurred in this material.

The male inflorescences of the *E. guineensis* cultivar were visited by 6010 *E. kamerunicus* adults during one day of anthesis, whereas approximately 42.8 of *E. kamerunicus* individuals frequent the female inflorescence. In contrast, Prada *et al.* (1998) determined that about 31 321 individuals of *E. kamerunicus* visit the female inflorescence of *E. guineensis* on one day of anthesis. Sánchez

et al. (2004) determined that the populations of *E. kamerunicus* per male inflorescence in anthesis ranged from 9606 to 156 753 individuals. Also, Arústegui *et al.* (2015) reported 124 527 and 224 219 adults of *E. kamerunicus* in male and female inflorescences in the anthesis of *E. guineensis* (Deli × La Mé), respectively.

Various factors, including the cultivated material, physiology of the inflorescence, number of male inflorescences at anthesis per hectare, climate (temperature, rainfall and dry periods), crop management practices (use of pesticides), the life cycle of pollinators, volatiles emitted by the inflorescences and the presence of natural enemies, influence the population fluctuation of *E. kamerunicus* (Nurul *et al.*, 2019; Prasetyo *et al.*, 2019; Sánchez *et al.*, 2004). The ratio of females to males is 2.9:1.0 for *E. guineensis*, whereas the ratio is 1.6:1.0 for the interspecific hybrid.

It was observed that there is a better activity of pollinating insects on the male inflorescence of *E. guineensis* between 09:30 hr and 12:00 hr (*Figure 9a-b*). The number of *E. kamerunicus* adults visiting the *E. guineensis* and the interspecific hybrid male inflorescences peaked at 11:00 hr (*Figure 9*). Prada *et al.* (1998), Sánchez *et al.* (2004), and Yue *et al.* (2015) determined that the time of maximum activity of *E. kamerunicus* was between 10:30 hr and 12:00 hr. Notably, the population dynamics of pollinating insects are regulated by the volatile compounds emitted by inflorescences. Therefore, the higher the emission of volatile compounds, the greater the activity of pollinators.

Identification of Volatile Organic Compounds

The chromatographic elution order of the main compounds identified is as follows: Ethyl salicylate, estragole, *cis*-Anethole, and *trans*-Anethole. In our results, estragole corresponds to the highest peak area, revealing it to be the most prevalent among the volatile organic compounds detected. Based on the chromatographic peak areas, the volatile organic compound emitted by the inflorescence differs depending on whether it is male or female. Female inflorescences emit fewer compounds than male inflorescences (*Figure 10*). The variation in pollinators visiting each inflorescence correlates with this difference (*Figure 10*).

The HS-SPME test facilitated a qualitative characterisation of the compounds emitted by inflorescences, and their subsequent identification was obtained using GC–MS. This tool has proven helpful in identifying volatile organic compounds involved in the interaction between insects and inflorescences (Basaglia *et al.*, 2014). Studies conducted by Lajis *et al.* (1985) and Yue *et al.* (2015) suggested that estragole was the compound responsible for the *E. kamerunicus* insect's attraction. In our results, estragole corresponds to the highest peak area, revealing it to be the most prevalent among the volatile compounds detected.

Furthermore, it was observed that the interspecific hybrid (Coari × La Mé) inflorescences emit minority compounds not detected in the *E. guineensis* (IRHO 1001) inflorescences. These were identified as styrene, benzaldehyde, isopropyl methoxypyrazine, dimethyl nonatriene, isobutyl methoxypyrazine, beta-elemene and triacetin. Methoxypyrazines have been reported as attractants to some pollinating insects (Maia *et al.*, 2018). In contrast, benzaldehyde has been reported as a repellent and insecticide against *Galleria mellonella* (Lepidoptera: Pyralidae), causing 100% insect mortality was observed at 108 hours after the injections (Ullah *et al.*, 2015). The interactions of these compounds with *E. kamerunicus* have not been reported to date. Therefore, whether these compounds have an attractive or repulsive effect on the insect remains unknown. These differences in the presence and concentration of volatile organic compounds could explain the population dynamics of *E. kamerunicus* in each cultivar.

CONCLUSION

Elaeidobius kamerunicus adults visit the inflorescences of the cultivar *E. guineensis* (IRHO 1001) during anthesis in more significant numbers than the interspecific hybrid (Coari × La Mé). The ratio of females to males was 2.9:1.0 for *E. guineensis* and 1.6:1.0 for the interspecific hybrid.

The most significant activity of *E. kamerunicus* was between 09:30 hr and 12:00 hr. They copulate between 09:30 hr and 11:30 hr, and the females oviposit on the stamens of the male flowers. The life cycle of *E. kamerunicus* from egg to pupa was 8.6 days, with a life expectancy of 40.8 days for males and 51.4 days for females. The oviposition rate of the females was 1.3 eggs day^{-1}, with a development time of 0.5 days.

Pachycondyla harpax was the most abundant natural enemy observed in the inflorescences, and the other identified enemies were *Hololepta* sp., Chrysopidae, Dermaptera, Araneae and Pseudoscorpiones. Methyl salicylate, estragole, *cis*-anethole, and *trans*-anethole were identified as the main compounds emitted by the male and female inflorescences of the two cultivars studied.

The behaviour of the adult population of *E. kamerunicus* in the two cultivars studied could be modulated by the emission of organic compounds identified from the male and female inflorescences. The knowledge of these compounds is essential for developing attractants that improve interspecific hybrids' productivity.

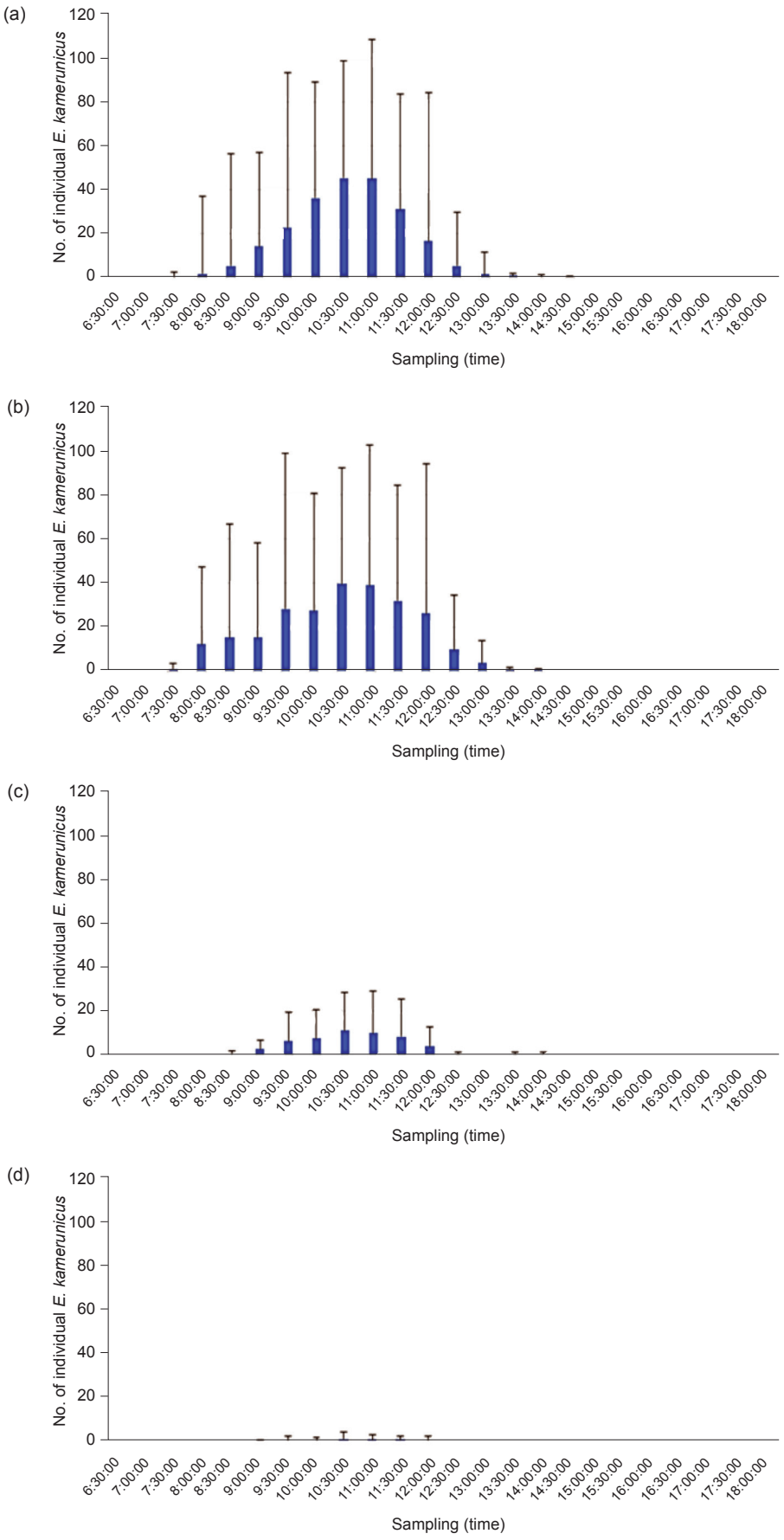


Figure 9. Population fluctuation of E. kamerunicus *on inflorescences of* E. guineensis *(IRHO 1001) during anthesis; (a) male inflorescence, (b) female inflorescence, and in inflorescences of the interspecific hybrid (Coari × La Mé); (c) male inflorescence, and (d) female inflorescence.*

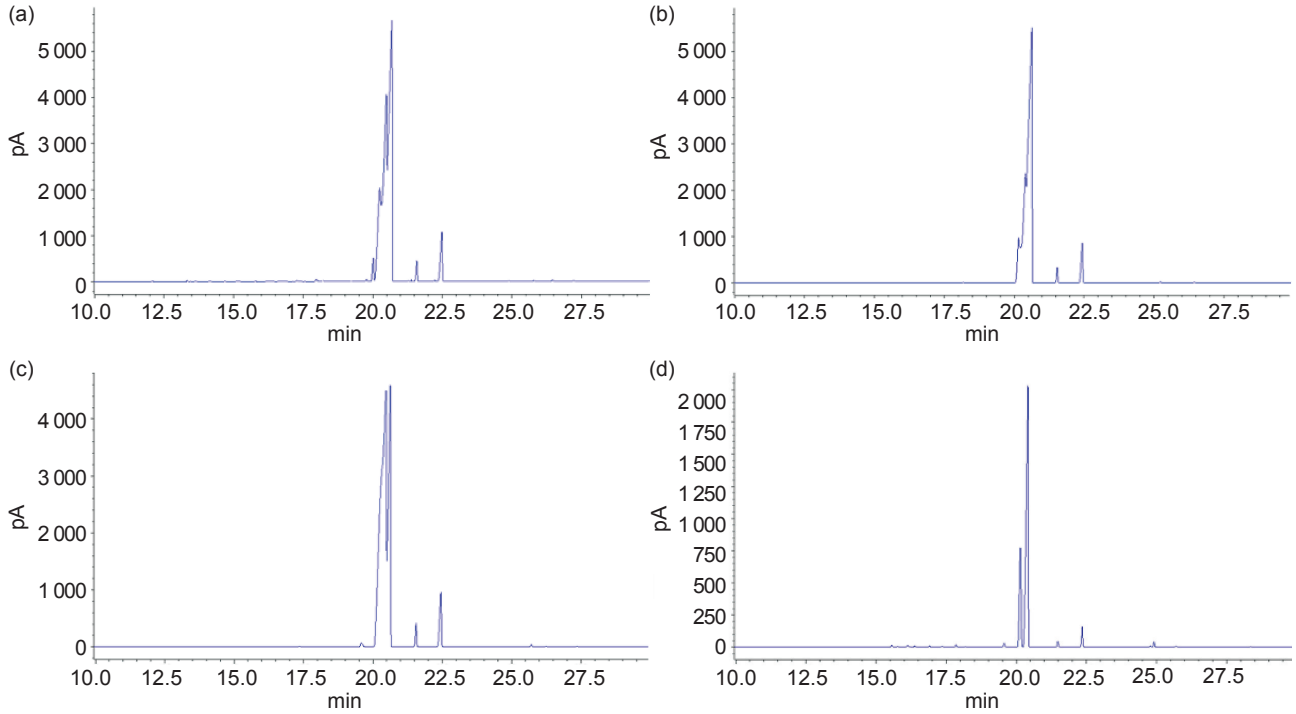


Figure 10. Chromatogram of the inflorescences of E. guineensis *(IRHO 1001) duringanthesis: (a) Male inflorescence and (b) female inflorescence. From the interspecific hybrid (Coari × La Mé): (c) male inflorescence and (d) female inflorescence.*

ACKNOWLEDGEMENT

The authors thank the Oil Palm Development Fund (Fondo de Fomento Palmero – FFP), administered by the National Federation of Oil Palm Growers (Federación Nacional de Cultivadores de Palma de Aceite – Fedepalma), for funding this study and the Palmar de la Vizcaína Experimental Field for logistical support.

CAS-C, NFU-M, and JDC-M carried out the experiment. CAS-S and NFU-M wrote the manuscript with support from AEB-P and AM-R. All authors provided critical feedback and helped shape the research, analysis and manuscript. AEB-P and AM-R supervised the project.

REFERENCES

Abd, N; Abd, I; Riza, I and Muhammad, D (2022). Starvation levels affect behaviours of wild-caught and laboratory-reared oil palm pollinator weevil, *Elaeidobius kamerunicus* (Coleoptera: Curculionidae). *Insects*, *13(10)*: 940. DOI: 10.3390/insects13100940.

Arústegui, M; Pinedo, H and Julca, A (2015). Insectos polinizadores de *Elaeis guineensis* Jacquin en el Distrito de Campoverde, Ucayali. *Saber y Hacer, 2(2)*: 110-126.

Basaglia, G; Fiori, J; Leoni, A and Gotti, R (2014). Determination of estragole in fennel herbal teas by HS-SPME and GCMS. *Anal. Lett., 47(2)*: 268-279. DOI: 10.1080/00032719.2013.834444.

Corley, R and Tinker, P (2003). *The Oil Palm*. Oxford: Blackwell Science Ltd. 608 pp.

Dilleephan, K (1992). Pollen carrying capacity, pollen load, and pollen transferring ability of the oil palm pollinating weevil *Elaeidobius kamerunicus* Faust in India. *OCL-Oilseed Fats, Crops Lipids, 47(2)*: 55-61.

Egonyu, J; Sisye, S; Baguma, J; Otema, M and Ddamulira, G (2021). Insect flower-visitors of African oil palm *Elaeis guineensis* at different sites and distances from natural vegetation in Uganda. *Int. J. Trop. Insect Sci.*, *41*: 2477-2487. DOI: 10.1007/s42690-021-00426-6.

Fedepalma (2022). Anuario estadístico 2022. Principales cifras de la agroindustria de la palma de aceite en Colombia y en el mundo 2017-2021. Federación Nacional de Cultivadores de Palma de Aceite, Bogotá. 256 pp.

Forero, D; Hormaza, P; Moreno, L and Ruíz, R (2017). Generalidades sobre la fenología y morfología de la palma de aceite. Cenipalma. 150 pp.

Genty, P (1985). Polinización entomófila de la palma africana en América Tropical, Colombia. *Revista Palmas*, *6(3)*: 90-101.

Hardon, J and Tan, G (1969). Interspecific hybrids in the genus *Elaeis* I. Crossability, cytogenetics and fertility of hybrids of *E. guineensis* x *E. oleifera*. *Euphytica, 18(1)*: 372-379.

Hormaza, P; Forero, C; Ruiz, R and Romero, H (2011). Fenología de la palma de aceite africana (*Elaeis guineensis* Jacq.) y del híbrido interespecífico (*Elaeis oleífera* x *Elaeis guineensis*). Cenipalma. 110 pp.

Hussein, M; Lajis, N; Van Heemert, C and Ali, J (1991). Biological and chemical factors associated with the successful introduction of *Elaeidobius kamerunicus* Faust, the oil palm pollinator in Malaysia. *Acta Hortic., 288*: 81-87. DOI: 10.17660/ActaHortic.1991.288.7.

Lajis, N; Hussein, M and Toia, R (1985). Extraction and identification of the main compound present in *Elaeis guineensis* flower volatiles. *Pertanika*, *8(1)*: 105-108.

Maia, A; Santos, G; Goncalves, E; Navarro, D and Nuñez-Alellaneda, L (2018). 2-Alkyl-3-methoxypyrazines are potent attractants of *Florivorous scarabs* (Melolonthidae, Cyclocephalini) associated with economically exploitable Neotropical palms (Arecaceae). *Pest Manag. Sci.*, *74(9)*: 2053-2058. DOI: 10.1002/ps.4895.

Mondragón, V and Roa, J (1985). Censo de entomofauna nativa asociada con inflorescencias masculinas y femeninas y análisis de polinización en palma africana (*Elaeis guineensis* Jacq.), palma americana (*Elaeis melanococca*) e híbrido interespecífico (*E. guineensis* × *E. melanococca*) en Colombia, Colombia. *Revista Palmas*, *6(1)*: 43-69.

Montes, L; Sánchez, L; Prada, F; Daza, E; Bustillo, A and Romero, H (2018). Relationships between inflorescences and pollinators and their effects on bunch components in *Elaeis guineensis*, in Colombia. *J. Entomol. Sci.*, *53(4)*: 554-568. DOI: 10.18474/JES18-06.1.

Muhammad, H; Dzulhelmi, M; Idris, A and Izfa, H (2017). The potential natural predators of *Elaeidobius kamerunicus* Faust, 1878 (Coleoptera: Curculionidae) in Malaysia. *Serangga, 22(2)*: 239-252.

Nurul, A; Muhamad, M; Luqman, H; Syarifah, S; Teo, T; Izfa, H and Idris, A (2019). Effects of rainfall, number of male inflorescences, and spikelets on the population abundance of *Elaeidobius kamerunicus* (Coleoptera: Curculionidae). *Sains Malays., 48(1)*: 15-21. DOI: 10.17576/jsm-2019-4801-03.

Prada, M; Molina, D; Villaroel, D; Barrios, R and Díaz, A (1998). Efectividad de dos especies del género *Elaeidobius* (Coleoptera: Curculionidae) como polinizadores en palma aceitera. *Bioagro*, *10(1)*: 3-10.

Prasetyo, A; Purba, W and Susanto, A (2014). *Elaeidobius kamerunicus*: Application of hatch and carry technique for increasing oil palm fruit set. *J. Oil Palm Res.*, *26(3)*: 195-202.

Prasetyo, A; Perdana-Rozziansha, T; Priwiratama, H; Susanto, A and De-Chenon, R (2019). Perspectiva bioecológica de *Elaeidobius kamerunicus* en relación con el llenado de frutos de palma de aceite en Indonesia, Colombia. *Revista Palmas*, *40(1)*: 94-110.

Sánchez, E; Salamanca, J; Calvache, H; Ortiz, L and Rivera, D (2004). Evaluación de poblaciones de polinizadores y su relación con la formación de racimos en la zona de Tumaco, Colombia. *Revista Palmas*, *25*: 84-92.

Syed, R (1984). Los insectos polinizadores de la palma africana, Colombia. *Revista Palmas*, *5(3)*: 19-64.

Syed, R (1986). Factibilidad de la introducción de *Elaeidobius kamerunicus* en Colombia, Colombia. *Revista Palmas*, *7(1)*: 11-15.

Tuo, Y; Koua, H and Hala, N (2011). Biology of *Elaeidobius kamerunicus* and *Elaeidobius plagiatus* (Coleoptera: Curculionidae) main pollinators of oil palm in West Africa. *European J. Sci. Res., 49(3)*: 426-432.

Ullah, I; Khan, A; Ali, L; Khan, A; Waqas, M; Hussain, J; Lee, I and Shin, J (2015). Benzaldehyde as an insecticidal, antimicrobial and antioxidant compound produced by *Photorhabdus temperata* M1021. *J. Microbiol., 53(2)*: 127-133. DOI: 10.1007/s12275-015-4632-4.

Yue, J; Yan, Z; Bai, C; Chen, Z; Lin, W and Jiao, F (2015). Pollination activity of *Elaeidobius kamerunicus* (Coleoptera: Curculionidae) on oil palm on Hainan Island. *Fla. Entomol.*, *98(2)*: 499-505. DOI: 10.1653/024.098.0217.

Journal of Oil Palm Research Vol. 36 (4) December 2024 p. 598-607
DOI: https://doi.org/10.21894/jopr.2023.0052

NITROGEN UPTAKE MODEL OF OIL PALM IN MAIN NURSERY

ADINDA N H MANURUNG[1,2]*; SUWARTO[3]; SUDIRMAN YAHYA[3] and BUDI NUGROHO[4]

ABSTRACT

Optimising the use of nitrogen (N) fertiliser in the main nursery will save costs, optimise seedling growth and minimise N leaching. Appropriate N fertiliser recommendations can be approached by modelling growth and nitrogen uptake. This study aimed to obtain a model of nitrogen uptake from oil palm seedlings in the main nurseries. The trial was conducted at the Leuwikopo Experimental Farm, IPB University, Indonesia, from May 2021-January 2022. The experiment consisted of five levels of N replicated five times. Treatments N0, N1, N2, N3 and N4 consisted of 0%, 50%, 100%, 150% and 200% standard fertiliser, respectively. The developed growth and N uptake model can only be used to predict oil palm growth and nutrient uptake in the main nurseries. The model was built from the dry matter partition coefficient, nutrient partition coefficient, and the actual amount of nutrient requirement. The model validation results during the main nursery showed that the model developed generally corresponded to the observed values for dry weight and nutrient uptake in the field. The developed model can predict oil palm seedlings' dry weight and nutrient uptake in the main nurseries under various conditions of deficiency or excess of N fertiliser level and climate conditions.

Keywords: dry weight, growth, nutrient demand, optimisation, precision.

Received: 26 September 2022; **Accepted:** 14 August 2023; **Published online:** 12 October 2023.

INTRODUCTION

Indonesia is the largest palm oil producer and exporter in the world. In 2022, the area of oil palm plantations has increased to 15.38 million hectares (DJP, 2023). The expansion of the planting area should increase productivity. Oil palm productivity is generally affected by land issues, seedling quality and agronomic practices such as fertilising activity. Nurseries are one of the stages of cultivation that can be optimised to support oil palm productivity. Indeed, Tao *et al*. (2017) reported that the bunch index increased by 12% under best management and fertiliser application practices compared to standard plantation practices. In addition, plants from good seeds will grow and develop faster and, in the end, produce earlier and provide higher yields (Sudradjat *et al*., 2014). Good seedling care in nurseries through the right dose of fertiliser application is one of the efforts to achieve optimal seedling growth (Santi and Goenadi, 2016).

Optimal and balanced fertiliser application will maximise the growth of oil palm seedlings. However, currently, Indonesia only uses the same fertiliser recommendations for oil palm seedlings in all nurseries. According to Broschat (2009), oil palm fertiliser application should be based on the type of soil and climate at the place of planting (specific location). In addition, location-specific fertiliser dosage recommendations can also overcome low

[1] Study Program of Agronomy and Horticulture, Graduate School, IPB University, Jl. Meranti Kampus Darmaga, 16680 Bogor, Indonesia.

[2] Department of Agrotechnology, Faculty of Industrial Technology, Gunadarma University, Jl. Margonda Raya No. 100, 16424 Depok, Indonesia.

[3] Department of Agronomy and Horticulture, Faculty of Agriculture, IPB University, Jl. Meranti Kampus Darmaga, 16680 Bogor, Indonesia.

[4] Department of Soil Science and Land Resource, Faculty of Agriculture, IPB University, Jl. Meranti Kampus Darmaga, 16680 Bogor, Indonesia.

* *Corresponding author e-mail: adinda.nhm@gmail.com*

fertiliser efficiency (Chen *et al.*, 2014b). However, it is difficult to implement site-specific fertiliser application recommendations because Indonesia has various weather and soil types. Creating a nutrient uptake model is an approach to getting site-specific fertiliser recommendations. A model is a simple representation of a system and simulation for building mathematical models and studying plants that refer to the system. The model helped estimate the best growth and nutrient uptake for regions with different soil and weather nutrient conditions.

In oil palm, plants at the juvenile stage have a particular need for N (Rowe *et al.*, 2005). Nitrogen (N), which mainly enters the plant as a soluble nitrate ion, is a building block for tissue growth and essential components, including chlorophyll and nucleic acids (Ikhajiagbe *et al.*, 2022). N modeling is important because N is a mobile macronutrient, easily lost in the fields. Efficient N fertiliser application would reduce costs, optimise seedling growth, and minimise N leaching (Prado *et al.*, 2006). It is thus essential to obtain an accurate understanding of N dynamics and losses in plantations in order to optimise the management of N and the use N fertilisers.

Numerous models on oil palm have been established. In Nye and Tinker's model, nutrient uptake was discussed based on root morphology and soil reactions (Roose *et al.*, 2001). However, this model is challenging to apply because the input requirements are large and difficult to obtain. Growth modelling and other production predictions, such as PALSIM, have not considered water and nutrient limitations (Hoffmann *et al.*, 2014). Thus far, oil palm modelling has only focused on predicting bunches and dry matter production in the field (>1 yr). Thus, modelling for nurseries has yet to be reported. This study was established to obtain a model of nitrogen uptake from oil palm seedlings in the main nursery, which can predict growth and N uptake in various soil and weather conditions.

MATERIALS AND METHODS

Modelling research was carried out in four stages: Model concept assessment, model concept development, model simulation and verification, and model validation. The assessment and preparation of the model concept were carried out using a literature study. Model simulation and verification were carried out with the Stella 9.02 application. Model validation was carried out by paired T-test between the absorption of the N model and the results of experiments in the field.

The literature study was conducted to review the model concept and obtain existing models' input coefficients. The coefficients obtained from the literature study are:

- Extinction coefficient = 0.72 (Squire, 1984).
- The respiration coefficient of oil palm (g CH_2O kg^{-1} dry weight day^{-1}) of oil palm for roots, petiole, and leaves were 15.04, 9.35 and 38.28, respectively (Henson, 1992).
- The basic temperature of oil palm growth is 15°C (Hartley, 1988).

Field trials were conducted to obtain coefficients for model input that did not yet exist and to obtain growth and N uptake data for model validation. The field trial was conducted at Leuwikopo Experimental Farm, IPB University, Indonesia, from May 2021-January 2022. Uniform 3 month old oil palm seedlings (Damimas variety) were selected and transplanted in 40 x 50 cm polybags. The experiment was carried out in a randomised block design of five levels N replicated five times. The treatments of N0, N1, N2, N3 and N4 consisted of 0%, 50%, 100%, 150% and 200% standard fertiliser, respectively. The total N fertiliser dose of 100% using the standard fertiliser application for oil palm seedlings of the Damimas variety in the main nursery. Each seedling in the experiment was fertilised with a 100% dose of phosphorus (P), potassium (K) and magnesium (Mg) of the standard dose for the Damimas variety. Fertiliser application was done every two weeks with a predetermined dose. The total N, P, K and Mg fertiliser application standards for each seedling were 28 g N, 28 g P, 33 g K and 14 g Mg. Each experimental plot consisted of six seedlings.

Oil palm seedlings from pre-nursery (3 months old) were selected to obtain uniform seedlings with average growth. The planting medium for the main nursery was topsoil [pH (H_2O) of 5.9, 4.00% C, 0.29% N (Kjeldahl), 0.47% total P, 0.20% total K and 0.23% total Mg]. The media was filled in 40 x 50 cm black polybags. Polybags containing seedlings were arranged according to treatment blocks with a spacing of 90 x 90 x 90 cm. Watering was done every morning and evening. Fertiliser application was carried out according to the treatment dose every two weeks. Fertiliser application was done by spreading the fertiliser on the soil surface at ± 5 cm from the seedlings, and different types of fertilisers were placed on different sides of the plant. Measurement of actual nutrient uptake by the seedlings in the nursery was carried out by adding up the product of the dry weight of each organ (DWx) with its N content (Nx) [Equation (1)]:

$$\text{Total N uptake} = \begin{matrix}(DW_{root} \times N_{root}) + \\ (DW_{petiole} \times N_{petiole}) + \\ (DW_{leaf} \times N_{leaf})\end{matrix} \quad (1)$$

Variables of the dry weight of plant organs (roots, petiole, and leaves), leaf area index (LAI), radiation

use efficiency (ε) [Equation (3)], and partition coefficient of dry weight and N partition [Equation (12)] were measured at 3, 6, 9 and 12 months after planting. LAI was derived by calculating the leaf area and the leaf dry weight [Equation (4)]. The plant dry weight was calculated destructively by weighing the plant organs that had been dried for 48 hr at 80°C. N content was measured at the Laboratory of Soil Research Centre, Bogor.

The N uptake model consists of the growth model and the N uptake submodel. The growth simulation model (Handoko, 1992) is based on plant growth response to N and its interactions. Actual biomass estimation is calculated by:

$$Ba = wdf \times Bp = wdf \times \varepsilon \times Q_{int} \quad (2)$$

where, Bp is the potential biomass production (kg ha^{-1} day^{-1}); wdf is the water deficit factor (actual transpiration/maximum transpiration). Actual transpiration is calculated based on potential evapotranspiration (ETp) by the Penman method, which is considered as maximum evapotranspiration (ETm) (Handoko, 1994); ε is the radiation use efficiency (kg MJ^{-1}). ε is calculated based on the ratio of the dry weight of plants produced over a certain period (ΔDW) to the amount of solar radiation energy intercepted (Q_{int}) by plants. Q_{int} (MJ^{-1} ha^{-1} day^{-1}) is the difference between the amount of radiation that comes above the canopy (Qs) and the radiation below the plant canopy (Ql).

$$\varepsilon = \frac{\Delta DW}{Q_{int}}, \; Q_{int} = Qs\text{-}Ql = (1\text{-}e^{-k\,LAI})\,Qs \quad (3)$$

where, k is the extinction coefficient = 0.72 (Squire, 1984) and LAI is the leaf area index. LAI changes are calculated by:

$$dILD = SLA \times dWL \quad (4)$$

SLA is the specific leaf area (ha kg^{-1}); dWL is the difference in leaf mass change (kg ha^{-1} day^{-1}).

Net biomass production is the actual biomass estimation reduced by maintenance respiration. The maintenance respiration coefficients (g CH_2O kg^{-1} dry weight day^{-1}) of oil palm for roots, petiole and leaves were 15.04, 9.35 and 38.28 (Henson, 1992).

The availability of N in the soil is estimated by the actual rate of soil nitrification (d_{NO_3}) minus the estimated N leaching. Calculation of the rate of soil nitrification and N-leaching followed that of Handoko (1992):

$$d_{NO_3} = Q_{10} * d_{NO_3P} * FKat \quad (5)$$

$$FKat = -0.039 + (1.02 * SWC/FC) \quad (6)$$

$$Q_{10} = 2^{(T-20)/10} \quad (7)$$

where, d_{NO_3P} is the potential rate of soil nitrification; T is the daily temperature (°C); SWC is the soil water content (mm); FC is the field capacity (mm). Nitrogen leaching from soil (L_{NO_3}) was calculated based on the amount of percolation water:

$$L_{NO_3} = \frac{(Percolation * [NO_3\ contentration])}{soil\ water\ content + Percolation} \quad (8)$$

$$Nitrogen\ soil\ availability = d_{NO_3} * wdf - L_{NO_3} \quad (9)$$

N uptake by plants takes into consideration the available soil N-content and N-demand of the plant. N requirements during plant growth are determined by the actual N concentration in plant organs and the maximum organ concentration (Handoko, 1992):

$$N_{demand} = dW * [N_{max}] \quad \text{if } [N_{act}] < [N_{max}];$$

$$N_{demand} = 0 \quad \text{if } [N_{act}] \geq [N_{max}] \quad (10)$$

$$N_{actual} = N_{plant} * W_{plant}/100 \quad (11)$$

where, dW is the plant biomass increment; N_{act} is the actual N concentration (%); N_{max} is the maximum N concentration (%); N_{plant} is the initial N plant concentration; W_{plant} is the plant dry weight. The maximum N concentration was determined as the highest plant concentration during the observation period. N partition (p_i) is the ratio of the increase in nitrogen uptake of certain plant organs (roots, petiole, leaves) at a certain age (dDW_i) to the total increase in nitrogen uptake of plants at the same age (dDW_{total}).

$$pi = \frac{dDw_i}{dDW_{total}} \quad (12)$$

When there is sufficient available N in the soil to cover the plant demand for N, root uptake is driven by the demand. The maximum N concentration of the daily growth of the plant determines the demand. However, the demand is also limited to staying within the maximum N concentration of the standing biomass that decreases with plant biomass and decreasing day length. The plant N demand is limited to the difference between the maximum plant N and its actual N content. The N uptake submodel is shown in *Figure 1*.

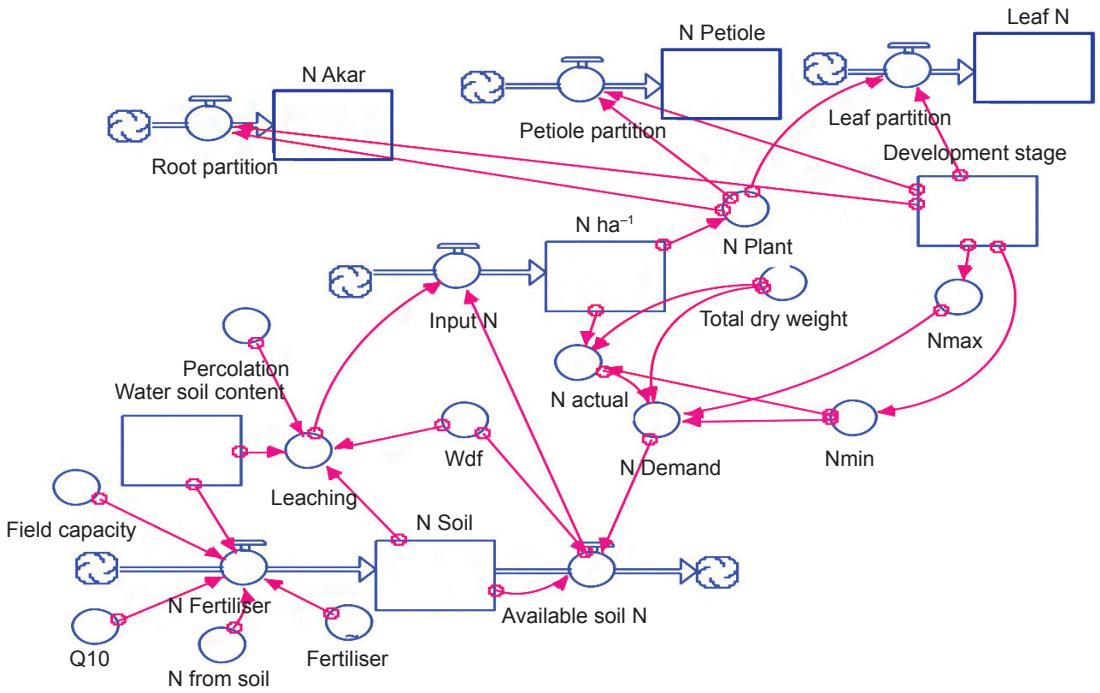


Figure 1. Approximate schematic description of N dynamics of the N uptake model. Total biomass and soil mineral N are simulated with linked models programmed in Stella.

RESULTS AND DISCUSSION

Initial soil conditions and daily weather are inputs in the growth model. Monthly weather conditions consist of total rainfall, average temperature, radiation intensity, light exposure length and relative humidity during the study, as seen in *Table 1*. The average rainfall during the study was 310 mm month^{-1}. The average daily temperature was 27.1°C. The average radiation intensity was 18.8 MJ m^{-2}. The average light exposure length was 7.4 hr day^{-1}. The average relative humidity was 83.1%.

Leaf Area Index (LAI)

The results of LAI measurements on oil palm seedlings at various doses of N fertiliser are shown in *Table 2*.

TABLE 1. WEATHER ON TRIAL SITE IN MAY 2021-JANUARY 2022

Month	Total rainfall (mm month^{-1})	Temperature (°C)	Radiation intensity (MJ m^{-2})	Light exposure length (hr day^{-1})	Relative humidity (%)
May 2021	510.3	26.8	20.4	9.3	84.2
June 2021	311.1	25.9	16.0	7.8	84.1
July 2021	115.6	26.0	19.3	9.2	79.8
August 2021	399.5	26.0	19.2	8.9	81.9
September 2021	317.3	30.0	21.8	9.0	81.0
October 2021	566.5	31.0	23.2	8.5	82.6
November 2021	183.6	26.4	16.0	4.2	83.7
December 2021	279.1	26.1	16.7	3.8	85.2
January 2022	106.6	26.0	16.5	6.0	85.0

TABLE 2. LEAF AREA INDEX OF OIL PALM ON SEVERAL DOSAGES OF N FERTILISER APPLICATION

Treatment	Leaf area index (LAI)		
	6 MAP	9 MAP	12 MAP
N0	0.17	0.95	2.11
N1	0.24	1.09	1.66
N2	0.22	1.57	2.63
N3	0.21	1.29	3.03
N4	0.20	1.14	1.88

Note: MAP - month after planting.

Radiation Use Efficiency (ε) (g MJ^{-1})

Table 3 presents data on oil palm's radiation use efficiency at various N fertiliser doses. Increasing the dose of N fertiliser causes an increase in the value of ε up to a dose limit of 100%. Higher fertiliser application in the N3 and N4 treatments caused a decrease in the value of ε.

TABLE 3. RADIATION USE EFFICIENCY OF OIL PALM ON SEVERAL DOSAGES OF N FERTILISER APPLICATION

Treatment	Radiation use efficiency (g MJ^{-1})		
	3-6 MAP	6-9 MAP	9-12 MAP
N0	1.10	0.70	0.91
N1	1.02	0.72	1.07
N2	1.02	0.73	1.20
N3	1.07	0.69	1.05
N4	1.01	0.67	0.89

Note: MAP - month after planting.

Partition of Dry Weight and Nitrogen

The dry-weight partition of oil palm is shown in *Table 4*. The dry weight of oil palm in the nursery phase was more partitioned into shoots. At 12 MAP, the N1, N2 and N3 treatments, the dry weight partition to roots was higher than N0 and N4. *Table 5* shows the N partitions on roots, petioles and leaves. Nutrient partitioning also indicated that more N produces a lengthy canopy (*Table 5*). N accumulation in roots increased during the main nursery. The highest N accumulation was found in leaves.

Growth Model Validation

Dry weight simulation was carried out according to Equations (2-4). A comparison of the dry weight of each organ in the actual and model conditions can be seen in *Figure 2*. At 3 MAP, the dry weight of the roots was 0.84 g, the petiole was 0.91 g, and the leaves was 1.87 g. Dry matter accumulation was focused on above-ground biomass enlargement. At 9 MAP, root growth was increased to compensate for shoot growth. At 12 MAP, treatments N1, N2 and N3 showed a similar trend of dry matter accumulation among roots, petiole, and roots. On the other hand, N4 treatment tended to accumulate dry matter in the canopy (leaf and petiole). A comparison of actual and simulated growth data for each treatment is shown in *Figure 2*.

Figure 2 shows an agreement between the simulation results of oil palm seedlings' dry weight at various N fertiliser application doses with the measurement results. The data from the simulation results are still included in the confidence interval ($1-\alpha = 0.95$) of the measurement results. Paired T-test showed no difference between the actual dry weight in the field and the model simulation results (*Table 6*).

TABLE 4. DRY WEIGHT PARTITION OF OIL PALM ON SEVERAL DOSAGES OF N FERTILISER APPLICATION

Age (months)	Organ	Treatment				
		N0	N1	N2	N3	N4
3-6	Roots	0.28	0.26	0.28	0.29	0.27
	Petiole	0.30	0.30	0.30	0.29	0.29
	Leaves	0.43	0.45	0.43	0.43	0.45
6-9	Roots	0.34	0.27	0.26	0.22	0.26
	Petiole	0.28	0.33	0.35	0.32	0.31
	Leaves	0.38	0.40	0.39	0.45	0.43
9-12	Roots	0.15	0.33	0.36	0.37	0.24
	Petiole	0.42	0.34	0.31	0.19	0.32
	Leaves	0.43	0.34	0.33	0.43	0.44

TABLE 5. N PARTITION OF OIL PALM ON SEVERAL DOSAGES OF N FERTILISER APPLICATION

Age (months)	Organ	Treatment				
		N0	N1	N2	N3	N4
3-6	Roots	0.20	0.13	0.13	0.18	0.17
	Petiole	0.29	0.28	0.23	0.23	0.24
	Leaves	0.51	0.58	0.64	0.59	0.59
6-9	Roots	0.30	0.26	0.26	0.13	0.18
	Petiole	0.10	0.24	0.23	0.25	0.18
	Leaves	0.60	0.50	0.51	0.62	0.65
9-12	Roots	0.10	0.26	0.36	0.33	0.23
	Petiole	0.19	0.17	0.08	0.00	0.13
	Leaves	0.71	0.57	0.56	0.67	0.64

Nitrogen Uptake Validation

At the beginning of seedling growth in the main nursery (6 MAP), there was no difference in treatments (*Figure 3*). At 9 MAP, the highest N accumulation in N1 was in roots, while at N2, N3 and N4, the highest N accumulation was in leaves. At 12 MAP, the trend of N accumulation in roots and leaves was high in N2 and N3, while N1 and N4 tended to be lower. A comparison of simulation data and measured N absorption can be seen in *Figure 3*.

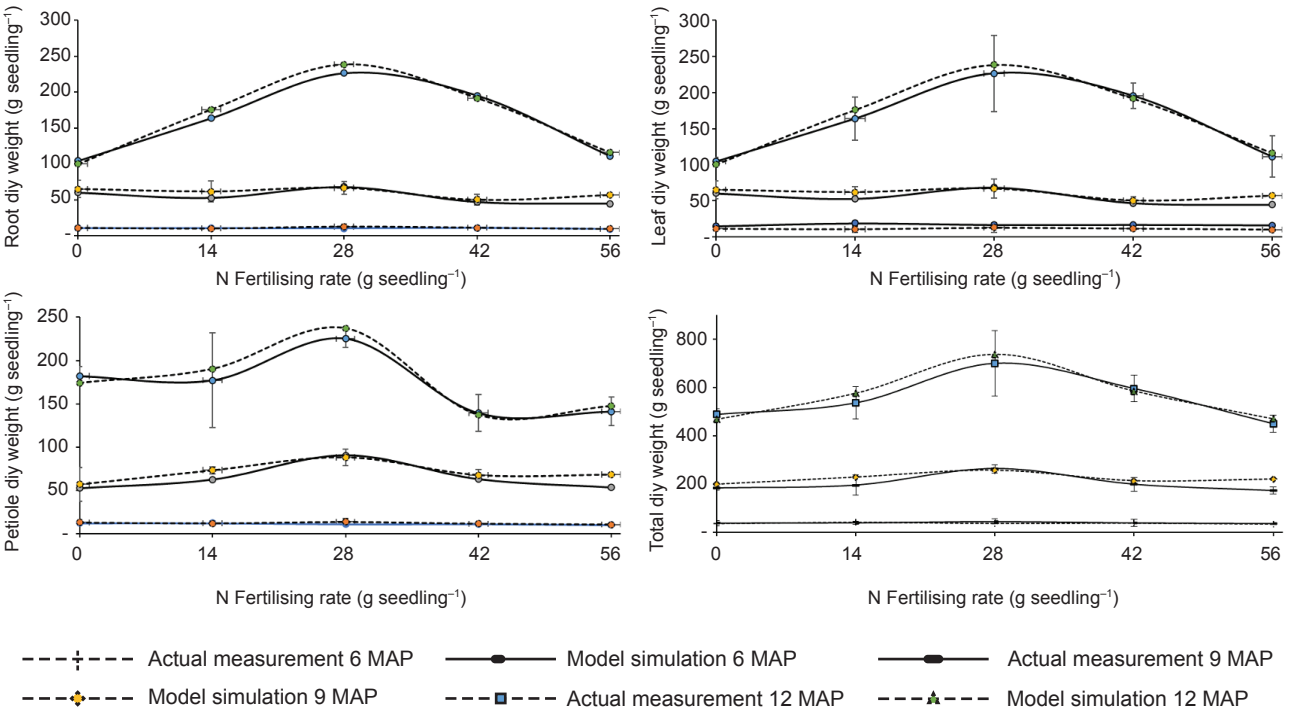


Figure 2. Simulated (dotted line) and measured dry weight (solid line) of N0, N1, N2, N3 and N4.

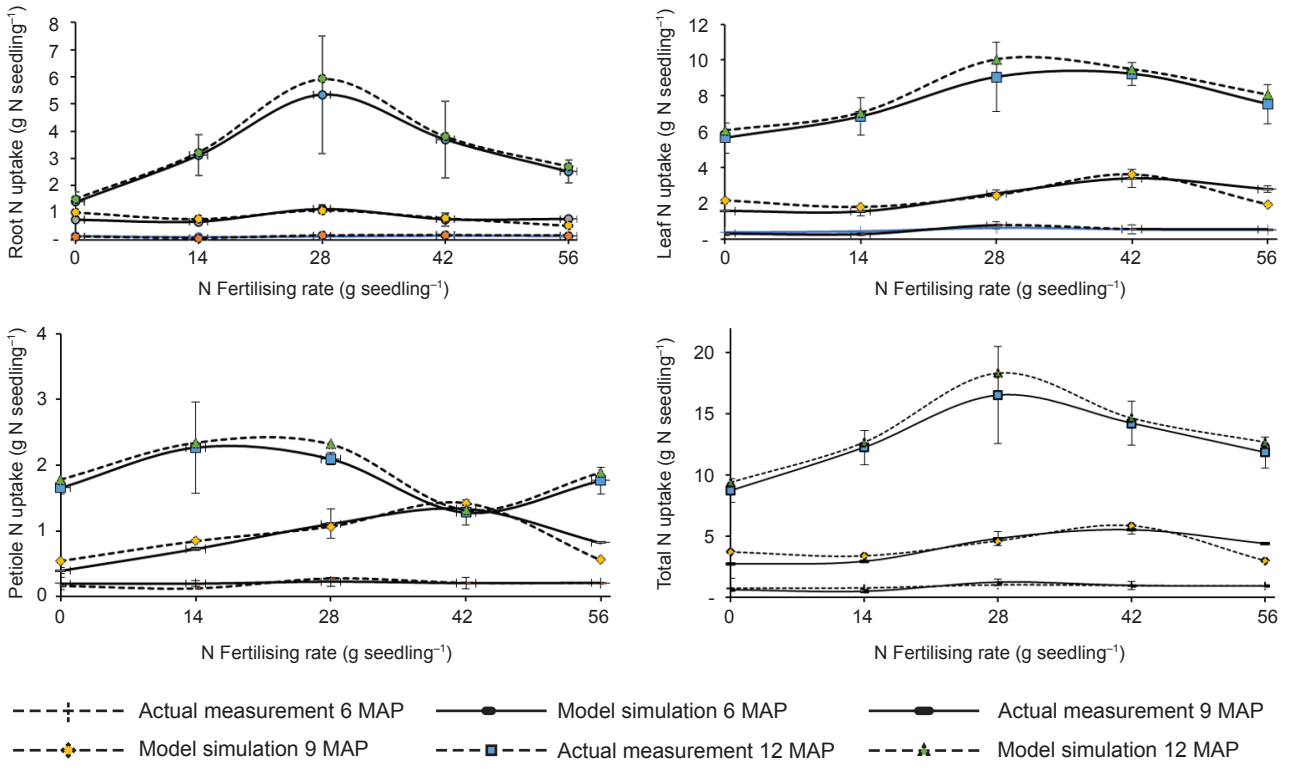


Figure 3. Simulated (dotted line) and measured N uptake (solid line) of N0, N1, N2, N3 and N4.

TABLE 6. DRY WEIGHT AND N-UPTAKE T-TEST RESULT OF ACTUAL MEASUREMENT AND MODEL SIMULATION

Parameter	Treatment				
	N0	N1	N2	N3	N4
Growth model					
Dry weight 6 MAP					
t	0.07	0.06	-0.37	0.04	0.18
$t_{0.05}$	2.31	2.31	2.31	2.31	2.31
Result	ns	ns	ns	ns	ns
Dry weight 9 MAP					
t	0.65	0.32	0.15	0.21	1.34
$t_{0.05}$	2.31	2.31	2.31	2.31	2.31
Result	ns	ns	ns	ns	ns
Dry weight 12 MAP					
t	0.38	-0.23	-0.11	0.08	-0.22
$t_{0.05}$	2.31	2.31	2.31	2.31	2.31
Result	ns	ns	ns	ns	ns
N uptake model					
N uptake 6 MAP					
t	0.05	0.92	0.36	0.02	0.02
$t_{0.05}$	2.31	2.31	2.31	2.31	2.31
Result	ns	ns	ns	ns	ns
N uptake 9 MAP					
t	3.43	0.33	0.22	0.17	1.61
$t_{0.05}$	2.31	2.31	2.31	2.31	2.31
Result	*	ns	ns	ns	ns
N uptake 12 MAP					
t	0.28	0.12	0.18	0.09	0.27
$t_{0.05}$	2.31	2.31	2.31	2.31	2.31
Result	ns	ns	ns	ns	ns

At 3-6 MAP, the accumulation of N nutrient partitions in each plant organ for all treatments tended to be the same (*Table 4*). The highest N accumulation was found in the leaves. At 6-9 MAP, the partitioning of N in the leaf in N3 and N4 is higher than that of N1 and N2. On the other hand, the partition N at the root of N1 and N2 is higher than that of N3 and N4. In 9-12 MAP, N1 and N4 had a similar trend of accumulation N, as well as N2 and N3.

Figure 3 shows the agreement between the simulation results of the N uptake of oil palm seedlings at various doses of N fertiliser and the measurement results. The suitability is based on the data from the simulation results, which are still included in the confidence interval (1-α = 0.95) of the measurement results. T-test result can be seen at *Table 6*.

From *Figure 4*, increasing N fertiliser affected the N uptake to the optimum limit. At the same time, the higher application of N fertiliser increased the leaching of N in the soil.

Discussion

The LAI of the oil palm plantation can be described as the ratio of the total leaflet area of the plantation to the total ground area of that plantation. LAI describes a fundamental property of the oil palm canopy. It is an important index related to the growth and metabolism of the plant, as well as the accumulation of dry matter and yield (Awal *et al.*, 2010). *Table 2* shows that increasing the dose of N will increase LAI to the optimum fertiliser application and then decrease at excessive fertiliser application doses. Increasing the LAI shows that N fertiliser application causes an increase in leaf area per unit area of planting area.

Increasing N fertiliser application increases the growth and biomass of oil palm seedlings to the 100% dose. The increase in plant dry weight caused increased plant shoot, which could be seen from the LAI. Moradi *et al.* (2014) showed that N fertiliser application positively increased palms trunk

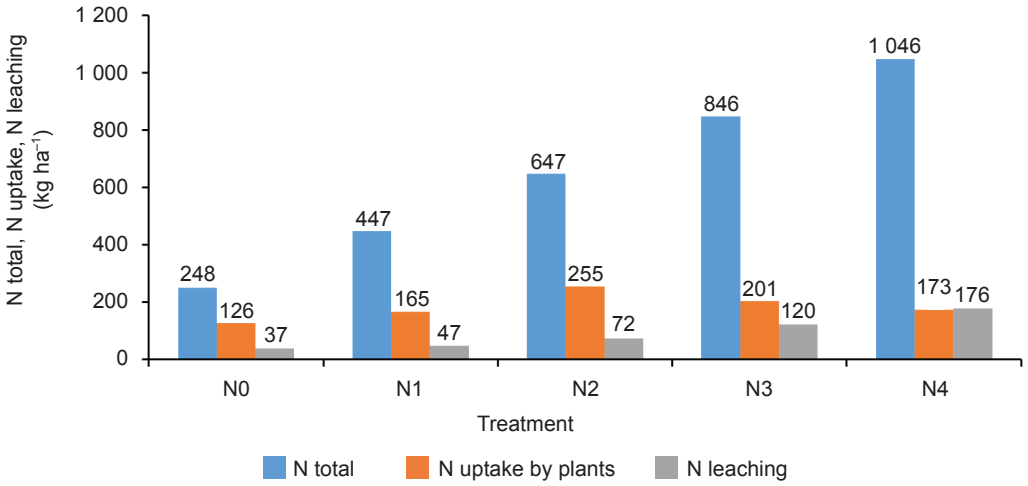


Figure 4. Simulation N total, N uptake and N leaching by model.

measurements and leaf area. The LAI determines the amount of intercepted of radiation (Q_{int}). The Q_{int} value determines the amount of potential biomass production. The accumulation of dry matter reflects the ability of plants to bind energy from radiation through the process of photosynthesis, as well as interactions with other environmental factors (Fried and Hademenos, 2000). Furthermore, leaf N content is a solid factor influencing optimum canopy radiation use efficiency and photosynthesis rate (Sastrohartono *et al.*, 2016).

Furthermore, the growth rate was slower with increased excessive N fertiliser application. Excess N fertiliser application causes disorders on the uptake of nutrients by plant roots and nutrient balance in plant tissues (Fairhurst and Hardter, 2003). Excessive application of N also causes the oil palm growth to be inhibited due to antagonistic interactions among several nutrients (Uexkull and Fairhurst, 1991). Excess N content in plant tissues also causes stunted growth and reduced crop production, making plants vulnerable to attack by pests (Goh and Hardter, 2003).

Higher N levels in plants with higher N fertiliser application cause plants to reduce N demand. This decreased demand in turn causes N uptake to decrease, even though N is available in the soil. Reduction in demand and biomass cause N uptake at higher N doses to be lower. Sugihara *et al.* (2012) reported that changes in inorganic N concentration would affect N assimilation by plants and the potential for nitrogen loss. Subsequent N demand may also help to explain differences in species' response to increases in soil N (Boardman, 1977).

The N partition in oil palm seedlings depends on the condition of N availability in the plant. Optimal N content causes N to be partitioned less in the petiole. Deficiency or excess of N in treatments N0, N1 and N4 treatments resulted in more partitioning of N in the petiole than in leaves. This condition caused N to be preferentially partitioned in the shoot of oil palm seedlings, probably due to an increase in the rate of amino acid translocation to the shoot than the roots (Mohidin *et al.*, 2015). Regarding the proportion of biomass partitioning, the portion partitioned of the shoot consisting of leaves and stems accounted for the most significant proportion of dry matter partitioning, 81.1%-90.9%, while root accounted for only 9.1%-18.9%, (Mohidin *et al.*, 2015). However, the partition distribution of dry matter is influenced by various environmental factors such as air temperature, drought and nutrient deficiencies (Wardlaw, 1990). In plants that experience a deficiency of N and P, more dry matter will be partitioned in the roots than the shoots (Ericsson, 1994).

Increasing N fertiliser application was positively correlated with increased N leaching in the soil (*Figure 4*). The availability of N in soil and high rainfall are associated with the leaching of N. According to Tung *et al.* (2009), leaching losses are related to rainfall patterns, fertiliser treatment and nutrient uptake by roots. Chen *et al.* (2014a) reported that nitrogen loss might occur if excessive nitrogen is available during the seedling stage. Estimates of total losses of N are highly variable, ranging from 21 to 139 kg N ha^{-1} yr^{-1} around an average of 77 kg N ha^{-1} yr^{-1} (Pardon *et al.*, 2016).

Model verification in this study was only carried out on plant dry weight and N uptake variables. The model can estimate the dry weight of oil palm seedlings, so with the model's input, the model, in principle, can be used as a tool to distinguish the level of N adequacy in oil palm

seedlings. The advantages of the model constructed in this study are follows:

- The growth and nutrient uptake models were constructed specifically for the main oil palm nursery.
- The model can be used in conditions of lack/excess of water and nutrients (N, P, K and Mg).
- The nutrient uptake model is built based on nutrient partitioning so that the model can predict nutrient uptake in each seedling organ (leaves, petioles and roots).
- The demand for nutrients (N-demand) in the model is determined based on the actual needs of the seedlings.
- The constructed model requires simple data input (easy to apply).

CONCLUSION

The developed growth and N uptake model can only be used to predict oil palm growth and nutrient uptake in main nurseries. The model requires relatively fewer input data (weather elements and soil fertility) than other models, so the model becomes more applicable than other models. The model was built from the dry matter partition coefficient, nutrient partition coefficient and actual nutrient requirement amounts. The model validation results during the main nursery (nine months) showed that the model developed generally corresponded to the observed values for dry weight and nutrient uptake in the field. The developed model can predict oil palm seedlings' dry weight and nutrient uptake in main nurseries under various conditions of deficiency or excess of N fertiliser level.

ACKNOWLEDGEMENT

The first author would like to express the deepest gratitude to the Indonesia Endowment Fund of Education (LPDP) for granting a study fellowship to the first author and supporting this study.

REFERENCES

Awal, M A; Ishak, W I W and Bockari-Gevao, S M (2010). Determination of leaf area index foroil palm plantation using hemispherical photography technique. *Pertanika J. Sci. Technol., 18(1).*

Boardman, N K (1977). Comparative photosynthesis of sun and shade plants. *Ann. Rev. Plant Physiol., 28*.

Broschat, T K (2009). Palm nutrition and fertilization. *Hortechnology*, *19(4)*: 690-694.

Chen, B; Liu, E; Tian, Q; Yan, C and Zhang, Y (2014a). Soil nitrogen dynamics and crop residues. A review. *Agron. Sustain. Dev., 34(2)*: 429-442. DOI: 10.1007/s13593-014-0207-8.

Chen, C; Pan, J and Lam, S K (2014b). A review of precision fertilization research. *Environ. Earth Sci., 71(9)*: 4073-4080. DOI: 10.1007/s12665-013-2792-2.

DJP (2023). Statistik Unggulan 2020-2022. Direktorat Jendral Perkebunan Kementerian Pertanian Republik Indonesia.

Ericsson, T (1994). Nutrient dynamics and requirements of forest crops. *N. Z. J. For. Sci., 24(2)*: 133-167.

Fairhurst, T and Hardter, R (2003). *Oil Palm: Management for Large and Sustainable Yields*. International Potash Institute.

Fried, G and Hademenos, G (2000). *Scahum's Outlines Biology.* 2nd edition. Erlangga.

Goh, K and Hardter, R (2003). *General Oil Palm Nutrition*. Intern Potash Institute.

Handoko (1992). *Analysis and Simulation of Water-Nitrogen Interaction of Wheat Crop*. The University of Melbourne.

Handoko (1994). *Dasar Penyusunan dan Aplikasi Model Simulasi Komputer untuk Pertanian*. Geomet FMIPA-IPB.

Hartley, W (1988). *The Oil Palm.* 3rd edition. Longman Scientific Technical.

Henson, E I (1992). Carbon assimilation, respiration and productivity of young oil palm (*Elaeis guineensis*). *J. Oil Palm Res., 4(2)*: 51-59.

Hoffmann, M P; Castaneda Vera, A; van Wijk, M T; Giller, K E; Oberthür, T; Donough, C and Whitbread, A M (2014). Simulating potential growth and yield of oil palm (*Elaeis guineensis*) with PALMSIM: Model description, evaluation and application. *Agric. Sys., 131*: 1-10. DOI: 10.1016/j.agsy.2014.07.006.

Ikhajiagbe, B; Aituae, W and Ogwu, M C (2022). Morpho-physiological assessment of oil palm (*Elaeis guineensis* Jacq.) seedlings exposed to simulated drought conditions. *J. Oil Palm Res., 34(1)*: 26-34. DOI: 10.21894/jopr.2021.0018.

Mohidin, H; Hanafi, M M; Rafii, Y M; Abdullah, S N A; Idris, A S; Man, S; Idris, J and Sahebi, M (2015). Determination of optimum levels of nitrogen,

phosphorus, and potassium of oil palm seedlings in solution culture. *Bragantia*, *74(3)*: 247-254. DOI: 10.1590/1678-4499.0408.

Moradi, A; Teh, C B S; Goh, K J; Husni, M H A and Ishak, C F (2014). Decomposition and nutrient release temporal pattern of oil palm residues. *Ann. Appl. Biol.*, *164(2*): 208-219. DOI: 10.1111/aab.12094.

Pardon, L; Bessou, C; Nelson, P N; Dubos, B; Ollivier, J; Marichal, R; Caliman, J P and Gabrielle, B (2016). Key unknowns in nitrogen budget for oil palm plantations. A review. *Agron. Sustain. Dev.*, *36(1*): 1-21. DOI: 10.1007/s13593-016-0353-2.

Prado, A D; Brown, L; Schulte, R; Ryan, M and Scholefield, D (2006). Principles of development of a mass balance N cycle model for temperate grasslands: An Irish case study. *Nutr. Cycl. Agroecosystems*, *74(2*): 115-131. DOI: 10.1007/s10705-005-5769-z.

Roose, T; Fowler, A C and Darrah, P R (2001). A mathematical model of plant nutrient uptake. *J. Math. Biol.*, *42(4*): 347-360. DOI: 10.1007/s002850000075.

Rowe, E C; Van Noordwijk, M; Suprayogo, D and Cadisch, G (2005). Nitrogen use efficiency of monoculture and hedgerow intercropping in the humid tropics. *Plant Soil*, *268(1*): 61-74. DOI: 10.1007/s11104-004-0227-2.

Santi, L P and Goenadi, D H (2016). Pupuk organo-kimia untuk pemupukan bibit kelapa sawit organo-chemical fertilizer for oil palm seedling fertilization. *E-Journal Menara Perkebunan*, *76(1).* DOI: 10.22302/ppbbi.jur.mp.v76i1.94.

Sastrohartono, H; Renjani, R A; Suryotomo, A P and Uktoro, A I (2016). Unmanned aerial vehicle application for plantation mapping and automatic oil palm trees counting on oil palm plantation management oil palm. https://www.researchgate.net/publication/316880425, accessed on 10 March 2021.

Squire, G (1984). *Light interception, productivity, and yield of oil palm*. PORIM Internal Report. Palm Oil Research Institute of Malaysia, Kuala Lumpur, Malaysia.

Sudradjat, Darwis, A and Wachjar, A (2014). Optimasi dosis pupuk nitrogen dan fosfor pada bibit kelapa sawit (*Elaeis guineensis* Jacq.) di pembibitan utama. *J. Agron. Indonesia*, *42(3*): 222-227.

Sugihara, S; Funakawa, S; Kilasara, M and Kosaki, T (2012). Effect of land management on soil microbial N supply to crop N uptake in a dry tropical cropland in Tanzania. *Agric. Ecosystems Environ.*, *146(1)*: 209-219. DOI: 10.1016/j.agee.2011.11.008.

Tao, H H; Donough, C; Hoffmann, M P; Lim, Y L; Hendra, S; Rahmadsyah, Abdurrohim, G; Indrasuara, K; Lubis, A; Dolong, T and Oberthür, T (2017). Effects of best management practices on dry matter production and fruit production efficiency of oil palm. *Eur. J. Agronomy*, *90*: 209-215. DOI: 10.1016/j.eja.2017.07.008.

Tung, P G A; Ah Tung, P G; Yusoff, M K; Majid, N M; Joo, G K and Huang, G H (2009). Effect of N and K fertilizers on nutrient leaching and groundwater quality under mature oil palm in sabah during the monsoon period. *Amer. J. Applied Sci.*, *6(10*): 1788-1799.

Uexkull, H R V and Fairhurst, T H (1991). *Fertilizing for High Yield and Quality: The Oil Palm: Vol. IPI-Bulletin No. 12*. International Potash Institute.

Wardlaw, I F (1990). The control of carbon partitioning in plants. *New Phytol.*, *116*: 341-381.

Journal of Oil Palm Research Vol. 36 (4) December 2024 p. 608-617
DOI: https://doi.org/10.21894/jopr.2023.0053

FISH ASSEMBLAGES IN ARTIFICIAL DRAINAGE SYSTEMS ACROSS OIL PALM PLANTATION DEVELOPMENT PHASES ON PEATLAND IN SARAWAK

ANGIE SAPIS[1]*; BETTYCOPA AMIT[1]; NIK SASHA KHATRINA KHAIRUDDIN[1] and IDRIS ABU SEMAN[1]

ABSTRACT

Development of oil palm plantations on peatland requires drainage for water level regulation which often creates new artificial habitats for aquatic inhabitants. We assessed the changes in fish communities of the artificial drainage systems in Betong, Sarawak, Malaysia. Fish were sampled from three sampling stations at the man-made drainage from July 2013 until July 2019. A total of 1546 individuals represented by 12 species were recorded across oil palm plantation development phases. Although it is an artificial habitat, the conversion of logged peat swamp forest to cleared land reduced fish species richness by at least 25%. Not many changes were observed when the land was initially planted with palms. As the oil palm reached 2 years old, fish species richness increased and was comparable to the prior conversion phase. The fish abundance fluctuated as the peat swamp forest was being cleared, and throughout the oil palm development phases.

Keywords: blackwater, fish abundance, land use, loss forest, man-made drainage.

Received: 29 November 2022; **Accepted:** 27 August 2023; **Published online:** 13 October 2023.

INTRODUCTION

Peat swamp forest (PSF) is a waterlogged forest that grows on a layer of organic materials, such as dead leaves and plants, up to 20 m thick (UNDP, 2006). Despite having a low level of nutrients and low dissolved oxygen with acidic water, this forest is an important component of the wetland due to its unique ecosystem (Leete *et al*., 2006). The freshwater habitat of the peat swamp is known as a habitat for diverse and interesting fish fauna that have narrow niches and a restricted range (Norhisyam *et al*., 2012).

Until 1968, only 26 fish species were known from blackwaters (colour of PSF water) in Peninsular Malaysia, of which only *Spharichthys osphromenoides* can be regarded as restricted to blackwater (Ng *et al*., 1994). In the North Selangor PSF, a total of 47 blackwater fish species have been recorded in this habitat thus, showing that PSF does support diverse fish fauna which makes it of great interest to ecologists (Davies and Abdullah, 1989). In addition, fish exhibit the highest endemicity to peat swamps compared to other faunal groups such as vertebrate species and there is no vertebrate except fish that is considered entirely dependent or restricted to peat swamp habitat (Posa *et al*., 2011). Up to 33% of the known freshwater fish species are associated with peat swamps (Kottelat *et al*., 2006; Ng *et al*., 1994; Posa *et al*., 2011). The PSFs are known to have some of the highest freshwater fish diversity in the world (Wetland International, 2010). The study by Ng *et al*. (1994) reported that diverse and interesting fish fauna with narrow niches and restricted ranges were present in PSFs. According to Rahim and Esa (2006), most of the fishes that inhabit the peat swamp system are those species that are tolerant to low oxygen conditions and acidic water that is rich in decaying organic matter. About 66% of the total fish found in the North Selangor peat swamp have the ability to breathe atmospheric air, whether they are air breathers or often swim near the surface (Ng *et al*., 1994). Additionally, blackwater, characterised

[1] Malaysian Palm Oil Board,
6, Persiaran Institusi, Bandar Baru Bangi,
43000 Kajang, Selangor, Malaysia.

* *Corresponding author e-mail: angie@mpob.gov.my*

by its black appearance or tea-coloured water, acidic and low dissolved oxygen has been regarded as an extreme and inhospitable habitat and, thus was poorly explored in the early days.

Over the past few decades, the conversion of PSF for oil palm agriculture has been common, particularly in the Southeast Asia region (Miettinen *et al*., 2016). Peatland has become the potential land for oil palm cultivation since the land mineral soil has become scarce. By the year 2018, about 657 000 ha of peatland in Sarawak were planted with oil palm, which covered about 34% of the total oil palm planted area in the region (Wan Mohd Jaafar *et al*., 2020). Fewer studies related to the fish community are being carried out in oil palm plantations in Malaysia. Dosi *et al.* (2019) conducted a fish study in Sungai Kulak of Tinbarap Conservation Area (TCA), located in Tinbarap Estate Miri, Sarawak, and documented a total of 106 fish representing 13 species and seven families. Another study by Chong (2014) on the diversity and abundance of freshwater fish fauna in various landscapes (drainage systems and streams or rivers within conservation areas) within oil palm plantations recorded a total of 503 fish represented by 35 species. From the species caught, two species were endemic to Borneo (namely, *Nematabramis everetti* and *Barbonymus collingwoodii*), three exotic species [*Cherax quadricarinatus* (red-claw crayfish), *Macrobranchium rosenbergii* (giant freshwater prawn) and *Oreochromis niloticus* (tilapia)], while the remaining were native species. Both studies recorded the dominance of Cyprinidae in the conservation area in oil palm plantations which are similar to other peat swamp habitats (Chong, 2014; Dosi *et al*., 2019).

Being a waterlogged forest with a high water table under natural conditions, the removal of excess water to lower the water table as required for oil palm cultivation is essential before cultivating oil palm on peatland (Lim *et al*., 2012). Therefore, the drainage network is often established for water table regulation which will create a new artificial habitat for aquatic inhabitants, particularly fish. Thus, a fish study covering an area in artificial habitat in response to the conversion of drained peat swamp forest to oil palm monoculture was conducted. This study hypothesises that the fish community in the artificial drainage system changes throughout the development phases in relation to the change in water quality and habitat conditions.

MATERIALS AND METHODS

Study Site

The aquatic fauna study was focused on the fish community and assemblages throughout the oil palm development phases in Ladang Lingga 2, Betong, Sarawak, Malaysia (*Figure 1*).

The sampling sites selected were located at the man-made drainage within the area with ongoing development activity. There was no river present in this development area hence the fish study was conducted at artificial drainage systems which were constructed to control water-table. However, the drainage system is connected to the adjacent mature oil palm plantation and Lupar River. Lupar River is located 1 km apart from the oil palm plantation and is covered with peat swamp forest that acts as a buffer

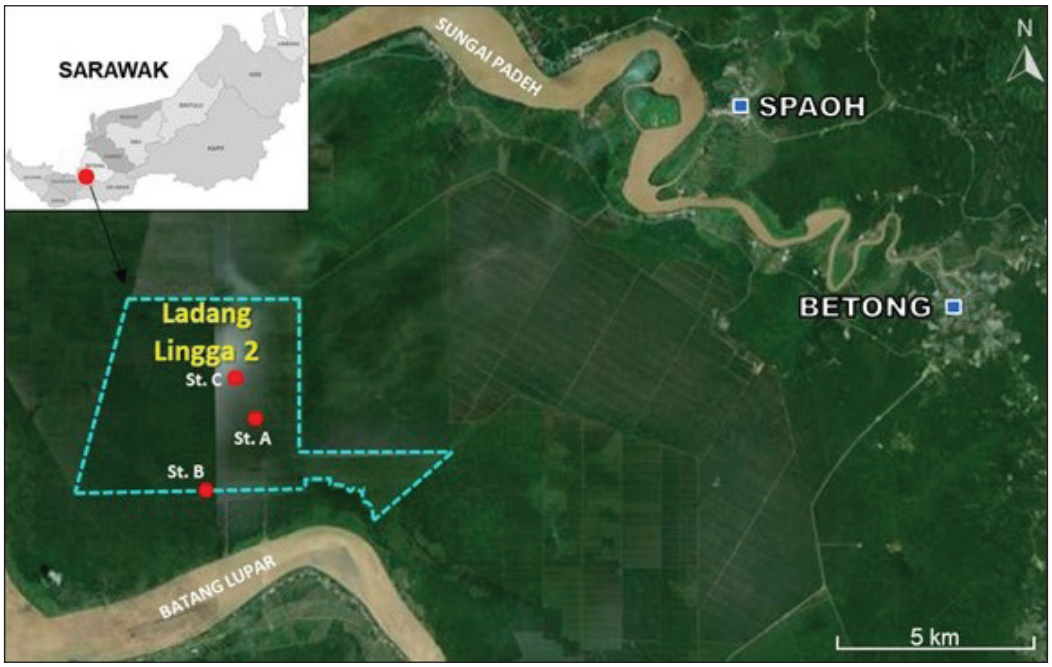


Figure 1. Location of the fish fauna sampling points in Ladang Lingga 2, Betong Division, Sarawak, Malaysia.

zone. The drainage system is very important for water-table management in oil palm development on peat to get high and sustainable yield production and to reduce carbon dioxide emission (Othman *et al*., 2011). Fish sampling was initiated at the early drainage (main and collection drains) system that was constructed together with the road system. Once the road and drainage systems were established, the area was cleared and the field drain was created. After the clearing was done, the planting was immediately commenced with oil palm. As the area was planted with oil palm, the fish study was divided into three different drainage systems: Collection drain (St. A), perimeter drain (St. B), and main drain (St. C). Fish sampling was conducted throughout the oil palm plantation development phases, from July 2013 to July 2019, with the frequency of every three months at all stations. Sampling before oil palm planting was carried out in two phases: Drained peat swamp forest (DPSF) and cleared land (CL) that was converted to oil palm plantation. Meanwhile, samplings after planting involved five phases of the oil palm development phase, namely, 1 year oil palm (YOP), 2-YOP, 3-YOP, 4-YOP and 5-YOP.

Fish Sampling

Fish were sampled using three layer gill nets, monofilament gill nets (mesh size of 5.5 and 2.5 cm), and kick nets. The gill nets were deployed for three days and two nights. Fish species were identified *in-situ* while fishes that were unable to be identified were preserved in formalin (10%) and brought back to the laboratory for further identification. After identification, fish samples were transferred to ethanol (70%) for long-term preservation. Fish identification was carried out at the species level with reference to Froese and Pauly (2019), Kotellat and Whitten (1993), and Inger and Chin (2002). The Conservation Status of the fish was listed based on The IUCN Red List of Threatened Species Version 2021-3 (IUCN, 2022).

***In-situ* Parameter Water Quality Sampling**

Triplicate readings of water temperature, dissolved oxygen (DO), pH and conductivity were measured at the subsurface of all sampling stations using YSI 6600 V202 Multi-parameter Water Quality Sonde (YSI Inc., Ohio, USA).

Statistical Analyses

One-way analysis of variance (ANOVA) was used to determine the significant differences in environmental data, water quality, species richness and abundance of fish community among development phases, with a *posteriori* Tukey HSD test at a significance level of 95% (Calloway *et al*., 2017; Gyawali *et al*., 2013; Ndungu *et al*., 2013; Zakeyuddin *et al*., 2016). These analyses were computed using SPSS 17.0 Software. Variation in the fish community of different oil palm plantation development phases was investigated using the ordination method. Non-metric multidimensional scaling (NMDS) was carried out using the metaMDS function from the vegan package in R version 3.6.3. Sites that were most similar to one another in species composition are closest together on the NMDS plot (Oksanen *et al*., 2015). Subsequently, the statistical difference between groups was tested using the function "ANOSIM" from the vegan package.

RESULTS AND DISCUSSION

A total of 1546 fish representing 12 species belonging to six families (*Table 1* and *Figure 2*) were recorded throughout this study. Meanwhile, Khairul-Adha *et al.* (2009) recorded 36 species of fish from brownish and blackish water habitats of Batang Kerang in Balai Ringin, Sarawak. Rahim *et al.* (2009) also studied the fish fauna in blackwater and waters originating from PSFs at Batang Kerang, Balai Ringin, Sarawak and reported 12 species of fish from 12 families, and the Kissing Gourami fish was the dominant species. Hassan *et al.* (2010) found seven out of 15 fish species were from a water body with peat-like characteristics in Nanga Merit area and Giam *et al.* (2012) recorded 13 fish species from the peat swamps of Rajang and Sadong in Sarawak. Sule *et al.* (2016) stated that a total of 198 peat swamp species have been recorded in Malaysia whereby 114, 49, 13, 58, 31 and 40 species were recorded from North Selangor PSF, PSF of Perak, PSF of Johor, PSF of Pahang, East Peninsular Malaysia (parts of Pahang and Terengganu), and East Malaysia (Sarawak and Sabah), respectively.

The most dominant fish family was Anabantidae with 51.4% of the total number of individuals caught followed by Helostomatidae (22.8%), Osphronemidae (17.0%), Clariidae (5.1%), and finally, Channidae (3.8%). The least dominant fish family in this area was Siluridae, with 0.1% of the total number of fish caught. Similarly, as reported by Rahim *et al*. (2009), these families of fish species are occupied with accessory respiratory organs and suprabranchial cavities that assist them in adaptation to water with low concentrations of dissolved oxygen and high acidity. Of the 12 species caught, *Anabas testudineus* was the most abundant comprising 51.4% of the total number of fish caught, followed by *Helostoma temminckii* (22.8%), *Trichopodus trichopterus* (16.8%), *Clarias leiacanthus* (2.3%), *C. meladerma* (2.0%), *Channa striata* (1.8%) and *C. lucius* (1.5%). Meanwhile, fishes such as *Channa bankanensis*, *Clarias nieuhofii*, *Trichopodus pectoralis*,

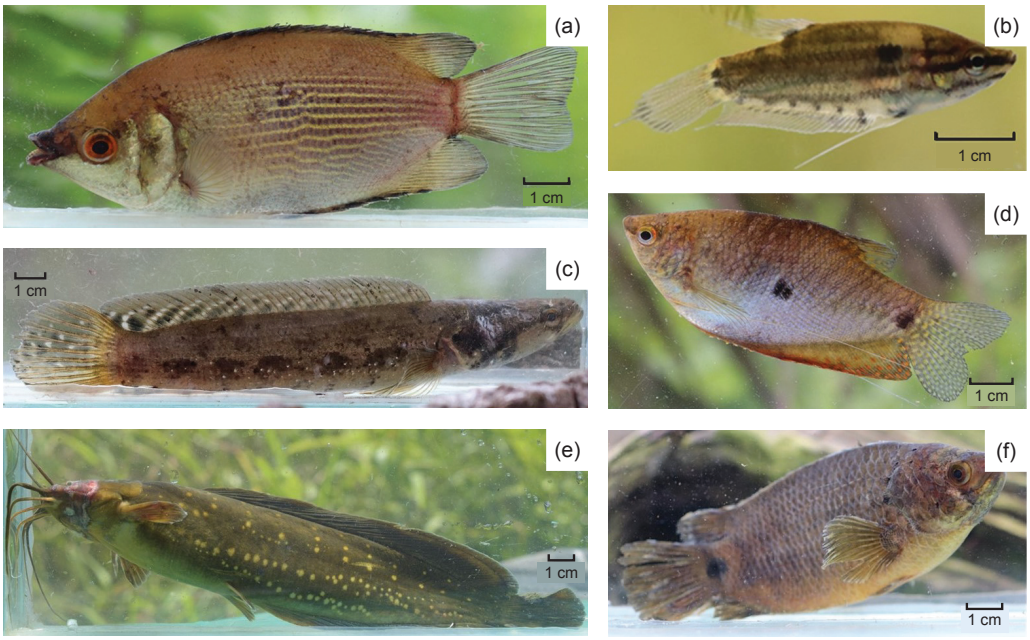


Figure 2. Fish species recorded from the study: (a) Helostoma temminckii, *(b)* Trichopsis vittata, *(c)* Channa lucius, *(d)* Trichopodus trichopterus, *(e)* Clarias leiacanthus *and (f)* Anabas testudineus.

TABLE 1. LIST OF FISH SPECIES, RELATIVE ABUNDANCE AND THEIR CONSERVATION STATUS RECORDED AT LADANG LINGGA 2, BETONG, SARAWAK

Family name	Common name	Scientific name	IUCN	Relative abundance (%)	Oil palm development phase						
					DPSF	CL	1YOP	2YOP	3YOP	4YOP	5YOP
Anabantidae	Climbing Perch	*Anabas testudineus*	LC	51.4	+	+	+	+	+	+	+
Channidae	Bangka Snakehead	*Channa bankanensis*	LC	0.5	+	-	-	+	-	-	+
	Forest Snakehead	*Channa lucius*	LC	1.5	+	+	+	+	-	+	+
	Striped Snakehead	*Channa striata*	LC	1.8	+	+	+	+	+	+	+
Clariidae	Forest Catfish	*Clarias leiacanthus*	LC	2.3	+	+	+	+	+	+	+
	Blackskin Catfish	*Clarias meladerma*	LC	2.0	+	+	+	+	+	+	+
	Slender Catfish	*Clarias nieuhofii*	LC	0.8	+	+	+	+	-	+	-
Helostomatidae	Kissing Gourami	*Helostoma temminckii*	LC	22.8	+	+	+	+	+	+	+
Osphronemidae	Snakeskin Gourami	*Trichopodus pectoralis*	LC	0.1	-	-	-	-	-	+	-
	Three Spot Gourami	*Trichopodus trichopterus*	LC	16.8	-	+	+	+	+	+	+
	Croaking Gourami	*Trichopsis vittata*	LC	0.1	-	-	-	-	-	-	+
Siluridae	Ompok Catfish	*Ompok leiacanthus*	NT	0.1	-	-	-	-	-	-	+

Note: Conservation Status based on the IUCN Red List of Threatened Species Version 2021-3 (IUCN, 2022): NT - near threatened (includes LR/nt - lower risk/near threatened); LC - least concern (includes LR/lc - lower risk, least concern). For oil palm development phase: DPSF - drained peat swamp forest; CL - cleared land; 1YOP - 1 year oil palm; 2YOP - 2 years oil palm; 3YOP - 3 years oil palm; 4YOP - 4 years oil palm; and 5YOP - 5 years oil palm. "+" denotes the presence of species and "-" denotes the absence of species in the study area.

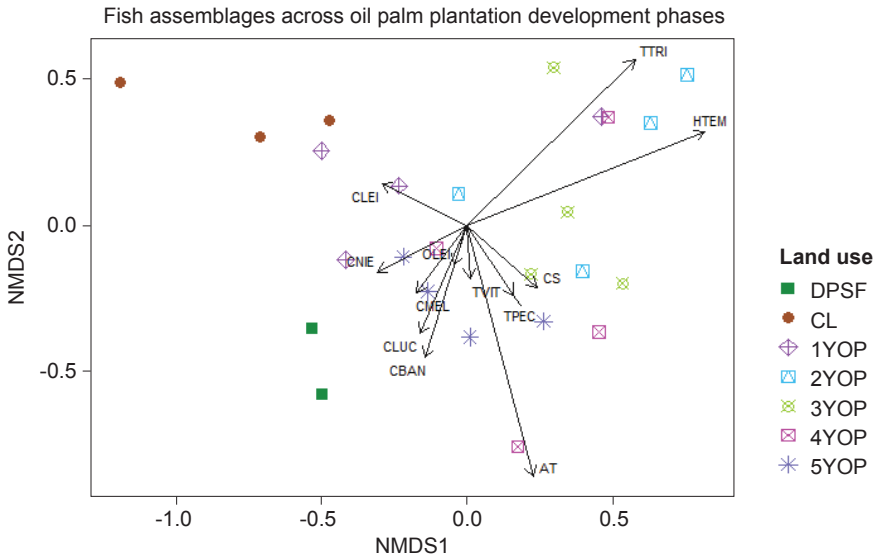
T. vittate and *Ompok leiacanthus* were considered least dominant as they only contributed less than 1% of the total number of individuals caught. Fish species recorded in this study were similar to those recorded in the North Selangor peat swamp forest Selangor, Paya Beriah peat swamp forest Perak, Southeast Pahang peat swamp forest and Sarawak peat swamp forest (Ahmad *et al*., 2005; 2013; Ismail *et al*., 2013; Khairul-Adha *et al*., 2009; Rezawaty, 2004; Shah *et al*., 2006; Siow *et al*., 2013).

Non-metric multidimensional scaling (NMDS) ordination using Bray-Curtis similarities was used to summarise the variations that may occur within the fish assemblage in the oil palm plantation throughout the sampling period (*Figure 3*). The ordination displayed DPSF and CL were grouped

on the left of the graph while 1YOP, 2YOP, 3YOP, 4YOP and 5YOP were clustered to the right, which indicated a gradual change in fish assemblage structure in the oil palm plantation throughout the oil palm development phases. This variation was also found to be significant by ANOSIM test among all sites at $p < 0.05$.

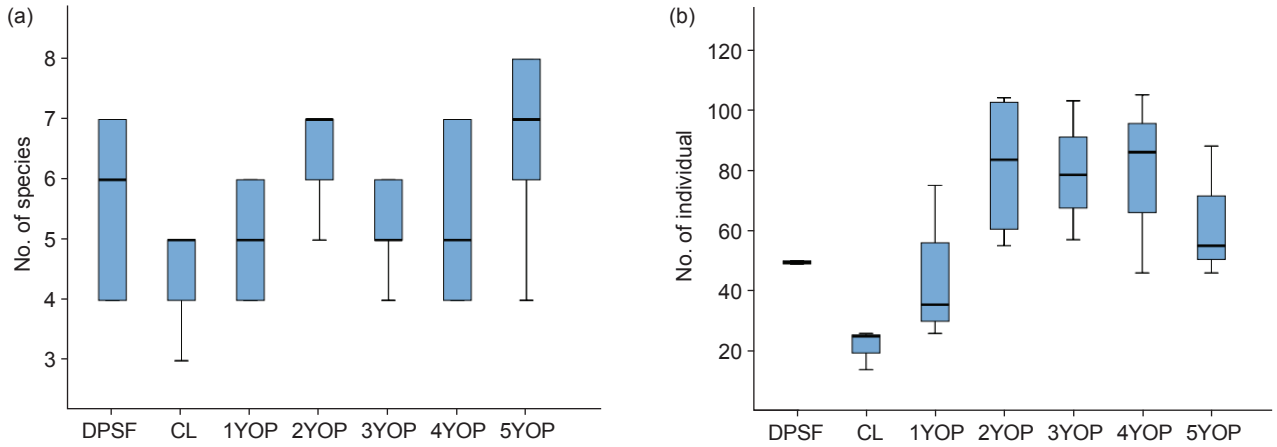
Seven fish species were recorded from the aquatic habitat of drained peat swamp forest. As the area was being cleared, fish species richness and abundance decreased by at least 25% and 48% respectively (*Figure 4*).

There is no significant difference in fish species richness at the artificial drainage system along the oil palm development phases ($F_{(6,18)} = 1.404$, $p = 0.267$). After planting, during 1YOP, species richness showed an increment by at least 10% compared to the CL phase but remained lower by at least 14% as compared to DPSF. Meanwhile, fish abundance increased by at least 48% as compared to DPSF and double that of those recorded during the CL phase. As it reached 2YOP, fish species richness was comparable to the DPSF phase and more than those recorded during the CL phase. The abundance of fish ($F_{(6, 18)} = 4.430$, $p=0.006$) was significantly greater in 2YOP (mean = 81 individuals), 3YOP (mean = 75 individuals), and 4YOP (mean = 80 individuals) than CL (mean = 21 individuals), DPSF (mean = 50 individuals), 1YOP (mean = 43 individuals) and 5YOP (mean= 61 individuals). Fish abundance was doubled as compared to the DPSF phase and was fourfold greater than in the CL phase.



Note: Oil palm development phase: DPSF - drained peat swamp forest; CL - cleared land; 1YOP - 1 year oil palm; 2YOP - 2 years oil palm; 3YOP - 3 years oil palm; 4YOP - 4 years oil palm; and 5YOP - 5 years oil palm.

Figure 3. Non-metric Multidimensional Scaling (NMDS) ordination of fish assemblage in different oil palm plantation development phases.



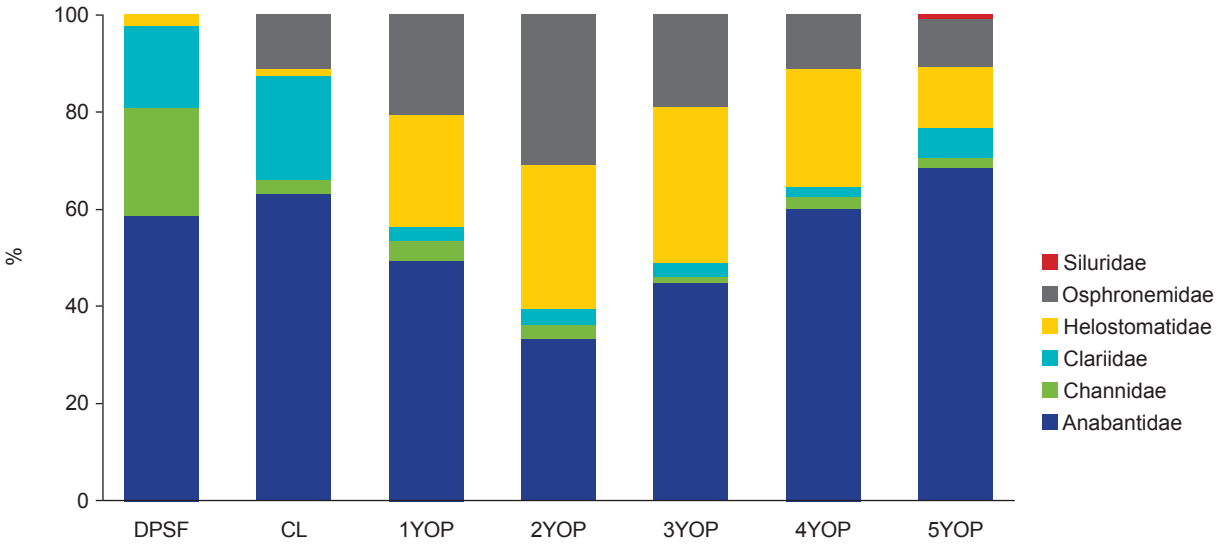
Note: Abbreviation for oil palm development phase: DPSF - drained peat swamp forest; CL - cleared land; 1YOP - 1 year oil palm; 2YOP - 2 years oil palm; 3YOP - 3 years oil palm; 4YOP - 4 years oil palm; and 5YOP - 5 years oil palm.

Figure 4. Boxplots of fish, (a) species richness and (b) abundance across oil palm plantation development phases.

Fish composition in each development phase of the oil palm plantation shows that Anabantidae was dominant during each phase (*Figure 5*). Helostomatidae constituted a very small percentage of the population before oil palm planting (*i.e.*, during DPSF and CL phase). After oil palm planting (1YOP-5YOP) the proportion increased. Likewise, Osphronemidae which was only recorded after the forest was cleared showed increments in the community composition as palms aged. In contrast to Helostomatidae and Osphronemidae, the composition of Channidae was lower after conversion and remained low after oil palm planting. *Channa bankanensis* for instance was recorded during the DPSF phase but was not recorded as the forest was being cleared. It was until the palm reached 2YOP that this species was recorded again. Similarly, the composition of Clariidae was lower compared to DPSF and CL phases after oil palm planting. Siluridae which was represented by *Ompok leiacanthus* was only recorded during the 5YOP which suggests that it might have entered the plantation drainage network from the nearby river.

One-way ANOVA results show significant differences in water temperature, pH, dissolved oxygen, and conductivity throughout the oil palm development phases (*Table 2*). After planting with oil palm, the pH of the water became more acidic, water temperature and dissolved oxygen were lower, and conductivity was higher. This may be the reflection of agricultural activities in the oil palm plantation similar to those reported in the MAAH oil palm plantation in Selangor by Azizan *et al*. (2021). Shabalala *et al*. (2013) also reported high conductivity in the oil palm plantation could be due to the application of fertiliser on the palm trees. These results indicate that fish inhabiting the water habitat in oil palm plantations were able to tolerate the acidic, low dissolved oxygen and water temperature and higher conductivity.

The fish study was conducted at artificial drainage systems as the river is not present in this area, similar to those conducted by Azizan *et al*. (2021) in drains in oil palm plantations in the southern part of Selangor. This artificial drainage system is connected with adjacent mature oil palm plantations and rivers (1 km apart). In this artificial drainage system, a total of 12 species of fish were recorded across the development phases, of which all seven species of the DPSF fish species continued to be recorded after the forest conversion to oil palm plantation, while four fish species were additional species from DPSF species, appearing following clearing process and planting of oil palm. The presence of these species might be due to the drainage system in this plantation being connected to an adjacent mature oil palm plantation drainage system. Azizan *et al*. (2021) recorded five fish species in an oil palm plantation in the southern part of Selangor with the species also recorded in this study. A fish study conducted by Chong (2014) in oil palm plantations in different ecosystems including rivers within peat swamp conservation areas and oil palm drainage recorded 35 species of fish. Also, Dosi *et al*. (2019) conducted a fish study at a river located within the peat swamp conservation area and recorded a total of 13 species. Both studies showed that the family Cyprinidae was the most diverse species recorded at rivers within conserved peat swamp forests in oil palm plantations. Family Cyprinidae



Note: Abbreviation for oil palm development phase: DPSF - drained peat swamp forest; CL - cleared land; 1YOP - 1 year oil palm; 2YOP - 2 years oil palm; 3YOP - 3 years oil palm; 4YOP - 4 years oil palm; and 5YOP - 5 years oil palm.

Figure 5. Percentage of fish abundance according to family recorded across different phases of oil palm plantation developments.

TABLE 2. *In-situ* WATER QUALITY PARAMETERS RECORDED ACCORDING TO DIFFERENT OIL PALM DEVELOPMENT PHASES

Parameter	Oil palm development phase							*p*-value
	DPSF	CL	1YOP	2YOP	3YOP	4YOP	5YOP	
Cond (mS/cm)	0.074 ± 0.001^{a}	0.89 ± 0.001^{a}	0.091 ± 0.001^{a}	0.094 ± 0.001^{ab}	0.119 ± 0.005^{b}	0.178 ± 0.008^{c}	0.260 ± 0.005^{d}	0.01
Temperature (°C)	31.5 ± 0.80^{bc}	30.1 ± 0.45^{b}	31.5 ± 0.24^{bc}	31.9 ± 0.21^{c}	30.9 ± 0.34^{bc}	27.7 ± 0.19^{a}	28.3 ± 0.30^{a}	0.01
pH	4.2 ± 0.03^{b}	4.3 ± 0.03^{b}	4.4 ± 0.014^{b}	3.76 ± 0.06^{a}	3.81 ± 0.034^{a}	3.81 ± 0.07^{a}	3.9 ± 0.06^{a}	0.02
DO (mg L^{-1})	0.98 ± 0.56^{a}	2.39 ± 1.74^{b}	4.32 ± 0.75^{d}	3.65 ± 2.33^{cd}	2.84 ± 1.59^{bc}	1.29 ± 0.79^{a}	1.18 ± 1.63^{a}	0.01

Note: Means with the same letters (in alphabet) in the same row are not significantly different with $p>0.05$. Abbreviation for oil palm development phase: DPSF - drained peat swamp forest; CL - cleared land; 1YOP - 1 year oil palm; 2YOP - 2 years oil palm; 3YOP - 3 years oil palm; 4YOP - 4 years oil palm; and 5YOP - 5 years oil palm.

was found to commonly dominate the rivers in Southeast Asia (Rahim *et al*., 2009). The diversity and composition of the freshwater fish fauna are associated with several factors in the streams and rivers such as availability of food sources, topography, physicochemical properties of water, and water current (Rahim *et al*., 2009). Freshwater fishes that can adapt to the environment are likely to have a higher possibility of surviving (Chong, 2014). The increment of species richness and abundance in the artificial drainage habitat of a newly developed oil palm plantation on peatland after planting could be due to the extension of the drainage network, which increases the connectivity of fishes from the nearby plantation drainage network and river to the newly created habitat.

It was different for artificial drainage systems whereby the family Clariidae (air-breathing Catfish) are the most diverse species recorded during DPSF, CL, and oil palm phases (except 3YOP and 5YOP) with three species. In Borneo, catfishes are the most abundant component of freshwater fish fauna together with the family Cyprinidae and they also tend to display an overwhelming rate of endemic species (Kottelat and Whitten, 1993). Catfishes of the *Ompok leiacanthus* recorded in this study were listed as Near Threatened species under IUCN Red List. Overall, the species recorded consisted of hardy species that can tolerate harsh water conditions. In this study, climbing perch, *Anabas testudineus*, was the most abundant fish species recorded along the development phases followed by Kissing Gourami, *Helostoma temminckii,* and Three Spot Gourami, *Trichopodus trichopterus,* and these species are air-breathing species. Air-breathing fishes are bimodal breathers where their organ enable them to obtain oxygen from atmospheric air and also when in water (Nelson, 2014). During the oil palm phases, all these species are present in all drainage systems, *i.e*., the main drain and collection drain. The dominance of *Anabas testudineus* could be related to its ability to tolerate low oxygen levels and turbid water conditions, thus enabling its succession in the new habitat, especially after forest clearance (Bhattacharjee *et al*., 2009; Habib and Hassan, 1994). This species is also equipped with the labyrinth, thus enabling it to take oxygen from the air and can tolerate turbid stagnant waters (Kottelat, 2001; Velmurugan *et al*., 2015).

Low dissolved oxygen (DO) levels in the drainage system might be due to high conductivity caused by the agricultural activity after planting with oil palm. DO value in this study was recorded lower as compared to the study conducted by Gandaseca *et al*. (2015) at Sibu and Mukah District, Sarawak. Gandaseca *et al*. (2015) found that rivers at newly planted oil palm plantations recorded DO values of 3.37+0.07 at Sibu and 3.86+0.10 at Tatau while at undisturbed peat swamp forest recorded 4.98+0.14 at Pandan and 5.02+0.09 at Sepadok. Water temperature decreased and became cooler after the drainage system was shaded by the palm canopy. Water temperature is influenced by the lack of canopy cover, its shallowness and stagnant water condition (Gandaseca *et al*., 2015). In addition, *A. testudineus* possesses a special accessory air-breathing organ, situated just above the gills in a large extension on the upper part of each gill chamber, which facilitates the utilisation of atmospheric air for respiration (Hughes *et al*., 1973). During the larval and juvenile stage, *A. testudineus* prefers to feed on plankton while in the adult stage, they mainly feed on insects, invertebrates, small fish, and plants (Davenport and Matin, 2006). *Helostoma temminckii* constitutes a very small percentage of the fish community before oil palm planting. However, after oil palm planting starting from 1YOP to 5YOP they proliferated to a larger number. It feeds on a variety of plants and animals including green algae, zooplankton, and aquatic insects near the water surface (Rainboth, 1996; Ukkatawewat, 2005). *Trichopodus trichopterus* was the third most abundant species in this study. This species is small and native to Southeast Asia (Knight, 2010). They successfully colonised new aquatic habitats because of their wide environmental tolerance, ability to colonise anthropogenically disturbed habitats, tropic opportunism, and fast growth rate (Pinter, 1986). In addition, the presence of *T. trichopterus* after the clearing of land could be influenced by the forming of feeding aggregations for

short-term temporal patterns of resource availability (Azizan *et al*., 2021; Syarifuddin and Kramer, 1996). Dosi (2017) found that an artificial drainage system in oil palm plantation on peat recorded high water temperature, turbidity, total suspended solid (TSS), conductivity, biochemical oxygen demand (BOD), pH and nitrite but low dissolved oxygen. This could be related to agricultural activities and fish species that are recorded in oil palm plantation drainage systems can tolerate to these water quality conditions.

After conversion phases, four additional species of fish have been recorded from DPSF phase fish species: *Trichopodus trichopterus* at CL, *T. pectoralis* at 4YOP and *T. vittata* and *Ompok leiacanthus* at 5YOP. The appearance of additional fish species in this study might be due to the connection between the drainage system and Lupar River nearby. Fish abundance slightly decreased after 4YOP and this could be attributed to the vegetation removal which resulted in the loss of vegetation cover responsible to shade the water surface and subsequently increase the water surface exposure to sunlight, which then increases the water temperature. In addition, dredging activities might have resulted in the increase in sedimentation of water habitat during the process and thus negatively affecting the fish. It is also important to note that prior to conversion, *i.e.*, during the DPSF phase, samplings were conducted at the artificial drainage system that was previously made to regulate the water table as preparation for oil palm planting. During this phase, the drainage network has been established but not extensive. During the CL phase, more areas were dredged to extend the drainage network. Even though the extension of the drainage network creates new habitat for fish, the reduction in species richness and abundance could be attributed to the vegetation removal which resulted in the loss of vegetation cover responsible for shading the water surface and subsequently increasing the water surface exposure to sunlight, therefore, increase the water temperature.

CONCLUSION

This study assesses the response of fish assemblages in artificial drainage systems as the drained peat swamp forest was being converted to oil palm monoculture. Species richness and abundance fluctuated as forest area was cleared and throughout the oil palm development phases. However, after oil palm planting, fish abundance showed an early recovery as the palm reached one year old meanwhile fish species richness recovered as the palm reached two years old. Letting natural plants grow along the drainage system for better water quality creates habitats for aquatic and wetland carnivorous fauna.

ACKNOWLEDGEMENT

We would like to thank the Malaysian Palm Oil Board for their financial and logistical support. We are also grateful for field assistance from the staff of the Peat Ecosystem and Biodiversity Unit, Institute of Biodiversity and Environmental Conservation of Universiti Malaysia Sarawak (UNIMAS), and Ella Michael Dosi. We would also like to thank the Forestry Department of Sarawak for the research permission.

REFERENCES

Ahmad, A; Mazlan, A G; Syed Ahmad Rizal, T N; Abdul Rahman, A R; Jamil, M; Jacqueline, L and Abdullah, S (2005). Freshwater fishes of Sungai Bebar and adjacent areas. *Summary Findings PSF Technical Series No. 4. Peat Swamp Forest Project*. UNDP, GEF, Pahang Forestry Department and Universiti Kebangsaan. p. 145-148.

Ahmad, A B; Ahmad, M F and Nek, S A R T (2013). Freshwater fishes recorded from north Selangor peat swamp forest, Selangor. *Proc. of the Seminar on Scientific Biodiversity Expedition, North Selangor Peat Swamp Forest*. Shah Alam, Selangor, Malaysia. p. 72-76.

Azizan, S N F; Huynh, M N; Padfield, R; Evers, S L; Noborio, K and Hara, H (2021). The effects of oil palm plantation on fish composition in Selangor Peatlands, Malaysia. *J. Adv. Res. Applied Sci. Eng. Technol., 25(1)*: 19-336.

Bhattacharjee, I; Aditya, G and Chandra, G (2009). Laboratory and field assessment of the potential of larvivorous, air-breathing fishes as predators of culicine mosquiteos. *Biol. Contr., 49*: 126-133.

Calloway, M T; Roberts, M E and Taylor, C M (2017). Temporal and spatial patterns of fish distribution and diversity in the Noxubee River, Mississippi and Alabama. *Copeia*, *105(1)*: 100-107.

Chong, M D (2014). Diversity and abundance of freshwater fish fauna in fragmented forest of Wilmar palm oil plantation in Miri. Degree Thesis, Universiti Malaysia Sarawak.

Davenport, J and Matin, A K M A (2006). Terrestrial locomotion in the climbing perch, *Anabas testudineus* (Bloch) (Ananbantidae, Pisces). *J. Fish Biology, 37(1)*: 175-184.

Davies, J and Abdullah, A R (1989). Freshwater fish survey of the north Selangor peat swamp forest.

Asian Wetland Bureau Publication No. 46, IPT Asian Wetland Bureau/WWF Malaysia, Kuala Lumpur.

Dosi, E M (2017). Effects of conversion of peat swamp forest to oil palm plantation on biodiversity of aquatic fauna and water quality. *MPOB VIVA Report 2017*.

Dosi, E M; Tuen, A A; Yaman, I C and Khoon, K L (2019). Fishes of a conserved peat swamp forest in an oil palm plantation. *Oil Palm Bulletin*, *78*: 1-5.

Froese, R and Pauly, D (2019). FishBase version (10/2016). https://www.fishbase.in/search.php, accessed on 26 April 2016.

Gandaseca, S; Rosli, N; Idris, M H; Ahmed, O H and Pazi, A M M (2015). Effects of converting tropical peat swamp forest into oil palm plantation on water quality. *Amer. J. Applied Sci., 12(8)*: 525-532.

Giam, X; Koh, L P; Tan, H H; Miettinen, J; Tan, H T and Ng, P K (2012). Global extinctions of freshwater fishes follow peatland conversion in Sundaland. *Front. Ecol. Environ., 10(9)*: 465-470.

Gyawali, S; Techato, K; Yuangyai, C and Musikavong, C (2013). Assessment of relationship between land uses of riparian zone and water quality of river for sustainable development of river basin, a case study of U-Tapao river basin, Thailand. *Procedia Environ. Sci., 17*: 291-297.

Habib, M A B and Hasan, M R (1994). Evaluation of dietary protein and lipid requirements of climbing perch, *Anabas testudineus*. *Proc. of the Workshop of BAU Research Progress, 8B*: 340-347.

Hassan, R; Esa, F A and Harith, M N (2010). Fish assemblages in Nanga Merit area, Kapit, Sarawak. *Sarawak Mus. J., 88*: 274-284.

Hughes, G M; Dube, S C and Munshi, J D (1973). Surface area of the respiratory organs of the climbing perch, *Anabas testudineus* (Pisces: Anabantidae). *J. Zool., 170(2)*: 227-243.

Inger, R F and Chin, P K (2002). *The Freshwater Fishes of North Borneo*. Natural History Publication, Borneo.

International Union for Conservation of Nature (IUCN) (2022). The IUCN Red List of threatened Species. Version 2022-2. Retrieved from https://www.iucnredlist.org, accessed on 25 March 2022.

Ismail, A; Amal, M N A; Abdullah, T; Johari, S; Azizul, A; Nur-Illiani, H and Amiruddin, M H (2013). Fish diversity in north Selangor peat swamp forest. *Proc. of the Seminar on Scientific Biodiversity Expedition, North Selangor Peat Swamp Forest.* Shah Alam, Selangor, Malaysia. p. 57-71.

Khairul-Adha, A R; Siti, K D; Siti, S S; Aziz, A; Yuzine, E and Eza, R I (2009). Freshwater fish diversity and composition in Batang Kerang floodplain, Balai Ringin, Sarawak. *Pertanika J. Tropical Agric. Sci., 32(1)*: 7-16.

Knight, J D M (2010). Invasive ornamental fish: A potential threat to aquatic biodiversity in Peninsular India. *J. Threatened Taxa*. p. 700-704.

Kotellat, M and Whitten, A J (1993). *Freshwater Fisheries of Western Indonesia and Sulawesi*. Periplus Limited Edition, Jakarta. 221 pp.

Kotellat, M (2001). *Fishes of Laos*. WHT Publication, Colombo.

Kottelat, M; Britz, R; Tan, H H and Witte, K E (2006). *Paedocypris*, a new genus of Southeast Asian cyprinid fish with a remarkable sexual dimorphism, comprises the world's smallest vertebrate. *Proc. of the Royal Society B, 273(1589)*: 895-899.

Leete, R; Abdul, R N; Efransjah; Neville, N; Ragavan, H R; Sayok, A; Khali, A H and Rashid, A S (2006). *Malaysia's Peat Swamp Forests Conservation and Sustainable Use*. United Nation Development Programme (UNPP), Malaysia.

Lim, K H; Lim, S S; Parish F and Suharto, R (2012). *RSPO Manual on Best Management Practices (BMPs) for Existing Oil Palm Cultivation on Peat*. RSPO, Kuala Lumpur.

Miettinen, J; Shi, C and Liew, S C (2016). Land cover distribution in the peatlands of Peninsular Malaysia, Sumatra and Borneo in 2015 with changes since 1990. *Glob. Ecol. Conserv., 6*: 67-78.

Ndungu, J; Augustijn, D C; Hulscher, S J; Kitaka, N and Mathooko, J (2013). Spatio-temporal variations in the trophic status of Lake Naivasha, Kenya. *Lakes and Reservoirs: Res. Manag., 18(4)*: 317-328.

Nelson, J A (2014). Breaking wind to survive: Fishes that breathe air with their gut. *J. Fish Biology, 84*: 554-576.

Ng, P K L; Tay, J B and Lim, K K P (1994). Diversity and conservation of blackwater fishes in Peninsular Malaysia, particularly in the north Selangor peat swamp forest. *Hydrobiologia, 285(1-3)*: 203-218.

Norhisyam, M S; Roshani, O; Zuhairi, A N M; Akmal, S N; Mohd Syahril, M Z; Ainil Hawa, S; Wahidah, M N and Harmin, S A (2012). Water quality,

diversity and distribution of blackwater fishes in selected locations of Raja Musa Peat Swamp Forest Reserve. *In Conf.: Malaysian Sciences and Technology Congress 2012*.

Oksanen, J; Blanchet, F G; Kindt, R; Legendre, P; O'Hara, R B; Simpson, G L; Solymos, P; Henry, M; Stevens, H and Wagner, H (2015). Vegan: Community ecology package. R package version 2. 10 pp.

Othman, H; Mohammed, A T; Darus, F M; Harun, M H and Zambri, M P (2011). Best management practices for oil palm cultivation on peat: Ground water-table maintenance in relation to peat subsidence and estimation of CO_2 emissions at Sessang, Sarawak. *J. Oil Palm Res.*, *23*: 1078-1086.

Pinter, H (1986). *Labyrinth Fish*. Barrons Educational Series, New York.

Posa, M R C; Wijedasa, L S and Corlett, R T (2011). Biodiversity and conservation of tropical peat swamp forests. *BioScience*, *61(1)*: 49-57.

Rahim, K A A; Siti, K D; Siti, S S; Aziz, A; Yuzine, E and Eza, R I (2009). Freshwater fish diversity and composition in Batang Kerang floodplain, Balai Ringin, Sarawak. *Pertanika J. Tropical Agric. Sci., 32(1)*: 7-16.

RSPO (2020). About. Retrieved from https://rspo.org/about, accessed on 6 August 2020.

Rainboth, W J (1996). *Fishes of the Cambodian Mekong, FAO Species Identification Field Guide for Fishery Purposes*. FAO, Rome. 265 pp.

Rezawaty, K (2004). *Taburan ikan di tiga batang sungai di Paya Beriah*. B.Sc. thesis, Universiti Sains Malaysia.

Shabalala, A N; Combrinck, L and McCrindle, R (2013). Effect of farming activities on seasonal variation of water quality of Bonsma Dam, KwaZulu-Natal. *South African J. Sci.*, *109(7)*: 1-7.

Shah, A S R M; Zarul, H H; Chan, K Y; Zakara, R; Khoo, P and Mashhor, M (2006). A recent survey of freshwater fishes of the Paya Beriah peat swamp forest, North Perak, Malaysia. *J. Bioscience*, *17(1)*: 51-64.

Siow, R; Ramli, M N; Shakori, M H M and Asmuni, M (2013). Fish fauna assemblages and their distribution patterns in the north Selangor peat swamp forest. *Proc. of the Seminar on Scientific Biodiversity Expedition, North Selangor Peat Swamp Forest*. Shah Alam, Selangor, Malaysia. p. 77-82.

Sule, H A; Ismail, A and Amal, M N A (2016). A review of the ichthyofauna of Malaysian peat swamp forest. *Pertanika J. Tropical Agric. Sci.*, *39(4).*

Syarifuddin, S and Kramer, D L (1996). The effect of group size on space use and aggression at a concentrated food source in blue gouramis, *Trichogaster trichopterus* (Pisces: Belontiidae). *Environ. Biol. Fishes*, *46*: 289-296.

Ukkatawewat, S (2005). *The Taxonomic Characters and Biology of Some Important Freshwater Fishes in Thailand*. National Inland Fisheries Institute, Department of Fisheries, Ministry of Agriculture, Bangkok, Thailand. 55 pp.

UNDP (2006). Malaysia's Peat Swamp Forest, Conservation and Sustainable Use. Malaysia: United Nation Development Programme.

Velmurugan, B; Selvanayagam, M; Cengiz, E I and Ugurlu, P (2015). Scanning electron microscopy study of the gills, scales and erythrocytes of *Anabas testudineus* upon exposure to chlorpyrifos. *Toxicol. Environ. Chem.*, *97(2)*: 208-220.

Wan Mohd Jaafar, W S; Said, N F S; Abdul Maulud, K N; Uning, R; Latif, M T; Muhmad Kamarulzaman, A M; Mohan, M; Pradhan, B; Saad, S N M; Broadbent, E N and Cardil, A (2020). Carbon emissions from oil palm induced forest and peatland conversion in Sabah and Sarawak, Malaysia. *Forests, 11(12)*: 1285.

Zakeyuddin, M S; Shah, A S M; Mohammad, M S; Fazlinda, N; Fadzil, M; Hashim, Z and Omar, W M W (2016). Spatial and temporal variations of water quality and trophic status in Bukit Merah Reservoir, Perak. *Sains Malays.*, *45(6)*: 853-863.

Journal of Oil Palm Research Vol. 36 (4) December 2024 p. 618-629
DOI: https://doi.org/10.21894/jopr.2023.0059

OIL PALM LEVEL OF RIPENESS CLASSIFICATION USING EFFICIENTDET-LITE CNN ARCHITECTURE

YOSUA ALVIN ADI SOETRISNO[1]*; EKO HANDOYO[1]; SUMARDI[1] and ENDA WISTA SINURAYA[1]

ABSTRACT

Determining the category of ripeness of oil palm fresh fruit bunches (FFB) based on maturity is essential in estimating suitable fruit for processing. Ripeness classification could prevent the oil palm from becoming over-ripe. When the oil palm becomes over-ripe, the quality of oil extracted is not optimal because of the increase in free-fatty acid level. The deep learning approach usually used in object detection could help in object classification based on the model trained with the oil palm dataset. Many kinds of research used shared convolutional neural network (CNN) architecture to detect the ripeness of oil palms fruits. This research contributes to finding the suitable CNN model specialised in oil palm FFB ripeness using an unequal scalable feature known as EfficientDet. We propose the most proper coefficient for object detection scaling with the following configuration. The compound coefficient D2's resolution is used as EfficientDet-Lite2 input size. EfficientDet-Lite2's backbone network is nearly identical to EfficientDet using D2. The bi-directional feature pyramid network (Bi-FPN) layer is five, and the box class per layer is three. The accuracy of the proposed EfficientDet-Lite2 using EfficientDet D2 input is 84% and has been tested in Indonesian plantations.

Keywords: CNN, EfficientDet, feature pyramid network, oil palm.

Received: 31 October 2022; **Accepted:** 27 August 2023; **Published online:** 3 November 2023.

INTRODUCTION

The development of Deep Learning (DL) makes functions such as image classification, object detection, image tracking, and image manipulation more accessible and accurate (Prasetyo *et al.*, 2020). The DL system has a layered architecture which could be organised as a convolutional and fully connected layer. The convolutional layer is for extracting automatic features based on the properties of the windowing filter applied in a particular area of the image. The fully connected layer collects the critical component of the object with an activation function to ensure that the feature belongs to the category. The activation function is a mathematical function that can activate the next layer based on previous criteria with various weights to be considered as a category based on the feature that belongs to that category.

DL has been applied in many applications, including agriculture. Palm oil is one strategic commodity in Indonesian agriculture known as crude palm oil (CPO) that is being exported to many countries because of the need for cooking oil and other industrial application. Oil palm ripeness as the CPO source must be detected on the right time sequence. A farmer harvests based on experience, and sometimes the decision is wrong because of unfocussed observation. The farmer could be assist by a computer vision system to select for ripe fresh fruit bunches (FFB) is ripe based on the grade classification (Suharjito *et al.*, 2021).

There are two categories of research: Detecting the ripeness of oil palm FFB from a close range and detecting the ripeness and classifying the trees from

[1] Department of Electrical Engineering, Faculty of Engineering, Diponegoro University, Semarang, Indonesia.

* *Corresponding author e-mail: yosua@live.undip.ac.id*

remote sensing images. Image classification can be achieved through the use of traditional machine learning methods, as well as through the application of deep learning techniques. Traditional machine learning combines image processing techniques to obtain unique features from statistical Red, Green, Blue (RGB) distribution in images of oil palm FFB, while deep learning extracts specific features through filter combinations.

In general, mature FFB is transformed from black to red but not completely red, so it needs to be considered the most significant region of interest (ROI) with red color (Alfatni *et al*., 2020). The image processing technique combines machine learning to properly get the ROI's feature distribution. An artificial neural network (ANN) and support vector machine (SVM) algorithms classify the oil palm ripeness category. The SVM algorithm is used in the grain, not the whole oil palm fruit image.

Regarding DL, there is a variation in convolutional neural network (CNN) usage from simple to complicated. Simple CNN uses EfficientNet B0 with an accuracy of 89.3% (Suharjito *et al*., 2021). There is a need for simple CNN because it will be implemented in the embedded device. Based on the architecture of EfficientNet, it would be developed with extra scaling fusion parametrisation in the term of EfficientDet in this research. Mounting the filter with unequal dimensions in EfficientDet could give another insight base on the oil palm's ripeness characteristic. There is a surrounding edge to each bunch and a color transition to determine which part is ripe.

Several kinds of research on the maturity level of oil palm FFB use different classification and DL models and additional techniques to help obtain more specific characteristics of the oil palm bunch. Machine learning needs several feature engineering. Feature engineering that needs to be tinkered with is wavelength input and RGB decomposition, preprocessing using the principal component analysis (PCA) method, and the artificial neural network (ANN) hyperparameter tuning.

The ANN approach is explained in research for near-bunch images and remote sensing. ANN uses a different approach to CNN architecture. Transfer learning is used from the typical architecture like AlexNet, which outperforms machine learning with SVM and extra preprocessing like Histogram of Oriented Gradient (HOG) (Ibrahim *et al*., 2018). *Table 1* shows the comparison of methods and improvement suggestions of each research done in oil palm detection based on image processing and artificial neural network.

This research was not using regional segmentation because the complexity of the segmentation could affect the performance of the DL model applied to the Android device. There is also a need for more examples to represent the state of the oil palms (Prasetyo *et al*., 2020). Although this research primarily focuses on the dataset derived from the plantations in Sumatra, it should be noted that the dataset from Kalimantan was relatively limited in size and scope. We incorporated data from both regions to understand plantation conditions across different areas better.

An extension for CNN is R-CNN, a combination of region proposals. There is extra insight from complex sight, overlapping objects, and diverse backgrounds, which could exclude the intersection of an object with another object, so the region of interest becomes clearer. Faster R-CNN consists of regional proposal network (RPN) and detector modules. RPN is a small network neuron in the last row of convolutional layers and is used to predict the existence of the required object and bounding box.

This research also aimed to build observation tools to validate the model directly on the plantation area, given the variation in tree height, ranging from approximately 2-20 m. Before utilising the observation tools in this research, farmers would employ elevated stationary platforms or tall observation towers to observe the upper sections of trees where the fruit bunches are located at heights of 10 m or higher. In this case, following the tools from this research, farmers and researchers could practically approach the task by utilising their smartphones' cameras along with a long stick. Farmers and researchers could extend their reach by attaching their phones to the stick and capturing images or videos of the FFB located at heights of 10 m or higher. This method allowed them to observe and monitor the FFB without needing elevated stationary platforms or tall observation towers. Subsequently, these captured images were classified using deep learning techniques, thereby enhancing the accuracy and efficiency of the classification process.

Several CNN is used to classify the oil palm FFB: LeNet, AlexNet, EfficientNet B0, and Faster R-CNN. The reason for choosing EfficientDet-Lite as the backbone for classification was that EfficientDet is based on the CNN model that achieved state-of-the-art performance (Guo *et al*., 2022). A lighter and improved version of EfficientDet, called EfficientDet-Lite, does away with the squeeze-and-excite module because it is not mobile-optimised and replaces the ReLU6 activation function with a swish activation mechanism. This research began with a trial with MobileNetV2 and NasNetMobile before using the EfficientDet-Lite. The problem was that the MobileNetV2 could not do a stable classification with cases; sometimes, the object was undetected. Another research also showed that EfficientDet-D5 using a variation of scaling D5 gives better accuracy than YOLOv4 (Ammar *et al*., 2021).

TABLE 1. FFB RIPENESS DETECTION COMPARISON

Researcher	Method	Algorithm	Sample size, number of classes, accuracy	Insight and improvement suggestions
Shiddiq *et al*. (2016)	Image Processing	RGB quantisation	Not mentioned, 4 classes not mentioned	The comparison should also be made using soft computing programs.
Septiarini *et al*. (2019)	Image Processing and Machine Learning	Histogram statistical spread, otsu method, and morphology using SVM	160 images, 4 classes, about 90.00%	Need development of segmentation and classification methods to reduce error.
Sukemi and Sukrisno (2019)	Image Processing	Gray Level Co-occurrence Matrix (GLCM)	50 images, 2 classes, 90.00%	Need lighting for getting the 90% accuracy.
Prasetyo *et al*. (2020)	ANN	Faster R-CNN	100 images, counting and giving a bunch's region area, 80.00%	Some things that caused the detection of bunches were the high level of occlusion, and there is the presence of several objects that covered the bunch.
Suharjito *et al*. (2021)	ANN	EfficientNetB0	103 images, 4 classes, 89.3.0%	A tradeoff exists between accuracy, classification time, and the need for a more significant parameter.
Saleh and Liansitim (2020)	ANN	CNN	Accuracy is calculated in different research	Need to use datasets outside the training because the accuracy is high when using the training dataset.
Harsawardana *et al*. (2020)	ANN with Smart Crane Hardware	CNN using ResNet	400 images, 7 classes, 71.34%	The accuracy is only about 71%, and need for optimisation.
Ibrahim *et al*. (2018)	ANN	Compare Fast Retina Keypoint, HOG using SVM, and CNN using AlexNet	120 images, 4 classes, 92.00%	A deep layer can lead to better results but at a slow processing time and need a deeper pre-trained CNN model.
Ammar *et al*. (2021)	ANN for Geospatial Image	YOLOv4 and EfficientDet-D5	258 images, not detecting oil palm ripeness, 99.00%	There is a tradeoff between speed and accuracy which are YOLOv4 and EfficientDetD5 are suitable for accuracy, while Faster R-CNN and YOLOv3 were significantly less accurate.
Khalid and Shahrol (2022)	ANN for Geospatial	CNN inside ArcGIS Pro compared with SVM	Not mentioned, not detecting oil palm ripeness, 91.00%	CNN gets better accuracy than SVM, but by using built-in CNN, the architecture could not be described clearly.
Wibowo *et al*. (2022)	ANN for Remote Sensing	YOLOv3, YOLOv4, YOLOv5	Not mentioned, not detecting oil palm ripeness, 97.00%	There is a certain resolution that affects the result, and for the model, YOLOv3 and YOLOv4 are the best models.
Mubin *et al*. (2019)	ANN	CNN using LeNet	260 images, 2 classes of remote sensing, 95.11%	There is a need for an optimiser like AdaGrad because the lowest loss value and high accuracy could be further improved by using high-resolution hyperspectral remote-sensing images.

Considering all the aspects above, this research contributes by optimising the hyperparameters and input size of the EfficientDet-Lite model, which leads to improved performance in the ripeness classification of the Dumpy variety. The findings suggest that with appropriate adjustments to the hyperparameters and input size, the model can achieve favourable results in accurately classifying the ripeness of Dumpy variety fruit bunches.

MATERIALS AND METHODS

The total dataset of oil palm FFB used as training data were 240 images. There were four classes: Unripe, underripe, ripe, and overripe, and each class consisted of 60 images. The consideration of choosing 240 images was because, as in *Table 1*, the usage of the sample images was about 100-200 images if they consisted of 2-4 classes. There is no specific minimum image standardisation that could be used in DL. The validation used 15 images for each category, totaling 60 images outside the training data. A variation of 170 images of unique oil palm FFB has been used. EfficientDet supports a variety of image preprocessing procedures. By default, the supplied image has a 50% probability of being horizontally flipped, serving as a simple image enhancement method.

There was a consideration that some oil palm FFB images were rotated and zoomed in to get an additional number of samples for about 2-5 images from the original 170 images. The variety of oil palms captured was all Dumpy from Pusat Penelitian Kelapa Sawit (PPKS) or Research Centre of Oil Palm. Dumpy is a variety of oil palm with the advantage of a slow growth rate, allowing it to grow for an economic lifespan of 30 years or longer compared to other types. The Dumpy variety of oil palm, also known as DyP Sungai Pancur I (SP-I), can be found in various locations, including Kebun Rayon B, PT Raya Padang Langkat, Ds. Bukit Mas II, Kec Besitang, Kab. Langkat, North Sumatra, Indonesia. The site of the plantation can be accessed through the following Google Maps link: https://maps.app.goo.gl/omzqUWJusKfNCnTs7. The Dumpy variety picture was also taken from several private plantations in Kalimantan. The distance between the camera and the oil palm FFB was about 3-5 m. The smartphone used to take the picture was the Samsung Galaxy J7 with specifications 13 MP, f/1.9, 28 mm (wide). A variation of the camera has been used: An X85 HD 720P Webcam with 5 MP high definition with a resolution of 1920 × 1080.

The researcher collected images of the oil palm FFB using a smartphone camera and varied the shooting angles and backgrounds to create different datasets. With the guidance of experts from Perhutani, predetermined classes were determined, and the data collection was supervised on the plantation. A strong foundation was laid for the oil palm FFB ripeness detection research by working directly with the experts and gathering a comprehensive data set. The criteria used to determine the class was based on the experience of the expert. The main reason for taking an image with supervision was to ensure that the photo's angle could describe the proper criteria for classification.

The second stage was image preprocessing based on the specification in *Table 2*. EfficientDet needs a specific resolution for the input, so the input images were considered using EfficientDet D2 because the backbone layer structure is the same as EfficientDet-Lite2. The image was resized to 768 × 768 from the original resolution of about 1080 × 1920.

The third stage was labeling and annotating each dataset image. Labeling is crucial in EfficientDet object detection by providing ground truth annotations as the reference standard for training the model. The assigned bounding boxes and class labels during the labeling process are used to instruct the model on identifying and locating objects of different classes within an image, considering the diverse backgrounds and conditions in the dataset shown in *Figure 1*. These annotations are instrumental in teaching the model the visual characteristics of various objects, enhancing its ability to generalise and make accurate predictions on unseen patterns. Four different environments and scenarios were used to collect oil palm images. There were 27 photos of palm bunches hanging from the tree, 183 photos on the ground, 11 photos capturing scenes with hanging FFB and 19 photos of groups with grass in the background. The labeling and annotation process results are saved in an XML file containing information about the labeling box coordinate and width.

The fourth stage was conducting data training on images that had been labeled and annotated. The training process was performed using the Google Collaboratory application. EfficientDet-Lite2 was chosen among other models because the mean Average Precision (mAP) score is above average compared with EfficientDet-Lite0 until EfficientDet-Lite4 (Repák, 2021). This model was implemented as the detection and counting program on the Android device.

EfficientNet, as the base of EfficientDet, introduced a brand-new compound scaling technique that uniformly scales the network's depth, width, and resolution. A new baseline network was created with a neural architecture search. The EfficientNet scaling method evenly



Figure 1. Background and camera angle variation of the oil palm FFB dataset.

scales network breadth, depth, and resolution using a set of preset scaling coefficients, in contrast to standard practice, which scales these variables arbitrarily.

Compound scaling uses a compound coefficient (Φ) to uniformly scale a network according to guiding principles. The parameters denote the user-specified coefficient in Equation (1) and parameters α, β and γ define how to apply this to the network depth, width and resolution.

$$\begin{gathered} \text{Depth: } d = \alpha^{\Phi} \text{ Width: } w = \beta^{\Phi} \\ \text{Resolution: } r = \gamma^{\Phi} \\ \mathrm{f} = \alpha \cdot \beta^2 \cdot \gamma^2 \approx 2 \\ \alpha \geq 1, \beta \geq 1, \gamma \geq 1 \end{gathered} \tag{1}$$

Compound scaling aims to increase the network's length (Li), width (Ci) and resolution (Hi, Wi) while maintaining the baseline network's preset Fi. Although the design space is supposed to be reduced by fixing Fi, since Li, Ci, Hi, and Wi can still be explored for each layer, the design space is still quite wide. Every layer must be scaled consistently with a constant ratio to constrict the design space further. Compounding scaling, described as an optimisation problem, aims to maximise the model's accuracy given the resource constraints in Equation (2).

$$\begin{aligned} &\max_{d,w,r} && \text{Accuracy } [N(d,w,r)] \\ &\text{s.t.} && N(d,w,r) = \bigodot_{i=1\ldots s} \hat{F}_i^{d\cdot\hat{L}_i}(X_{\langle r\cdot\hat{H}_i, r\cdot\hat{W}_i, w\cdot\hat{C}_i\rangle}) \\ &&& \text{Memory } (N) \leq \text{Target_memory} \\ &&& \text{FLOPS } (N) \leq \text{Target_flops} \end{aligned} \tag{2}$$

where N is Convnet, w, d, and r are coefficients for scaling the network width, depth, and resolution. A sign ⊙ is a list of a layer.

A bi-directional Feature Pyramid Network (BiFPN) improves cross-scale connections by deleting nodes with only one input edge. BiFPN adds an advantage from the original input to the output node based on some level conditions and treats each bidirectional path as a single feature network layer. Different input features have varied resolutions and typically contribute unequally to the output feature. Additional weight is applied to each input, allowing the network to learn the relative relevance of each input attribute.

BiFPN has five modifications over a normal FPN. Instead of only the top-down feature, it adds another bottom-up feature fusion branch, shown with the red arrow in *Figure 2*. It has to skip connections from the initial feature map to the fused feature map, so there is a repeated block with a purple arrow. Nodes with only one input are removed because they do not do much fusion as other nodes. The entire module is repeated multiple times. For different resolution feature maps to contribute to the fusion at various capacities, features are not added directly but instead using a weighted average. There is a normalisation of backpropagation because unbounded weights cause issues. Although it worked, applying softmax to the weight values slowed down training. A simple average following Relu activation is utilised to normalise the weights.

The BiFPN, as an additional module in the network, which may also be scaled, necessitates the development of a new scaling technique. The width of BiFPN increases exponentially while the input resolution and depth of BiFPN increase linearly.

This section shows the top-down convolution in the 6th layer of BiFPN. The illustration of feature fusion at level 6 is shown in *Figure 2*. A top-down fusion P_6^{td} has to be computed as in Equation (3). A bottom-up feature fusion is calculated to produce the output from the current level shown in Equation (4). There is a resizing mechanism from P_7^{in} The layer shows a connection for the convolution from top-down and bottom-up as

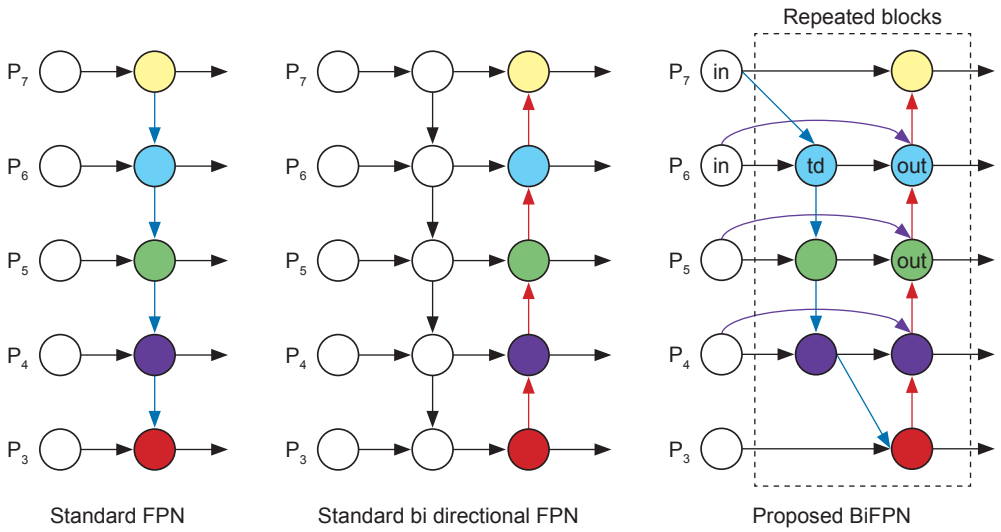


Figure 2. Weighted bi-directional Feature Pyramid Network (FPN).

the backbone of FPN. Equation (4) shows the P_6^{out} that affected the convolutional in Equation (2) and connected with P_5^{out} so it is connected bi-directional.

$$P_6^{td} = \text{Conv}\left(\frac{w_1 \cdot P_6^{in} + w_2 \cdot Resize\,(P_7^{in})}{w_1 + w_2 + \epsilon}\right) \quad (3)$$

$$P_6^{out} = \text{Conv}\left(\frac{w_1' \cdot P_6^{in} + w_2' \cdot P_6^{td} + w_3' \cdot Resize\,(P_5^{out})}{w_1' + w_2' + w_3' + \epsilon}\right) \quad (4)$$

In general, Pi represents an output from the backbone's i-th layer and is an input to the i-th Bi-FPN level. w_1', w_2', w_3', are the weighted feature fusion. ϵ is a small constant (configurable as part of the constructor arguments).

Top-down and bottom-up fusion are explained in *Figure 3*. The left side in *Figure 3* is the bottom-up approach, which down-sampled the resolution by a factor of 0.5. The middle part is the top-down approach, starting with a coarser-resolution feature map and upsampling by 2. The upsampled map is merged with the corresponding bottom-up map, which walks on a 1 × 1 convolutional layer to reduce channel dimension. This process is iterated until the finest resolution map is generated.

Inspired by the merge scaling used in EfficientNets, a new combined scaling method is proposed for object detection. This method uses coefficients (Φ) to improve the fusion of all dimensions of the backbone network, BiFPN network, class network, and resolution. This research proposes an EfficientDet-Lite2 model using a D2 input size of 768 × 768 in input layer resolution. EfficientDet D2 and EfficientDet-Lite2 use five BiFPN layers to fuse the upsampling and downsampling features. Three ClassNet and BoxNet are used to predict categories and draw the location of the bounding box. The bounding box is the box with the coordinate of the object. An XML file describes the bounding box location while the model was fed to EfficientDet. As a result of the classification, a bounding box was used to determine the exact object location. A complete table of comparison is shown in *Table 2*.

TABLE 2. EFFICIENTDET INPUT, BIFPN AND CLASSNET LAYER

Model	Input layer	BiFPN layers	ClassNet and BoxNet layers
D0 (Φ = 0)	512	3	3
D1 (Φ = 1)	640	4	3
D2 (Φ = 2)	768	5	3
D3 (Φ = 3)	896	6	4
D4 (Φ = 4)	1 024	7	4
D5 (Φ = 5)	1 280	7	4
D6 (Φ = 6)	1 280	8	5
D7 (Φ = 7)	1 536	8	5
Lite0	320	3	3
Lite1	384	4	3
Lite2	448	5	3
Lite3	512	6	4
Lite4	640	7	4

This research proposes EfficientDet-Lite2 based on the trial and error mechanism. The consideration for choosing EfficientDet-Lite2 is the size, latency, and mAP. Size describes the quantised integer model after optimisation. Integer quantisation is an optimisation technique that converts both model's weights and activation outputs from 32-bit floating-point numbers to the

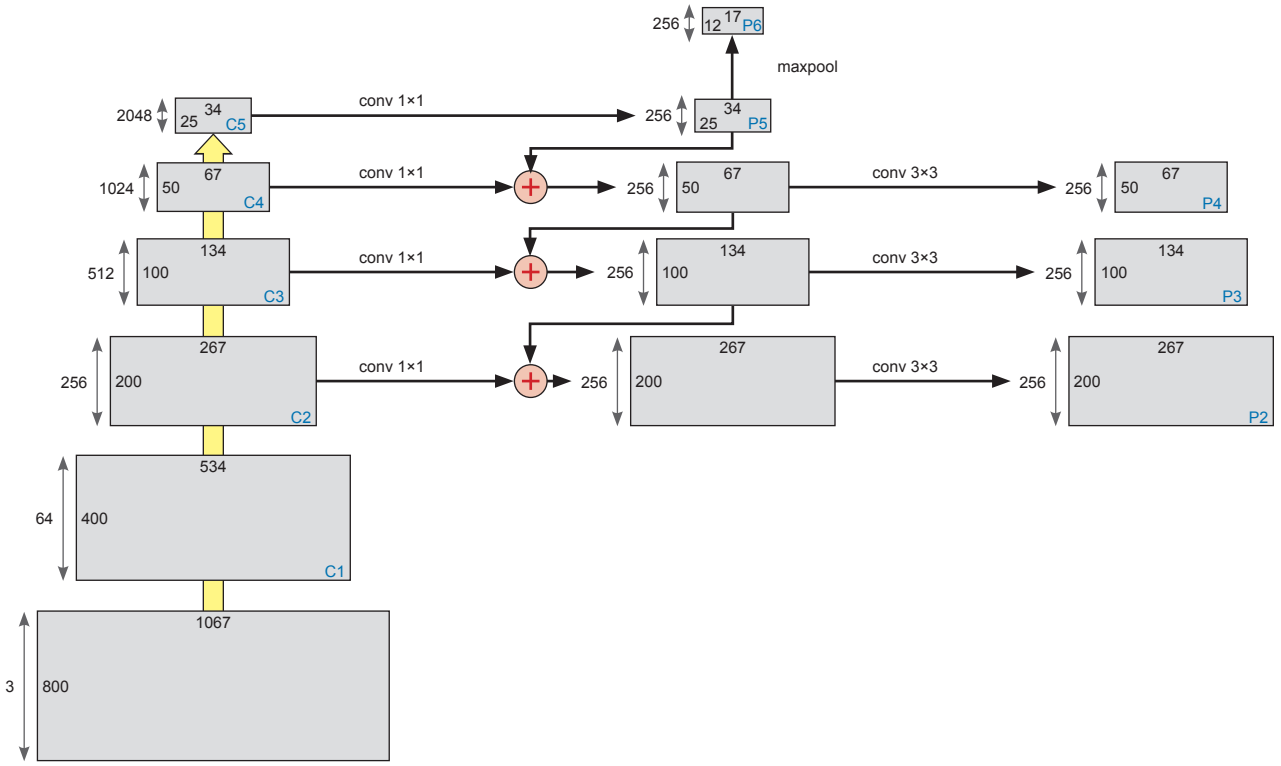


Figure 3. FPN bottom-up and top-down convolutional mechanism.

nearest 8-bit fixed-point numbers. Latency was measured on Google Pixel 4 Smartphone using four threads on the CPU. Average Precision is the mAP on the COCO 2017 validation dataset. EfficientDet-Lite3 mAP is higher but not very significant. The usage of EfficientDet-Lite2 is also a consideration that the model would be implemented on the Android device. The comparison of size, latency and mAP levels is shown in *Table 3*.

TABLE 3. EFFICIENTDET-LITE SIZE, LATENCY AND mAP COMPARISON

Model	Size (MB)	Latency (ms)	mAP (%)
EfficientDet-Lite0	4.4	37	25.69
EfficientDet-Lite1	5.8	49	30.55
EfficientDet-Lite2	7.2	69	33.97
EfficientDet-Lite3	11.4	116	37.70
EfficientDet-Lite4	19.9	260	41.96

Test on the system's performance was based on the data outside the dataset, batch and epoch variations, and independence accuracy testing. Data training with batch and epoch variations is divided into two: Original and preprocessing data training with batch variations: 8 and 16 and epochs: 20, 50, 100, 200, 300, 400 and 500. The results of data training with batch and epoch variations can be seen in *Table 4*.

RESULTS AND DISCUSSION

Batch size is the sample of images that propagate through the network. A larger batch size would make less backpropagation, so for the 240 samples, there was 15 backpropagation in batch 16 and 30 backpropagation in batch 8. The pattern was that in 300 epochs, each batch gained the top mAP percentage, and then the mAP decreased. There was no significant difference between batch 8 and batch 16 according to the duration of the training and the mAP score, but the mAP score was higher in batch 16.

Detection quality means recognising oil palm FFB objects and performing classification. The confidence level of the detection must be above 50%. The confidence score reflects how likely the box contains an object of interest and how confident the classifier is about it. If no object exists in that box, the confidence score should ideally be zero. Generally, the confidence score tends to be higher for tighter bounding boxes in the case of object detection. The TensorFlow model validation testing only shows one category with the highest confidence. A confidence level below 50% often shows incorrect results, so the threshold is set to 50%.

The test results were entered into a table called the confusion matrix or error matrix, which was used to deliver information on comparing the classification results. The confusion matrix is

shown in *Table 5*. The performance parameter of classification is shown in *Table 6*.

Testing is done on the 60 images beside the dataset captured directly in the plantation in variation with images provided on the internet. While color features in pictures on the internet can still offer some reliability, they may not be as accurate as images taken directly from the fruit on the plantation due to possible variations in lighting and other factors. Still, the aim is to test the possibility of the interpretation and how general the model could classify. The classification performance was not much higher than the accuracy in the previous literature finding, which is above 90% or more.

The testing scenario used images outside the training process and a direct capture at the plantation, as in *Figure 2*. For example, in *Figure 2*,

TABLE 4. EFFICIENTDET-LITE2 BATCH TRAINING 8 AND 16

No.	EfficientDet-Lite Version (Batch training 8)	Epoch	Duration (hh:mm:ss)	mAP (%)
1	2	20	00:06:20	58.00366
2	2	50	00:12:42	55.70173
3	2	100	00:23:59	55.09633
4	2	200	00:47:49	56.46802
5	2	300	01:10:00	57.66782
6	2	400	01:22:21	53.56957
7	2	500	02:12:50	52.73226

No.	EfficientDet-Lite Version (Batch traning 16)	Epoch	Duration (hh:mm:ss)	mAP (%)
1	2	20	00:07:08	55.47828
2	2	50	00:13:32	58.89936
3	2	100	00:26:18	57.62151
4	2	200	00:53:33	58.88936
5	2	300	01:20:00	59.80644
6	2	400	01:30:00	57.99332
7	2	500	02:16:34	55.68957

TABLE 5. CONFUSION MATRIX OF EFFICIENTDET-LITE2

Category		Prediction				Total
		Overripe	Ripe	Underripe	Unripe	
Actual	Overripe	21	4	0	0	25
	Ripe	1	22	2	0	25
	Underripe	0	3	17	4	25
	Unripe	0	0	1	24	25
	Total	22	29	20	28	100

TABLE 6. CLASSIFICATION PERFORMANCE

No.	CNN Model	Device	Accuracy (%)	Precision (%)	Recall (%)	F1-Score
1	EfficientDet-Lite2 (Proposed)	Android	84.00	82.00	85.00	84.00
2	LeNet (Mubin *et al.*, 2019)	PC	95.11			
3	EfficientDet-D5 and YOLOv4 (Ammar *et al.*, 2021)	PC	99.00			
4	AlexNet (Ibrahim *et al.*, 2018)	PC	92.00			
5	ResNet (Harsawardana *et al.*, 2020)	PC	71.34			
6	Fast R-CNN (Prasetyo *et al.*, 2020)	PC	80.00			

the image was directly downloaded from Google search. There were about 50 images that were downloaded from Google that were used for testing. Before the testing process, the consideration for each class was clarified with the expert. The result of the detection was underripe because the FFB was ripe but with juxtaposition with unripe. The detection threshold was set at about 0.5 to ensure that the confidence rate of the intersection of the detection box is relatively high. This mechanism is built on the EfficientDet-Lite2 and could prove that the classification could be done. *Figure 4* shows examples of the classification result for each class.

The flowchart of the Android detection application and usage process is shown in *Figure 3*. There are two modes of the camera: Directly using the mobile phone camera or using the webcam USB-based camera connected to the mobile phone. After choosing the camera mode, the classifier must scan the aiming process with the TensorFlow Lite model, as shown in *Figure 5*. If there is a detection, the process continues to capture the data. If no detection results have occurred, then the process of taking the picture is repeated.

TensorFlow Lite would determine the class and bounding box based on the classification of the EfficientDet-Lite2 embedded in the application.

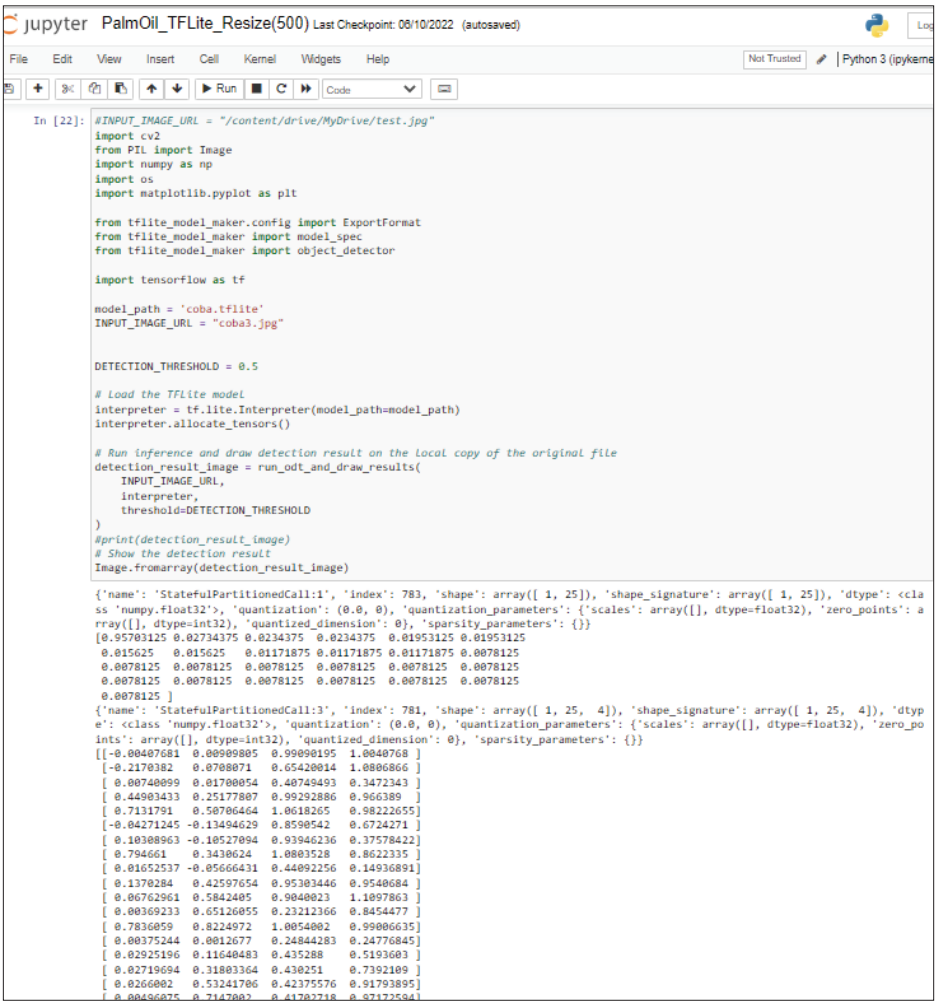




Figure 4. Classification mechanism in FFB ripeness detection.

After the detection was done and shown in the bounding box, the approved counting result was saved to the phone database. Approved counting result was done by selecting the save button icon, as shown in *Figure 6*. After being approved, the result was saved in the Android SQLite database.

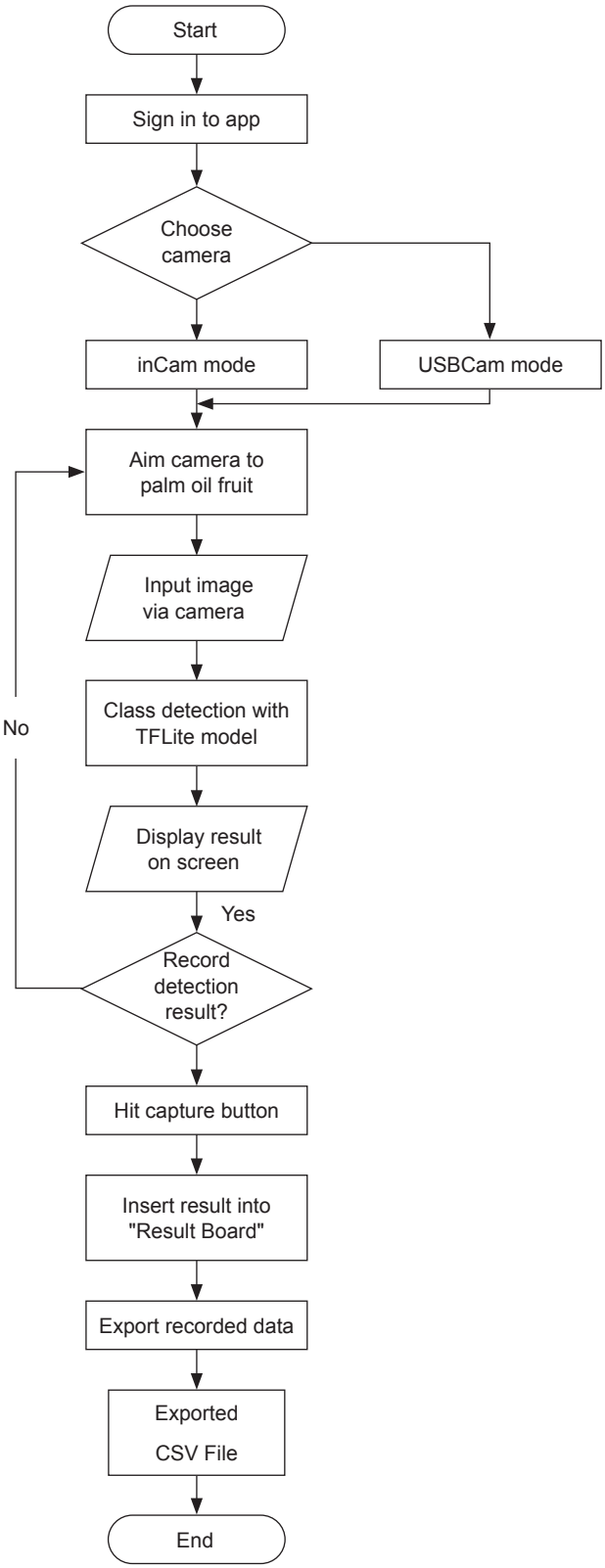


Figure 5. Classification flowchart on the mobile phone.

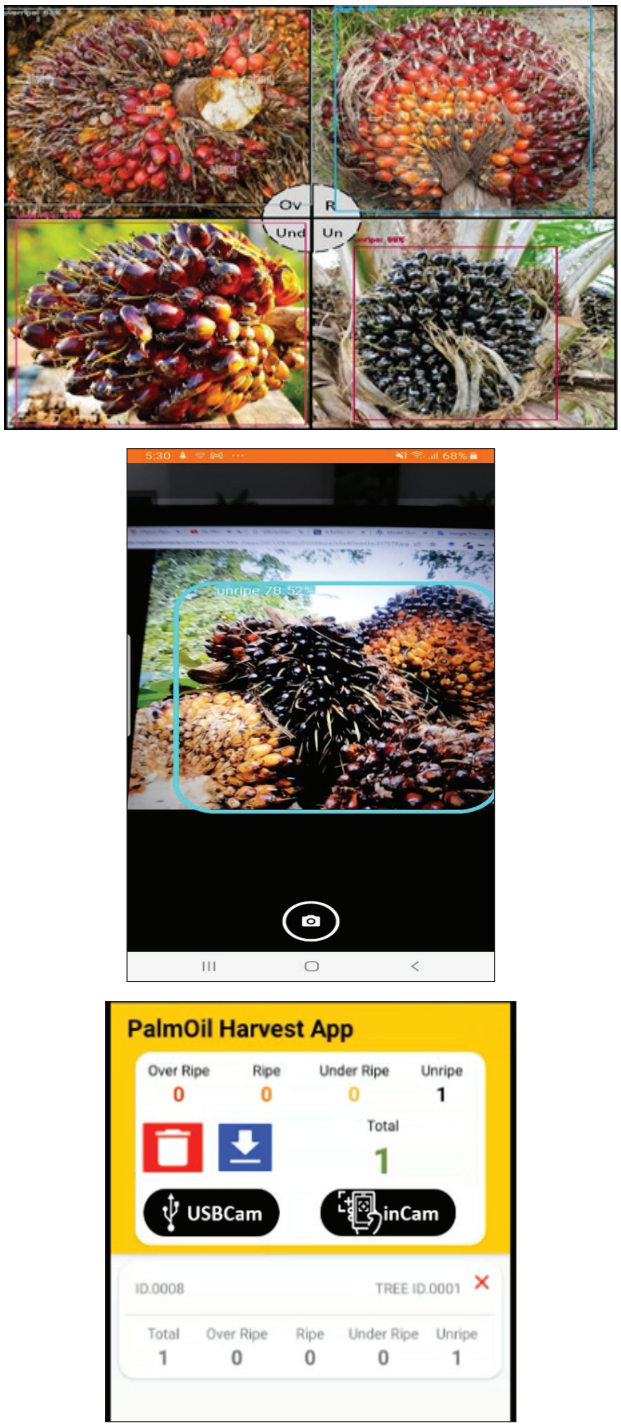


Figure 6. Classification result after taking a picture directly of the oil palm FFB.

The accuracy of EfficientDet-Lite2 is about 84%, which shows that the model could fit the situation using an image outside the dataset. Despite having slightly lower accuracy than previous models, with around 90% accuracy, the developed model demonstrated its feasibility for application in a real-world plantation setting, including FFB on the trees. The challenge is that the state-owned enterprise plantation has a high standard to determine ripeness, whereas, in private plantations,

the ripeness standard is lower, so the half-ripe or underripe can be considered ripe. In the testing scenario of the Android application, sometimes the class and bounding box results could differ in a flash condition when there is a fusion area between black-colored and orange-red parts. The overall performance is acceptable to be used in the big plantation situation.

CONCLUSION

This research applied the EfficientDet-Lite2 with proposed hyperparameter tuning in the Android application. This application can classify oil palm ripeness into four categories: Unripe, underripe, ripe and overripe. Using a back-and-forth convolutional process, Bi-FPN could do the scaling variation to capture the image's feature from the coarse once related until a more detailed feature. EfficientDet, as the embodiment of the EfficientNet backbone with the D model, showed that resolution variation could effectively help the detection of the oil palm with striking differences in certain conditions. The proposed model uses EfficientDet-Lite2 as the backbone network and uses the input size of EfficientDet D2 to get more detailed features. EfficientDet-Lite2 had a good mAP score and could be used on mobile phones with an accuracy of 84%.

ACKNOWLEDGEMENT

This work is supported and fully funded by the Strategic Research Annual Budget Grant from the Electrical Engineering Department, part of the Faculty of Engineering at Diponegoro University.

REFERENCES

Alfatni, M S M; Mohamed Shariff, A R; Ben Saaed, O M; Albhbah, A M and Mustapha, A (2020). Colour feature extraction techniques for real time system of oil palm fresh fruit bunch maturity grading. *IOP Conf. Series: Earth Environ. Sci., 540(1)*: 012092. DOI: 10.1088/1755-1315/540/1/012092.

Ammar, A; Koubaa, A and Benjdira, B (2021). Deep-learning-based automated palm tree counting and geolocation in large farms from aerial geotagged images. *Agronomy, 11(8)*: 1458. DOI: 10.3390/agronomy11081458.

Guo, J M; Yang, J S; Seshathiri, S and Wu, H W (2022). A light-weight CNN for object detection with sparse model and knowledge distillation. *Electronics, 11*: 575. DOI: 10.3390/electronics11040575.

Harsawardana; Rahutomo, R; Mahesworo, B; Cenggoro, T W; Budiarto, A; Suparyanto, T; Surya Atmaja, D B; Samoedro, B and Pardamean, B (2020). AI-based ripeness grading for oil palm fresh fruit bunch in smart crane grabber. *IOP Conf. Series: Earth Environ. Sci., 426(1)*: 012147. DOI: 10.1088/1755-1315/426/1/012147.

Ibrahim, Z; Sabri, N and Isa, D (2018). Palm oil fresh fruit bunch ripeness grading recognition using convolutional neural network. *J. Telecommun. Electron. Comput. Engin., 10(3-2)*: 109-113.

Khalid, N and Shahrol, N A (2022). Evaluation the accuracy of oil palm tree detection using deep learning and support vector machine classifiers. *IOP Conf. Ser.: Earth Environ. Sci., 1051(1)*: 012028. DOI: 10.1088/1755-1315/1051/1/012028.

Khan, N; Kamaruddin, M A; Sheikh, U U; Yusup, Y and Bakht, M P (2021). Oil palm and machine learning: Reviewing one decade of ideas, innovations, applications, and gaps. *Agriculture 2021, 11*: 832. DOI: 10.3390/agriculture11090832.

Mubin, N A; Nadarajoo, E; Shafri, H Z M and Hamedianfar, A (2019). Young and mature oil palm tree detection and counting using convolutional neural network deep learning method. *Int. J. Remote Sens., 40*: 7500-7515. DOI: 10.1080/01431161.2019.1569282.

Prasetyo, N A; Pranowo, P and Santoso, A J (2020). Automatic detection and calculation of palm oil fresh fruit bunches using faster R-CNN. *Int. J. Appl. Sci. Eng., 17*: 121-134. DOI: 10.6703/IJASE.202005_17(2).121.

Repák, T (2021). Fast object detection on mobile platforms using neural networks. Bachelor Thesis, Masaryk University.

Saleh, A Y and Liansitim, E (2020). Palm oil classification using deep learning. *Sci. Infor. Tech. Letters, 1(1)*: 1-8. DOI: 10.31763/sitech.v1i1.1

Septiarini, A; Hamdani, H; Hatta, H R and Kasim, A A (2019). Image-based processing for ripeness classification of oil palm fruit. *2019 5th International Conference on Science in Information Technology (ICSITech)*. IEEE, Indonesia. p. 23-26.

Septiarini, A (2021). Machine vision for the maturity classification of oil palm fresh fruit bunches based on color and texture features. *Sci. Hortic., 286(2021)*: 110245. DOI: 10.1016/j.scienta.2021.110245.

Shiddiq, M; Salambue, R; Poja, R and Solistio, A T (2016). Analysis of physical properties of oil palm

fresh fruit bunches using ImageJ. *Appl. Sci. Technol., 1(1)*: 388-394.

Suharjito; Elwirehardja, G N and Prayoga, J S (2021). Oil palm fresh fruit bunch ripeness classification on mobile devices using deep learning approaches. *Comput. Electron. Agric., 188*: 106359. DOI: 10.1016/j.compag.2021.106359.

Sukemi and Sukrisno, E (2019). Identification using the K-means clustering and gray level co-occurance matrix (GLCM) at maturity fruit oil head. *2019 Fourth International Conference on Informatics and Computing (ICIC)*. IEEE, Indonesia. p. 1-4.

Tan, M; Pang, R and Le, Q V (2020). EfficientDet: Scalable and efficient object detection. *Proc. of the IEEE Conference on Computer Vision and Pattern Recognition (2020)*. p. 1-10.

Wibowo, H; Sitanggang, I S; Mushthofa, M and Adrianto, H A (2022). Large-scale oil palm trees detection from high-resolution remote sensing images using deep learning. *Big Data Cogn. Comput. 2022, 6(3):* 89.

Journal of Oil Palm Research Vol. 36 (4) December 2024 p. 630-639
DOI: https://doi.org/10.21894/jopr.2023.0051

NUTRITIVE SCREENING AND FORAGE YIELD OF GUINEA AND HYBRID NAPIER GRASS VARIETIES UNDER DENSE SHADE OF MATURE OIL PALM PLANTATION

RAMACHANDRUDU KUMMARI[1]*; NARASIMHA RAO BEZAWADA[1] and MANORAMA KAMIREDDY[1]

ABSTRACT

Cattle grazing and sparse weed flora due to poor light infiltration in mature oil palm plantations have created a need for the identification of shade tolerant fodder grass varieties. A total of 14 varieties of Guinea grass and four varieties of hybrid Napier were screened for four years under dense shade of mature oil palm plantation. Significant differences were observed among the fodder grass varieties evaluated for fodder yield and nutritive quality attributes. Of all the varieties, Sampoorna (24.55 t ha^{-1}), CO-4 (22.52 t ha^{-1}) and KKM-1 (22.34 t ha^{-1}) among hybrid Napier grass and BG-1 (23.12 t ha^{-1}), DGG-1 (22.00 t ha^{-1}), CO-3 (21.38 t ha^{-1}) and Grazing Guinea-1 (20.28 t ha^{-1}) among Guinea grass have been identified as promising fodder yielders. Overall, better nutritive levels in fodder quality attributes like crude protein (11.88%), crude fat (2.15%), neutral detergent fibre (66.75%), acid detergent fibre (44.37%), lignin (8.91%) and acid insoluble ash (6.00%) were observed in Sampoorna. Because of unique/sturdy growth habit, better adaptation and optimum fodder yield, Sampoorna along with Grazing Guinea-1 can be the most suitable option for a sustainable oil palm-based farming system.

Keywords: fodder grass, growth, nutritive parameter, oil palm, shade.

Received: 9 October 2022; **Accepted:** 31 August 2023; **Published online:** 9 October 2023.

INTRODUCTION

Globally, oil palm (*Elaeis guineensis* Jacq.) is a promising edible oil-yielding crop which is cultivated to an extent of 0.40 million hectares in India (Anonymous, 2022). Equilateral triangular method with 9 x 9 x 9 m spacing is a recommended method for the establishment of oil palm plantations in India. Grazing of cattle is quite common and in fact, dairy farming has become an integral part of many oil palm plantations in Andhra Pradesh and Telangana in India. Due to the sparse growth of palatable weed flora in mature oil palm plantations, daytime grazing by cattle is supplemented with paddy straw/maize stalks/green fodder brought from outside. So, the existing situation offers a dire need for improving forage availability and quality through the introduction of improved fodder grass varieties in mature oil palm plantations. Oil palm requires about 40% area for its optimum growth and FFB yield and the rest of the area remains vacant which offers scope for intercropping (Ramachandrudu *et al*., 2018) with fodder crops. Cultivation of pastures in plantation crops will certainly enhance the availability of forage by using efficient natural resources like land and filtered sunlight. However, the presence of intense shade or poor light intensity (<30%) in mature oil palm plantations is the main limiting factor for the luxuriant growth of forage. In plantations, the shade environment changes gradually with the age of the tree crop. At maturity, levels of photon irradiance (PI) transmitted to the herbaceous layer at the ground may be very low in oil palm plantations (Chen, 1989). Light drives many vital processes in plants which show different

[1] ICAR-Indian Institute of Oil Palm Research, Pedavegi-534 435, Andhra Pradesh, India.

* *Corresponding author e-mail: chandrudu.KR@icar.gov.in*

morphophysiological responses to varying degrees of light intensity and quality as an adaptation (Formisano *et al*., 2022). Hence, shade-tolerant grass species/varieties are certainly needed for improving and sustaining forage production which can be a base for successful integrated/mixed farming in mature oil palm plantations.

Hybrid Napier and Guinea grasses are important forage grasses of the tropics known for good biomass production, palatability, persistence and fodder quality (Hindoriya *et al*., 2019). Further, it is proven that both grasses are highly suitable, productive, slightly shade tolerant and well-established in coconut-based cropping/farming systems in India. Guinea grass and bajra hybrid Napier (CO-5) grass were found to perform well under the shade of coconut garden (Vinodhini *et al*., 2022) and *Melia dubia* plantation (Ramah *et al*., 2022), respectively. Based on the available literature, fodder grasses Guinea and hybrid Napier were selected for screening in the microclimate of mature oil palm plantations. Demographic pressure and shifts in land use patterns have been creating a gap between the demand and supply of fodder in India. The limited availability of land for fodder production and the high cost of concentrates are the major constraints in dairy farming in India. Presently, the country faces a net shortfall of 35.6% green fodder, 10.5% dry crop leftover and 44% concentrate feed ingredients (Singh *et al*., 2022). Thus, the present situation created an opportunity/challenge for the identification of shade-tolerant fodder grass varieties to convert oil palm plantations into a self-sustainable farming system. Under-storey productivity is generally a function of photosynthetically active radiation (PAR) which varies considerably among tree species (Yirdaw and Luukkanen, 2004). There are few reports about the performance of fodder grass like Napier grass, forage sorghum and kenaf (Tohiran *et al*., 2014) and *Pennisetum purpurium* cv. Mott (Muhtarudin *et al*., 2020) under the shade of oil palm. However, information about suitable fodder grasses/their varieties is very limited in major oil palm-growing countries and totally lacking in India. There is a great need for transforming mature oil palm plantations for forage production to sustain livestock integration as the vast area is under oil palm in India. Therefore, the present experiment was conducted with the objective of identifying shade-tolerant grass varieties with quality nutrition under the dense shade of mature oil palm plantations.

MATERIALS AND METHODS

A field experiment was carried out at ICAR-Indian Institute of Oil Palm Research, Pedavegi, Andhra Pradesh state, India for four consecutive years. The experimental site is located at 16° 43′ N and 81° 09′ E with a mean sea level of 13.41 m. Weather conditions of the location *i.e*., average annual temperature, relative humidity, rainfall and photosynthetically active radiation (PAR) in oil palm plantation recorded during the experimental period were described in *Table 1*. Photosynthetically active radiation was measured at monthly intervals by LI-COR Line Quantum Sensor between 11.00 am-12.00 pm. The average temperature and relative humidity of oil palm plantation measured by HTC Thermohygrometer were 3°C-5°C lesser and 12%-15% higher, respectively when compared with outside conditions. Reduced solar light infiltration/dense shade, moderate temperature regime, higher humidity, lower rate of evaporation and higher soil moisture level are features of the microclimate of oil palm plantations as compared with the open condition. Experiment was laid out in randomised block design (RBD) with 18 treatments and two replications. Age of the oil palm plantation was 10 years when the study was initiated and the soil of the experimental site is sandy loam.

Fourteen varieties of Guinea grass (*Megathyrsus maximus*/*Panicum maximum*) and four varieties of hybrid Napier grass (*Pennisetum purpureum* x *Pennisetum typhoides*) were used for the study. The varieties are CO-1 (Coimbatore-1), CO-3 (Coimbatore-3), Samruddhy, Harithasree, BG-1 (Bundel Guinea-1), BG-2 (Bundel Guinea-2), DGG-1 (Dharwar Guinea Grass-1), DGG-2 (Dharwar Guinea Grass-2), Grazing Guinea-1 (GG-1), Tanzania,

TABLE 1. WEATHER CONDITIONS PREVAILED DURING THE EXPERIMENTATION PERIOD AT ICAR-INDIAN INSTITUTE OF OIL PALM RESEARCH, PEDAVEGI, ANDHRA PRADESH, INDIA

Weather parameter	Year			
	1	2	3	4
Temperature (°C)	22.94-32.47	23.55-34.81	21.82-31.24	23.04-33.74
Relative humidity (%)	52.40-96.02	48.09-91.97	49.56-90.89	49.98-94.38
Sun light infiltration (µmol m^{-2} s^{-1})/shade (%)	359.75/23.12	292.79/18.82	347.52/22.34	356.94/22.92
Rainfall (mm)	1 287	705	423	996

Riversdale, Colonel, Mumbasa and Hamil of Guinea grass and KKM-1 (Killikulum-1), Sampoorna, APBN-1 (Andhra Pradesh Bajra Napier-1) and CO-4 (Coimbatore-4) of hybrid Napier grass planted under shaded condition of mature oil palm. All the fodder grass varieties were irrigated with drip system whereas oil palm with micro jet system in palm basins.

Fodder grass varieties were introduced into oil palm plantations where the trees are planted established in hexagonal/equilateral triangular method with 9 x 9 x 9 m spacing. Root slips of grass varieties were planted in four rows in interspace at 60 x 45 cm spacing. Intra space of the plantation was left vacant for the free movement of farm workers and ease of cultural operations around the year. Oil palm and fodder grass were maintained as per the recommended package of practices to avoid competition for nutrients and water. Observations on plant growth and yield parameters *i.e.*, plant height, number of tillers/clump, days to cutting of fodder, number of cuttings/yr, fresh and dry weight of grass were recorded by employing standard methods. Similarly, observations like fresh fruit bunches (FFB) production, bunch weight and annual FFB yield were recorded at the time of FFB harvesting. Chlorophyll and carotenoid contents were estimated by UV-VIS spectrophotometer (*Simadzu UV-1800*) by following dimethyl sulfoxide (DMSO) method. Third leaf from the top of the shoot was taken for pigment estimation.

Fodder grass quality parameters *viz*., crude protein (CP), crude fat (CF), lignin, silica and acid insoluble ash (AIA) were estimated as per AOAC method (2005) and neutral detergent fibre (NDF), acid detergent fibre (ADF), hemicellulose (HC) and cellulose by Van Soest *et al*. (1991) method. Data were analysed statistically as per the procedure given by Gomez and Gomez, (1984) for analysis of variance (ANOVA) for RBD design and analysed data are presented in tabular and graphical forms. ANOVA of growth and yield parameters of fodder grass varieties grown in mature oil palm plantations are presented in *Table 2*.

RESULTS AND DISCUSSION

Results of the present experiment revealed that there were significant differences among the grass varieties for all the characters studied except cellulose and silica. Morphological and physiological adaptation to shade is common for all plants but the extent of changes varies with plant species and genotype (Pierson *et al*., 1990). In the present study, maximum plant height (237.93 cm) was observed in KKM-1 which was significantly superior to other varieties (*Figure 1*). Except for Sampoorna (184.78 cm), shoots were taller in hybrid Napier grass varieties as compared with Guinea grass varieties. Among the Guinea grass varieties, CO-1 recorded the maximum plant height (194.17 cm) whereas plants were short and bushy in stature in Grazing Guinea-1 (107.65 cm) which is a short-statured variety by nature. Enhanced plant height was mainly attributed to the uptake of more nutrients by the variety which resulted in more vegetative growth and increase in protoplasmic constituent and acceleration in the process of cell division, expansion and differentiation thereby resulting in luxuriant growth (Dahipahle *et al*., 2015).

Tillering in grasses is a complex phenomenon which is due to the combined effect of genetic, physiological and environmental factors (Assuero and Tognetti, 2010). It is clear from the results that there was a significant variation among the varieties for tiller production (*Figure 2*). Maximum tiller production per clump was noticed with Grazing Guinea-1 (101.04) while the minimum production was recorded in APBN-1 (18.90). The highest number of tillers recorded in Grazing Guinea-1

TABLE 2. ANOVA OF VARIOUS GROWTH AND YIELD PARAMETERS OF FODDER GRASS VARIETIES

Parameter	Treatment mean sum of square	Replication mean sum of square	Error mean sum of square	Coefficient of variation
Plant height	5 678.31 (0.0001)	124.70 (0.396)	120.65	6.42
Tillers	1 516.94 (0.0001)	84.77 (0.188)	53.43	19.42
Green fodder yield	18.63 (0.0001)	0.0001 (0.991)	1.388	6.16
Dry fodder yield	2.650 (0.0001)	0.209 (0.286)	0.172	10.960
Chlorophyll	0.702 (0.022)	0.453 (0.200)	0.255	12.990
Carotenoids	0.064 (0.015)	0.139 (0.008)	0.019	13.670

Note: Values in parentheses are F probability values.

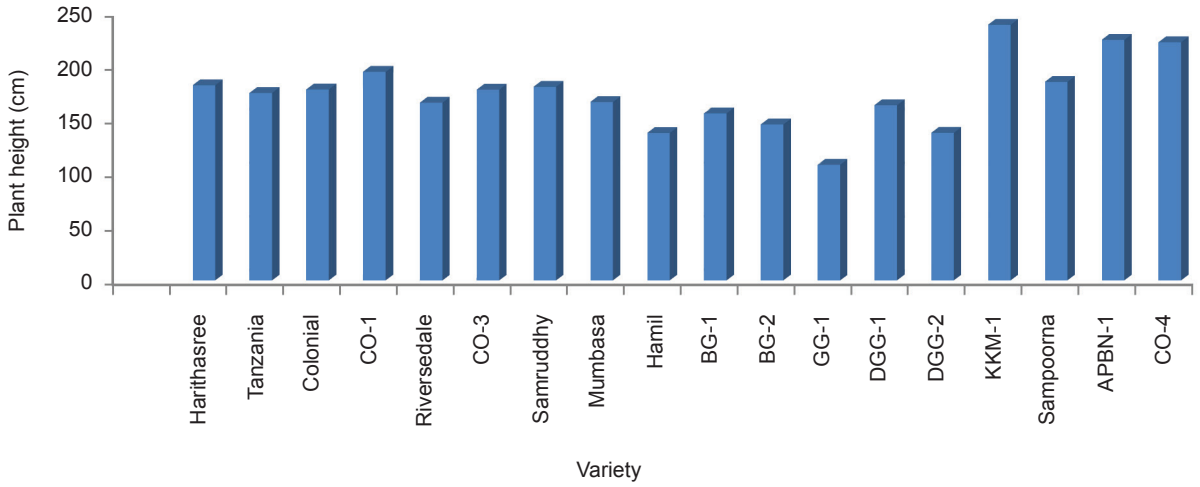


Figure 1. Plant height in Guinea and hybrid Napier grass varieties grown in mature oil palm (pooled mean) plantation.

which was markedly superior to other varieties and this may be due to better photosynthetic rate and acclimatisation to shade of oil palm. Further, profuse tiller production in Grazing Guinea-1 may be due to higher leaf area index which in turn might have resulted in more carbohydrate assimilation (Anita and Lakshmi, 2011). However, tillers did not have solid stem and mostly they are soft in texture and leafy in Grazing Guinea-1. Mean tiller production was significantly higher in many varieties of Guinea grass when compared to hybrid Napier grass varieties. By nature, Guinea grass has more tiller production capacity when compared with hybrid Napier grass. The increase in number of tillers in Guinea grass may be due to higher leaf area index which might have resulted in more carbohydrate assimilation (Anita and Lakshmi, 2011). High density of shade in oil palm might have suppressed the tiller production in hybrid Napier grass by delaying the development of tiller buds into tillers (Gautier *et al*., 1999). The results of the current study are in tune with the findings of Jose *et al*. (2019) that inverse relation of tiller production with increasing shade levels and the rate of tillering existed among fodder grasses grown in mature coconut and rubber plantations. Tiller production was relatively better in Sampoorna (32.15) among hybrid Napier grass varieties. Malaviya *et al*. (2020) reported the differential response among Guinea grass varieties for yield attributes under shade.

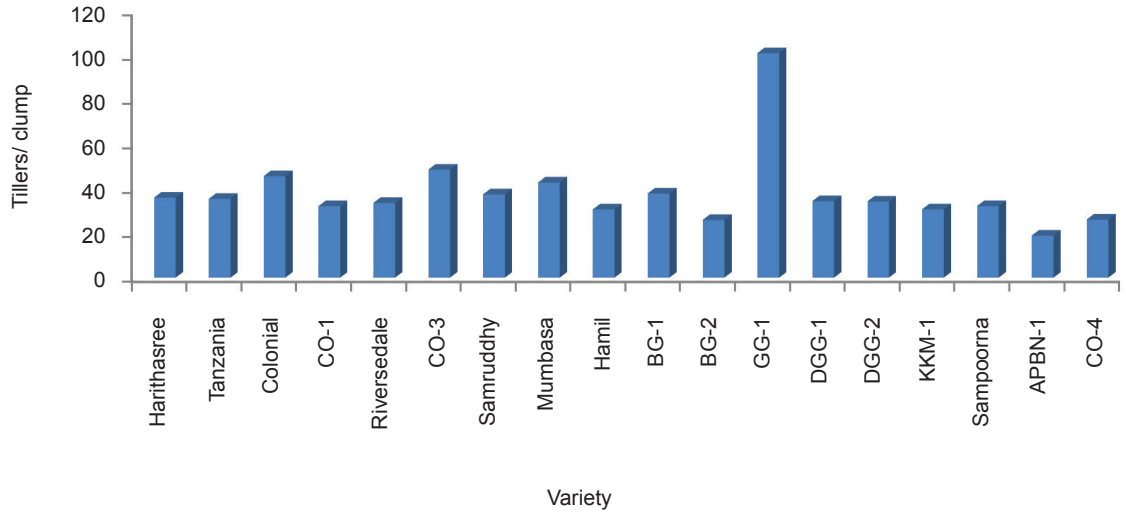


Figure 2. Tiller production in Guinea and hybrid Napier grass varieties grown in mature oil palm (pooled mean) plantation.

Biomass or fodder production in the understory is a function of the PAR reaching the ground. Of all the grass varieties, Sampoorna recorded the highest average green fodder yield (24.55 t ha^{-1}) over the years (*Figure 3*) and it was significantly superior to other varieties except BG-1 (23.12 t ha^{-1}), CO-4 (22.52 t ha^{-1}) and KKM-1 (22.34 t ha^{-1}). Among the Guinea grass varieties, BG-1 (23.12 t ha^{-1}), DGG-1 (22.00 t ha^{-1}), CO-3 (21.38 t ha^{-1}) and Grazing Guinea-1 (20.28 t ha^{-1}) were the promising fodder yielders. More or less, the same trend (*Figure 4*) was observed with respect to dry fodder yield among the varieties. The varieties CO-4 (6.23 t ha^{-1}) and Sampoorna (6.11 t ha^{-1}) recorded the highest dry fodder yield and both were more or less equal in yield and markedly superior to the rest of the varieties. The growth and development of Sampoorna indicated the sturdiness, compactness and anti-lodging properties. Higher fodder yield was due to enhanced plant growth attributes like plant height, increased number of tillers and leaf/stem ratio and because of these characteristics this variety is highly suitable for oil palm plantations. Similar to green fodder yield, more dry fodder yield levels were noticed in Guinea grass varieties like BG-1 (4.43 t ha^{-1}), CO-3 (4.09 t ha^{-1}), DGG-1 (3.88 t ha^{-1}) and GG-1 (3.87 t ha^{-1}). Except APBN-1 (18.55 t ha^{-1}), other hybrid Napier grass varieties like Sampoorna, CO-4 and KKM-1 emerged as good forage yielders. Mean dry fodder yield was relatively higher in hybrid Napier grass varieties as compared with Guinea grass ones. Overall, higher forage yield in hybrid Napier grass varieties might be due to more stem weight though tiller production was less as compared with Guinea grass varieties. Fodder yield is mainly dependent on tiller and foliage production in Guinea grass whereas tillers and sturdy stem growth in hybrid Napier grass varieties. By nature, stem growth is weak in Guinea grass as compared with hybrid Napier grass which has strong and large stems. Higher biomass (green and dry fodder) production under a poor light intensity of mature oil palm plantations indicates a better adaptation of the above-mentioned varieties. Similarly, differential Guinea (Malaviya *et al*., 2020) and hybrid Napier grass (Antony and Thomus, 2015) genotypic response was observed for green and dry fodder yields under shade.

Results shown in *Figure 3* reflect an increasing trend in fodder yield in all the varieties of Guinea and hybrid Napier grass over the years. This can be attributed to better morphological and physiological adaptation of fodder grasses under prevailing microclimate of oil palm plantation. In the present study, the number of fodder cuttings per annum was four times in all the varieties and this indicated the delayed and slow growth of Guinea and hybrid Napier grasses under high shade of oil palm. Reasons for lower fodder yield and less number of cuttings in all the varieties must be due to reduced photosynthesis under poor light intensity in oil palm. This is in consistent with the statement of Salisbury and Rose (1986) that shade causes the light compensation point at lower irradiance levels and

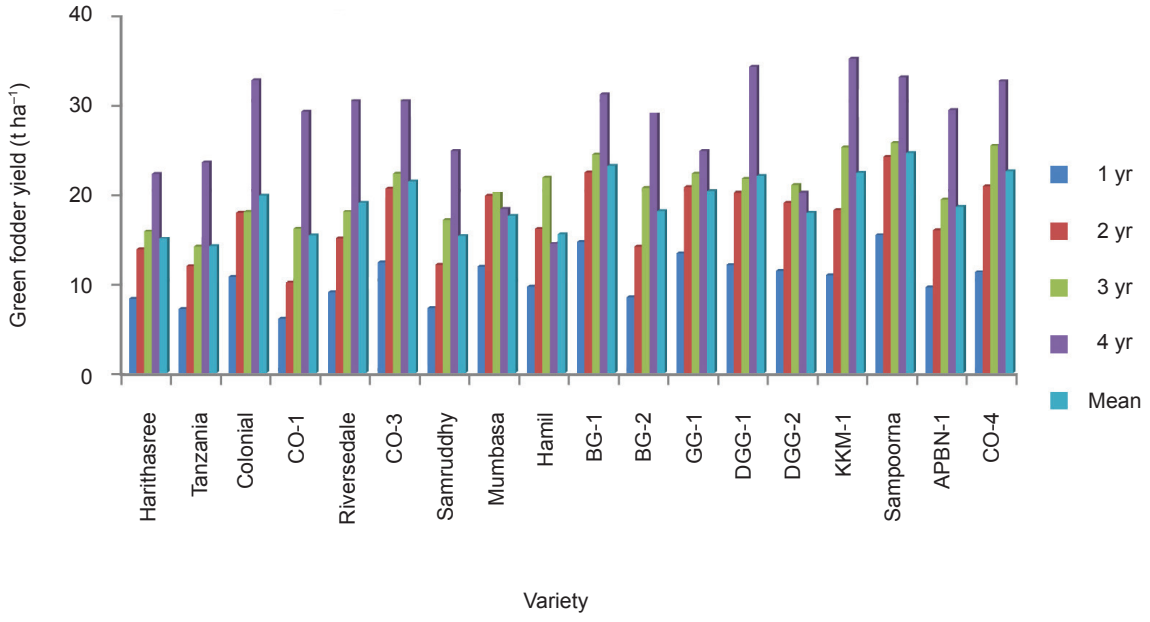


Figure 3. Green fodder yield of Guinea and hybrid Napier grass varieties grown in mature oil palm plantation.

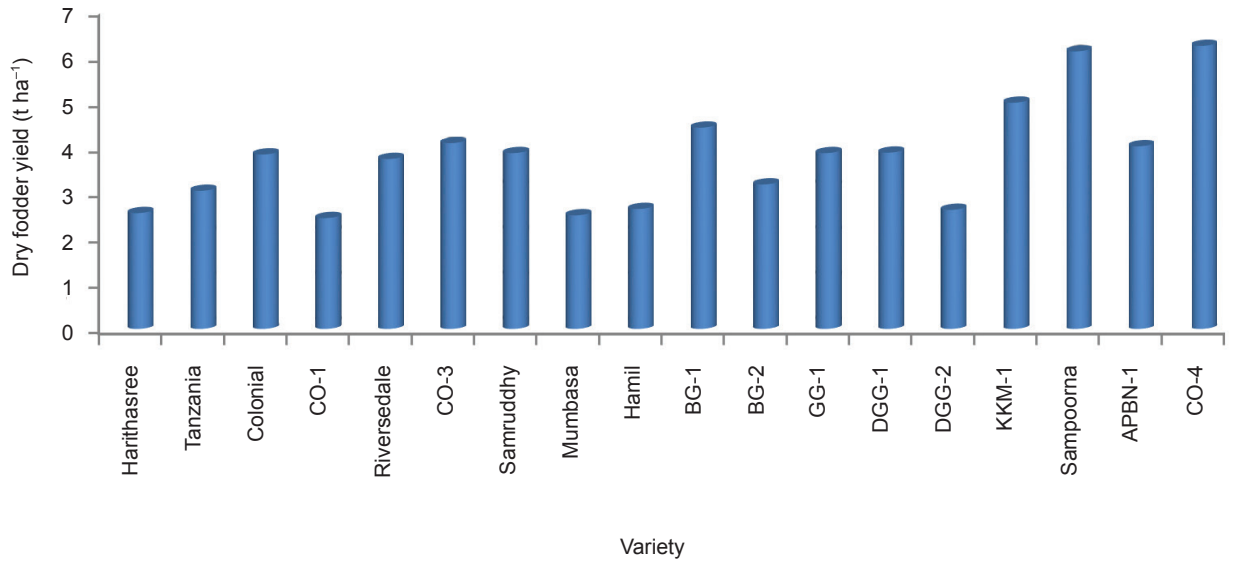


Figure 4. Dry fodder yield of Guinea and hybrid Napier grass varieties grown in mature oil palm (pooled mean) plantation.

stunted grass growth by developing ability to grow under shade. Even though grasses are fairly tolerant to shade, showed a reduction in forage production under intense shade, especially when the level of shade exceeds 50% of the incident radiation (Paciullo *et al*., 2007). Further, plants do show elasticity only in a limited range and beyond that, plants do not make any adaptation attempts (Valladares *et al*., 2007). Similarly, Jose *et al.* (2019) reported decreased yields in Guinea and hybrid Napier grasses in understory of rubber plantation.

Chlorophyll and carotenoids play a vital role in light reactions of photosynthesis and photosynthetic electron transport system in plants (Gardener *et al*., 2010). Among the tested grass varieties, the maximum chlorophyll content (4.61 mg g^{-1}) was recorded in variety DGG-2 (*Figure 5*) which was closely followed by Riversedale (4.54 mg g^{-1}) and Sampoorna (4.52 mg g^{-1}) whereas the minimum was estimated in Samruddhy (3.23 mg g^{-1}). Similarly, the variety DGG-2 (1.24 mg g^{-1}) recorded the maximum carotenoid content while the minimum was estimated in Harithasree [(0.82 mg g^{-1}) and BG-2 (0.82 mg g^{-1})]. Chlorophyll plays a crucial role in plant growth and in general the content is relatively higher in shady situation as compared with partial and open conditions. Because of this, foliage of all the grass varieties was dark green in colour and reflecting the direct relation between chlorophyll content and photosynthesis rate. Increased levels of chlorophyll were also reported in Guinea grass genotypes grown under dense shading (Malaviya *et al*., 2020). The higher chlorophyll density influences efficiency of interception and use of solar radiation with growth potential at low level of radiation (Shelton *et al*., 1991).

Fodder grass plays a key role in growth and performance of livestock. Forage fed to the cattle must have good nutritional value and palatability. Crude protein, crude fat and crude fibre are the major components which decide the nutritive quality of forage. There were significant differences among the varieties for most of the nutritive quality parameters (*Table 3*). Among all the varieties, Harithasree recorded the highest crude protein (12.98%) content and closely followed by Sampoorna (11.88%) and CO-4 (11.28%) and these varieties were more or less consistent in crude protein content among themselves. The higher the crude protein level, the more digestible is the forage. Higher crude protein yield must be due to higher photosynthetic activity leading to beneficial effects like cell division and cell elongation which in turn resulted in more fodder production and accumulation of photosynthates (Dahipahle *et al*., 2015). The present results are in accordance with findings of Dahipahle *et al.* (2015) in Guinea grass.

Extractable ether/crude fat improves the palatability of fodder by providing essential fatty acids. Crude fat content was ranged from 2.15% in Sampoorna to 1.10% in DGG-1. Of all the tested varieties, higher crude fat level was observed in Sampoorna (2.15%), BG-2 (2.09%) and Mumbasa (2.00%) and these were found equal to one another. Neutral detergent fibre (NDF) is total fibre present in fodder which influences level of intake. Though high level limits intake but minimum level is

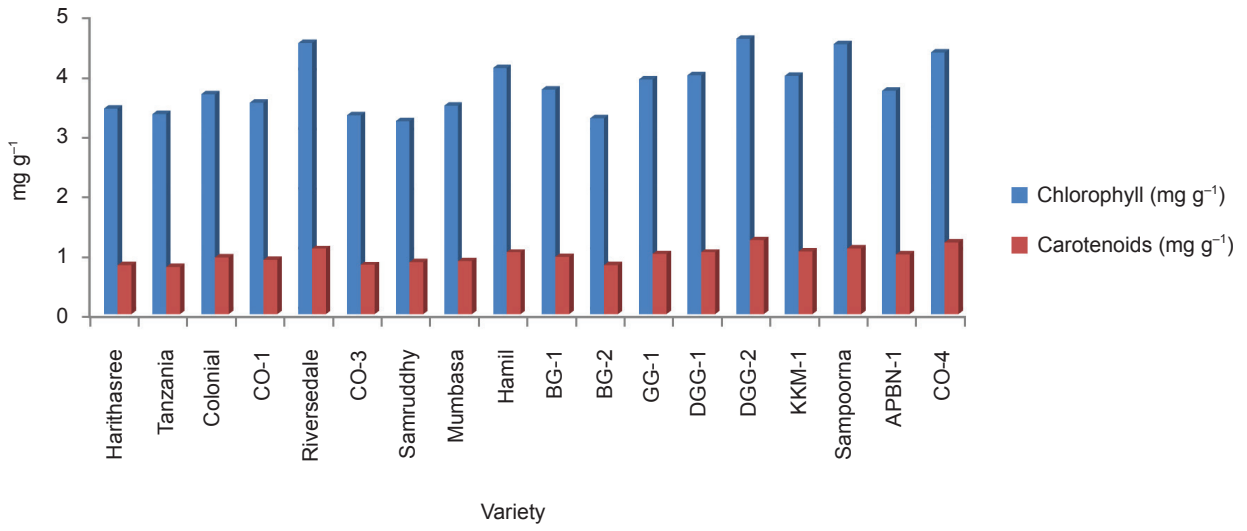


Figure 5. Chlorophyll and carotenoid content of Guinea and hybrid Napier grass varieties grown in mature oil palm (pooled mean) plantation.

necessary for healthy rumen in ruminants. The variety DGG-2 contained the maximum quantity of NDF (78.02%) which was markedly superior to most of the varieties and it was closely followed by CO-4 (77.72%), KKM-1 (77.33%) and CO-3 (77.11%). Out of all the grass varieties, NDF was lesser in Sampoorna (66.75%), BG-1 (68.90%) and Harithasree (69.46%) which were similar with one another. Acid detergent fibre (ADF) is the least digestible portion of fibre which affects a feed digestibility. The lower the ADF content, the higher the digestibility of fodder. Acid detergent fibre ranged from 44.37% in Sampoorna to 54.63% in Hamil. It is observed from the results that fodder of Sampoorna is more digestible as compared to other varieties.

Hemicellulose content was the highest in the variety Mumbasa (26.62%) while the lowest level was recorded in Harithasree (16.05%) followed by BG-1 (17.13%). Hemicellulose in plants possesses inverse relation with nitrogen uptake and crude protein content. Results were not significant among the varieties of Guinea and hybrid Napier grass for cellulose and silica content. Comparatively, higher cellulose and silica content were observed with CO-3 and Hamil, respectively. Lignin has no known nutritive value except a bulk factor which limits organic matter digestibility and nutrient availability in forages by interfering with microbial enzymatic activity (Moore and Jung, 2001). At high levels, it reduces digestibility of other nutrients in a ration. Higher level of lignin content was recorded in CO-1 (11.48%) and closely followed by CO-3 (11.45%), KKM-1 (11.25%) and Tanzania (11.16%). Varieties like Harithasree (7.86%), DGG-2 (8.40%), DGG-1 (8.50%), Sampoorna (8.91%) and BG-1(8.95%) contained lesser lignin in their fodder. Acid insoluble ash (IAA) is the measure of total mineral content of forage and its quantity was varied from 3.00% in BG-2 and KKM-1 to 7.17% in Riversedale. Similarly, Hindoriya *et al*. (2019) in various fodder crops and Singh and Chauhan (2018) in bajra Napier hybrids reported proximate principles and fibre fractions.

Increased FFB yield in oil palm over the years was recorded in intercropped (28.24 t ha^{-1}) area as compared with mono crop (25.92 t ha^{-1}). This indicates that intercropping with fodder crop promoted the yield of oil palm which must be due to drawing of nutrients and water by oil palm from the inter cropped area owing to its dense mat like growth of root system (data not shown) in inter cropped area. In fact, oil palm has the capacity to produce lot of feeder roots wherever water and nutrients are available even beyond its active feeder root zone (Corley and Tinker, 2016). Experiments clearly demonstrated that intercropping has complementary effect on coconut productivity if proper nutrient management practices are adopted for the fodder crops (Subramanian *et al*., 2019).

CONCLUSION

Results revealed the relative performance of Guinea and hybrid Napier grass varieties under dense shade of mature oil palm plantation. Varieties Sampoorna, CO-4 and KKM-1 of hybrid Napier grass and BG-1, DGG-1, CO-3 and Grazing Guinea-1 of Guinea grass have been identified as most promising shade tolerant and high yielding varieties under microclimate of mature oil palm plantation. Of all the varieties tested, the hybrid

TABLE 3. NUTRITIVE QUALITY (% DRY MATTER BASIS) OF FODDER IN GUINEA AND HYBRID NAPIER GRASS VARIETIES GROWN IN MATURE OIL PALM PLANTATION (POOLED MEAN)

Variety	CP	CF	NDF	ADF	HC	Cellulose	Lignin	Silica	AIA
Harithasree	12.98	1.42	69.46	53.41	16.05	40.97	7.86	2.51	6.20
Tanzania	10.98	1.45	75.22	53.03	22.19	37.84	11.16	2.86	4.90
Colonial	10.68	1.45	75.09	54.01	21.08	41.03	10.53	3.29	6.20
CO-1	10.11	1.40	73.36	50.85	22.51	38.52	11.48	3.15	5.70
Riversedale	9.59	1.31	76.17	51.67	24.50	38.35	10.01	3.40	7.15
CO-3	9.04	1.30	77.11	53.95	23.16	42.43	11.45	3.92	5.50
Samruddhy	10.92	1.85	72.41	50.32	22.09	42.12	9.87	3.54	6.05
Mumbasa	9.05	2.00	76.83	50.21	26.62	39.13	10.46	3.86	7.10
Hamil	9.56	1.40	73.59	54.63	18.96	40.42	10.90	4.53	5.90
BG-1	9.76	1.53	68.90	51.77	17.13	38.29	8.95	4.41	5.70
BG-2	9.64	2.09	72.56	50.85	21.71	41.97	9.16	4.15	3.00
GG-1	10.11	1.16	72.68	49.31	23.37	38.24	10.61	4.20	6.95
DGG-1	8.16	1.10	75.97	54.40	21.57	37.17	8.50	4.03	5.90
DGG-2	8.15	1.81	78.02	52.55	25.47	39.43	8.40	3.87	6.00
KKM-1	10.89	1.40	77.33	52.05	25.28	39.63	11.25	3.96	3.00
Sampoorna	11.88	2.15	66.75	44.37	22.38	39.13	8.91	4.15	6.00
APBN-1	9.96	1.42	71.03	49.06	21.97	37.15	10.10	4.16	6.20
CO-4	11.28	1.45	77.72	53.39	24.33	40.16	10.97	3.72	4.90
CV	8.93	9.32	3.44	4.32	8.62	6.55	8.72	15.14	10.78
CD-5%	1.91	0.31	5.36	4.71	4.25	NS	1.85	NS	1.31

Note: CP - crude protein; CF - crude fat; NDF - neutral detergent fibre; ADF - acid detergent fibre; HC - hemicellulose; AIA - acid insoluble ash; NS - not significant.

Napier grass variety Sampoorna possessed better nutritive levels in fodder. A combination of varieties Sampoorna and Grazing Guinea-1 can be ideal for oil palm plantations due to their better adaptability and suitability. Cropping system with fodder grass in oil palm provides potential alternative to overcome fodder problem to some extent in India as it utilises natural resources like available light and space more efficiently. Further, results of the study clearly reflected the complementary effect of intercropping over the productivity of oil palm. This study also revealed appreciable variability for shade tolerance among various grass genotypes which can be used in crop improvement programmes. Thus, the successful performance of fodder grass varieties can certainly pave the way for sustainable integrated/mixed farming system in mature oil palm plantations which in turn leads to optimising land productivity and doubling farmer's income.

REFERENCES

Anita, M R and Lakshmi, S (2011). Response of Guinea grass varieties to shade and potash. *Madras Agril. J., 98(1-3)*: 41-43.

Anonymous (2022). *Annual Report 2022*. ICAR-Indian Institute of Oil Palm Research, Pedavegi-534 435, Andhra Pradesh, India.

Antony, S and Thomus, C G (2015). Shade tolerance of selected hybrid Napier cultivars under rainfed conditions. *J. Tropical Agri., 53(1)*: 35-41.

AOAC (2005). *Official Methods of Analysis*. 18th edition. Association of Official Analytical Chemists, Washington DC, USA.

Assuero, S G and Tognetti, J A (2010). Tillering regulation by endogenous and environmental factors and its agricultural management. *American J. Plant Sci. Biotechnol., 4(1)*: 35-48.

Chen, C P (1989). Problems and prospects of integration of forage into permanent crops. *Grasslands and Forage Production in South-East Asia* (Halim, R A ed.). Serdang, Malaysia. p. 128-139.

Corley, R H V and Tinker, P B 2016. *The Oil Palm*. 5th edition. Wiley Blackwell, West Sussex, UK. 680 pp.

Dahipahle, A V; Bhagat, S B; Shinde, D B and Mahadkar, U V (2015). Performance of Guinea grass

varieties in North Konkan zone of Maharashtra. Paper presented during the 23rd International Grassland Congress (Sustainable use of grassland resources for forage production, biodiversity and environmental protection). New Delhi.

Formisano, L; Miras-Moreno, B; Ciriello, M; Zhang, L; De Pascale, S; Lucini, L and Rouphael, Y (2022). Between light and shading: Morphological, biochemical and metabolomics insights into the influence of blue photoselective shading on vegetable seedlings. *Front. Plant Sci*., *13*: 890830. DOI: 10.3389/fpls.2022.890830.

Gardner, F P; Brent Pearce, R and Roger, L M (2010). *Physiology of Crop Plants*. Scientific Publishers (India), Jodhpur, India. p. 7-17.

Gautier, H; Claude, V and Hazard, L (1999). Tillering responses to the light environment and to defoliation in populations of perennial rye grass selected for contrasting leaf growth length. *Annals. Botany*, *83*: 423-429.

Gomez, K A and Gomez, A A (1984). *Statistical Procedures for Agricultural Research*. 2nd edition. John Wiley and Sons, New York. p. 316-356.

Hindoriya, P S; Meena, R K; Magan Singh and Rajesh Kumar (2019). Evaluation of kharif forage crops for biomass production and nutritional parameters in Indo-Gangetic plains of India. *Indian J. Animal Nutri.*, *36(1)*: 25-29.

Jose, R M; Jamaludheen, V; Kunhamu, T K; Santhosekumar, A V and Raj, A K (2019). Growth and productivity of selected fodder grasses intercropped under mature coconut and rubber plantations. *Indian J. Agroforestry*, *21(1)*: 21-26.

Malaviya, D R; Baig, M J; Kumar, B and Kaushal, P (2020). Effects of shade on guinea grass genotypes *Megathyrsus maximus*. *Revista de Biologia Tropical*, *68(2)*: 563-572.

Moore, K J and Jung, H J G (2001). Lignin and fiber digestion. *J. Range Manage.*, *54*: 420-430.

Muhtarudin; Winda Puspita Sari; Desi Savitri; Farida Fathul; Erwanto Liman; Gung Kusuma Wijaya; Akhmad Dakhlan and Kusuma Adhianto (2020). Effect of grass variety and shade under oil palm plantation on production and proportion of stems, leaves and nutrition content of grass. *J. Biol. Sci.*, *20*: 116-122.

Paciullo, D S C; de Carvalho, C A B; Aroeira, L J M; Morenz, M J F; Lopes, F C F and Rossiello, R O P (2007). Morphophysiology and nutritive value of *Brachiaria decumbense* under natural shade and full sun. *Pesquisa Agropecuaria Brasileira*, *42(4)*: 573-579.

Pierson, E A; Mack, N M and Alan Black, R (1990). The effect of shading on photosynthesis, growth and regrowth following defoliation for *Bromus tactorum*. *Oecologia*, *84(4)*: 534-543.

Ramachandrudu, K; Suneetha, V; Suresh, K; Rao, B N and Manorama, K (2018). Systems approach in oil palm for higher productivity and profitability. *Technical Bulletin*. Indian Institute of Oil Palm Research, Pedavegi, Andhra Pradesh. p. 1-52.

Ramah, K; Parthiban, K T; Sivakumar, K; Sekhar, I and Rajendran, P (2022). Evaluation of shade tolerant fodder crops in *Melia dubia* based silvipastoral system. *Range Manag. Agrofor., 43(1)*: 74-79.

Salisbury, F B and Ross, C W (1986). *Plant Physiology*. 3rd edition. CBS Publishers and Distributers, Delhi, India. p. 216-228.

Shelton, H M and Stilr, W W (1991). Forages for Plantation Crops. *Proc. of Workshop*. Sanur Beach, Bali, Indonesia. 27-29 June 1990. *ACIAR Proceedings No. 32*: p. 168.

Singh, D N; Bohra, J S; Vishal, T; Tejpal, S; Banjara, T R and Gaurendra, G (2022). A review of India's fodder production status and opportunities. *Grass Forage Sci.*, *77(1)*: 1-10. DOI: 10.1111/gfs.12561.

Singh, D and Chauhan, A (2018). Fodder yield and quality assessment of different bajra Napier hybrids in Central Gujarath of India. *Range Manag. Agrofor.*, *39(2)*: 269-273.

Subramanian, P; Surekha, K; Ravi Bhat and Thamban, C (2019). Fodder grass cultivation in coconut garden. *Indian Coconut J.*, *62(1)*: 17-19.

Tohiran, K A; Omar, R Z R; Norkaspi Khasim; Rodi, M Z R M; Basri, N K M and Wahid Omar (2014). Transforming oil palm plantation for forage and livestock integration. *Oil Palm Bulletin*, *69*. p. 1-4.

Valladares, F; Gianoli, E and Gomez, J M (2007). Ecological limits to plant phenotypic plasticity. *New Phytol.*, *176(4)*: 749-763.

Van Soest, P J; Robertson, J B and Lewis, B A (1991). Methods for dietary fibre, neutral detergent fibre and non-starch polysaccharides in relation to animal nutrition. *J. Dairy Sci., 74*: 3583-3597.

Vinodhini, S M; Sivakumar, S D; Karthikeyan, R and Thirunavukkarasu, M (2022). Assessment of suitable grass and legume fodders for the development of pastures under coconut garden. *Int. J. Plant Soil Sci*., *34(21)*: 201-202.

Yirdaw, E and Luukkanen, O (2004). Photosynthetically active radiation transmittance of forest plantation canopies in the Ethiopian highlands. *For. Ecol. Manage.*, *188*: 17-24.

Journal of Oil Palm Research Vol. 36 (4) December 2024 p. 640-649
DOI: https://doi.org/10.21894/jopr.2023.0058

EVALUATION OF DIFFERENT RATES AND TYPES OF MOROCCAN PHOSPHATE ROCKS ON OIL PALM SEEDLINGS

NORAKMAL KHAIRUANUAR[1]; TAN NGAI PAING[1]*; MOHAMED HANAFI MUSA[1] and ADIBAH MOHD AMIN[1]

ABSTRACT

Phosphorus (P) deficiency has consistently been a major limitation in crop production, especially in acidic tropical soils such as those in Malaysia. Since Morocco has the world's largest reserve of phosphate mines, its phosphate rocks (PR) can be examined for their agronomic effectiveness in Malaysian soil. This study investigated the effects of various types of Moroccan phosphate rocks (MPR) as well as Egyptian phosphate rocks (EPR) on the growth performance of different oil palm genotype seedlings. Five different rates of MPR Type B was used to assess the effect of different rate of PR on oil palm seedlings' performance; 0 (control), 50, 100, 200 and 400 mg P kg^{-1}. Meanwhile, four different types of PR were used to assess the effect of different types of PR on oil palm seedlings' performance: MPR Type A, MPR Type B, MPR Type C, EPR and control (no PR application). The results showed that the rates and types of PR application had significant effects on the P concentration and P uptake of oil palm seedlings. MPR Type B at 100 mg P kg^{-1} was found to produce the optimum rate of P concentration and P uptake in the oil palm seedlings. In terms of different sources of PR, MPR Type B was found to provide oil palm seedlings with a higher concentration of P than EPR.

Keywords: Moroccan phosphate rocks, oil palm seedlings, phosphorus fertilisers.

Received: 9 February 2023; **Accepted:** 14 September 2023; **Published online:** 3 November 2023.

INTRODUCTION

Malaysia has vast areas of oil palm plantations, which were estimated to be 5.67 million hectares in 2022 (MPOB, 2023). Despite this, the cultivation and production of oil palm are often limited by the available nutrients in the soil, in particular, phosphate. Phosphorus (P) limitations are also a major productivity constraint in many natural (Augustine *et al*., 2003) and managed (Bünemann *et al*., 2011) grassland systems. A study done by Balemi and Negisho (2012) estimated that crop productivity of the world's arable land is limited by a P deficiency of >40% which can severely reduce crop production. This challenge, however, can be easily overcome by applying phosphate fertiliser to raise the P levels in soils. Two main categories of P fertilisers can be identified: 1) water-soluble P fertilisers such as superphosphate, triple super phosphate ad, and diammonium phosphate; and 2) ground phosphate rocks (PR) originating from different mines. As Malaysian soil is highly weathered, acidic and inherently low in P, the application of fertilisers is crucial and can satisfy the nutrient deficiency in acid soils (Chien *et al*., 2011), but however, the cost of fertilisers, particularly of P fertilisers, has increased markedly worldwide (Chien *et al*., 2011; Van Straaten, 2002; 2006). Planters generally choose P fertilisers based on the agronomic efficiencies of the materials and the price. The performances of water soluble phosphate in acid soils are reported to be very low. This is due to the the presence of iron (Fe) and aluminum (Al) in these soils (Basak and Biswas, 2016). Thus, it is not suitable to use in acid

[1] Department of Land Management,
Universiti Putra Malaysia,
43400 UPM Serdang, Selangor, Malaysia.

* *Corresponding author e-mail: ngaipaing@upm.edu.my*

soil. Direct application of PR has been a standard practice since the 1930s in supplying the P demand of the oil palm crops (Zaharah *et al*., 1996). Zin *et al*. (2001) reported that direct application of PR is highly practical in correcting P deficiency in most Malaysian soils. The use of ground PR also shows a positive result in liming as it has high calcium (Ca) content (Isenmila *et al*., 2006). Furthermore, the PR was found to have significant residual effects in acid soils for at least a few years (Chan, 1981; Tan *et al*., 2015). In addition, several studies have demonstrated that the application of PR directly to the soil was agronomically comparable to phosphate fertilisers of a lower price; PR was also an economically attractive substitute to the use of the more expensive soluble phosphate fertilisers (Chien *et al*., 1990; Chien and Friesen, 1992; Hammond *et al*., 1986; Khasawneh and Doll, 1978; Sale and Mokwunye, 1993). Correa *et al*. (2005) performed a study on corn plants in Ultisol and found an increase in shoot dry matter production when treated with Gafsa PR. The production of crop plants incorporated with Gafsa PR was as sufficient as the production of crop plants treated with triple superphosphate. On the other hand, Barrow (2017) showed that for soybeans, the decrease in soil pH (6 to 4) had increased the phosphate uptake by roots.

The principal mineral in most PR sources is apatite, but these PR sources vary extensively in their physical, chemical, and crystallographic properties (Chien *et al*., 2010). They originate from various places being mined and include marine, igneous, metamorphic, biogenic, and phosphate deposits as a result of weathering. However, most of the PR is extracted from sedimentary marine deposits, and a small amount is obtained from igneous sources. According to Lin and Schorr (1997), PR of sedimentary origin yield typically 30%-35% of phosphorus pentoxide (P_2O_5), whereas those of igneous origin contain marginally higher P_2O_5 at typically 35%-40%. Meanwhile, 90% of PR is being processed as raw material into water-soluble P fertiliser, while some of it is used for direct application to the soil. The direct application of PR can be a source of P for crops, but not all PR is readily available and agronomically effective when applied directly to the soil. This can be attributed to PR's natural variation in reactivity and occurring mineral impurities, such as clay, carbonate (CO_3^{2-}), Fe, and Al. Furthermore, these properties most often differ with geological location, which will affect their use for direct application. At present, several PR varieties have been used in Malaysia; these are mined from different regions of the world, mostly from Christmas Island, China and Northern Africa. This PR have different reactivity and agronomic effectiveness, and this will eventually affect the performance of the plant. Thus, a reactive source of PR is crucial to improve the soil P levels and boost plant productivity.

Several studies have indicated that PR reserves could be depleted within 50 to 100 years (Cordell, 2010; De Haes *et al*., 2009; Smit *et al*., 2009; Steen, 1998; Vaccari, 2009), whilst others suggest that PR reserves will extend well into the future (Van Kauwenbergh, 2010; Van Vuuren *et al*., 2010). Regardless of these timelines, it is evident that most of the PR reserves are held by only a few countries in Northern Africa, primarily Morocco. According to the USGS (2011), it is estimated that Morocco possesses around 77% of the world's PR reserves.

Some PR from these mines are used for direct application in soils for agricultural purposes. Accordingly, Moroccan phosphate rocks (MPR) have the potential to be a good alternative to P fertilisers in Malaysia. Various P fertilisers have been evaluated for oil palm under nursery and field conditions (Foong, 1993; Foster *et al*., 1988; Goh *et al*., 1994; Ng, 1986). However, there are limited studies on MPR, for oil palm in Malaysia, in terms of its solubility/reactivity in soils and agronomic effectiveness. Therefore, the objective of this study was to evaluate the effects of PR on the growth performance of different oil palm seedling genotypes with different types of MPR applications. This is the first study to investigate the use of MPR on oil palm seedlings in Malaysian soils.

MATERIALS AND METHODS

Experimental Design

Four types of PR from two geological locations were used in this study: PR from three different mines in Khouribga, Morocco, hence designated as MPR Type A, MPR Type B, and MPR Type C, and PR from Egypt hence designated as EPR. EPR was used in this experiment because; 1) It is commonly found in Malaysian oil palm plantation/market and 2) EPR is from Northern Africa, which is same as MPR. Thus, it is a good indicator in comparing both phosphate rocks. As a control group, a treatment without the addition of PR was included in the experiment. Before the study, all the PR materials were sampled and subjected to a 2% formic acid and 2% citric acid solubility test. *Table 1* shows the results of the solubility test.

X-ray diffraction (XRD) analysis was also performed (to identify the mineral content) on MPR Type A, Type B and Type C and the results showed the initial presence of Arrojadite, Cacoxenite and Lesukite respectively as their phosphate minerals.

Four month old oil palm seedlings (*Dura* x *Pisifera*) comprising AVROS and Yangambi planting materials were used in this study. The oil palm seedlings were selected according to the average height and frond sizes. On receiving the seedlings from the supplier, they were transplanted into

TABLE 1. THE CHEMICAL AND PHYSICAL CHARACTERISTICS OF THE TWO APPLIED PR FERTILISERS

P sources		P_2O_5 (%)	Solubility as a percent of rocks (%)	
			2% Formic acid	2% Citric acid
MPR	Type A	32.7	17.2	10.3
	Type B	30.8	16.8	10.2
	Type C	31.4	16.9	10.4
EPR		26.6	11.4	9.2

Note: P - phosphorus; P_2O_5 - phosphorus pentoxide; MPR - Moroccan phosphate rocks; EPR - Egyptian phosphate rocks.

prepared polybags (20′ x 20′) containing 20 kg of soil (the soils were allowed to acclimatise for a week before treatment application). The soil used in this study was sandy clay loam; it has a low P content which can be classified as Haplic Hapludox (Soil Survey Staff, 1998). The characteristics of the soils are shown in *Table 2*.

TABLE 2. CHARACTERISTICS OF SOIL

Treatment		Topsoil
pH	H_2O	3.98
Organic carbon (%)		0.29
Total nitrogen (%)		0.03
C:N ratio		0.10
Available P (mg P kg^{-1})		2.57
Exchangeable cations [cmol(+)kg^{-1} soil]	Ca	0.24
	Na	0.05
	Mg	0.07
	K	0.12
Soil texture (%)	Clay	26.78
	Silt	6.22
	Sand	66.99

Note: C:N ratio - carbon to nitrogen ratio; P - phosphorus; H_2O - water; Ca - calcium; Na - sodium; Mg - magnesium; K - potassium.

To assess the effects of different rates of PR application, we applied MPR Type B at the rates of 0 mg P kg^{-1} (control), 50 mg P kg^{-1}, 100 mg P kg^{-1}, 200 mg P kg^{-1} and 400 mg P kg^{-1} to the four month old oil palm seedlings (two genotypes) at an open field area. The treatments were arranged in a randomised complete block design (RCBD) with four replications for each. Meanwhile, to assess the effects of different types of PR application, we treated four different types of PR including control (0 mg P kg^{-1}) with PR at the rate of 100 mg P kg^{-1} per polythene bag. The PRs used were MPR (Type A, Type B, Type C), EPR and control (without PRs). The treatments were arranged in an RCBD with four replications.

After eight months, the plants were harvested, dried, ground, sieved using 1 mm sieve and analysed. The third leaf of each plant was used for plant nutrient analyses of P, potassium (K), Ca, and magnesium (Mg) levels. All plant samples were digested using the wet digestion method before further nutrient analysis. The plants' P was determined using the procedure described by Murphy and Riley (1962), with absorbance at 693 nm, while K, Ca and Mg were analysed using atomic absorption spectrophotometer (AAS).

Statistical Analysis

All the data collected during the study were recorded and analysed using General Linear Models (GLM) analysis by Statistical Analysis System (SAS 9.4) (SAS, 1985). Differences between means were separated using Duncan multiple range test (DMRT) at $P<0.05$ (Gomez and Gomez, 1980).

RESULTS AND DISCUSSION

Effects of Different Rates and Types of PR Application on Plant Total Dry Weight

The total dry weight of oil palm seedlings with different rates of MPR Type B is presented in *Figure 1*. The result shows that the minimum yield was obtained in the control for both oil palm seedling genotypes with a value of 195.1 g for Yangambi and 290.2 g for AVROS, respectively. The application of PR into the soil had a significant effect on total dry weight compared to the control ($P<0.0001$). However, no significant effect was observed between the oil palm seedlings with MPR Type B at the rates of 50, 100, 200 and 400 mg P kg^{-1}.

Generally, the application of PR improved the total dry weight of oil palm seedlings. Nevertheless, our study showed that the oil palm seedling genotype treatments had no statistically significant effects on total dry weight. This could be because of the characteristics and nature of PR, where PR are a slow-release fertiliser that require more time to be dissolved completely in soil.

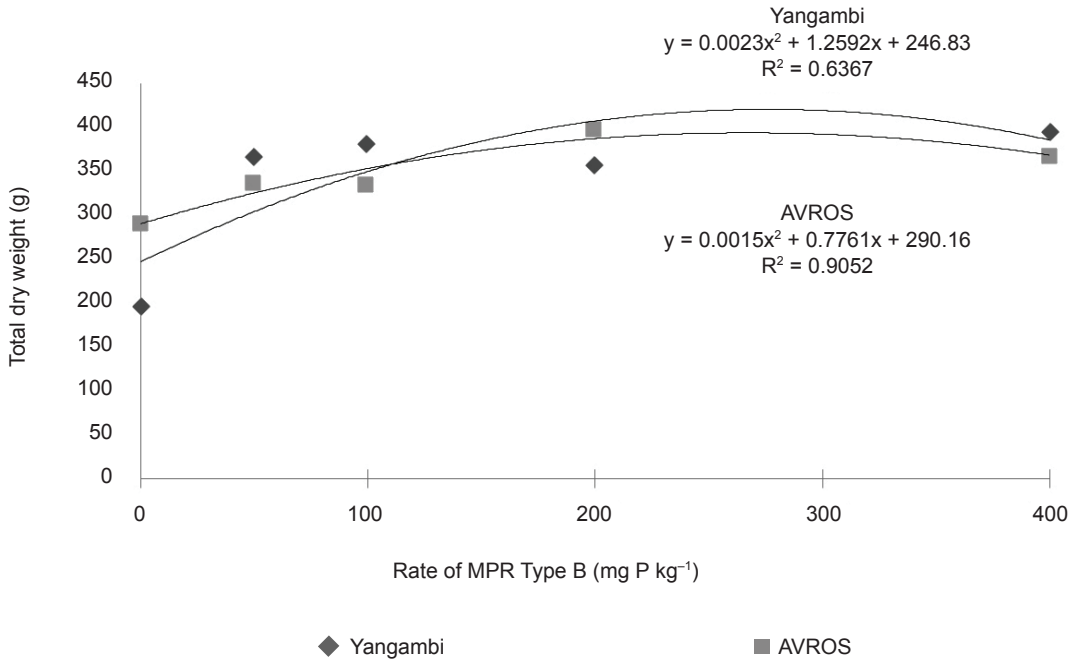


Figure 1. Effect of different rates MPR Type B application and oil palm seedlings genotypes on plant total dry weight.

Meanwhile, a significant interaction in dry weight was found between oil palm seedling genotypes and rates of PR application ($P = 0.0124$). *Avros* seedlings showed the highest value at the rate of 200 mg P kg^{-1} (397.1 g). Also, a significant interaction was found between oil palm seedling genotype and types of PR application ($P = 0.0458$), where the *Yangambi* seedling showed the highest value when applied with MPR Type A (490.5 g). Our results showed that different types and rates of PR application did not produce much difference in the total dry weight of oil palm seedlings, which agreed with the study done by Foong (1993) and Syahputra (1997) on oil palm seedlings. Additionally, the study found that there was not much difference between treatments in terms of total dry weight, regardless of the PR source. Thus, dry yield may not be a good parameter in assessing the effectiveness of P sources.

Effects of Different Rates and Types of PR Application on Plant P Concentration and P Uptake

This study found that both the rates and types of PR application influenced the P levels in oil palm leaves. There were significant differences found in the P concentration as affected by the rates of MPR Type B in both genotypes ($P<0.005$) (*Figure 2*). The least P concentration was in the control group (0.150% for Yangambi and 0.123% for AVROS), and the highest P concentration was in oil palm seedlings treated with MPR Type B at the rate of 400 mg P kg^{-1} for both oil palm seedlings (0.244% for Yangambi and 0.215% for AVROS). However, there was no significant difference found in the P concentration between oil palm seedlings with MPR Type B application at the rate of 100, 200 and 400 mg P kg^{-1} in both genotypes. Significant differences were also found in the P concentration as affected by the type of MPR in both genotypes ($P<0.005$) (*Figure 3*) where the highest P concentration was MPR Type B.

In terms of plant genotype, there were no significant differences found in P concentrations between different oil palm seedling genotypes used in this study. Both of the oil palm seedling genotypes showed a similar trend in P concentration. This result coincides with a study done by Tan *et al*. (2010) on different genotypes of oil palm seedlings treated with Gafsa PR, where the plant total dry weights and P accumulations did not give a clear estimation of the phosphate concentration in the oil palm seedlings.

As for the P uptake, there were significant differences for both genotypes at different rates of MPR Type B application (*Figure 4*). The least P uptake was found in the control group, while the highest P uptake was at the rate of 400 mg P kg^{-1} for both Yangambi and AVROS. However, there was no significant difference found at the rate of 100, 200 and 400 mg P kg^{-1}, which suggests 100 mg P kg^{-1} of MPR Type B as the optimum rate.

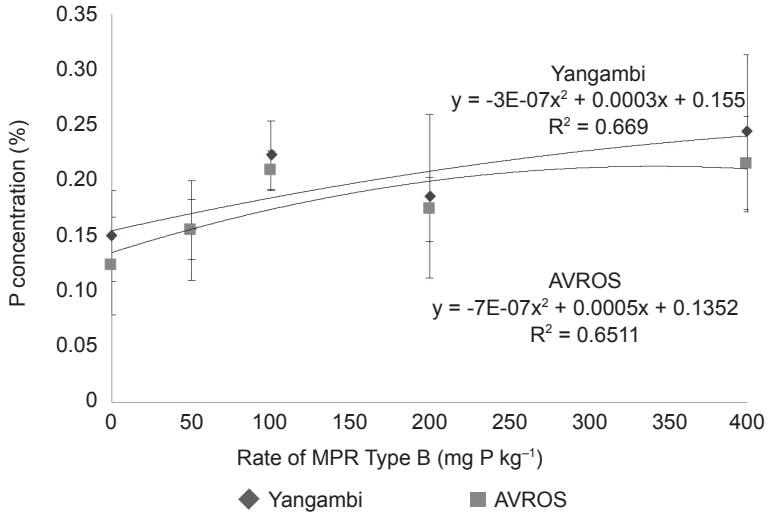
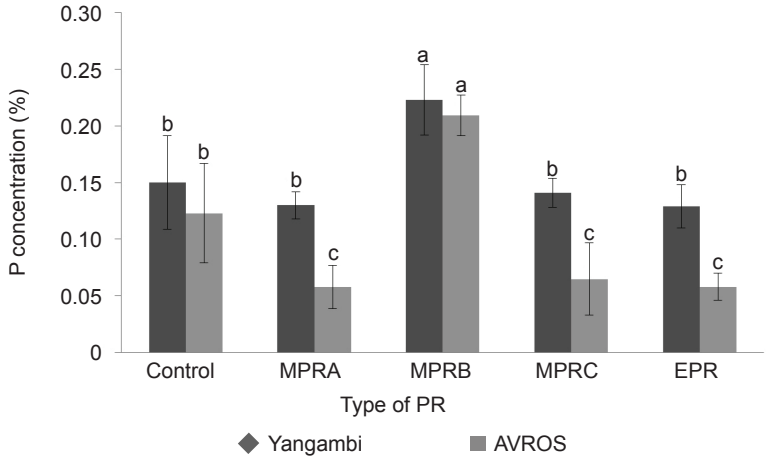


Figure 2. Effect of different rates of MPR Type B application on the P concentration of Yangambi and AVROS oil palm seedlings.



Note: **Mean values with the same letter are not significantly different using DMRT at *P*>0.05.

Figure 3. Effect of different types of PR application on the P concentration of Yangambi and AVROS oil palm seedlings.

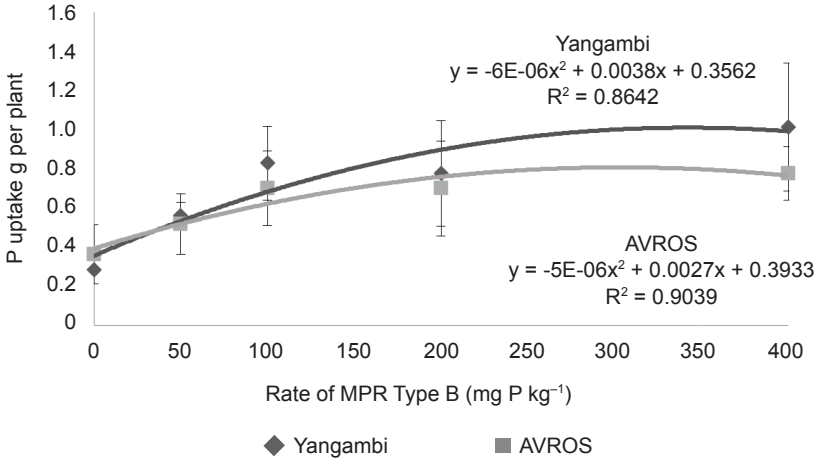


Figure 4. Effect of different rates of MPR Type B (mg P kg^{-1}) application on the P uptake g per plant of Yangambi and AVROS oil palm seedlings.

On the other hand, there were statistical differences in plant P uptake between the control group and different types of PR applications. This indicates that the application of PR into the soil does affect the P uptake in plants. MPR Type B showed the highest P uptake in both oil palm seedling genotypes compared to the others (*Figure 5*).

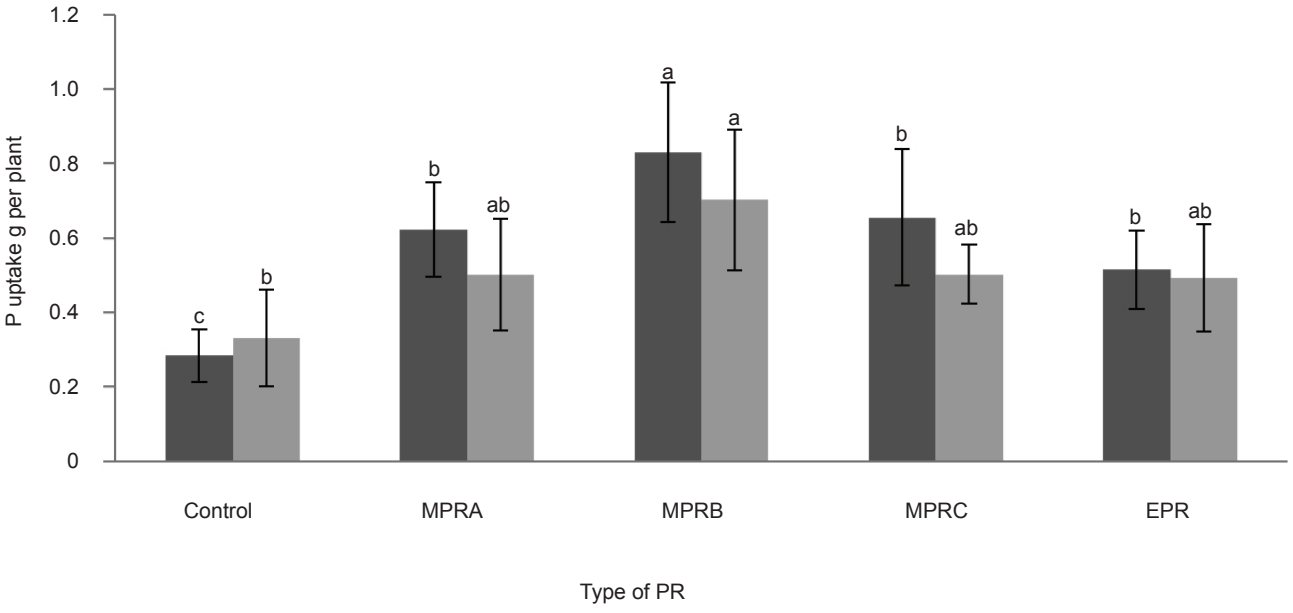
Based on the results above, MPR Type B at the rate of 100 mg P kg^{-1} is the optimum rate of PR application for both genotypes; it is sufficient to fulfil the plant's P requirement. However, in this study, the P uptake of the plant did not correspond to the solubility and P_2O_5 percentage of MPR. This can be attributed to MPR's similar solubility (around 10%) in 2% citric acid, which complies with SIRIM's (2015) requirement for direct application in soil. Thus, all MPRs are suitable for direct application. On the other hand, despite the similar percentage of P_2O_5 of the three types of MPR, XRD analysis showed that Type A, Type B and Type C contained Arrojadite, Cacoxenite and Lesukite respectively as their phosphate minerals, which may contribute to the different agronomic performance. Meanwhile, in comparison between different types of MPR (Type A, Type B and Type C) and EPR, the solubility of EPR is lower than MPR which corresponds to the lower P uptake in plants. This result aligned with a study done by Zaharah *et al.* (2014) on matured oil palm, where treatments with high soluble PR showed the highest P concentration compared to the treatment with less soluble PR.

Regression Analysis Between Rate of MPR Type B and Plant P Concentration and P Uptake

As there was no statistical difference found in plant genotypes, regression analysis was performed to establish the relationship between the effects of different rates of MPR Type B on plant P concentration and plant P uptake between Yangambi and AVROS oil palm seedlings as shown in *Figure 6* and *7* respectively. The increasing rate of PR significantly increased the plant P concentration [in both seedlings, Yangambi (R^2 = 0.6554; P<0.001) and AVROS (R^2 = 0.5559; P<0.001)] and plant P uptake [in both seedlings, Yangambi (R^2 = 0.7386; P<0.001) and AVROS (R^2 = 0.6768; P<0.001)], respectively. From the trend and regression equation, Yangambi seedlings were more responsive towards the rate of MPR Type B compared to the AVROS seedlings as the gradient of the linear line was higher than AVROS seedlings.

Effects of Different Rates and Types of PR Application on Plant Ca Concentration and Ca Uptake

The Ca concentration and Ca uptake in oil palm seedlings for all treatments showed low values. The highest Ca concentration recorded



Note: **Mean values with the same letter are not significantly different using DMRT at P>0.05.

Figure 5. Effect of different types of PR application on the P uptake g per plant of Yangambi and AVROS oil palm seedlings.

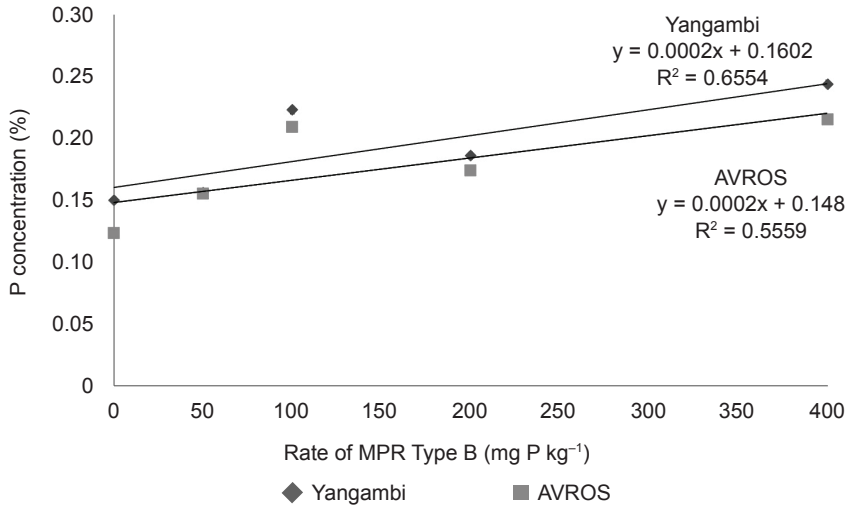


Figure 6. Regression analysis of plant P concentration on Yangambi and AVROS oil palm seedlings.

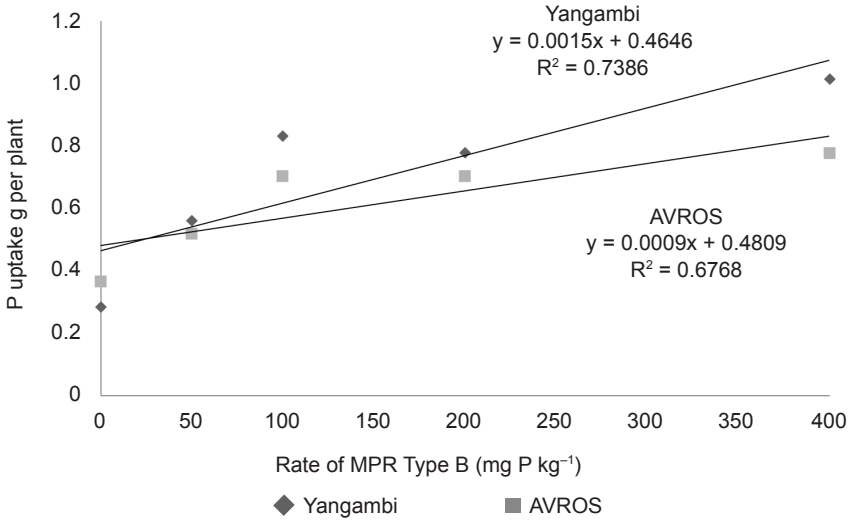


Figure 7. Regression analysis of plant P uptake g per plant on Yangambi and AVROS oil palm seedlings.

was just 0.043%, which is from the Yangambi oil palm seedling treated with 200 mg P kg^{-1} of MPR Type B. The Ca concentration in oil palm seedlings with different types of PR application also showed low values, where the highest value of Ca concentration recorded was 0.034%, in the Yangambi oil palm seedling treated with EPR. Meanwhile, the highest Ca uptake recorded was just 0.185 g in the Yangambi oil palm seedling treated with 200 mg P kg^{-1} of PR. The Ca uptake by oil palm seedlings with different types of PR applications also showed low values. The highest value of Ca uptake recorded was 0.162 g, which was obtained by Yangambi treated with EPR.

As Ca is a major constituent of PR, the release of Ca as affected by the PR application should be positively correlated to the P uptake of the plant (Zaharah *et al.*, 2014). There were positive correlations between P concentration and Ca concentration in the oil palm seedlings as affected by different rates of MPR Type B and types of PR (*Table 3*). However, all oil palm seedlings in this experiment showed low values of Ca concentration and suffered from Ca deficiency, thus suggesting that the Ca solubility in PR is low. Therefore, additional Ca application in other forms is required.

Despite the low values of Ca concentration obtained by the oil palm seedlings, application of

TABLE 3. CORRELATION COEFFICIENTS (IN BOLD) AND PROBABILITIES FOR PLANT CONCENTRATION IN OIL PALM SEEDLINGS AS AFFECTED BY DIFFERENT RATES OF MPR TYPE B APPLICATION

Parameters	P	K	Ca	Mg
P	1.00000			
K	**0.46478 (**0.1759)	1.00000		
Ca	**0.06610 (**0.8560)	**0.08054 (**0.8249)	1.00000	
Mg	**-0.07471 (**0.8375)	**0.72575 (**0.0175)	**-0.17152 (**0.6356)	1.00000

Note: P - phosphorus; K - potassium; Ca - calcium; Mg - magnesium.
Bold values: Pearson's correlation coefficients.

PR at different rates and types did increase the Ca concentration in the oil palm seedling considerably above the control. This corresponds to the study done by Zaharah *et al.* (2014) on matured oil palm, where the leaf Ca concentration increased with increasing PRs application rates in comparison to the control in both PR of Christmas Islands and Morocco origin. A study done by Dodor (2016) on maize crops also revealed the same trend where the application of African PR increased the Ca content in the crop.

Effects of Different Rates and Types of PR Application on Plant K and Mg Concentration

Based on statistical analysis, there were no significant differences in K and Mg leaf concentration in the oil palm seedlings for both rate and PR type treatments: K and Mg levels in foliar were constant among all treatments. This finding concurs with another study done by Zaharah *et al*. (2014) on peat soils and Charles *et al*. (1998) on Italian ryegrass. K concentration as affected by the different rates of MPR Type B showed a positive correlation (*Table 3*). Conversely, Mg showed a very small negative correlation (r = -0.07471, *P* = 0.8375) towards P. For different types of PR, the correlation coefficients were the same with the different rates of MPR Type B.

CONCLUSION

MPR was able to supply adequate P in soils for oil palm growth, thus suggesting that MPR is a viable source of P for direct application in Malaysian soils. However, PR from different locations may affect the agronomic effectiveness of the plant; MPR Type B was found to provide the highest levels of P for plant concentration as well as plant uptake. By taking regression analysis into account, our study showed that the Yangambi seedlings are more responsive to plant P concentration and P uptake compared to the AVROS seedlings.

ACKNOWLEDGEMENT

This research was funded under Trans-Disciplinary Research Grant Schemes by the Ministry of Higher Education Malaysia [grant number TRGS/1/2016/UPM/01/6/2] and OCP S.A.

REFERENCES

Augustine, D J; McNaughton, S J and Frank, D A (2003). Feedbacks between soil nutrients and large herbivores in a managed savanna ecosystem. *Ecol. Appl., 13(5)*: 1325-1337.

Bünemann, E K; Prusisz, B and Ehlers, K (2011). Characterization of phosphorus forms in soil microorganisms. *Phosphorus in Action: Biological Processes in Soil Phosphorus Cycling*. Springer Berlin, Heidelberg. p. 37-57.

Balemi, T and Negisho, K (2012). Management of soil phosphorus and plant adaptation mechanisms to phosphorus stress for sustainable crop production: A review. *J. Soil Sci. Plant Nutr., 12*: 574-562.

Basak, B B and Biswas, D R (2016). Potentiality of Indian rock phosphate as liming material in acid soil. *Geoderma, 263*: 104-109.

Chan, K W (1981). Phosphorus requirement of oil palm in Malaysia: Fifty years of experimental results. *Phosphorus and Potassium in the Tropics* (Pushparajah, E and Hamid Sharifuddin, H A eds.). The Malaysian Society of Soil Science, Kuala Lumpur. p. 395-436.

Charles, I S; Ando, T; Kouno, K and Nagaoka, T (1998). Residual effects of organic acid-treated phosphate rocks on some soil properties and phosphate availability. *Soil Sci. Plant Nutr., 44(4)*: 627-634. DOI: 10.1080/00380768.1998.10414486.

Chien, S H; Prochnow, L I; Tu, S and Snyder, C S (2011). Agronomic and environmental aspects of phosphate fertilizers varying in source and solubility: An update review. *Nutr. Cycl. Agroecosys., 89*: 229-255.

Chien, S N; Prochnow, L I and Mikkelsen, R (2010). Agronomic use of phosphate rock for direct application. *RAE, 75(50)*: 25.

Chien, S H; Sale, P W G and Hammond, L L (1990). Comparison of the effectiveness of phosphorus fertilizer products. *Proc. Symposium on Phosphorus Requirements for Sustainable Agriculture in Asia and Oceania*. International Rice Research Institute, Manila, Philippines. p. 143-156.

Chien, S H and Friesen, D K (1992). Phosphate rock for direct application. *Workshop on Future Directions for Agricultural Phosphorus Research*. TVA Bull. Y-224. Tennessee Valley Authority, Muscle Shoals, AL. p. 47-52.

Cordell, D (2010). *The Story of Phosphorus. Sustainability Implications of Global Phosphorusscarcity for Food Security.* Linköping University.

Corrêa, R M; Nascimento, C W A D; Souza, S K D S; Freire, F J and Silva, G B D (2005). Gafsa rock phosphate and triple superphosphate for dry matter production and P uptake by corn. *Scientia Agricola, 62(2)*: 159-164.

De Haes, H A U; Jansen, J; Van Der Weijden, L A and Smit, W J A L (2009). Phosphate - from surplus to shortage. *Policy memorandum of the Steering Committee for Technology Assessment. Utrecht: Ministry of Agriculture, Nature and Food Quality*.

Dodor, D E (2016). Relative agronomic effectiveness of some African rock phosphate fertilizers in an ultisol of Okinawa, Japan. *West Afr. J. Appl. Ecol., 24(2)*: 45-55.

Foong, S F (1993). Comparative efficacy of various PR on the growth of oil palm seedling using radio isotop and conventional technique. Paper presented at PORIM International Palm Oil Congress: Update and Vision. Hotel Istana Kuala Lumpur. 20-25 September 1993.

Foster, H L; Tarmizi, A M; Tayeb, M D and Zin, Z Z (1988). Oil palm yield responses to P fertiliser in Peninsular Malaysia. *PORIM Bull., 17*: 1-8.

Goh, K J; Chew, P S and Teo, C B (1994). Maximising and maintaining oil palm yields on commercial scale in Malaysia. *Proc. Inter. Planters Conf. on Management for Enhanced Profitability in Plantations, 1994*. Inc. Soc. Planters, Kuala Lumpur, Malaysia. p. 121-142.

Gomez, K A and Gomez, A A (1984). *Statistical Procedures for Agricultural Research*. John Wiley and Sons. 704 pp.

Hammond, L L; Chien, S H and Easterwood, G W (1986). Agronomic effectiveness of Bayovar phosphate rock in soil with induced phosphorus retention. *Soil Sci. Soc. Am. J., 50(6)*: 1601-1606.

Isenmila, A E; Omoti, U and Oviasogie, P O (2006). Development of alternative, cheap, easily available and affordable fertilizers from local rock minerals for the palms: The journey so far. *NIFOR Seminar*. p. 1-20.

Khasawneh, F E and Doll, E C (1978). The use of phosphate rock for direct application to soils. *Advances in Agronomy*. New York: Academic Press. p. 159-206.

Lin, I J and Schorr, M (1997). A challenge for the phosphate industry: Cd removal. *Phosphorus and potassium, (208)*: 27-32.

MPOB (2023). Oil palm planted area 2022. Available online: https://bepi.mpob.gov.my/images/area/2022/Area_summary2022.pdf. accessed on 31 January 2023.

Murphy, J and Riley, J P (1962). A modified single solution method for the determination of phosphate in natural waters. *Anal. Chim. Acta, 27*: 31-36.

Ng, S K (1986). Phosphorus nutrition and fertilisation of oil palm. *Oleagineux, 41*: 307-313.

Sale, P W and Mokwunye, A U (1993). Use of phosphate rocks in the tropics. *Fertilizer Research, 35*: 33-45.

SAS Institute (1985). SAS User's Guide: Statistics. SAS Institute.

SIRIM (1995). Method for the determination of phosphorus. *The Analysis of Fertilizers, Part 4*. Malaysian Bureau of Standards: Kuala Lumpur, Malaysia.

Smit, A L; Bindraban, P S; Schröder, J J; Conijn, J G and Van Der Meer, H G (2009). *Phosphorusin Agriculture: Global Resources Trends and Developments*. Wageningen, The Netherlands *(Plant Research International B.V)*. 42 pp.

Soil Survey Staff (1998). Keys to Soil Taxonomy. USDA - Natural Resources Conservation Service.

Steen, I (1998). Phosphorus availability in the 21st century: Management of a non-renewable resource. *Phosphorus and Potassium, 217*: 25-31.

Syahputra, M E (1997). *Comparative efficacy of various sources and rates of phosphate rocks to oil palm seedlings.* MSc Thesis, Universiti Putra Malaysia.

Tan, N P; Zaharah, A R; Akma, A S N and Jamaluddin, N (2010). Evaluating the variability of Gafsa phosphate rock uptake by oil palm genotypes at nursery stage. *Pertanika J. Trop. Agric. Sci., 33(2)*: 223-231.

Tan, N P; Wong, M K; Yusuyin, Y; Abdu, A B; Iwasaki, K and Tanaka, S (2015). Distribution of soil phosphorus fractions influenced by chemical fertilizer application and frond heaping practices in an oil palm plantation in Pahang, Peninsular Malaysia. *Pedologist, 59(1)*: 12-24.

USGS (2011). *Mineral Commodity Summaries 2011*. U.S. Geological Survey, U.S. Department of the Interior.

Vaccari, D A (2009). Phosphorus: A looming crisis. *Scientific American, 300*: 54-59.

Van Kauwenbergh, S J (2010). World phosphate rock reserves and resources. *International Fertilizer Development Center (IFDC).*

Van Straaten, P (2002). *Rocks for Crops: Agrominerals of Sub-Saharan Africa*. ICRAF, Nairobi.

Van Straaten, P (2006). Farming with rocks and minerals: Challenges and opportunities. *An Acad. Bras. Ci^enc., 78*: 731-747.

Van Vuuren, D P; Bouwman, A F and Beusen, A H W (2010). Phosphorus demand for the 1970-2100 period: A scenario analysis of resource depletion. *Glob. Environ. Change, 20*: 428-439.

Zaharah, A R; Zulkifli, H and Sharifuddin, H A H (1996). Evaluating the efficacy of various phosphate fertiliser sources for oil palm seedlings. *Nutr. Cycl. Agroecosystems, 47*: 93-98.

Zaharah, A R; Gikonyo, E W; Silek, B; Goh, K J and Amin, S (2014). Evaluation of phosphate rock sources and rate of application on oil palm yield grown on peat soils of Sarawak, Malaysia. *J. Agronomy, 13(1)*: 12-22.

Zin, Z Z; Foong, S F; Jamaludin, N; Lee, C T; Hamdan, A B; Tarmizi, A M and Khalid, H (2001). Evaluation of various sources of phosphate fertilizer for mature oil palm in Peninsular Malaysia. *Proc. of the 2001 PIPOC International Palm Oil Congress, Agriculture Conference.* Kuala Lumpur, Malaysia, 20-22 August 2001. MPOB, Bangi. p. 272-281.

Journal of Oil Palm Research Vol. 36 (4) December 2024 p. 650-663
DOI: https://doi.org/10.21894/jopr.2023.0054

PALM KERNEL MEAL ACTIVATED CARBON VIA GLASS WOOL-PYROLYSIS METHOD FOR CEFTRIAXONE ADSORPTION

ACHMAD GUS FAHMI[1]; ZAENAL ABIDIN[2]*; CECEP KUSMANA[3] and ERLIZA NOOR[4]

ABSTRACT

Antibiotic residues are a primary environmental concern because they are difficult to remove, including in wastewater treatment plants. A one-pot glass wool-pyrolysis method was developed and utilised to convert palm kernel meal (PKM) into activated carbon from palm kernel meal (AC-PKM) over process temperatures 750°C for 5 hr as an adsorbent for antibiotic residues. Physicochemical properties, semi-quantitative specific surface area, surface functional group profiles, and scanning electron microscopy (SEM) were evaluated. The physicochemical properties of AC-PKM meet the standards set by SNI 06-3730-1995 with a semi-quantitative specific surface area of 751 m^2 g^{-1}. Fourier transform infrared (FTIR) analysis shows that the active functional groups are scattered on the surface of AC-PKM. The maximum adsorption capacity is 82.64 mg g^{-1} adsorbent and can be explained by the Langmuir isotherm and pseudo-second-order type I kinetic model. The thermodynamic investigation showed that the adsorption process is a spontaneous endothermic reaction. The AC-PKM can remove 26% ceftriaxone (as a model residue antibiotic) for 2 hr of contact at a neutral pH at room temperature. The results show great promise of the one-pot glass wool-pyrolysis method to produce desirable activated carbon for removing ceftriaxone (CFT) application and an alternative treatment for the reuse of palm kernel meal waste.

Keywords: adsorption, ceftriaxone, glass wool, palm kernel meal, pyrolysis.

Received: 21 July 2022; **Accepted:** 14 August 2023; **Published online:** 26 October 2023.

INTRODUCTION

Antibiotics are drugs used to treat bacterial infections. There is no doubt about the benefits of using antibiotics. However, if used excessively or not according to indications, it will lead to strains of bacteria resistant to antibiotics. Repeated and irrational use of the same antibiotic can increase microbial resistance to that antibiotic (Olesen *et al*., 2018). Its increasing use in COVID-19 pandemic and antimicrobial resistance is a severe threat to public health that is experienced globally (Browne *et al*., 2021). Previous studies have explained that excessive use of antibiotics can lead to other diseases, such as diabetes mellitus (Mensah and Ansah, 2016) and cancer (Prajwal *et al*., 2017). The results of research conducted by Widayati *et al*. (2011) showed that antibiotic abuse does not only occur in health facilities but also in the community. Antibiotics are also used in livestock and fisheries, so antibiotic residues are considered persistent micropollutants in the aquatic environment.

Among various antibiotics, ceftriaxone (CFT) is the most common group in production and use in Indonesia because it has antimicrobial activity against various bacterial pathogens (Ayele *et al*., 2018). However, the CFT residue will enter the hospital wastewater treatment plant, which harms the aquatic environment and can hinder

[1] Graduate School of Natural Resources and Environmental Management Science, IPB University, 16127 Bogor, Indonesia.

[2] Department of Chemistry, Faculty of Mathematics and Natural Science, IPB University, 16680 Bogor, Indonesia.

[3] Department of Silviculture, Faculty of Forest and Environment, IPB University, 16680 Bogor, Indonesia.

[4] Department of Agro-Industrial Engineering, Faculty of Agriculture Engineering, IPB University, 16680 Bogor, Indonesia.

* *Corresponding author e-mail: abidinzed@apps.ipb.ac.id*

the progress of water treatment processes that use microbes. In addition, irrational use can lead to increased resistance to microorganisms and become a significant public health crisis (Al-Riyami *et al*., 2018). Therefore, efforts are needed to remove CFT residues from water so they are not harmful to the environment.

In recent years, various techniques have been investigated for the removal of CFTs from wastewater, including photocatalytic treatment, oxidation degradation (Kordestani *et al*., 2020), ultrasonic wave degradation (Shi *et al*., 2020), adsorption (Mahmoud *et al*., 2020), bio-electrochemical degradation (Hassan *et al*., 2021) and biological treatment (Bozorginia *et al*., 2021). Among these techniques, adsorption has been considered one of the most prospective approaches in the future because of its attractive advantages for the application of drug waste management in wastewater (de Ilurdoz *et al*., 2022). Several alternative adsorbents to overcome this problem are kaolin, bentonite (Song *et al*., 2019), polymer resins (Rivas *et al*., 2020), metal-organic framework (MOF) (Zango *et al*., 2020) and activated carbon (Schultz *et al*., 2020).

Important factors that constrain the selection and use of adsorbents are raw material availability, adsorption effectiveness, manufacturing method and production price. The challenges for raw material availability are overcome by using alternative raw materials derived from waste or recycling. In contrast, adsorption effectiveness, manufacturing methods and production prices are overcome by modifying production methods to produce adsorbents that have large surface areas, are easy, simple, and do not require expensive costs in manufacturing. One of the most widely used adsorbents, activated carbon, is the best alternative that can be chosen. Activated carbon (AC) can be produced from waste and has sustainable and environmentally friendly properties (Sharma *et al*., 2020). This potential can be an opportunity for tropical countries such as Indonesia because it fulfils promising aspects for providing such activated carbon adsorbents. However, even poorly managed biomass can cause serious environmental problems.

As one of the most widely used adsorbents, activated carbon is also considered a reliable solution for CFT removal due to its good performance (Schultz *et al*., 2020). On the other hand, activated carbon from palm fibres have a good adsorption capacity (57.47 mg g^{-1} adsorbent) in removing antibiotic residues in water (Acelas *et al*., 2021). One of the palm oil wastes that can be converted into activated carbon is palm kernel meal (PKM). PKM is a solid by-product of palm kernel oil extraction. Oil palm biomass waste from empty fruit bunches, core meat, shells, and a mixture of them, has been widely used as activated carbon as an adsorbent of organic compounds (Ukanwa *et al*., 2020). Rugayah *et al*. (2014) used steam activation at high temperatures to make activated carbon from palm shells. This condition produces activated carbon with an adsorption capacity of 80.7% or 8.83 mg g^{-1} compared to commercial activated carbon. However, the continuous high-temperature steam method causes the production cost to increase. According to Osman *et al*. (2016), the one-step physical activation method can reduce production costs. The single-step physical activation method has a surface area of 523 m^2 g^{-1} with an organic compound adsorption capacity of 13-38 mmol g^{-1} adsorbent (Fahmi *et al*., 2019). In addition, modification of glass wool in the process of making activated carbon has the benefit of increasing the percentage yield, reducing the amount of ash formed and providing activated carbon with surface functional groups maintained (Fahmi *et al*., 2022). However, applying activated carbon products from PKM with physical activation has not been widely used to remove antibiotic waste in water. Therefore, this study discusses the properties of activated carbon from palm kernel meal (AC-PKM) by the one-pot glass wool pyrolysis method developed by Fahmi *et al*. (2019) and relevant factors for CFT removal in wastewater.

MATERIALS AND METHODS

Materials

Granule PKM waste was collected at a palm oil plant in South Kalimantan, Indonesia. All the chemicals used were obtained from Sigma-Aldrich®, while the commercially activated carbon used as control (ACC) was purchased from a chemical store in Bogor. The antibiotics model used in all the experiments was CFT, a sodium salt. The structure of CFT is given in *Figure 1*.

Procedures

Sample preparation. Waste PKM was collected from the oil palm industry in South Kalimantan. To remove contaminants, the sample was washed with distilled water before drying in the oven for 24 hr at 105°C. The dried materials were cut into small pieces and ground to 100 mesh using fibre grinder (Model 4 Wiley Mill Machine, Thomas Scientific, USA) at 5000-6000 rpm. Synthesis of AC-PKM followed the modified method by Fahmi *et al*. (2019). A total of 5 g of PKM powder was added in crucible porcelain-coated glass wool all around. Then the porcelain crucible was heated at 750°C in a *47900 Thermocline furnace* (Barnstead International, USA) for 5 hr. This process took 3 hr for carbonisation and 2 hr for physical activation

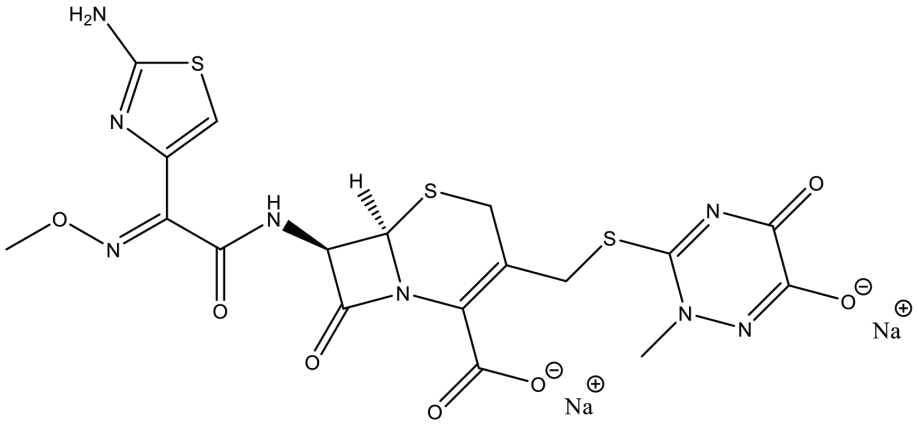


Figure 1. Structure of sodium ceftriaxone.

with characteristics of activated carbon showed in Fahmi *et al.* (2022). It was then cooled naturally to room temperature.

Characterisation of activated carbon. Physico-chemical properties of AC-PKM, PKM, and ACC (as a control), such as pH, ash content and moisture content, were determined using standard methods for activated carbon. The pH value of activated carbon was determined according to American Standard Testing Method (ASTM) D3838-5 with 1 g of sample added to 100 mL of distilled water in a 250 mL beaker. After stirring continuously for 10 min, the activated carbon was filtered, and the filtrate solution acidity was determined using a pH metre. The ash content of activated carbon was determined using the ASTM D2866-96 method. Moisture content was determined using the oven drying method as described in ASTM D2867-09. The specific surface area of activated carbon was calculated using semi-quantitative measurements (Okeola *et al*., 2012). Surface functional groups were identified using Spectrum One Fourier transform infrared (FTIR) (Perkin-Elmer, USA). The morphology of AC-PKM was identified using a scanning electron microscope (JEOL JSM-IT 300, Tokyo, Japan). All chemical ingredients were obtained from Sigma-Aldrich®.

Adsorption of CFT. CFT was employed as an antibiotic model because this drug is often used in hospital therapy. In evaluating the stability of CFT under acidic, alkaline, and heat conditions, the CFT solution (25 mg L^{-1}) was treated with acid at pH 1, alkaline at pH 13, and temperature at 40°C (313 K). After being stored for 24 hr, the CFT solution was scanned using a Genesys 10S Ultraviolet visible (UV-Vis) spectrophotometer (Thermo Fischer Scientific, USA) at 200-400 nm wavelength to identify degradation or peak shift. Adsorption was carried out at pH neutral with the batch method for 24 hr at 25°C (298 K). A total of 10 mL of CFT solution with a concentration of 25-1000 mg L^{-1} was added to a tube containing AC-PKM sample as much as 0.01 g. After equilibrium, the adsorbent was separated under centrifugation, and the concentration of CFT on the supernatant was measured using Genesys 10S UV-Vis spectrophotometer (Thermo Fischer Scientific, USA) at the maximum wavelength (274 nm). The adsorption capacity followed Equation (1).

$$q_e = \frac{(C_o\text{-}C_e) \times V}{(m \times 1000)}. \quad (1)$$

where q_e is adsorption capacity (mg g^{-1} adsorbent), V is the volume of solution (mL), C_o is the initial concentration of CFT (mg L^{-1}), C_e is the residual concentration of CFT (mg L^{-1}), and m is mass of adsorbent (g). Mathematical representation from the isotherm adsorption model was used to interpret CFT adsorption on the surface adsorbent, and its calculation refers to Langmuir and Freundlich isotherm model. The Langmuir isotherm model in its nonlinear form is expressed as in Equation (2) (Jasper *et al.*, 2020).

$$q_e = \frac{q_{max} K_L C_e}{1 + K_L C_e} \quad (2)$$

where, q_e being adsorption capacity equilibrium of the adsorbent (mg g^{-1} adsorbent), C_e being the residual concentration (mg L^{-1}), q_{max} being adsorption maximum in Langmuir model (mg g^{-1} adsorbent), K_L being Langmuir's constant (L mg^{-1}) that represents affinity side active bond. The Freundlich isotherm model in nonlinear form is expressed as in Equation (3) (Jasper *et al.*, 2020).

$$q_e = K_f C_e^{\frac{1}{n}} \quad (3)$$

where, q_e as adsorption capacity equilibrium (mg g^{-1} adsorbent), C_e is the residual concentration (mg L^{-1}), K_f (mg g^{-1}) (L $mg^{-1})^{(1/n)}$, and $1/n$ is Freundlich

constant denoting capacity adsorption and intensity adsorption. The process was solely based on C_e measurements. Following the statistical premise, Cassol *et al*. (2014) state that the method is more trustworthy and must be used to estimate the adsorption equilibrium parameters.

Kinetic and thermodynamic models. The method for analysing the adsorption kinetics was carried out with the same experiment as the adsorption measurement. The treatment was repeated by measuring the supernatant at different contact times (0-180 min). In addition, the effect of temperature on the adsorption process of CFT on AC-PKM was studied by varying the adsorption temperature at 30°C (303 K) until 40°C (313 K).

Removal of CFT. CFT removal was carried out at a CFT concentration of 250 mg L^{-1} as artificial wastes. The quantity of CFT removal (%R) by AC-PKM was calculated as follows [Equation (4)].

$$\%R = \frac{V\,(C_O - C_e)}{C_O} \times 100 \quad (4)$$

where $\%R$ is percentage removal CFT (%), V is volume of solution (mL), C_o is initial concentration of CFT (mg L^{-1}), and C_e is the residual concentration of CFT (mg L^{-1}).

RESULTS AND DISCUSSION

Adsorbent Characteristics

Generally, activated carbon is synthesised at temperatures of 700°C-1000°C. In high-temperature condition, some of the carbon loses various functional groups on its surface and convert to ash. The presence of this surface functional group is significant because it plays a role in chemical processes for adsorption and catalysis. Xiao *et al*. (2018) used a unique pyrolysis process to retain functional groups on the surface, and this method can increase specific surface area, porosity, and absorptivity. Thus, maintaining functional groups on the surface of activated carbon has benefits in utilising the activated carbon.

This study concentrated on the physical activation approach using glass wool as a material that can isolate heat and reduce oxygen during the activation process. Furthermore, adding glass wool to coat the reactor can cause the heat generated to be concentrated in the reactor core, making the pyrolysis process more efficient (Santhiarsa, 2021). Our previous experiment used the glass wool pyrolysis method for coconut shell waste samples, effectively conducted at 750°C to produce activated carbon with large surface functional groups. This method can also increase biomass conversion into activated carbon (Fahmi *et al*., 2019). In addition, the modification of glass wool in the process of making activated carbon has the benefit of increasing the percentage yield, reducing the amount of ash formed, and providing activated carbon with surface functional groups maintained (Fahmi *et al*., 2022). Therefore, in this study, we used the similar method with different biomass effluents to apply ceftriaxone removal in hospital wastewater.

The physicochemical properties of the activated carbon are presented in *Table 1*. Based on the measurement results, it is shown that the pH values of AC-PKM and ACC were found to be in proximity of neutral pH, namely 6.80 and 6.98, respectively. Generally, the acceptable pH range is 6.00-8.00 for applications in wastewater treatment (Ashtaputrey and Ashtaputrey, 2016). The presence of surface-active functional groups can affect the surface charge of the adsorbent (variable charge), which will affect the adsorption ability. Therefore, the pH value is crucial for adsorbents with surface-active functional groups to achieve the most excellent application performance.

TABLE 1. PHYSICOCHEMICAL PROPERTIES OF AC-PKM COMPARED WITH COMMERCIAL ACTIVATED CARBON (ACC) AND BIOMASS (PKM)

Parameter	AC-PKM	ACC	PKM
pH	6.80 ± 0.2	6.98 ± 0.2	-
Ash content (%)	5.10 ± 1.0	3.10 ± 1.0	5.15 ± 1.0
Moisture content (%)	4.94 ± 1.0	3.94 ± 1.0	14.94 ± 1.0
Specific surface area ($m^2\ g^{-1}$)	751 ± 10	783 ± 10	407 ± 10

Another physicochemical property is ash content. Based on the measurement, the ash content of AC-PKM and PKM had the same values, which were 5.10% and 5.15%, respectively, while ACC has a lower ash content value of 3.10%. Ash content can affect the activated carbon quality, with the maximum in activated carbon being 15.00% (SNI 06-3730-1995). High ash content can reduce the absorption and specific surface area (De Gisi *et al*., 2016). In addition, the selection of biomass raw materials also affects the ash content in activated carbon. Low ash-content biomass has the potential as an excellent raw material for the manufacture of activated carbon (Feng *et al*., 2020).

Furthermore, AC-PKM has a relatively low water moisture of 4.94%, with the accepted standard value for activated carbon samples of 3.00%-6.00% (Gumus and Okpeku, 2015). In addition, the high water moisture in activated carbon will dilute the adsorbent concentration, thus requiring more weight of the adsorbent to maintain the same adsorption capacity. Furthermore, the water moisture decreases with the carbonisation temperature due to the

smaller pores of the activated carbon. The high water moisture is usually caused by the concentration of activator in chemical activation (Maulina *et al*., 2020). Ultimately, this phenomenon will increase the hygroscopic properties of absorbing water from the air (Tani *et al*., 2014). Hence, the selection of activator compounds and activation methods have an essential role in influencing the characteristics of the water moisture in activated carbon.

Based on the written reports, the value of X_m was used to calculate the specific surface area of monolayer coverage (Okeola *et al*., 2012). The specific surface area of AC-PKM is 751 m^2 g^{-1}, slightly lower than that of ACC (783 m^2 g^{-1}). According to Hu and Gao (2018), a high surface area can increase the adsorbability so that it will affect the adsorption capacity of the adsorbent. In addition, another factor that affects the adsorption ability is the surface interaction of the adsorbent with the adsorbate, which is predicted through the adsorption isotherm model (Wu *et al*., 2020). Activated carbon has various pores, so further analysis is needed to show the presence of macropores, mesopores and micropores.

In addition, the adsorption performance of carbon-based adsorbents is highly dependent on the surface-active functional groups (Kharrazi *et al*., 2021). In this study, the various surface-active functional groups of AC-PKM, ACC, and PKM was identified using FTIR spectroscopy (*Figure* 2). The AC-PKM and PKM show a broad spectrum around 3445 cm^{-1} and 600 cm^{-1} with different intensities and shapes of the spectra. Meanwhile, the ACC found that the peak loss was at the wavenumber at 3445 cm^{-1}, which is a stretch of O-H and 600 cm^{-1} from the =C-H bending of the aromatic ring. Another FTIR spectrum of ACC differed in intensity from the spectrum of AC-PKM and PKM. The C=O (1500-1650 cm^{-1}) and C-O (1000-1050 cm^{-1}) stretches had low intensity in the spectrum of ACC, and the CC (2366 cm^{-1}) stretch band was weak. However, the similarity of the spectrum of AC-PKM with the initial biomass (PKM) is identical, which indicates that there are similar functional groups. Thus, the glass wool-pyrolysis method can maintain the intensity of the spectrum compared to ACC, where the spectrum is significantly weakened or even disappears.

Based on the spectrum data analysed for each adsorbent produced, it can be seen that AC-PKM has a peak in the FTIR spectrum in the form of some active surface groups. Therefore, the morphology of AC-PKM was confirmed using Scanning Electron Microscope (SEM). The identification results using SEM showed that on the surface of the AC-PKM pore, there was an unshaped bulk solid. In addition, these unshaped bulk solids can also reduce the pore size but provide interaction with the adsorbate adsorbed. As for ACC, there are no such shapeless bulk solids, which corroborates the statement of the presence of functional groups on the AC-PKM pore surface (*Figure 3*).

CFT stability experiments showed that CFT has high stability in heat treatment because there was no significant change (24 hr, 40°C) (*Figure 4*). Roca *et al*. (2011) suggest that β-lactam antibiotics such as CFT will undergo thermal decomposition gradually at a temperature of 60°C-100°C following pseudo-first-order kinetics. Meanwhile, at room temperature (23 ± 2°C), structurally, CFT is very stable for up to four days (De Diego *et al*., 2010). However, in the acid-base treatment, there were (hyperchromic and bathochromic) shifts in the peak of the CFT, which indicated that it was unstable (*Figure 4*). This condition is caused by the side reactions, such as hydrolysis, and side functional groups, such as

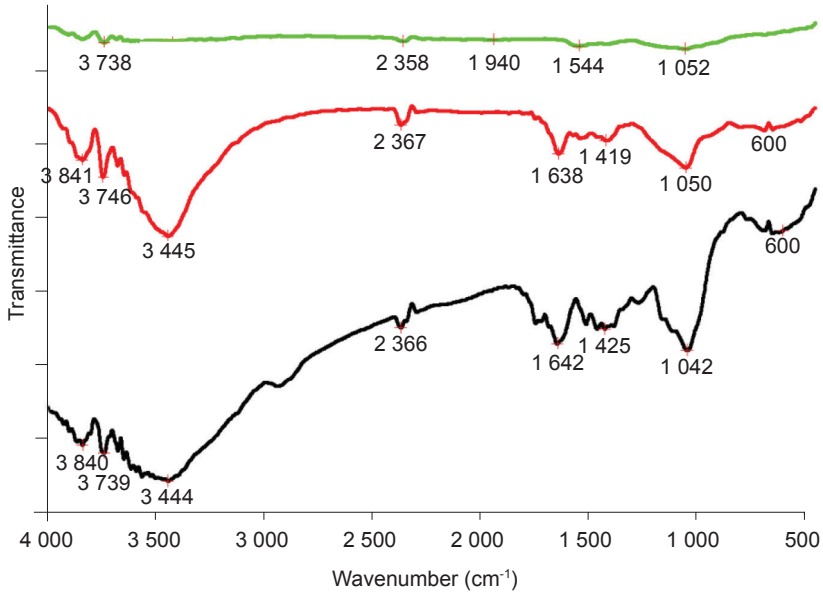


Figure 2. The infrared spectrum of ACC (green line), AC-PKM (red line) and PKM (black line).

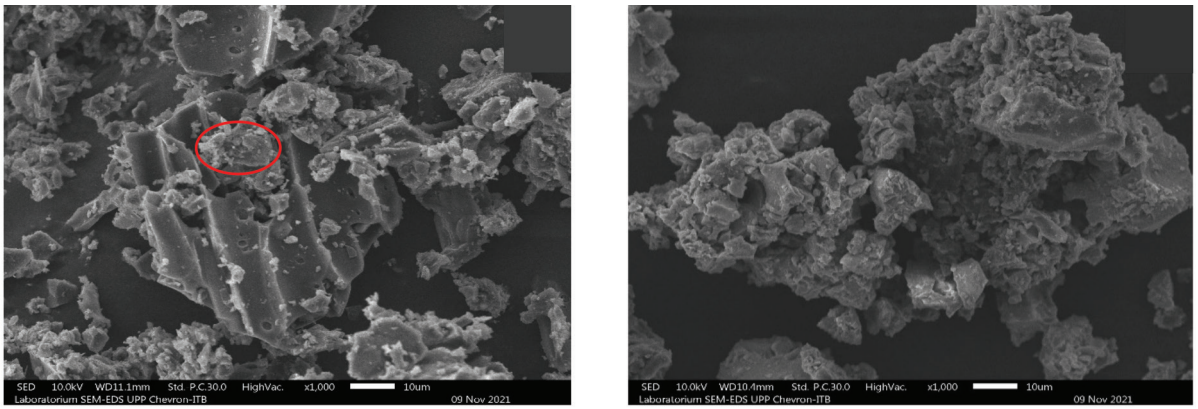


Figure 3. Scanning electron microscope photograph of (a) AC-PKM, and (b) ACC.

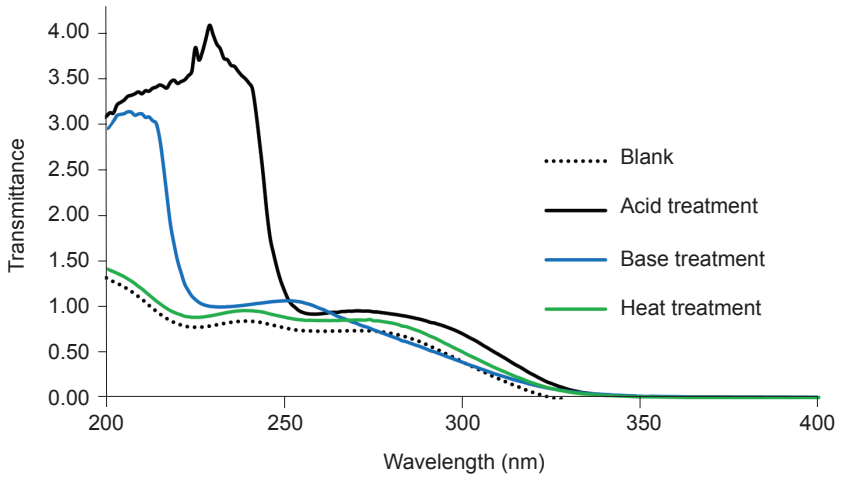


Figure 4. UV spectrum of CFT in 200-400 nm with various treatments (acid, base and heat).

amines and carboxyls, that affect the structural changes of CFT (Alekseev, 2010). Based on these results, adsorption measurements were carried out under neutral conditions according to the pH of the activated carbon and CFT.

CFT Adsorption

Sorption processes are well described by isotherms whose purpose is to help elucidate the interaction between sorbate and sorbent. They also provide information on the affinity of the sorbent for the sorbate. In this study, the Langmuir and Freundlich isotherm models were applied to observe the sorption of CFT onto the AC-PKM. All three adsorbents (ACC, AC-PKM and PKM) followed the Langmuir adsorption isotherm, consistent with the statistical premise with non-linear evaluation (*Figure 5*).

The isotherm models shown in *Table 2* follow the Langmuir model for all three adsorbent types ACC, AC-PKM, and PKM. The linearity (R^2) of the Langmuir adsorption isotherm model for ACC, AC-PKM, and PKM significantly differed from the linearity (R^2) of the Freundlich adsorption isotherm model. According to Cassol *et al*. (2014), this method is more reliable and should be used to determine adsorption equilibrium parameters. This isotherm model is routinely used to explore the adsorption characteristics of an adsorbent (Karri *et al*., 2017). As for the two adsorption isotherm models, they have differences from the adsorption mechanism that occurs with various assumptions in each model. The Freundlich isotherm model predicts sites that do not interact with heterogeneous surfaces and exponential adsorption. In contrast, the Langmuir model predicts sites that interact with the heterogeneous surface and exponential adsorption.

TABLE 2. LANGMUIR AND FREUNDLICH ADSORPTION ISOTHERM MODEL CONSTANTS

Adsorbent	Langmuir			Freundlich		
	qm	b	R^2	Kf	n	R^2
PKM	24.86	0.033	0.9891	20.19	44.05	0.1572
AC-PKM	82.64	0.037	0.9982	14.56	3.71	0.9162
ACC	153.85	0.029	0.9988	16.64	2.75	0.9091

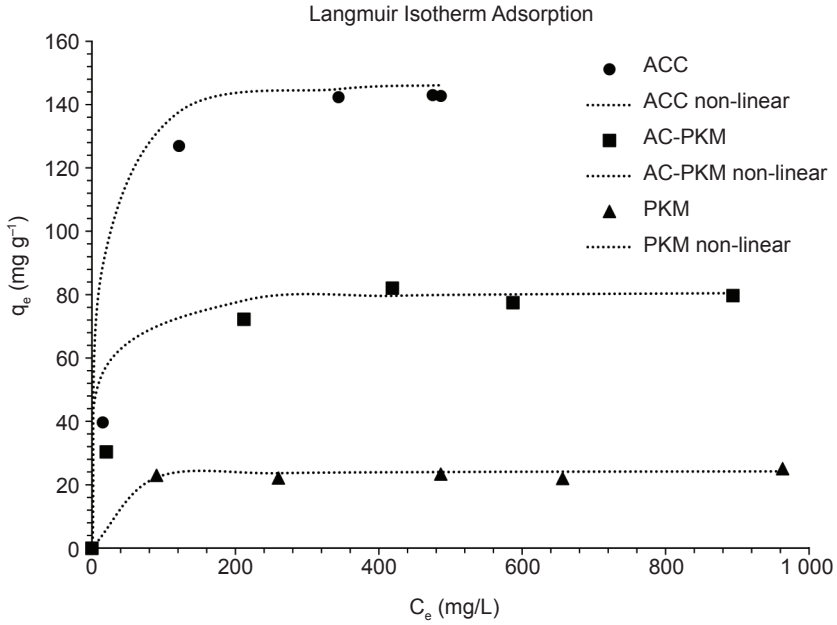


Figure 5. Nonlinear the Langmuir isotherm model fittings for CFT adsorption onto ACC, AC-PKM and PKM at room temperature.

The maximum adsorption capacity of each sample was determined by calculating the Langmuir adsorption isotherm (*Figure 5*). The maximum adsorption capacity value of PKM is 24.86 mg g^{-1} adsorbent was the lowest when compared to AC-PKM (82.64 mg g^{-1} adsorbent), and ACC (153.85 mg g^{-1} adsorbent). The activated carbon adsorption mechanism generally utilises wide pores or follows the Freundlich adsorption isotherm model (Ayawei *et al*., 2017). However, the presence of surface functional groups can affect the adsorption capacity. CFT adsorption in water was carried out at neutral pH, so the anionic CFTs dominated. However, the negatively charged surface of AC-PKM electrostatically repels the incoming CFT anions and affects their absorption. Furthermore, competition of hydroxyl (-OH) functional groups for the active binding site on AC-PKM with CFT anions may contribute to the markedly perceived decrease in adsorption rates (Saied *et al*., 2022). Therefore, the adsorption capacity will decrease as the surface functional groups increase. The maximum monolayer adsorption capacity (q_{max}) was 82.64 mg g^{-1} adsorbent, comparable to values reported for CFT adsorption with several adsorbents (*Table 3*).

The dependence of pH on CFT stability (*Figure 4*) implies that the removal of CFTs under neutral conditions cannot be ascribed to electrostatic interactions. This is because the CFT used as a drug is a sodium salt compound easily soluble in water with a pH of around 6.7 (Khan *et al*., 2017). In addition, the crystal structure of CFT has many OH---O hydrogen bonds involving water molecules and an ionised portion of the anion (Gonzalez *et al*., 2020), so it will produce a high electrostatic repulsion force with the surface-active group of activated carbon, which is also negatively charged. The electrostatic repulsion between AC-PKM and CFT can reduce the adsorption capacity of AC-PKM compared to commercial activated carbon (ACC).

TABLE 3. COMPARISON OF MAXIMUM ADSORPTION CAPACITY OF CFT USING SAVERAL ADSORBENTS

Adsorbent	q_{max} (mg g^{-1} adsorbent)	References
Activated carbon-Fe_2O_3	28.930	Badi *et al.* (2018)
ZVI/$SrFe_{12}O_{19}$	8.084	Amiri *et al.* (2020)
NBent-$NTiO_2$-Chit nanocomposite	90.910	Mahmoud *et al.* (2020)
Bi_2WO_6/g-C_3N_4 photocatalyst	3.400	Zhao *et al.* (2018)
ACC	153.850	Present study
AC-PKM	82.640	Present study

The interactions that may form so AC-PKM can adsorb CFT are non-electrostatic interactions such as H-bonds, -π interactions, *n*-π electron donor-acceptor interactions, and hydrophobic-hydrophobic interactions (Saied *et al*., 2022). Although there is a possible interaction between CFTs with π-π bonds in the activated carbon pores (*Figure 6*). Hydrogen bonds occur between the hydroxyl functional groups on the activated carbon surface and *S*, *N*, and *O* atoms in the CFT structure (C-OH---S, C-OH---N, and C-OH---O). Gonzales *et al*. (2020) report that hydroxyl molecules act as donors for ionised carboxylates and carbonyls. In addition, there are also intramolecular hydrogen

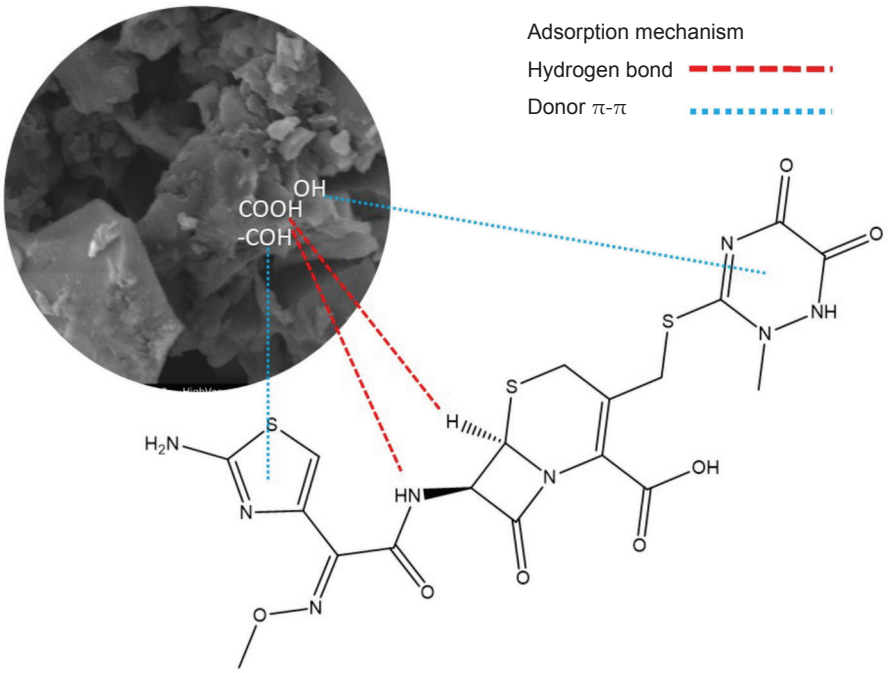


Figure 6. Proposed adsorption mechanism of ceftriaxone as a model antibiotics residue in this study to activated carbon from PKM.

bonds C13-H48-C10 with the carbon of the ionised carboxyl group. Another interaction that may occur in this adsorption process is between the carbonyls found on the activated carbon surface and triazine (aromatic) in the CFT structure. The *n*-π electron donor-acceptor interaction occurs when the carbonyl donates a lone pair of electrons (*n*), and the triazine accepts electrons in its system structure. According to Biasutti *et al*. (1992), nitrogen-substituted benzene, such as triazine, is an acceptor in the *n*-π electron donor-acceptor interaction. Therefore, the adsorption mechanism can be illustrated in *Figure 6*.

Kinetics and Thermodynamics Model of CFT Adsorption

Experiments to obtain CFT removal percentage were carried out at room temperature and neutral pH using an artificial CFT waste (250 mg L^{-1}). Gradually, the concentration of CFT in the residual solution was measured to obtain a stable condition at several points (*Figure 7*). Based on the measurements, the results showed that PKM could absorb the lowest value of 8%. The AC-PKM conversion using the glass wool-pyrolysis method can increase the percentage of CFT removal is to 26%. However, this value is still lower when compared to ACC (32%). This percentage value has been able to eliminate the content of CFT in hospital wastewater with a concentration of 1.25-29.15 g mL^{-1} (Shipingana *et al.*, 2022).

Adsorption is also a multistep process involving the transfer of dissolved substances to the surface, followed by diffusion of internal pores. Thus, kinetics adsorption gives valuable information for the design need of big-scale adsorption columns. There are two types of kinetic study models, *i.e.*, pseudo-first-order model and pseudo-second-order model. The pseudo-first-order assumes that the interaction surface controls the adsorption process. In contrast, pseudo-second-order assumes that intra-particle diffusion controls the adsorption rate. Lagergren first proposed this kinetic study model to describe the adsorption of pollutant liquid on the surface solid and differentiate it from the kinetic system based on concentration (Vafakhah *et al.*, 2016). The experimental results of the kinetic parameters are given in *Table 4* and *Figure 8*. The linear correlation coefficient of AC-PKM (R^2) against the pseudo-second-order kinetic model type I (R^2 = 0.9961) was higher than that of the other kinetic model. In addition, the experimental adsorption capacity value on pseudo-second-order kinetics model type I (q_{exp} = 82.64 mg g^{-1}) was close to the calculated one (q_{cal} = 72.9927 mg g^{-1}), indicating this kinetic model is more suitable for describing the data. Therefore, the phenomenon of CFT adsorption with AC-PKM is chemisorption (Yu *et al.*, 2020).

Thermodynamic analysis was also carried out to predict changes in free energy ($G°$), enthalpy ($H°$), and entropy ($S°$) (Bhandari and Gogate, 2018). The adsorption usually involves dropping Gibbs free energy (ΔG), accompanied by decreased entropy (ΔS), because the adsorbed molecule is bound to the side of the active surface. The loss of degrees of freedom of adsorbed molecules compared with the state before adsorption causes a drop in free energy (ΔG) and entropy (ΔS). At the same time, enthalpy (ΔH) depends on temperature during adsorption. Temperature plays a vital role in adsorption. Change

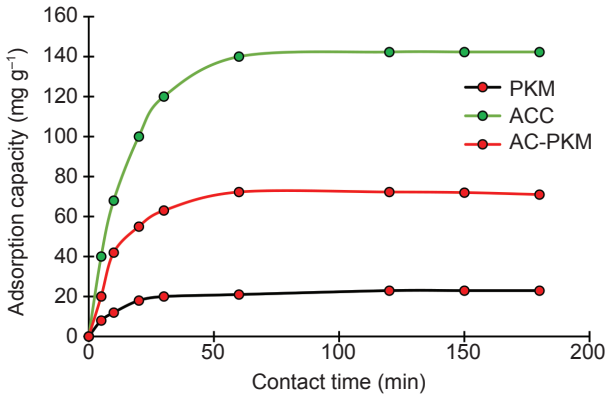


Figure 7. Adsorption capacity of CFT removal (mg g^{-1} adsorbent) with the effect of contact time on ACC, AC-PKM and PKM biomass.

TABLE 4. ADSORPTION KINETICS CONSTANTS OF PSEUDO-FIRST-ORDER AND PSEUDO-SECOND-ORDER ADSORPTION

Type	Non-linear form	Linear form	Plot	Parameters
Pseudo first-order	$q = q_e(1 - exp^{-K_1 t})$	$\log(q_e - q) = \log(q_e) - \frac{K_1 t}{2.303}$	$\log(q_e - q)$ vs. t	$K_1 = -2.303$ x slope
Type 1 pseudo second-order		$\frac{t}{q} = \frac{1}{K_2 q_e^2} + \frac{1}{q_e} t$	t/q vs. t	$q_e = 1/\text{slope}, K_2 = \text{slope}^2/\text{intercept}$
Type 2 pseudo second-order		$\frac{1}{q} = \left(\frac{1}{K_2 q_e^2}\right)\frac{1}{t} + \frac{1}{q_e}$	$1/q$ vs. $1/t$	$q_e = 1/\text{intercept}, K_2 = \text{intercept}^2/\text{slope}$
Type 3 pseudo second-order	$q = \frac{K_2 q_e^2 t}{1 + K_2 q_e t}$	$\frac{1}{t} = \frac{K_2 q_e^2}{q} - \frac{K_2 q_e^2}{q_e}$	$1/t$ vs. $1/q$	$q_e = -\text{slope}/\text{intercept}, K_2 = \text{intercept}^2/\text{slope}$
Type 4 pseudo second-order		$\frac{q}{t} = K_2 q_e^2 - \frac{K_2 q_e^2 q}{q_e}$	q/t vs. q	$q_e = -\text{intercept}/\text{slope}, K_2 = \text{slope}^2/\text{intercept}$
Type 5 pseudo second-order		$\frac{1}{q_e - q} = \frac{1}{q_e} + K_2 t$	$1/(q_e - q)$ vs. t	$q_e = 1/\text{intercept}, K_2 = \text{slope}$

	Pseudo 1st			Type I Pseudo 2nd			Type II Pseudo 2nd		
	R^2	q_{cal}	K_1	R^2	q_{cal}	K_2	R^2	q_{cal}	K_2
PKM	0.0094	0.3887	0.0005	0.9966	21.5054	0.0044	0.9823	25.9740	0.0019
AC-PKM	0.4074	1.1220	0.0044	0.9961	72.9927	0.0008	0.9956	80.6452	0.0005
ACC	0.4750	1.5545	0.0039	0.9947	87.7193	0.0009	0.9830	98.0392	0.0005
	Type III Pseudo 2nd			Type IV Pseudo 2nd			Type V Pseudo 2nd		
	R^2	q_{cal}	K_1	R^2	q_{cal}	K_2	R^2	q_{cal}	K_2
PKM	0.9823	26.4738	0.0018	0.8447	24.5563	0.0023	0,4038	11,2867	0,0005
AC-PKM	0.9956	81.1957	0.0005	0.9348	79.6690	0.0005	0,3849	12,1359	0,0004
ACC	0.9830	99.5606	0.0005	0.8310	100.2432	0.0005	0,3582	33,3333	0,0001

in Gibbs free energy (ΔG) during the adsorption process could be calculated from its connection with thermodynamics based on Equation (5):

$$\Delta G^o = \Delta H^o - T\Delta S^o \quad (5)$$

where $G°$ is the change energy free standard (J mol^{-1}), $H°$ is the heat adsorption standard (J mol^{-1}), $S°$ is the change in entropy during adsorption [J $(mol\ K)^{-1}$] and T is the temperature (K). The Van't Hoff Equation (6) shows a relationship between the equilibrium constant and the free energy change.

$$\Delta G^o = -RT \ln K^o \quad (6)$$

where R is an ideal gas constant of 8.314 (J/mol K) and K is an equilibrium constant. The equilibrium constant was calculated from the ratio of equilibrium adsorbate concentration still in solution, C_e (mg L^{-1}), to the quantity of adsorbate adsorbed per gram of adsorbent at equilibrium, q_e (mg g^{-1}). The following is how the equation for K is represented mathematically.

$$K = \frac{q_e}{C_e}^{o} \quad (7)$$

In calculating the free energy change, equilibrium constant values were employed. The adsorption is usually confirmed to be spontaneous when the free energy change is negative. In order to derive the model parameters, Equation (5) was converted into a straight-line equation and plotted as $G°/T$ *vs.* $1/T$.

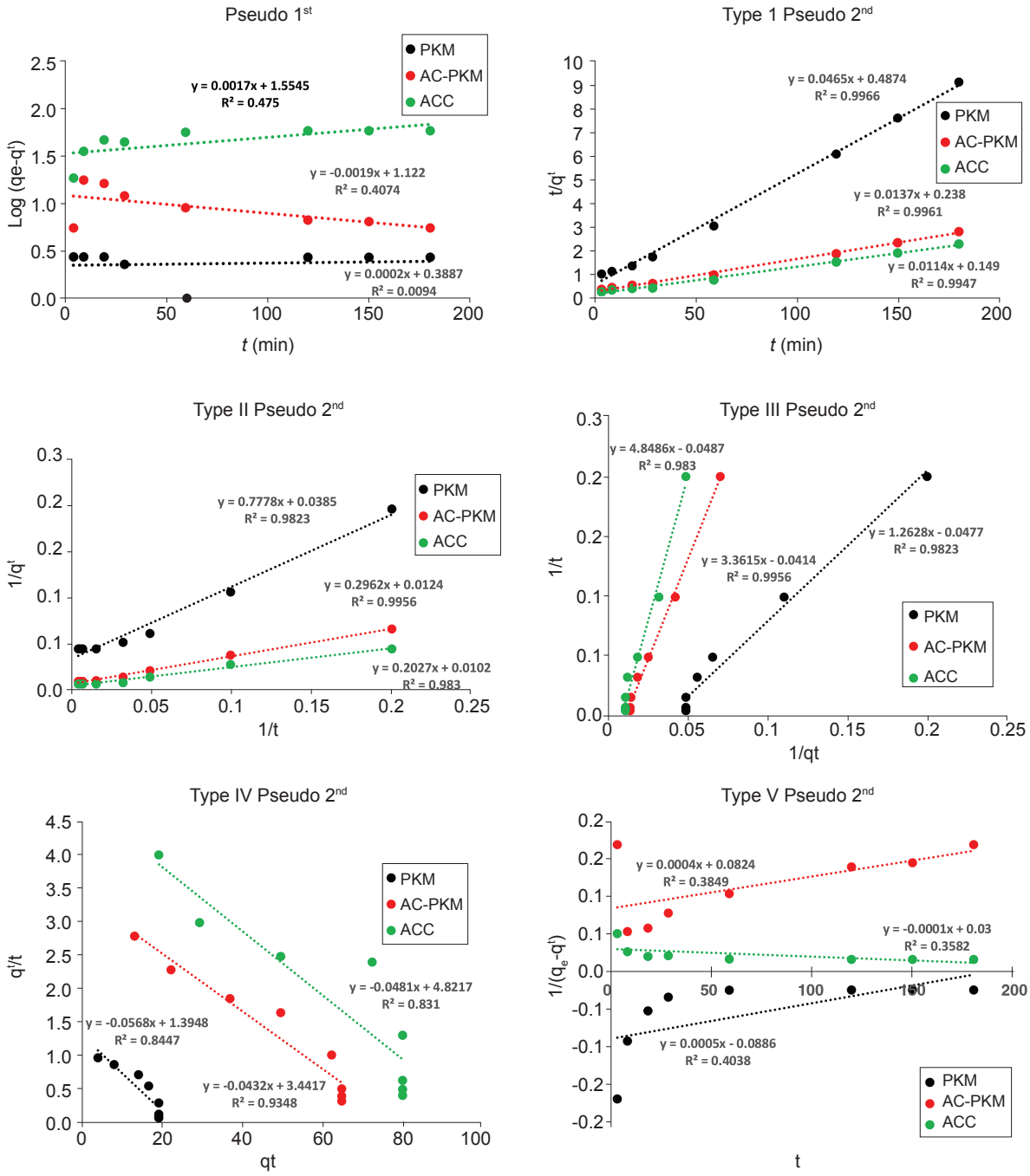


Figure 8. Pseudo-first-order and pseudo-second-order adsorption kinetics type I, II, III, IV, V plot of CFT removal on ACC, AC-PKM and PKM biomass.

Enthalpy and entropy values for adsorption were calculated using slope and intercept values. *Table 5* includes the information obtained for *G*, *H*, and *S*.

The change in free energy ($\Delta G°$), enthalpy ($\Delta H°$) and entropy ($\Delta S°$) were all predicted using thermodynamic analysis. The data for $G°$, $H°$, and $S°$ are shown in *Table 5* and *Figure 9*. The adsorption process is endothermic with a positive adsorption enthalpy value. On the other hand, the entropy was positive, associated with an increase in the system's randomness during adsorption. This thermodynamic parameter also shows that an increase in adsorption capacity will be obtained with an increase in temperature. However, it should be noted that at temperatures above 60°C (353 K), β-lactam antibiotics such as CFTs can degrade rapidly (Roca *et al.*, 2011).

CFT is an antibiotic widely used for surgical prophylaxis, pneumonia, respiratory infections and sepsis. The WHO (2014) recommended maximum daily dose of CFT is 2 g for adults (Anatomical Therapeutic Chemical/ATC J01DD04). Improper target use can increase the potential for CFT contamination in the waters. When the length of time the pollutant acts is examined, pollution

TABLE 5. THERMODYNAMIC MODEL FROM SAMPLE

Sample	Temperature (K)	ΔG (J mol^{-1})	ΔH (J mol^{-1})	ΔS [J (mol K)$^{-1}$]
PKM	298	289.73	8 812.7	17 251
	303	268.30		
	313	176.65		
AC-PKM	298	-1 455.92	19 496.0	55 346
	303	-1 435.98		
	313	-1 344.59		
ACC	298	-2 071.71	25 768.0	78 193
	303	-1 763.25		
	313	-1 603.37		

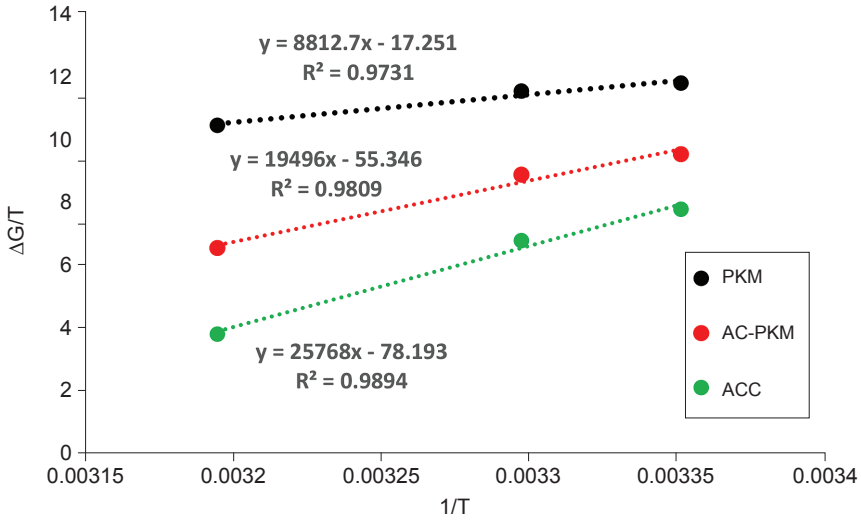


Figure 9. Van't Hoff Plot of CFT removal on ACC, AC-PKM and PKM biomass.

might be permanent, systematic, periodic, or accidental. The repercussions of water pollution have an impact on both the environment and human health (Gavrilescu, 2021). For this reason, reducing the risk of antibiotic residues from waste in hospitals is necessary. In this paper, adsorbent regeneration is not carried out because it is less economical and efficient. Thus, after adsorption, the adsorbent will be used as an alternative fuel. Further research is needed to investigate the release of carbon dioxides and other gases produced, thereby avoiding more harmful side pollutants.

Indonesia is the world's largest palm oil producer and produces PKM waste of 6 million tonnes yr^{-1}. In addition, PKM waste is generally found in palm oil processing plants, making it easier to process it into activated carbon at a lower production price. Therefore, activated carbon based on PKM waste has great potential as an adsorbent that can be used as an alternative material in reducing antibiotic residues in water.

CONCLUSION

Modifying the glass wool-pyrolysis method at 750°C for 5 hr was developed to synthesize AC-PKM from palm kernel meal as an adsorbent for antibiotic residues. This method can maintain the surface-active functional groups on AC-PKM with a large specific surface area. The adsorption isotherm model for AC-PKM follows the Langmuir isotherm model at room temperature. The adsorption process is endothermic and spontaneous. Kinetics studies showed that CFT adsorption on AC-PKM followed a pseudo-second-order kinetic model. AC-PKM adsorbent can remove CFT levels greater than PKM, which is 26%. Although the percentage removal of AC-PKM is still lower than that of ACC. AC-PKM has potential in removing CFT and is an alternative treatment for reuse PKM biomass waste.

ACKNOWLEDGEMENT

This work was funded by PMDSU Scholarship, the Ministry of Educational and Culture of Republic Indonesia (Grant Number 4160/IT3.L1/PN/2020).

REFERENCES

Acelas, N; Lopera, S M; Porras, J and Torres-Palma, R A (2021). Evaluating the removal of the antibiotic cephalexin from aqueous solutions using an adsorbent obtained from palm oil fibre. *Molecules*, *26(11)*: 3340. DOI: 10.3390/molecules26113340.

Al-Riyami, I M; Ahmed, M; Al-Busaidi, A and Choudri, B S (2018). Antibiotics in wastewaters: A review with a focus on Oman. *Water Science App*., *8(7)*: 1-10. DOI: 10.1007/s132010180846-z.

Alekseev, V G (2010). Drug synthesis methods and manufacturing technology acid-base properties of penicillins and cephalosporins (A review). *Pharm. Chem. J., 44(1)*: 14-24.

Amiri, S; Sohrabi, M R and Motiee, F (2020). Optimization removal of the ceftriaxoxne drug from aqueous media with novel zero-valent iron supported on doped strontium hexaferrite nanoparticles by response surface methodology. *Anal. Chem., 5*: 5831-5840.

Ashtaputrey, S D and Ashtaputrey, P D (2016). Preparation and characterization of activated charcoal derived from orange peel. *J. Adv. Chem. Sci*., *2(3)*: 360-362.

Ayawei, N; Ebellegi, A N and Wankasi, D (2017). Modelling and interpretation of adsorption isotherms. *J. Chem., 2017*: 11. DOI: 10.1155/2017/3039817.

Ayele, A A; Gebresillassie, B M; Erku, D A; Gebreyohannes, E A; Demssie, D G; Mersha, A G and Tegegn, H G (2018). Prospective evaluation of ceftriaxone use in medical and emergency wards of Gondar University referral hospital, Ethiopia. *Pharmacol. Res. Perspect*., *6(1)*: 1-7. DOI: 10.1002/prp2.383.

Badi, Y M; Azari, A; Pasalari, H; Esrafili, A and Farzadkia, M (2018). Modification of activated carbon with magnetite Fe_3O_4 nanoparticle composite for removal of ceftriaxone from aquatic solutions. *J. Mol. Liq*., *261*: 146-154.

Bhandari, P S and Gogate, P R (2018). Kinetic and thermodynamic study of adsorptive removal of sodium dodecyl benzene sulfonate using adsorbent based on thermo-chemical activation of coconut shell. *J. Mol. Liq*., *252*: 495-505. DOI: 10.1016/j.molliq.2017.12.018.

Biasutti, M A; Anunziata, J D and Silber, J J (1992). N-π electron-donor-acceptor complexes-IV. The interaction of aliphatic amines with 1,3-dicyanobenzene in n-hexane. The importance of preferred orientation in the stability of the complexes. *Spectrochim. Acta Part A Mol. Spectrosc., 48(2)*: 169-173. DOI: 10.1016/0584-8539(92)80019-S.

Bozorginia, S; Jaafari, J; Taghavi, K; Ashraf, S D; Roohbakhsh, E and Naghipour, D (2021). Biosorption of ceftriaxone antibiotic by *Pseudomonas putida* from aqueous solutions. *Int. J. Environ. Anal. Chem*., *108*: 1-15. DOI: 10.1080/03067319.2021.18787858.

Browne, A J; Chipeta, M G; Haines-Woodhouse, G; Kumaran, E P A; Hamadani, B H K; Zaraa, S; Henry, N J; Deshpande, A; Reiner, R C; Day, N P J; Lopez, A D; Dunachie, S; Moore, CE; Stergachis, A; Hay, S I and Dolecek, C (2021). Global antibiotic consumption and usage in humans, 2000-18: A spatial modelling study. *Lancet Planet. Health*., *5(12)*: e893-e904. DOI: 10.1016/S2542-5196(21)00280-1.

Cassol, O G; Gallon, R; Schwaab, M; Barbosa-Coutinho, E; Júnior, J B and Pinto, J C (2014). Statistical evaluation of non-linear parameter estimation procedures for adsorption equilibrium models. *Adsorp. Sci. Technol., 32(4)*: 257-273.

De Diego, M; Godoy, G and Mennickent, S (2010). Chemical stability of ceftriaxone by a validated stability-indicating liquid chromatographic method. *J. Chil. Chem. Soc*., *55(3)*: 335-337. DOI:10.4067/S0717-97072010000300013.

De Gisi, S; Lofrano, G; Grassi, M and Notarnicola, M (2016). Characteristics and adsorption capacities of low-cost sorbents for wastewater treatment: A review. *Sustain. Mater. Technol*., *9*: 10-40. DOI: 10.1016/j.susmat.2016.06.02.

Fahmi, A G; Abidin, Z; Kusmana, C; Kharisma, D; Prajaputra, V and Rahmawati, W R (2019). Preparation and characterization of activated carbon from palm kernel shell at low temperature as an adsorbent for methylene blue. *IOP Conference Series: Earth and Environmental Science*. 399 pp.

Fahmi, A G; Abidin, Z; Kusmana, C and Noor, E (2022). Versatile synthesis of activated carbon from coconut shells: A method for cyanide adsorption in artisanal and small-scale gold mining wastewater. *J. Degrade. Min. Land Manage., 9(4)*: 3685-3693.

Feng, P; Li, J; Wang, H and Xu, Z (2020). Biomass-based activated carbon and activators: Preparation of activated carbon from corncob by chemical activation with biomass pyrolysis liquids. *ACS Omega*., *5(37)*: 24064-24072. DOI: 10.1021/acsomega.0c03494.

Gavrilescu, M (2021). Water, soil and plants interactions in a threatened environment. *Water*, *13*: 2746. DOI: 10.3390/w13192746.

Gonzalez, D; Golab, J T; Eilert, J Y; Wang, R and Kaduk, J A (2020). Crystal structure of ceftriaxone sodium hemiheptahydrate, $C18H16N8O7S3Na_2(H_2O)3.5$. *Powder Differ., 35(3)*: 206-212. DOI: 10.1017/S0885715620000299.

Gumus, R H; and Okpeku, I (2015). Production of activated carbon and characterization from snail shell waste. *Adv. Chem. Eng. Sci.*, *05(01)*: 51-61. DOI: 10.4236/aces.2015.51006.

Hassan, M; Zhu, G; Lu, Y Z; Al-Falahi, A H; Lu, Y; Huang, S and Wan, Z (2021). Removal of antibiotics from wastewater and their problematic effects on microbial communities by bioelectrochemical technology: Current knowledge and future perspectives. *Environ. Eng. Res., 26(1)*: 1-15. DOI: 10.4491/eer.2019.405.

Hu, Z and Gao, Z (2018). High-surface-area activated red mud for efficient removal of methyleneblue from wastewater. *Adsorpt. Sci. Technol*., *36(1-2)*: 62-79. DOI: 10.1177/0263617416684348.

de Ilurdoz, M S; Sadhwani, J J; and Reboso, J V (2022). Antibiotic removal processes from water and wastewater for the protection of the aquatic environment - A review. *J. Water Process. Eng., 45*: 102474. DOI: 10.1016/j.jwpe.2021.102474.

Jasper, E E; Ajibola, V O and Onwuka, J C (2020). Nonlinear regression analysis of the sorption of crystal violet and methylene blue from aqueous solutions onto an agro-waste derived activated carbon. *Appl. Water Sci., 10*: 132. DOI: 10.1007/s13201-020-01218-y.

Karri, R R; Sahu, J N and Jayakumar, N S (2017). Optimal isotherm parameters for phenol adsorption from aqueous solutions onto coconut shell based activated carbon: Error analysis of linear and non-linear methods. *J. Taiwan Inst. Chem. Eng., 80*: 472-487. DOI: 10.1016/j.jtice.2017.08.004.

Khan, M Y; Roy, M; Rawal, R K and Bansal, U K (2017). Ceftriaxone for life. *Asian J. Pharm. Res., 7(1)*: 35-48. DOI: 10.5958/2231-5691.2017.00007.

Kharrazi, S M; Soleimani, M; Jokar, M; Richards, T; Pettersson, A and Mirghaffari, N (2021). Pretreatment of lignocellulosic waste as a precursor for synthesis of high porous activated carbon and its application for Pb (II) and Cr (VI) adsorption from aqueous solutions. *Int. J. Biol. Macromol., 180*: 299-310. DOI: 10.1016/j.ijbiomac.2021.03.078.

Kordestani, B; Takdastan, A; Jalilzadeh Yengejeh, R and Neisi, A K (2020). Photo-Fenton oxidative of pharmaceutical wastewater containing meropenem and ceftriaxone antibiotics: Influential factors, feasibility, and biodegradability studies. *Toxin. Rev., 39(3)*: 292-302. DOI: 10.1080/15569543.2018.1520261.

Mahmoud, M E; El-Ghanam, A M; Mohamed, R H A and Saad, S R (2020). Enhanced adsorption of levofloxacin and ceftriaxone antibiotics from water by assembled composite of nanotitanium oxide/chitosan/nano-bentonite. *Mater. Sci. Eng., 108(2019)*: 110199. DOI: 10.1016/j.msec.2019.110199.

Maulina, S; Handika, G; Irvan and Iswanto, A H (2020). Quality comparison of activated carbon produced from oil palm fronds by chemical activation using sodium carbonate versus sodium chloride. *J. Korean Wood Sci. Technol*., *48(4)*: 503-512. DOI: 10.5658/WOOD.2020.48.4.503.

Mensah, K B and Ansah, C (2016). Irrational use of antibiotics and the risk of diabetes melitus in Ghana. *Ghana Med. J., 50(2)*: 107-114. DOI: 10.4314/gmj.v50i2.9.

Okeola, O F; Odebunmi, E O and Ameen, O M (2012). Comparison of sorption capacity and surface area of activated carbon prepared from *Jatropha curcas* fruit pericarp and seed coat. *Bull. Chem. Soc. Ethiopia*., *26(2)*: 171-180. DOI: 10.4314/bcse.v26i2.2.

Olesen, S W; Barnett, M L; Macfadden, D R; Brownstein, J S; Hernández-Díaz, S; Lipsitch, M and Grad, Y H (2018). The distribution of antibiotic use and its association with antibiotic resistance. *Elife*, *7*: 1-15. DOI: 10.7554/eLife.39435.

Osman, N B; Shamsuddin, N and Uemura, Y (2016). Activated carbon of oil palm empty fruit bunch (EFB): Core and shaggy. *Procedia Eng*., *148*: 758-764. DOI: 10.1016/j.proeng.2016.06.610.

Prajwal, S; Vasudevan, V N; Sathu, T; Irshad, A and Pame, K (2017). Antibiotic residues in food animals: Causes and health effects. *Pharma. Innov. J., 6(12)*: 01-04.

Rivas, B L; Oñate, P and Palacio, D A (2020). Removal of oxytetracycline by polimers: An overview. *J. Chil. Chem. Soc*., *4*: 4943-4947.

Roca, M; Villegas, L; Kortabitarte, M L; Althaus, R L and Molina, M P (2011). Effect of heat treatments on stability of β-lactams in milk. *J. Dairy Sci*., *94*: 1155-1164. DOI: 10.3168/jds.2010-3599.

Rugayah, A F; Astimar, A A and Norzita, N (2014). Preparation and characterisation of activated carbon from palm kernel shell by physical activation with steam. *J. Oil Palm Res*., *26(3)*: 251-264.

Saied, M El; Shaban, S A; Mostafa, M S and Naga, A O A (2022). Efficient adsorption of acetaminophen from the aqueous phase using low-cost and renewable adsorbent derived from orange peels. *Biomass Convers. Biorefin., March 2022*. 18 pp. DOI: 10.1007/s13399-022-02541-x.

Santhiarsa, I G N N (2021). Effect of variations in pyrolysis reactor with glass wool equipped and without glass wool on the weight of the oil produced. *J. Mech. Eng. Sci. Technol*., *5(2)*: 89-95.

Schultz, J; Capobianco, G; da Silva Veiga, P A; Fornari, M R; Antonangelo, A R; Tebcherani, S M; Mangrich, A S and Pianaro, S A (2020). Sustainable activated carbon obtained as a by-product of the sugar and alcohol industry for removal of amoxicillin from aqueous solution. *Energy, Ecol. Environ*., *5(6)*: 433-443. DOI: 10.1007/s40974-020-00173-3.

Sharma, G; Kaur, M; Punj, S and Singh, K (2020). Biomass as a sustainable resource for value-added modern materials: A review. *Biofuels, Bioprod. Biorefin*., *14(3)*: 673-695. DOI: 10.1002/bbb.2079.

Shi, X; Karachi, A; Hosseini, M; Yazd, M S; Kamyab, H; Ebrahimi, M and Parsaee, Z (2020). Ultrasound wave assisted removal of Ceftriaxone sodium in aqueous media with novel nanocomposite g-C3N4/MWCNT/Bi2WO6 based on CCD-RSM model. *Ultrason. Sonochem., 68*: 104460. DOI: 10.1016/j.ultsonch.2019.01.018.

Shipingana, L N N; Shivaraju, H P and Yashas, S R (2022). Quantitative assessment of pharmaceutical drugs in a municipal wastewater and overview of associated risks. *Appl. Water Sci., 12(16)*: 1-9.

Song, Y; Sackey, E A; Wang, H and Wang, H (2019). Adsorption of oxytetracycline on kaolinite. *PLoS ONE*, *14(11)*: 1-13. DOI: 10.1371/journal.pone.0225335.

Tani, D; Setiaji, B; Trisunaryanti, W and Syoufian, A (2014). Effect of activation time on chemical structure and quality of coconut shell activated carbon. *Asian J. Sci. Technol*., *5(9)*: 553-556.

Ukanwa, K S; Patchigolla, K; Sakrabani, R and Anthony, E (2020). Preparation and characterization of activated carbon from palm mixed waste treated with trona ore. *Molecules, 25(21)*: 1-18. DOI: 10.3390/molecules25215028.

Vafakhah, S; Bahrololoom, M E and Saeedikhani, M (2016). Adsorption kinetics of cupric ions on mixture of modified corn stalk and modified tomato waste. *J. Water Resource Prot*., *8*: 1238-1250.

WHO (2014). Safe management of wastes from healthcare activities.

Widayati, A; Suryawati, S; De Crespigny, C and Hiller, J E (2011). Self medication with antibiotics in Yogyakarta City Indonesia: A cross sectional population-based survey. *BMC Res Notes, 4(1)*: 491. DOI: 10.1186/1756-0500-4-491.

Wu, Z; Ye, X; Liu, H; Zhang, H; Liu, Z; Guo, M; Li, Q and Li, J (2020). Interactions between adsorbents and adsorbates in aqueous solutions. *Pure Appl. Chem., 92(10)*: 1655-1662. DOI: 10.1515/pac-2019-1110.

Xiao, F; Bedane, A H; Zhao, J X; Mann, M D and Pignatello, J J (2018). Thermal air oxidation changes surface and adsorptive properties of black carbon (char/biochar). *Sci. Total Environ., 618*: 276-283. DOI: 10.1016/j.scitotenv.2017.11.008.

Yu, J; Kang, Y; Yin, W; Fan, J and Guo, Z (2020). Removal of antibiotics from aqueous solutions by a carbon adsorbent derived from protein-waste-doped biomass. *ACS Omega*, *5(30)*: 19187-19193. DOI: 10.1021/acsomega.0c02568.

Zango, Z U; Jumbri, K; Sambudi, N S; Ramli, A; Bakar, N H H A; Saad, B; Rozaini, M N H; Isiyaka, H A; Jagaba, A H; Aldaghri, O and Sulieman, A (2020). A critical review on metal-organic frameworks and their composites as advanced materials for adsorption and photocatalytic degradation of emerging organic pollutants from wastewater. *Polymers (Basel)*, *12(11)*: 1-42. DOI: 10.3390/polym12112648.

Zhao, Y; Liang, X; Wang, Y; Shi, H; Liu, E; Fan, J and Hu, X (2018). Degradation and removal of ceftriaxone sodium in aquatic environment with Bi2WO6/g-C3N4 photocatalyst. *J. Colloid Interface Sci., 523*: 7-17. DOI: 10.1016/j.jcis.2018.03.078.

Journal of Oil Palm Research Vol. 36 (4) December 2024 p. 664-673
DOI: https://doi.org/10.21894/jopr.2023.0055

BACTERIAL CELLULOSE PRODUCTION FROM OIL PALM FROND JUICE AND ITS IMPREGNATION WITH SILVER NANOPARTICLES FOR ANTIBACTERIAL WOUND DRESSING

TAN SOU MIN[1]; NOR SYAHIRAH ABD KARIM[1]; SHAHRIL MOHAMAD[1]; JUNAIDI ZAKARIA[1]; MOHD HAFIZ ARZMI[2]; HASSAN FAHMI ISMAIL[3] and ROHANA ABU[1]*

ABSTRACT

Bacterial cellulose-silver nanoparticles (BC-AgNPs) composite was prepared for a bacterial wound dressing. The oil palm frond (OPF) juice was utilised as a low-cost raw material for BC production. The AgNPs were incorporated in the BC composite by thermal reduction of 1 mM silver nitrate for their antibacterial agent. The BC-AgNPs composite had dense nanofibrils with an average diameter of 61.5 ± 1.0 nm as shown in the field emission scanning electron microscope (FESEM) images. The composite had a crystallinity index of 86.5% and the nanoparticles had a face-centred cubic geometry with a crystal size of 26.5 nm as determined by X-ray diffraction analysis (XRD). The Ag content was 1.463 mg/100 cm² in the composite analysed by atomic absorption spectrophotometry (AAS). 10.4% of the total Ag content was released from AgNPs in 72 hr as measured by inductively coupled plasma mass spectrometry (ICP-MS). The composite also demonstrated excellent antibacterial action against Staphylococcus aureus, giving a 29 ± 0.8 mm inhibition zone by the disk diffusion assay. Pure BC composite exhibited no cytotoxicity effect on the HSF1184 fibroblast cells and 10%-40% BC-AgNPs composite extracts were compatible with the cell growth. The study suggests the BC-AgNPs composite is a good material for antibacterial wound dressing.

Keywords: bacterial cellulose, oil palm frond, silver nanoparticles, wound dressing.

Received: 7 April 2023**; Accepted:** 20 August 2023**; Published online:** 26 October 2023.

INTRODUCTION

The developments of new value-added products from agricultural biomass as low-cost raw materials are of great prospects in various fields such as biocompost, biofuel, bioplastic and biomaterial (Aziz *et al*., 2023; Harrison *et al*., 2023). Most palm oil-producing countries like Malaysia and Indonesia contribute significant biomass resources including oil palm trunk (OPT) and oil palm frond (OPF). The OPF is generated after fruit harvesting at the plantation area and it was estimated that 42 million tonnes yr^{-1} of OPF were abundantly available (Gan *et al*., 2023). Various value-added products have been developed due to the availability of biomass resources from the sustainable Malaysian palm oil industry (Parveez *et al*., 2023; Rashidi *et al*., 2022). The current industrial utilisation of OPF is in producing paper, animal feed, bio-alcohol, bio-char and biogas (Gan *et al*., 2023; Norrrahim *et al*., 2022; Zakaria *et al*., 2023). More recently, the OPF juice which contains high-carbon sugars has been found suitable to be utilised as a low-cost fermentation medium for bacterial growth in bacterial cellulose production (BC) (Lim *et al*., 2022; Mohamad *et al*., 2022; Said Azmi *et al*., 2023).

[1] Faculty of Chemical and Process Engineering Technology, Universiti Malaysia Pahang Al-Sultan Abdullah, 26300 Kuantan, Pahang, Malaysia.

[2] Department of Fundamental Dental and Medical Sciences, Kulliyyah of Dentistry, International Islamic University Malaysia, 25200 Kuantan, Pahang, Malaysia.

[3] Institute of Marine Biotechnology, Universiti Malaysia Terengganu, 21030 Kuala Terengganu, Terengganu, Malaysia.

* *Corresponding author e-mail: rohanaa@umpsa.edu.my*

BC composite is an extracellular product mainly synthesised by *Komagataeibacter xylinus*, a cellulose-producing bacteria also known as *Acetobacter xylinus* and *Gluconacetobacter xylinus*. This product is considered suitable for treating wounds because of its high purity and crystallinity with good mechanical strength, water holding capacity and biocompatibility (Avcioglu, 2022). The application of BC composite as a wound dressing has been reported to promote cell adhesion, proliferation and differentiation in wound healing phases, including hemostasis, inflammation, proliferation, and remodelling (Pang *et al*., 2020).

Despite its excellent role as a wound dressing, bacterial infection is still a concern as BC does not have intrinsic antibacterial properties that limit its application. BC-based antibacterial wound dressing can be developed by incorporating antibacterial agents into the BC matrix to prevent possible bacterial infection (Alyamani *et al*., 2023). BC's nanofibril network has been found to facilitate the penetration of various antibacterial agents through different impregnation methods that attracted many researchers' attention recently (Chandana *et al*., 2022). Interestingly, the BC containing inorganic nanoparticles like Ag, Au, CuO and ZnO showed significant efficacy against bacterial pathogens like *Staphylococcus aureus, Candida albicans, Escherichia coli*, *Salmonella enterica* and *Pseudomonas aeruginosa* (Araújo *et al*., 2018; Ayyappan *et al*., 2022; Heidari *et al*., 2022; Shaaban *et al*., 2023). Skin cells such as keratinocytes and fibroblasts have also demonstrated good biocompatibility with the BC composite loaded with nanoparticles (Sabarees *et al*., 2022). Moreover, our recent study has shown that AgNPs impregnated into BC composite can provide a favourable moisture environment with good water holding and release properties comparable to pure BC (Abu *et al*., 2021; 2022).

Therefore, this study aimed to develop the BC-AgNPs composite for bacterial wound dressing. The BC was produced using the OPF juice by *A. xylinum* and subsequently, the BC was impregnated with AgNPs by hydrothermal reduction. The composite properties were further analysed by FTIR, FESEM and XRD. The Ag content in the composite and the slow release of Ag^+ ions from the composite were measured by AAS and ICP-MS, respectively. The antibacterial activity against *S. aureus* was studied using the disk diffusion assay and the biocompatibility was tested in human skin fibroblast HSF1184 cells using the MTT assay.

MATERIALS AND METHODS

Materials

Silver nitrate was purchased from Bendosen Laboratory Chemicals, Norway. Acetic acid, sulphuric acid, nitric acid and MTT [3-(4,5-dimethylthiazol-2-yl)-2,5-diphenyltetrazolium bromide] were acquired from Sigma-Aldrich, USA. Sodium hydroxide was procured from R&M Chemicals, UK. Bacterial strain *A. xylinum* 0416 was bought from MARDI (Malaysian Agriculture and Research Development Institute). *Staphylococcus aureus* ATCC 6538 and human skin fibroblasts HSF1184 were provided by IIUM (International Islamic University Malaysia) and UMT (Universiti Malaysia Terengganu), respectively.

Production of BC by OPF Juice

OPF petioles were collected at LCSB Lepar palm oil plantation, Pahang. The petioles were mechanically pressed to extract the OPF juice. Before being autoclaved at 121°C for 10 min, the pH of the fermentation medium (60% v/v) was adjusted to 4.0 using 50% v/v acetic acid. 10% v/v *A. xylinum* 0416 inoculum was cultivated in 24-well plates and statically incubated at 30°C for 10 days (Mohamad *et al*., 2022). The boiling NaOH solution was used to purify the BC composites for 20 min. The composites were then stored at 4°C after soaking in distilled water.

BC-AgNPs by Hydrothermal Reduction

BC composite was submerged in a glass vial containing 25 mL of 1.0 mM $AgNO_3$ solution. The vial was wrapped with aluminium foil and autoclaved for 10 min at 121°C and 0.103 MPa for hydrothermal reduction. The composite was left at room temperature in distilled water to stop the reduction process. After that, it was freeze-dried for 24 hr at -70°C and 0.011 Mba before the characterisation studies.

BC-AgNPs Characterisation

The cellulose functional groups present in the BC-AgNPs composite were identified using Fourier transform infrared (FTIR) spectroscopy (Thermo-Scientific NICOLET iS50), equipped with the attenuated total reflectance (ATR). The average of each spectrum was 16 scans in the range of 4000 to 500 cm^{-1} at 4 cm^{-1} spatial resolution. The surface morphology of sputter-coated platinum of BC and BC-AgNPs composites was identified at 5 kV acceleration voltage using a JEOL JSM-7800F field emission-scanning electron microscope (FESEM). The size distribution was analysed by histogram using ImageJ software. The presence of elemental silver in the composite was determined by Energy dispersive X-ray (EDX) attached to the FESEM. The crystalline structure of the composite was analysed by a PANalytical X'Pert Pro X-ray diffractometer (XRD) using Cu Kα irradiation at λ =1.54060A°. The XRD data was measured in 2θ between 10°-80° range at 1° per min scan speed. The crystallite index and

size were calculated using empirical method (Zeng *et al.*, 2014) and Scherrer equation (Manosalva *et al.*, 2019), respectively.

Silver Content and Release Studies

The quantity of silver in the BC-AgNPs composite was measured by flame atomic absorption spectrometry (AAS) (Hitachi Z-5000 Polarised Zeeman, Japan). The composite was heated for 2 hr at 600°C using a furnace. The remaining substance was dissolved in 2 mL of concentrated nitric acid before diluting to 100 mL with distilled water for AAS analysis. The Ag^+ ions released from the composite were measured using inductively coupled plasma mass spectrometry analysis (ICP-MS) (7500a Agilent Technologies, USA). The composite was immersed in 10 mL of PBS solution at pH 7.4 and was placed in a water bath at 37°C. 200 µL of the solution was taken at 1.5, 2.5, 6.0, 24.0, 48.0 and 72.0 hr for the analysis.

Antibacterial Activity

The antibacterial susceptibility testing was conducted using the disk diffusion method. The inhibitory effect of AgNPs in the BC composite was assessed on the bacterial strain *S. aureus* grown onto the Mueller Hinton agar plate after overnight incubation at 37°C. The diameter of zone inhibition was measured in three biological replicates.

Cytotoxicity Test

The *in vitro* cytotoxicity test was conducted using Human skin fibroblast HSF1184 cells. Cell culture medium was prepared using Dulbecco's Modified Eagle's Medium (DMEM) supplemented with 10% fetal bovine serum and 1% penicillin-streptomycin (Invitrogen, CA, USA). 1.0×10^4 cells per well were cultured in 96-well plates and incubated overnight at 37°C, 5% CO_2 and 95% humidity. After removing the medium, the cells were treated with BC composite extract and the serially diluted BC-AgNPs extract in DMEM (100%, 80%, 60%, 40% and 10%) for 24 hr (Horue *et al.*, 2020). Cells that were treated with only DMEM were used as a control. After the treatment, 100 µL MTT solution was added to each well and then incubated for an additional 3 hr. The formed MTT formazan was dissolved with 100 mL of dimethyl sulphoxide and the solution's absorbance was measured at 570 nm using an ELISA microplate reader.

Statistical Analysis

Statistical analysis was performed using Origin 2022 software (OriginLab, Northampton, MA, USA). Results are expressed as mean value ± standard error of the mean. The statistical significance of the results was determined using Student's T-test ($P \leq 0.05$).

RESULTS AND DISCUSSION

Synthesis of BC-AgNPs Composite

Prior studies found that the pressed juice from OPF has a high concentration of fermentable sugar, which can be utilised as a cheap carbon source for microbial growth in BC production (Mohamad *et al.*, 2022; Said Azmi *et al.*, 2023). The BC yield can be obtained up to 2.33 g L^{-1} using 60% v/v of OPF juice after 14 days of static fermentation (Mohamad *et al.*, 2022). In this study, the BC was produced using the same fermentation conditions with a shorter incubation time of 10 days as a thick BC film was obtained due to a lower surface area of 24-well plates. The produced BC was then hydrothermally incorporated with AgNPs to explore its potential use as an antibacterial wound dressing. It was found that the pure BC composite was colourless while the BC-AgNPs composite was yellowish, indicating that AgNPs were successfully incorporated into the BC composite. The schematic representation in *Figure 1* served as an illustration of how the BC-AgNPs composite was developed.

Characterisation of BC-AgNPs Composite

From the FESEM images, the nanofibril mean diameter of 60.2 ± 1.5 nm was obtained with the loose arrangement in the pure BC composite (*Figure 2a*). While the BC-AgNPs composite exhibits denser cellulose fibrils with a mean diameter of 61.5 ± 1.0 nm and the presence of 24.7 ± 2.9 nm mean diameter of Ag spherical particle attached to the surface of nanofibrils (*Figure 2b* and *2c*). It can be seen from the image that each particle is either individually or aggregately attached to the nanofibril surface. The presence of elemental Ag on the surface was also confirmed by the EDX analysis as shown in the EDX spectrum (*Figure 2d*). A similar characteristic was also observed in other BC-AgNPs studies (Pal *et al.*, 2017; Shidlovskiy *et al.*, 2018).

BC produced from OPF juice shows the typical FTIR spectra of cellulose with broad vibration at 3335 cm^{-1} and 1625 cm^{-1}, indicating the OH stretching of the hydroxyl group (Pal *et al.*, 2017) and the C=O stretching of the carbonyl group (Liu *et al.*, 2015), respectively. These functional groups exhibit good hydrophilicity for the BC composite. Similarly, the BC-AgNPs composite had the same strong peaks but a shift occurred in the spectra (*Figure 3*). The same spectra suggest that the cellulose structure was maintained after the impregnation of AgNPs.

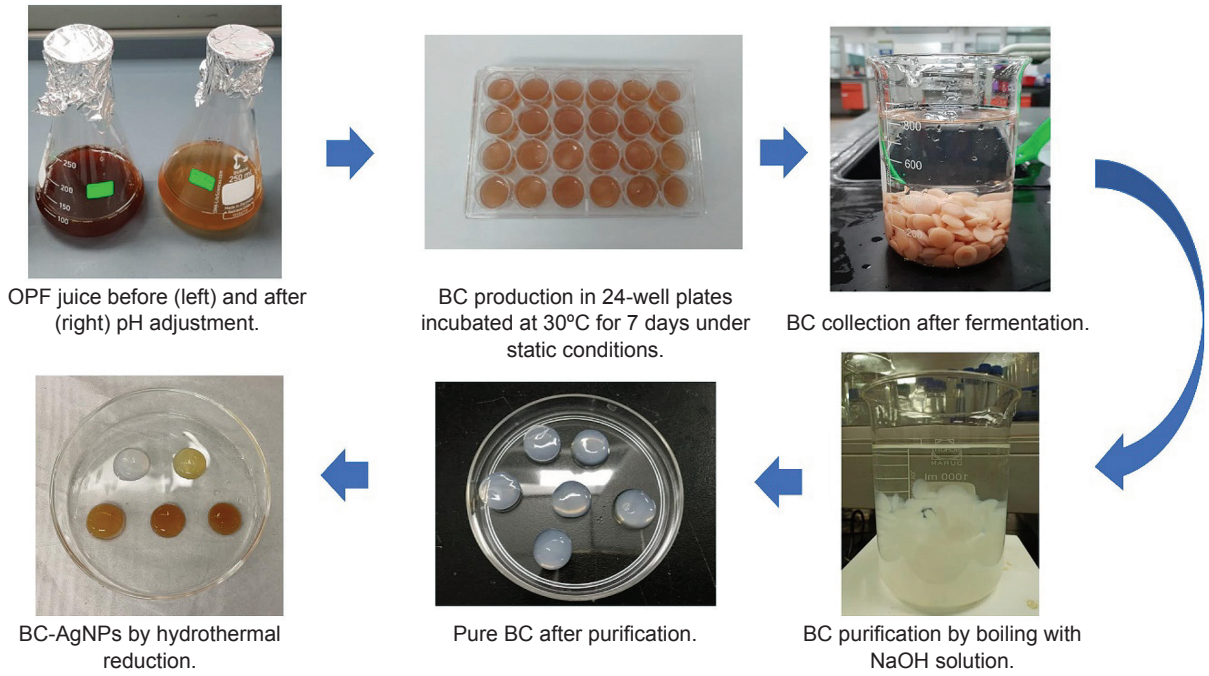


Figure 1. Schematic diagram of the development of the BC-AgNPs composite.

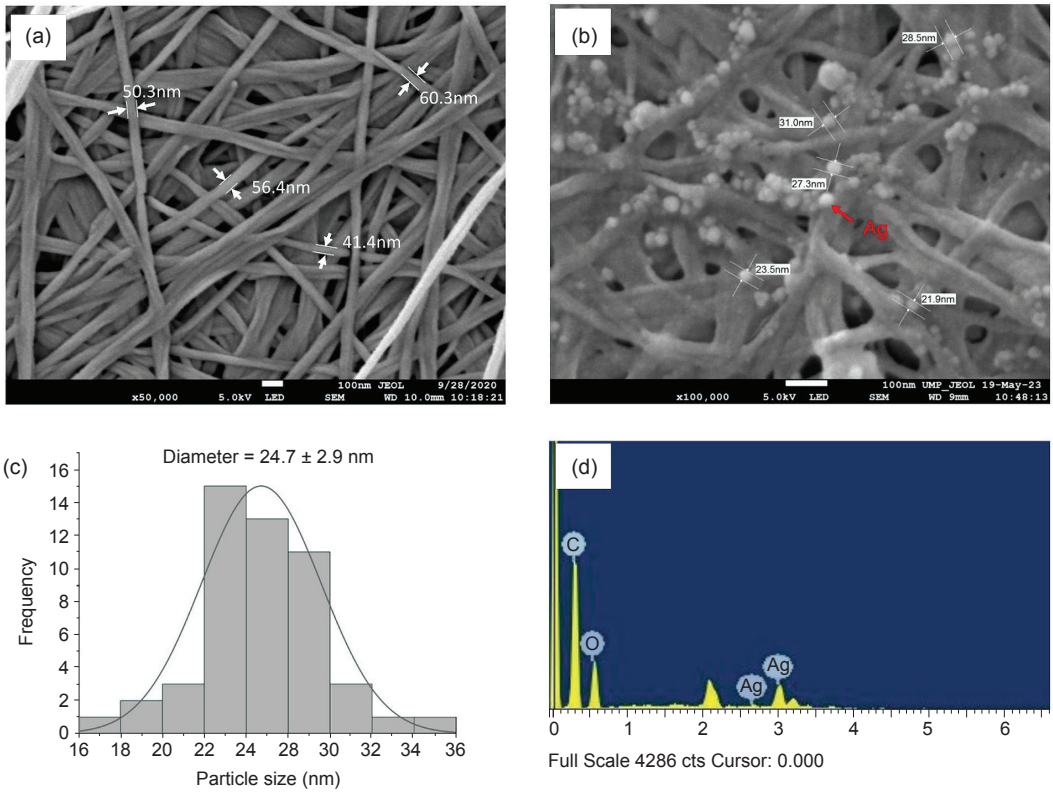


Figure 2. FESEM images of (a) pure BC, (b) BC-AgNPs, (c) particle size distribution of BC-AgNPs and (d) EDX spectrum of BC-AgNPs. The red arrow indicates the elemental Ag.

XRD was used to identify the possible structural change in the BC-AgNPs composite compared to pure BC (*Figure 4*). The XRD pattern of pure BC had three typical diffraction peaks of crystalline cellulose I at 14.4°, 16.7° and 22.6° which correspond to the crystal planes of (1$\bar{1}$0), (110) and (200), respectively (Li *et al.*, 2015). BC-AgNPs composite had the same crystalline structure of cellulose I with the additional crystalline peaks of face-centred cubic (FCC) of AgNPs (Ganesh Babu and Gunasekaran, 2009). The FCC peaks can be seen at 38.2°, 44.1°, 64.4° and 77.4° which correspond to the crystal planes of (111), (200), (220) and (311),

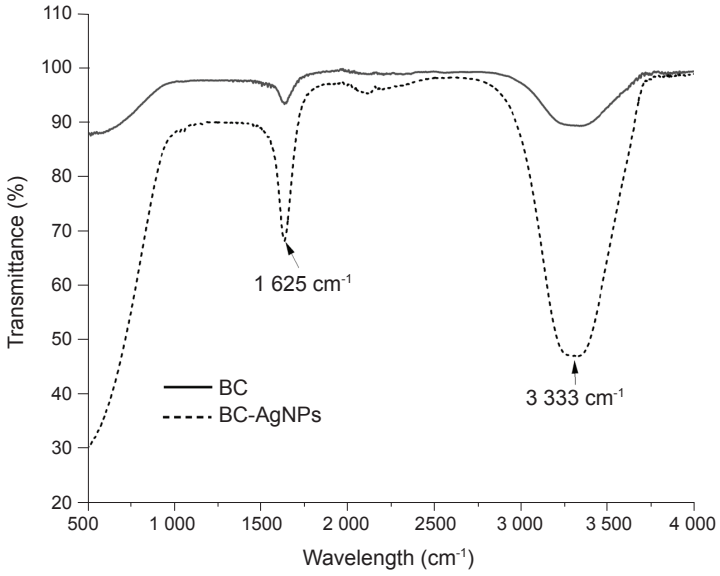


Figure 3. FTIR spectra of BC and BC-AgNPs.

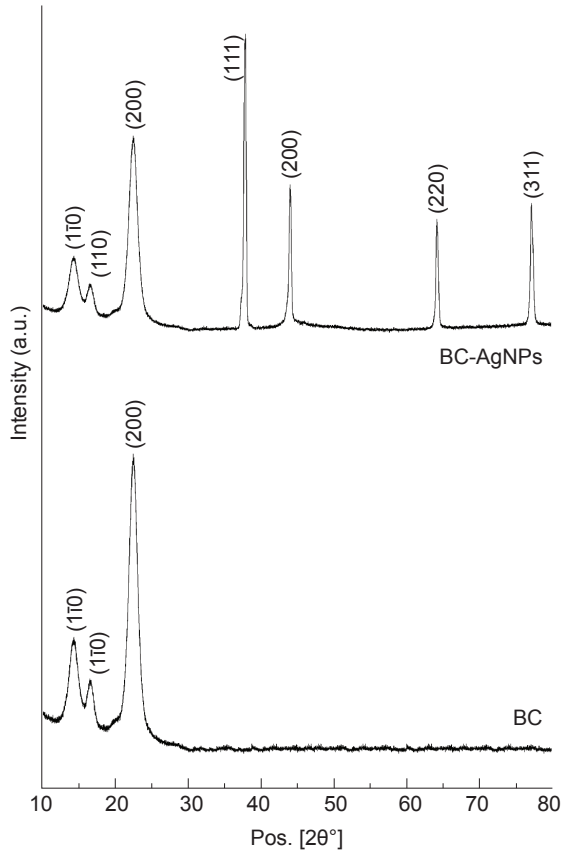


Figure 4. XRD patterns of BC and BC-AgNPs composites.

respectively. The crystallinity index of the BC-AgNPs composite had slightly decreased to 86.5% from 87.0% of the BC composite, showing minor structural change from the hydrothermal method. Moreover, the Ag in the BC composite had a nanosized crystal of 26.5 nm, calculated using the Scherrer equation.

Silver Content and Release of BC-AgNPs Composite

The Ag content in the BC-AgNPs composite was determined by AAS analysis. It was found that 1.463 mg of Ag was incorporated into 100 cm^2 of BC-AgNPs composite when prepared using 1 mM $AgNO_3$ concentration. The result is comparable to those reported in previous studies with values ranging from 0.04-16.00 mg Ag per 100 cm^2 composite, using the same hydrothermal method to prepare BC-AgNPs composite (Li *et al*., 2015; Volova *et al*., 2018).

The Ag ions profile diffused from the BC-AgNPs composite into the PBS solution at pH 7.4 and 37°C was demonstrated in *Figure 5*. It can be seen that the Ag^+ ions released rapidly in the initial 6 hr. After that, the release rate was sustained slowly until it reached a plateau. There was 10.4% of the total Ag^+ ions deposited from the composite in 72 hr. The initial rapid release of Ag^+ ions into PBS solution can be due to the fast ionisation of AgNPs that adhered on the nanofibril surface as shown in FESEM image. Besides, the slow-release rate of Ag^+ ions from the composite may be elucidated by the strong electrostatic interaction between the Ag^+ ions and the hydroxyl group of cellulose. The free ions are associated with the antibacterial potential of this composite. Excessive release of antibacterial agents can harm human cells and limit their antibacterial efficacy (Pal *et al*., 2017).

Antibacterial Activity of BC-AgNPs Composite

The susceptibility of *S. aureus* ATCC 6538 towards antibacterial agent in BC composite was observed using the disk diffusion method.

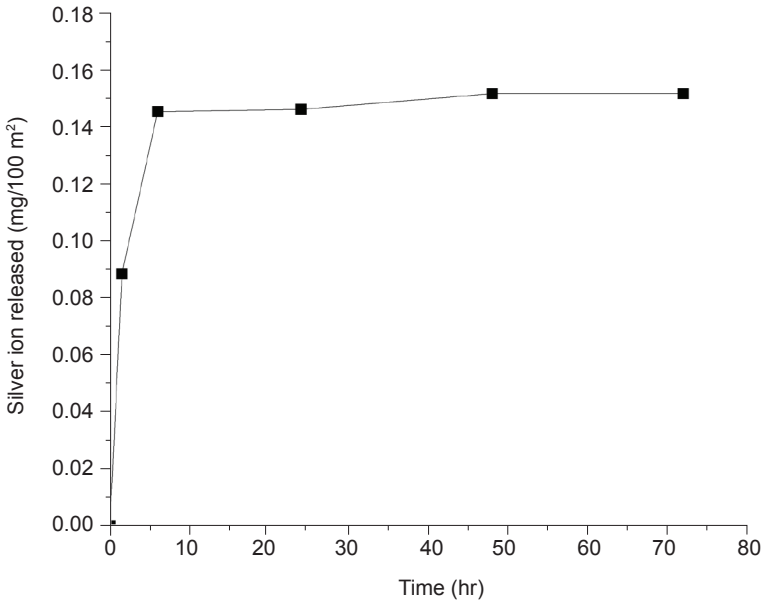


Figure 5. Ions released from BC-AgNPs composite as a function of the incubation time in PBS solution at 37°C and pH 7.4. The value was measured using inductively coupled plasma mass spectrometry (ICP-MS) analysis.

As expected, there was no inhibition for the BC composite indicating that the composite itself did not have antibacterial property against the bacterial strain which limits its wound dressing application (*Figure 6a*). Remarkably, the large inhibition zone of 29 ± 0.8 mm was measured for the BC-AgNPs composite, showing the susceptibility of *S. aureus* to the bactericidal effect of AgNPs (*Figure 6b*). Likewise, the effect was observed in other studies where the inhibition zones of 15 mm (Volova *et al*., 2018) and 9 mm (Yang *et al*., 2012) were shown by BC-AgNPs composites prepared by 1 mM $AgNO_3$ against the Gram-positive bacterium *S. aureus*. The different inhibition zone values may be caused by the use of different impregnation methods as well as the quantity of Ag^+ ions released from the BC composites (Wu *et al*., 2014).

Besides, the different biological activity of AgNPs can also be affected by several factors including particle size, morphology, surface charge, surface chemistry, capping agents as well as microorganism type (Barabadi *et al*., 2020; Saravanan *et al*., 2021; Talank *et al*., 2022). The high susceptibility of gram-positive bacteria to BC-AgNPs composite might be due to the strong electrostatic force between Ag ions that are released from the AgNPs and the sulphur proteins on the bacterial cell wall and cytoplasm membrane. The accumulation of the ions on the cell wall and cytoplasm membrane eventually causes cell disruption (More *et al*., 2023). AgNPs might also induce reactive oxygen species (ROS) formation in the cell which leads to the damage of DNA and membrane proteins (Talank *et al.*, 2022).

In addition to their excellent antibacterial activity, AgNPs have other biological potential such as antiviral (Barabadi *et al*., 2022a), antiparasitic (Jain *et al*., 2021), biofilm inhibitory (Barabadi *et al*., 2022b; Ibraheem *et al*., 2022), and antioxidant (Alzubaidi *et al*., 2023; Barabadi *et al*., 2020). The combination of BC with these biological activities is a feasible research direction for wound treatment.

Cytotoxicity of BC-AgNPs Composite

For wound healing applications, the dressing material must be biocompatible with skin cells. The cytotoxicity of BC-AgNPs composite was evaluated in human skin fibroblast HSF1184 cells using MTT assay. After 24 hr of exposure, the BC composite extract was found to be non-toxic to the cell lines when compared to control cells (*Figure 7*). The results are in agreement with previously reported biocompatibility of BC composite produced from various carbon sources (Jutakridsada *et al*., 2023; Lin *et al*., 2013; Qiu *et al*., 2016; Wu *et al*., 2014). Besides, the BC-AgNPs composite extracts showed non-toxicity up to 40% dilution after 24 hr of incubation. Nevertheless, 60% and 80% BC-AgNPs extracts started to inhibit fibroblast growth. This is because the antibacterial agent like AgNPs cannot differentiate between healthy cells and pathogenic bacteria. To some extent, the cytotoxic effects on cell growth strongly correlate with the amount of Ag in the composite and the amount of Ag^+ ions released from the composite (Jabbari and Babaeipour, 2023). Therefore, *in vitro* study is needed to test the biocompatibility of potential dressing material.

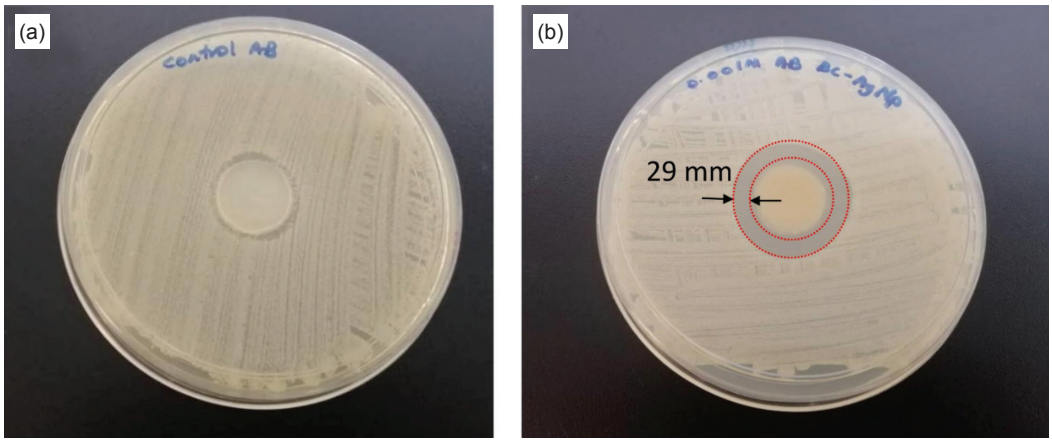


Figure 6. Antibacterial activity against Staphylococcus aureus *by the disk diffusion method. (a) No inhibition zone of BC composite and (b) inhibition zone of 29 ± 0.8 mm of BC-AgNPs composite.*

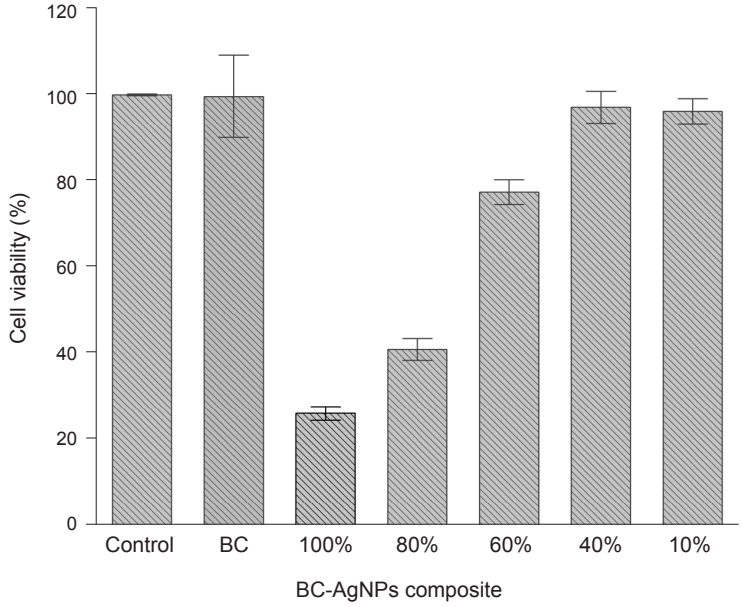


Figure 7. Cytotoxicity of BC-AgNPs composite after 24 hr incubation in HSF1184 cell lines using MTT assay. In the figure, control (untreated cells), BC composite and BC-AgNPs composite extracts in serial dilutions (10% to 100%). The results were expressed in the mean ± standard error (n = 3).

CONCLUSION

In summary, we prepared BC composite from OPF juice and incorporated AgNPs into the composite through hydrothermal synthesis. The results from characterisation studies confirmed the incorporation of AgNPs in the BC matrix was successful with the presence of 24.7 ± 2.9 nm mean diameter of Ag spherical particle attached to the surface of BC nanofibrils. The slow release of Ag^+ ions from the composite as analysed by ICP-MS might prevent wound infection. The composite exhibits excellent antibacterial activity with inhibition zone of 29 ± 0.8 mm against a gram-positive bacterium *S. aureus* and good biocompatibility in fibroblast cell growth. This study showed oil palm biomass could be efficiently used for BC production and the developed BC-AgNPs composite has the potential as a bacterial wound dressing. Future research is necessary to determine the biological potential of the BC-AgNPs composite for ideal wound dressing.

ACKNOWLEDGEMENT

The authors with gratitude acknowledge the Ministry of Higher Education Malaysia for supporting this work under Fundamental Research Grant Scheme (FRGS/1/2018/TK10/UMP/03/4) with UMP Vote No.: RDU190177.

REFERENCES

Abu, R; Mohamad, S; Zakaria, J; Mortan, S H and Yah, N A (2021). Water holding capacity and water release rate of bacterial cellulose-silver nanoparticles. *Proc. of Malaysian Technical Universities Conference on Engineering and Technology*. p. 472-473.

Abu, R; Mohamad, S; Zakaria, J; Mohd Amin, W N and Yin, C G C (2022). Water holding and release properties of bacterial cellulose produced from oil palm frond juice. *Mater. Sci. Forum, 1056*: 179-184.

Alyamani, A A; Al-Musawi, M H; Albukhaty, S; Sulaiman, G M; Ibrahim, K M; Ahmed, E M; Jabir, M S; Al-karagoly, H; Aljahmany, A A and Mohammed, M K A (2023). Electrospun polycaprolactone/ chitosan nanofibers containing *Cordia myxa* fruit extract as potential biocompatible antibacterial wound dressings. *Molecules, 28*: 2501.

Alzubaidi, A K; Al-Kaabi, W J; Ali, A A; Albukhaty, S; Al-Karagoly, H; Sulaiman, G M, Asiri, M and Khane, Y (2023). Green synthesis and characterization of silver nanoparticles using flaxseed extract and evaluation of their antibacterial and antioxidant activities. *Appl. Sci., 13*: 2182.

Araújo, I M S; Silva R R; Pacheco, G; Lustri, W R; Tercjak, A; Gutierrez, J; Júnior, J R S; Azevedo, F H C; Figuêredo, G S; Vega, M L; Ribeiro, S J L and Barud, H S (2018). Hydrothermal synthesis of bacterial cellulose–copper oxide nanocomposites and evaluation of their antimicrobial activity. *Carbohydr. Polym., 179*: 341-349.

Avcioglu, N H (2022). Bacterial cellulose: Recent progress in production and industrial applications. *World J. Microbiol. Biotechnol., 38(5)*: 1-13.

Ayyappan, V G; Vhatkar, S S; Bose, S; Sampath, S; Das, S K; Samanta, D and Mandal, A B (2022). Incorporations of gold, silver and carbon nanomaterials to kombucha-derived bacterial cellulose: Development of antibacterial leather-like materials. *J. Indian Chem. Soc., 99(1)*: 100278.

Aziz, T; Haq, F; Farid, A; Kiran, M; Faisal, S; Ullah, A; Ullah, N; Bokhari, A; Mubashir, M; Chuah, L F and Show, P L (2023). Challenges associated with cellulose composite material: Facet engineering and prospective. *Environ. Res., 223*: 115429.

Barabadi, H; Jounaki, K; Pishgahzadeh, E; Morad, H; Sadeghian-Abadi, S; Vahidi, H and Hussain, C M (2022a). Antiviral potential of green-synthesized silver nanoparticles. *Handbook of Microbial Nanotechnology* (Chaudery, M H ed.). Elsevier. p. 285-310.

Barabadi, H; Mohammadzadeh, A; Vahidi, H; Rashedi, M; Saravanan, M; Talank, N and Alizadeh, A (2022b). *Penicillium chrysogenum* derived silver nanoparticles: Exploration of their antibacterial and biofilm inhibitory activity against the standard and pathogenic *Acinetobacter baumannii* compared to tetracycline. *J. Clust. Sci., 33*: 1929-1942.

Barabadi, H; Webster, T J; Vahidi, H; Sabori, H; Kamali, K D; Shoushtari, F J; Mahjoub, M A; Rashedi, M; Mostafavi, E; Cruz, D M; Hosseini, O and Saravana, M (2020). Green nanotechnology-based gold nanomaterials for hepatic cancer therapeutics: A systematic review. *Iran. J. Pharm. Res., 19(3)*: 3-17.

Chandana, A; Mallick, S P; Dikshit, P K; Singh, B N and Sahi, A K (2022). Recent developments in bacterial nanocellulose production and its biomedical applications. *J. Polym. Environ., 30*: 4040-4067.

Gan, S; Chen, R S; Mohammad Padzil, F N; Moosavi, S; Tarawneh, M A; Loh, S K and Idris, Z (2023). Potential valorization of oil palm fiber in versatile applications towards sustainability: A review. *Ind. Crops Prod., 199*: 116763.

Ganesh Babu, M M and Gunasekaran, P (2009). Production and structural characterization of crystalline silver nanoparticles from *Bacillus cereus* isolate. *Colloids Surf B: Biointerfaces, 74(1)*: 191-195.

Harrison, T R; Gupta, V K; Alam, P; Perriman, A W; Scarpa, F and Thakur, V K (2023). From trash to treasure: Sourcing high-value, sustainable cellulosic materials from living bioreactor waste streams. *Int. J. Biol. Macromol., 233*: 123511.

Heidari, H; Teimuri, F and Ahmadi, A R (2022). Nanocellulose-based aerogels decorated with Ag, CuO and ZnO nanoparticles: Synthesis, characterization and the antibacterial activity. *Polyhedron, 213*: 115629.

Horue, M; Cacicedo, M L; Fernandez, M A; Rodenak-Kladniew, B; Torres Sánchez, R M and Castro, G R (2020). Antimicrobial activities of bacterial cellulose – Silver montmorillonite nanocomposites for wound healing. *Mater. Sci. Eng. C, 116*: 111152.

Ibraheem, D R; Hussein, N N; Sulaiman, G M; Mohammed, H A; Khan, R A and Al Rugaie, O (2022). Ciprofloxacin-loaded silver nanoparticles as potent nano-antibiotics against resistant pathogenic bacteria. *Nanomater., 12*: 2808.

Jabbari, F and Babaeipour, V (2023). Bacterial cellulose as a potential biopolymer for wound care.

A review. *Int. J. Polym. Mater. Polym. Biomater.* DOI: 10.1080/00914037.2023.2167080.

Jain, A S; Pawar, P S; Sarkar, A; Junnuthula, V and Dyawanapelly, S (2021). Bionanofactories for green synthesis of silver nanoparticles: Toward antimicrobial applications. *Int. J. Mol. Sci.*, *22*: 11993.

Jutakridsada, P; Suwannaruang, T; Kasemsiri, P; Weerapreeyakul, N; Knijnenburg, J T N; Theerakulpisut, S; Kamwilaisak, K and Chindaprasirt, P (2023). Controllability, antiproliferative activity, Ag^{+} release, and flow behavior of silver nanoparticles deposited onto cellulose nanocrystals. *Int. J. Biol. Macromol.*, *225*: 899-910.

Li, Z; Wang, L; Chen, S; Feng, C; Chen, S; Yin, N; Yang, J; Wang, H and Xu, Y (2015). Facilely green synthesis of silver nanoparticles into bacterial cellulose. *Cellulose, 22(1)*: 373-383.

Lim, H J; Cheng, W K; Tan, K W and Yu, L J (2022). Oil palm-based nanocellulose for a sustainable future: Where are we now? *J. Environ. Chem. Eng., 10(2)*: 107271.

Lin, W C; Lien, C C; Yeh, H J; Yu, C M and Hsu, S H (2013). Bacterial cellulose and bacterial cellulose-chitosan membranes for wound dressing applications. *Carbohydr. Polym.*, *94(1)*: 603-611.

Liu, Y; Lu, T; Sun, Z; Chua, D H C and Pan, L (2015). Ultra-thin carbon nanofiber networks derived from bacterial cellulose for capacitive deionization. *J. Mater. Chem. A, 3(16)*: 8693-8700.

Manosalva, N; Tortella, G; Cristina Diez, M; Schalchli, H; Seabra, A B; Durán, N and Rubilar, O (2019). Green synthesis of silver nanoparticles: Effect of synthesis reaction parameters on antimicrobial activity. *World J. Microbiol. Biotechnol.*, *35(6)*: 1-9.

Mohamad, S; Abdullah, L C; Jamari, S S; Osman Al Edrus, S S; Aung M M and Mohamad, S F S (2022). Production and characterization of bacterial cellulose nanofiber by *Acetobacter xylinum* 0416 using only oil palm frond juice as fermentation medium. *J. Nat. Fibers*, *19(17)*: 16005-16016.

More, P R; Pandit, S; Filippis, A D; Franci, G; Mijakovic, I and Galdiero, M (2023). Silver nanoparticles: Bactericidal and mechanistic approach against drug resistant pathogens. *Microorganisms*, *11*: 369.

Norrrahim, M N F; Farid, M A A; Lawal, A A; Tengku Yasim-Anuar, T A; Samsudin, M H and Zulkifli, A A (2022). Emerging technologies for value-added use of oil palm biomass. *Environ. Sci.: Advances, 1(3)*: 259-275.

Pal, S; Nisi, R; Stoppa, M and Licciulli, A (2017). Silver-functionalized bacterial cellulose as antibacterial membrane for wound-healing applications. *ACS Omega, 2(7)*: 3632-3639.

Pang, M; Huang, Y; Meng, F; Zhuang, Y; Liu, H and Du, M (2020). Application of bacterial cellulose in skin and bone tissue engineering. *Eur. Polym. J.*, *122*: 109365.

Parveez, G K A; Rasid, O A; Ahmad, M N; Taib, H M; Bakri, M A M; Hafid, S R A; Ismail, T N M T; Loh, S K; Abdullah, M O; Zakaria, K and Idris, Z (2023). Oil palm economic performance in Malaysia and R&D progress in 2022. *J. Oil Palm Res., 35(2)*: 193-216.

Qiu, Y; Qiu, L; Cui, J and Wei, Q (2016). Bacterial cellulose and bacterial cellulose-vaccarin membranes for wound healing. *Mater. Sci. Eng. C, 59*: 303-309.

Rashidi, N A; Chai, Y H and Yusup, S (2022). Biomass energy in Malaysia: Current scenario, policies, and implementation challenges. *BioEnergy Res., 15*: 1371-1386.

Sabarees, G; Velmurugan, V; Tamilarasi, G P; Alagarsamy, V and Raja Solomon, V (2022). Recent advances in silver nanoparticles containing nanofibers for chronic wound management. *Polymers, 14*: 3994.

Said Azmi, S N N; Samsu, Z A; Mohd Asnawi, A S F; Ariffin, H and Syed Abdullah, S S (2023). The production and characterization of bacterial cellulose pellicles obtained from oil palm frond juice and their conversion to nanofibrillated cellulose. *Carbohydr. Polym. Technol. Appl., 5*: 100327.

Saravanan, M; Barabadi, H; Vahidi, H; Webster, T J; Medina-Cruz, D; Mostafavi, E; Vernet-Crua, A; Cholula-Diaz, J L and Periakaruppan, P (2021). Emerging theranostic silver and gold nanobiomaterials for breast cancer: Present status and future prospects. *Handbook on Nanobiomaterials for Therapeutics and Diagnostic Applications* (Anand, K; Saravanan, M; Chandrasekaran, B; Kanchi, S; Panchu, S J and Chen, Q S eds.). Elsevier. p. 439-456.

Shaaban, M T; Zayed, M and Salama, H S (2023). Antibacterial potential of bacterial cellulose impregnated with green synthesized silver nanoparticle against *S. aureus* and *P. aeruginosa*. *Curr. Microbiol., 80(2)*: 1-9.

Shidlovskiy, I P; Shumilova, A A; Shishatskaya, E I and Volova, T G (2018). Properties of bacterial cellulose composites with silver nanoparticles. *Biophys., 63(4)*: 519-525.

Talank, N; Morad, H; Barabadi, H; Mojab, F; Amidi, S; Kobarfard, F; Mahjoub, M A; Jounaki, K; Mohammadi, N; Salehi, G; Ashrafizadeh, M and Mostafavi, E (2022). Bioengineering of green-synthesized silver nanoparticles: *In vitro* physicochemical, antibacterial, biofilm inhibitory, anticoagulant, and antioxidant performance. *Talanta*, *243*: 123374.

Volova, T G; Shumilova, A A; Shidlovskiy, I P; Nikolaeva, E D; Sukovatiy, A G; Vasiliev, A D and Shishatskaya, E I (2018). Antibacterial properties of films of cellulose composites with silver nanoparticles and antibiotics. *Polym. Test., 65*: 54-68.

Wu, J; Zheng, Y; Song, W; Luan, J; Wen, X; Wu, Z; Chen, Z; Wang, Q and Guo, S (2014). *In situ* synthesis of silver-nanoparticles/ bacterial cellulose composites for slow-released antimicrobial wound dressing. *Carbohydr. Polym., 102(1)*: 762-771.

Yang, G; Xie, J; Hong, F; Cao, Z and Yang, X (2012). Antimicrobial activity of silver nanoparticle impregnated bacterial cellulose membrane: Effect of fermentation carbon sources of bacterial cellulose. *Carbohydr. Polym., 87(1)*: 839-845.

Zakaria, M R; Ahmad Farid, M A; Andou, Y; Ramli, I and Hassan, M A (2023). Production of biochar and activated carbon from oil palm biomass: Current status, prospects, and challenges. *Ind. Crops Prod., 199*: 116767.

Zeng, M; Laromaine, A and Roig, A (2014). Bacterial cellulose films: Influence of bacterial strain and drying route on film properties. *Cellulose, 21(6)*: 4455-4469.

Journal of Oil Palm Research Vol. 36 (4) December 2024 p. 674-686
DOI: https://doi.org/10.21894/jopr.2023.0050

STRUCTURAL ALTERATION OF OIL PALM EMPTY FRUIT BUNCH BY PERACETIC ACID COMBINED WITH ULTRASONIC PRETREATMENT FOR XYLANASE PRODUCTION BY *Neosartorya* sp.

RAMA MOHAN POLUDASU[1]*; BENJAMAS CHEIRSILP[1] and PIYARAT BOONSAWANG[1]

ABSTRACT

The excess of oil palm empty fruit bunches (OPEFB) has caused significant ecological issues. Combined peracetic acid (PAA) and ultrasonication were used for OPEFB pretreatment. PAA solutions of varying strengths and duration of ultrasonication at a frequency of 37 kHz at 60°C were examined for OPEFB pretreatment. At 10% PAA for 60 min, the highest levels of cellulose (52.0 ± 0.2%), hemicellulose (39.5 ± 0.2%), and decreased lignin (11.3 ± 0.4%) were achieved. In the ideal pretreatment condition, the highest glucose levels (28 mg g^{-1}) and xylose (19 mg g^{-1}) was observed. Under a scanning electron microscope (SEM), a significant structural change in OPEFB before and after pretreatment was discovered. FTIR of OPEFB fibre had an absorption peak at 1727 cm^{-1}, which relates to the hemicellulose's C=O stretching. From the XRD studies, both crystalline and semi-crystalline zones may be seen in the diffractogram curves of OPEFB cellulose. Neosartorya *sp. BCC 18065 produced more xylanase (92 ± 0.03 IU g^{-1}) on pretreated OPEFB compared to untreated OPEFB (61 ± 0.01 IU g^{-1}). With more xylanase enzymes present during fermentation, xylose production was enhanced. The results demonstrate that structural changes in OPEFB can be changed by PAA-assisted ultrasonication pretreatment, which also improves enzymatic hydrolysis and saccharification.*

Keywords: characterisation, OPEFB, peracetic acid, ultrasonication, xylanase.

Received: 14 April 2023; **Accepted:** 25 August 2023; **Published online:** 6 October 2023.

INTRODUCTION

Up to 85% (or around 49.56 million tonnes) of the world's palm oil was produced in Indonesia and Malaysia in 2016, making them the two biggest producers in the world (Nurika *et al*., 2023). The oil palm empty fruit bunch (OPEFB) which is frequently discarded and incinerated at the palm oil mill, can be used as fertiliser at the plantation. Therefore, the OPEFB must be converted to protect the environment (reduce greenhouse gas emissions) and secure the future of the oil palm industry. The country would certainly benefit from the conversion of this waste into useful products. More and more people are becoming interested in regulating OPEFB, especially in industrial conversion. By utilising all fractions derived from the OPEFB as the raw material, it is expected that OPEFB valorisation to be maximised and thus, reduces the residues in the process of producing fuels and various chemical products of commercial interest (Rame, 2018; Tahir *et al*., 2022).

The majority of palm solid residues are lignocellulosic components, which have different compositions of lignin, cellulose and hemicellulose (Farhan *et al*., 2021). Currently, lignocellulosic substrates promote alternative feedstocks for the synthesis of bioethanol (Selvakumar *et al*., 2023). Typically, a substrate with a good proportion

[1] Center of Excellence in Innovative Biotechnology for Sustainable Utilisation of Bioresources, Biotechnology Program, Faculty of Agro-Industry, Prince of Songkla University, Hat Yai, 90110 Songkhla, Thailand.

* *Corresponding author e-mail: bioraam@gmail.com*

of cellulose and hemicellulose is utilised for the enzymatic synthesis of ethanol. OPEFB is suggested as an alternative feedstock for ethanol production, which indicates that the majority of its primary components are fermentable sugars, including xylose and glucose (Mardawati *et al*., 2022).

Cellulose is generally present as a linear polymer of glucose and hemicelluloses, which are branched copolymers of many sugars (*i.e.*, uronic acid, arabinose, mannose, galactose, and xylose), and lignin being the aromatic heterogeneous polymer of three monolignans units (*p*-coumaryl, sinapyl, and coniferyl) (Zhu and Pan, 2022). It is possible to hydrolyse cellulose and hemicelluloses to produce sugar. Due to the recalcitrant character of lignocellulosic biomass, an effective pretreatment step is required to maximise the yield of fermentable sugar and the intensity of enzymatic hydrolysis. Pretreatment is consequently required to delignify and promote the breakdown of the lignocellulosic moiety (Tran *et al*., 2019). Pretreatment involves modifying the biomass so that hemicelluloses and cellulose may be hydrolysed (enzymatically) more quickly, with higher sugar yields. Certain pretreatment conditions are required to eliminate lignin through sugar retention.

There are many pretreatment procedures, involving physical, chemical, and biological treatments which have been used to change the structural and chemical structure of the lignocellulosic substrate and to increase the yield of fermentable sugars (Kucharska *et al*., 2018). The steam pretreatment which employs a high-temperature-pressure reactor, is a viable pretreatment strategy to improve the enzymatic saccharification of OPEFB. Small-scale batch operating equipment, such as laboratory flasks, were mainly used in the research on the auto-hydrolysis process of biomass for the generation of bioethanol (Sari *et al*., 2021). The oxidative pretreatments involve various mechanisms, depending on the situation. The options for pretreatment include the utilisation of ozone or oxygen, moist oxidation, and the application of oxidising solvents like hydrogen peroxide (H_2O_2) and peracetic acid (PAA) (Bussemaker and Zhang, 2013). The hydroxonium ions produced by strong oxidising agents like PAA target the electron sites of lignin, and thus have been described as selective and effective as delignification agents (Jia *et al*., 2015). In the presence of a sulfuric acid catalyst, PAA can be made by combining H_2O_2 with acetic acid. By removing as little lignin as possible, this PAA pretreatment process effectively de-lignifies biomass, thereby improving the probability that the cellulose fraction will be converted (Gill *et al*., 2021).

The ultrasonic solution treatment is an innovative emerging technique which has the potential to replace pretreatment technology. By dividing the intermolecular connection, sonication uses ultrasonic radiation to agitate the particles and facilitate the disintegration of molecules. There is a chance to successfully replace traditional hydrolysis techniques with ultrasonication (Wong *et al*., 2009). However, lignocellulosic biomass sonication depends on several parameters, including ultrasonic intensity, frequency, power, medium used, temperature, time and solid loading (Luo *et al*., 2014). Aqueous mediums are subjected to ultrasonic treatment to cause cavitation, which generates conditions of high temperature, pressure, and powerful shear forces. Lignin is released after the breaking of lignin-carbohydrate linkages that occur as a result of ultrasound exposure (Subhedar and Gogate, 2014). Studies by Subhedar *et al.* (2015) and Olughu *et al.* (2021), demonstrated the impact of ultrasonication on the destruction of lignocellulosic substrates, however, there is not much current information existing on the effectiveness of PAA-assisted ultrasonication on OPEFB. Due to this, we predicted that using PAA and ultrasonication together, it might significantly improve the enzymatic saccharification of OPEFB fibre residues.

The main enzymes which are responsible for destroying the xylosidic linkages in the biomass xylan structure are known as xylanases. Microbial xylanases exhibit a range of substrate specificities and biochemical characteristics, thus making them appropriate for use in a variety of biotechnological and industrial applications (Bhardwaj *et al*., 2019). *Neosartorya* spp. is a member of the *Aspergillaceae* family and is known as an ascomycete. They have special heat-resistance features that enable them to survive in extreme temperatures. *Neosartorya glabra* is used for the production of exo-polygalacturonase (Desagiacomo *et al*., 2021). The genus *Neosartorya fischeri* produces β-Glucosidase enzyme, which has a broad substrate specificity and shows glucanase, cellobiase, xylanase, and glucosidase activities (Yang *et al*., 2014).

Utilising inexpensive substrate is beneficial economically from an industrial perspective for synthesising enzymes. The ability of PAA-aided ultrasonication to pretreat the OPEFB and increase enzyme production was the primary focus of the current study. The effects of pretreatment-induced structural and compositional changes to OPEFB on solid substrate fermentation (SSF) production of value-added bioproducts including xylanase and sugars were investigated. This is the first study to report the use of the fungus *Neosartorya* sp. BCC 18065 to produce xylanase and sugar on pretreated OPEFB.

MATERIALS AND METHODS

OPEFB Substrate

OPEFB was collected from the palm oil mill industry (Trang Province, Thailand). The collected OPEFB was then continually cleaned with purified water to eliminate any debris, dust, or other unwanted contaminants, and then dried in an oven for 24 hr at 70°C-80°C to get a constant dry weight. The necessary particle size of 1 to 2 mm was achieved by using a hammer mill to crush the dried OPEFB fibre, which was then processed through a sieve shaker (18 mm meshes) before being kept in sealed plastic bags at ambient temperature until used in the experiment. For the proximate analysis, a fresh OPEFB substrate was also created.

Peracetic Acid-assisted Ultrasonication Pretreatment of Biomass

In three separate 250 mL Erlenmeyer flasks, 5 g of dried OPEFB substrate and 100 mL of PAA were combined at three different concentrations (w/v): 5%, 10%, and 15%. After thoroughly mixing the contents, the flasks were submerged in an ultrasonic bath (Germany's Elma E series) and sonicated for various lengths of time: 40, 60, and 80 min at 37 kHz frequency with an ultrasonic power of 200-250W at 60°C. For the control treatment, no sonication is required. The produced slurry residue was then divided into solid and liquid parts, once the experiment finished. The solid filtrate was oven-dried for 24 hr at 60°C-70°C and then kept for future research, following a distilled water rinse. Exactly 20 mL of 1% v/v H_2SO_4 was mixed with 1 g of solid substrate when its pH was around 7.0. After that, they undergo autoclave hydrolysis for 1 hr at 121°C. Whatman No. 1 filter paper was used to filter the hydrolysed samples after the reaction finished. The quantitative and qualitative characteristics of reducing sugars were ascertained by the obtained supernatant.

Assay Methods

The components of the OPEFB substrates (cellulose, hemicelluloses and lignin) were evaluated, and moisture and ash content were also analysed according to the AOAC (1990) methods. The hydrolysate's total soluble sugars (TS) were measured using the simple, rapid phenol-sulfuric acid method (Dubois *et al*., 1956). The 3, 5-dinitro salicylic acid (DNS) method (Miller, 1959) was employed to quantify the concentration of reducing sugars. By using the stated method (Khabarov *et al*., 2006), the amounts of xylose and arabinose were determined.

FTIR Spectrum of OPEFB

The surface functional groups of both untreated and pretreated OPEFB were recognised by Fourier transform infrared (FT-IR) spectroscopy (Perkin Elmer Spectrometer, England). Before the examination, tests were blended in with potassium bromide (KBr), and the resultant combination was squeezed into a pellet. The IR spectrum was gathered with a resolution value set at 4 cm^{-1} across a range of 500-4000 cm^{-1}.

Scanning Electron Microscopy (SEM) of OPEFB

Utilising SEM and imaging, morphological and structural alterations in pretreated and untreated OPEFB were found. First, double-sided carbon tape was used to attach the solid samples to the aluminium sample stabs. After that, a picture was captured using an acceleration voltage of 10 kV.

X-ray Diffraction of OPEFB

An X-ray diffractometer (XRD, PHILIPS, X'Pert MPD) was used with a 40 kV applied voltage and a 30 mA current to observe the complex crystalline structure of OPEFB both before and after pretreatment. With a step size of 0.03° in the range of 2 = 5°-50° and the Equation (1) presented below (Segal *et al*., 1959) as a reference, the crystallinity index (CrI) was calculated from the samples.

$$CrI\ (\%) = \frac{I_{002}\text{-}I_{18.0°}}{I_{002}} \times 100 \quad (1)$$

where I_{002} denotes the maximum diffraction intensity at the 002 lattice, and $I_{18.0°}$ denotes the maximum diffraction intensity at 18.0°, 2θ°.

Xylanase Producing Fungus Strain and Inoculum Preparation

Neosartorya sp. BCC 18065 was purchased from the National Center for Genetic Engineering and Biotechnology (BIOTEC), Pathum Thani, Thailand. Stock cultures of the organism were preserved on Potato Dextrose Agar (PDA) Slant at 40°C.

A 250 mL clean Erlenmeyer flask was utilised to make a 100 mL broth that included (% w/v): xylan (Birchwood) (0.5), KCl (0.01), Peptone (0.09), $(NH_4)_2HPO_4$ (0.04), and $MgSO_4.7H_2O$ (0.01). The pH was then adjusted to 7.0, and the flask was then sterilised at 121°C for 15 min. To get the mycelial suspension as inoculum, *Neosartorya* sp. BCC 18065 spore suspension was then injected and incubated in a continuous rotating shaker (at 120 rpm) at 33°C-340°C for 72 hr.

Solid Substrate Fermentation (SSF)

Separate SSF tests employing untreated and pretreated OPEFB were conducted. Along with the 5 g of OPEFB substrate, the 500 mL conical flasks contained a basal fermentation medium made up of the following ingredients: (g L^{-1}): $MgSO_4.7H_2O$ 0.6; $(NH_4)_2SO_4$ 1.4; KH_2PO_4 1.6; $CaCl_2.2H_2O$ 0.4; urea 0.2; yeast extract 0.2; proteose peptone 0.25; together with a mineral salt solution with traces of elements [$MnSO_4.7H_2O$, 4.60; $CoCl_2.2H_2O$, 1.50; $ZnSO_4.7H_2O$, 3.34; $FeSO_4.7H_2O$, 3 mg L^{-1} (pH 7.0)]. The fermentation medium's moisture percentage was retained between 70% and 72% using a basal medium. They were autoclaved at 121°C for 15 min, after uniformly mixing the contents of the Erlenmeyer flasks. The flasks were then allowed to reach room temperature. Following this, flasks were inoculated with a 5 mL *Neosartorya* sp. BCC 18065 spore suspension (1×10^8 spores mL^{-1}) and cultured at ambient temperature for 6-7 days under aseptic conditions. To eliminate the fungal biomass, the broth was centrifuged after being collected under the laminar airflow hood chamber during fermentation. The collected supernatant was then analysed for xylanase and estimate xylose sugars.

Assay of Xylanase

The xylanase activity was calculated following Bailey *et al*. (1992). For this assay, 1.8 mL of a 1.0% (w/v) Azo-xylan (birch wood) solution was made in 50 mM sodium citrate buffer (pH 5.3) with 0.2 mL of enzyme dilution (in 50 mM sodium citrate buffer, pH 5.3) and allowed to incubate for 5 min at 50°C. The DNS method which required mixing 3 mL of DNS reagent and incubating the mixture for 5 min at 95°C, was employed to calculate the quantity of released reducing sugars. The end reaction was stopped by conditioning it with cold water. The solution's 540 nm wavelength was then measured with a UV-visible spectrophotometer. The quantity of enzyme that generates 1 mol of xylose equivalent every min is considered one international unit of enzyme activity.

RESULTS AND DISCUSSION

PAA/Ultrasonic Pretreatment of OPEFB

Pretreatment is a vital step in converting lignocellulose into fermentable sugars. The purpose of the pretreatment is to separate the lignin and disrupt the lignocellulose's structure, and in this study, it is typically carried out using PAA and ultrasonication. *Table 1* displays the chemical and proximate composition of untreated OPEFB. The primary constituents of untreated OPEFB are cellulose (32.6 ± 0.4%), hemicelluloses (28.4 ± 0.2%), and lignin (25.0 ± 0.4%). This reveals that cellulose and hemicellulose together make up around 50% of the dry weight of OPEFB. A pretreatment was applied to increase the cellulose and hemicellulose yields from untreated OPEFB biomass.

TABLE 1. CHEMICAL COMPOSITION OF UNTREATED OPEFB

No.	Components	%
1	Moisture	10.0 ± 0.2
2	Ash	1.5 ± 0.3
3	Cellulose	32.6 ± 0.4
4	Hemicellulose	28.4 ± 0.2
5	Lignin	25.0 ± 0.4
	Sugars	**mg g^{-1}**
6	Total sugars	20.2 ± 0.1
7	Reducing sugars	18.4 ± 0.3
8	Glucose	10.8 ± 0.1
9	Xylose	7.4 ± 0.2
10	Arabinose	3.6 ± 0.8

Note: Except moisture in OPEFB, all the remaining composition of substrate was analysed based on dry weight basis (%). Values are mean of two replicates.

The PAA concentrations of around 5%, 10%, and 15% (w/v) were examined against three different ultrasonication durations (40, 60, and 80 min) at 60°C to establish the most efficient ratio of PAA concentration and ultrasonication duration for OPEFB biomass hydrolysis. The composition of the pretreated OPEFB was determined under various circumstances and shown in *Figure 1*. It indicates that pretreatment makes lignin soluble, increasing the quantity of cellulose and hemicellulose.

The ideal pretreatment conditions for achieving the highest yield were observed to be 10% PAA with a 60 min ultrasonication period at 60°C. The findings showed that both cellulose (52.0 ± 0.2%) and hemicellulose (39.5 ± 0.2%) were increased along with a decrease in lignin (11.3 ± 0.4%). Delignification is a crucial indicator of an efficient pretreatment process because lignin prevents the enzymatic breakdown of carbohydrates. The proportion of lignin removed during the pretreatment under various circumstances ranged from 5.5%-54.8% (*Figure 1*). This demonstrates that PAA might respond selectively to lignin without significantly degrading cellulose and that it can help separate cellulose from other components. This present result was compared with Palamae *et al*. (2014), who found that acid-insoluble lignin, hemicellulose, and cellulose made up around 16%, 36%, and 47% respectively, in the pretreated

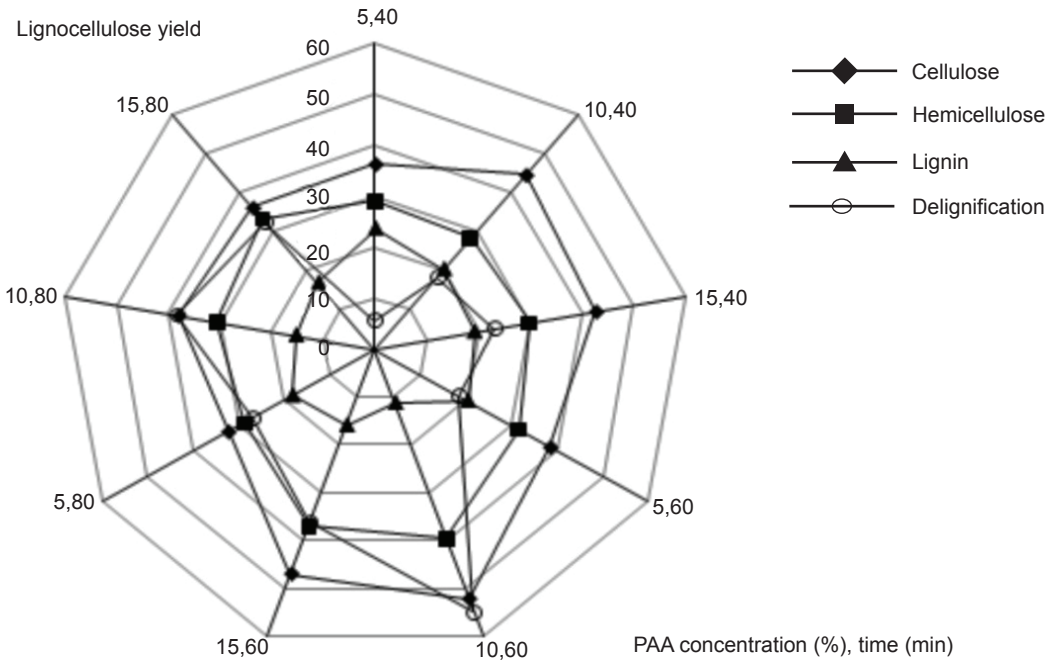


Figure 1. PAA assisted ultrasonication pretreatment of lignocellulose yield.

EFB fibre under optimal circumstances (20 mL PAA per g of OPEFB, 35°C, reaction time for 9 hr). The majority of the hemicellulose was retained, whereas around 53% of the lignin was removed. The extended pretreatment duration (80 min), however, was the cause of the lower cellulose and hemicellulose yields. To successfully delignify and increase the carbohydrate content of OPEFB, a shorter pretreatment period (40 min) with a lower PAA concentration (5%) is insufficient. The sonication time has the biggest impact on the pretreatment that is obtained. As the duration of sonication increases, the amount of delignification and sugar released from the biomass also increases, but the sonication which lasts longer than a specific period of time, has no further advantage.

Switchgrass (*Panicum virgatum* L.) was subjected to ultrasonic irradiation, and Olughu *et al*. (2021) studied the molecular, microstructural, and delignification alterations that occurred. The percentage of delignification, according to their research, varied between 1.86% and 20.11%. The results demonstrated that sonication time, followed by acoustic power, has the greatest influence on ultrasonic delignification. Switchgrass undergoes chemical and structural changes as a result of ultrasonic irradiation. The improvement in delignification was made possible by the hydrodynamic shear forces brought on by sonication. The variation in lignin percentage between pretreated and untreated EFB suggests that lignin was degraded during combined pretreatment. The extent of delignification increases from 16.00% to 44.00% with a change in temperature from 313 K to 373 K, with 353 K being the optimum temperature, above which an increase in temperature has only a minimal impact on delignification, as reported by Subhedar *et al*. (2015) in their study of delignification of waste newspaper using ultrasound. Different types of biomass must have different optimum temperatures; hence, it is critical to investigate how temperature influences EFB for a specific ultrasonic reactor configuration. Moreover, studies show that ultrasonication may shorten pretreatment periods and be beneficial for the extraction of cellulose and hemicellulose from lignocellulosic material. Chemical pretreatment is used to delignify lignocelluloses, and this recovery may be mainly due to the reduction in lignin. Based on the difference in lignin percentage between pretreated and untreated EFB, the lignin was eliminated during combined pretreatment.

Additionally, the pretreatment may produce a higher percentage of glucan and xylan in the pretreated OPEFB. *Figure 2* shows the yields of various sugars during the PAA/ultrasonic pretreatment of the OPEFB substrate. The findings of this investigation suggested that the PAA/ultrasonic pretreatment might significantly increase the yield of fermentable sugar. The pretreated OPEFB had a much higher quantity of sugar than the untreated OPEFB. Research by Patil *et al*. (2019) showed that when compared to traditional methods used for sawdust, the ultrasonic-assisted operations resulted in effective delignification as well as a higher yield of reducing



Figure 2. Effect of PAA assisted ultrasonication on different sugar yields.

sugars in a treatment time of 3 hr at 50°C. Overall, it was found that compared to traditional treatment methods, ultrasonic-assisted delignification and enzymatic hydrolysis produced around 1.5 times more lignin removal and 1.6 times more reducing sugar yield, respectively. The findings of the present experiment suggest that pretreated OPEFB produced more glucose than untreated OPEFB. PAA pretreatment greatly decreased lignification rates in the OPEFB, especially when it was combined with ultrasonication. The pretreatment, however, was completed using 10% PAA and a 60 min ultrasonication time when the temperature was low (60°C).

To avoid losing the reaction mixture due to substantial heating, experiments were not carried out over 60°C. The yield of reducing sugars in the hydrolysis process may be negatively impacted by the degradation of polysaccharides, particularly cellulose, which can occur when temperatures are much higher than normal (Subhedar and Gogate, 2014). This mild pretreatment condition facilitates the delignification process by preserving cellulose and hemicellulose in the final OPEFB substrate and promoting cellulolysis and xylanolysis. Under ideal pretreatment conditions, pretreatment with PAA improves the high-yield recovery of carbohydrate (Glucose) content in the solid phase and reduces carbohydrate loss (Kundu *et al*., 2021). After pretreatment, the hardwood and softwood recovered 90%-95% of their glucan content. The recovery of all sugars except glucan declined as response time increased.

Based on the findings depicted in *Table 1*, the original, untreated OPEFB substrate had low quantities of both total and additional sugars. At 10% PAA and 60 min of ultrasonication, the pretreated OPEFB produced higher concentrations of reducing sugar (42.0 mg g^{-1}), glucose (28.0 mg g^{-1}), xylose (19.0 mg g^{-1}), and arabinose (7.8 mg g^{-1}). The yield of sugar was extremely low at both short retention (40 min) and high retention (80 min) times. The yield of the released sugar, however, decreased as the concentration of acid increased (15%). The formation of furfural, hydroxyl methyl furfural, and acetic acid in more challenging conditions appears to be the reason for the drop in sugar yields. When these by-products were produced during the pretreatment, there may be less cellulose in the solid residue, which would reduce the yield of released sugars. Increasing pretreatment time and temperature would result in a decrease in the output of xylose and arabinose since hemicelluloses are frequently more easily degraded than cellulose. Furfural production was linked to a greater xylose content than glucose in hydrolysates.

Based on these findings, pretreatment duration and PAA concentration significantly influenced sugar yields. Sugar yields decrease as the pretreatment time exceeds the optimal point (80 min). The present

study is compared with that of Song *et al*. (2015), who used three levels of ultrasound power (0%, 30%, and 70%) to prepare poplar wood biomass, and they discovered that the ultrasound-assisted 15 min dilute acid pretreatment will increase the sugar production by roughly 10% to 40%. They also reported that the longer periods at relatively low power densities of around 0.5 W mL^{-1} showed minimal impact and increased ultrasonic power, and time during ultrasonic treatment, all which had substantial effects on hydrolysis efficiency.

FTIR Spectrum of OPEFB

OPEFB's structural modification was successfully achieved via PAA/ultrasonic treatment. The hydroxonium ion or H_3O^+, which PAA generates in acidic media attacks the electron sites of lignin and causes electrophilic substitution with ring hydroxylation, oxidative ring-opening, oxidative demethylation, cleavage of β-aryl ether bonds, displacement of side chains, and epoxidation of olefin structure (Zhao *et al*., 2017).

The FTIR spectra of untreated and pretreated OPEFB are shown in *Figure 3*. In both the untreated and pretreated OPEFB, they displayed strong peaks at 3100-3400 and 1000-1100 cm^{-1}. The large absorption band in the spectral region of 3100-3400 cm^{-1} is a result of the particular hydrogen-bonded -OH stretching vibration of cellulose, which appeared in the FTIR spectra of both untreated and pretreated OPEFB (Senusi *et al*., 2020). In addition, the lignin's C-O-C stretching vibrations are represented by the peak at 1000-1100 cm^{-1}. The OPEFB fibre also had an absorption peak at 1727 cm^{-1}, which relates to the hemicellulose's C=O stretching (Ghali *et al*., 2012). These peaks, which were seen in both the pretreated and untreated OPEFB, suggest that hemicellulose was still available after pretreatment. A single absorption peak at 1319 cm^{-1}, which represented the C-H in-plane bending of cellulose (Shi and Li, 2012), was only found in the pretreated OPEFB. The untreated OPEFB missed this peak. It appears that a portion of the lignin was solubilised during the PAA pretreatment procedure and may have been lost. Chemical analysis of the (*Figure 1*) sample clearly shows that lignin has been solubilised, whereas cellulose and hemicellulose have been maintained in the pretreated OPEFB. After the pretreatment, the vibrational peak of about 2900 cm^{-1}, which is connected to the C-H stretching vibration in cellulose and hemicelluloses was reduced, suggesting partial lignin removal and hemicelluloses (Shang *et al*., 2020). The peak at 1645 cm^{-1} in the pretreated OPEFB may be caused by the adsorbed water's bending mode when it interacts with the cellulose fibre (Inamuddin *et al*., 2019).

The pretreated OPEFB sample did, however, show enhanced intensities in the ranges of 3400, 1200 and 1500 cm^{-1}, as well as 600-850 cm^{-1}. These findings, however, suggested that the OPEFB substrate has a variety of absorption bonds that are often observed at 1030, 1239, 1457 and 1727 cm^{-1}. Both untreated and pretreated OPEFB exhibited

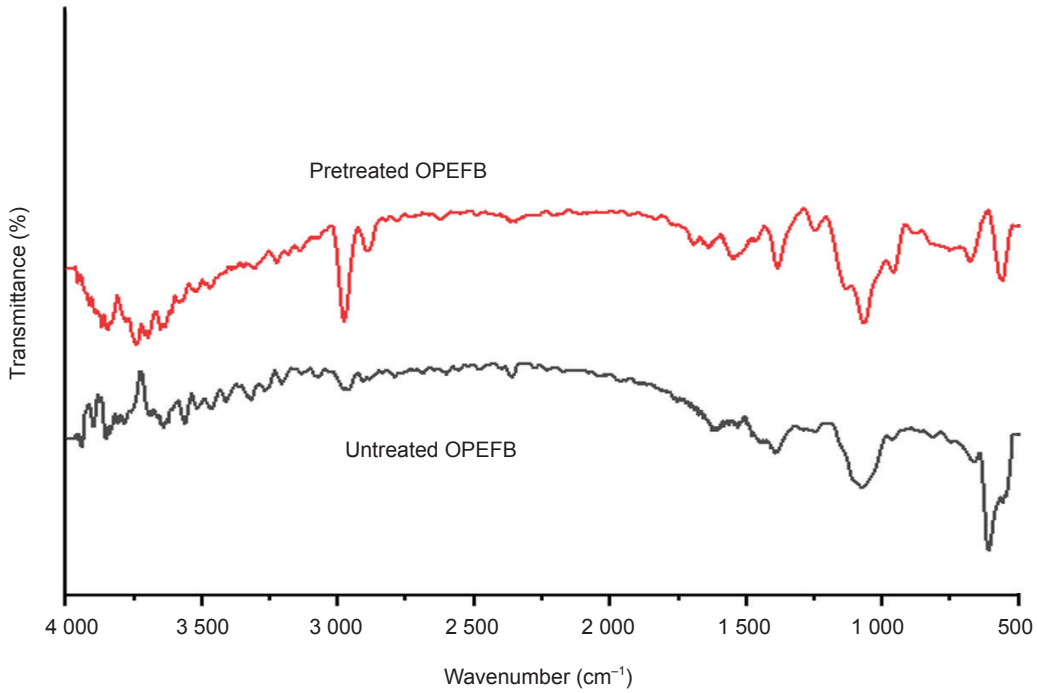


Figure 3. FTIR spectra of untreated and pretreated OPEFB.

hemicellulose assignment at 1727.00 cm^{-1} (C=O conjugates in xylans). However, a well-defined peak with high intensity at 1030.00 cm^{-1} was discovered and gradually disappeared as PAA concentration increased (Pandey and Pitman, 2003). This peak is also attributed to guaiacyl moieties. As the temperature rises, the peak of about 1239.00 cm^{-1} is the first to start decreasing in size, and data indicates that this band has a mixed origin. According to Acquah *et al*. (2016), it is created via syringyl nuclei in lignin and C=O linkages in hemicelluloses. All spectra had the same peak at 1457.00 cm^{-1}, which is connected to the asymmetric bending of the CH_3 and methoxy ($-OCH_3$) groups found in lignin, demonstrating the retention of lignin in the matrix (Labbe *et al*., 2005).

The absorption spectral bands in the 1200.00-800.00 cm^{-1} region may indicate the type of polysaccharide present. According to Labbe *et al*. (2005), typical arabinoxylan peaks have regions of between 1152.00 and 995.00 cm^{-1}, due to the vibrational stretching and bending of C-O, C-C, and C-OH. The degree of branching at the O-2 and/or O-3 sites is strongly correlated with the absorption intensity in this region (Inamuddin *et al*., 2019). Furthermore, all hemicellulosic fractions have a high absorbance at 896.00 cm^{-1}, which is relevant to either the C-1 group frequency or the ring frequency, indicating the occurrence of β-glycosidic connections between xylose units in the hemicelluloses (Revanappa *et al*., 2010). The spectral band identified in the current study was in the region of 898.05 cm^{-1} in both untreated and pretreated OPEFB.

SEM of OPEFB

To further examine the effectiveness of pretreatment on the OPEFB surface, SEM analysis was also performed. SEM images of both untreated and pretreated OPEFB are shown in *Figure 4a* and *4b*. The untreated OPEFB surface had a rough, hard appearance and was covered with silica bodies (*Figure 4a*). The structure is compact and densely arranged, and there are no holes or pores observed on the OPEFB surface. Due to the presence of high levels of lignin and hemicellulose, the structure looks highly compact. Hence, little cellulose and hemicellulose were accessed by enzymes. The most well-known mineral seen on the exterior of woody plants is often silica bodies (silicon dioxide), which are created when soil minerals invade and solidify in sedimentary cavities between and inside the cell wall during plant growth (Yoon and Kim, 2008). As can be observed, the surface shape of the untreated fibre is the main physical barrier preventing enzymes from accessing the surface, cellulose, and hemicellulose hydrolysis for the creation of sugar. Pretreatment is, therefore, necessary to remove these silica solids and destroy the resistant fibre surface in order to permit the entrance of an enzyme. The surface morphology of OPEFB after 60 min of 10% PAA-assisted ultrasonication is displayed in *Figure 4b*. It was found that the pretreatment effectively removed the silica bodies deposited on the outside of the fibre strands by leaving unfilled sedimentary cavities. The degradation of the lignocellulosic structure was increased by pretreatment. The compact structure of the OPEFB was significantly damaged as a result of the removal of the binding polymers. Intra- and intermolecular linkages are present in lignocellulosic biomass components, which contribute to the compact structure of the biomass. SEM images demonstrate the breakdown of these structures, which is consistent with the decomposition of the chemical constituents of the treated OPEFB. The processing caused the lignin covering and fibre surface to become disturbed. Surface disturbance might make cellulose and hemicellulose more accessible to microorganisms and enzymatic processes for future bioconversion. Additionally, it was shown that pretreatment reduced the fiber bundle size, which could expand the area accessible for enzyme entry and improve enzyme accessibility. The creation of holes and cracks along the internal components of the OPEFB suggested that PAA-assisted ultrasonication had been effectively utilised to alter the structure of the OPEFB.

According to Mesa *et al*. (2011), the pretreatment disintegrated the lignin and lignin-carbohydrate connections, leaving behind thick residues that were primarily composed of cellulose and hemicellulose. Another physical barrier preventing enzyme action on both cellulose and hemicelluloses is the coating of lignin on the fibre surface. Delignification is therefore an important stage in the pretreatment process to remove this physical barrier to enzymatic saccharification.

X-ray Diffraction (XRD) of OPEFB

XRD experiments were conducted to ascertain the degree to which raw OPEFB and chemically treated fibers are crystalline. The findings of the XRD examination of untreated and pretreated OPEFB are shown in *Figure 5*. Untreated OPEFB cellulose has a maximum cellulose I content of roughly 28.10%, whereas pretreatment lowers the cellulose I concentration to around 25.23%. However, after 60 min of hydrolysis, it was determined that the fiber crystallinity index had somewhat decreased, possibly as a result of excessive PAA exposure. After 60 min of sulphuric acid hydrolysis, the pretreated OPEFB had a CrI of about 54%, which was lower than the untreated OPEFB data, which had a CrI of 55% (Fahma *et al*., 2010). The CrI values of the regenerated cellulose-rich solids were reduced, making them more amenable to

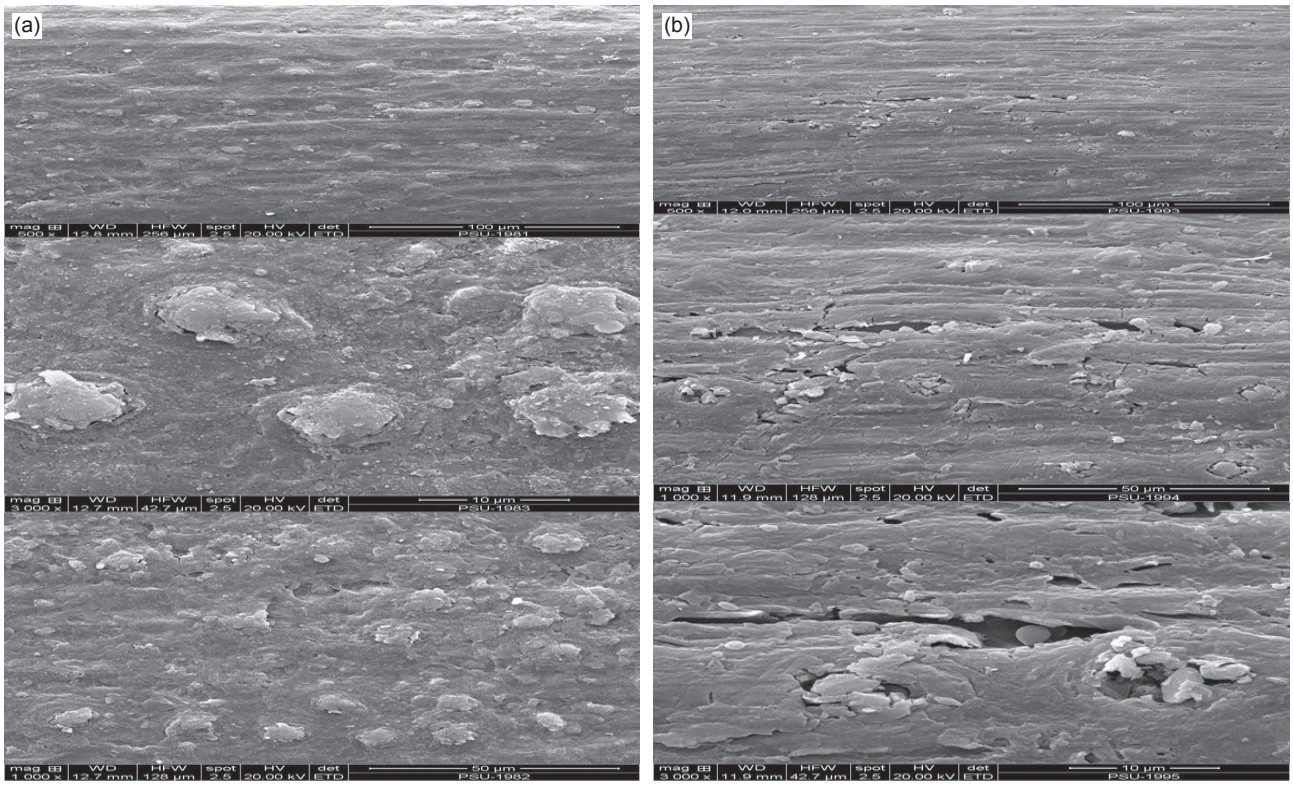


Figure 4. (a) Scanning electron microscope (SEM) images of untreated OPEFB at 500x, 1000x and 3000x magnification. (b) Scanning electron microscope (SEM) images of OPEFB treated at 600°C for 60 min (10% PAA), at 500x, 1000x and 3000x magnification.

enzymatic hydrolysis. The materials' CrI was not considerably impacted by pretreatment, but a more significant decrease in CrI was seen for straw, which explains the reduced recalcitrance of straw cellulose. A correlation exists between the stiffness of the cellulose structure and crystallinity, which can lead to fibres with higher tensile strengths. Both crystalline and semi-crystalline zones may be seen in the diffractogram curves of OPEFB cellulose in *Figure 4a* and *4b*. The existance of a visible peak on the shoulder at two diffraction angles between 22.0° and 25.4° shows that this type of behaviour is caused by the presence of a minimal amount of cellulose II. During the ultrasonication pretreatment procedure, the potential energy of the expanded bubble is converted into the kinetic energy of a liquid jet that passes through the interior of the bubble, penetrates the opposing bubble, and strikes the surface molecule of the cellulose. Continuous physical pressures contribute to particle breakage and initiate the process of cellulose polymers being cut into shorter chains of cellulose. The combined PAA treatment improved the cellulose yield. Comparable to untreated OPEFB, pretreated OPEFB has a lower crystallinity index. This could be because the non-selective processes like ultrasonication, can remove both amorphous and crystalline celluloses.

Xylanase Production in SSF

The goal of the current work was to produce xylanase enzyme using *Neosartorya* sp., a fungus, from OPEFB, which had been made with PAA-assisted ultrasonication and left untreated. It was discovered that OPEFB prepared with 10% PAA/ultrasonic for 60 min produced more enzymes (92 ± 0.02 IU/g) than untreated OPEFB (61 ± 0.01 IU/g) (*Figure 6*). The enzyme activity was higher on the fifth day, and as fermentation continued, the enzyme activity on both OPEFB substrates continued to decline. The lack of hemicellulose (xylan) and the depletion of the medium's micro- and macronutrients may be the causes of the decrease in enzyme synthesis.

Additionally, *Figure 7* displays the yield of xylose sugar during enzymatic hydrolysis. Compared to the pretreated substrate (46 ± 0.02 mg g^{-1}), less xylose was generated from the untreated OPEFB (34 ± 0.03 mg g^{-1}). On the fifth day, the xylose output reached its maximum; subsequently, it declined, possibly because of the consumption of sugar for fungal development. The results of this study showed that OPEFB pretreatment seemed to promote the synthesis of xylanase, which was associated with a higher level of xylose. The hemicellulose in the pretreated OPEFB was predicted to be broken down more

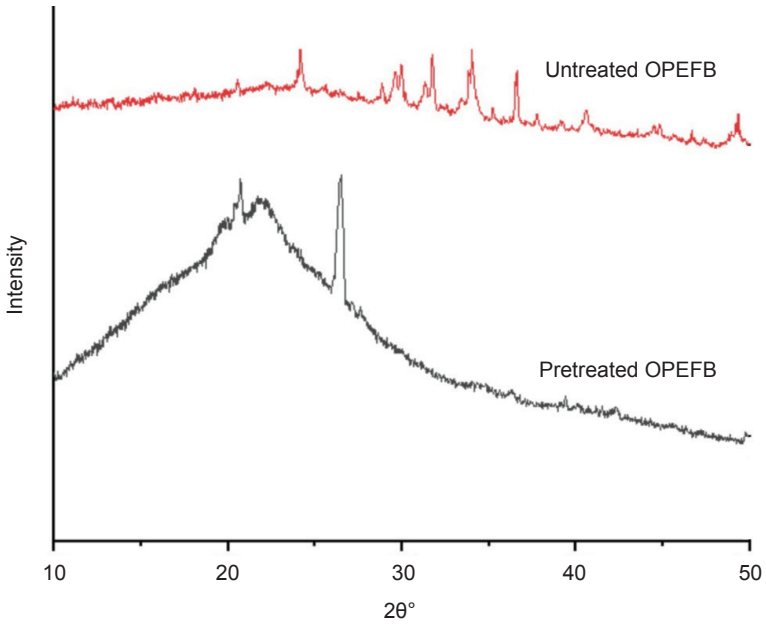


Figure 5. X-ray diffraction of untreated and pretreated OPEFB.

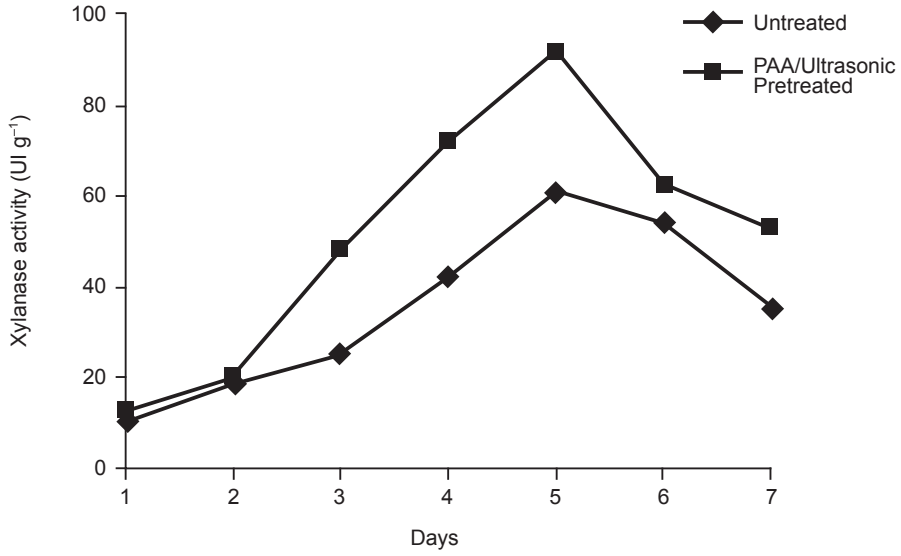


Figure 6. Xylanase enzyme activity (IU/g) on untreated and PAA/Ultrasonic pretreated OPEFB.

effectively, and theoretically, more xylose would be produced with higher xylanase activity. It has been demonstrated that pretreatment efficiently delignifies OPEFB substrates by lowering cellulose crystallinity and loosening the lignin structure, thereby increasing the substrate's porosity. The results of this study reveal that the fungus ability to produce xylanase may vary depending on the substrate used. As a result, xylanase production is enhanced when the substrate has more readily available hemicellulosic components. The results of this study were compared to those of Alves-Prado *et al*. (2010), whom reported that *Neosartorya spinosa* was an effective producer of xylanase when cultured on SSF using wheat bran and corncobs after a 72 hr fermentation.

CONCLUSION

According to the current findings, PAA-assisted ultrasonication is appropriate for the generation of fermentable sugars with holo-cellulose (cellulose and hemicellulose). Additionally, the pretreatment increases the quantity of lignin removed from the treated substrate. The elimination of lignin is indicated by an FTIR result, and XRD examination supported the reduction in cellulose crystallinity,

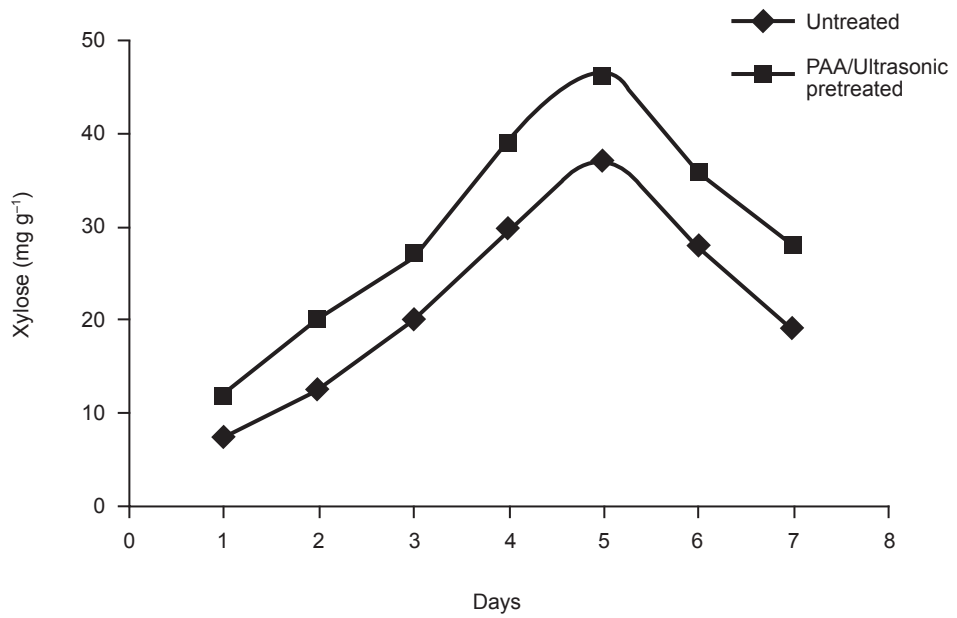


Figure 7. Yield of xylose sugar during enzymatic hydrolysis on untreated and PAA/Ultrasonic pretreated OPEFB.

which is crucial for the yields of fermentable sugar in pretreated OPEFB. As opposed to alternative pretreatment techniques, the current method is appealing since it is low-energy, low-cost, and economically feasible because the procedure is done at room temperature. Additional research will concentrate on statistical optimisation techniques (RSM, Taguchi, *etc.*) to increase enzyme production from a fungus strain.

ACKNOWLEDGEMENT

We acknowledge the Prince of Songkhla University, Hat Yai, for supporting this research with funding under the Postdoctoral Fellowship Program. The corresponding author and third authors are supported by the Thailand Research Fund under Grant No. RTA6280014.

REFERENCES

Acquah, G E; Via, B K; Fasina, O O and Eckhardt, L G (2016). Rapid quantitative analysis of forest biomass using Fourier transform infrared spectroscopy and partial least squares regression. *J. Anal. Methods. Chem.*, *2016*: 1-10. DOI: 10.1155/2016/1839598.

Alves-Prado, H F; Pavezzi, F C; Leite, V M; Sette, L D and Silva, R (2010). Screening and production study of microbial xylanase producers from Brazilian Cerrado. *Appl. Biochem. Biotechnol., 161*: 333-346. DOI: 10.1007/s12010-009-8823-5.

AOAC (1990). *Official Methods of Analysis of the Association of Official Chemists*. 15th edition. Helrich K., ed., AOAC Inc., Arlington, VA., USA.

Bailey, M J; Biely, P and Poutanen, K (1992). Inter laboratory testing of methods for assay of xylanase activity. *J. Biotechnol., 23*: 257-270. DOI: 10.1016/0168-1656(92)90074-J.

Bhardwaj, N; Kumar, B and Verma, P (2019). A detailed overview of xylanases: An emerging biomolecule for current and future prospective. *Bioresour. Bioprocess., 6*: 40. DOI: 10.1186/s40643-019-0276-2.

Bussemaker, M J and Zhang, D (2013). Effect of ultrasound on lignocellulosic biomass as a pretreatment for biorefinery and biofuel applications. *Ind. Eng. Chem. Res., 52*: 3563-3580. DOI: 10.1021/ie3022785.

Desagiacomo, C C V; Alnoch R C; Pinheiro, V E; Cereia, M; Machado C B; Damasio A; Augusto M J; Pedersoli W; Silva R N and de Moraes Polizeli M D L T (2021). Structural model and functional properties of an exo-polygalacturonase from *Neosartorya glabra*. *Int. J. Biol. Macromol., 186*: 909-918. DOI: 10.1016/j.ijbiomac.2021.07.065.

Dubois, M; Gills, K A; Hamilton, J A and Rebers, P A (1956). Colorimetric method for determination of sugars and related substances. *Anal. Chem., 28*: 350-356. DOI: 10.1021/ac60111a017.

Fahma, F; Iwamoto, S; Hori, N; Iwata, T and Takemura, A (2010). Isolation, preparation, and characterization of nanofibers from oil palm empty-fruit-bunch (OPEFB). *Cellulose, 17*: 977-985. DOI: 10.1007/s10570-010-9436-4.

Farhan, M S; Hamid, N F; Razali, M A and Daud, N F S (2021). Lignocellulosic of oil palm biomass to chemical product via fermentation. *Elaeis guineensis*. Intech Open, London. DOI: 10.5772/intechopen.99312.

Ghali, A E; Marzoug, I B; Baouuab, M H V and Roudesli, M S (2012). Separation and characterization of new cellulosic fibers from the *Juncus acutus* plant. *Bioresour., 7:* 2002-2018. DOI: 10.15376/biores.7.2.2002-2018.

Gill, M K; Kocher, G S and Panesar, A S (2021). Optimization of acid-mediated delignification of corn stover, an agriculture residue carbohydrate polymer for improved ethanol production. *Carbohyd. Polym. Technolo. Appl., 2*: 100029. DOI: 10.1016/j.carpta.2020.100029.

Inamuddin; Thomas, S; Mishra, R K and Asiri, A M (2019). *Sustainable Polymer Composites and Nanocomposites*. Springer Cham, Springer Nature Switzerland AG. 1440 pp. DOI: 10.1007/978-3-030-05399-4.

Jia, L; Goncalves, G A L; Takasugi, Y; Mori, Y; Noda, S; Tanaka, T; Ichinose, H and Kamiya, N (2015). Effect of pretreatment methods on the synergism of cellulase and xylanase during the hydrolysis of bagasse. *Bioresour. Technol., 185*: 158-164. DOI: 10.1016/j.biortech.2015.02.041.

Khabarov, Y G; Kamakina, N D; Gusakov, L V and Veshnyakov, V A (2006). New spectrophotometric method for determination of furfural and pentoses. *Russ. J. Appl. Chem., 79*: 103-106. DOI: 10.1134/S1070427206010228.

Kucharska, K; Rybarczyk, P; Holowacz, I; Lukajtis, R; Glinka, M and Kaminski, M (2018). Pretreatment of lignocellulosic materials as substrates for fermentation processes. *Molecules, 10; 23(11)*: 2937. DOI: 10.3390/molecules23112937.

Kundu, C; Samudrala, S P; Kibria, M A and Bhattacharya, S (2021). One-step peracetic acid pretreatment of hardwood and softwood biomass for platform chemicals production. *Sci. Rep., 27;11(1)*: 11183. DOI: 10.1038/s41598-021-90667-9.

Labbe, N; Rials, T G; Kelley, S S; Cheng, Z M; Kim, J Y and Li, Y (2005). FT-IR imaging and pyrolysis-molecular beam mass spectrometry: New tools to investigate wood tissues. *Wood Sci. Tech., 39*: 61-77. DOI: 10.1007%2Fs00226-004-0274-0.

Luo, J; Fang, Z and Smith, R L (2014). Ultrasound-enhanced conversion of biomass to biofuels. *Prog. Energy Combust. Sci., 41*: 56-93. DOI: 10.1016/j.pecs.2013.11.001.

Mardawati, E; Febrianti, E A; Fitriana, H N; Yuliana, T; Putriana, N A; Suhartini, S and Kasbawati (2022). An integrated process for the xylitol and ethanol production from oil palm empty fruit bunch (OPEFB) using *Debaryomyces hansenii* and *Saccharomyces cerevisiae*. *Microorganisms*, *10(10)*: 2036. DOI: 10.3390/microorganisms10102036.

Mesa, L; Gonzalez, E; Cara, C; Gonzalez, M; Castro, E and Mussatto, S I (2011). The effect of organosolv pretreatment variables on enzymatic hydrolysis of sugarcane bagasse. *Chem. Eng. J., 168*: 1157-1162. DOI: 10.1016/j.cej.2011.02.003.

Miller, G L (1959). Use of dinitrosalicylic acid reagent for determination of reducing sugar. *Anal. Chem., 31*: 426-428. DOI: 10.1021/ac60147a030.

Nurika, I; Aristya, Y I; Azizah, N; Sunyoto, N M S; Suhartini, S; Bugg, T D H and Barker, G C (2023). Enhancement of the ligninolytic activity of *Lysinibacillus sphaericus* by the addition of $MnSO_4$ and its impact on subsequent methane production from oil palm empty fruit bunches (OPEFB). *Bioresour. Technol. Rep., 22*: 101394. DOI: 10.1016/j.biteb.2023.101394.

Olughu, O; Tabil, L G and Dumonceaux, T (2021). Ultrasonic delignification and microstructural characterization of switchgrass. *Energies., 14*: 263. DOI: 10.3390/en14020263.

Palamae, S; Palachum, W; Chisti, Y and Choorit, W (2014). Retention of hemicellulose during delignification of oil palm empty fruit bunch (EFB) fiber with peracetic acid and alkaline peroxide. *Biomass. Bioenerg., 66*: 240-248. DOI: 10.1016%2Fj.biombioe.2014.03.045.

Pandey, K K and Pitman, A J (2003). FTIR studies of the changes in wood chemistry following decay by brown-rot and white-rot fungi. *Int. Biodeter. Biodegr., 52*: 151-160. DOI: 10.1016%2FS0964-8305(03)00052-0.

Patil, R S; Joshi, S M and Gogate, P R (2019). Intensification of delignification of sawdust and subsequent enzymatic hydrolysis using ultrasound. *Ultrason. Sonochem., 58:* 104656. DOI: 10.1016/j.ultsonch.2019.104656.

Rame (2018). Oil palm empty fruit bunches (OPEFB): Existing utilisation and current trends bio refinery in Indonesia. *E3S. Web. Conference., 31*: 03014. DOI: 10.1051/e3sconf/20183103014.

Revanappa, S B; Nandini, C D and Salimath, P V (2010). Structural characterisation of pentosans from hemicellulose B of wheat varieties with varying chapati-making quality. *Food Chem., 119(1)*: 27-33. DOI: 10.1016/j.foodchem.2009.04.064.

Sari, F P; Falah, F; Anita, S H; Ramadhan, K P; Laksana, R P B; Fatriasari, W and Hermiati, E (2021). Pretreatment of oil palm empty fruit bunch (OPEFB) at bench-scale high temperature-pressure steam reactor for enhancement of enzymatic saccharification. *Int. J. Renew. Energy Dev., 10(2)*: 157-169. DOI: 10.14710/ijred.2021.32343.

Segal, L; Creely, J; Martin, A and Conrad, C (1959). An empirical method for estimating the degree of crystallinity of native cellulose using the X-ray diffractometer. *Text Res. J., 29*: 786-794. DOI: 10.1177%2F004051755902901003.

Selvakumar, P; Isabel, J B; Kavitha, S; Karthik, V; Mohamed, B A; Getachew, G D; Sivashanmugam, P and Aminabhavi, T M (2023). Recent advances in consolidated bioprocessing for conversion of lignocellulosic biomass into bioethanol - A review. *Chem. Eng. J., 453*: 1:139783. DOI: 10.1016/j.cej.2022.139783.

Senusi, N A; Shohaimi, N A M; Halim, A Z A; Shukri, N M; Abdul Razab, M K A; Mohamed , M; Mohd Amin, M A; Wan Mokhtar, W N; Ismardi, A and Mohamed Noor, A (2020). Preparation and characterization of microcrystalline cellulose from agriculture waste. *IOP Conf. Ser. Earth Environ. Sci., 596*: 012035. DOI: 10.1088/1755-1315/596/1/012035.

Shang, W; Liu, Y; He Q; Liu S; Zhu Y; Tong, T and Liu, B (2020). Efficient adsorption of organic matters and ions by porous biochar aerogel as pre-treatment of ultrafiltration for shale gas wastewater reuse. *Chem. Eng. J. Adv., 2*: 100011. DOI: 10.1016/j.ceja.2020.100011

Shi, J and Li, J (2012). Metabolites and chemical group changes in the wood forming tissue of *Pinus koraiensis* under inclined condition. *Bioresources, 7*: 3463-3475. DOI: 10.15376/BIORES.7.3.3463-3475.

Song, X; Zhang, M; Pei, Z J and Wang, D (2015). Ultrasonic-assisted dilute acid pretreatment of poplar wood biomass for biofuel manufacturing: A preliminary study. *ASME Proceedings, 1*: 8. DOI: 10.1115/MSEC2015-9340.

Subhedar, P B and Gogate, P R (2014). Alkaline and ultrasound assisted alkaline pretreatment for intensification of delignification process from sustainable raw-material. *Ultrason. Sonochem., 21*: 216-225. DOI: 10.1016/j.ultsonch.2013.08.001.

Subhedar, P B; Babu, N R and Gogate P R (2015). Intensification of enzymatic hydrolysis of waste newspaper using ultrasound for fermentable sugar production. *Ultrason. Sonochem., 22*: 326-332. DOI: 10.1016/j.ultsonch.2014.07.005.

Tahir, P M; Fei, A A; Ashaari, Z; Lee, S H and Al-Edrus, S S O (2022). Oil palm empty fruit bunch as a potential feedstock for composting. *Lett. Appl. Nanobioscience., 11(4)*: 3961-397. DOI: 10.33263/LIANBS114.39613974.

Tran, T T A; Le, T K P; Mai, T P and Nguyen, D Q (2019). Bioethanol production from lignocellulosic biomass. *Alcohol Fuels - Current Technologies and Future Prospect*. Intech Open, London. DOI: 10.5772/intechopen.86437.

Wong, S S; Kasapis, S and Tan, Y M (2009). Bacterial and plant cellulose modification using ultrasound irradiation. *Carbohydr. Polym., 77*: 280-287. DOI: 10.1016/j.carbpol.2008.12.038.

Yang, X; Ma, R; Shi, P; Huang, H; Bai, Y; Wang, Y; Yang, P; Fan, Y and Yao, B (2014). Molecular characterization of a highly-active thermophilic β-Glucosidase from *Neosartorya fischeri* P1 and its application in the hydrolysis of soybean isoflavone glycosides. *PLoS ONE, 9*: e106785. DOI: 10.1371/journal.pone.0106785.

Yoon, C J and Kim, K W (2008). Anatomical descriptions of silicified woods from Madagascar and Indonesia by scanning electron microscopy. *Micron., 39*: 815-831. DOI: 10.1016/j.micron.2007.12.011.

Zhao, X; Li, S; Wu, R and Liu, D (2017). Organosolv fractionating pretreatment of lignocellulosic biomass for efficient enzymatic saccharification: Chemistry, kinetics, and substrate structures. *Biofuel Bioprod. Biorefining, 11*: 567-590. DOI: 10.1002/bbb.1768.

Zhu, J Y and Pan, X (2022). Efficient sugar production from plant biomass: Current status, challenges, and future directions. *Renew. Sust. Energ. Rev., 164*: 112583. DOI: 10.1016/j.rser.2022.112583.

Journal of Oil Palm Research Vol. 36 (4) December 2024 p. 687-707
DOI: https://doi.org/10.21894/jopr.2024.0004

COMPOSITE OF ZnO/SBE AS CATALYST MATERIALS FOR PHOTODEGRADATION OF RHODAMINE-B

DIAH SUSANTI[1]*; SHAFIRA MARELLIA[1]; AZZAH DYAH PRAMATA[1]; I D A A WARMADEWANTHI[2]; ERVIN NURHAYATI[2]; HANIFFUDIN NURDIANSAH[1] and JHY-CHERN LIU[3]

ABSTRACT

Spent Bleaching Earth (SBE) is a solid waste material from the palm oil refining process, and its abundance poses environmental challenges. Meanwhile, Rhodamine B (RhB) is a liquid pollutant produced by the textile industry. SBE could potentially be a viable solution for RhB treatment, as it can adsorb on its surface. However, SBE lacks the ability to chemically degrade the RhB pollutant. Therefore, in this study, SBE was combined with zinc oxide (ZnO), a highly effective photocatalyst semiconductor, to create a composite material for the photodegradation of RhB. This experiment aimed to investigate the effect of SBE pyrolysis temperature on the morphology and structure of the ZnO/SBE composite, as well as its capability to degrade RhB. The pyrolysis temperatures chosen for variation were 450°C, 500°C, and 550°C. The experiments have shown that SBE activated at 500°C exhibited the highest surface area, measuring 106.851 $m^2 g^{-1}$. Consequently, the corresponding composite ZnO/SBE photocatalyst activated at 500°C demonstrated the most efficient performance in RhB degradation, achieving a rate of 67.8%. The ability of ZnO/SBE to photodegrade RhB was confirmed by the GC-MS results, which demonstrated the degradation of RhB into various other chemicals.

Keywords: photodegradation, pyrolysis, Rhodamine-B, SBE, ZnO.

Received: 8 May 2023; **Accepted:** 23 October 2023; **Published online:** 9 January 2024.

INTRODUCTION

The textile industry is a significant contributor to pollutant production, with 8000 kg of cloth produced globally in 2019 (Pinto *et al*., 2019). One of the main sources of textile pollutants is textile colouring agents, which contain organic compounds that are not easily degraded in nature (Dianggoni *et al*., 2017). Rhodamine B (RhB) is a commonly used synthetic dye in the textile industry due to its affordability, accessibility, and vibrant red colour (Aristanti *et al*., 2019). However, RhB is known to be harmful to both human health and the environment, necessitating appropriate pollutant treatment methods to prevent pollution. One environmentally friendly method is adsorption (Bahram *et al*., 2014), which involves binding molecules in fluids to solid surfaces (Yustinah *et al*., 2019). However, adsorption alone does not degrade the dyes and requires an additional process, such as photodegradation, to achieve complete degradation (Trivana *et al*., 2015).

Photodegradation is a process in which molecules are degraded through the absorption of photons from light (photo) (Yousif and Haddad, 2013). Zinc oxide (ZnO), a semiconductor material, is a potential photocatalyst that can be used to facilitate the photodegradation process (Khan *et al*., 2022). ZnO offers several advantages, including low production costs, non-toxicity, and widespread availability (Cambrussi *et al*., 2019). However, ZnO

[1] Materials and Metallurgical Engineering Department, Institut Teknologi Sepuluh Nopember (ITS), Kampus ITS, Keputih, Sukolilo, Surabaya, 60111 Indonesia.

[2] Environmental Engineering Department, Institut Teknologi Sepuluh Nopember (ITS), Kampus ITS, Keputih, Sukolilo, Surabaya, 60111 Indonesia.

[3] Chemical Engineering Department, National Taiwan University of Science and Technology (NTUST), Sec. 4 No. 43, Keelung Road, Taipei, 106335 Taiwan-ROC.

* *Corresponding author e-mail: santiche@mat-eng.its.ac.id*

has a limitation in terms of its low adsorption capacity (Saraswati *et al*., 2015).

Spent Bleaching Earth (SBE), a waste product from the crude palm oil (CPO) bleaching process, can be utilised for adsorption due to its porous characteristics. However, activation is required to enhance its adsorption capacity, typically achieved by using mineral acids such as hydrochloric acid (HCl), sulphuric acid (H_2SO_4), or nitric acid (HNO_3) (Lesaoana *et al*., 2019). Liu *et al.* (2021) conducted research on the synergistic carbonisation of residual oil in SBE and the activation process of SBE using KOH, resulting in the creation of a novel clay (SBE)/carbon composite. This composite was then employed as an effective adsorbent for the removal of Pb^{2+} (Liu *et al*., 2021). The carbon produced through the carbonisation process is commonly referred to as 'biochar' (Foong *et al*., 2022).

The amount of solid SBE waste from palm oil production is increasing significantly every year. According to the Ministry of Environment and Forestry in the Republic of Indonesia, for every 600 million tonnes of palm oil produced, there is an estimated 600 000 t of solid SBE waste generated (Kementerian Lingkungan Hidup dan Kehutanan Republik Indonesia, 2020). It is worth noting that SBE still contains a significant amount of valuable palm oil, ranging from 25% to 40%. As a result, it is highly flammable and poses a risk of causing fires (Lee *et al*., 2000). Therefore, it is essential to handle the disposal of SBE with utmost care to prevent any adverse impact on the environment.

SBE is a group of montmorillonite clay, in which montmorillonite is a typical of aluminosilicate of 2:1 layered structure. The structure theoretically composed of two silicon tetra oxide (SiO_4) tetrahedral layers sandwiched with one aluminum dioxide tetra hydroxide [$AlO_2(OH)_4$] octahedral layer making it a member of phyllosilicates family. Montmorillonite is known for its exceptional adsorption properties, high active surface area, and ability to exchange ions or molecules. The ions or molecules exchange capabilities were influenced by isomorphous substitutions of lower-valent metal cations, such as Al^{3+} to substitute Si^{4+} in the tetrahedral layer and Mg^{2+} to substitute Al^{3+} in octahedral layer. Hence the surface structure of montmorillonite is negatively charged and can attract positively charged cations, such as Fe^{2+}, Ca^{2+}, Mg^{2+}, and Na^{2+}, to balance the surface charge (Chen *et al*., 2022a; Ferreira *et al.*, 2019; Sani *et al*., 2017).

Montmorillonite has great capacity to accommodate new species and assist in the formation of product through chemical reactions. Due to its unique properties, montmorillonite has various applications. Besides being used as a chemical reaction catalyst, it serves as an excellent adsorbent for diverse purposes, including waste water treatment, pollutant removal, oil bleaching processes, and radioactive waste management. Moreover, montmorillonite can act as a support material for other substances, such as ZnO and g-C_3N_4, to enhance the material functionality, such as for photocatalyst (Chen *et al*, 2022a; Sani *et al*, 2017).

Pyrolysis is a thermochemical technique employed to decompose lignocellulosic materials or biomass, primarily for the purpose of activation. This process transpires in an environment devoid of oxygen or with controlled oxygen concentrations, resulting in the creation of a substance referred to as biochar. Biochar is a solid product distinguished by its elevated carbon content (Faramarzi *et al*., 2015; Foong *et al*, 2022; Sukiran *et al*., 2018). During pyrolysis, volatile matter from the biomass evaporates, leading to increased porosity and active surface area of the material (Fu *et al*., 2020). The temperature during pyrolysis is critical as it determines the pyrolysis rate and the amount of lost volatile matter (Hu and Gholizadeh, 2019).

Pyrolysis can be categorised into two main types: Slow pyrolysis and fast pyrolysis. Slow pyrolysis is characterised by a gradual heating rate, typically ranging from 0.02 to 1.00°C s^{-1}, and an extended residence period spanning from several hours to days occurring within 300°C-700°C. In contrast, fast pyrolysis involves a rapid heating rate exceeding 2.00°C s^{-1} and a much shorter residence time of less than 10 s occurring within 300°C-1000°C (Foong *et al*., 2021).

Previous studies by the authors' research group have shown that SBE activated through pyrolysis at 500°C resulted in a surface area of 158.7 $m^2 g^{-1}$ (Rizqiyah, *et al*., 2022). Other research reported that SBE when further activated with KOH, exhibited an adsorption rate of 206.65 mg g^{-1} for Pb^{2+} (Liu *et al*., 2021). Similarly, Chen *et al*. (2022b) activated iron-based SBE at 700°C, resulting in a surface area of 90.98 $m^2 g^{-1}$ and a degradation efficiency of 91.0% for tetracycline hydrochloride. Therefore, pyrolysis proves to be effective in activating SBE by opening the pores and removing impurities.

ZnO/SBE composites offer several advantages as photocatalyst materials for dye degradation, such as enhanced photocatalytic activity, improved adsorption capacity, cost-effectiveness, and environmental friendliness. However, they also have some limitations, including limited visible-light absorption, photocorrosion and stability issues, recyclability challenges, and potential substrate compatibility concerns.

Numerous studies have been conducted on the photocatalytic degradation and removal of colorant/dye wastes, leading to significant achievements. For instance, Hindryawati *et al*. (2020) investigated the photocatalytic degradation of methylene blue (MB) using SBE impregnated with WO_3, while Saputra *et al*. (2020) studied the

photocatalytic degradation of MB with $CeFeO_3$/calcinated SBE. In another investigation, Slamet *et al*. (2021) explored the application of SBE/ZnO composite for the removal of RhB, comparing its adsorption ability in both dark and ambient light conditions. Furthermore, Rahayu and Nurhayati (2023) compared the adsorption capacities of SBE and activated SBE for RhB dye. Additionally, Yulikasari, *et al*. (2023) employed SBE/ZnO in a catalytic ozonation process to remove RhB. However, it is essential to note that the methods used in the reported studies differ from those in this research.

Another avenue of research involves the application of semiconductor and montmorillonite composite materials for photodegrading RhB. Haounati *et al*. (2023) demonstrated the use of ZnO/montmorillonite photocatalyst in RhB degradation under UV light irradiation and the presence of scavenger agents. Similarly, Djellabi *et al*. (2014) employed a TiO_2/montmorillonite composite for RhB photodegradation under UV-A irradiation. Notably, the reported studies utilised fresh montmorillonite, whereas this research focuses on spent montmorillonite (SBE).

Despite extensive efforts to find studies employing the same materials, pollutant, and methodology, there was a lack of research on the photocatalytic degradation of RhB using ZnO/SBE. Consequently, this study remains relatively rare and presents ample opportunities for further development and exploration.

Furthermore, the papers reported by other groups seldom mention the examination of the photodegradation products. According to the mass conservation law, mass cannot be created nor destroyed; it simply transfers from one substance to another. As a result, it is crucial to conduct meticulous observations to identify the products formed after the photocatalytic process. This study has taken the initiative to identify these products using gas chromatography-mass spectrometry (GC-MS).

By focusing on the identification of the photodegradation products, this work aims to shed light on the complete mechanism of the photocatalytic process and provide valuable insights into the fate of the reactants and the formation of new substances. This comprehensive understanding is essential in assessing the efficiency and environmental impact of photocatalytic applications. Hence, this research not only explores the photodegradation process but also demonstrates a novel approach to examining the photodegradation products using GC-MS, offering valuable contributions to the field, and laying the foundation for further exploration in this area.

In this research, a composite material consisting of SBE and ZnO was synthesised for use as a photocatalyst in the photodegradation process of RhB. The variable studied was the pyrolysis temperature, which was set at 450°C, 500°C, and 550°C for activating SBE. The structure, morphology, active surface area, and chemical composition of SBE, ZnO, and ZnO/SBE composites were characterised using various material characterisation techniques. The photocatalytic performance of the synthesised materials was evaluated through photocatalytic tests. The correlations between pyrolysis temperatures and the chemical and physical properties of the materials were investigated, as well as their effects on the photocatalytic performance. At the end of the research, an investigation of the photodegradation products was conducted using GC-MS instrumentation. This analytical technique was utilised to identify the substances produced during the photocatalytic process.

MATERIALS AND METHODS

Prior to the activation process, as received or pure SBE was characterised using Scanning Electron Microscope (SEM), X-Ray Diffractometer (XRD), Fourier-Transformed Infra-Red (FTIR), and Brunauer-Emmet-Teller (BET) instruments. To start the activation process of SBE, a total of 1000 g of pure SBE was dried at 200°C for 10 hr in a muffle furnace, followed by soaking in 0.1 M KOH for 24 hr to decompose organic impurities such as the remaining CPO in SBE. The SBE was then dried in a vacuum oven at room temperature for 12 hr. The dried SBE was subjected to pyrolysis under a nitrogen flow in a horizontal vacuum furnace at temperatures of 450°C, 500°C and 550°C for 2 hr. The resulting pyrolysed SBE samples were washed with 2 M HCl and distilled water until neutral (pH = 7), dried at 200°C for 10 hr in a muffle furnace, and then filtered using 100 mesh filter paper. At the end of these processes the activated SBE was produced. The volatile matter compositions of the pyrolysed samples were examined following the American Society for Testing Materials (ASTM) D-3174 procedure (Isnugroho *et al*., 2016). The SBE samples activated at 450°C, 500°C and 550°C were denoted as ASBE1, ASBE2 and ASBE3, respectively.

The synthesis of the ZnO/SBE composite involved dissolving 78.7 g of zinc acetate dihydrate ($Zn(CH_3CO_2)_2{\cdot}2H_2O$) in 337.5 mL of distilled water and then mixing it with 120 mL of ethanol. The complete formation of ZnO can be described by the following reaction in Equation (1) (Ha *et al*., 2013).

$$Zn(CH_3COOH)_2.2H_2O_{(s)} + 2NaOH_{(aq)} \longrightarrow ZnO_{(s)} + 2NaCH_3COO_{(aq)} + H_2O_{(l)} \quad (1)$$

Subsequently, 12.5 g of activated SBE was added to the solution. The mixture was refluxed at 80°C for 2 hr and then transferred to a 1000 mL glass

beaker, where 225 mL of 2 M NaOH was added while stirring with a magnetic stirrer for 1 hr to form a gel composed of wet precipitate. The precipitate was filtered using 100 mesh filter paper, and the resulting ZnO/SBE composite precipitate was dried in a vacuum oven at 60°C for 12 hr. The composite material formed by combining activated SBE (ASBE) with ZnO was designated as KSBE. Specifically, KSBE1, KSBE2 and KSBE3 were used to represent the composites of ASBE1, ASBE2 and ASBE3 with ZnO, respectively.

The structure, morphology, and composition of the materials were characterised using X-ray diffractometer (XRD Panalytical X'pert Cu Ka = 1.5406 Å), Scanning Electron Microscope equipped with Energy Dispersive X-Ray Spectrometer (SEM/EDX, FEI Tecnai S50) and Fourier Transformed Infra-Red (FTIR Shimadzu) instrument, respectively. The active surface area was measured using a Brunauer-Emmet-Teller (BET Quantachrome Nova 4200e) instrument and the photocatalytic test results were measured using a UV-Vis spectrophotometer (Thermo Fischer Scientific Genesys) and GC-MS (Perkin Elmer) instrument.

Photocatalytic testing was performed to analyse the effect of SBE activation temperature on the performance of ZnO/SBE composite (KSBE) in degrading RhB. Standard RhB solutions with concentrations of 2, 4, 6, 8, 10, and 12 ppm were prepared to build a linear curve showing the correlation between absorbance and concentration values. A 12 ppm RhB solution was then mixed with 0.5 g of SBE in a 50 mL beaker glass, which was tightly covered and irradiated using a 20 W TL blue light source (Philips TL blue light 20 W/52 l = 400 - 500 nm, peak l = 450 nm) for varying durations of 0, 2, 4, 6, 8, and 10 hr. This process was repeated for the photocatalyst materials, including ZnO, KSBE1 (450°C), KSBE2 (500°C), and KSBE3 (550°C). Each sample was measured using a UV-Vis instrument every 2 hr, and the absorbance data were converted into concentration in ppm.

Before conducting the photocatalytic measurements on each material, the RhB solution was pre-conditioned in the dark with the photocatalyst materials, namely SBE, ZnO, KSBE1, KSBE2 or KSBE3. This pre-conditioning step aimed to ensure that the adsorption of RhB reached equilibrium prior to exposing it to UV irradiation. By doing so, it could be confirmed that any reduction in RhB absorption observed was solely attributed to photodegradation rather than the adsorption of RhB in the ZnO/SBE composite.

RESULTS AND DISCUSSION

Figure 1a shows the X-ray diffraction peaks of the samples SBE, ASBE1, ABSE2 and ASBE3, which consist of quartz and montmorillonite (Al_2O_3, SiO_2, CaO, and Fe_2O_3) phases (Yulikasari *et al*., 2022). The findings were in line with the characteristics of SBE which is classified as a group of montmorillonite clay (Sabour and Shahi, 2018). The SiO_2 diffraction peaks are observed at 2θ = 20.7°, 21.5°, 26.5°, 27.3°, 39.3°, 59.7° and 68°, corresponding to (110), (002), (022), (141), (321), and (262) planes, respectively, as per JCPDS 46-1045 (Amritphale *et al*., 2016). The diffraction peaks of Al_2O_3 are observed at 2θ = 35.4°, 42.2°, 43.1° and 47.3°, corresponding to (200), (202), (024) and (213) planes, respectively, as per JCPDS 12-0219 (Yulikasari *et al*., 2022). Fe_2O_3 peaks are observed at 2θ = 27.6°, 29.1° and 45.7°, corresponding to (121), (112), and (231) planes, respectively, according to International Crystallographic Diffraction Data (ICDD) No. 01-089-0597 (Ilmi *et al*., 2021). The diffraction peak of CaO is observed at 49.9° for the (143) plane, as per JCPDS No. 82-1691 (Singh *et al*., 2018).

Figure 1b shows the diffraction patterns of ZnO and activated ZnO/SBE composites. In addition to the diffraction patterns shown in *Figure 1a* there are diffraction peaks of ZnO observed at 2θ = 30.90°, 31.71°, 34.30°, 36.14°, 47.34°, 56.51° and 62.67° which correspond to (100), (002), (101), (102), (110), (103), (112) and (201) planes, respectively, according to JCPDS card 36-1451 (Nurbayasari and Saridewi, 2017). Based on the XRD diffraction peaks, the crystallite size of the materials was calculated using the Scherrer formula, and the results were summarised in *Table 1*.

The Scherrer formula for calculating crystallite size is given by (Cullity and Stock, 2014):

$$d = \frac{K\lambda}{B\ cos\ \theta} \quad (2)$$

where, d is the crystallite size (nm), K is the constant (taken as 0.9), λ is the X-ray wavelength Cu K-α source = 0.15406 nm, B is the breadth or full width at half maximum (radian) and θ is the diffraction angle (radian).

The crystallite sizes of SBE, ASBE1, ASBE2 and ASBE3 materials were calculated to be 127.5, 72.8, 56.6 and 102.0 nm, respectively. Similarly, the crystallite sizes of ZnO, KSBE1, KSBE2 and KSBE3 were found to be 61.2, 65.2, 57.9 and 57.9 nm, respectively. Interestingly, the crystallite sizes of ZnO decreased upon composite formation with ASBE, possibly due to reduced inter-atomic collisions caused by the presence of ASBE, as suggested by previous studies (Septiani *et al*., 2014). Notably, there were significant changes in the crystallite sizes of SBE before and after the activation process, indicating a structural transformation. In general, the SBE pyrolysed at 500°C exhibited the smallest crystallite size.

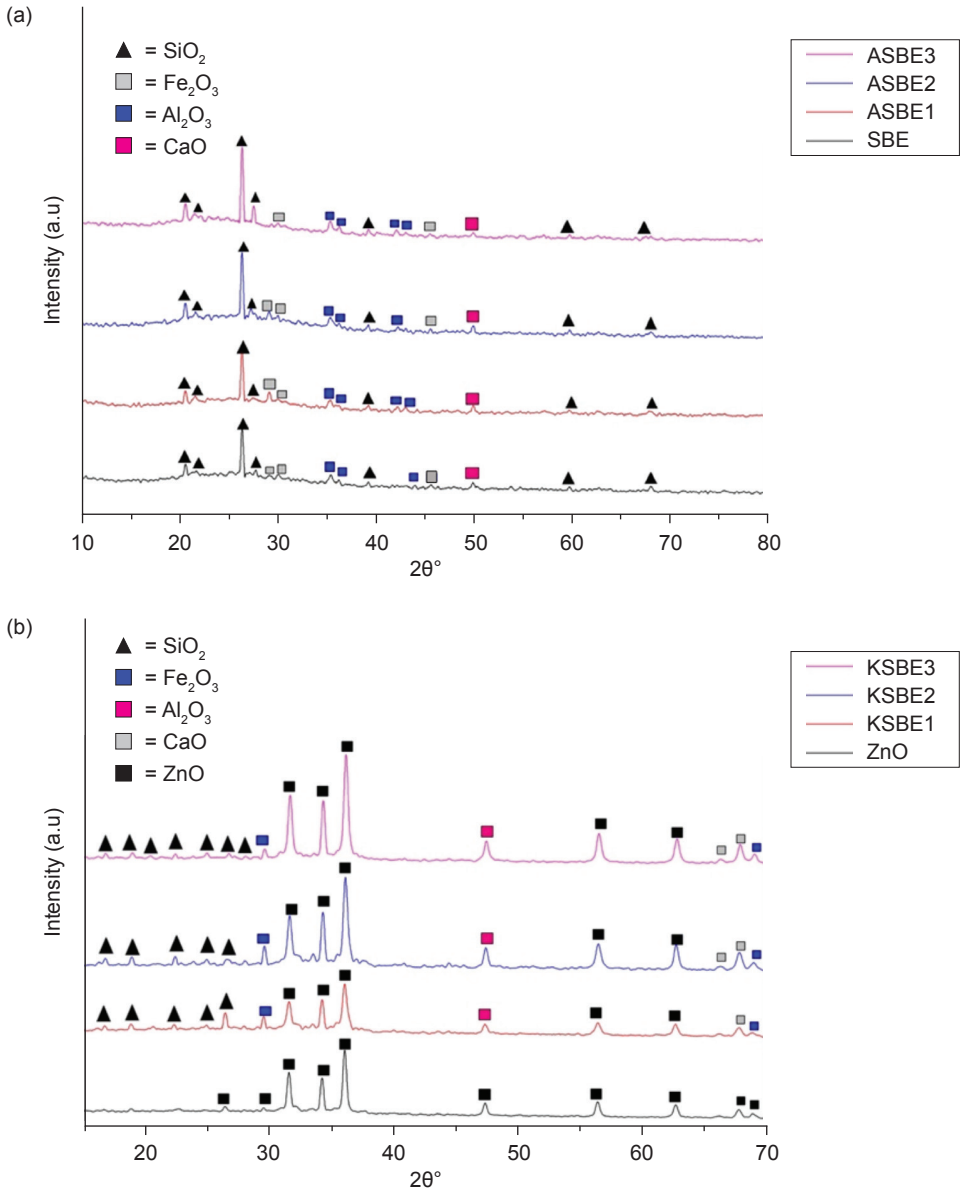


Figure 1. XRD results of (a) SBE, ASBE1, ASBE2 and ASBE3, (b) ZnO, KSBE1, KSBE2 and KSBE3.

TABLE 1. THE CRYSTALLITE SIZE OF THE SAMPLES WAS CALCULATED USING DEBBYE-SCHERRER FORMULA

No.	Sample	2θ°	FWHM (rad)	Crystallite size (nm)	$d_{spacing}$ (Å) SBE	$d_{spacing}$ (Å) ZnO
1	SBE	26.6214	0.0669	127.5	3.344	-
2	ASBE1	26.4618	0.1171	72.8	3.370	-
3	ASBE2	26.4396	0.1506	56.6	3.368	-
4	ASBE3	26.4480	0.0836	102.0	3.371	-
5	ZnO	36.2141	0.1428	61.2	-	2.478
6	KSBE1	36.0449	0.1338	65.2	3.368	2.62
7	KSBE2	36.0696	0.1506	57.9	3.37	2.49
8	KSBE3	36.1714	0.1506	57.9	3.36	2.48

As reported by Mana *et al.* (2011) on the TGA/DSC of SBE, there was a sharp TG decreasing curve corresponding to ~ 42% mass loss from room temperature to 500°C which was attributed to the evaporation of water content (represented by an exothermic peak at 278°C), the release of volatile products or remaining oil, and the decomposition as well as the burning of organic matters (represented by two exothermic peaks at 341°C and 400°C). After 500°C to 800°C, the TG curve sloped and

the mass loss was only ~2%. The DSC curve also showed an endothermic peak at 500°C which was attributed to the breakage of the hydroxyl group. Hence, the crystallite size of SBE pyrolysed at 500°C was the smallest due to the greatest mass loss of impurities from room temperature to 500°C. The loss of impurities caused the SBE to restructure the atomic arrangement nearly to the structure of pure BE. The energy given in the form of high pyrolysis temperature was used to erase the impurities. However, when the temperature increased to more than 500°C, the remaining energy was used to decompose further the material and enlarge the crystallite size as well.

The lattice spacing ($d_{spacing}$) of material can be calculated using Bragg's law [Equation (3)] which is expressed as follows (Cullity and Stock, 2014):

$$d_{spacing} = \frac{n\lambda}{2\ sin\ \theta} \quad (3)$$

In which, $d_{spacing}$ is the lattice spacing (Å), λ is the X-ray wavelength Cu K-a source = 0.15406 nm, θ is the diffraction angle (°), n is the integer number (1, 2, 3, *etc*.).

The lattice spacings of the materials are presented in *Table 1*. For SBE, the lattice spacing was calculated from the SiO_2 peak at 2θ = 26.6214°, resulting in a value of 3.344 Å. This value closely matched the SiO_2 lattice spacing of SiO_2 (quartz) with a trigonal crystal structure, which is 3.34347 Å (Heriyanti *et al*., 2018). Upon activation of SBE at 450°C, 500°C and 550°C (ASBE1, ASBE2 and ASBE3), the peaks shifted slightly to the left, causing an increase in the $d_{spacing}$ to approximately 3.37 Å, 3.368 Å, and 3.371 Å, respectively. Interestingly, the activation temperatures did not seem to significantly affect the $d_{spacing}$ of activated SBE.

The lattice spacing of ZnO calculated from ZnO peak at 2θ = 36.2141° was measured to be 2.4785 Å. Once ZnO was composited with SBE, the peaks slightly shifted to the left, and the $d_{spacings}$ of ZnO in KSBE1, KSBE2 and KSBE3 slightly increased to 2.62 Å, 2.49 Å and 2.48 Å, respectively. Meanwhile, the $d_{spacings}$ of SBE were calculated from the highest peak of SBE at 2θ ~ 26.4° in KSBE1, KSBE2, and KSBE3, resulting in values of 3.368 Å, 3.37 Å and 3.36 Å, respectively.

As SBE belongs to the family of montmorillonite clays, it can undergo intercalation, similar to other members of this group. Intercalation involves the insertion of certain species through cation exchange in the interlayer of the clay, thereby preserving its layered structure. This process results in an increased basal spacing within the clay. Upon heating, the layered structure transforms into a thermally stable mesoporous and/or microporous material, all the while retaining its original layer structure. This modified form of montmorillonite is commonly referred to as "pillared montmorillonite" (Al Kasour *et al*., 2022).

Prior studies on ZnO nanocomposites with montmorillonite reported that introducing ZnO into the clay resulted in a noticeable shift in the X-ray diffraction (XRD) peak of montmorillonite towards a lower angle. Furthermore, this incorporation of ZnO caused an increase in the $d_{spacing}$ of montmorillonite from 0.99 - 1.19 nm (Sani *et al*., 2017). In contrast, our research suggests that the compositing process of ZnO with SBE did not follow the typical pillaring or intercalating process. This conclusion is based on the observation that the $d_{spacings}$ of ZnO and SBE after the compositing process did not exhibit significant changes compared to their respective values before the process. Indeed, it is likely that the bonding mechanisms involved are of a low physical or mechanical nature. This suggests that the interaction between SBE and ZnO might not involve strong chemical bonds or substantial structural alterations. Instead, the compositing process may rely on weaker physical forces such as Van der Waals interactions or mechanical mixing.

Figure 2 displays the FTIR diagrams of the samples, namely pure SBE, pyrolysed SBE at 450°C (ASBE1), 500°C (ASBE2), and 550°C (ASBE3), as well as composite ZnO/SBE at 450°C (KSBE1), ZnO/SBE at 500°C (KSBE2), and ZnO/SBE at 550°C (KSBE3). FTIR analysis was employed to identify the chemical functional groups present in these samples and characterise their compositions. Pure SBE and activated SBE (*Figure 1a*) exhibit characteristic peaks corresponding to the –OH functional group at a wavelength of 3392 cm^{-1} (Majid and Mat, 2017). Additionally, peaks corresponding to Si-O functional groups are observed in the wavelength range of 420-485 cm^{-1}, Si-O-Si functional groups at 1017 cm^{-1}, and a C=C bond at 1636 cm^{-1}. Notably, no significant changes in the functional groups of SBE materials are observed before or after the activation process, even with temperature variations of 450°C, 500°C, and 550°C (Yulikasari *et al*., 2022), as evident from the FTIR results above. Furthermore, *Figure 1b* reveals additional peaks in the activated SBE samples, including –OH functional groups at wavelengths of 3277 cm^{-1} and 1408 cm^{-1}, a C=O functional group at 1637 cm^{-1} and a Zn-O functional group at 300-650 cm^{-1} (Hernández *et al*., 2007).

SEM characterisations were conducted on pure SBE, ASBE1, ASBE2, ASBE3, ZnO, KSBE1, KSBE2 and KSBE3 samples. As depicted in *Figure 3a*, the surface morphology of SBE exhibits a porous structure with montmorillonite phases, displaying irregular and nearly spherical shapes with sizes ranging from ~5-40 µm. *Figure 3b-3c* illustrate the surfaces of ASBE1, ASBE2 and ASBE3 samples,

which exhibit increased pore openness as a result of the activation process with KOH and pyrolysis at high temperatures. *Figure 3e-3h* depict the surface morphologies of ZnO, KSBE1, KSBE2 and KSBE3. In *Figure 3e*, white lumps on the surface indicate the formation of ZnO. Meanwhile, in *Figure 3f-3g*, the presence of white lumps of ZnO on the surface of ASBE samples partially obstructs the pores of ASBE.

The elemental compositions of the samples, as shown in *Table 2* and *Figure 4a-4d*, were determined by EDX analysis. The main constituent elements of SBE were found to be Silicon (Si) at 38.54%, Oxygen (O) at 49.03% and Carbon (C) at 7.97%. Among the activated SBE samples, ASBE1, ASBE2 and ASBE3, oxygen had the highest composition with levels of 54.73%, 53.5% and 53%, respectively. Moreover, an increase in carbon content was observed with increasing temperature during the activation process, from 7.97% in pure SBE to 16.52% in ASBE activated at 500°C. Notably, the activated SBE at 500°C exhibited the highest carbon content compared to pure SBE and ASBE activated at 450°C and 550°C, respectively.

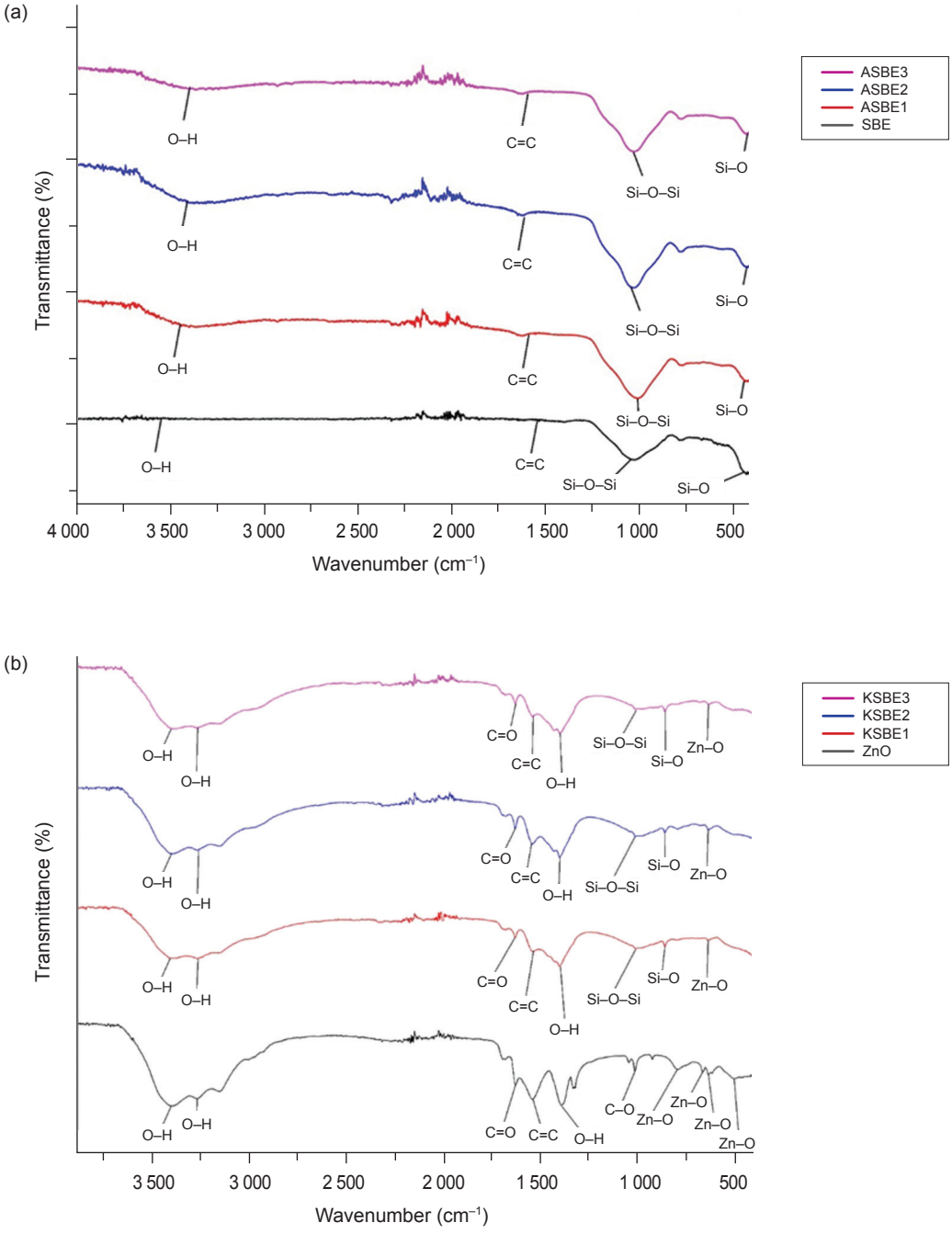


Figure 2. FTIR results of (a) SBE, ASBE1, ASBE2 and ASBE3, (b) ZnO, KSBE1, KSBE2 and KSBE3.

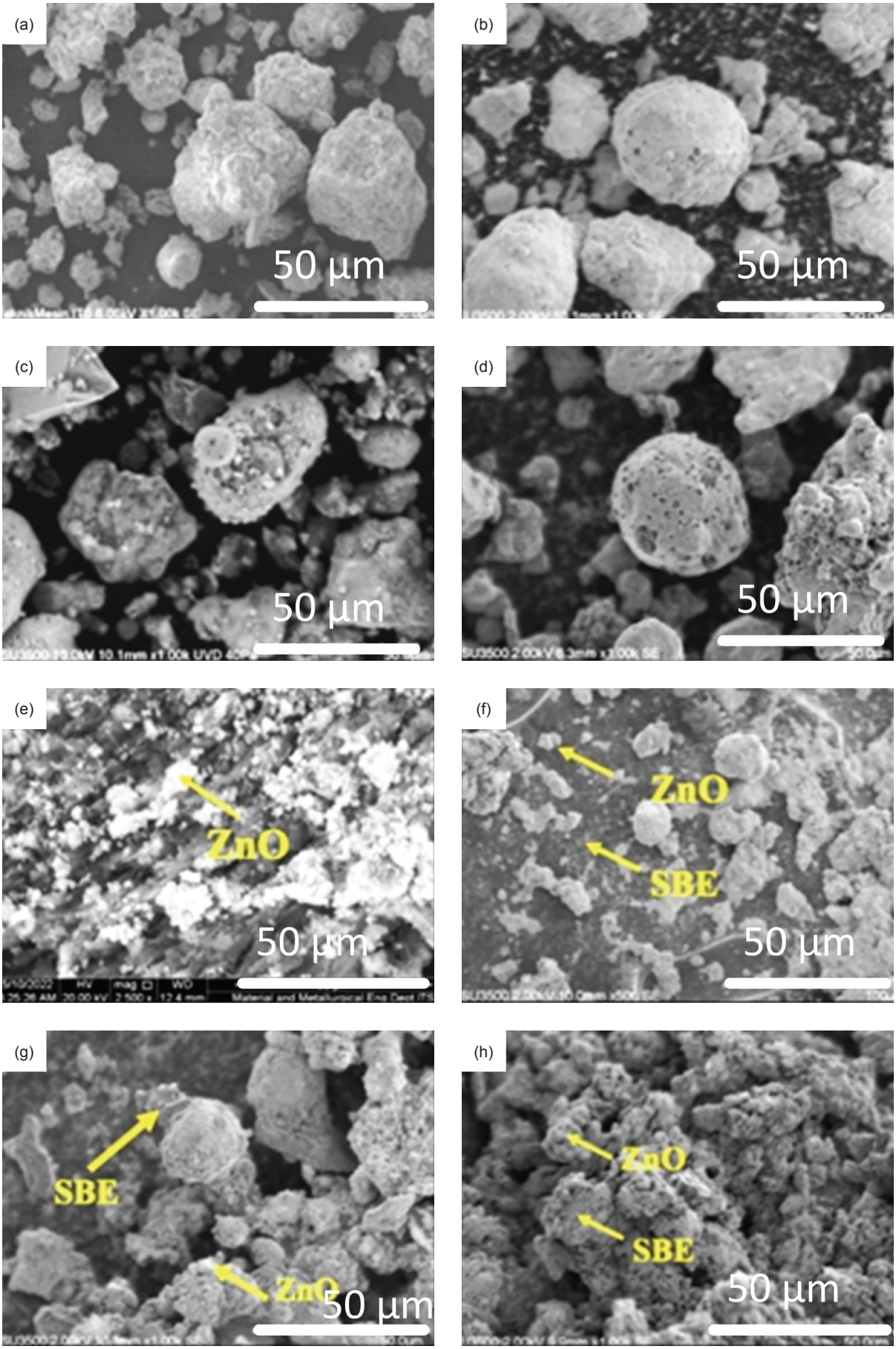


Figure 3. Bright Field Secondary Electron SEM images of (a) SBE, (b) ASBE1, (c) ASBE2, (d) ASBE3, (e) ZnO, (f) KSBE1, (g) KSBE2 and (h) KSBE3.

Table 2 and *Figure 4e-4h* also reveal that Zinc (Zn) was the major constituent element in ZnO and ZnO/SBE composite samples, with percentages of 43.30%, 44.06%, and 40.06% for KSBE1, KSBE2 and KSBE3, respectively. Additionally, the activated ZnO/SBE composite samples exhibited increased carbon content, similar to the activated SBE (ASBE) samples in *Table 2*. The highest carbon content of 21.68% was observed in the ZnO/SBE composite activated at 500°C. This carbon content originated from the remaining CPO in the SBE, which was thermally degraded during the pyrolysis process and formed 'biochar' (Foong *et al.*, 2022). Overall, these results were consistent with the XRD and FTIR findings, confirming the elemental composition of SBE as Si, O, and C.

The active surface area and pore total volume of pure SBE before and after activation at different temperatures (450°C for ASBE1, 500°C for ASBE2 and 550°C for ASBE3) were measured using the BET (Brunauer-Emmett-Teller) instrument. The tabulated results are provided in *Table 3*.

Table 3 shows that SBE, ASBE1, ASBE2, and ASBE3 have pore volumes of 0.038, 0.051, 0.119 and 0.098 $cm^3 g^{-1}$, respectively. It is evident that there is an increase in pore volume for SBE after activation. However, when the activation temperature was set at 550°C, the pore volume decreased. This trend is also supported by the surface area measurements of SBE, ASBE1, ASBE2 and ASBE3. The surface area of SBE increased from 11.217 $m^2 g^{-1}$ to 20.313 $m^2 g^{-1}$ and 106.851 $m^2 g^{-1}$ when activated at temperatures of 450°C and 500°C, respectively. However, when the pyrolysis temperature was set at 550°C, the surface area decreased to 74.600 $m^2 g^{-1}$. The average pore diameters were 13.819 nm before the activation process, 5.048, 2.237 and 2.636 nm after activation at 450°C, 500°C and 550°C, respectively. Therefore, the SBE activated at 500°C exhibited the highest active surface area and total volume of pores due to the lowest average pore diameter. It is worth mentioning that the active surface area was not solely contributed by SBE, but also by the remaining carbon, which transformed into activated carbon, as confirmed by FTIR and EDX results. At higher temperatures, the functional groups of carbon were decomposed, resulting in a decrease in carbon content according to the EDX results, and consequently, a reduction in active surface area as well (Bazan *et al.*, 2016)

According to Rizkiyah *et al.* (2022), the active surface areas of SBE were reported as 88.7, 158.7 and 124.5 $m^2 g^{-1}$ when activated at 400°C, 500°C, and 600°C, respectively. Similarly, Wafti *et al.* (2011) reported the active surface areas of SBE as 186, 206 and 72 $m^2 g^{-1}$ when activated at 400°C, 500°C, and 800°C, respectively. These studies revealed that there is a turning point temperature where the maximum active surface area is achieved, and beyond this temperature, the active surface area reduces due to the decomposition of the activated carbon, which contributes to the formation of new pores. This finding is also supported by the XRD measurements of crystallite size, where smaller crystallite size corresponds to larger active surface area (Hossain *et al.*, 2018).

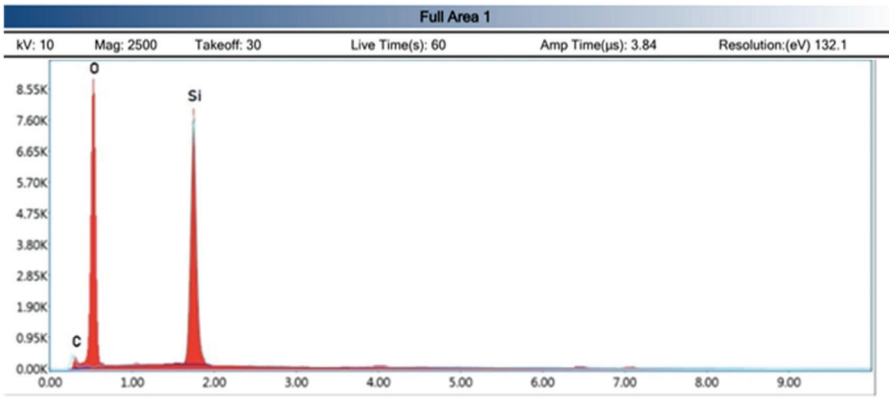
TABLE 2. THE ELEMENTAL COMPOSITIONS OF SBE, ASBE1, ASBE2, ASBE3, ZnO, KSBE1, KSBE2, KSBE3 BASED ON EDX MEASUREMENTS

No.	Sample	Wt (%)			
		Zn	Si	C	O
1	SBE	-	38.54	7.97	53.03
2	ASBE1	-	32.51	12.43	54.73
3	ASBE2	-	29.53	16.51	53.50
4	ASBE3	-	30.48	16.06	53.00
5	ZnO	63.96	-	-	36.04
6	KSBE1	43.30	7.89	12.23	36.58
7	KSBE2	44.06	3.68	21.68	30.58
8	KSBE3	40.06	6.69	20.80	31.55

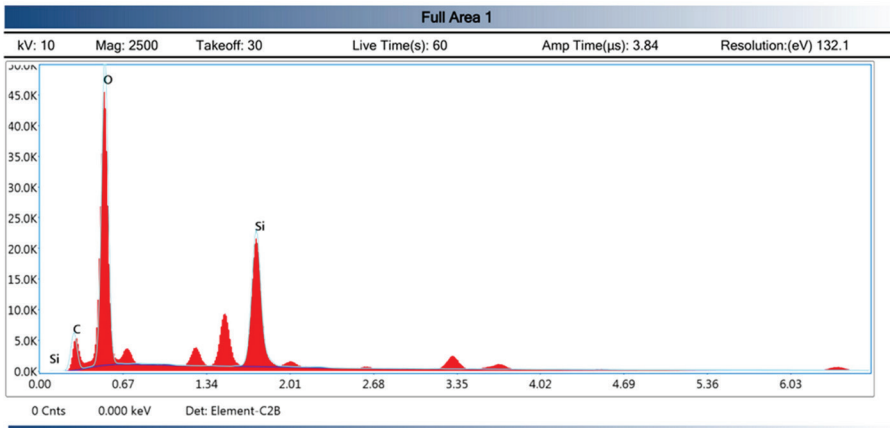
TABLE 3. BET AND VOLATILE MATTER RESULTS OF SBE, ASBE1, ASBE2, ASBE3

No.	Sample	Active surface area ($m^2 g^{-1}$)	Total volume of pores ($cm^3 g^{-1}$)	Average pore diameter (nm)	Volatile matter (%)
1	SBE	11.217	0.038	13.819	-
2	ASBE1	20.313	0.051	5.048	6.14
3	ASBE2	106.851	0.119	2.237	3.54
4	ASBE3	74.600	0.098	2.636	4.02

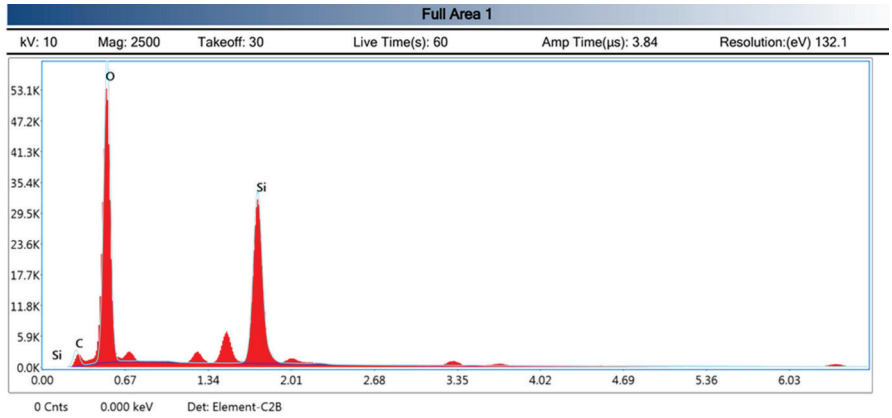
(a)


Full Area 1
kV: 10 Mag: 2500 Takeoff: 30 Live Time(s): 60 Amp Time(μs): 3.84 Resolution:(eV) 132.1
O
Si
C
8.55K
7.60K
6.65K
5.70K
4.75K
3.80K
2.85K
1.90K
0.95K
0.00K
0.00 1.00 2.00 3.00 4.00 5.00 6.00 7.00 8.00 9.00

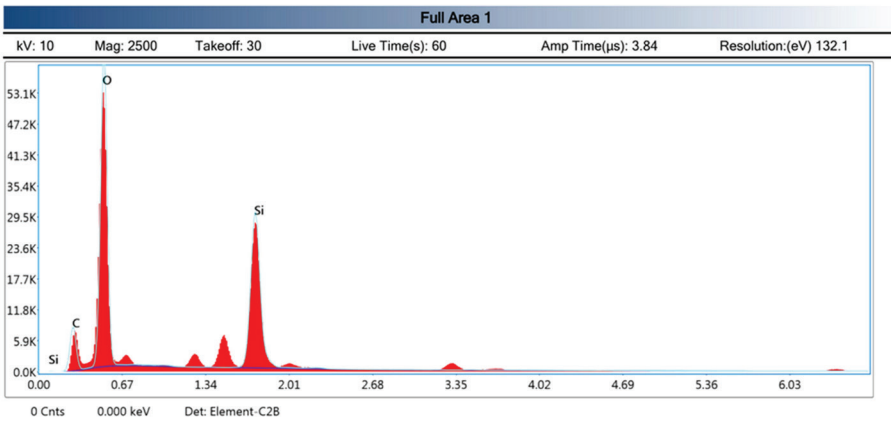
(b)


Full Area 1
kV: 10 Mag: 2500 Takeoff: 30 Live Time(s): 60 Amp Time(μs): 3.84 Resolution:(eV) 132.1
O
Si
C
Si
45.0K
40.0K
35.0K
30.0K
25.0K
20.0K
15.0K
10.0K
5.0K
0.0K
0.00 0.67 1.34 2.01 2.68 3.35 4.02 4.69 5.36 6.03
0 Cnts 0.000 keV Det: Element-C2B

(c)


Full Area 1
kV: 10 Mag: 2500 Takeoff: 30 Live Time(s): 60 Amp Time(μs): 3.84 Resolution:(eV) 132.1
O
Si
C
Si
53.1K
47.2K
41.3K
35.4K
29.5K
23.6K
17.7K
11.8K
5.9K
0.0K
0.00 0.67 1.34 2.01 2.68 3.35 4.02 4.69 5.36 6.03
0 Cnts 0.000 keV Det: Element-C2B

(d)


Full Area 1
kV: 10 Mag: 2500 Takeoff: 30 Live Time(s): 60 Amp Time(μs): 3.84 Resolution:(eV) 132.1
O
Si
C
Si
53.1K
47.2K
41.3K
35.4K
29.5K
23.6K
17.7K
11.8K
5.9K
0.0K
0.00 0.67 1.34 2.01 2.68 3.35 4.02 4.69 5.36 6.03
0 Cnts 0.000 keV Det: Element-C2B

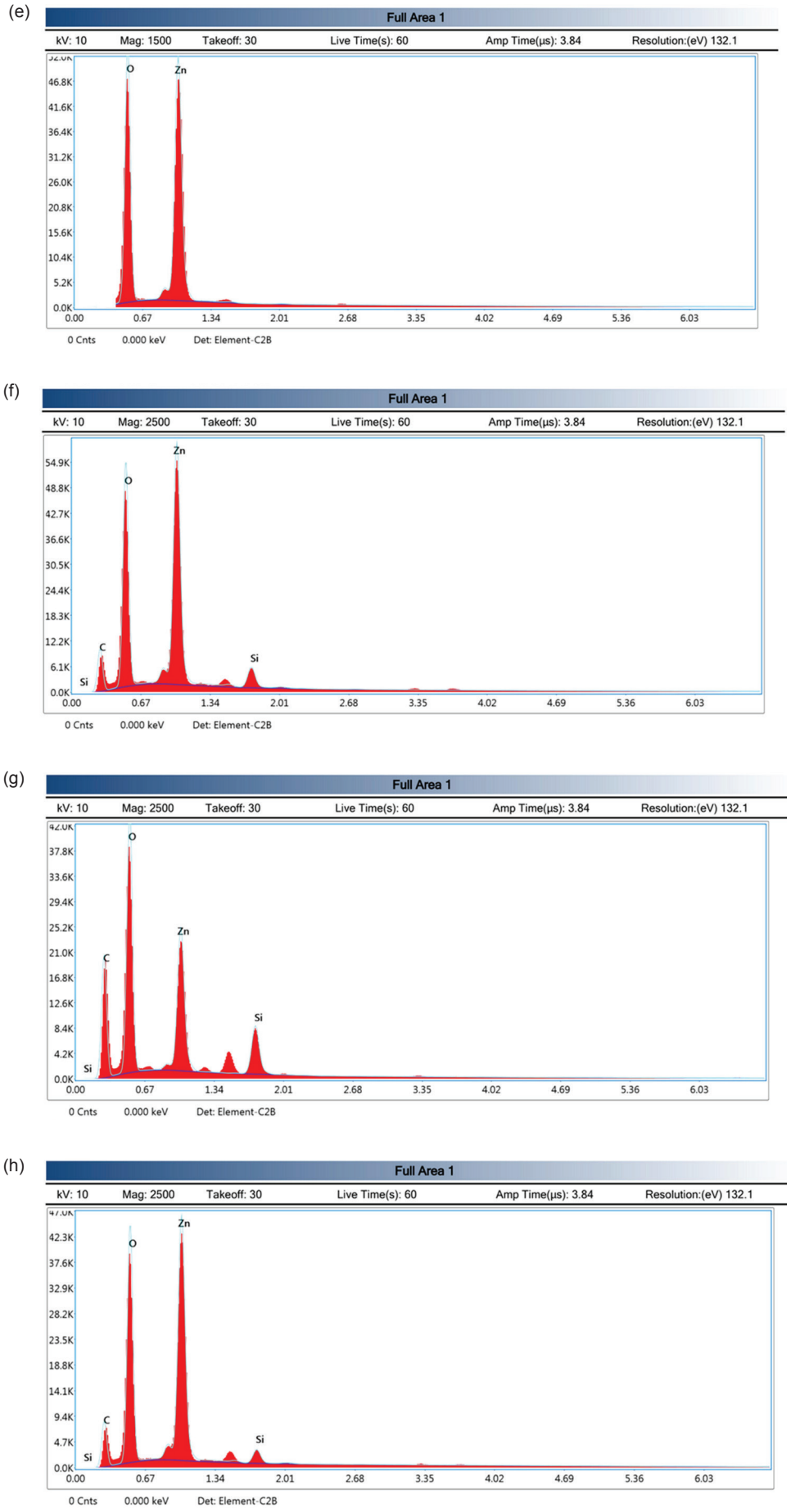


Figure 4. EDX analysis of (a) SBE, (b) ASBE1, (c) ASBE2, (d) ASBE3 (e) ZnO, (f) KSBE1, (g) KSBE2 and (h) KSBE3.

Similar findings were reported by Liu *et al.* (2021), where a decrease in surface area and pore volume was observed at higher activation temperatures. This decrease in surface area was attributed to pore damage caused by excessively high activation temperatures. On the other hand, the increase in surface area of SBE was generally attributed to the decomposition of organic matter and the release of volatile components during the activation process.

Furthermore, research has shown that the amount of carbon formed during the activation process is directly correlated with the pore volume and surface area of SBE. Additionally, pre-soaking of SBE with KOH prior to the activation process has been found to increase the surface area and adsorption capacity of SBE, as reported in previous research (Liu *et al*., 2021).

Table 3 also presents the percentage of volatile matter for ASBE1, SBE2, and ASBE3 as 6.14%, 3.54% and 4.02%, respectively. Research conducted by Kusdarini *et al.* (2017) indicated that if the activation temperature increased, the percentage of volatile matter would decrease. This is because non-carbon compounds do not decompose during the activation process, resulting in less volatile matter being released. Furthermore, an increase in the number of pores formed due to the released volatile matter results in a decrease in the material's surface area. Based on the BET test results shown in *Table 3*, the ASBE2 sample has the largest surface area and corresponds to the percentage of low volatile matter.

Figure 5 displays the adsorption-desorption isotherm curves obtained from BET measurements of the samples plotted as volume adsorbed (STP $cm^3 g^{-1}$) *vs.* relative pressure (P/P_0). *Figure 5a* shows the curve of SBE which fits to type III adsorption isotherm classified by IUPAC. According to IUPAC, type III represents the nonporous or macro porous adsorbents (Zhang *et al.*, 2020). As classified by IUPAC, macroporous materials have pores with diameter > 50 nm, mesoporous materials have pores with diameter between 2-50 nm, while microporous materials have pores with diameter ≤ 2 nm (Alothman, 2012). However, referring to *Table 3*, the average pore diameter of SBE is 13.819 nm, indicating that SBE is a mesoporous material. The isotherm curve had a shape similar to that of type III, likely due to the presence of remaining CPO that covered the pores. This explanation is further supported by the desorption curve in *Figure 5a*, which was lower than the adsorption curve at $P/P_0 \leq 0.4$ (low pressure). It is possible that the sample was not degassed sufficiently, and some impurities may still be present.

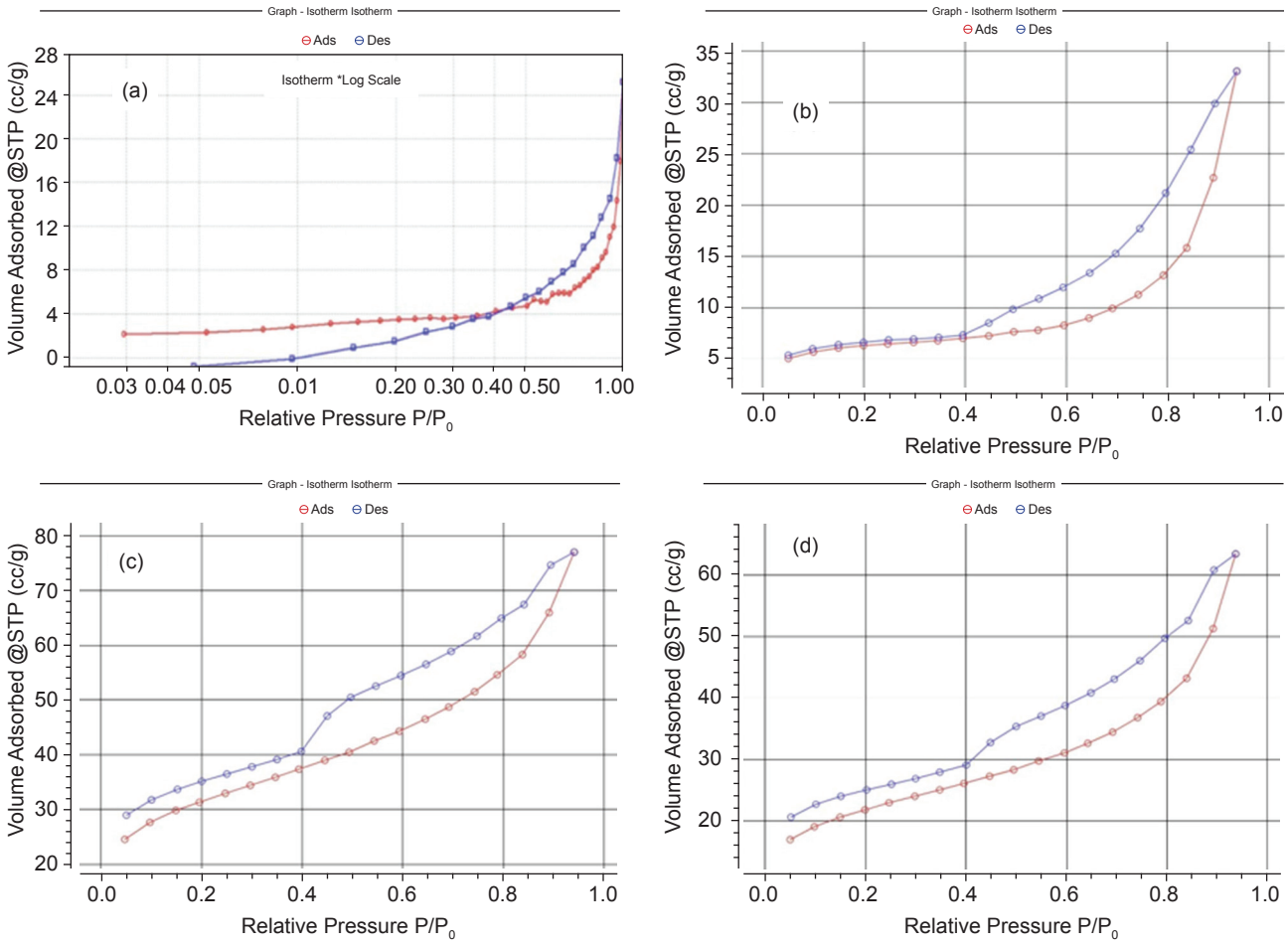


Figure 5. Adsorption-desorption curves from BET measurements (a) SBE, (b) ASBE1, (c) ASBE2, and (d) ASBE3.

Figure 5b appears to be a transition from *Figure 5a-5c*, because the desorption curve was only slightly higher than the adsorption curve. Therefore, the temperature of 500°C was likely not sufficient to activate the SBE. Additionally, the active surface area and the total volume of pores of ASBE1 were not significantly different from those of SBE, as shown in *Table 3*.

Figure 5b-5d exhibit adsorption-desorption hysteresis of type H_3, as classified by IUPAC. The three basic models of pores include cylindrical, ink-bottle, and slit-shape pores. Type H_3 represents the slit-shaped pores formed by non-rigid aggregates of plate-like particles (Alothman, 2012). Thus, the activated SBE samples had slit-shaped pores and were classified as mesoporous materials, with pore diameters ranging from 2.237 to 5.048 nm.

Figure 5 illustrates that the volume adsorbed of SBE (y axis) was the lowest, followed by ASBE1, ASBE3, and ASBE2. This trend is consistent with the results presented in *Table 3*, where ASBE2 had the smallest average pore diameter size and highest active surface area and total pore volumes, while SBE had the largest average pore diameter size and lowest active surface area and total pore volumes.

Figure 6a illustrates the UV-Vis measurement of RhB with a concentration of 12 ppm before undergoing photocatalysis. The maximum wavelength was observed at approximately 554 nm with an absorbance of around 2. This outcome served as the baseline to determine the absorbances of other concentrations in *Figure 6b*, which were then used to establish a standard for assessing changes in RhB concentration during the photocatalytic test based on UV-Vis absorbance.

In *Figure 6b*, RhB was subjected to varying concentrations of 2, 4, 6, 8, 10 and 12 ppm, yielding absorbance values of 0.295, 0.591, 1.104, 1.454, and 1.872, respectively. The resulting linear regression equation is y = 0.1861x–0.0731, where y denotes the absorbance of the solution, and x represents the concentration of the RhB solution (ppm). The coefficient of correlation (R^2) is equal to 0.98847, which indicates a strong linear relationship between concentration and absorbance based on the Lambert-Beer law, since the R^2 value approaches 1.

The results of UV-Vis measurements on the ZnO, SBE, KSBE1, KSBE2 and KSBE3 samples are presented in *Figure 6c* as absorbance *vs.* time of the photocatalytic experiments. Based on *Figure 6b*, these results were then converted into % degradation of RhB *vs.* time of the photocatalytic experiments,

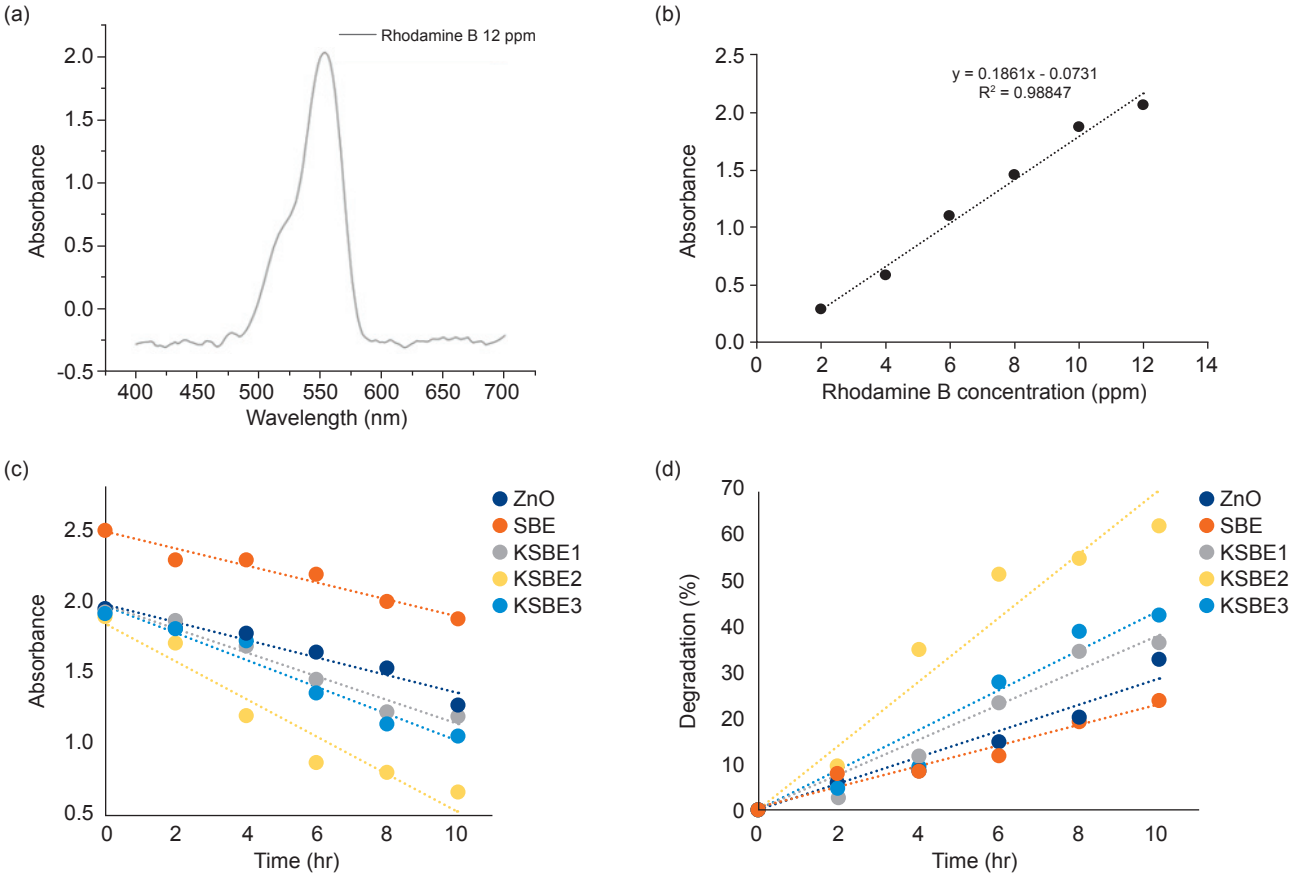


Figure 6. (a) UV-Vis measurement result of RhB 12 ppm. (b) Linear regression of UV-Vis measurement of RhB at concentrations of 2, 4, 6, 8, 10, and 12 ppm plotted as absorbance vs. *RhB concentration. (c) UV-Vis measurements on the ZnO, SBE, KSBE1, KSBE2, and KSBE3 samples. (d) The conversion of RhB UV-Vis measurements in* Figure 6c *into % degradation of ZnO, SBE, ASBE1, ASBE2 and ASBE3 samples.*

as shown in *Figure 6d*. After 10 hr of photocatalytic testing, KSBE2 showed the highest percentage degradation of RhB (62.5%), followed by KSBE3 (42.8%), KSBE1 (36.5%), ZnO (33.2%) and SBE (24%). Hence, drawing upon the aforementioned results and focusing on the most significant outcome, if we were to assess the contribution of SBE adsorption within the composite, an approximate estimation would be at 26.2%.

The percentage degradation results were consistent with the active surface area, with KSBE2 having the highest active surface area, followed by KSBE3, KSBE1, and SBE. The high active surface area allowed more RhB to be stored in the pore volume, resulting in an increased photodegradation process. The compositing process of ZnO with SBE significantly improved the ability of ZnO as a photocatalyst semiconductor to degrade RhB. Moreover, if the trendline of KSBE2 in *Figure 6d* is extended to reach 100% degradation, the photocatalytic process will need approximately 14.3 hr to complete.

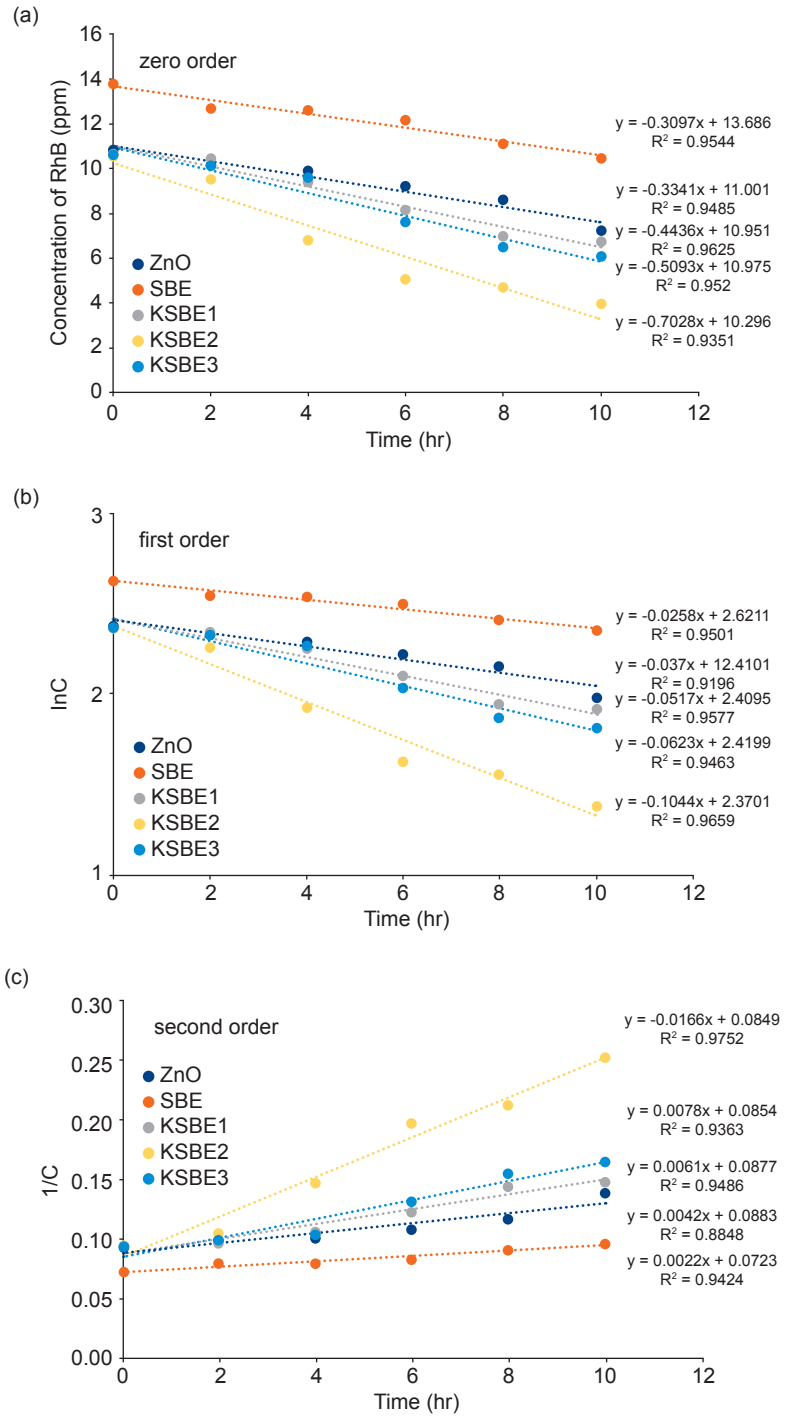


Figure 7. (a) Plot of RhB concentration (C) vs. times follows zero order reaction, (b) plot of lnC vs. times follows first order reaction, and (c) plot of 1/C vs. times follows second order reaction to determine the pollutant degradation kinetic.

Figure 7 displays linear plots of reaction rates for all samples to study the pollutant degradation kinetics. Zero order reaction rate can be expressed as follows (Upadhyaya and Dube, 1985):

$$\frac{dC}{dt} = -k \quad (4)$$

$$C = -kt + C_0 \quad (5)$$

where, C_0 is RhB concentration (ppm) at t = 0, C is RhB concentration (ppm) at any time, t (hr) and k (ppm hr^{-1}) is the reaction rate constant. After integration with initial value of $C = C_0$ at $t = 0$ and final value of $C = C$ at $t = t$, Equation (4) becomes Equation (5). Equation (5) was plotted as seen in *Figure 7a*.

For the first order reaction, the reaction rate can be expressed as follows (Upadhyaya and Dube, 1985):

$$\frac{dC}{dt} = -kC \quad (6)$$

Integration of Equation (6) results in Equation (7):

$$lnC = -kt + lncC_0 \quad (7)$$

And for the second order reaction, the reaction rate can be expressed as follows:

$$\frac{dC}{dt} = -kC^2 \quad (8)$$

In the same way, integration of Equation (8) results in Equation (9) (Upadhyaya and Dube, 1985):

$$\frac{1}{C} = kt + \frac{1}{C_0} \quad (9)$$

Equation (7) and (9) were linearly plotted in *Figure 7b* and *7c*, respectively.

The reaction rate constants (k) and the correlation coefficients (R^2) are listed in *Table 4*, as follows:

Notably, all experimental data exhibit a strong correlation with linear trendlines, boasting correlation coefficients (R^2) exceeding 93.51% for zero order reaction kinetic, 91.96% for first order reaction kinetic and 88.48% for second order reaction kinetic. Consequently, it can be inferred that the degradation kinetics of RhB adhere to the zero-order reaction model. The reaction rate constants ranked from the highest to lowest for all the kinetic models were as follows: KSBE2, KSBE3, KSBE1, ZnO, and SBE. Hence the reaction rates ranked from the fastest to the slowest were KSBE2, KSBE3, KSBE1, ZnO, and SBE.

The results of RhB degradation in *Figure 6d* were probably less than reported in other papers. For example, Slamet *et al*. (2021) conducted a study comparing the adsorption ability of SBE/ZnO composite towards RhB waste in both dark and ambient light conditions. The results revealed that the presence of ambient light significantly enhanced the adsorption ability, reaching up to 147.059 mg g^{-1}. In a study by Rahayu and Nurhayati (2023), the abilities of SBE and activated SBE to adsorb RhB dye were compared. The highest removal efficiency reported was 76.77% for SBE and 81.8% for activated SBE. The adsorption kinetics followed a pseudo-second order reaction.

In another study conducted by Yulikasari *et al*. (2023), a catalytic ozonation process using SBE/ZnO was employed to remove RhB. Remarkably, the RhB dye was removed by 97.43% within just 12 min, with a catalyst dose of 0.5 g L^{-1}, a pH of 7, and an ozone flow rate of 3 L min^{-1}. However, the methods of the reported research mentioned above were different from our research.

The ZnO/montmorillonite photocatalyst, as reported by Haounati *et al*. (2023), exhibited an impressive 99% maximum degradation efficiency of RhB after 70 min of UV light irradiation when there was no scavenger agent added to the RhB solution. The degradation followed a first-order reaction kinetic. In contrast, the TiO_2/montmorillonite composite studied by Djellabi *et al*. (2014) achieved a degradation efficiency of 79.8% for RhB under UV-A irradiation over a longer duration of 6 hr. It is worth noting that both

TABLE 4. COMPARISON OF ZERO ORDER, FIRST ORDER, AND SECOND ORDER RHB DEGRADATION KINETICS PARAMETERS

Sample	Zero order		First order		Second order	
	k (ppm hr^{-1})	R^2	k (ppm hr^{-1})	R^2	k (ppm hr^{-1})	R^2
ZnO	0.3341	0.9544	0.037	0.9196	0.0042	0.8848
SBE	0.3097	0.9485	0.0258	0.9501	0.0022	0.9424
KSBE1	0.4436	0.9625	0.0517	0.9577	0.0061	0.9486
KSBE2	0.7028	0.952	0.1044	0.9659	0.0166	0.9752
KSBE3	0.5093	0.9351	0.0623	0.9463	0.0078	0.9363

studies involved photocatalyst composites using fresh montmorillonite, unlike SBE, which utilises spent montmorillonite.

Hindryawati *et al.* (2020) reported the degradation of 99.12% of methylene blue (MB) by SBE impregnated with WO_3 catalyst during 2 hr of photocatalytic experiment and Saputra *et al.* (2020) reported the degradation of 99.5% of MB by $CeFeO_3$/calcinated SBE after 2 hr photocatalytic test. The experiment conducted by Pinto *et al.* (2019) reported the RhB degradation of maximum 80.46% after 24 hr photocatalytic contact using geopolymer material. Hence, research of ZnO/SBE as a photocatalyst for photodegradation of RhB is still rarely found, so comparison of the same photocatalyst material and solution waste was difficult to find.

SBE, a type of montmorillonite clay, is categorised as an insulator material. The electrical conductivity of montmorillonite shows temperature dependence; at 100°C, it ranges from 7.94×10^{-13} to 1.58×10^{-9} Ω^{-1} cm^{-1}, while at 1000°C, it ranges from 5.01×10^{-6} to 8.71×10^{-4} Ω^{-1} cm^{-1}. The activation energy of montmorillonite's electrical conductivity is relatively low, ranging from 0.2 to 4.1 eV (Guseinov, 2017). Lower activation energy corresponds to a higher energy band gap, while higher activation energy indicates a smaller energy band gap (Sawicki *et al.*, 2016). Consequently, with its low activation energy of electrical conductivity, montmorillonite exhibits a relatively high energy band gap. Previous studies have reported the energy band gap of montmorillonite as 4.75 eV (Horwarth and Liang, 2011), 4.63 eV for Mg^{2+}-doped montmorillonite, and 4.3 eV for Fe^{2+}-doped montmorillonite (Ferreira *et al.*, 2019). These values further support the insulating properties of montmorillonite. On the other hand, ZnO is a semiconductor material with an energy band gap of 3.21 eV (Haounati *et al.*, 2023). Hence in this research, the photocatalytic activity was solely governed by ZnO without heterojunction mechanism of ZnO and SBE.

Figure 8 represents the schematic diagram of RhB photodegradation by composite of ZnO/SBE. Theoretically, when a photocatalyst semiconductor material such as ZnO is exposed to light energy, such as sunlight, its electrons (e^-) are excited from the valence band to the conduction band. This leaves holes (h^+) in the valence band which directly oxidise the pollutant (RhB). Additionally, the electrons (e^-) in the conduction band can react with oxygen to produce superoxide anion radicals $\bullet O_2^-$. The O_2^- can react with H_2O to form •OH radicals. These •OH and $\bullet O_2^-$ radicals then participate in redox reactions with organic compounds, such as RhB, causing the breakage of chemical bonds and the production of new compounds (Rajendrachari *et al.*, 2021) and (Irfan *et al.*, 2019).

Further explanation, the conduction band potential (E_{CB}) and valence band potential (E_{VB}) of ZnO, as determined by Haounati *et al.* (2023) using the Butler and Ginley method, were -0.32 eV and +2.88 eV *vs.* the normal hydrogen electrode

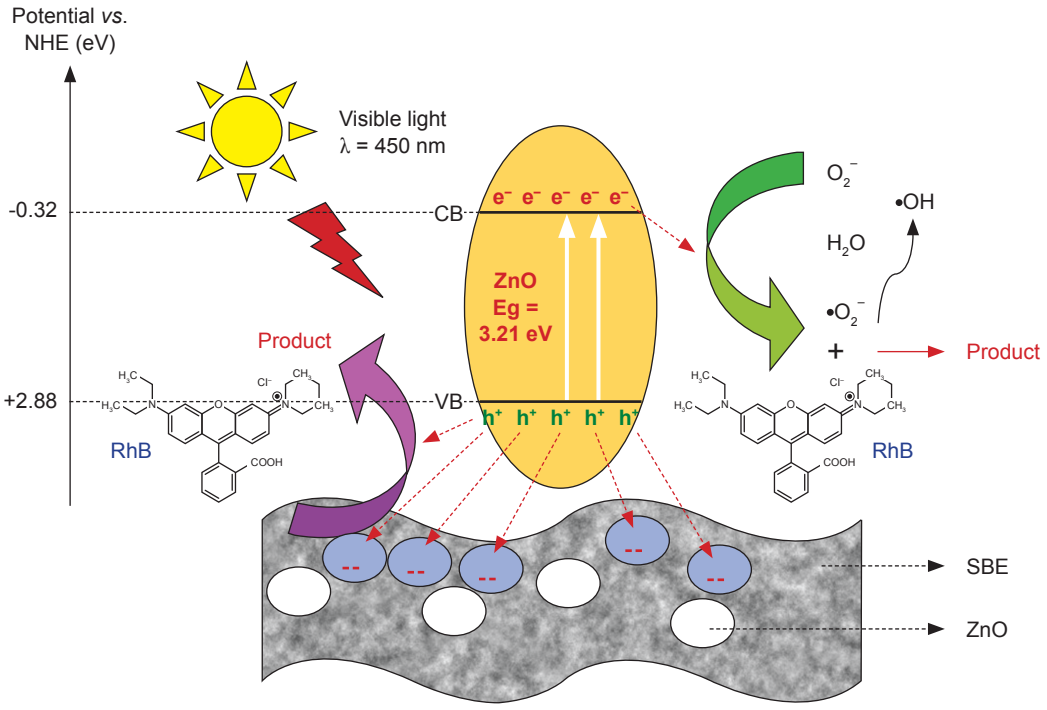


Figure 8. Schematic illustration of RhB photodegradation assisted by ZnO/SBE composite photocatalyst.

(NHE), respectively. Due to the E_{CB} potential of ZnO (-0.32 eV) being more positive than the reduction potential of O_2/O_2^- (-0.33 eV *vs.* NHE), the electrons are unable to reduce O_2 into O_2^-. Instead, the electrons in ZnO conduction band react with dissolved O_2 to produce H_2O_2, given that the potential of the electron is more negative than the reduction potential of O_2 to H_2O_2 (+0.682 eV *vs.* NHE). Furthermore, the produced H_2O_2 reacts with ZnO electrons in conduction band to generate •OH radicals and OH^- (Haounati *et al.*, 2023).

Meanwhile, the potential of the ZnO conduction band electrons is more negative than that of OH/H_2O (~2.72 eV *vs.* NHE), resulting in the inability of the holes to react with OH^- to produce •OH. Consequently, the holes directly react with RhB, degrading it through an oxidation reaction to form products such as CO_2 and H_2O.

The incorporation of SBE led to a homogeneous dispersion of ZnO species and the establishment of a well-connected interface between ZnO particles and SBE layers, facilitated by electrostatic interactions or weak physical bonds, such as Van der Waals forces, as previously observed in XRD results. Consequently, the excited electron-hole pairs of ZnO could efficiently migrate due to the electrostatic repulsion between the negatively charged electrons and the negatively charged SBE layers. In comparison to pure ZnO, the likelihood of electron-hole recombination in ZnO photocatalysts was substantially reduced, enabling more electrons to react with adsorbed O_2, thereby generating sufficient $\bullet O_2^-$ and resulting in an improved photocatalytic activity (Li *et al.*, 2016). The enhanced adsorption of RhB and O_2 facilitated by the increased active surface area of SBE led to a higher percentage of RhB degradation. As a result, the sample KSBE2 exhibited the most significant degradation performance due to its highest active surface area among the tested samples.

The remaining RhB solution, with a molecular structure of $C_{28}H_{31}ClN_2O_3$ and a molecular weight of 479.017 g mol^{-1}, underwent Gas Chromatography-Mass Spectroscopy (GC-MS) analysis to determine if it had been degraded after photocatalytic test. The results, shown in *Table 5*, indicate that RhB was broken down into 6 new compounds, confirming the effectiveness of the photocatalytic process.

Figure 6d and *Table 5* provide evidence that the degradation of RhB resulted from both photocatalytic and adsorption mechanisms. If degradation were exclusively attributed to the photocatalytic process, one would anticipate the most substantial photodegradation percentage to appear in *Figure 6d*, corresponding to the ZnO photocatalyst material. Nevertheless, if the degradation were primarily prompted by the adsorption mechanism, the transformation of RhB into different materials, as outlined in *Table 5*, would not be observed.

These findings support the conclusion that the degradation of RhB involved a combination of both photocatalysis and adsorption processes.

CONCLUSION

Composites of ZnO and activated SBE have been successfully synthesised and used as photocatalyst materials for the photodegradation process of RhB through combination of two mechanisms, photocatalytic by ZnO and adsorption by activated SBE and follow zero order reaction kinetic. The pyrolysis process has proven to be effective in enhancing the properties of SBE, and a pyrolysis temperature of 500°C yielded the best photocatalytic result due to the superior structure and properties of the material, as indicated by the material characterisation measurements. Based on BET analysis, the surface area of SBE, ASBE1, ASBE2 and ASBE 3 were 11.217, 20.313, 106.851 and 74.6 $m^2 g^{-1}$, respectively. After 10 hr of photocatalytic testing, KSBE2 showed the highest % degradation of RhB (62.5%), followed by KSBE3 (42.8%), KSBE1 (36.5%), ZnO (33.2%), and SBE (24%). These results were certainly in line with the BET results. SBE facilitated the creation of a larger active area for the dispersion of ZnO, adsorption of RhB and O_2 and played a role in impeding the recombination of ZnO's electron-hole pairs through a repulsion mechanism between the negatively charged electrons and the negatively charged SBE surface. GC-MS analysis revealed that RhB was decomposed into six new compounds after the photocatalytic test. Thus, the photocatalyst material was effective in decomposing RhB, demonstrating its potential for

TABLE 5. GC-MS RESULTS OF RHB SOLUTION AFTER PHOTOCATALYTIC TEST

No.	Compound name	Chemical formula	Percentage (%)
1	9,12-Octadecadienoic acid	$C_{18}H_{32}O_2$	9.720
2	Methyl Octadetanoate	$C_{19}H_{38}O_2$	23.292
3	8-Octadecenoic acid, methyl ester	$C_{19}H_{36}O_2$	23.068
4	Octadecadienoic acid, methyl ester	$C_{19}H_{34}O_2$	23.019
5	Hexadecanoic acid, methyl ester	$C_{17}H_{34}O_2$	7.840
6	Methylbenzene	C_7H_8	4.140

environmental remediation applications despite of the lower degradation percentage compared to the other reported research.

ACKNOWLEDGEMENT

The authors would like to acknowledge the funding support provided by the Taiwan-Indonesia Science and Technology Innovation Centre for Circular Economy and Green Innovative Resources year 2022, under the National Taiwan University of Science and Technology (NTUST). The authors also acknowledge the research facilities provided by the Materials and Metallurgical Engineering Department, Institut Teknologi Sepuluh Nopember (ITS). The valuable support and contributions to this research project were sincerely appreciated.

REFERENCES

Alothman, Z A (2012). A review: Fundamental aspects of silicate mesoporous materials. *Materials*, *5(12)*: 2874-2902. DOI: 10.3390/MA5122874.

Al Kausor, M; Gupta, S S; Bhattacharyya, K G and Chakrabortty, D (2022). Montmorillonite and modified montmorillonite as adsorbents for removal of water soluble organic dyes: A review on current status of the art. *Inorg. Chem. Comm.*, *143(109686)*: 1-23. DOI: 10.1016/j.inoche.2022.109686.

Amritphale, S S; Mishra, D; Mudgal, M; Chouhan, R K and Chandra, N (2016). A novel green approach for making hybrid inorganic - organic geopolymeric cementitious material utilizing fly ash and rice husk. *J. Enviro. Chem. Eng.*, *4(4)*: 3856-3865. DOI: 10.1016/J.JECE.2016.08.015.

Aristanti, Y; Minandar, N; Marliani and Soepriyanto, S (2019). Analisis laju degradasi Rhodamine B (RhB) pada proses fotokatalisis TiO_2. *Ensains*, *2(3)*: 188-194.

Bahram, M; Talebi, R; Naseri, A and Nouri, S (2014). Modeling and optimization of removal of Rhodamine - B from wastewaters by adsorption on modified clay. *Chiang Mai J. Sci.*, *41(5.2)*: 1230-1240.

Bazan, A; Nowicki, P; Półrolniczak, P and Pietrzak, R (2016). Thermal analysis of activated carbon obtained from residue after supercritical extraction of hops. *J. Therm. Anal. Cal.*, *125(3)*: 1199-1204. DOI: 10.1007/S10973-016-5419-5/TABLES/4.

Cambrussi, A N C O; Morais, A Í S; Neris, A de M; Osajima, J A; Filho, E C da S and Ribeiro, A B (2019). Photodegradation study of TiO_2 and ZnO in suspension using miniaturized tests. *Revista Materia (Rio de Janeiro)*, *24(4)*. DOI: 10.1590/s1517-707620190004.0807.

Chen, Y; Yu, Y; Yan, Z; Li, T; Jing, Q and Liu, P (2022a). Montmorillonite induced assembly of multi-element doped g-C_3N_4 nanosheets with enhanced activity for Rhodamine B photodegradation. *Appl. Clay Sci.*, *218*(*106432)*: 1-12. DOI: 10.1016/j.clay.2022.106432

Chen, Y; Shi, Y; Wan, D; Zhao, J; He, Q and Liu, Y (2022b). Synergistic adsorption and advanced oxidation activated by persulfate for degradation of tetracycline hydrochloride using iron-modified spent bleaching earth carbon. *Enviro. Sci. Pollut. Res.*, *29(17)*: 24704-24715. DOI: 10.1007/S11356-021-17435-0/METRICS.

Cullity, B D and Stock, S R (2014). *Elements of X Ray Diffraction*. 3rd edition. Pearson Education Limited, England. p. 95 and 402.

Djellabi, R; Ghorab, M F; Cerrato, G; Morandi, S; Gatto, S; Oldani; V; Di Michele, A and Bianchi, C L (2014). Photoactive TiO_2-montmorillonite composite for degradation of organic dyes in water. *J. Photochem. Photobio. A: Chem.*, *295*: 57-63.

Dianggoni, I; Saputra, E and Pinem, J A (2017). Pengolahan zat warna tekstil (Rhodamine B) dengan teknologi AOP (advance oxidation processes) menggunakan katalis ce@carbon sphere dan oksidan *peroxymonosulfate*. *Jom Fteknik*, *4(2)*: 1-7.

Faramarzi, A H; Kaghazchi, T; Ebrahim, H A and Ebrahimi, A A (2015). Experimental investigation and mathematical modeling of physical activated carbon preparation from pistachio shell. *J. Anal. Appl. Pyrolysis*, *114*: 143-154. DOI: 10.1016/J.JAAP.2015.05.012.

Ferreira, C R; Pulcinelli, S H; Scolfaro, L and Borges, P D (2019). Structural and electronic properties of iron-doped sodium montmorillonite clays: A first-principles DFT study. *ACS Omega*, *4(11)*: 14369-14377. DOI: 10.1021/acsomega.9b00685.

Foong, S Y; Chan, Y H; Cheah, W Y; Kamaludin, N H; Ibrahim, T N B T; Sonne, C; Peng, W; Show, P L and Lam, S S (2021). Progress in waste valorization using advanced pyrolysis techniques for hydrogen and gaseous fuel production. *Biores. Tech.*, *320*: 124299. DOI: 10.1016/j.biortech.2020.124299.

Foong, S Y; Chan, Y H; Chin, B L F; Lock, S S M; Yee, C Y; Yiin, C L; Peng, W and Lam, S S (2022). Production of biochar from rice straw and its application for wastewater remediation - An overview. *Biores. Tech.*, *360(2)*: 127588. DOI: 10.1016/j.biortech.2022.127588.

Fu, J; Zhang, J; Jin, C; Wang, Z; Wang, T; Cheng, X and Ma, C (2020). Effects of temperature, oxygen and steam on pore structure characteristics of coconut husk activated carbon powders prepared by one-step rapid pyrolysis activation process. *Biores. Tech.*, *310*: 123413. DOI: 10.1016/J.BIORTECH.2020.123413.

Guseinov, A A (2017). Electrical properties of montmorillonite studied together with the processes occurring under thermal activation. *Izvestiya, Phys. Sol. Earth*, *53*: 845-854. DOI: 10.1134/S1069351317060015.

Ha, T T; Canh, T D and Tuyen, N V (2013). A quick process for synthesis of ZnO nanoparticles with the aid of microwave irradiation. *Inter. Scho. Res. Not.*, *2013*: 1-8. DOI: 10.1155/2013/497873.

Haounati, R; Ighnih, H; Malekshah, R E; Alahiane, S; Alakhras, F; Alabbad, E; Alghamdi, H; Ouachtak, H; Addi, A A and Jada, A (2023). Exploring ZnO/montmorillonite photocatalysts for the removal of hazardous RhB Dye: A combined study using molecular dynamics simulations and experiments. *Mater. Today Comm.*, *35*: 105915. DOI: 10.1016/j.mtcomm.2023.105915.

Heriyanti; Prendika, W; Ashyar, R and Sutrisno (2018). Thermal behaviour and microanalysis of coal subbituminus. *IOP Conf. Series: Mater. Sci. Eng.*, *345(1)*: 012015. DOI: 10.1088/1757-899X/345/1/012015.

Hernández, A; Maya, L; Sánchez-Mora, E and Sánchez, E M (2007). Sol-gel synthesis, characterization and photocatalytic activity of mixed oxide ZnO-Fe_2O_3. *J. Sol-Gel Sci. Tech.*, *42(1)*: 71-78. DOI: 10.1007/S10971-006-1521-7/METRICS.

Hindryawati, N; Julia, R N D; Panggabean, A S and Wilsoma (2020). Ultrasound assisted the degradation of methylene blue using WO_3-deoiled spent bleaching earth as a catalyst. *IOP Conf. Series: Mater. Sci. Eng.*, *854(1)*: 012058. DOI: 10.1088/1757-899X/854/1/012058.

Horwath, W and Liang, Y L (2011). Variations of chemical composition and band gap energies in hectorite and montmorillonite clay minerals on sub-micron length scales. *Final Report. Kearney Foundation of Soil Science*. p. 1-62.

Hu, X and Gholizadeh, M (2019). Biomass pyrolysis: A review of the process development and challenges from initial researches up to the commercialisation stage. *J. Energy Chem.*, *39*: 109-143. DOI: 10.1016/J.JECHEM.2019.01.024.

Hossain, M K; Pervez, M F; Uddin, M J; Tayyaba, S; Mia, M N H; Bashar, M S; Jewel, M K H; Haque, M A S; Hakim, M A and Khan, M A (2018). Influence of natural dye adsorption on the structural, morphological and optical properties of TiO_2 based photoanode of dye-sensitized solar cell. *Mater. Sci. - Poland*, *36(1)*: 93-101. DOI: 10.1515/MSP-2017-0090.

Ilmi, M M; Nurdini, N; Maryanti, E; Setiawan, P and Ismunandar, I (2021). X-ray diffraction peak profile for determination of microstructural properties of hematite (Fe_2O_3). *J. Res. Develop. Nanotech.*, *1(1)*: 11-17. DOI: 10.5614/JRDN.2021.1.1.16667.

Irfan, S; Zhuanghao, Z; Li, F; Chen, Y X; Liang, G X, Luo, J T and Ping, F (2019). Critical review: Bismuth ferrite as an emerging visible light active nanostructured photocatalyst. *J. Mater. Res. Tech.*, *8(6)*: 6375-6389. DOI: 10.1016/J.JMRT.2019.10.004.

Isnugroho, K; Birawidha, D C and Hendronursito, Y (2016). The biomass waste use as a secondary energy source for metal foundry process. *AIP Conf. Proc.*, *1746(1)*: 20001. DOI: 10.1063/1.4953926/1020418.

Kementerian Lingkungan Hidup dan Kehutanan Republik Indonesia (2020). Peraturan Menteri LHK Nomor 10 Tahun 2020, Alternatif Solusi KLHK untuk Pengelolaan Limbah B3 SBE - Kementerian LHK. https://www.menlhk.go.id/site/single_post/3003, accessed on 7 May 2023.

Khan, I; Saeed, K; Zekker, I; Zhang, B; Hendi, A H; Ahmad, A; Ahmad, S; Zada, N; Ahmad, H; Shah, L A; Shah, T and Khan, I (2022). Review on methylene blue: Its properties, uses, toxicity and photodegradation. *Water, 14(2):* 242. DOI: 10.3390/w14020242.

Kusdarini, E; Budianto, A and Ghafarunnisa, D (2017). Produksi karbon aktif dari batubara bituminus dengan aktivasi tunggal H_3PO_4, kombinasi H_3PO_4-NH_4HCO_3, dan termal. *Reaktor*, *17(2)*: 74-80. DOI: 10.14710/REAKTOR.17.2.74-80.

Lee, C G; Seng, C E and Liew, K Y (2000). Solvent efficiency for oil extraction from spent bleaching clay. *J. Am. Oil Chem. Soc.*, *77(11)*: 1219-1223. DOI: 10.1007/S11746-000-0190-6.

Lesaoana, M; Mlaba, R P V; Mtunzi, F M; Klink, M J; Edijike, P and Pakade, V E (2019). Influence of inorganic acid modification on Cr(VI) adsorption performance and the physicochemical properties of activated carbon. *South Afr. J. Chem. Eng.*, *28*: 8-18. DOI: 10.1016/j.sajce.2019.01.001.

Li, C; Sun, Z; Huang, W and Zheng, S (2016). Facile synthesis of g-C_3N_4/montmorillonite composite with enhanced visible light photodegradation of rhodamine B and tetracycline. *J. Taiwan Inst. Chem. Eng.*, *66*: 363-371. DOI: 10.1016/j.jtice.2016.06.014.

Liu, W; Yuan, K; Yin, K; Zuo, S and Yao, C (2021). Clay-activated carbon adsorbent obtained by activation of spent bleaching earth and its application for removing Pb(II) ion. *Enviro. Sci. Pollut. Res.*, *28(1)*: 711-723. DOI: 10.1007/s11356-020-10473-0.

Mana, M; Ouali, M S; de Menorval, L C; Zajac, J J and Charnay, C (2011). Regeneration of spent bleaching earth by treatment with cethyltrimethylammonium bromide for application in elimination of acid dye. *Chem. Eng. J.*, *174(1)*: 275-280. DOI: 10.1016/J.CEJ.2011.09.026.

Majid, R A and Mat, C R C (2017). Regenerated spent bleaching earth for the decolourisation and BOD reduction of palm oil mill effluent. *J. Oil Palm Res.*, *29(4)*: 579-587. DOI: 10.21894/jopr.2017.0006.

Nurbayasari, R and Saridewi, N (2017). Biosynthesis nnd characterization of ZnO nanoparticles with extract of green seaweed *Caulerpa* sp. *Jurnal Perikanan Universitas Gadjah Mada*, *19(1)*: 17-28. DOI: 10.22146/JFS.24488.

Pinto, L F; Montaño, A M; González, C P and Barón, G C (2019). Removal of Rhodamine B in wastewater from the textile industry using geopolymeric material. *J. Phys: Conf. Series*, *1386(1)*: 012040. DOI: 10.1088/1742-6596/1386/1/012040.

Rahayu, D P and Nurhayati, E (2023). Pemanfaatan activated spent bleaching earth sebagai adsorben untuk menyisihkan Rhodamine-B: Studi adsorpsi secara batch. *Envirotek: Jurnal Ilmiah Teknik Lingkungan*, *15(1)*: 91-97. DOI: 10.33005/envirotek.v15i1.41.

Rajendrachari, S; Taslimi, P; Karaoglanli, A C; Uzun, O; Alp, E and Jayaprakash, G K (2021). Photocatalytic degradation of Rhodamine B (RhB) dye in waste water and enzymatic inhibition study using cauliflower shaped ZnO nanoparticles synthesized by a novel One-pot green synthesis method. *Arab. J. Chem.*, *14(6)*: 103180. DOI: 10.1016/J.ARABJC.2021.103180.

Rizqiyah, M; Susanti, D; Pramata, A D and Nurhayati, E (2022). *Analisis pengaruh temperatur pada proses aktivasi material komposit spent bleaching earth/zinc oxide (SBE/ZnO) dengan metode pirolisis terhadap kemampuan degradasi Rhodamine B*. Undergraduate Thesis, Institut Teknologi Sepuluh Nopember (ITS).

Sabour, M R and Shahi, M (2018). Spent bleaching earth recovery of used motor-oil refinery. *Civ. Eng. J.*, *4(3)*: 572-584. DOI: 10.28991/cej-0309116.

Sani, H A; Ahmad, M B; Hussein, M Z; Ibrahim, N A; Musa, A and Saleh, T A (2017). Nanocomposite of ZnO with montmorillonite for removal of lead and copper ions from aqueous solutions. *Proc. Safety Enviro. Prot.*, *109*: 97-105. DOI: 10.1016/j.psep.2017.03.024.

Saputra, E; Utama, P S; Irdoni, H S; Simatupang, M D V; Prawiranegara, B A; Abid, H R and Muraza, O (2020). Spent bleaching earth supported $CeFeO_3$ perovskite for visible light photocatalytic oxidation of methylene blue. *J. Appl. Mater. Tech.*, *1(2)*: 81-87. DOI: 10.31258/JAMT.1.2.81-87.

Saraswati, I; Diantariani, N and Suarya, P (2015). Fotodegradasi zat warna tekstil congo red dengan fotokatalis ZnO-arang aktif dan sinar ultraviolet (UV). *J. Kim.*, *9(2)*: 175-182.

Sawicki, B; Tomaszewicz, E; Piątkowska, M; Groń, T; Duda, H and Górny, K (2016). Correlation between the band-gap energy and the electrical conductivity in $MPr_2W_2O_{10}$ tungstates (Where M= Cd, Co, Mn). *Acta Pyhs. Pol. A, 129(1-A)*: A94-96. DOI: 10.12693/APhysPolA.129.A-94.

Septiani, U; Bella, I and Syukri, D (2014). Pembuatan dan karakterisasi katalis ZnO/karbon aktif dengan metode solid state dan uji aktifitas katalitiknya pada degradasi Rhodamin B. *Jurnal Riset Kimia*, *7(2)*: 180-180. DOI: 10.25077/JRK.V7I2.186.

Singh, J P; Lim, W C; Won, S O; Song, J and Chae, K H (2018). Synthesis and characterization of some alkaline-earth-oxide nanoparticles. *J. Kor. Phys. Soc.*, *72(8)*: 890-899. DOI: 10.3938/JKPS.72.890/METRICS.

Slamet, A; Yulikasari, A; Nurhayati, E and Cornelio, F X F (2021). Pengaruh cahaya ambient terhadapt efektivitas penyisihan rhodamine b menggunakan material komposite spent bleaching earth-ZnO. *Jurnal Purifikasi*, *20(2)*: 58-63. DOI: 10.12962/j25983806.v20.i2.438.

Sukiran, M A; Loh, S K and Bakar, N A (2018). Conversion of pre-treated oil palm empty fruit bunches into bio-oil and bio-char via fast pyrolysis. *J. Oil Palm Res.*, *30(1)*: 121-129. DOI: 10.21894/jopr.2018.0006.

Trivana, L; Sugiarti, S and Rohaeti, E (2015). Sintesis zeolit dan komposit zeolit/TiO_2 dari kaolin serta uji adsorpsi-fotodegradasi biru metilena. *ALCHEMY Jurnal Penelitian Kimia*, *11(2)*: 147-162.

Uphadyaya, G S and Dube, R K (1985) *Problems in Metallurgical Thermodynamics and Kinetics.* 1st edition. Pergamon Press, Oxford, England. p. 203-207.

Wafti, N S A; Yoo, C K; Lin, S W; Yaw, T C S and Abdullah, L C (2011). Regeneration and characterization of spent bleaching clay. *J. Oil Palm Res.*, *23*: 999-1004.

Yousif, E and Haddad, R (2013). Photodegradation and photostabilization of polymers, especially polystyrene: Review. *SpringerPlus 2(1):* 1-32. DOI: 10.1186/2193-1801-2-398.

Yulikasari, A; Nurhayati, E; Utama, W and Warmadewanthi, I (2022). Characterization of spent bleaching earth as an adsorbent material for dye removal. *J. Ecol. Eng., Vol. 23(4)*: 96-104. DOI: 10.12911/22998993/146353.

Yulikasari, A; Nurhayati, E and Warmadewanthi, I (2023). *Aplikasi komposit fotokatalis SBE/ZnO pada proses ozonasi katalitik untuk mendegradasi Rhodamine B*. Master Thesis, Institut Teknologi Sepuluh Nopember (ITS), Surabaya - Indonesia.

Yustinah, Y; Hudzaifah, H; Aprilia, M and Ab, S (2019). Kesetimbangan adsorpsi logam berat (Pb) dengan adsorben tanah diatomit secara batch. *Jurnal Konversi*, *9(1)*: 17-27. DOI: 10.24853/konversi.9.1.12.

Zhang, W; Lan, Y; Ma, M; Chai, S; Zuo, Q; Kim, K H and Gao, Y (2020). A novel chitosan–vanadium-titanium-magnetite composite as a superior adsorbent for organic dyes in wastewater. *Enviro. Inter., 142(105798)*: 1-12. DOI: 10.1016/J.ENVINT.2020.105798.

Journal of Oil Palm Research Vol. 36 (4) December 2024 p. 708-717
DOI: https://doi.org/10.21894/jopr.2023.0046

DETERMINATION OF TRIACYLGLYCEROL COMPOSITION AND ITS CONTENT IN REFINED AND FRACTIONATED PALM OIL BY USING LC-MS/MS WITH MULTIPLE NEUTRAL LOSS SCAN

SEONGEUNG LEE[1]*; SEUNGCHUL BAEK[1]; SIYOUNG YANG[1] and GYEONGHWEON LEE[1]

ABSTRACT

Palm oil is widely consumed as an edible vegetable oil in many countries. Triacylglycerol (TAG) is the main component of palm oil, and its composition and contents have been extensively linked with physical and chemical properties. However, the identification and quantitation of TAGs is a challenge due to the complexity of the TAG molecule. This study employed LC-MS/MS with multiple neutral loss scans (NLS) to analyse TAG composition and contents in refined and fractionated palm oil. Identifying and quantifying TAGs using LC-MS/MS in combination with multiple-NLS was an efficient way to improve accuracy and timeliness. For accurate quantification of TAGs, isotopic deconvolution and the adjustment factor (AF) were applied. A total of 31 TAGs were identified and quantified, and C50:1 (16:0/16:0/18:1) (20.5%-36.0%), C52:2 (16:0/18:1/18:1) (17.8%-25.0%), C52:3 (16:0/18:1/18:2) (7.8%-12.2%), C48:0 (16:0/16:0/16:0) (0.4%-17.4%), and C52:1 (16:0/18:0/18:1) (4.1%-9.3%) were the predominant TAGs depending on refined and fractionated palm oil. The obtained information has been elucidated concerning the fundamental properties of refined and fractioned palm oil, such as hardness and degree of oxidation.

Keywords: fatty acid, LC-MS/MS, neutral loss scan, palm oil, triacylglycerol.

Received: 14 February 2023**; Accepted:** 30 July 2023**; Published online:** 11 September 2023.

INTRODUCTION

Palm oil, extracted from palm fruit, is the major export of Southeast Asian countries such as Indonesia and Malaysia. Palm oil's widespread popularity stems from its lower cost when compared to other edible vegetable oils such as sunflower oil, olive oil, rapeseed oil and soybean oil and its various forms (Carter *et al.*, 2007; Chandrasekharan *et al.*, 2000; Murphy, 2009). Palm olein is the liquid fraction of refined palm oil, and palm stearin and palm mid-fraction is the solid fractions (Braipson-Danthine and Gibon, 2007). According to Gee (2007), the physical and chemical properties of fractionated palm oils were influenced by the composition of various lipid compound. The triacylglycerol (TAG) is the major compound of lipids in fractionated palm oil like other edible vegetable oils. The composition and the contents of TAGs have been most extensively linked with the structure and hardness of lipid and fats (Himawan *et al.*, 2006; Noor Lida *et al.*, 2002; Sato, 2001). Also, changes in TAG and fatty acid composition may impact lipid oxidative stability (Bates *et al.*, 2012; Mateos *et al.*, 2005). Therefore, analysing the composition of TAG species and its content is crucial to especially understanding more of the physical and chemical properties of refined and fractionated palm oil. However, the identification and quantification of TAG is a great challenge due to the complexity of the TAG molecule. TAGs are esters of a glycerol molecule linked to three fatty acid molecules. The fatty acid, in particular, has various characteristics depending on the number of carbons and double bonds (Li *et al.*, 2014b).

[1] Lotte R&D Center, 201, Magokjungang-ro, Gangseo-gu, Seoul, 07594 Republic of Korea.

* *Corresponding author e-mail: sungoung.lee@lotte.net*

The composition of TAG species and its content has been determined by various analytical methods such as thin layer chromatography (TLC) (Khor *et al.*, 1980; Tan *et al.*, 1981), GC with flame ionisation detector (GC-FID) (Toschi *et al.*, 1993), HPLC (Buchgraber *et al.*, 2000), and liquid chromatography with tandem mass spectrometry (LC-MS/MS) (Beccaria *et al.*, 2014; Cheong *et al.*, 2014). The TAG composition of various forms of palm oil including refined palm oil, fractionated palm oil and palm kernel oil have been especially determined by TLC, GC-FID and HPLC (Braipson-Danthine and Gibon, 2007; Chen *et al.*, 2007; Oboh, 2004). Recently, LC-MS/MS with multiple neutral loss scan (NLS) has been employed to determine TAG composition and its contents (Pizzo *et al.*, 2022; Sirbu *et al.*, 2018; Xie *et al.*, 2019; Xu *et al.*, 2018). The NLS continuously determined mass offset scanned data between the first and second analysers (Han *et al.*, 2012). In other words, the chemical components in the sample were scanned in the first analyser and then are fragmented in the collision cells, followed by scanning fragment ions at the second analyser. The mass offset was calculated using the difference of masses scanned in the first and second analysers. Notably, it is an effective method to identify TAGs since they have neutral loss parts like fatty acid chains. (Li *et al.*, 2014b). Multiple-NLS was used to determine the composition and contents of TAG in salmon muscle tissue. In this research, the author elaborated on TAG metabolism in Atlantic salmon where for example the TAG containing linoleic acid is metabolised in salmon muscle (Yeo and Parrish, 2020). However, this method has not been yet applied to study TAG contents and its composition in refined and fractionated palm oil.

Therefore, the objective of this study was to analyse the TAG composition and its contents in refined and fractionated palm oil using LC-MS/MS with multiple-NLS. Herein, the obtained multiple-NLS data were deconvoluted to reduce isotopic interference. These findings will be used to determine the chemical and physical properties of refined and fractionated palm oil.

MATERIALS AND METHODS

Materials

Refined and fractionated palm oil, including palm olein, palm stearin and palm mid-fraction were obtained from Lotte Confectionery Co. (Seoul, Korea). Ammonium acetate, 14% boron-trifluoride in methanol solution, 37-component fatty acid methyl ester (FAME) standard mixture and TAG standards including glyceryl triundecanoate (C33:0, tri-11:0, internal standard for fatty acid analysis), glyceryl tridodecanoate (C36:0, tri-12:0), glyceryl trimyristate (C42:0, tri-14:0), glyceryl tripalmitoleate (C48:3, tri-16:1), glyceryl tripalmitate (C48:0, tri-16:0), glyceryl triheptadecanoate (C51:0, tri-17:0), glyceryl tristearate (C54:0, tri-18:0), glyceryl trioleate (C54:3, tri-18:1), glyceryl trilinoleate (C54:6, tri-18:2), glyceryl tri-linolenate (C54:9, tri-18:3), and glyceryl trinonadecanonate (C57:0, tri-19:0) were purchased from Sigma Aldrich Chemical Co. (St. Louis, MO, USA). TAG standard such as tripentadecanoin (C45:0, tri-15:0), triheptadecenoin (C51:3, tri-17:1, internal standard for TAG), trinonadecenoin (C57:3, tri-19:1), trinonadecadienoin (C57:6, tri-19:2), trieicosanoin (C60:0, tri-20:0), trieicosenoin (C60:3, tri-20:1), trieicosadienoin (C60:6, tri-20:2) and trieicosatrienoin (C60:9, tri-20:3) were obtained from Nu-check prep, Inc. (Elysian, MN, USA). Methanol, chloroform, isooctane and sodium hydroxide solution were purchased from J.T. Baker (Phillipsburg, NJ, USA).

Determination of Fatty Acid

The fatty acid analysis by GC-FID is an essential step since the fatty acid composition, and the molecular weight is the fundamental information for multiple-NLS. The analysis of fatty acids followed the modified method of Korean food code (KFDA, 2022). Refined and fractionated palm oil samples (50 mg) were placed in glass tubes. 1.5 mL of 0.5 N methanolic sodium hydroxide solution and 1.0 mL of internal standard (glyceryl triundecanolate) were added to the glass tube and heated for 5 min at 100°C. And then, 2.0 mL of 14% boron-trifluoride in methanol solution was added and incubated for 30 min at 100°C. During this step, fatty acid was converted into FAME. After heating, 1.0 mL of isooctane and 5.0 mL of saturated sodium chloride solution were added, mixed and centrifuged. The upper isooctane layer was determined by GC-FID (Model 7890a, Agilent, Santa Clara, CA, USA) with sp-2560 column (Supleco, Bellefonte, PA, USA). The sample (1.0 μL) was injected into the inlet of GC-FID using the split ratio of 200:1 at 250°C. The carrier gas was nitrogen with a flow rate of 1.0 mL min^{-1}. The initial temperature of the oven was 100°C for 3 min, then increased by 4°C min^{-1} to 190°C for 5 min, finally, ramped to 240°C at 3°C min^{-1} and kept at that temperature for 23 min. FAMEs were identified by comparing their retention time with the standard mixture (37 components of FAME standard mixture) and quantified by their peak area using internal standard and conversion coefficient.

Determination and Quantitation of TAG

First, refined and fractionated palm oil samples (50 mg) were placed in the glass tube, and diluted using 20.0 mL solvent (Chloroform:Methanol = 2:1). The mixture was thoroughly vortexed for 10 min and the upper layer mixture (0.5 mL) was mixed with 0.5 mL internal standard (C51:3, tri-17:1, 0.5 nmol) and 4.0 mL ammonium acetate mixture solution (Chloroform:Methanol:300 mM ammonium acetate = 300:665:35) and then vortexed for 2 min. In this step, TAG reacted with ammonium acetate to form ammonium-adducted TAG. The prepared samples were directly infused into the LC-MS/MS (Model Xevo TQ-S, Waters, Milford, MA, USA) with electrospray ionisation (ESI) to identify and quantify TAGs. The sample (300 µL) was direct infused at a flow rate of 20 µL min^{-1}. The TAG was identified and quantified in the positive mode with 4.0 kV capillary voltage, 60 V cone voltage, and 450°C desolvation temperature. The gas flow of desolvation and cone were 600 and 150 L hr^{-1}, respectively. The collision gas was nitrogen, and the collision energy was 25 V. TAG analysis was carried out as ammonium-adducted ion using multiple-NLS in positive mode. The content and molecular weight of fatty acid was used for multiple-NLS. The obtained data were processed using MassLynx software version 4.1 (Waters, Milford, MA, USA).

The acquired spectrum intensity was corrected by deconvolution to reduce the effect of isotopic interference and improve quantification accuracy. The calculation of isotopic deconvolution was followed, as shown by Li *et al.* (2014a), and the detailed process is explained below. The corrected spectrum intensity was applied to quantify the TAG by applying it to the statistically estimated equations using adjustment factors (AF). The AF was calculated using the correlation between commercial TAG and internal standard (Li *et al.*, 2014b). And then, the factor, which was unavailable to calculate, was estimated by a regressive curve generated by statistical software SPSS version 25 (IBM, Armonk, NY, USA).

Statistical Analysis

One-way analysis of variance (ANOVA) was performed using SPSS version 25 (IBM, Armonk, NY, USA). Means were compared using Duncan's test with a significance level of 0.05.

RESULTS AND DISCUSSION

Fatty Acid Composition of Refined and Fractionated Palm Oil

The fatty acid composition of refined and fractionated palm oil was analysed using GC-FID. The fatty acids, including myristic acid (C14:0), palmitic acid (C16:0), palmitoleic acid (C16:1), stearic acid (C18:0), oleic acid (C18:1), linoleic acid (C18:2), arachidic acid (C20:0) and linolenic acid (C18:3) were determined (*Figure 1*). The quantification data of fatty acids are shown in *Table 1*. In this study,

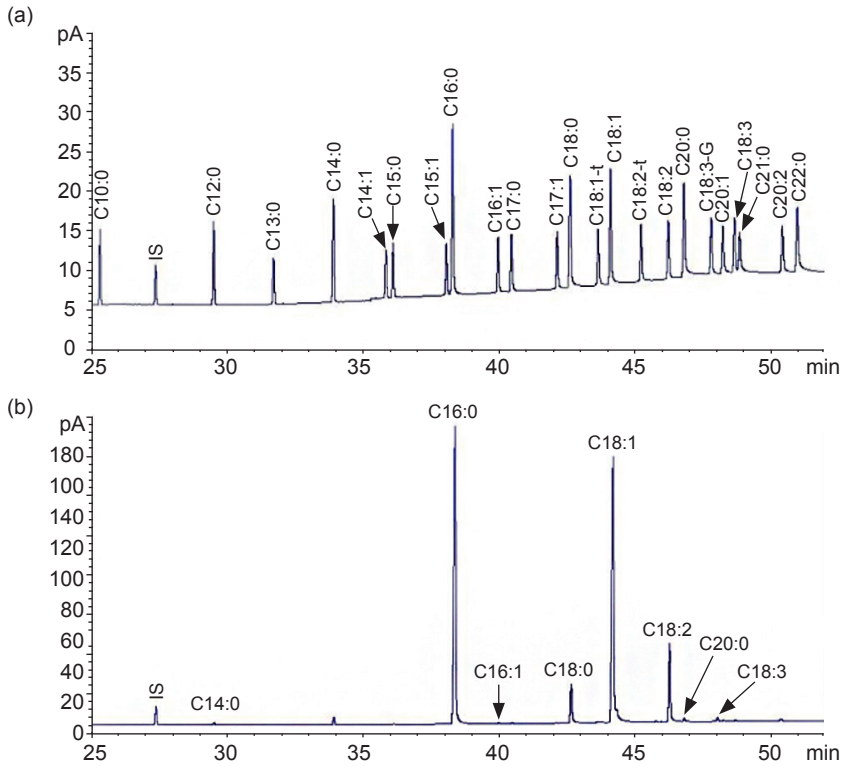


Figure 1. Chromatogram of FAME determined by GC-FID. (a) Standard (FAME 37 mixture) and (b) refined palm oil.

palmitic acid and oleic acid showed higher contents other than fatty acids. Palm stearin showed 63.38 g/100.00 g of palmitic acid, which could influence the hardness characteristics. On the other hand, palm olein showed 44.92 g/100.00 g of palmitic acid, which could impact their soft characteristics. Also, palm olein showed the highest oleic acid content (37.84 g/100.00 g). Myristic acid, palmitoleic acid, arachidic acid and linolenic acid were less abundant at level under 1.00 g/100.00 g. Gee (2007) and Koushki *et al.* (2015) showed similar results in fatty acid composition and its contents of refined and fractionated palm oil. Especially, according to Gee (2007), iodine value and melting point which could explain the properties of oils and fats including oxidative stress were different between palm olein and palm stearin. These differences were influenced by the composition and contents of fatty acids. Moreover, the composition and contents of TAGs would specifically explain the differences in the physical and chemical properties of fractionated palm oils. The fatty acid composition from this study and molecular weight of ammoniated ion was utilised based on the condition of multiple-NLS.

Identification of TAG using Multiple Neutral Loss Scan (NLS)

The multiple NLS is an effective scan method for the identification of lipids that possess neutral loss moieties such as fatty acyl chains in the TAG structure. The condition of multiple NLS was established using the fatty acids profile obtained by GC-FID, including NLS 245 (C14:0), NLS 273 (C16:0), NLS 271 (C16:1), NLS 301 (C18:0), NLS 299 (C18:1), NLS 297 (C18:2), NLS 329 (C20:0), NLS 295 (C18:3) and NLS 285 (C17:1, IS). The range of multiple NLS was at m/z 600-1050. The spectrum obtained from multiple NLS were utilised to confirm combinations of fatty acid chain and identify each TAG using their molecular masses of ammoniated ion form (*Figure 2*). For example, the spectrum at 875 was found in NLS 273, 297 and 299 means the loss of C16:0, C18:2 and C18:1 fatty acid from its TAG compounds. Besides the confirmation of the three fatty acids determined using multiple-NLS, the masses of ammoniated ion of TAG matched with 875, leading to confirmation of C54:3 (16:0/18:1/18:2). This process was repeated using different NLS conditions of fatty acid to identify TAG in refined and fractionated palm oil. A total of 32 TAGs were detected depending on the sample type and the range of m/z 797-993 in neutral loss scan with positive mode. Depending on the sample, various numbers of carbon (46-56) and double bonds (0-6) were identified. Most TAGs identified from the multiple-NLS were composed of palmitic acid (C16:0), oleic acid (C18:1) and linoleic acid (C18:2), similar to fatty acid analysis data.

Isotopic Deconvolution

The spectrums of identified TAGs were corrected using isotopic deconvolution. The main atoms of TAG are carbon, oxygen and hydrogen which have their own isotope, causing the interference in the mass spectrometry analysis. Particularly, this interference is influenced by carbon variants, including ^{13}C and ^{12}C. In other words, one TAG molecule (M) may have isotopes such as M+1, M+2, M+3, *etc*., and some of them may interfere with different mass (Li *et al*., 2014b). For example, C50:1 has a monoisotopic spectrum (M) at 851. On the other hand, its second isotopic spectrum (M+2) with two ^{13}C isotopic carbon is at m/z 853. The M+2 spectrum of C50:1 interferes with the monoisotopic spectrum of C50:0, which has m/z 853 *(Figure 3a*). C50:1 has one more double bond than C50:0, which means the loss of two hydrogen atoms.

Thus, the interference of isotope affects the accurate quantification of TAGs in mass spectrometry analysis, causing the requirement of isotopic deconvolution, which means removing the effect of isotope. This study conducted isotopic deconvolution for a spectrum determined using LC-MS/MS with multiple-NLS.

TABLE 1. FATTY ACID COMPOSITION AND CONTENTS OF REFINED AND FRACTIONATED PALM OIL

Fatty acid	Abbreviation	Fatty acid contents (g/100 g)			
		Refined palm oil	Palm olein	Palm stearin	Mid-fraction
Myristic acid	C14:0	1.07 ± 0.08^{ab}	0.93 ± 0.10^{b}	1.19 ± 0.07^{a}	0.95 ± 0.10^{b}
Palmitic acid	C16:0	46.08 ± 0.49^{bc}	44.92 ± 0.65^{c}	63.38 ± 0.57^{a}	51.59 ± 0.58^{b}
Palmitoleic acid	C16:1	0.14 ± 0.01^{a}	0.15 ± 0.02^{a}	0.10 ± 0.00^{a}	0.09 ± 0.08^{a}
Stearic acid	C18:0	4.60 ± 0.10^{bc}	4.33 ± 0.19^{c}	5.05 ± 0.10^{a}	4.63 ± 0.17^{b}
Oleic acid	C18:1	37.51 ± 0.35^{a}	37.84 ± 3.03^{a}	24.38 ± 0.55^{b}	35.36 ± 0.98^{a}
Linoleic acid	C18:2	9.32 ± 0.08^{a}	9.09 ± 2.63^{a}	5.04 ± 0.11^{b}	6.35 ± 0.26^{b}
Arachidic acid	C20:0	0.14 ± 0.25^{a}	0.35 ± 0.06^{a}	0.35 ± 0.06^{a}	0.20 ± 0.17^{a}
Linolenic acid	C18:3	0.17 ± 0.01^{a}	0.15 ± 0.03^{a}	0.07 ± 0.01^{b}	0.11 ± 0.01^{b}

Note: All values are means ± SD of triplicate analysis. Mean values in a row followed by different superscript letters are significantly (p<0.05) different (Duncan's multiple range test).

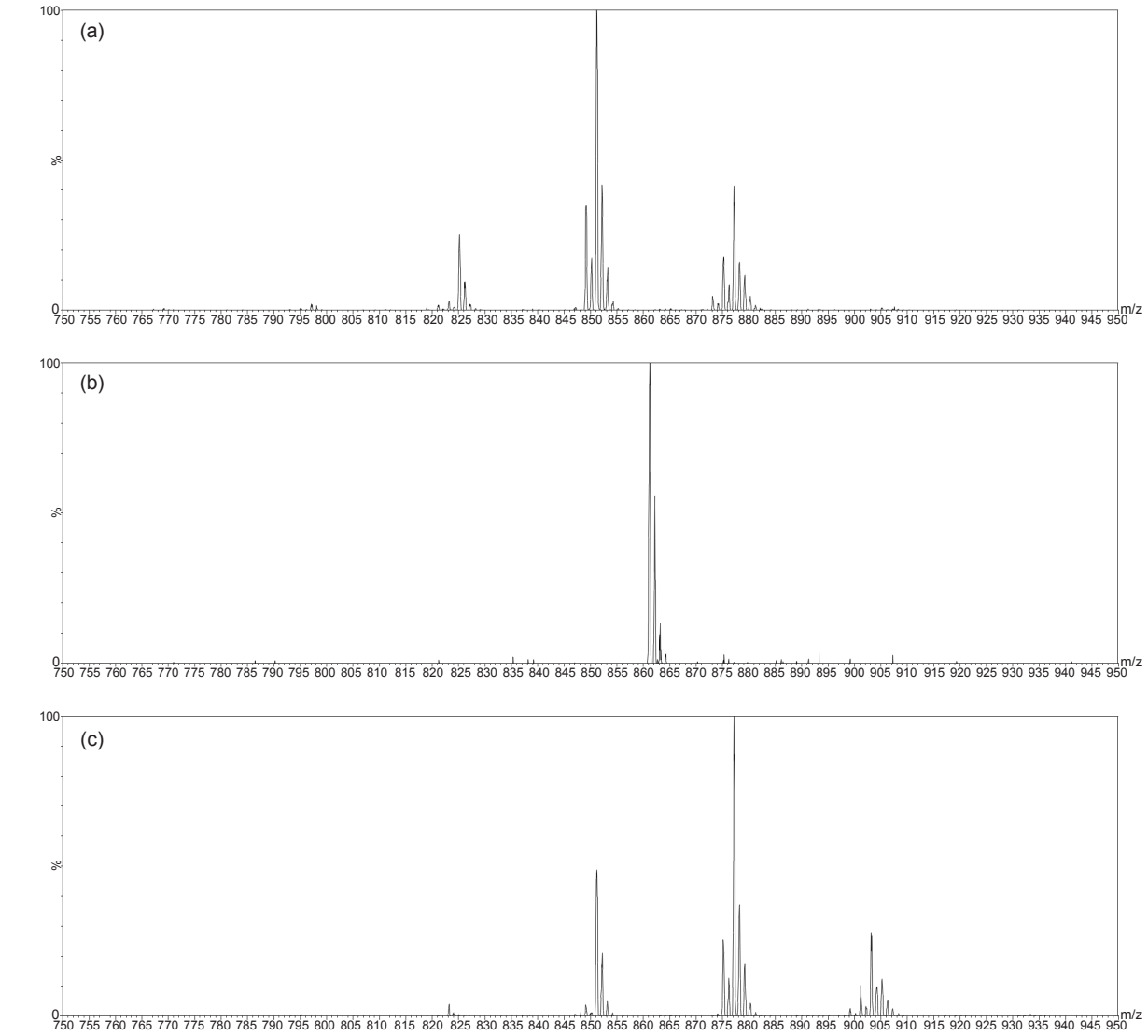


Figure 2. Partial spectrum of multiple NLS of ammoniated TAG ion in refined palm oil. (a) NLS 273 (Loss of C16:0), (b) NLS 285 (Loss of C17:1, internal standard), and (c) NLS 299 (Loss of C18:1).

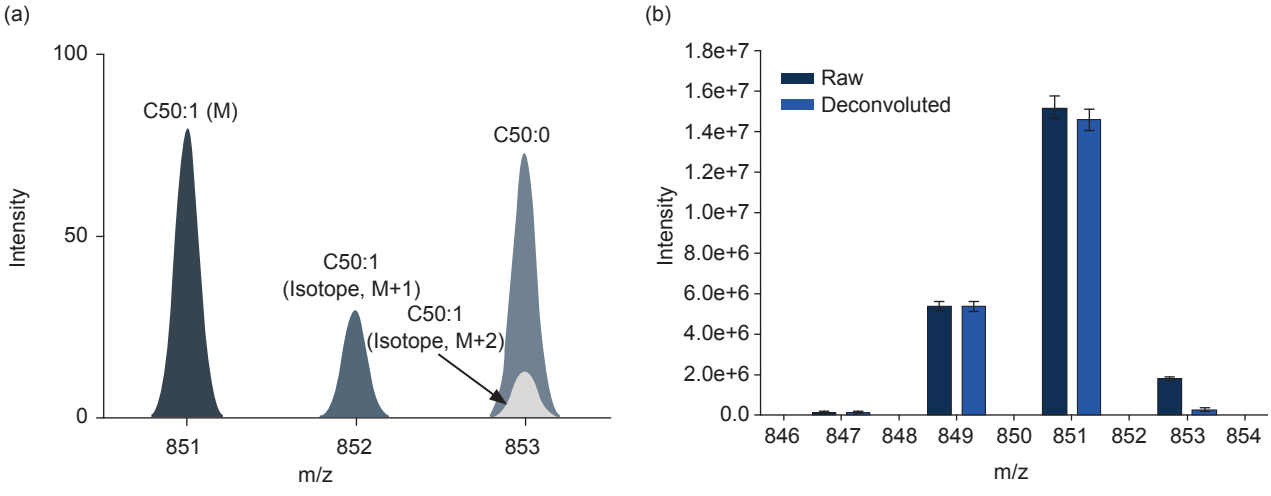


Figure 3. (a) Example of deconvolution to reduce effect of isotopic interference, and (b) partial result of isotopic deconvolution in NLS 217.

The calculation for deconvolution was followed as given by Li *et al.* (2014a; 2014b). First, the Z_M was calculated using Equation (1):

$$Z_M = [(N_C \times 1.12) \times (N_C \times 1.12) / 200 + (N_O \times 0.204)] / 100 \quad (1)$$

where N_C and N_O means the numbers of carbon and oxygen atoms of the diacylglycerol (DAG) product ion from fragmented TAGs. And then, the Z_M was applied to the following Equation (2) to compute the corrected peak signal:

$$^{C}I_{M+2} = I_{M+2} - {}^{C}I_M \times Z_M \quad (2)$$

where I_{M+2} means the gained raw spectrum intensity, and $^{C}I_M$ means the corrected spectrum intensity of molecule M. In this process, 32 TAG spectrum were deconvoluted depending on the sample, and the spectrum of C50:0 (16:0/16:0/18:0) TAG was removed because of isotopic interference. The partial results of isotopic deconvolution in NLS 217 are shown in *Figure 3b*. In this figure, the spectrum at m/z 847 showed the same intensity after isotopic deconvolution. On the other hand, the spectrum at m/z 853 showed the most decreasing intensity after isotopic deconvolution.

Calculation and Estimation of AF

After performing isotopic deconvolution on the spectrum signal obtained at individual NLS, the adjustment factors were used to correct the variable NLS spectrum of acquired TAGs that varied in the number of carbon atoms and double bonds in the fatty acid chain. The AF is defined as a coefficient where the NLS spectrum intensity of the internal standard (C51:3) is divided by the NLS spectrum intensity of each TAG, when the TAG and internal standard are equimolar (Li *et al.*, 2014a). The AF was calculated by utilising commercially purchased TAG standards, and then statistical estimation for regressive curve was conducted by using calculated factors. First, the regressive curve for saturated TAG was obtained using the calculated AF of saturated TAGs (*Figure 4a*). After that, the regressive curve was obtained for unsaturated TAG, including three double bond (*Figure 4b*) and six double bonds (*Figure 4c* and *4d*). Lastly, the final regressive curve was deduced about each carbon of TAGs (48-60) using acquired AF from calculation and estimation (*Figure 4e*). All deduced and computed AF are shown at *Table 2*.

These factors were applied to the isotopically deconvoluted spectrum intensity of NLS. For instance, the AF for m/z at 903 (C54:3) was 1.81, which means that 1.85 moles of C54:3 and 1.00 mole of internal standard (C51:3) would show the same spectrum intensity. Thus, the amount at m/z 903 (C54:3) from NLS 299 was corrected by multiplying 1.85. The increase in the AF indicated a decrease in the intensity of the NLS spectrum, which was found to increase with the number of carbons in the range of C46-C60 in a fatty acid chain. The results are consistent with the findings of Li *et al.* (2014a) in which the TAGs with short fatty acid chains were shown to have higher sensitivity than that of long fatty acid chain. The AF was increased depending on the increase in unsaturation of TAGs in the range of 3-6 double bonds. On the other hand, it was decreased in the range of 0-3 double bonds in the TAGs, which means the highest intensity of NLS spectrum at 3 double bonds. The similar results were reported in the study by Han and Gross (2001) and Li *et al.* (2014a).

Quantitation of TAG in Refined and Fractionated Palm Oil

The contents of individual TAG species in refined and fractionated palm oil were quantified

TABLE 2. CALCULATED AND DEDUCED ADJUSTMENT FACTOR (AF) FOR QUANTIFICATION OF TAG DETECTED IN REFINED AND FRACTIONATED PALM OIL (TAG 51:3, INTERNAL STANDARD = 1.0)

TAG	AF[1)]	TAG	AF	TAG	AF	TAG	AF	TAG	AF
46:0	0.51	50:2	0.80	52:5	1.89	56:1	3.47	58:4	3.81
48:0	0.78	50:3	0.88	52:6	2.51	56:2	2.85	58:5	4.51
48:1	0.55	50:4	1.14	54:0	2.89	56:3	2.58	58:6	5.81
48:2	0.49	50:5	1.59	54:1	2.28	56:4	2.67	60:0	10.65
48:3	0.62	50:6	2.23	54:2	1.92	56:5	3.11	60:1	7.69
48:4	0.92	52:0	1.87	54:3	1.81	56:6	3.92	60:2	5.90
48:5	1.39	52:1	1.46	54:4	1.96	58:0	6.89	60:3	5.28
48:6	2.05	52:2	1.26	54:5	2.36	58:1	5.23	60:4	5.83
50:0	1.21	52:3	1.26	54:6	3.01	58:2	4.17	60:5	7.55
50:1	0.91	52:4	1.47	56:0	4.46	58:3	3.69	60:6	10.44

Note: [1)] The adjustment factor is defined as NLS intensity of internal standard divided by NLS intensity of commercially purchased TAG standard for each.

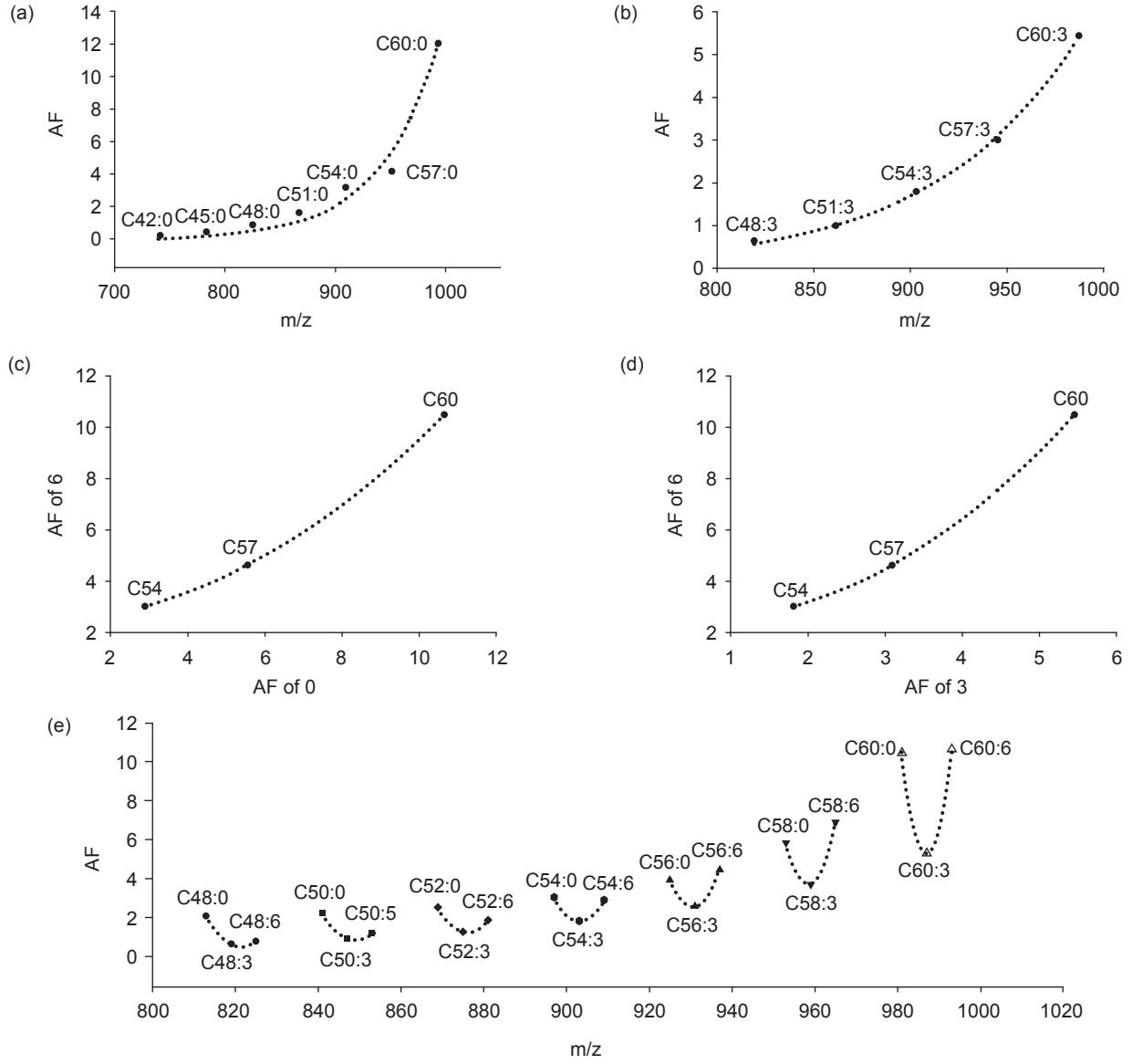


Figure 4. The process of estimation of AF using regression curve to determine TAG in refined and fractionated palm oil. (a) Regression curve of saturated TAG, (b) regression curve of TAG with 3 double bonds, (c) estimation of TAG with 6 double bonds (TAG:0 ➛ TAG:6), (d) estimation of TAG with 6 double bonds (TAG:3 ➛ TAG:6), and (e) combination of regression curve to estimate AF along with carbon number.

using a spectrum acquired from multiple-NLS with isotopic deconvolution and adjustment factor. The calculation for TAG quantification was followed as given by Li *et al.* (2014a). First, each fatty acid in TAGs (Am) at a particular m/z was calculated (in nmol) following the Equation (3):

$$A_m = \frac{\text{(Observed TAG intersity} \times \text{Internal standard amount)} \times \text{Adjustment factor}}{\text{Observed internal standard intensity}} \quad (3)$$

The calculated amount of fatty acid in TAG at each m/z was used to calculate the amount of each TAG molecule. For instance, TAG mass m/z at 877.0 (C52:2) has various fatty acid chains. The most amount of fatty acid chain at C52:2 and they are C16:0, C18:1, C18:0 and C18:2, in this order. Based on the number of carbons and double bonds on the three fatty acid chains, two kinds of fatty acid combinations were deduced for C52:2, such as 16:0/18:1/18:1 and 16:0/18:0/18:2. The amount of 16:0/18:1/18:1 was represented by the amount of 18:1, $A_{18:1}$. The 16:0/18:1/18:1 have two C18:1 acyl chains. Thus, the amount of this TAG was calculated using the formula, *i.e.*, $A_{18:1}/2$. Also, the level of 16:0/18:0/18:2 was represented by the amount of C18:0, $A_{18:0}$ and the amount of C18:2, $A_{18:2}$. The formula to calculate the level of 16:0/18:0/18:2 was $(A_{18:0} + A_{18:2})/2$. Individual TAGs (31) identified by their fatty acyl chain were calculated this way, depending on samples. The final calculated results

are shown in *Table 3*, and the results are presented as nmol/g and % portion separately. The two most abundant TAGs, C50:1 (16:0/16:0/18:1) (1415.8-1943.9 nmol/g, 20.5%-36.0%) and C52:2 (16:0/18:1/18:1) (962.0-1717.8 nmol/g, 17.8%-25.0%) accounted for nearly 40% of the TAGs found in refined and fractionated palm oil. In contrast, the TAG, which exhibited the third highest content, varied greatly depending on the samples.

The third highest TAG of refined palm oil and palm olein was C52:3 (16:0/18:1/18:2) (814.5-911.9 nmol/g, 12.2%-13.3%), however, palm stearin did not contain this TAG. Whereas, palm stearin showed the third highest contents of C48:0 (16:0/16:0/16:0) (1057.7 nmol/g, 17.4%). On the other hand, palm olein and mid-fraction showed relatively lower contents at 29.1 and 53.8 nmol/g, respectively. Braipson-Danthine and Gibon (2007) determined the TAG composition in fractionated palm oil by HPLC and reported similar results with our study. In their study, palm olein showed relatively higher contents of C52:2 (16:0/18:1/18:1) at 25.41%-43.03%. Whereas, palm stearin showed relatively higher contents of C50:1 (16:0/16:0/18:1) at 30.01%-40.67%. Palm stearin especially showed the TAG composition of C48:0 (16:0/16:0/16:0), however, palm olein did not contain this TAG. Chen *et al.* (2007) and Oboh (2004) also determined the TAG composition in refined palm oil by HPLC and TLC with GC-FID, respectively. In their studies, the refined palm oil mainly contained the TAG of C52:2 (16:0/18:1/18:1) and C50:1 (16:0/16:0/18:1). The other analysis methods such as HPLC, TLC and GC-FID had been used to determine the TAG compositions and contents in refined and fractionated palm oil due to its relatively effective values. However, a quantitative literature of TAG species in absolute amount, *e.g.*, nmol/g, is still lacking for various forms of palm oil.

TABLE 3. IDENTIFICATION AND QUANTIFICATION DATA OF TAG IN REFINED AND FRACTIONATED PALM OIL

m/z[1)]	TAG	Composition	Refined palm oil		Palm olein		Palm stearin		Mid-fraction	
			nmol/g	Portion	nmol/g	Portion	nmol/g	Portion	nmol/g	Portion
797	46:0	14:0-16:0-16:0	17.0 ± 0.2^{b}	0.3	5.2 ± 0.1^{d}	0.1	50.6 ± 1.6^{a}	0.8	7.9 ± 0.9^{c}	0.2
821	48:2	14:0-16:0-18:2	19.4 ± 1.5^{a}	0.3	18.9 ± 0.2^{a}	0.3	0.0	0.0	18.4 ± 0.7^{a}	0.3
823	48:1	14:0-16:0-18:1	39.4 ± 5.4^{bc}	0.6	47.9 ± 1.5^{a}	0.7	43.2 ± 1.1^{ab}	0.7	34.7 ± 1.3^{c}	0.7
825	48:0	14:0-16:0-18:0	9.7 ± 0.4	0.1	N.D	0.0	N.D	0.0	N.D	0.0
825	48:0	16:0-16:0-16:0	222.9 ± 6.3^{b}	3.3	29.1 ± 2.3^{d}	0.4	1066.7 ± 18.4^{a}	17.4	53.8 ± 0.8^{c}	1.0
847	50:3	14:0-18:1-18:2	20.8 ± 1^{a}	0.3	17.2 ± 0.8^{b}	0.3	4.1 ± 1.3^{c}	0.1	15.1 ± 3.2^{b}	0.3
847	50:3	16:0-16:1-18:2	27.2 ± 0.4^{a}	0.4	14.9 ± 2.2^{b}	0.2	10.8 ± 1^{c}	0.2	N.D	0.0
847	50:3	16:0-16:0-18:3	N.D	0.0	15.3 ± 0.8^{a}	0.2	15.1 ± 0.9^{a}	0.3	10.2 ± 0.8^{b}	0.2
847	50:3	16:1-16:1-18:1	4.3 ± 1.3^{b}	0.1	3.8 ± 1.5^{b}	0.1	10.1 ± 1.7^{a}	0.2	N.D	0.0
849	50:2	14:0-18:1-18:1	28.7 ± 0.7^{b}	0.4	33.8 ± 2.9^{a}	0.5	17.7 ± 1.5^{c}	0.3	6.7 ± 1.7^{d}	0.1
849	50:2	16:0-16:1-18:1	21.5 ± 1.7^{c}	0.3	25.9 ± 1.5^{b}	0.4	17 ± 2.4^{d}	0.3	32.5 ± 2.5^{a}	0.6
849	50:2	16:0-16:0-18:2	403.4 ± 8.9^{b}	6.0	476.4 ± 2.0^{a}	6.9	304.6 ± 4.3^{d}	5.0	347 ± 1.2^{c}	6.5
851	50:1	14:0-18:0-18:1	N.D	0.0	N.D	0.0	N.D	0.0	11.4 ± 0.8	0.2
851	50:1	16:0-16:0-18:1	1437.5 ± 11.1^{c}	21.4	1410.6 ± 11.5^{c}	20.5	1686.1 ± 5.2^{b}	27.4	1934.3 ± 30^{a}	36.0
853	50:0	16:0-16:0-18:0	112.6 ± 1.9^{b}	1.7	N.D	0.0	302.7 ± 3.2^{a}	4.9	N.D	0.0
873	52:4	16:0-18:1-18:3	42.3 ± 1.4^{b}	0.6	48.2 ± 1.4^{a}	0.7	N.D	0.0	25.7 ± 0.7^{c}	0.5
873	52:4	16:0-18:2-18:2	216 ± 2.6^{b}	3.2	248.7 ± 4.0^{a}	3.6	129.5 ± 4.8^{c}	2.1	91.6 ± 2.2^{d}	1.7
875	52:3	16:0-18:1-18:2	815.8 ± 19.7^{b}	12.2	911.0 ± 7.1^{a}	13.3	N.D	0.0	416.6 ± 7.1^{c}	7.8
877	52:2	16:0-18:0-18:2	218.2 ± 100.8^{a}	3.3	133.7 ± 2.0^{ab}	2.0	102.9 ± 4.2^{c}	1.7	156.4 ± 43.1^{ab}	2.9
877	52:2	16:0-18:1-18:1	1487.9 ± 27.8^{b}	22.2	1718.9 ± 24.7^{a}	25.0	1109.9 ± 39.6^{c}	18.1	956.5 ± 20.3^{d}	17.8
879	52:1	16:0-18:0-18:1	277.4 ± 9.1^{d}	4.1	335.8 ± 19.4^{c}	4.9	424.3 ± 8.7^{b}	6.9	501.7 ± 16.8^{a}	9.3
897	54:6	18:2-18:2-18:2	20.7 ± 1.4^{c}	0.3	33.0 ± 2.1^{a}	0.5	8.9 ± 1.7^{d}	0.1	24.6 ± 0.9^{b}	0.5
899	54:5	18:1-18:2-18:2	186.2 ± 7^{a}	2.8	113.9 ± 1.9^{b}	1.7	51.6 ± 1.6^{c}	0.8	49.5 ± 0.8^{c}	0.9
901	54:4	18:1-18:1-18:2	219.7 ± 7.9^{b}	3.3	251.1 ± 3.3^{a}	3.7	158.7 ± 3.1^{c}	2.6	123.7 ± 6.5^{d}	2.3
901	54:4	18:0-18:2-18:2	51.7 ± 3.5^{a}	0.8	50.2 ± 1.7^{a}	0.7	34.6 ± 1.8^{a}	0.6	66.9 ± 40.4^{a}	1.3
903	54:3	18:0-18:1-18:2	118.1 ± 2^{b}	1.8	144.7 ± 4.7^{a}	2.1	77.5 ± 6.1^{c}	1.3	63.6 ± 3.3^{d}	1.2
903	54:3	18:1-18:1-18:1	325.3 ± 13^{b}	4.8	410.2 ± 5.5^{a}	6.0	249.3 ± 1.8^{c}	4.1	199.6 ± 2.6^{d}	3.7
905	54:2	16:0-18:2-20:0	30.8 ± 1.3^{b}	0.5	37.3 ± 1.0^{a}	0.5	31.7 ± 1.6^{b}	0.5	N.D	0.0
905	54:2	18:0-18:1-18:1	230.2 ± 5.5^{b}	3.4	259.4 ± 12.2^{a}	3.8	137.2 ± 21.8^{c}	2.2	131.9 ± 0.9^{c}	2.5
907	54:1	16:0-18:1-20:0	79.1 ± 3.1^{a}	1.2	44.8 ± 1.0^{c}	0.7	71.9 ± 3.4^{b}	1.2	68.5 ± 4.1^{b}	1.3
933	54:2	18:1-18:1-20:0	31.6 ± 1.3^{a}	0.2	29.9 ± 1.5^{a}	0.4	32.2 ± 1.5^{a}	0.5	23.6 ± 0.7^{b}	0.4

Note: All values are means ± SD of triplicate analysis. Mean values in a row followed by different superscript letters are significantly (p<0.05) different (Duncan's multiple range test). [1)] - m/z is the molecular weight of ammoniated ion of TAG. N.D - not detected.

A quantitative TAG profiling method for the refined and fractionated palm oil is described in the present study based on multiple-NLS.

The differences in composition and content suggest that the TAGs have been closely related to the physical and chemical properties of palm oils which are refined and fractionated. For example, palm stearin is semi liquid form like butter and shortening. According to Gee (2007), palm stearin showed a higher melting point than palm olein. Palm stearin is thought to have more palmitic acid than other fractionated palm oil, including palm olein. Its predominant type of palmitic acid is C48:0 (16:0/16:0/16:0), making palm stearin harder than other fractionated palm oil. Because saturated TAGs strongly linked with each other. Also according to Almeida *et al.* (2018), palm stearin showed relatively higher oxidative stability than palm olein. Although both fractionated palm oil contained palmitic acid, but also their predominant type of palmitic acid is different.

CONCLUSION

In conclusion, LC-MS/MS with multiple-NLS was effectively used to determine the TAG composition and its contents in refined and fractionated palm oil. To obtain precise quantification, isotopic deconvolution and the AF of various TAG were used. A total of 31 TAGs were identified and quantified, and C50:1 (16:0/16:0/18:1) (20.5%-36.0%), C52:2 (16:0/18:1/18:1) (17.8%-25.0%), C52:3 (16:0/18:1/18:2) (7.8%-12.2%), C48:0 (16:0/16:0/16:0) (0.4%-17.4%) and C52:1 (16:0/18:0/18:1) (4.1%-9.3%) being the most abundant TAGs, depending on refined and fractionated palm oils. Using direct infusion LC-MS/MS with repeated neutral loss scans to identify and quantify TAG was an efficient approach that improved the detection accuracy. This approach effectively revealed the composition and content of TAG in refined and fractionated palm oil. This has ramifications for the physical and chemical properties and could be positively used to understand the phenomenon, like hardness, oxidation levels and other properties.

ACKNOWLEDGEMENT

We thank Sanghwa Jung from Lotte confectionery CO. (Seoul, Korea) for providing the palm oil samples.

REFERENCES

Almeida, D T D; Viana, T V; Costa, M M; Silva, C D S and Feitosa, S (2018). Effects of different storage conditions on the oxidative stability of crude and refined palm oil, olein and stearin (*Elaeis guineensis*). *Food Sci. Technol.*, *39*: 211-217. DOI: 10.1590/fst.43317.

Bates, P D; Fatihi, A; Snapp, A R; Carlsson, A S; Browse, J and Lu, C (2012). Acyl editing and headgroup exchange are the major mechanisms that direct polyunsaturated fatty acid flux into triacylglycerols. *Plant Physiol.*, *160(3)*: 1530-1539. DOI: 10.1104/pp.112.204438.

Beccaria, M; Sullini, G; Cacciola, F; Donato, P; Dugo, P and Mondello, L (2014). High performance characterization of triacylglycerols in milk and milk-related samples by liquid chromatography and mass spectrometry. *J. Chromatogr. A, 1360*: 172-187. DOI: 10.1016/j.chroma.2014.07.073.

Braipson-Danthine, S and Gibon, V (2007). Comparative analysis of triacylglycerol composition, melting properties and polymorphic behavior of palm oil and fractions. *Eur. J. Lipid Sci. Technol.*, *109(4)*: 359-372. DOI: 10.1002/ejlt.200600289.

Buchgraber, M; Ulberth, F and Anklam, E (2000). Comparison of HPLC and GLC techniques for the determination of the triglyceride profile of cocoa butter. *J. Agric. Food Chem.*, *48(8)*: 3359-3363. DOI: 10.1021/jf991000p.

Carter, C; Finley, W; Fry, J; Jackson, D and Willis, L (2007). Palm oil markets and future supply. *Eur. J. Lipid Sci. Technol.*, *109(4)*: 307-314. DOI: 10.1002/ejlt.200600256.

Chandrasekharan, N; Sundram, K and Basiron, Y (2000). Changing nutritional and health perspectives on palm oil. *Brunei Int. Med. J.*, *2*: 417-427.

Chen, C W; Chong, C L; Ghazali, H M and Lai, O M (2007). Interpretation of triacylglycerol profiles of palm oil, palm kernel oil and their binary blends. *Food Chem., 100(1)*: 178-191. DOI: 10.1016/j.foodchem.2005.09.044.

Cheong, W F; Wenk, M R and Shui, G (2014). Comprehensive analysis of lipid composition in crude palm oil using multiple lipidomic approaches. *J. Genet. Genomics*, *41(5)*: 293-304. DOI: 10.1016/j.jgg.2014.04.002.

Gee, P T (2007). Analytical characteristics of crude and refined palm oil and fractions. *Eur. J. Lipid Sci. Technol.*, *109(4)*: 373-379. DOI: 10.1002/ejlt.200600264.

Han, R H; Wang, M; Fang, X and Han, X (2013). Simulation of triacylglycerol ion profiles: Bioinformatics for interpretation of triacylglycerol

biosynthesis. *J. Lipid Res.*, *54(4)*: 1023-1032. DOI: 10.1194/jlr.M033837.

Han, X, and Gross, R W (2001). Quantitative analysis and molecular species fingerprinting of triacylglyceride molecular species directly from lipid extracts of biological samples by electrospray ionization tandem mass spectrometry. *Anal. Biochem.*, *295(1)*: 88-100. DOI: 10.1006/abio.2001.5178.

Han, X; Yang, K and Gross, R W (2012). Multi-dimensional mass spectrometry-based shotgun lipidomics and novel strategies for lipidomic analyses. *Mass Spectrom. Rev.*, *31(1)*: 134-178. DOI: 10.1002/mas.20342.

Himawan, C; Starov, V M and Stapley, A G (2006). Thermodynamic and kinetic aspects of fat crystallization. *Adv. Colloid Interface Sci.*, *122(1-3)*: 3-33. DOI: 10.1016/j.cis.2006.06.016.

KFDA (2022). *Food Code.* 84th edition. Korea Food and Drug Administration. p. 377-385.

Khor, H; Goh, S and Tan, W (1980). Glycolipids of Malaysian palm oil. *Oil Palm News, (24)*: 12-13.

Koushki, M; Nahidi, M and Cheraghali, F (2015). Physico-chemical properties, fatty acid profile and nutrition in palm oil. *Arch. Adv. Biosci.*, *6(3)*: 117-134.

Li, M; Baughman, E; Roth, M R; Han, X; Welti, R and Wang, X (2014a). Quantitative profiling and pattern analysis of triacylglycerol species in *Arabidopsis* seeds by electrospray ionization mass spectrometry. *Plant J.*, *77(1)*: 160-172. DOI: 10.1111/tpj.12365.

Li, M; Butka, E and Wang, X (2014b). Comprehensive quantification of triacylglycerols in soybean seeds by electrospray ionization mass spectrometry with multiple neutral loss scans. *Sci. Rep.*, *4*: 6581. DOI: 10.1038/srep06581.

Mateos, R; Trujillo, M; Pérez-Camino, M C; Moreda, W and Cert, A (2005). Relationships between oxidative stability, triacylglycerol composition, and antioxidant content in olive oil matrices. *J. Agric. Food Chem.*, *53(14)*: 5766-5771. DOI: 10.1021/jf0504263.

Murphy, D J (2009). Oil palm: Future prospects for yield and quality improvements. *Lipid Technol.*, *21(11-12)*: 257-260. DOI: 10.1002/lite.200900067.

Noor Lida, H M D; Sundram, K; Siew, W L; Aminah, A and Mamot, S (2002). TAG composition and solid fat content of palm oil, sunflower oil, and palm kernel olein blend before and after chemical interesterification. *J. Am. Oil Chem. Soc.*, *79(11)*: 1137-1144. DOI: 10.1007/s11746-002-0617-0.

Oboh, F O J (2004). Triacylglycerols of palm oil. *Benin. Sci. Dig.*, *2*: 79-85.

Pizzo, J S; Cruz, V H M; Santos, P D S; Silva, G R; Souza, P M; Manin, L P; Santos, O O and Visentainer, J V (2022). Instantaneous characterization of crude vegetable oils via triacylglycerols fingerprint by atmospheric solids analysis probe tandem mass spectrometry with multiple neutral loss scans. *Food Contr., 134*: 108710. DOI: 10.1016/j.foodcont.2021.108710.

Sirbu, D; Corno, M; Ullrich, M S and Kuhnert, N (2018). Characterization of triacylglycerols in unfermented cocoa beans by HPLC-ESI mass spectrometry. *Food Chem., 254*: 232-240. DOI: 10.1016/j.foodchem.2018.01.194

Sato, K (2001). Crystallization behaviour of fats and lipids - A review. *Chem. Eng. Sci.*, *56(7)*: 2255-2265. DOI: 10.1016/S0009-2509(00)00458-9.

Tan, B K; Hamilton, R J and Berger, K G (1981). Glyceride analysis of palm oil after solvent fractionation. *J. Am. Oil Chem. Soc.*, *58(1)*: 1-5. DOI: 10.1007/BF02666043.

Toschi, T G; Christie, W W and Conte, L S (1993). Capillary gas chromatography combined with high performance liquid chromatography for the structural analysis of olive oil triacylglycerols. *J. High Resolut. Chromatogr.*, *16(12)*: 725-730. DOI: 10.1002/jhrc.1240161211.

Xie, Y; Wei, F; Xu, S; Wu, B; Zheng, C; Lv, X; Wu, Z; Chen, H and Huang, F (2019). Profiling and quantification of lipids in cold-pressed rapeseed oils based on direct infusion electrospray ionization tandem mass spectrometry. *Food Chem.*, *285*: 194-203. DOI: 10.1016/j.foodchem.2019.01.146.

Xu, S-l; Wei, F; Xie, Y; Lv, X; Dong, X-y and Chen, H (2018). Research advances based on mass spectrometry for profiling of triacylglycerols in oils and fats and their applications. *Electrophor., 39(13)*: 1558-1568. DOI: 10.1002/elps.201700481.

Yeo, J and Parrish, C C (2020). Evaluation of triacylglycerol (TAG) profiles and their contents in salmon muscle tissue using ESI-MS/MS spectrometry with multiple neutral loss scans. *Food Chem.*, *324*: 126816. DOI: 10.1016/j.foodchem.2020.126816.

Journal of Oil Palm Research Vol. 36 (4) December 2024 p. 718-727
DOI: https://doi.org/10.21894/jopr.2023.0047

In Vitro EVALUATION OF MELANOGENESIS INHIBITION BY TOCOTRIENOL RICH FRACTION

NUR ANIS ALBAKRY[1]*; YUSRABBIL AMIYATI YUSOF[1] and ZAFARIZAL ALDRIN AZIZUL HASAN[1]

ABSTRACT

Melanogenesis is a process of melanin production, the leading cause of pigmentation in human skin. However, ultraviolet (UV) irradiation can stimulate melanocytes and enhance melanin production. This study aimed to evaluate the effects of tocotrienol-rich fraction (TRF), a potent antioxidant, on UVA-induced melanogenesis in melanocytes. Melanocytes were treated with different concentrations of study materials [TRF, alpha-tocopherol (α-TP) and kojic acid (KA)] to determine the cell viability and the effect of TRF on melanin synthesis. Then, the optimum concentration of study materials was used to assess their effect on melanin synthesis in the UVA-irradiated melanocytes. Treatment of melanocytes with different concentrations of TRF and α-TP increased the number of viable cells. The optimum concentration of 62.5 µg mL^{-1} for study materials was used to determine their effects on melanin synthesis. After seven days, the irradiated and untreated melanocytes showed a significant 10.8% increase in melanin content, indicating that UVA irradiation directly influences melanogenesis. Melanocytes treated with TRF and irradiated with UVA showed a slight decrease in melanin content of about 4.0% compared to the negative control (irradiated), indicating that TRF may effectively protect cells from UVA irradiation. From findings, TRF could be a useful therapeutic agent for treating skin hyperpigmentation and a practical component to support skin lightening in skincare products.

Keywords: melanin content, melanocytes, TRF, UVA.

Received: 9 February 2023**; Accepted:** 7 August 2023**; Published online:** 11 September 2023.

INTRODUCTION

Melanogenesis is a highly regulated process in human skin. Melanogenesis occurs within melanosomes (Hida *et al*., 2020), the specialised lysosome-related organelles of melanocytes located in the basal layer of the epidermis (Le, 2020; Maranduca *et al*., 2019). Melanocytes are dendritic cells that synthesise melanin in melanosomes and transfer it to surrounding keratinocytes, where the cells are protected from DNA damage (Ramsden and Riley, 2014). Melanosomes protect epidermal cells from damage by limiting the penetration of ultraviolet (UV) radiation through the epidermal layers of the skin and scavenging reactive oxygen species (ROS) that are generated by UV radiation (Yi *et al*., 2018).

UV exposure is recognised as a well-known external risk factor for melanoma development (Sample and He, 2018), and a better strategy to prevent UV-induced melanoma is to inhibit both UVA and UVB cell damage pathways (Sun *et al*., 2020). Studies have shown that UVA strongly influences skin melanogenesis by activating the oxidative stress pathway involving ROS generation (Dumbuya *et al*., 2020). It is well established that UVA irradiation, especially UVA (340-400 nm), induces pigmentation and oxidative stress to a greater extent than UVB (290-320 nm) irradiation and is also more prominently associated with oxidative stress (Lohan *et al*., 2016; Nahhas *et al*., 2018). In another study, Chen *et al*. (2021) reported a link between oxidative stress and UVA-mediated exacerbation of melanogenesis, due to the overproduction of reactive oxidants.

[1] Malaysian Palm Oil Board,
6, Persiaran Institusi, Bandar Baru Bangi,
43000 Kajang, Selangor, Malaysia.

* *Corresponding author e-mail: nuranis@mpob.gov.my*

Plants are a rich source of biologically active substances that significantly affect human skin. Plants can exhibit a variety of properties, both medicinal for certain skin diseases and beneficial for skin health, including antioxidant effects (Michalak, 2020). Several botanical extracts have been found to have high antioxidant capacity and the ability to protect the skin from UV-induced effects (Dunaway *et al*., 2018). The ability to scavenge free radicals and the antioxidant properties of plants are associated with the presence of components such as polyphenols, tocopherols, carotenoids and ascorbic acid (Song *et al*., 2020). Tocopherols and tocotrienols are isoforms of vitamin E that inhibit the formation of new free radicals and neutralise existing free radicals.

Oil palm is the most efficient oil crop in the world, contributing to 31.6% (76.39 million tonnes) of global total oil and fats (Parveez *et al*., 2022). Palm oil is a rich source of vitamin E which comprises tocopherols and tocotrienols. It plays a pivotal role as an essential, fat-soluble nutrient that functions as an antioxidant in the human body. Both tocopherols (-TP) and tocotrienols (-T3) have isomers, designated as alpha (α-), beta (β-), gamma (γ-) and delta (δ-), which differ by the number and position of methyl groups on the chromanol ring. The mechanism of antioxidant activity of tocopherols and tocotrienols is partly related to the presence of a hydroxyl group in the chromanol ring, which donates a hydrogen atom to reduce free radicals (Adwas *et al*., 2019). In addition, tocotrienols have a beneficial effect on various chronic diseases, such as cardiovascular and neurodegenerative (Marelli *et al*., 2016). It also has an anti-proliferative effects on human breast cancer cells (Loganathan *et al*., 2021).

Tocopherol is commonly and widely used in anti-ageing and skin-whitening products, although most scientific studies evaluating the potential benefits of tocopherol have been conducted in animals (Makpol *et al*., 2014). α-TP of vitamin E is a well-known antioxidant, reported to be the most abundant non-enzymatic, lipid-soluble antioxidant in human tissues. Topically applied α-TP can inhibit UV radiation-induced DNA damage in human keratinocytes *in vitro* pre and post-UVA exposure (Delinasios *et al*., 2018).

Kojic acid (KA) is an organic metabolite produced by fungi that inhibits tyrosinase activity in the formation of melanin (Saeedi *et al*., 2019). KA is a well-known depigmenting agent often used as a positive control in screening new components or extracts that successfully inhibit melanin production (Wang *et al*., 2022). Despite the numerous advantages of using KA in topical products, there are some drawbacks, such as contact dermatitis and potential skin photodamage (Saeedi *et al*., 2019). Tocopherols and tocotrienols, on the other hand, are widely used in dermatology and cosmeceutical for their antioxidant and UV protective properties that provide photoprotection to the skin.

There are many reports on the effects of vitamin E isomers on the inhibition of skin cancer cells, reduction of tyrosinase enzyme and melanin production. In mouse B16 melanoma cells, γ-TP inhibited up to 39% of melanin synthesis and 45% of tyrosinase activity. δ-T3 inhibited melanin synthesis significantly in B16 melanoma cells (Yap *et al.*, 2010). A study done by Ng *et al.* (2014) showed that the inhibitory effects of δ-T3 on melanogenesis are mediated by the activation of extracellular signal-regulated kinase signaling, thus resulting in downstream suppression of melanogenesis-related proteins and melanin production. The potent antioxidant property of δ-T3 decreased the melanin levels in murine B16 melanocyte cells by preventing the oxidative reactions of tyrosinase (Michihara *et al*., 2010; Yap *et al*., 2010).

TRF consists of 70% tocotrienols (T3) and 30% tocopherols (TP) (Sen *et al*., 2010). It has been reported that treatment with palm TRF (500 μg mL^{-1}) possessed anti-melanogenic properties and may be useful in improving skin pigmentation caused by UVA (Makpol *et al*., 2014). However, the exact compositions of TRF used were not provided. Moreover, there are limited studies reporting the use of TRF to inhibit melanogenesis.

Therefore, the present work aimed to determine the effects of TRF (70% tocotrienols, 30% tocopherols) on UVA-induced melanogenesis. The optimum concentration of TRF, α-TP and KA was assessed by analysing cell viability, measuring melanin content and UVA-induced melanogenesis using human epidermal melanocytes. We hypothesised that TRF has beneficial effects as an anti-melanogenic agent to protect the skin from UVA-induced melanogenesis.

MATERIALS AND METHODS

Reagents

Ethanol with a purity of 99% was obtained from RCI Labscan, Thailand. TRF with a purity of 70% was obtained from Sime Darby, Malaysia. Kojic acid (KA), alpha-tocopherol (α-TP), thiazolyl blue tetrazolium bromide (MTT) and synthetic melanin were purchased from Sigma-Aldrich, US. Isopropanol, potassium phosphate buffer (potassium dihydrogen phosphate and dipotassium hydrogen phosphate) and sodium hydroxide (NaOH) were purchased from Merck, Germany. Normal human epidermal melanocyte, reagents and Dulbecco's Phosphate

Buffered Saline (PBS) were purchased from Sciencell Research Laboratories (Carlsbad, CA, USA).

Cell Culture

Melanocytes were cultured in a complete medium containing melanocyte medium, supplemented with a low percentage of Fetal Bovine Serum (FBS) (0.5%), 100 U mL^{-1} penicillin, 100 µg mL^{-1} streptomycin and melanocyte growth supplement. The cells were grown in a humidified chamber containing 5% CO_2 at 37°C.

Cell Viability Assay

When 90% confluency of melanocyte was attained at passage four, trypsinisation and seeding were done in 96-well plates ($2x10^4$ cells/well) in a complete medium. After overnight incubation, the medium was replaced with a new medium containing cells treated with various concentrations of TRF, α-TP and KA (7.8, 15.6, 31.3, 62.5, 125.0, 250.0 and 500.0 µg mL^{-1}) and incubated for 24 hr at 5% CO_2 at 37°C. After incubation, the wells were washed with PBS to remove debris and dead cells. The fresh medium was replaced with 10 µL of MTT (5 mg mL^{-1} in PBS), and MTT was added to each well and incubated for 4 hr at 5% CO_2 at 37°C. The solution in each well was replaced with dimethyl sulfoxide to solubilise the formed formazan crystals, and the wells were further incubated at room temperature for 10 min. The absorbance of each well was measured at 540 nm using a BioTek Synergy™ H1 Reader (BioTek Instrument, Winooski, VT, USA). The cell viability assay was performed to determine the optimum dose of TRF for subsequent experiments. The medium for untreated cells (control) was changed in parallel to the treated cells.

Melanin Content Measurement

Melanin content was determined using the method described by Zaidi *et al.* (2016) with slight modifications. A total of $1x10^5$ cells/well were seeded in 24-well plates. After overnight incubation, the medium was refreshed with a new medium. TRF, α-TP and KA at a concentration of 62.5 µg mL^{-1} were added and incubated for 24, 48, 72 hr and seven days. Melanocyte cells were harvested with EDTA/trypsin after treatments with TRF, α-TP and KA at each period for 1 hr. Then melanocyte cells were centrifuged at 10 000 g for 10 min. The supernatants were discarded, while pellets were dissolved in one normality (N) sodium hydroxide (NaOH) and incubated at 80°C for 1 hr. After incubation, the solution was centrifuged at 10 000 g for 10 min. The supernatants were transferred into 96-well plates in triplicate, and optical density (OD) was measured at 450 nm using BioTek Synergy™ H1 Reader.

Determination of Optimum Dose for UVA Irradiation

The optimum dosage for UVA irradiation was determined by exposing the skin melanocytes to UVA for seven consecutive days at doses of 0, 0.2, 0.4, 0.6, 0.8, 1.0, 2.0, 4.0, 6.0, 8.0 and 10.0 J cm^{-2}. UVA irradiation was carried out according to Makpol *et al.* (2014) with slight modification. Melanocytes were exposured to UVA stress with one stress per day for seven consecutive days. After an optimised UVA dosage was determined, $1x10^5$ melanocytes at passage five were directly exposed to 0.4, 0.6 and 0.8 J cm^{-2} UVA in a thin layer of PBS (pH 7.4) in an uncovered 12-well plate. The irradiation was carried out at room temperature using a light UVL-56 Handheld UV lamp (UVP, USA) which emits UVA at 365 nm. The emitted radiation was checked using a UVX-digital radiometer with UVA 365 nm sensor (UVP, USA). After irradiation, the PBS was replaced with a medium, and cells were cultured under standard culture conditions.

Determination of Melanin in UVA-induced Melanogenesis

A total of $1x10^5$ melanocytes were incubated with palm TRF, KA and α-TP at 62.5 µg mL^{-1} per sample before UVA irradiation. The culture plates were placed at a distance of 20 cm from the UVA lamp and exposed for 6, 9, or 12 min to achieve a single dose of 0.4, 0.6 and 0.8 J cm^{-2}, respectively. The UVA irradiation was performed once a day for seven consecutive days. The control cells were maintained in the same culture conditions without treatment with test samples and UVA exposure. After irradiation, PBS was discarded, and cells were incubated in the growth medium for 24 hr and analysed for melanin content.

Melanin content was measured spectrophotometrically at 450 nm after heating the cell lysates for 1 hr with one normality NaOH at 80°C as described by Zaidi *et al.* (2016) with slight modification. Melanin content was expressed as the percentage of the controls (Chatatikun *et al.*, 2019).

Statistical Analysis

The results were presented as means ± standard deviation. One-way analysis of variance ANOVA (SPSS version 16.0) was performed, and sequential differences between the means were identified at the level of $P<0.05$ using Bonferroni post-test analysis.

RESULTS AND DISCUSSION

Cell Viability

Incubation of melanocytes with different concentrations of TRF (7.8, 15.6, 31.3, 62.5, 125.0, 250.0 and 500.0 μg mL^{-1}) caused an increase in the number of viable cells (*Figure 1*).

After 24 hr of treatment, increasing the concentration of TRF and α-TP increased the percentage of viable cells. In contrast, increasing the concentration of KA did not significantly affect cell viability. The survival rate of melanocyte cells treated with TRF and α-TP was found to be high, indicating that TRF and α-TP promoted melanocyte cell proliferation. Therefore, 62.5 μg mL^{-1} of TRF was used in the subsequent experiment to determine its effect on melanocyte cells. Prolonged treatment of seven days using the optimal dose (62.5 μg mL^{-1}) of TRF and α-TP on melanocyte cells improved cell viability (*Figure 2*).

Melanin Content

Melanocyte cells were treated with TRF, α-TP and KA for 24, 48, 72 hr and seven days at 62.5 μg mL^{-1}. The melanin concentration was determined

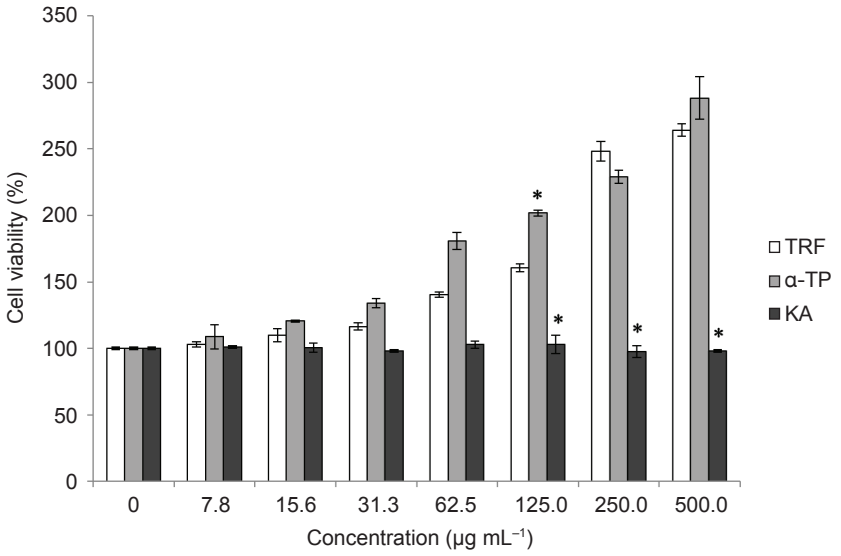


Figure 1. Effects of TRF, α-TP and KA on melanocyte proliferation at 24 hr of treatment, as assessed by MTT assay. Data are presented as mean ± SD, n=3. Statistical significance was set at $P<0.05$ *(ANOVA+Dunnett). * Significant difference with TRF within the same concentration.*

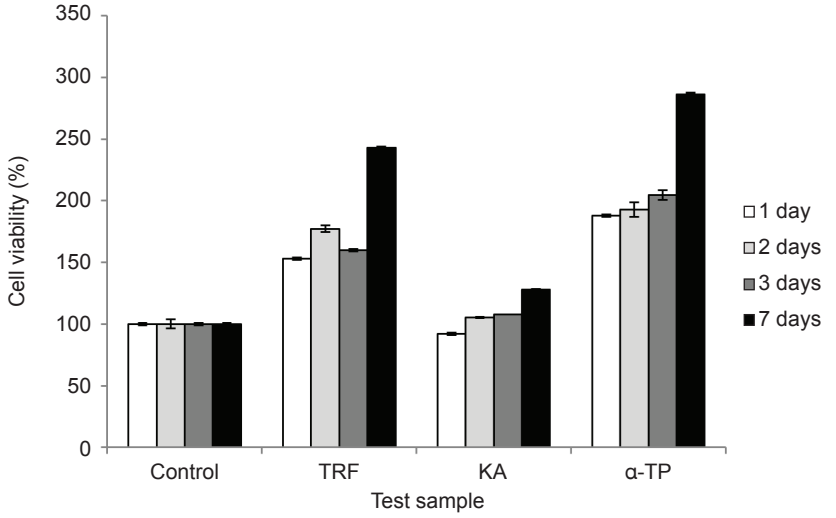


Figure 2. Effect of TRF, KA and α-TP at dose 62.5 μg mL^{-1} on cell viability within seven days.

by comparing the optical density of TRF, α-TP and KA at OD_{450nm}. *Figure 3* shows a standard curve of melanin concentration which was highly correlated with the OD_{450nm}, where R^2 was 0.999.

Effect of Different Doses of UVA on Cell Viability

Figure 4 shows the effects of increasing UVA (0-10 J cm^{-2}) on the viability of melanocyte cells after seven days of treatment. After daily exposure to UVA for seven consecutive days at different doses, the percentage of viable melanocytes decreased compared to the control (non-irradiated cells). In this study, the UVA dose of 0.6 J cm^{-2} was less toxic than the other doses. It was observed that at doses beyond 0.6 J cm^{-2}, the melanocytes were swollen or enlarged cell bodies and ruptured membranes compared to non-irradiated cells and cells exposed to lower doses of UVA. The results of our study showed that cell viability was increased in melanocytes exposed to 0.6 J cm^{-2} UVA and produced the highest melanin content, which is consistent with the report of Makpol *et al*. (2014). Melanocytes with high melanin content showed increased resistance to UVA cytotoxicity and those with low melanin content showed low resistance to UVA cytotoxicity.

Figure 5 shows the melanin level of melanocyte cells exposed to single UVA stress daily for seven consecutive days at a dose of 0 to 1 J cm^{-2}.

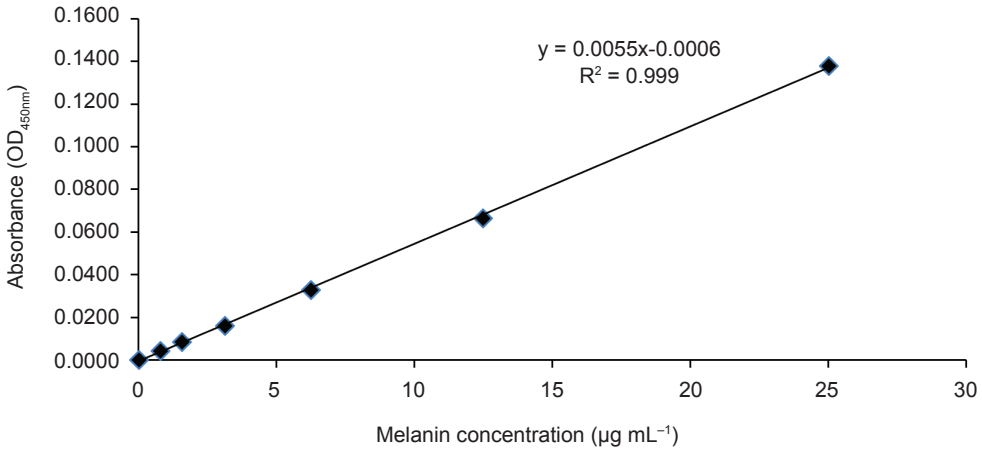


Figure 3. Standard curve for synthetic melanin at concentration ranges between 0-25 µg mL^{-1}.

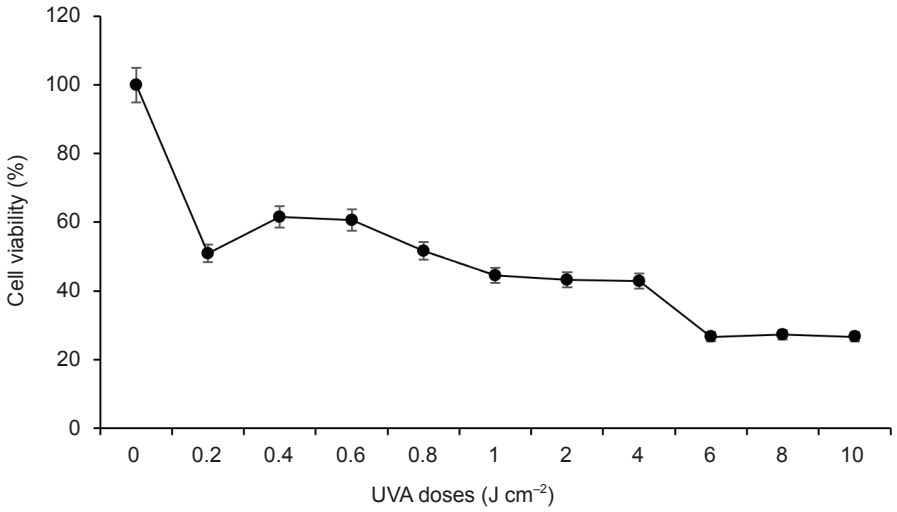


Figure 4. Effect of different doses of UVA on melanocyte cell viability.

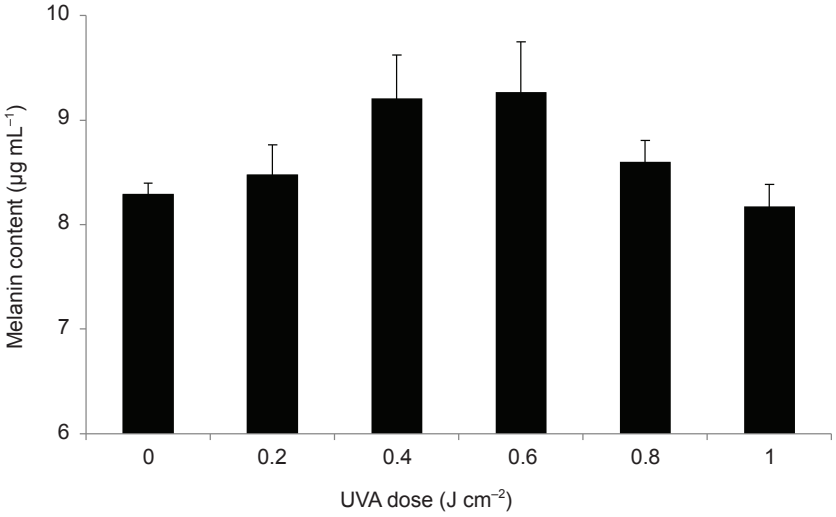


Figure 5. Effect of different doses of UVA on melanin level.

Exposure to increasing amounts of UVA increased the level of melanin content compared to cells without exposure to UVA. The melanin content of melanocytes exposed to UVA reached a maximum level at 0.6 J cm^{-2} and decreased beyond 0.6 J cm^{-2}. Thus, further study on the photoprotective effect of test samples against UVA irradiation was limited to the UVA dose of 0.6 J cm^{-2}.

Photoprotective Effect of Palm TRF

Figure 6 shows the melanin content of melanocyte cells treated with TRF, KA and α-TP (62.5 µg mL^{-1}) in the absence of UVA irradiation. After seven days, there was no significant difference in melanin content for negative control and melanocyte cells treated with TRF and KA compared to day one. However, there was a significant increase (P<0.05) in melanin content when melanocyte cells were treated with α-TP compared to day one. This may be due to the ability of melanocyte cells to proliferate when treated with α-TP, thus increasing the melanin level as well. However, in the presence of UVA irradiation, melanocyte cells treated with KA (known as a universal whitening agent) showed significantly lower (P<0.05) melanin content than TRF and α-TP at day seven. Meanwhile, the melanin content of melanocyte cells treated with TRF significantly decreased (P<0.05) compared to α-TP on day seven. This data was supported by a study by Yap *et al.* (2010) which stated that treatment with tocotrienol isomers (δ- and γ-) was able to lower melanin content in cells but not α-TP.

Melanogenesis is intensified in melanocytes in response to harmful conditions, including UVA radiation (Rok *et al.*, 2018). Thus, the photoprotective effect of TRF on UVA-irradiated melanocyte cells was evaluated. The melanocyte cells were irradiated with UVA light with a single UVA dose of 0.6 J cm^{-2} for seven consecutive days. After seven days, the irradiated and untreated melanocyte cells showed a 10.8% increase in melanin content, indicating that UVA irradiation directly influences melanogenesis. Melanocytes treated with TRF and irradiated with UVA showed a slight 2.8% increase in melanin content, indicating that TRF may effectively protect the cells against UVA irradiation. KA-treated and UVA-irradiated melanocyte cells did not indicate any significant increase in melanin content. However, melanocytes treated with α-TP showed a 16.6% increase in melanin content. A previous study reported that a UVA dose of 0.6 J cm^{-2} was identified as the non-toxic dose (Makpol *et al.*, 2014).

Discussion

In this study, we investigated the potential of TRF on melanogenesis, including inhibition of melanin synthesis and UV-induced melanogenesis in melanocytes.

We found that treatment with increasing concentrations of TRF and α-TP caused a significant increase in the number of viable cells for skin melanocytes. The viable cells' percentage increased at doses of 62.5 to 500.0 µg mL^{-1} (*Figure 1*). A previous study by Khor *et al.* (2016) reported that TRF and α-TP could increase cell viability and improve cellular morphology at a concentration of 50.0 µg mL^{-1}. Also, treatment with both TRF and α-TP for 24 hr promoted higher cell proliferation than KA. Data was supported by Khor *et al.* (2016), wherein TRF increases cell viability and enhances the proliferation capacity of senescent myoblasts. These findings proved the potential of TRF in

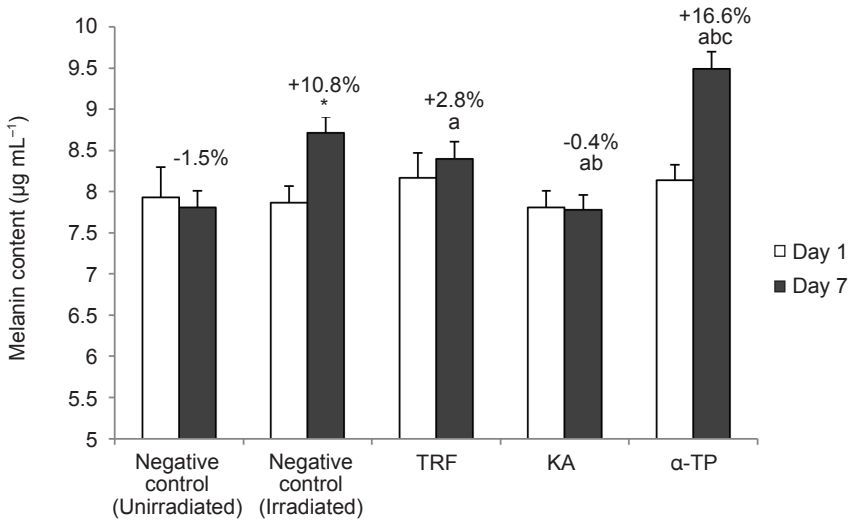


*Figure 6. Evaluation of photoprotective properties of melanocyte cells treated with TRF, KA and α-TP and irradiated with UVA 0.6 J cm^{-2}. *P<0.05 compared to Day 1; [a]P<0.05 compared to control at Day 7; [b]P<0.05 compared to TRF at Day 7; [c]P<0.05 compared to KA at Day 7.*

improving the proliferation capacity of melanocytes in culture. Also, treatment with both TRF and α-TP for 24 hr promoted higher cell proliferation than KA. Prolonged treatment for seven days using the dose of 62.5 µg mL^{-1} improved cell viability in melanocyte cells (*Figure 2*). In this study, the data indicated that TRF and α-TP not only increase cell viability but also enhance the proliferation capacity of melanocyte cells. Vitamin E can act as a cellular antioxidants and promote cell growth. Tocotrienol has also been reported to promote proliferation, differentiation, and mineralised nodule formation in osteoblastic cells (Xu *et al.*, 2018). In another study it was reported that low doses (50.0 µg mL^{-1}) of TRF stimulated the proliferative capacity of myoblasts (Lim *et al.*, 2019). Recently, treatments with α-T3, δ-T3 or γ-T3 significantly increased the viability of the murine splenocytes. These results suggest that tocotrienol isoforms do not have cytotoxic effects on the murine splenocytes, *i.e.*, normal primary cells and tocotrienols may have less impact on the proliferation of normal cells (Loganathan *et al.*, 2021). From this study, it was evident that TRF improves the proliferative capacity of melanocytes in culture without being cytotoxic.

Figure 4 shows that the percentage of viable cells decreased when exposed to an increasing dose of UVA as compared to the control (non-irradiated cells). The UVA dose of 0.6 J cm^{-2} was less cytotoxicity than doses beyond 0.6 J cm^{-2} in primary human melanocytes. This is in agreement with what was reported by Makpol *et al.* (2014). Meanwhile, *Figure 5* shows the melanin content in melanocytes at different doses of UVA. Exposure to increasing doses of UVA (up to 0.6 J cm^{-2}) raised the level of melanin content compared to cells without exposure to UVA (*Figure 5*). This is because UVA-induced ROS oxidises proteins and lipids, disrupting normal cellular signaling and possibly promoting abnormal cell proliferation (Dunaway *et al.*, 2018). The presence of melanin may protect against the effects of direct UVA exposure, and it is possible that melanin may have heterogeneous effects and may simultaneously absorb UVA photons and intracellular ROS.

Melanocytes treated with TRF and irradiated with UVA showed a significant reduction in melanin content (+2.8%) compared to untreated control melanocytes (+10.8%), as shown in *Figure 6*. In this study, melanocytes treated with α-TP and irradiated with UVA showed the highest melanin content (+16.6%), indicating that α-TP is ineffective in protecting the melanocytes compared to TRF. The significant difference in melanin content in melanocytes treated with TRF or tocopherol may be due to the difference in molecular structure. Tocotrienols have a unique structure with three unsaturated double bonds in their side chains, while tocopherols have a saturated phytyl tail. The unsaturated side chain of the tocotrienol molecule allows for better penetration into the cell membrane compared to tocopherols (Serbinova *et al.*, 1991; Wong and Radhakrishnan, 2012). The presence of these double bonds in tocotrienols allows them to interact more effectively and neutralise free radicals. Free radicals are highly reactive molecules that cause oxidative damage to cells (Adwas *et al.*, 2019; Drotleff and Ternes, 2001; Musa, 2021). This unique property increases the efficiency of tocotrienols in reducing the formation of ROS in melanocytes when irradiated with UVA and indirectly reduces the formation of

melanin, as observed in this experiment compared to melanocytes treated with tocopherol. Another study showed that TRF protects the cells and thus reduces oxidative damage caused by UV radiation (Sample and He, 2018; Solano, 2020).

Vitamin E and its derivatives act as a melanogenesis inhibitor in epidermal melanocytes *in vitro* and inhibit tyrosinase activity, a key enzyme in melanisation. Moreover, the study found that tocotrienols effectively reduce skin redness and pigmentation after UV exposure (Yap, 2018).

KA is a well-known skin whitening agent and a potent tyrosinase inhibitor (Masum *et al*., 2019) and in this study, KA was used as the positive control. As shown in *Figure 6*, there was a significant reduction in melanin levels of melanocyte cells treated with KA after UVA radiation compared to the control on day seven. This is because KA is a naturally occurring metabolite produced by fungi that can inhibit tyrosinase activity in synthesis of melanin. Tyrosinase is composed of copper ions. When exposed to UV light, the copper ion induced tyrosinase to become more active. The copper ion is captured by KA, preventing it from activating the tyrosinase. By inhibiting tyrosinase activity, KA can also prevent melanin formation (Saeedi *et al*., 2019).

Vitamin E has been proven for its antioxidant and UV protection effects, providing photoprotection (de Oliveira Pinto *et al*., 2021), moisturising and delaying skin aging (Ijaz and Akhtar, 2020). Different studies have shown that supplementation with vitamins C and E significantly reduces UV-induced skin damage than supplementation with vitamin C alone (Pullar *et al*., 2017), possibly due to vitamin E regeneration. Vitamin E protection against UV-induced cytotoxicity has been linked to the extent of its uptake into cells. It also has been reported that vitamin E interacts with endogenous antioxidant enzymes and plays a crucial role in recycling the antioxidant defence system in human cells (Miyazawa *et al*., 2019).

Our findings revealed that TRF protects the melanocyte cells from UVA irradiation. Inhibition of melanin synthesis might be the possible mechanism of TRF as an anti-melanogenic agent that protects against UVA-induced melanogenesis.

CONCLUSION

In conclusion, palm TRF can inhibit melanin synthesis and thus, may act as an anti-melanogenic agent that protects against UVA-induced melanogenesis. Interestingly, this study found that the inhibitory effect of TRF on melanin synthesis was higher than KA and α-TP. Therefore, TRF may potentially be developed as an anti-melanogenic agent for topical skin care applications.

ACKNOWLEDGEMENT

The authors would like to thank the Malaysian Palm Oil Board (MPOB) for permission to conduct this study. We would also like to thank Nur'Ain Ali and Nurul Ain Mohd Arzani from Safety and Efficacy Assessment Group, Oleo Product Development Unit, AOTD, MPOB for their technical assistance.

REFERENCES

Adwas, A A; Elsayed, A S I; Azab, A E and Quwaydir, F A (2019). Oxidative stress and antioxidant mechanisms in human body. *J. Appl. Biotechnol. Bioeng., 6*: 43-47.

Chatatikun, M; Yamauchi, T; Yamasaki, K; Chiabchalard, A and Aiba, S (2019). *Phyllanthus acidus* (L.) Skeels and *Rhinacanthus nasutus* (L.) Kurz leaf extracts suppress melanogenesis in normal human epidermal melanocytes and reconstitutive skin culture. *Asian Pac. J. Trop. Med., 12(3)*: 98-105.

Chen, J; Liu, Y; Zhao, Z and Qiu, J (2021). Oxidative stress in the skin: Impact and related protection. *Int. J. Cosmetic Sci., 43(5)*: 495-509.

Delinasios, G J; Karbaschi, M; Cooke, M S and Young, A R (2018). Vitamin E inhibits the UVAI induction of "light" and "dark" cyclobutane pyrimidine dimers, and oxidatively generated DNA damage, in keratinocytes. *Sci. Rep., 8(1)*: 1-12.

de Oliveira Pinto, C A S; Martins, T E A; Martinez, R M; Freire, T B; Velasco, M V R and Baby, A R (2021). Vitamin E in human skin: Functionality and topical products. *IntechOpen*. DOI: 10.5772/intechopen.98336.

Drotleff, A M and Ternes, W (2001). Determination of RS, E/Z-tocotrienols by HPLC. *J. Chromatogr. A., 901*: 215-223.

Dumbuya, H; Hafez, S Y and Oancea, E (2020). Cross talk between calcium and ROS regulate the UVA-induced melanin response in human melanocytes. *FASEB J., 34(9)*: 11605-11623.

Dunaway, S; Odin, R; Zhou, L; Ji, L; Zhang, Y and Kadekaro, A L (2018). Natural antioxidants: Multiple mechanisms to protect skin from solar radiation. *Front. Pharmacol., 9*: 392.

Hida, T; Kamiya, T; Kawakami, A; Ogino, J; Sohma, H; Uhara, H and Jimbow, K (2020). Elucidation of melanogenesis cascade for identifying pathophysiology and therapeutic approach of

pigmentary disorders and melanoma. *Int. J. Mol. Sci.*, *21(17)*: 1-23.

Ijaz, M and Akhtar, N (2020). Fatty acids based α-tocopherol loaded nanostructured lipid carrier gel: *In vitro* and *in vivo* evaluation for moisturizing and anti-aging effects. *J. Cosmet. Dermatol.*, *19(11)*: 3067-3076.

Khor, S C; Razak, A M; Ngah, W Z W; Yusof, Y A M; Karim, N A and Makpol, S (2016). The tocotrienol-rich fraction is superior to tocopherol in promoting myogenic differentiation in the prevention of replicative senescence of myoblasts. *PLoS ONE*, *11(2)*: 1-21.

Le, L (2020). Novel insights into the cellular basis of pigmentation using mouse models of albinism. PhD Thesis. University of Pennsylvania.

Lim, J J; Wan Zurinah, W N; Mouly, V and Norwahidah, A K (2019). Tocotrienol-rich fraction (TRF) treatment promotes proliferation capacity of stress-induced premature senescence myoblasts and modulates the renewal of satellite cells: Microarray analysis. *Oxid. Med. Cell. Longev.*, *2019*: 1-19.

Loganathan, R; Selvaduray K R; Nesaretnam, K and Radhakrishna, A K (2021). Palm tocotrienols cause cleavage of poly- (ADP)-ribose polymerase enzyme and down-regulation of cyclooxygenase-2 protein level in human breast cancer cells. *J. Oil Palm Res.*, *33(1)*: 119-128.

Lohan, S B; Müller, R; Albrecht, S; Mink, K; Tscherch, K; Ismaeel, F; Lademann, J; Rohn, S and Meinke, M C (2016). Free radicals induced by sunlight in different spectral regions-*in vivo* versus *ex vivo* study. *Exp. Derm.*, *25(5)*: 380-385.

Makpol, S; Jam, F A; Rahim, N A; Khor, S C; Ismail, Z; Yusof, Y A M and Wan Ngah, W Z (2014). Comparable down-regulation of TYR, TYRP1 and TYRP2 genes and inhibition of melanogenesis by tyrostat, tocotrienol-rich fraction and tocopherol in human skin melanocytes improves skin pigmentation. *Clin. Ter.*, *165(1)*: e39-45.

Maranduca, M A; Branisteanu, D; Serban, D N; Branisteanu, D C; Stoleriu, G; Manolache, N and Serban, I L (2019). Synthesis and physiological implications of melanic pigments. *Oncol. Lett.*, *17(5)*: 4183-4187.

Marelli, M M; Marzagalli, M; Moretti, R M; Beretta, G; Casati, L; Comitato, R; Gravina, G L; Festuccia, C and Limonta, P (2016). Vitamin E δ-tocotrienol triggers endoplasmic reticulum stress-mediated apoptosis in human melanoma cells. *Sci. Rep.*, *6(1)*: 30502.

Masum, M N; Yamauchi, K and Mitsunaga, T (2019). Tyrosinase inhibitors from natural and synthetic sources as skin-lightening agents. *Rev. Agri. Sci.*, *7*: 41-58.

Michihara, A; Ogawa, S; Kamizaki, Y and Akasaki, K (2010). Effect of delta-tocotrienol on melanin content and enzymes for melanin synthesis in mouse melanoma cells. *Biol. Pharm. Bull.*, *33(9)*: 1471-1476.

Michalak, M (2022). Plant-derived antioxidants: Significance in skin health and the ageing process. *Int. J. Mol. Sci.*, *23(2)*: 585.

Miyazawa, T; Burdeos, G C; Itaya, M; Nakagawa, K and Miyazawa, T (2019). Vitamin E: Regulatory redox interactions. *IUBMB Life*, *71(4)*: 430-441.

Musa, A F (2021). Tocotrienol: An underrated isomer of vitamin E in health and diseases. *IntechOpen*. DOI: 10.5772/intechopen.96451.

Nahhas, A F; Abdel-Malek, Z A; Kohli, I; Braunberger, T L; Lim, H W and Hamzavi, I H (2018). The potential role of antioxidants in mitigating skin hyperpigmentation resulting from ultraviolet and visible light-induced oxidative stress. *Photodermatol. Photoimmunol. Photomed.*, *35*: 420-428.

Ng, L T; Lin, L T; Chen, C L; Chen, H W; Wu, S J and Lin, C C (2014). Anti-melanogenic effects of δ-tocotrienol are associated with tyrosinase-related proteins and MAPK signaling pathway in B16 melanoma cells. *Phytomedicine*, *21(7)*: 978-983.

Parveez, G K A; Kamil, N N; Zawawi, N Z; Ong-Abdullah, M; Rasuddin, R; Loh, S K; Selvaduray, K R; Hoong, S S and Idris, Z (2022). Oil palm economic performance in Malaysia and R&D progress in 2021. *J. Oil Palm Res.*, *34(2)*: 185-218.

Pullar, J M; Carr, A C and Vissers, M C M (2017). The roles of vitamin C in skin health. *Nutrients*, *9(8)*.

Ramsden, C A and Riley, P A (2014). Tyrosinase: The four oxidation states of the active site and their relevance to enzymatic activation, oxidation and inactivation. *Bioorganic Med. Chem.*, *22(8)*: 2388-2395.

Remigante, A; Spinelli, S; Marino, A; Pusch, M; Morabito, R and Dossena, S (2023). Oxidative stress and immune response in melanoma: Ion channels as targets of therapy. *Int. J. Mol. Sci.*, *24(1)*.

Rok, J; Wrześniok, D; Beberok, A; Otręba, M; Delijewski, M and Buszman, E (2018). Phototoxic

effect of oxytetracycline on normal human melanocytes. *Toxicol. Vitr.*, *48*: 26-32.

Saeedi, M; Eslamifar, M and Khezri, K (2019). Kojic acid applications in cosmetic and pharmaceutical preparations. *Biomed. Pharmacother.*, *110*: 582-593.

Sample, A and He, Y Y (2018). Mechanisms and prevention of UV-induced melanoma. *Photodermatol. Photoimmunol. Photomed.*, *34(1)*: 13-24.

Sen, C K; Rink, C and Khanna, S (2010). Palm oil-derived natural vitamin E α-tocotrienol in brain health and disease. *J. Am. Coll. Nutr.*, *29 (3 Suppl)*: 314S-323S.

Serbinova, E; Kagan, V; Han, D and Packer, L (1991). Free radical recycling and intramembrane mobility in the antioxidant properties of alpha-tocopherol and alpha-tocotrienol. *Free Radic. Biol. Med.*, *10(5)*: 263-275.

Solano, F (2020). Photoprotection and skin pigmentation: Melanin-related molecules and some other new agents obtained from natural sources. *Molecules*, *25(7)*: 1537.

Song, R; Wu, Q; Yun, Z and Zhao, L (2020). Advances in antioxidative bioactive macromolecules. *IOP Conf. Ser. Earth Environ. Sci.*, *512*: 012094.

Sun, X; Zhang, N; Yin, C; Zhu, B and Li, X (2020). Ultraviolet radiation and melanomagenesis: From mechanism to immunotherapy. *Front. Oncol.*, *10*: 951.

Wang, W; Gao, Y; Wang, W; Zhang, J; Yin, J; Le, T; Xue, J; Engelhardt, U H and Jiang, H (2022). Kojic acid showed consistent inhibitory activity on tyrosinase from mushroom and in cultured B16F10 cells compared with arbutins. *Antioxidants*, *11(3): 502*.

Wong, R S Y and Radhakrishnan, A K (2012). Tocotrienol research: Past and present. *Nutr. Rev.*, *70(9)*: 483-490.

Xu, W; He, P; He, S; Cui, P; Mi, Y; Yang, Y; Li, Y and Zhou, S (2018). Gamma-tocotrienol stimulates the proliferation, differentiation, and mineralization in osteoblastic MC3T3-E1 cells. *J. Chem.*, *2018*: 3805932.

Yap, W N (2018). Tocotrienol-rich fraction attenuates UV-induced inflammaging: A bench to bedside study. *J. Cosmet. Dermatol.*, *17(3)*: 555-565.

Yap, W N; Zaiden, N; Xu, C H; Chen, A; Ong, S; Teo, V and Yap, Y L (2010). Gamma- and delta-tocotrienols inhibit skin melanin synthesis by suppressing constitutive and UV-induced tyrosinase activation. *Pigment Cell Melanoma Res.*, *23(5)*: 688-692.

Yi, W J; Su, M Y; Shi, Y; Jiang, S; Xu, S Z and Lei, T C (2018). Degraded melanocores are incompetent to protect epidermal keratinocytes against UV damage. *Cell Cycle*, *17(7)*: 844-857.

Zaidi, K U; Ali, S A and Ali, A S (2016). Effect of purified mushroom tyrosinase on melanin content and melanogenic protein expression. *Biotechnol. Res. Int.*, *2016*: 1-8.

Journal of Oil Palm Research Vol. 36 (4) December 2024 p. 728-738
DOI: https://doi.org/10.21894/jopr.2023.0057

DEVELOPMENT OF SOLID FAT CONTENT-BASED PREDICTIVE MODEL FOR MARGARINE FORMULA DESIGN

JIAJIA GONG[1]; NANXI SHU[1]; XIAN SUN[1]; XINYU CAO[1]; YUANFA LIU[1] and YONG-JIANG XU[1]*

ABSTRACT

The curve of solid fat content (SFC) is a fundamental but significant physical characteristic of fat, which markedly affects the texture and sense of food. A bivariate Gompertz model with temperature and saturated fatty acids (SFAs) as variables was used in this study to fit the SFC curve of enzymatically interesterified vegetable oil from palm oil (PO) and palm stearin (ST), to determine the ideal proportion of plant-based fat substrate. The fitting result (R^2 = 0.99) showed that this model had respectable predictive power. When the PO/ST ratio was 83:17, the SFC curve of the prepared plant-based margarine was close to that of butter, as calculated using the acquired SFC curve fitting formula. Bread characteristics and sensory analysis showed that the acceptance level of the bread made with this formulation was similar to that of natural animal fats. The results demonstrated that using the Gompertz function to build a simulated fit of SFC curves for enzymatically interesterified fat blends is a beneficial tool for optimising margarine formulation.

Keywords: bread, enzymatic interesterification, plant-based margarine, solid fat content.

Received: 28 March 2023; **Accepted:** 13 September 2023; **Published online:** 26 October 2023.

INTRODUCTION

In recent years, to meet the needs of mass consumers while reducing production costs (Sabate *et al.*, 2014; Silva *et al.*, 2021), plant-based margarine that substitutes animal fats has gradually become a hot research topic in the food industry (Aini and Miskandar, 2007; Collier *et al.*, 2022; Patel *et al.*, 2020; Zhang *et al.*, 2019). Changes in the chemical composition of margarine naturally lead to changes in its physical properties (Doan *et al.*, 2018; Li *et al.*, 2022; Zhang *et al.*, 2004). Physical characteristics, especially the solid fat content (SFC) (Dollah *et al.*, 2016; Engelen *et al.*, 2008), determine many of the fundamental characteristics of margarines, including their general appearance, ease of packaging, spread ability (Zhou *et al.*, 2021), grease exudation, and sensory properties (Soares *et al.*, 2012). The use of SFC to characterise margarine is the most practical way for selecting margarine fat feedstocks (Zhang *et al.*, 2014). Meanwhile, the measurement of SFC is relatively quick and simple (Nelis *et al.*, 2021; Reiner *et al.*, 2018), making the process easy to monitor.

The SFC curve generally describes the variations in the consistency and plasticity of food at different temperatures (Naeli *et al.*, 2018; Saghafi *et al.*, 2019). The most important factors that affect the SFC curve are fat composition (TAG and fatty acid profile), fat storage temperature and polymorphic crystal morphology (Schmid *et al.*, 2020). Saberi *et al.* (2012) developed a hybrid formula in which a high proportion of diacylglycerol oil was incorporated into plastic fat as a functional oil to substitute full-fat products. To calculate the SFC curve of mixed fat, Dos Santos *et al.* (2013; 2014) merged the solid-liquid equilibrium model with the direct minimisation approach of the Gibbs free energy function. However, the above method requires a large amount of input data, and the steps

[1] State Key Laboratory of Food Science and Technology, School of Food Science and Technology, National Engineering Research Center for Functional Food, National Engineering Laboratory for Cereal Fermentation Technology, Collaborative Innovation Center of Food Safety and Quality Control in Jiangsu Province, Jiangnan University, 1800 Lihu Road, Wuxi, 214122, Jiangsu, China.

* *Corresponding author e-mail: yjxutju@gmail.com*

are tedious. And by comparing three different S-shaped function models (Gompertz model, power decay model and logistic model), Augusto *et al.* (2012) discovered that the Gompertz model can better characterise changes in the SFC curve. Later, Farmani (2015) expanded on these findings by presenting a two-variable Gompertz model that describes SFC as a simultaneous function of both temperature and saturated fatty acid content. Since this method is relatively fast and reliable, the Gompertz model was also used to forecast the kinetics of mould growth (Wawrzyniak, 2021) and the texture and colour development of chicken breast meat during thermal processing (Rabeler *et al.*, 2018).

To satisfy the specific performance requirements of plant-based margarine, oil products with varying physical and chemical properties are frequently modified by hydrogenation (Pimentel *et al.*, 2003; Zhu *et al.*, 2020), separation and transesterification in the food industry (Alan *et al.*, 2019; Sivakanthan *et al.*, 2019). Palm oil is generated in huge amounts at affordable prices from a steady source, is high in vitamin A and E, has strong oxidative stability, and is suitable for high-temperature baked products processing. In addition, palm oil fractionated products have similar textural characteristics and fatty acid composition to butter, are solid at room temperature, and have the same β′ crystalline behaviour as butter and can be used as a first choice for margarine manufacture. We use palm stearin (ST) and palm oil (PO) as feedstock oil for the enzymatic interesterification. The main goal of this work is to use the Gompertz fitting model to express the SFC curve of binary esterified fats in relation to temperature and saturated fatty acid (SFA) content. The emphasis is on finding the ratio of plant-based margarine formulation that is similar to the change in SFC of the target butter by constructing a simulation. This plant-based margarine formulation was applied to a bread system to compare with the textural and organoleptic properties of bread made with traditional animal fats. The model suggested in this research may be used to forecast and design the SFC of esterified fats, and this method has the potential to boost formulation development efficiently, minimise product development cost and time.

MATERIAL AND METHODS

Materials

Samples of commercially acceptable margarine were purchased from a local store in Wuxi. Beef tallow (BT) was purchased from Muge Co., Ltd. (Chongqing, China). Refined, bleached, and deodorised ST and PO were provided by Kerry Specialty Oils Co., Ltd. (Shanghai, China). The oils and fats were stored at room temperature in a dark place until use. The immobilised lipase Lipozyme 435 was donated by Novozymes (Bagsvaerd, Denmark). Supelco 37 Component FAME Mix was purchased from Sigma-Aldrich China (Shanghai, China). All other reagents and solvents used were of analytical or chromatographic grade from local suppliers.

Preparation of Enzymatic Interesterification

Before interesterification, ST and PO were melted by heating. Blends of ST and PO (12.5%, 25.0%, 37.5%, 50.0%, 62.5%, 75.0%, 87.5%, ST w/w) were interesterified using Lipozyme 435 (4.0%, w/w) by heating and magnetic stirring with agitation of 400 rpm at 90°C for 4 hr. At the end of the reaction, the immobilised enzyme was immediately removed by centrifugation to obtain an interesterified oil sample (Pang *et al.*, 2019).

Determination of SFC

The SFC of all samples was performed by using PQ001-20-010V low-resolution pulsed nuclear magnetic resonance (pNMR) (Niumag Instruments, Suzhou, China). The pNMR tubes (diameter = 10 mm) were filled with 2.5 mL of the samples. Approximately 2.5 mL of each sample in the NMR tube was first kept at 90°C to melt for 30 min. The NMR tubes were rapidly placed in a DC-0506 constant low temperature bath (Sunny Hengping Scientific Instrument, Shanghai, China) and maintained at 0°C, for 90 min. The temperature rose from 5°C to 60°C, and the SFC was measured at every increment of 5°C, with each temperature maintained for 30 min before measurement (Li *et al.*, 2018).

Determination of SFA Content

Gas chromatography (Nexis GC2030, Shimadzu, Japan) was used to assess the fatty acid compositions of the samples, which included an autoinjector (AOC-20i Plus, Shimadzu, Japan), a flame ionisation detector and a capillary column (60 m × 0.25 mm × 0.25 μm, Thermo Fisher Scientific, Waltham, MA, USA). Fatty acid determination was carried out using the method of Ye *et al.* (2019) with slight improvement. 2-3 drops of the samples were mixed successively with KOH-CH_3OH (0.5 M, 2 mL), incubated for 30 min with shaking at 65°C for saponification, and BF_3-CH_3OH (1:3, v/v, 2 mL) and then incubated for 10 min at 70°C for the methyl esterification reaction. After cooling to room temperature, the fatty acid methyl ester was extracted with 2 mL of chromatographic grade n-hexane, and the supernatant was transferred to

a 2 mL centrifuge tube by vigorous shaking for 3-4 min, and a small amount of water was sucked up by adding anhydrous Na_2SO_4, before being passed through a 0.22 μm organic filtration membrane into a 2 mL injection vial for gas chromatographic analysis.

Gas chromatography conditions; the whole procedure took 42 min, the column was first retained at 130°C for 3 min, then warmed up to 200°C and retained for 10 min within 14 min; then warmed up to 220°C and retained for 5 min within 10 min; the flow rate of the constant carrier gas (nitrogen) was set at 1.8 mL/min; the split ratio was 20; and the injection volume was 1 μL. Fatty acid characterisation and relative quantification using 52 fatty acid methyl ester mixed standards.

Modelling and Statistical Analyses

Temperature and SFA were the most influential factors and were chosen as independent variables for modelling the SFC curves (Farmani, 2015). The sigmoidal Gompertz function was used to simulate the SFC of enzymatically interesterified ST/PO blends [Equation (1)] by SigmaPlot 14.0 (Systat Software Inc., USA).

$$Y = \alpha^{e-e^{-\left(\frac{X-c}{b}\right)}} \quad (1)$$

SigmaPlot 14.0 was used to assess the goodness-of-fit of the models, which included the correlation coefficient (r), determination coefficient (R^2) and standard error of estimate (SE) between the experimental and predicted values.

Baking Application

Bread making. The breadmaking process undergoes two-steps alcoholic fermentation using the ingredients mentioned in *Table 1*. All the materials, condensed milk and lipid matrix except egg, were placed in an electric mixer (Shuangmai Bakery Equipment Co., Ltd., Wuxi, China) and mixed into a smooth dough. The dough was removed from the machine and fermented at a temperature of 40°C and a humidity level of 90% for 30 min. The dough was then enriched with egg, condensed milk and lipid matrix. The stirring process was continued until the dough was formed. After that, the dough was divided into small pieces and kneaded into a spherical form, with each piece weighing 50 g. Similarly, these doughs were fermented before being cooked in a preheated oven (Shuangmai Bakery Equipment Co., Ltd., Wuxi, China) at 180°C for 15 min. The bread samples were cooled at room temperature before placing into sample bags and stored at 25°C until analysis.

Bread characteristics. The baking loss, specific volume and texture properties of bread were measured. Baking loss is defined as the ratio of quality loss to dough weight before and after baking. The specific volume of bread was calculated from the ratio of weight to volume measured by the millet displacement. Texture properties were measured by TA-XTPlus (Stable Microsystems, Surrey, United Kingdom). Test conditions included probe type P/36R, a 25% compression ratio, a pre-test speed of 2.0 mm s^{-1}, a test speed of 1.0 mm s^{-1}, and a post-test speed of 2.0 mm s^{-1}.

Sensory analysis. The evaluation group was made up of seven female and 13 male assessors, all of whom were from the Department of Food Science and Technology at Jiangnan University. They were asked to evaluate the shape, colour, smell, taste and texture of the bread with a 5-hedonic scale from 1 to 5 (dislike very to like exceedingly). Every assessor received instruction on how to provide a grade for each sensory prosperity.

Statistical Analysis

Each experiment was carried out in triplicate. Statistical analysis was performed by SigmaPlot 14.0 and SPSS 16.0 (SPSS, Inc., Chicago, IL, USA). The data are expressed as the mean ± standard deviation (SD). The significant differences among samples were considered at a level of 5% ($P< 0.05$).

TABLE 1. THE INGREDIENTS OF BREADS MADE WITH DIFFERENT FATS

Ingredient	Weight (g)	Source
High-gluten bread flour	300	Commercial
Water	120	Commercial
Yeast	3	Commercial
Bread improver	0.9	Commercial
Salt	3	Commercial
Sugar	42	Commercial
Whole egg	50	Commercial
Condensed milk	25	Commercial
Butter, beef tallow or plant-based margarine	30	Commercial or EIE ST/PO blend

RESULTS AND DISCUSSION

SFC and SFA Content

In general, the two most important factors affecting SFC are the temperature during measurement and the composition of fat (Haupler *et al.*, 2014). The results of the SFC and SFA content of the fat samples obtained before and after enzymatic esterification at different ratios of PO and ST are shown in *Table 2*. The SFC curve for each oil sample has an S-shape that degrades with rising temperature. The high content of SFA in ST gives it a wider plasticity range than PO, whose SFC only drops to 0 when the temperature rises to 60°C, whereas PO is no longer present as a solid at 30°C. Accordingly, the SFA and SFC steadily rise as the ST content in the blends increased. When the ST content is lower than 50%, the plastic range of the SFC curve of the initial binary blend is lower than that after enzymatic interesterification. After enzymatic interesterification, the SFCs of binary blends of PO and ST are greater than 20% when the temperature is 25°C. The enhanced flexibility of the binary blends after the transesterification reaction when compared to single components or the initial binary blend demonstrates its bread processing potential. Puffing performance in bread applications is best achieved at processing temperatures of 15% to 25% SFC, with SFC values too low resulting in an oily feel and lower sensory attribute scores. The SFC of butter should be more than 10% at 20°C -25°C, while that of bakery shortening should be more than 20% at 25°C (Aini and Miskandar, 2007). Therefore, the enzymatically interesterified binary blends of PO and ST can be used as a potential substitute for butter or bakery shortening in bread recipes.

Modelling of SFC of Enzymatic Interesterification

Modelling of a single factor (temperature or SFA). Taking temperature and SFA as independent variables and SFC as dependent variables, the SFC curves were depicted using the sigmoidal Gompertz model [Equation (2) and (3)].

$$SFC = ae^{-e^{-\left(\frac{T-c}{b}\right)}} \quad (2)$$

$$SFC = ae^{-e^{-\left(\frac{SFA-c}{b}\right)}} \quad (3)$$

The Gompertz fit curves for the enzymatically interesterified binary blends temperature ($SFC_{f(T)}$) model and the SFA content ($SFC_{f(SFA)}$) model are presented in *Figure 1*. The coefficients a, b and c were calculated for each enzymatically interesterified fat using sigma plot software. The results of the fits are shown in *Table 3*. For the $SFC_{f(T)}$ model, α values ranged between 59 and 94, b ranged between -15 and -5, and c ranged between 17 and 27. The values of α, b, and c for the $SFC_{f(SFA)}$ model ranged from 97 to 177, 12 to 22, and 45 to 74 respectively. Both models displayed high determination coefficients ($R^2 > 0.96$), where r and R^2 of the $SFC_{f(T)}$ model were both as high as 0.99. The results showed that both models adequately captured the experimental data, and that the Gompertz function could be used to simulate how temperature or SFA content would affect SFC.

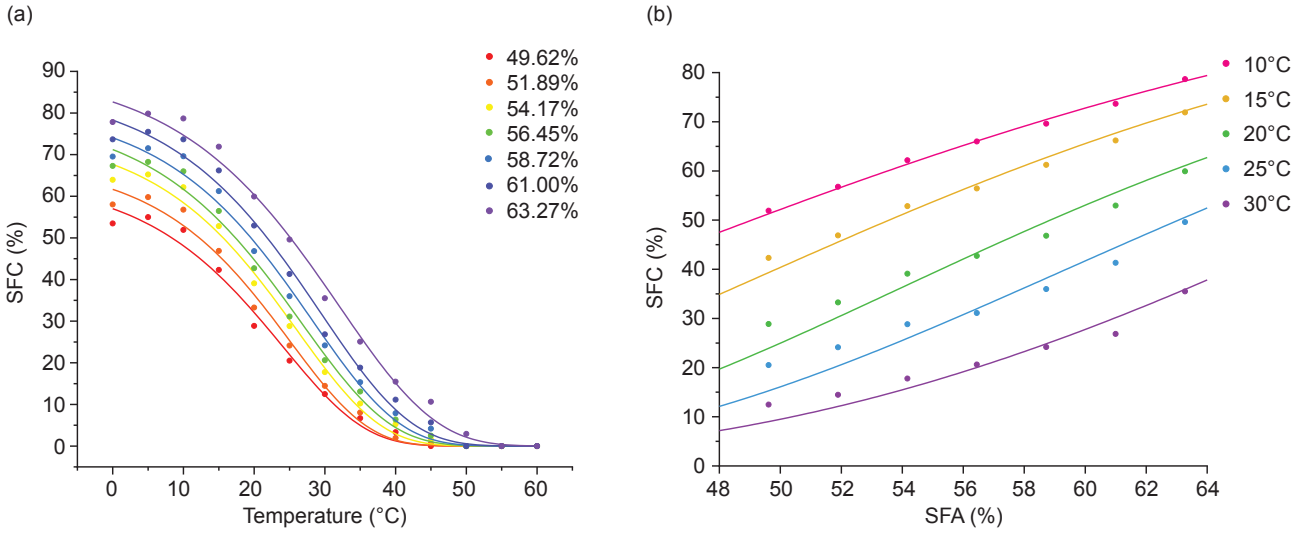


Figure 1. Gompertz fitting curves for the solid fat content (SFC) curves of interesterified binary blends as (a) a function of temperature ($SFC_{f(T)}$) and (b) saturated fatty acids (SFA)($SFC_{f(SFA)}$). The dashed dots reflect the experimental results, and the lines show the corresponding fitting results.

TABLE 2. SOLID FAT CONTENT (SFC) AND SATURATED FATTY ACID (SFA) CONTENT OF ST/PO MIXTURES BEFORE (NIE) AND AFTER (EIE) ENZYMATIC TRANSESTERIFICATION AND SFC AND SFA CONTENT OF BUTTER

Sample	SFC (%)													Fatty acid composition (%)
	0°C	5°C	10°C	15°C	20°C	25°C	30°C	35°C	40°C	45°C	50°C	55°C	60°C	SFA
0%[a]	55.0420	55.7366	45.1330	29.8808	11.3472	2.3508	0	0	0	0	0	0	0	47.34
12.5%[a]-NIE	61.6182	59.6689	48.4927	31.6786	17.4298	8.1464	0	0	0	0	0	0	0	49.62
12.5%[a]-EIE	53.4623	54.9795	51.9072	42.3090	28.8541	20.5037	12.4815	6.6877	3.3256	0	0	0	0	
25%[a]-NIE	65.0612	62.7384	54.8077	40.1981	25.9753	14.9924	3.2108	0	0	0	0	0	0	51.89
25%[a]-EIE	58.0329	59.8008	56.7847	46.8778	33.2569	24.1364	14.4646	8.0420	1.9497	0.6554	0	0	0	
37.5%[a]-NIE	67.9192	68.3934	60.6487	48.3791	34.6678	22.9779	9.4978	3.6729	0	0	0	0	0	54.17
37.5%[a]-EIE	63.9534	65.2303	62.1730	52.8297	39.0881	28.8184	17.7611	10.2172	5.2344	1.6182	0	0	0	
50%[a]-NIE	70.9692	71.3754	65.9377	55.1881	42.4448	30.1224	14.8853	7.7484	1.8758	0	0	0	0	56.45
50%[a]-EIE	67.2877	68.2418	65.9830	56.4444	42.7235	31.1107	20.6115	13.0862	6.3578	2.4988	0	0	0	
62.5%[a]-NIE	73.4672	74.6189	70.6447	61.8331	49.6828	37.8554	21.8983	13.6479	7.8638	4.3805	0.4054	0	0	58.72
62.5%[a]-EIE	69.5310	71.5462	69.6177	61.2337	46.8144	35.9789	24.1676	15.3244	7.8951	4.1770	0	0	0	
75%[a]-NIE	74.5712	77.8024	74.5557	67.9036	56.6178	44.9584	28.6208	20.4564	13.1008	8.7705	1.5369	0	0	61.00
75%[a]-EIE	73.6653	75.4786	73.6607	66.1881	52.9546	41.3178	26.8380	18.8330	11.1397	5.6702	0	0	0	
87.5%[a]-NIE	77.0707	79.9744	77.4587	72.1281	62.1258	51.3334	35.7878	27.4069	17.4293	12.8375	5.5579	0.137	0	63.27
87.5%[a]-EIE	77.8422	79.8660	78.6748	71.9053	59.9188	49.5963	35.5045	25.0776	15.4596	10.6471	2.9149	0	0	
100%[a]	80.8897	83.3384	82.1692	78.0216	69.2908	59.2899	43.7033	34.2419	24.7788	18.471	8.8189	0.5629	0	65.55
Butter	55.5229	55.5853	51.0080	42.1736	30.1547	22.7078	13.4762	8.96634	4.0529	0.9761	0	0	0	57.95

Note: [a] - ratio of ST in the binary blends.

TABLE 3. COEFFICIENTS OF THE SOLID FAT CONTENT (SFC) UNIVARIATE MODEL AND EVALUATION OF THE FITNESS OF MODELS

Model	α	b	c	r	R^2	SEE	p
$SFC_{f(T)}$							
47.34%	59.3259	-5.4818	17.2319	0.9991	0.9981	1.0753	<0.0001
49.62%	64.5227	-11.5390	24.1335	0.9957	0.9915	2.2698	<0.0001
51.89%	68.4122	-11.0720	25.0779	0.9967	0.9933	2.1944	<0.0001
54.17%	75.5154	-11.8076	26.0748	0.9971	0.9942	2.2340	<0.0001
56.45%	80.0798	-12.4763	26.7522	0.9968	0.9936	2.4483	0.0033
58.72%	81.9388	-12.3317	28.2465	0.9965	0.9930	2.6843	0.0033
61.00%	86.2383	-12.6469	29.5222	0.9965	0.9930	2.8328	0.0113
63.27%	90.6925	-13.5145	32.1371	0.9968	0.9936	2.8130	0.0464
65.55%	93.3588	-14.4349	36.0946	0.9957	0.9915	3.2774	0.2524
$SFC_{f(SFA)}$							
10°C	110.5578	17.0671	45.1177	0.9985	0.9971	0.7744	0.9129
15°C	104.1395	13.9546	49.2469	0.9915	0.9832	2.2676	0.2852
20°C	97.6734	12.4474	53.8619	0.9768	0.9541	4.2866	0.1863
25°C	107.0722	14.3258	59.1611	0.9664	0.9340	4.9609	0.0301
30°C	176.8545	21.8828	73.4819	0.9701	0.9410	3.6193	0.0361

Modelling of two factors (temperature and SFA together). The two models mentioned above can be used to forecast the SFC value of enzymatically interesterified fat at a prescriptive temperature or SFA content, but they are unable to explain the shared impact of these two variables on SFC. Consequently, to account for the combined influence of temperature and saturated fatty acid content on SFC, a bivariate Gompertz model was built. The coefficient of the univariate Gompertz model was expressed as the function of another variable to include both temperature and SFA in the model. In this way, the bivariate model was obtained by substituting the coefficients with the corresponding function. Based on this, Farmani (2015) developed a bivariate Gompertz model using temperature and SFA as variables. This model was used to predict the SFC of chemically interesterified blended oil with a correlation coefficient of 0.98 and an MAE of 1.02%. The fitting results (*Figure 2* and *Table 4*) were determined by evaluating the correlations (the coefficients of $SFC_{f(SFA)}$ Gompertz models and temperature, the coefficients of the $SFC_{f(T)}$ Gompertz models and SFA content). As can be observed from the results, there was a higher linear correlation between the coefficients α and c of $SFC_{f(T)}$ Gompertz models and SFA content, with $R^2 > 0.95$, indicating that the temperature model coefficient α and c can be accurately expressed by SFA. Therefore, it was preferable to replace the coefficients α and c of Equation (2) with the mathematical expressions [Equation (4) and (5)].

$$\alpha_{(T)} = \beta_1 + \beta_2 \times SFA \tag{4}$$

$$c_{(T)} = \beta'_1 + \beta'_2 \times SFA \tag{5}$$

Then, the final SFC model that was expressed as a function of two variables, temperature and SFA, was attained:

$$SFC = (\beta_1 + \beta_2 \times SFA)\, e^{-e^{-\left(\frac{T - (\beta'_1 + \beta'_2 \times SFA)}{b}\right)}} \tag{6}$$

The coefficients of the final model were calculated by Sigmaplot (*Figure 3*).

$$SFC = (-3.8915 + 1.4657 \times SFA) e^{-e^{-\left(\frac{T-(-8.7518+0.632\times SFA)}{-12.4418}\right)}} \tag{7}$$

$$R^2 = 0.9908$$

This result indicated that the model could accurately predict the SFC curves of ST and PO enzymatically interesterified lipids. This model can be used to calculate the formulations of plant-based margarine.

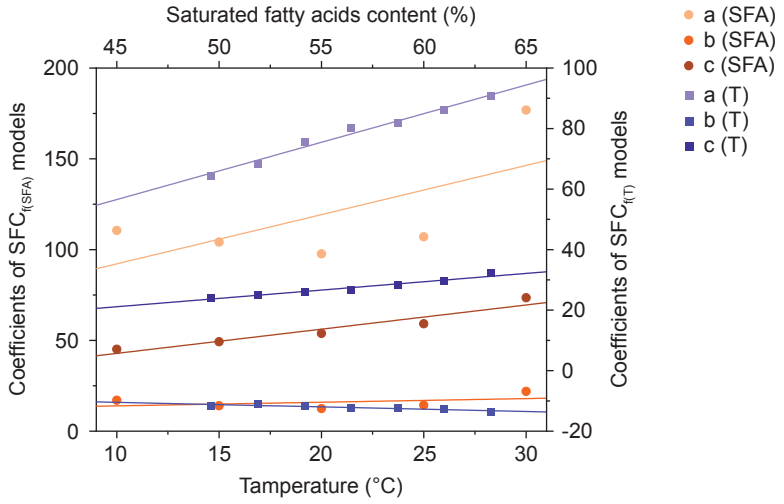


Figure 2. Correlation between each coefficient of solid fat content (SFC) univariate model and another factor. Markers are the experimental values; solid lines show linear regressions.

TABLE 4. EVALUATION OF FITNESS BETWEEN COEFFICIENTS OF SOLID FAT CONTENT $(SFC)_{F(T)}$ MODELS AND SATURATED FATTY ACIDS (SFA) CONTENT AND BETWEEN COEFFICIENTS OF $SFC_{F(SFA)}$ MODELS AND TEMPERATURE

Item	Function	R^2
f [a (SFA), T]	y = 65.0490 + 2.7105x	0.4336
f [b (SFA), T]	y = 11.9345 + 0.2001x	0.1808
f [c (SFA), T]	y = 29.5169 + 1.3329x	0.9175
f [a (T), SFA]	y = -28.5925 + 1.8920x	0.9831
f [b (T), SFA]	y = -3.6960 - 0.1506x	0.8474
f [c (T), SFA]	y = -3.6391 + 0.5503x	0.9571

The SFC of butter at 25°C was 22.7078% (*Table 2*), and this value was used as the objective. T = 25, and SFC = 22.7078 were substituted into Equation (7), in order to determine the SFA content of plant-based margarine which was 50.4698. Therefore, the final formulation of margarine was 83% PO + 17% ST (w/w), whose SFA was equal to the calculated result. The above formulation was used to make the plant-based margarine sample, and as a verification, the SFC was measured and compared to commercial butter. The results are displayed in *Figure 4*. It can be seen that the 83% PO+17% ST enzymatically interesterified binary blend fitted by this Gompertz model can simulate the SFC curve of commercial butter excellently. At 20°C, the SFC values of both fats and oils were greater than 10%, demonstrating that they could retain a suitable consistency without oil precipitation. Additionally, both fats and oils had SFC values at 40°C that were less than 10%, indicating that they would completely melt in the mouth and not provide a particle sensation. Thus, plant-based margarine has a wide plasticity range similar to butter and an ideal SFC profile for use in bread.

It was evident that the SFC of the interesterified blends can be accurately predicted by the Gompertz model. This method proved to be more beneficial than modelling and optimising reaction conditions based on the response surface method. It helps to

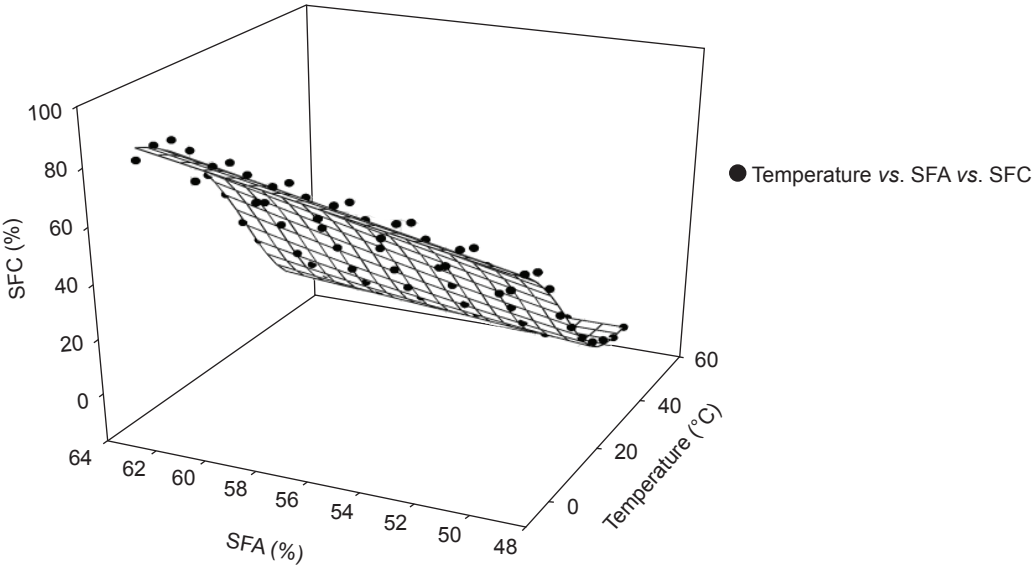


Figure 3. The model of solid fat content (SFC) as a function of temperature and saturated fatty acids (SFA).

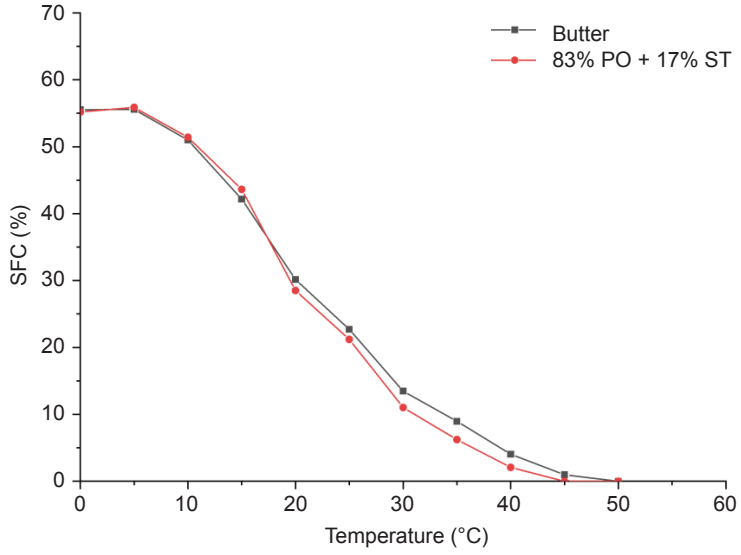


Figure 4. Solid fat content (SFC) of commercial butter and enzymatically interesterified blend.

preselect suitable plant oil raw materials to reproduce the SFC curves that were aimed at replacing animal fat and can effectively reduce the cost and time of new product development.

Application of Plant-based Margarine

In the baking field, fats are often used for shortening, and they can also soften gluten, prevent moisture loss, boost lustre and slow bread ageing, so they are also often used in bread making to improve the quality of bread (Patil *et al.*, 2019). Compared with liquid vegetable oil, adding solid oil can enhance the extensibility and plasticity of the dough hence making the bread more delicate, soft and delicious. Shortening (refined animal fats or hydrogenated vegetable oils and their mixtures) and butter are common fats used in traditional baking. Therefore, in this study we compared bread made from typical animal fats (butter and beef tallow) together with plant-based margarine. As shown in *Figure 5*, the bread with plant-based enzymatically interesterified fat shows a similar appearance to traditional breads with animal fats. All of the loaves also exhibit good shape and fermentation structure. *Table 5* lists the fundamental characteristics of bread, including specific volume, baking loss, and texture properties. The bread prepared from beef tallow was relatively the softest 519.53 g and had the highest specific volume (2.66 mL g^{-1}). It is possible that the higher SFC and SFA content of beef tallow further increased the internal network strength of the bread, which may have improved the bread's ability to hold gas. As a result, the bread may have displayed the lowest hardness and the highest specific volume (Meng *et al.*, 2019), though its elasticity and gumminess were somewhat diminished. Furthermore, bread made with plant-based margarine did not differ significantly from those made with butter and beef tallow in baking loss and texture properties.

The sensory evaluation results of different bread are shown in *Table 6*. Plant-based margarine bread had no significant differences in shape, smell, or texture when compared to butter and beef tallow, but they do differ significantly in terms of colour and flavour. Contrary to traditional concept, the bread with plant-based margarine received a higher rating. In general, butter and beef tallow can give bread a creamy flavour and alluring taste. Nevertheless, they failed to manifest a discernible advantage when subjected to meticulous sensory evaluation. In contrast, bread made with plant-based margarine has gained the favour of many tasters, perhaps due to the bland taste of palm oil, which accentuates the natural wheat flavour of the bread. This proved the feasibility of using plant-based margarine instead of animal fat in bread.

CONCLUSION

In summary, in this work, the SFC curve of plant-based margarine was modelled and fitted by the Gompertz equation model to reproduce the SFC variations of commercial butter and obtain the optimum margarine formula. The results demonstrated that the bread with this formula, 83% PO + 17% ST, had similar structural characteristics and sensory evaluation to butter or beef tallow bread.

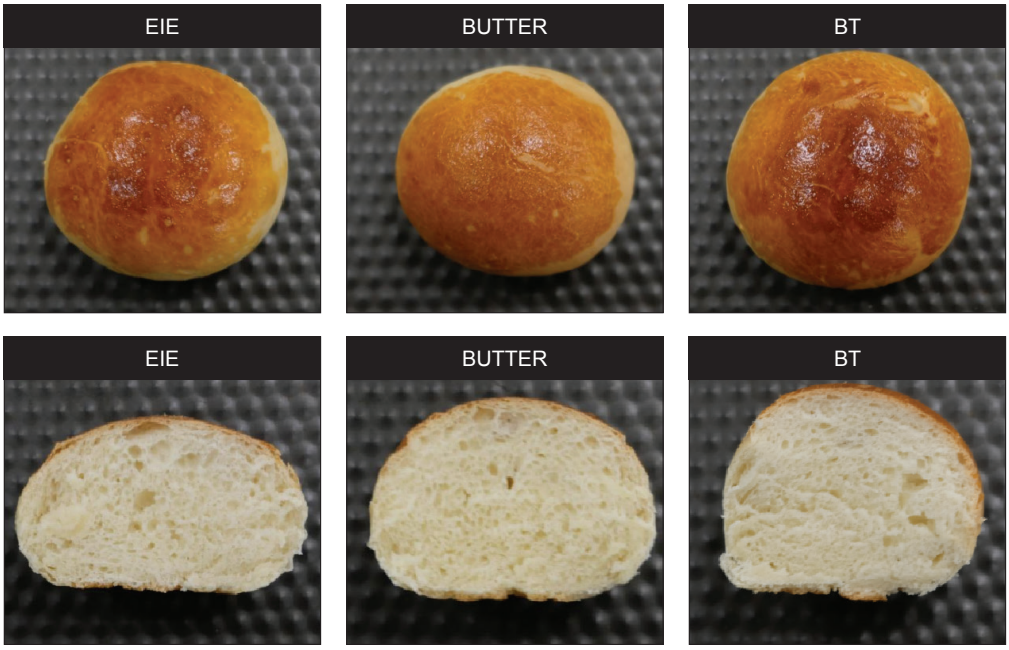


Figure 5. Upper surface crust appearance and breadcrumb structure of breads made with different fats.

TABLE 5. CHARACTERISTICS OF BREADS MADE BY DIFFERENT FAT

Item	EIE	Butter	BT
Baking loss	0.069 ± 0.0045[a]	0.078 ± 0.0040[a]	0.076 ± 0.0033[a]
Specific volume (mL g^{-1})	2.17 ± 0.030[a]	2.34 ± 0.047[b]	2.66 ± 0.078[c]
Hardness (g)	672.22 ± 169.82[a]	692.77 ± 173.05[a]	519.53 ± 45.33[a]
Adhesiveness (g)	-3.88 ± 3.44[a]	-1.16 ± 0.28[a]	-4.43 ± 1.75[a]
Springiness (g)	0.84 ± 0.027[a]	0.84 ± 0.037[a]	0.88 ± 0.0086[a]
Cohesiveness (g)	0.67 ± 0.037[a]	0.73 ± 0.079[a]	0.72 ± 0.024[a]
Gumminess (g)	443.65 ± 89.93[a]	496.72 ± 79.86[a]	376.11 ± 34.43[a]
Chewiness (g)	369.52 ± 66.73[a]	418.34 ± 73.90[a]	330.46 ± 30.55[a]

TABLE 6. EFFECT OF FAT TYPE ON THE SENSORY ANALYSIS OF BREADS

Item	EIE	Butter	BT
Shape	4.40 ± 0.50[a]	4.35 ± 0.49[a]	4.28 ± 0.75[a]
Colour	4.45 ± 0.69[a]	3.80 ± 0.62[b]	4.08 ± 0.57[ab]
Smell	3.68 ± 0.77[ab]	3.80 ± 0.83[a]	3.23 ± 0.73[b]
Taste	4.45 ± 0.60[a]	4.03 ± 0.90[ab]	3.85 ± 0.93[b]
Texture	3.98 ± 0.73[a]	3.70 ± 0.66[a]	3.75 ± 0.79[a]

These findings could offer a fresh approach for predicting the formula of plant-based margarine, recreate the application scenarios of target fats, drastically reducing the cost and time of product development, and significantly improve the efficiency of product development.

ACKNOWLEDGEMENT

This work was carried out under the laboratory support of the School of Food Science and Technology, Jiangnan University.

REFERENCES

Aini, I N and Miskandar, M S (2007). Utilization of palm oil and palm products in shortenings and margarines. *Eur. J. Lipid Sci. Technol.*, *109(4)*: 422-432. DOI: 10.1002/ejlt.200600232.

Alan, D F; Naeli, M H; Naderi, M; Jafari, S M and Tavakoli, H R (2019). Production of *trans*-free fats by chemical interesterified blends of palm stearin and sunflower oil. *Food Sci. Nutr.*, *7(11)*: 3722-3730. DOI: 10.1002/fsn3.1231.

Augusto, P E D; Soares, B M C; Chiu, M C and Goncalves, L A G (2012). Modelling the effect of temperature on the lipid solid fat content (SFC). *Food Res. Int.*, *45(1)*: 132-135. DOI: 10.1016/j.foodres.2011.10.026.

Collier, E S; Normann, A; Harris, K L; Oberrauter, L M and Bergman, P (2022). Making more sustainable food choices one meal at a time: Psychological and practical aspects of meat reduction and substitution. *Foods*, *11(9)*: 21. DOI: 10.3390/foods11091182.

Doan, C D; Tavernier, I; Danthine, S; Rimaux, T and Dewettinck, K (2018). Physical compatibility between wax esters and triglycerides in hybrid shortenings and margarines prepared in rice bran oil. *J. Sci. Food Agric.*, *98(3)*: 1042-1051. DOI: 10.1002/jsfa.8553.

Dollah, S; Abdulkarim, S M; Ahmad, S H; Khoramnia, A and Ghazali, H M (2016). Physico-chemical properties of *Moringa oleifera* seed oil enzymatically interesterified with palm stearin and palm kernel oil and its potential application in food. *J. Sci. Food Agric.*, *96(10)*: 3321-3333. DOI: 10.1002/jsfa.7510.

Dos Santos, M T; Gerbaud, V and Le Roux, G A C (2013). Modeling and simulation of melting curves and chemical interesterification of binary blends of vegetable oils. *Chem. Eng. Sci.*, *87*: 14-22. DOI: 10.1016/j.ces.2012.09.026.

Dos Santos, M T; Gerbaud, V and Le Roux, G A C (2014). Solid fat content of vegetable oils and simulation of interesterification reaction: Predictions from thermodynamic approach. *J. Food Eng.*, *126*: 198-205. DOI: 10.1016/j.jfoodeng.2013.11.012.

Engelen, L and Van Der Bilt, A (2008). Oral physiology and texture perception of semisolids. *J. Texture Stud.*, *39(1)*: 83-113. DOI: 10.1111/j.1745-4603.2007.00132.x.

Farmani, J (2015). Modeling of solid fat content of chemically interesterified fully hydrogenated soybean oil and canola oil blends as a function of temperature and saturated fatty acids. *J. Food Meas. Charact.*, *9(3)*: 281-289. DOI: 10.1007/s11694-015-9233-8.

Haupler, M; Peyronel, F; Neeson, I; Weiss, J and Marangoni, A G (2014). *In situ* ultrasonic characterization of cocoa butter using a chirp. *Food Bioproc. Technol.*, *7(11)*: 3186-3196. DOI: 10.1007/s11947-014-1273-2.

Li, S Y; Zhu, L; Wu, G C; Jin, Q Z; Wang, X G and Zhang, H (2022). Relationship between the microstructure and physical properties of emulsifier based oleogels and cookies quality. *Food Chem.*, *377*: 10. DOI: 10.1016/j.foodchem.2021.131966.

Li, Y; Zhao, J L; Xie, X D; Zhang, Z; Zhang, N and Wang, Y (2018). A low *trans* margarine fat analog to beef tallow for healthier formulations: Optimization of enzymatic interesterification using soybean oil and fully hydrogenated palm oil. *Food Chem.*, *255*: 405-413. DOI: 10.1016/j.foodchem.2018.02.086.

Meng, Z; Guo, Y; Wang, Y and Liu, Y F (2019). Oleogels from sodium stearoyl lactylate-based lamellar crystals: Structural characterization and bread application. *Food Chem.*, *292*: 134-142. DOI: 10.1016/j.foodchem.2018.11.042.

Naeli, M H; Farmani, J and Zargaraan, A (2018). Prediction of solid fat content curve of chemically interesterified blends of palm stearin and soyabean oil. *J. Oil Palm Res.*, *30(4)*: 579-590. DOI: 10.21894/jopr.2018.0053.

Nelis, V; De Neve, L; Danthine, S; Dewettinck, K; Martins, J C and van der Meeren, P (2021). Oil diffusion in fat crystal matrices: Characterization by NMR relaxometry and diffusometry. *Eur. J. Lipid Sci. Technol.*, *123(4)*: 10. DOI: 10.1002/ejlt.202000237.

Pang, M; Ge, Y F; Cao, L L; Cheng, J S and Jiang, S T (2019). Physicochemical properties, crystallization behavior and oxidative stabilities of enzymatic interesterified fats of beef tallow, palm stearin and camellia oil blends. *J. Oleo Sci.*, *68(2)*: 131-139. DOI: 10.5650/jos.ess18201.

Patel, A R; Nicholson, R A and Marangoni, A G (2020). Applications of fat mimetics for the replacement of saturated and hydrogenated fat in food products. *Curr. Opin. Food Sci.*, *33*: 61-68. DOI: 10.1016/j.cofs.2019.12.008.

Patil, S; Sonawane, S K and Arya, S S (2019). A fuzzy mathematical approach for selection of surface coating and its effect on staling kinetics in a formulated gluten-free flatbread. *Food Bioproc. Technol.*, *12(11)*: 1955-1965. DOI: 10.1007/s11947-019-02348-1.

Pimentel, D and Pimentel, M (2003). Sustainability of meat-based and plant-based diets and the environment. *Am. J. Clin. Nutr.*, *78(3)*: 660S-663S.

Rabeler, F and Feyissa, A H (2018). Kinetic modeling of texture and color changes during thermal treatment of chicken breast meat. *Food Bioproc. Technol.*, *11(8)*: 1495-1504. DOI: 10.1007/s11947-018-2123-4.

Reiner, J; Peyronel, F; Weiss, J and Marangoni, A G (2018). Monitoring the polymorphic transformation of a palm kernel-based emulsion using ultrasound. *Food Bioproc. Technol.*, *11(4)*: 797-808. DOI: 10.1007/s11947-018-2056-y.

Sabate, J and Soret, S (2014). Sustainability of plant-based diets: Back to the future. *Am. J. Clin. Nutr.*, *100(1)*: 476S-482S. DOI: 10.3945/ajcn.113.071522.

Saberi, A H; Lai, O M and Miskandar, M S (2012). Melting and solidification properties of palm-based diacylglycerol, palm kernel olein, and sunflower oil in the preparation of palm-based diacylglycerol-enriched soft tub margarine. *Food Bioproc. Technol.*, *5(5)*: 1674-1685. DOI: 10.1007/s11947-010-0475-5.

Saghafi, Z; Naeli, M H; Tabibiazar, M and Zargaraan, A (2019). Modeling the rheological behavior of chemically interesterified blends of palm stearin/canola oil as a function of physicochemical properties. *J. Am. Oil Chem. Soc.*, *96(11)*: 1219-1234. DOI: 10.1002/aocs.12272.

Schmid, T; Baumer, B; Ruegg, R; Naf, P; Kinner, M and Muller, N (2020). Evaluation of innovative technological approaches to replace palm fat with physically modified Swiss rapeseed oil in bakery products. *Int. J. Food Sci. Technol., 55(8)*: 2990-2999. DOI: 10.1111/ijfs.14564.

Silva, T J; Barrera-Arellano, D and Ribeiro, A P B (2021). Margarines: Historical approach, technological aspects, nutritional profile, and global trends. *Food Res. Int.*, *147*: 12. DOI: 10.1016/j.foodres.2021.110486.

Sivakanthan, S; Jayasooriya, A P and Madhujith, T (2019). Optimization of the production of structured lipid by enzymatic interesterification from coconut (*Cocos nucifera*) oil and sesame (*Sesamum indicum*) oil using Response Surface Methodology. *LWT-Food Sci. Technol.*, *101*: 723-730. DOI: 10.1016/j.lwt.2018.11.085.

Soares, F; da Silva, R C; Hazzan, M; Capacla, I R; Viccola, E R; Maruyama, J M and Gioielli, L A (2012). Chemical Interesterification of blends of palm stearin, coconut oil, and canola oil: Physicochemical properties. *J. Agric. Food Chem.*, *60(6)*: 1461-1469. DOI: 10.1021/jf204111t.

Wawrzyniak, J (2021). Model of fungal development in stored barley ecosystems as a prognostic auxiliary tool for postharvest preservation systems. *Food Bioproc. Technol.*, *14(2)*: 298-309. DOI: 10.1007/s11947-020-02575-x.

Ye, Z; Li, R Z; Cao, C; Xu, Y J; Cao, P R; Li, Q and Liu, Y F (2019). Fatty acid profiles of typical dietary lipids after gastrointestinal digestion and absorbtion: A combination study between *in-vitro* and *in-vivo*. *Food Chem.*, *280*: 34-44. DOI: 10.1016/j.foodchem.2018.12.032.

Zhang, H; Pedersen, L S; Kristensen, D; Adler-Nissen, J and Holm, H C (2004). Modification of margarine fats by enzymatic interesterification: Evaluation of a solid-fat-content-based exponential model with two groups of oil blends. *J. Am. Oil Chem. Soc.*, *81(7)*: 653-658. DOI: 10.1007/s11746-004-957-9.

Zhang, X; Li, L; Xie, H; Liang, Z L; Su, J Y, Liu; G Q and Li, B (2014). Effect of temperature on the crystalline form and fat crystal network of two model palm oil-based shortenings during storage. *Food Bioproc. Technol.*, *7(3)*: 887-900. DOI: 10.1007/s11947-013-1078-8.

Zhang, Z; Lee, W J; Zhou, H Y and Wang, Y (2019). Effects of chemical interesterification on the triacylglycerols, solid fat contents and crystallization kinetics of palm oil-based fats. *Food Funct.*, *10(11)*: 7553-7564. DOI: 10.1039/c9fo01648a.

Zhou, X R; Yeomans, M; Thomas, A; Wilde, P; Linter, B and Methven, L (2021). Individual differences in oral tactile sensitivity and gustatory fatty acid sensitivity and their relationship with fungiform papillae density, mouth behaviour and texture perception of a food model varying in fat. *Food. Qual. Prefer.*, *90*: 11. DOI: 10.1016/j.foodqual.2020.104116.

Zhu, T W; Zhang, X; Zong, M H; Linhardt, R J; Wu, H and Li, B (2020). Storage stability studies on interesterified blend-based fast-frozen special fats for oxidative stability, crystallization characteristics and physical properties. *Food Chem.*, *306*: 8. DOI: 10.1016/j.foodchem.2019.125563.

JOURNAL OF OIL PALM RESEARCH

GUIDE FOR AUTHORS

(for more details, kindly visit http://jopr.mpob.gov.my)

Type of Articles

1. **Regular Article**
   Full-length original empirical investigations, consisting of introduction, materials and methods, results and discussion, conclusions. Original work must provide references and an explanation on research findings that contain new and significant findings. Conclusion should be brief and focus on the research output, should not be in point form. These papers should not exceed 6000 words of text (including tables, figures and references) and generally not more than a total of 10 figures and tables. After peer-review, the article word count limit can be extended to a maximum of 8000 words to better address the reviewers' and editors' comments. Any additional figures or tables can be included in the supplementary data. Please note that papers submitted to JOPR will be sent back to authors because of poor figure resolution or exceeding the number of figures permitted.

2. **Short Communication**
   Significant new information to readers of the Journal in a short but complete form. Preferably not exceeding 3000 words (including tables, figures and references), and is intended for rapid publication. They are not intended for publishing preliminary results or to be a reduced version of regular article.

3. **Review Article**
   Critical evaluation of materials about current research that have already been published by organising, integrating, and evaluating previously published materials. Re-analyses as meta-analysis and systemic reviews are encouraged. Review articles provide systemic overview, evaluation and interpretation of research in a given field. They should not exceed 12 000 words (excluding references only) and should contain no more than a total of 20 figures and tables. Any additional figures or tables can be included in the supplementary data. Please note that papers submitted to JOPR will be sent back to authors because of poor figure resolution or exceeding the number of figures permitted. The same information should not be repeated in a figure and a table.

Language

Please write your text in good English (only British English is accepted). We do not accept American English or a mixture of these.

JOPR's Template

JOPR's template, which is a standard format that facilitates the manuscript writing and copyediting process. This template is created to provide a detail and clear house style of JOPR. The template is drafted according to JOPR's house style, but in standard word version format. When writing a paper, authors need to format their papers to fit into the journal's house style. To make this easier, Word templates are available for many of other established journals, ready for them to download and apply to their research paper format. It is crucial for author to write a research paper while considering formatting. Each journal has its own guidelines for formatting; hence, the template defines how an article will look when it is published online or in print.

JOPR's Aims & Scope

This is established to provide a detail and clear aims and scope for author reference. Authors should declare in the cover letter how the research fits the aims and scope of JOPR.

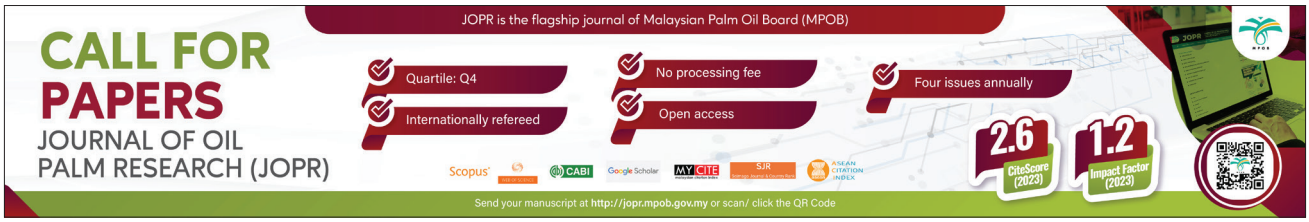
JOPR's House Style

A detail listing of JOPR's house style for authors and a checklist to facilitate the copyediting process and standardise the copyediting process. The JOPR's house style remains the same and is drafted into a detail version for author's reference.

Manuscript Submission

- Manuscripts should be submitted via: https://www2.cloud.editorialmanager.com/jopres/
- JOPR does not permit dual submission, publication and/or any archive platform (preprint) in violation of journal ethical practices.

For more details and to download the JOPR's House Style and Template, kindly surf http://jopr.mpob.gov.my



Contents of the Coming Issue
Journal of Oil Palm Research
Vol. 37 (1) March 2025*

- A Picture of Ripeness: Investigating Image-based Techniques for Oil Palm Fruit Grading
  Munirah Rosbi; Zaid Omar and Marsyita Hanafi

- Lignocellulosic Biomass-derived Biogas: A Review on Sustainable Energy in Malaysia
  Izzah Farhana Ab Aziz; Hasfalina Che Man; Ali Demirci; Muhammad Hazwan Hamzah; Rozita Omar; Nur Syakina Jamali; Kamil Kayode Katibi and Abdulsalam Mohammed

- Application of Seaweed Extracts in Oil Palm (*Elaeis guineensis*) Seedlings Subjected to Water Deficit: Physiological, Biochemical and Enzymatic Responses
  Muhammad Danial Mokhtaruddin; Nur Aifaa Abd Razak; Aisamuddin Ardi Zainal Abidin; Nor Izzati Husna Noorhisham; Nur Asna Faiqah Johari and Zetty Norhana Balia Yusof

- Species Composition of Birds in Oil Palm Areas, Northern Sarawak, Borneo, Malaysia
  Bettycopa Amit; Angie Sapis and Nik Sasha Khatrina Khairuddin

- Analysis of the Energy Consumption of Motorised Circular Saw When Cutting Oil Palm Frond
  Sun Qun and Zaidi Mohd Ripin

- Sediment Formation in a Palm Oil Biodiesel Blend in a Ship Fuel Tank
  Jajang Amir Hidayat; Bambang Sugiarto; Yulianto Sulistyo Nugroho; Ahmad Syihan Auzani; Hari Setiapraja and Siti Yubaidah

- Inverse Vulcanised Polysulphide Adsorbent from Waste Cooking Palm Oil for Cu^{2+} Removal
  Mohd Faizal Ali; Nancy Nubur Libat; Hannah Nisa Adawiyah; Abdullah Nayeem and Jun Haslinda Shariffuddin

Note: * Subject to change.